VYSOKÉ UČENÍ TECHNICKÉ V BRNĚ
FAKULTA CHEMICKÁ

NANOSTRUKTURNÍ SYSTÉMY V HYDRATOVANÝCH ALUMINOSILIKÁTOVÝCH MATERIÁLECH

Habilitační práce v oboru Chemie, technologie a vlastnosti materiálů

Ing. Eva Bartoníčková, Ph.D.

BRNO 2025

Abstrakt

Habilitační práce se zaměřuje na studium nanostrukturních hydratačních fází v anorganických pojivech na bázi aluminosilikátů, zejména systémů C-S-H, C-A-S-H a C-A-H. Tyto fáze představují klíčové produkty hydratace hydraulických pojiv a zásadně ovlivňují mikrostrukturu, mechanické vlastnosti a trvanlivost stavebních materiálů. Práce shrnuje poznatky získané analýzou hydratačních produktů vznikajících jak v přirozeném prostředí hydratace portlandských a kalcium aluminátových cementů, tak v řízených podmínkách laboratorní syntézy. Pomocí kombinace pokročilých analytických metod a modelových přístupů byly sledovány rozdíly v morfologii, chemickém složení, polymerizačním stupni Si–O–Si vazby a strukturním uspořádání vznikajících gelů. Zvláštní pozornost je věnována koloidní povaze C-S-H gelu, jeho fraktální struktuře a vlivu substituce prvků (např. Al, Fe, Cu, Li, S) na jeho vlastnosti. Práce rovněž diskutuje vliv různých syntetických metod (mechanochemická, hydrotermální, sol-gel, precipitační) na strukturu a reaktivitu připravených analogů. V kontextu současného trendu snižování emisí CO_2 ve stavebnictví, zejména prostřednictvím redukce obsahu portlandského slínku ve směsných cementech, dochází ke změnám ve složení hydratačních fází. Tyto změny se projevují zejména při použití příměsí s pucolánovými vlastnostmi nebo latentní hydraulicitou, jako jsou vysokopecní struska, popílky či metakaolin. Přítomnost těchto složek vede ke vzniku modifikovaných gelů typu (N, K)-C-(A, Fe)-S-H, schopných inkorporovat nebo substituovat doprovodné prvky, čímž dochází k jejich imobilizaci. Získané poznatky mají význam nejen pro vývoj nízkouhlíkových cementů, ale i pro cílené aplikace v oblasti žárovzdorných materiálů, jaderné infrastruktury či technologií pro úpravu odpadních vod.

Abstract

This habilitation thesis focuses on the study of nanostructured hydration phases in aluminosilicate-based inorganic binders, particularly the systems C-S-H, C-A-S-H, and C-A-H. These phases represent key products of hydraulic binder hydration and significantly influence the microstructure, mechanical properties, and durability of construction materials. The thesis summarizes findings obtained from the analysis of hydration products formed under both natural hydration conditions of Portland and calcium aluminate cements, as well as under controlled laboratory synthesis. Using a combination of advanced analytical techniques and model-based approaches, differences in morphology, chemical composition, degree of Si–O–Si polymerization, and structural arrangement of the resulting gels were investigated. Special attention is given to the colloidal nature of C-S-H gel, its fractal structure, and the impact of elemental substitution (e.g., Al, Fe, Cu, Li, S) on its properties. The work also discusses the influence of various synthesis methods (mechanochemical, hydrothermal, sol–gel, precipitation) on the structure and reactivity of prepared analogues. In the context of the current trend toward reducing CO_2 emissions in construction, particularly through the partial replacement of Portland clinker in blended cements, significant changes in the composition of hydration phases are observed. These changes are especially pronounced when using supplementary cementitious materials with pozzolanic or latent hydraulic activity, such as blast furnace slag, fly ash, or metakaolin. Their presence leads to the formation of modified gels of the (N, K)-C-(A, Fe)-S-H type, capable of incorporating or substituting accompanying elements, thereby achieving their immobilization. The insights gained are relevant not only for the development of low-carbon cements but also for targeted applications in refractory materials, nuclear infrastructure, and wastewater treatment technologies.

Klíčová slova:

Hydratace cementu; C-(A)-(S)-H gel; Sol-gel syntéza; Koloidní model; Spektroskopie; Nízkouhlíkové cementy; žárovzdorné kompozity

Key words:

Hydration of cement; C-(A)-(S)-H gel; Sol-gel synthesis; Colloidal model; Spectroscopy, Low-carbon cements; Refractory composites

Obsah

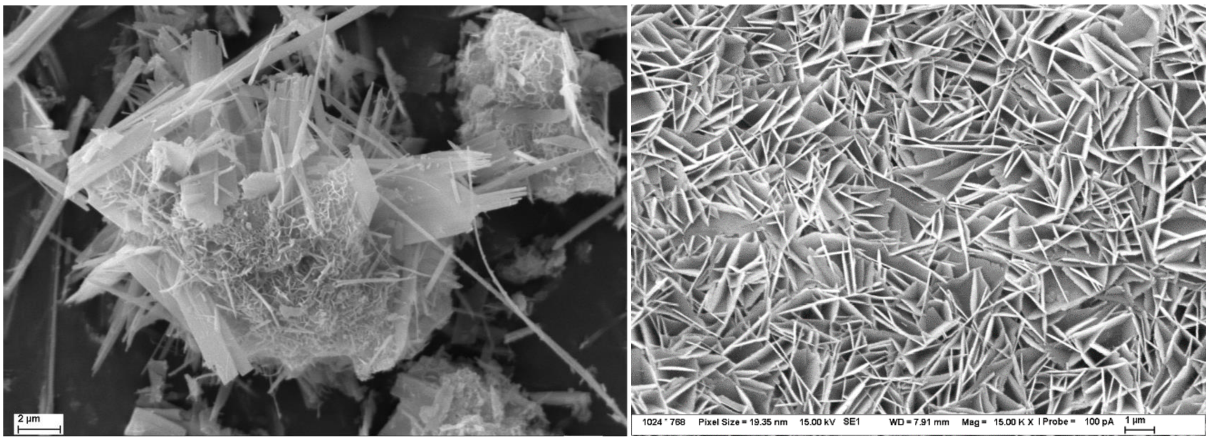

„Chlupatá krása“ - Morfologie syntetického krystalického tobermoritu zachycená pomocí SEM: Levý snímek ukazuje směs jehlicovitých, deskovitých a tabulárních krystalů, přičemž některé jehlice vyrůstají radiálně ze společného centra, což implikuje sférolitický růst. Pravý snímek dokumentuje hustou síť lamelárních krystalů s převážně paralelní orientací. Tato morfologická variabilita odráží rozdílné nebo měnící se podmínky syntézy krystalických C-S-H analogů – zatímco jehlicovité krystaly vznikají růstem z roztoku, lamelární a tabulární formy se tvoří topochemicky na povrchu pevných fází.

Poděkování

Mé poděkování patří všem kolegům, kteří se na letitém výzkumu podíleli – ať již odbornou spoluprací, kritickou diskusí či technickou podporou. Zvláštní uznání patří mentorům prof. Brandštetrovi, prof. Ptáčkovi a prof. Cihlářovi, kteří formovali mé vědecké uvažování, a také pracovním kolektivům, s nimiž jsem měla tu čest spolupracovat na různých mezioborových projektech i pracovištích. Důležitou součástí výzkumu byla a je spolupráce se studenty, kteří se podíleli na značné části prezentovaných výsledků. Významným faktorem pro uskutečnění bylo pracovní zázemí a dostupná infrastruktura, které mi umožnily přístup k moderním analytickým metodám (zejména různým typům spektroskopií – XPS, FT-IR a Ramanovy), díky nim bylo možné realizovat komplexní charakterizaci studovaných C-(A)-(S)-H systémů. V neposlední řadě děkuji své rodině za podporu a trpělivost, bez nichž by vznik této práce nebyl možný.

1. Úvod

V posledních desetiletích lze pozorovat zásadní posun v přístupu k návrhu a studiu anorganických materiálů, který je úzce spjat s rostoucím porozuměním jejich chování na nanoúrovni. Aluminosilikátové systémy představují významnou třídu materiálů s širokým spektrem využití – od tradičních pojiv až po pokročilé kompozity a nanostrukturované materiály. Klíčovým aspektem těchto systémů je jejich koloidní chování, které zásadně ovlivňuje výslednou mikrostrukturu i makroskopické vlastnosti připravených materiálů. Povrchové interakce a elektrostatické vlastnosti částic ve vodném prostředí hrají rozhodující roli při stabilizaci disperzí a při průběhu reakcí během syntézy a procesu hydratace a vytvrzování (tj. tuhnutí a tvrdnutí). Procesy probíhající na rozhraní pevné a kapalné fáze jsou rozhodující pro pochopení hydratačních mechanismů i pro predikci chování výsledného kompozitního systému, tj. betonu.

Interdisciplinární charakter výzkumu, propojující materiálové inženýrství, fyzikální chemii a analytický přístup, je nezbytný pro detailní popis mechanismů hydratačních reakcí na molekulové úrovni. Výzkum v oblasti aluminosilikátových systémů se pro mě stal více než jen profesní cestou – stal se výzvou k porozumění složitým interakcím na fázovém rozhraní, které významně ovlivňují makroskopické vlastnosti materiálů. Možnost pronikat do hloubky struktur hydratačních produktů, zkoumat dynamiku reakcí v čase, představuje praktickou výzvu s dopadem i na možné průmyslové aplikace a inovace v oblasti materiálového inženýrství. V průběhu posledních let jsem měla možnost sledovat, jak se pokroky v oblasti nanomateriálů promítají do studia anorganických pojiv a současně i vývoje pokročilých kompozitních systémů.

Předmětem této habilitační práce a současně i jejím největším přínosem je analýza a popis komplexních koloidních interakcí na povrchu různých aluminosilikátových matric během jejich hydratace. Cílem je systematicky zmapovat a interpretovat jevy spojené s povrchovým chováním částic v aluminosilikátových systémech, se zvláštním důrazem na popis nanostrukturních C-S-H, C-A-S-H a C-A-H hydratačních produktů, které byly analyzovány v přirozených procesech či v řízených experimentech. Výsledná práce je souhrnem komentovaných výsledků uveřejněných ve vědeckých publikacích autorky, které jsou uvedeny v seznamu komentovaných publikací a doloženy přílohou. Poznatky prezentované v jednotlivých kapitolách vycházejí jak z již publikovaných výsledků a experimentálního výzkumu, tak z analýzy dostupné literatury a slouží jako východisko pro další směřování v oblasti vývoje funkcionalizovaných anorganických systémů. Úvodní kapitola věnující se popisu C-S-H struktur je teoretickým základem pro kapitoly následující a je proto šířeji rozpracována z teoretického pohledu a následně doplněna komentovanými výsledky autorky z oblasti syntézy C-S-H analogů. Na kapitolu pak navazují publikace autorky týkající se dopované formy C-A-S-H v přirozeném systému směsných cementů či alkalicky aktivovaných materiálů, dále publikace hydratačních produktů C-A-H vznikajících při řízené hydrolýze syntetických kalcium aluminátů a kalcium aluminátových cementů.

Zvolené téma, propojující publikované vědecké práce, aplikované výsledky a vedené závěrečné práce, je zásadní oblastí výzkumu a pedagogického zaměření autora, ačkoliv není tématem jediným. Významná část publikovaných výsledků autorky týkající se syntézy a analýzy pokročilých keramických materiálů není z důvodu zachování tematické soudržnosti práce vybrána ke komentářům, ale je citována a uvedena v Podkladech k habilitačnímu řízení. Autorka je v současnosti spoluřešitelem a členem odborného týmu projektů VaVai (projekty *GA 23-05082S: „Výzkum kombinovaného účinku oxidů síry, mědi a lithia na tvorbu a vlastnosti slínku portlandského cementu“ a GA 25-16766S: „Řízená prostorová distribuce hydrátů v nízkouhlíkových cementech“)* a vedoucím bakalářských či diplomových prací, které úzce souvisejí s tématem habilitační práce.

Práce je členěna do tematických celků, které postupně rozvíjejí pohled na vznik a funkci nanostrukturních hydratačních fází v aluminosilikátových pojivech. Prvním celkem je skupina C-S-H struktur, včetně jejich historického vývoje, molekulového uspořádání a koloidních modelů. Následují části zaměřené na laboratorní syntézu C-S-H analogů různými metodami (mechanochemická, hydrotermální, sol–gel, precipitační), jejich morfologii a reaktivitu. Významná pozornost je věnována substituci prvků (např. Al, Cu, Li, S) a jejich vlivu na strukturu gelu, včetně schopnosti imobilizace doprovodných iontů. Práce dále rozebírá publikace autorky věnující se aplikaci těchto poznatků v oblasti směsných cementů, alkalicky aktivovaných materiálů a žárovzdorných kompozitů. Experimentální část je významně podpořena spektroskopickými analýzami (FT-IR, Raman, XPS, NMR), jejichž aplikace pro analýzu gelů na molekulární úrovni je významným přínosem práce a v současnosti stále aktuálním tématem. Výsledkem práce je zároveň propojení získaných poznatků o struktuře a chování C-(A,S)-H gelů s jejich praktickým využitím v návrhu funkčních a nízkoenergetických pojivových systémů vycházející z koncepce „*Low carbon economy*“ dané politikou evropského „*Green Deal*“ a strategií „*Fit-for 55*“.

2. Hydratace portlandského cementu

Maltovina je prášková hmota anorganického charakteru s měrným povrchem větším než 200 m^2/g, jejímž smícháním s vodou lze připravit pojivo. Po určitém čase tato směs ztvrdne a vytvoří pevný kompozit. Maltoviny lze rozdělit podle způsobu tuhnutí a tvrdnutí na [3]:

- Vzdušné – tuhnoucí pouze na vzduchu (např. vápno - karbonatací, sádra - hydratací, Sorelův cement – tj. cement na bázi oxidu hořečnatého v kombinaci s roztokem hořečnaté soli),
- Hydraulické – tuhnoucí i pod vodou (např. hydraulické vápno, portlandský cement),
- Latentně hydraulické – aktivující se až po smísení s vodou nebo s příměsemi či aditivy (tj. různé druhy kaolínů či strusek),
- Směsné – obsahující hydraulické i vzdušné složky, které po smísení s vodou hydratují.

Nejznámějším zástupcem hydraulických maltovin je portlandský cement (PC), který nabývá pevnost hydratací. Hydratací rozumíme proces transformace původního práškového materiálu za přítomnosti vody, tedy přijímání a vázání vody, na pevný monolitický kompozit. Tento proces probíhá formou soustavy chemických reakcí a fyzikálních jevů, které určují výsledné vlastnosti kompozitu, jako jsou pevnost, trvanlivost a celková životnost.

Na základě této definice a evropské normy EN 197-1 (českou verzí je ČSN EN 197-1, 2, 5 - LC^3) je cement hydraulická maltovina, která se vyrábí mletím vypáleného tzv. portlandského slínku se sádrovcem a příměsmi (vysokopecní struska, popílky, mikrosilika) či přísadami (např. plastifikační, stabilizační, provzdušňující, urychlující hydrataci, biocidní aj.). Norma udává, že portlandský cement musí obsahovat alespoň ze 2/3 tzv. silikátové slínkové minerály, tj. C_3S – trikalcium silikát (alit), C_2S – dikalcium silikát (belit), a z 1/3 tzv. aluminátových slínkových minerálů, tj. C_3A - trikalcium aluminát (tmavá spojovací hmota) a C_4AF – tetrakalcium aluminát ferit (světlá spojovací hmota) [3]. Normální cementy obsahují 50–75 % alitu, 5–20 % belitu a 5–15 % aluminátu a 5–15 % aluminát feritu, protože je portlandský cement velmi komplexní systém v soustavě CaO-SiO_2-Al_2O_3 (Obr. 1), je jeho hydratace procesem neméně složitým. Jak již bylo výše zmíněno, hydratace portlandského cementu je obecný proces reakcí probíhajících na fázovém rozhraní voda-částice, kdy částicí je myšleno zrno slínku v přítomnosti sádrovce, přísad a příměsí. Při kontaktu cementu s vodou se začnou uvolňovat jednotlivé ionty do roztoku, kde po dosažení kritické koncentrace, tj. stav přesycenosti, dochází k nukleaci nových systémů převážně na povrchu částic. V tomto komplexním systému dochází k rozpuštění jednotlivých složek v různém čase a při různých podmínkách, což ovlivňuje rychlost nukleace nových fází a vede k neustálým změnám fyzikálního i chemického stavu povrchu reagujících částic.

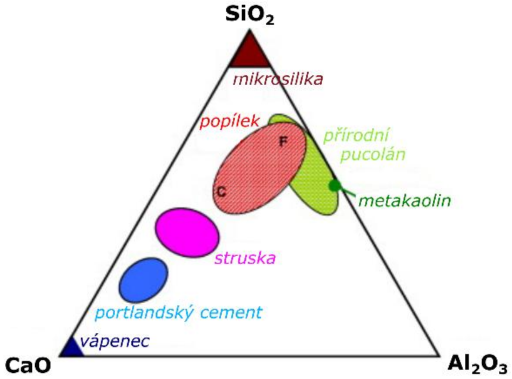

Obr. 1 Fázový diagram soustavy CaO-SiO_2- Al_2O_3 *(zpracováno z [4])*

Výsledkem hydratace je tvorba produktů na bázi hydratovaných kalcium silikátů (C-S-H fáze), kalcium aluminátů (C-A-H fáze), sulfoaluminátů a sulfoaluminoferitů (např. ettringit (AFt) a monosulfoaluminát (AFm)), či karboaluminátů (MC fáze). Tyto produkty hrají klíčovou roli při řízení procesu tuhnutí a tvrdnutí hydraulických pojiv a pucolánových příměsí. Tvorba hydratačních produktů je ovlivňována mnoha vzájemně provázanými faktory, což činí mechanismus vysoce komplexním, a jeho přesný popis je obtížně definovatelný.

3. C-S-H fáze

3.1. Historický vývoj popisu mechanismu hydratace kalcium silikátů

Studium povahy vznikajících částic a mechanismů hydratace bylo předmětem mnoha výzkumů [5-9]. Na základě těchto prací vznikla řada hydratačních a strukturních modelů, kterým se dále věnují samostatné kapitoly. Mnohé z modelů byly vyvráceny a mnohé naopak díky moderním experimentálním a analytickým přístupům potvrzeny. První pokusy o detailnější popis hydratace cementu se objevily již na konci 19. století, například krystaloidní teorie prof. Le Chateliera [10] a koloidní teorie prof. Michaëlise [11]. Ačkoli byly tyto teorie historicky vnímány jako neslučitelné, ve skutečnosti se vztahují k odlišným podmínkám hydratace – Le Chatelierova teorie předpokládá vysoký vodní součinitel a úplnou hydrolýzu slínkových minerálů, zatímco Michaëlisova teorie popisuje topochemický růst hydratačních produktů za praktických podmínek. Tato rozdílnost vedla k intenzivnímu empirickému ověřování, teoretickému objasňování a vzniku dalších koncepcí, jejichž vývoj trvá dodnes. Pro ilustraci komplexnosti tématu jsou na Obr. 2 a Obr. 3 uvedeny milníky v teorii hydratace, jejich autoři a přínos v časové ose od konce 19. století až po současnost.

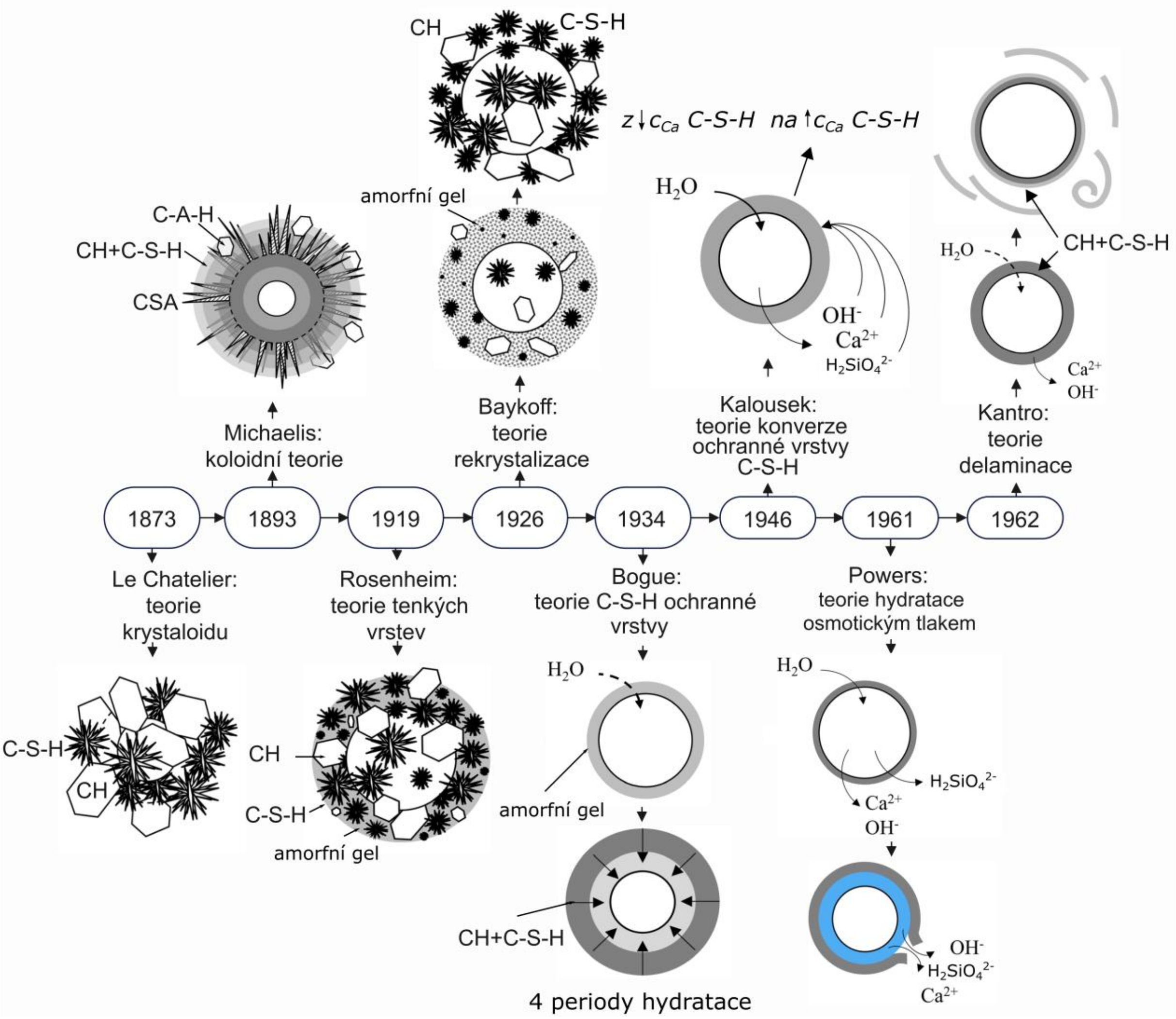

Obr. 2 Časové schéma jednotlivých modelů hydratace (do roku 1962) (zpracováno z [5])

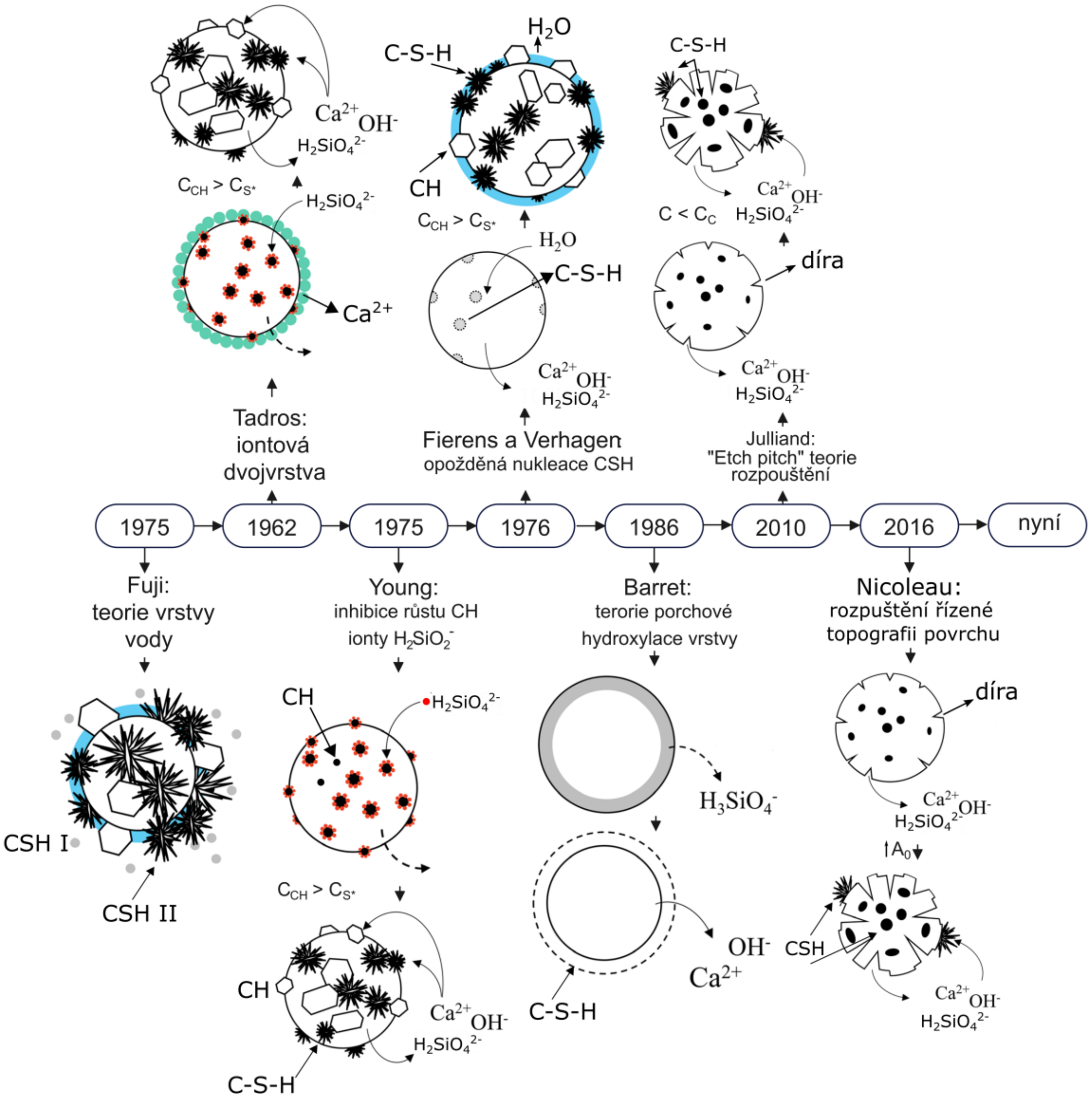

Obr. 3 Časové schéma jednotlivých modelů hydratace (1975 až nyní) (zpracováno z [5])

Popis reálné struktury hydrátů kalcium silikátů a kalcium aluminátů a objasnění mechanismu jejich vzniku za přítomnosti různých příměsí a přísad zůstává stálým předmětem zájmu vědecké komunity – v minulosti, současnosti i s výhledem do budoucnosti [5, 7, 8, 12].

Následující kapitola poskytuje teoretický přehled zaměřený na strukturu C–S–H fáze, včetně mechanismu jejich vzniku, morfologie, možností syntézy, termodynamických a kinetických charakteristik i přístupů k jejich numerickému modelování. Podrobnější analýza popisu nanostruktur tvoří základní rámec pro další kapitoly práce, které na dané poznatky navazují – zejména v kontextu substituovaných struktur alkalicky aktivovaných materiálů a interakcí s koloidní silikou.

Autorka se ve svých publikovaných vědeckých pracích věnuje vlivu podmínek, přísad a příměsí na hydrataci různých typů cementů. Jednotlivé studie přinášejí odlišné pohledy na vznik hydratačních produktů – od využití sekundárních surovin (např. popílky, vysokopecní struska, vápenec, metakaolin) [13-19], přes bezcementové systémy založené na alkalicky aktivované reakci [20-24] až po hydrataci kalcium aluminátů [25-27]. Tyto práce přispívají k hlubšímu porozumění mechanismům hydratace a zároveň mají praktický význam pro vývoj kalcium aluminátových cementů, zejména v oblasti žárovzdorných materiálů, kterým se věnuje kapitola 5.2. Studium C-S-H struktur je dlouhodobou součástí výzkumu, jak v rámci disertačních prací (Ing. Dlabajová [28]), tak i v současných projektech. Aktuálním tématem je příprava dopovaných koloidních C-S-H fází a jejich vliv na hydratačního mechanismus ve směsném cementu (GA 25-16766S). Následující kapitoly shrnují poznatky z těchto výzkumů a komentují jejich výsledky.

3.2. Molekulární struktura C-S-H fází

Stejně intenzivně, jako je diskutována teorie hydratace, probíhá i odborná diskuse o struktuře vznikajících hydratačních produktů. V padesátých a šedesátých létech minulého století prof. Powers či prof. Taylor [29, 30] definovali vznikající látky jako jeden z nejstarších <u>*nanočásticových systémů*</u> se strukturou kalcium hydrosilikátů xCaO-ySiO$_2$-zH$_2$O (dále C-S-H) [31]. Kalcium silikáty zjednodušeně řečeno reagují s vodou za vzniku kalcium hydrosilikátového gelu (tj. *C-S-H gelu*) a portlanditu (CH) dle obecných rovnic [32]:

$$C_3S \ + \ (3-x+y)H \ \rightarrow \ C_x - S - H_y \ + \ (3-x)CH, \tag{1}$$

$$C_2S \ + \ (2-x+y)H \ \rightarrow \ C_x - S - H_y \ + \ (2-x)CH, \tag{2}$$

kde se právě odlišný C/S (C = CaO, S = SiO$_2$) poměr a různě vázaná voda výrazně projevují. C-S-H vzniklý hydratací C$_2$S je odlišný od C-S-H gelu vzniklého hydratací C$_3$S [33]. S vyššími poměry C/S (tj. nad 2) se můžeme setkat při hydrataci za extrémních podmínek či v přítomnosti přímësí [4].

Porozumění procesům jako rozpouštění, difuze, nukleace, růst, komplexace, adsorpce a kinetika ve skutečném cementovém systému představuje velmi složitý a náročný úkol, jak již bylo zmíněno v úvodní části [12]. Nehomogenita vznikajících hydratačních produktů a jejich interakce s ostatními fázemi se odráží i v označeních typu C-S-H, C-A-H apod., která pomocí pomlček vyjadřují, že nejde o přesně definované chemické sloučeniny, ale o komplexní a proměnlivé struktury. Stěžejním se ukázal poměr mezi Ca a Si a množství vody v systému vyjádřené jako hydroxyl či hydrát. Prof. Richardson a jeho tým byli mezi prvními, kdo detailně popsal C-S-H i C-(A)-S-H struktury [34-42]. Poměr Ca/Si (vápník/křemík) se v reálném systému pohybuje mezi hodnotami 0,7 až 2,1 a množství vázané vody se mění ještě více [39, 43]. Skupina C-S-H fází byla dále během času a nástupu nových analytických metod různě dělena a označována. Taylor [44] ve své práci rozdělil C-S-H na dvě kategorie: na C-S-H I s C/S < 1.5 a C-S-H II s C/S > 1,5. Nonat [45] později první skupinu ještě rozdělil na C-S-H (α) pro 0,66 < C/S < 1 a C-S-H (β) v rozmezí 1 < C/S < 1,5. Dále najdeme rozdělení na LD („*low density*“ – nízkohustotní) a HD („*high density*“ = vysokohustotní) C-S-H, které vychází z novějšího koloidního modelu a říká nám o uspořádání jednotlivých C-S-H částic (v tomto případě globulí). Minerály krystalizující ze soustavy CaO-SiO$_2$-H$_2$O za různých podmínek jsou krystalickými analogy C-S-H sloučenin vznikajících přirozeně během hydratace a sehrály významnou roli při formulaci různých strukturních modelů [45-47]. Na Obr. 4 jsou uvedeny fázové diagramy soustavy C-S a C-S-H.

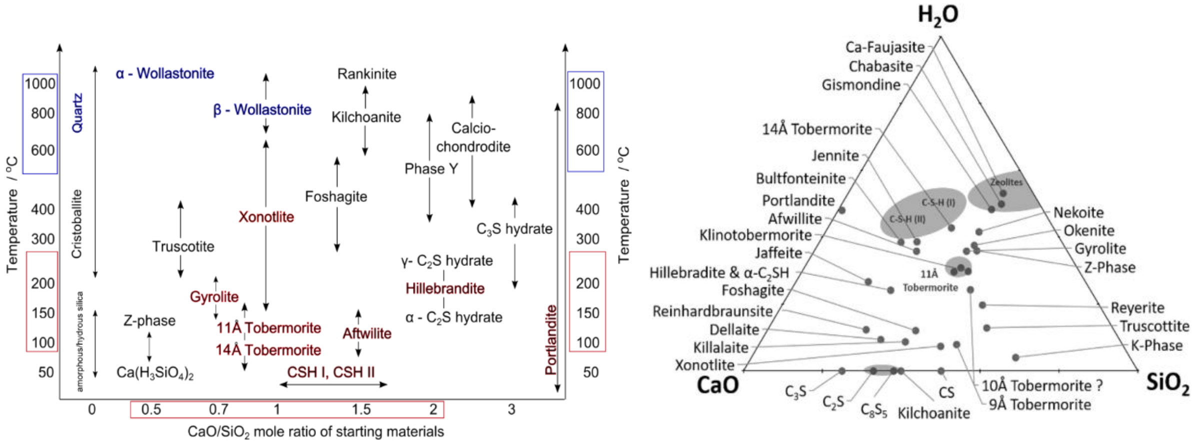

Obr. 4 Fázové diagramy soustavy CaO-SiO$_2$ a CaO-SiO$_2$-H$_2$O (převzato z [1] a [2])

C-S-H sloučeniny mohou vznikat v amorfní, semikrystalické i krystalické podobě, vše se odvíjí od podmínek jejich nukleace a růstu. Tyto látky jsou strukturně velmi podobné krystalickým analogům vznikajícím také ze systému CaO-SiO$_2$-H$_2$O, proto se pro popis reálných systémů využívají již od 90. let minulého století (prof. Taylor, viz. Tabulka 2). Na základě různých experimentálních dat můžeme C-S-

H gel popsat pomocí minerálů s různým C/S poměrem – tj. skupina *wollastonitu, jennitu, hillebranditu* a zejména *tobermoritu*.

Obecně je již uznávaným faktem, že *největší podobnost s reálným C-S-H gelem je přisuzována struktuře tobermoritu s určitým počtem strukturních defektů* [48], a dle posledních studií s atomárního pohledu je největší podobnost s clinotobermoritem (viz Tabulka 1) [49, 50].

Tzv. superskupina tobermoritu [51] vychází z jeho vrstevnaté struktury, tzv. *„order-disorder“* (OD) (Obr. 5) a jednotlivé minerály se liší rozdílnou bazální mezivrstevnou vzdáleností (d_{002}) danou stupněm hydratace a symetrií buňky. Centrální vrstva obsahuje CaO s atomy vápníku v cik-cak uspořádání a koordinačním číslem 7, které jsou podélně propojeny ve směru osy *b*. Vrstva CaO sdílí kyslíkové atomy se silikátovými řetězci typu *dreirketten* po obou stranách. Toto uspořádání se opakuje každé tři silikátové řetězce, přičemž dva jsou tzv. párové a jsou propojeny s centrální CaO vrstvou sdílením 2 kyslíkových atomů a třetí tzv. můstkový, který směruje do mezivrstevného prostoru [52-55]. Celá jednotka lze nazývat komplexním modulem [56]. C-S vrstvy leží v *xy* nebo rovině (001) s periodicitou 7,3 Å, zatímco periodicita v ose z je dána opakováním vrstev za sebou. Mezivrstevný prostor je vyplněný vodou a vápenatými ionty, které zajišťují kohezi způsobenou disperzním prostředím a elektrostatickými interakcemi [57].

Obr. 5 Schéma struktury vrstev v tobermoritu (a) a detail „dreierketten“ (b) uspořádání silikátových řetězců (upraveno z [58])

Rozlišujeme několik tzv. polytypů lišících se od sebe mezivrstevnou vzdáleností (d_{002}), která je větší s rostoucím hydratačním stupněm. Na Obr. 6 je zobrazena struktura 9, 11 a 14Å tobermoritu. Dále u tobermoritu hovoříme o tzv. MDO[1] struktuře, která rozlišuje typy tobermoritů dle krystalické mřížky a uspořádání vrstev. Všechny známé druhy jsou níže shrnuty v Tabulka 1.

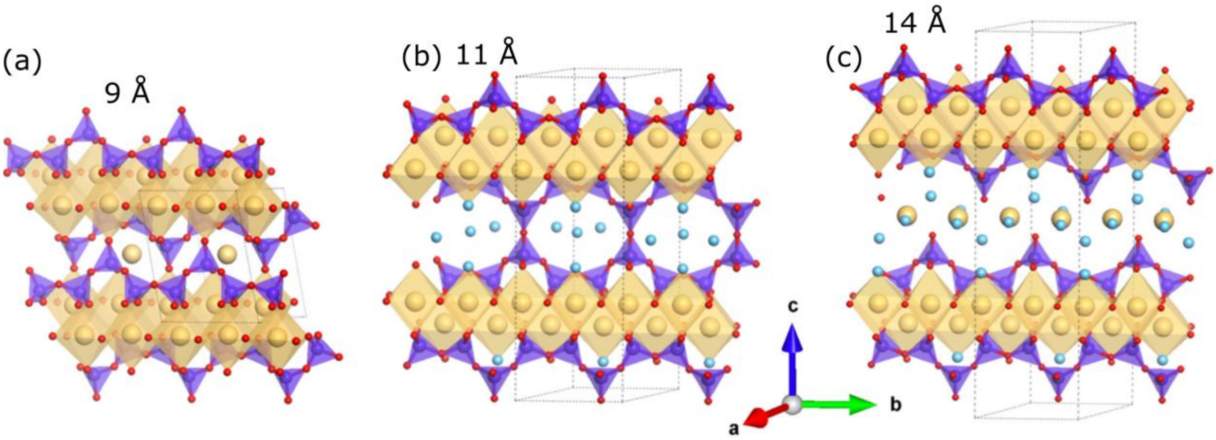

Obr. 6 Schéma polytypů tobermoritu: a) 9Å, b) 11Å, c) 14Å (upraveno z [58])

Rozdíl mezi jednotlivými typy není jen v mezivrstevné vzdálenosti, ale i v chování během tepelného namáhání. Ze 14Å tobermoritu lze získat polytypy s menší vzdáleností (jak 11Å tak i 9Å) a to pomocí dehydratace za zvýšené teploty (cca 200 °C). 11Å tobermorit vykazuje odlišné chování oproti ostatním

---

[1] MDO je *„maximum degree of order“* – představují ideální, pravidelně se opakující se uspořádání vrstev, které se liší typem translace vrstev.

polytypům, což souvisí s jeho schopností vytvářet kondenzačním mechanismem dvojité wollastonitové řetězce propojující můstkové silikátové řetězce sousedních vrstev. Tyto řetězce obsahují tzv. zeolitové kavity, v nichž se nacházejí intersticiální kationty Ca^{2+}. Jejich přítomnost je důsledkem substituce Si^{4+} za Al^{3+} v tetraedrických pozicích silikátových řetězců (zejména v Q^2 a Q^3 pozicích), která generuje záporný náboj vyžadující kompenzaci. Díky této struktuře lze při zahřívání rozlišit běžnou formu tobermoritu, bohatou na Ca, od anomální formy, která je na Ca ochuzená. U anomálního tobermoritu nedochází při dehydrataci ke zmenšení mezivrstevné vzdálenosti na 9,3 Å, jak je tomu u běžné formy, protože postrádá zeolitové kavity s výměnnými kationty. Tím pádem nedochází ani k přeuspořádání Ca^{2+} do koordinačního čísla 7. Při tepelném zpracování nad 800 °C se všechny C-S-H struktury rozpadají za vzniku wollastonitu [59, 60].

Tabulka 1 Polytypy tobermoritu dle nomenklatury Biaginiho [51]

d002 (Å)	*Název minerálu*	*Chemické složení*	*Krystalická mřížka*	*Citace*
14,0	Plombierit	$Ca_5Si_6O_{16}(OH)_2{\cdot}7H_2O$	ortorombická[1]/monoklinická[2]	[61]
11,3	Tobermorit	$Ca_5Si_6O_{17}{\cdot}5H_2O$	monoklinická[2]	[59]
	Kenotobermorit*	$Ca_4Si_6O_{15}(OH)_2{\cdot}5H_2O$	ortorombická[1]/monoklinická[2]	[59]
	Clinotobermorit	$Ca_5Si_6O_{17}{\cdot}5H_2O$	monoklinická[1]/triklinická[2]	[62][63]
9,3	Riversideit	$Ca_5Si_6O_{16}(OH)_2$	ortorombická[1]/monoklinická[2]	[63]
	Clinotobermorit 9 Å	$Ca_5Si_6O_{16}(OH)_2$	monoklinická[1]/triklinická[2]	[62]

*ve většině literatury označován jako anomální tobermorit;[1] typ MDO_1 ; [2] typ MDO_2

Z historického pohledu je potřeba zmínit i minerály skupiny jennitu. Dlouhou dobu se uvažovalo nad strukturním modelem C-S-H gelu s vysokým C/S poměrem vycházejícího z této struktury [64]. Jennit, se vzorcem $Ca_9Si_6O_{18}(OH)_6 \cdot 8H_2O$ a Ca/Si poměrem 1.55, je tobermoritu podobný díky jeho vrstevnaté struktuře obsahující silikátové řetězce wollastonitového typu a v přírodě se vedle tobermoritu i velmi často vyskytuje. V současnosti modely založené na struktuře jennitu ztrácejí na významu. Experimentální data ukazují, že struktury s vysokým poměrem Ca/Si mohou vznikat i při zachování tobermoritové strukturní architektury. Jak experimentální, tak teoretické studie navíc potvrzují, že charakteristické rysy struktury tobermoritu nejlépe odpovídají struktuře C-S-H gelu [50, 65, 66].

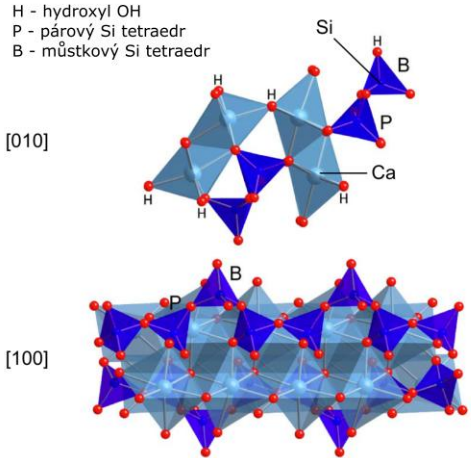

Obr. 7 Struktura jennitu (upraveno z [67])

Pro popis C-S-H můžeme využívat mnoho druhů modelů – empirických, numerických či atomistických. V dnešní době se empirické modely trochu upozaďují na úkor numerických simulací na atomární úrovni, je to opět v souvislosti s novými možnostmi analýz, které v minulosti nebyly. I přesto díky těmto modelům, byla struktura C-S-H gelů popsána a jsou důležitými milníky ve vědním oboru cementových pojiv.

3.2.1. Empirické modely struktury C-S-H

Vědci se dlouhodobě věnovali *empirickým popisům modelu struktury C-S-H fází* a s časem bylo navrženo, diskutováno i vyvráceno mnoho hypotéz. A právě koloidní povaha C-S-H gelu byla v minulosti upozaděna ve prospěch interpretace založené na strukturální podobnosti s minerály skupiny tobermoritu (Obr. 5) a jennitu (Obr. 7). *„Powersův koloidní model“* [29] vznikajícího C-S-H gelu byl nahrazen modelem *„vrstevnatým dle Bernala, Feldmana – Seredy“* [68], modelem „defektních struktur na bázi tobermoritu a jennitu“ dle Taylora, Conga a Kirkpatricka [46, 47]. Po roce 2000 se díky nástupu moderních analytických metod, jako jsou nukleární magnetická rezonance (MAS-NMR), rentgenová fotoelektronová spektroskopie (XPS) či vibrační spektroskopie (tj. FT-IR a Ramanovy), a všeobecného *„boomu nanomateriálů“* se diskuse opět vrátila ke *koloidní povaze C-S-H sloučenin* [69-75]. Opět se vracíme k již uvedenému, že navzdory rozsáhlému experimentálnímu i teoretickému zkoumání zůstává atomární struktura C-S-H fáze ne zcela jednoznačně vymezena. V Tabulka 2 jsou shrnuty vybrané empirické modely spolu s experimenty, které teorie podpořily.

Tabulka 2 Empirické modely C-S-H struktur (zpracováno z [58] a [6])

Kdo	*Kdy*	*Co*	*Jak*	*Čím*	*Reference*
Powers and Brownyard	1946	P-B: koloidní	Kapilární porozita; struktura gelu/absorbovaná a neabsorbovaná voda	Pyknometrie, Sorpce	[29]
Bernal	1952	Vrstevnatý	Tobermorite a silikátový monomer	XRD	[76]
Taylor and Howison	1956	Vrstevnatý	Tobermorit Ca/Si nad 0,83	XRD, měrná hmotnost, index lomu,	[77]
Kurczyk and Schwiete	1962	vrstevnatý	tobermorite	Tem, SEAD, XRD, FT-IR	[78]
Brunauer et al.	1967	Vrstevnatý	Struktura defektního tobermoritu a jennitu	N_2 adsorpce; porozimetrie	[79]
Witman	1976	Koloidní model	C-S-H jako xerogel	N_2 adsorpce; porozimetrie	[80]
Feldman a Sereda	1966, 1980	F-S: vrstevnatý	Vrstvy gelu s póry a mezivrstvy s vodou	N_2 adsoprce; mechanika	[68]
Stade, Wieker, Glasser	1980 1987	Tobermorit	Směs dimer a polymerních silikátových řetězců	Rozpustnost, termodynamika	[81] [82]
Taylor	1986	Defektní struktury tobermoritu a jennitu	Struktura na atomární úrovni 3n−1	XRD, TGA	[47]
Richardson a Groves	1992	Tobermorite, jenni a portlandit	Ukončené Silikátové řetězce s MCL[2] (3n – 1) a vrstvy CH	Stupeň hydratace, NMR	[83]
Cong a Kirkpatrick	1996-7	1,4nm tobermorit	Struktura Ca-OH a Si-OH dle C/S poměru	MAS-NMR	[46]
Nonat a Lecoq	1998	1,4nm tobermorit	MCL (3n – 1)	MAS-NMR	[84]

---

[2] MCL – „ mean chain lenght“, tj. délka silikátového řetezce

Jennings	2000, 2004	Koloidní a fraktální model - CM I	LD a HD C-S-H gel	SANX-NMR	[70, 71]
Chen	2004	Tobermorit and jennit	MCL (3*n* – 1)	MAS-NMR	[85]
Nonat	2004	Tobermorit, jennit	Různé struktury C-S-H dle C/S poměru	NMR, XRD, AFM	[86]
Jennings	2008	Koloidní model CM II	Uspořádání LD C-S-H globulí	Chemisorpce	[74, 75]

P-B (Powers-Brownyard) model jako jeden z prvních popsal vznikající C-S-H během procesu hydratace cementových past v závislosti na různém vodním součiniteli jako 3D systém (xerogel) skládající se z koloidních částic o velikosti 14 nm s nanoporezní strukturou (tzv. *„Munich model“*, Obr. 8a). Milníkem moderních koloidních modelů byla práce týmu prof. Allen (Obr. 8b), kteří využili experimentálních dat ze SANS (*„Small Angle Scattering“*) k popisu globulek gelu o velikosti 5 nm vznikajících již v raných fázích hydratace, jež s časem agregují do větších struktur (kolem 40 nm) [87].

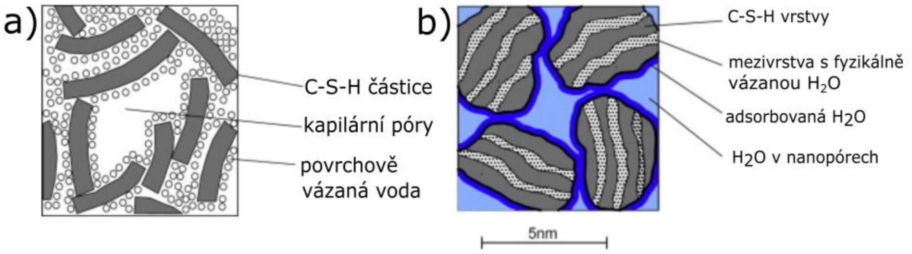

Obr. 8 „Munich (a) a Allenův (b)“ model C-S-H globulek (upraveno [71])

Na tyto práce navázal tým prof. Jenningse [70, 71, 75], který zformuloval postupně několik verzí koloidního modelu (CM I, fraktální CM I model, CM II). Na počátku jeho práce bylo potvrzení Munichova a Allenova zjištění sférického tvaru C-S-H částic o velikosti okolo 2,2 nm se strukturou podobnou jennitu či tobermoritu (Obr. 8). Tyto pevné částice se spojují do klastrů – <u>*globulí*</u> o velikosti 5,6 nm a na základě různých typů přítomných pórů se tyto globule uspořádávají (LD C-S-H a HD C-S-H[3], Obr. 9). HD C-S-H je výrazně pevnější a vzniká na rozhraní s nezreagovaných povrchem zrn a také bývá označován jako vnitřní C-S-H. Zatímco LD C-S-H vzniká napříč celou matricí zejména v počátečních fázích hydratace a je díky své hustotě přístupný vniku plynu (N_2), a proto je hlavní složkou hodnoty specifického povrchu, získaného metodou BET (Brunauer–Emmett–Teller). Koloidní model CM I byl později potvrzen i numerickým modelem založeným na Monte Carlo přístupu ([88, 89]).

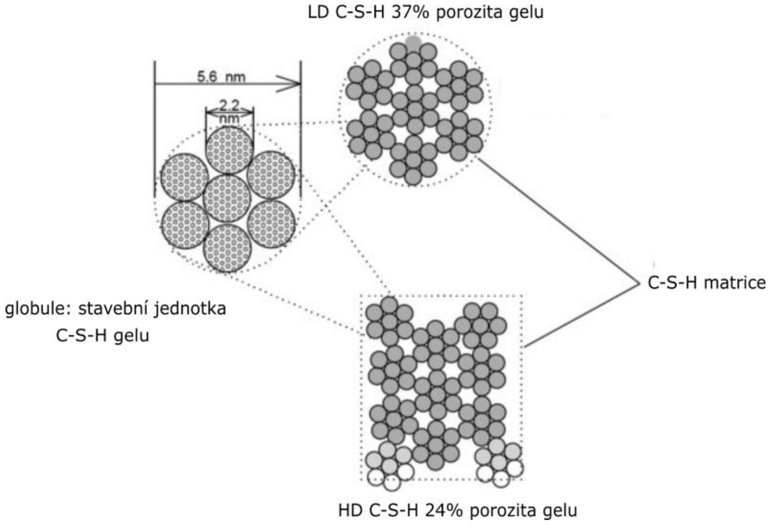

Obr. 9 C-S-H globule a jejich uspořádaní dle hustoty na LD a HD C-S-H (zpracováno z [71])

---

[3] LD – *„low density“* , nízkohustotní a HD – *„high density“*, vysokohustotní.

Koloidní model CM I v jeho původní formě, ale nebyl experimentálně potvrzen z hlediska HD C-S-H, rozšíření CM I se podařilo experimentálně doplnit prof. Jenningsovi. Ten vyšel z komplexních informací o pórové struktuře, nejenom v souvislosti s hustotou globulí, ale i z naměřeného obsahu vody, porozitě v gelu a měrného povrchu LD C-S-H získaného pomocí BET, doplněné o fyzikální data chemického smrštění hydratovaných cementových past v čase a různé vlhkosti [69, 90]. Model byl znovu přepracován v souvislosti s experimentálními daty získanými z NMR analýzy. Dává do souvislosti vztah pohybu C-S-H globulí během vysychání, mechanického namáhání či smršťování během procesu stárnutí spojeného s polykondenzací silikátových řetězců [6]. Z chemického pohledu se jedná o podstatu „sol-gel procesu“ [91] daného rovnicemi (3-5), kde se kondenzací uvolňuje voda a vznikají polymerní klastry (5), které mohou mít podobu gelu či částic [73, 92]:

$$\equiv Si - OH + H_2O \equiv \leftrightarrow \equiv Si - O^- + H_3O^+ \quad (3)$$

$$\equiv Si - OH + O^- - Si \equiv \leftrightarrow \equiv Si - O - Si \equiv + OH^- \quad (4)$$

$$\equiv Si - OH + HO - Si \equiv \xrightarrow{H^+ \text{ či } OH^-} \equiv Si - O - Si \equiv + H_2O \quad (5)$$

Porézní gel, který má schopnost vyplnit volný prostor, vzniká pouze tehdy, kdy je reakce (5) nevratná. Schematicky je závislost typu gelu na směru reakce (5) ukázána na Obr. 10, kdy je zcela zřetelné, že pro C-S-H gel tvořící hlavní pojivovou matrici je stěžejní mechanismus nevratné polykondenzace silikátových řetězců. Za podmínek, kdy v systému probíhají jak vratné reakce (např. reakce 4), tak nevratné (např. reakce 5), dochází k růstu silikátových zpolymerizovaných klastrů do takové velikosti, až samovolně vyprecipitují. Tyto precipitáty mají gelovou strukturu a vznikají agregací koloidních částic. Během stárnutí dochází k synerezi – vytlačování kapaliny z gelové sítě, která se následně odděluje jako volná fáze. Výsledný systém pak není schopen vyplnit celý dostupný prostor. Z hlediska klasifikace gelů se jedná spíše o koagel než o spojitý lyogel. Na základě fyzikálního pohledu na gely lze C-S-H gel vznikající v cementové matrici považovat za koloidní gel s částečně spojitou strukturou, která vzniká agregací globulí. Tento typ gelu je někdy označován jako *„nepravý gel“*, který lze chápat jako specifický případ koloidního gelu s fraktální strukturou [73, 93, 94]. Stárnutím dochází k postupné polykondenzaci silikátových řetězců, která zvyšuje stupeň polymerizace C-S-H gelu. Synereze gelu je významným jevem zejména u koloidních alkalických silikátů, alkalicky aktivovaných materiálů a geopolymerů [95]. Výsledky ^{29}Si NMR analýz publikované prof. Jenningsem potvrzují, že stupeň polymerizace se zvyšuje nejen s časem, ale i s rostoucí teplotou. Stárnutím dochází ke transformaci LD C-S-H na hutnější analogy HD C-S-H, a tedy dochází k poklesu měrného povrchu (měřeno metodu BET). Tomuto tématu se věnují publikace *(**Kalina, Bartoníčková a kol.*** [96]***, Kunovský, Bartoníčková a kol.*** [19]) studující vliv koloidních silikátů na tvorbu C-S-H gelu ve pórech již vytvrdnutého betonu. Jedná se o techniku vytvrzovačů, koloidních povlaků a nanoseedů, které jsou součástí tzv. *„self-healing“* systémů [96].

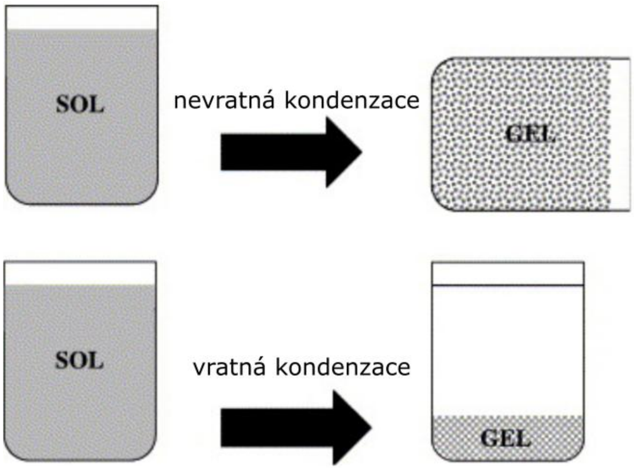

Obr. 10 Schéma C-S-H gelu vznikajícího polykondenzací (zpracováno z [73])

Novější poznatky ze SANS analýzy a nanoindentačních měření ukázaly, že základní stavební jednotka C-S-H gelu je větší, než bylo dříve určeno a odpovídá velikosti 4,4 nm, což je blíže k dříve stanovené velikosti C-S-H globule. Voda obsažená uvnitř globule nebyla v modelu CM I brána v potaz. Ve fraktální přístupu k CM I se C-S-H uspořádává stále do LD a HD struktury, ale nyní bylo LD C-S-H popsáno pomocí struktury s gelovými póry o různé velikosti (až 10 nm), což ukazuje na ještě nižší hustotu než v modelu předešlém [74, 97]. Jak již bylo zmíněno výše, koloidní model CM I nebere v potaz vodu uzavřenou uvnitř v C-S-H globulích, jejich změnu uspořádání během vysychání a smršťování, a proto byla vyvinuta snaha model přepracovat a upravit. Díky novým experimentálním datům byl původní koloidní model CM I přepracován do podoby koloidního modelu CM II, který spojuje vrstevnatý F-S model s modelem koloidním a byl nazván jako „granulární“ [75] (Obr. 11). Globule jsou tvořeny destičkovitými částicemi se strukturou podobnou tobermoritu či jennitu, kdy v jednotlivých mezivrstvách o velikosti menší než 1 nm je voda. Tato pronikající voda napomáhá ke tvorbě dvou typů gelových pórů o různé velikosti (SGP - „*Small Gel Pores*“ – 1-3 nm, LGP - „*Large Gel Pores*“ – 3-12 nm), ale model stále nepočítá s vodou v mezivrstvách a chování během mechanického namáhání. Struktura LD C-S-H není tedy jednoznačná, jelikož z experimentálních dat není jasné, zda zahrnují vodu v mezivrstvách či ne [75]. K objasnění souvislosti v nanopórovitostí a vodou v mezivrstvách přispěl experiment založený na mrazících cyklech pomocí nízkoteplotní DSC analýzy, který ukázal, že primární krystalický led s časem přechází na led amorfní a píky odpovídají malým a velkým gelovým pórům i pórům uvnitř globulí [98].

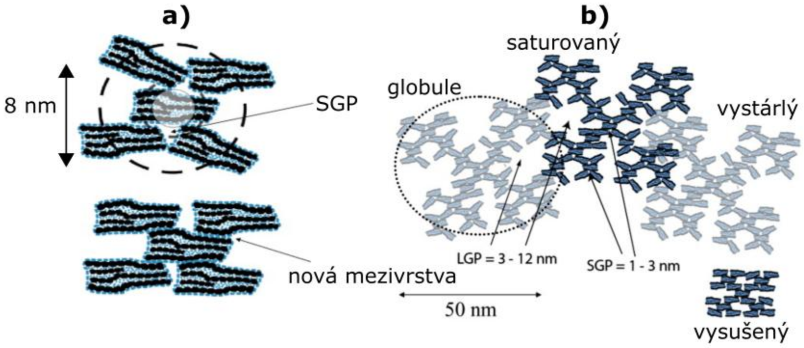

Obr. 11 Schéma uspořádání C-S-H částic do globulí dle koloidního CM II (upraveno z [75])

Porovnání empirických modulů a jejich finální kombinace v podobě „*granulárního“* modelu CM II je zobrazeno na Obr. 12.

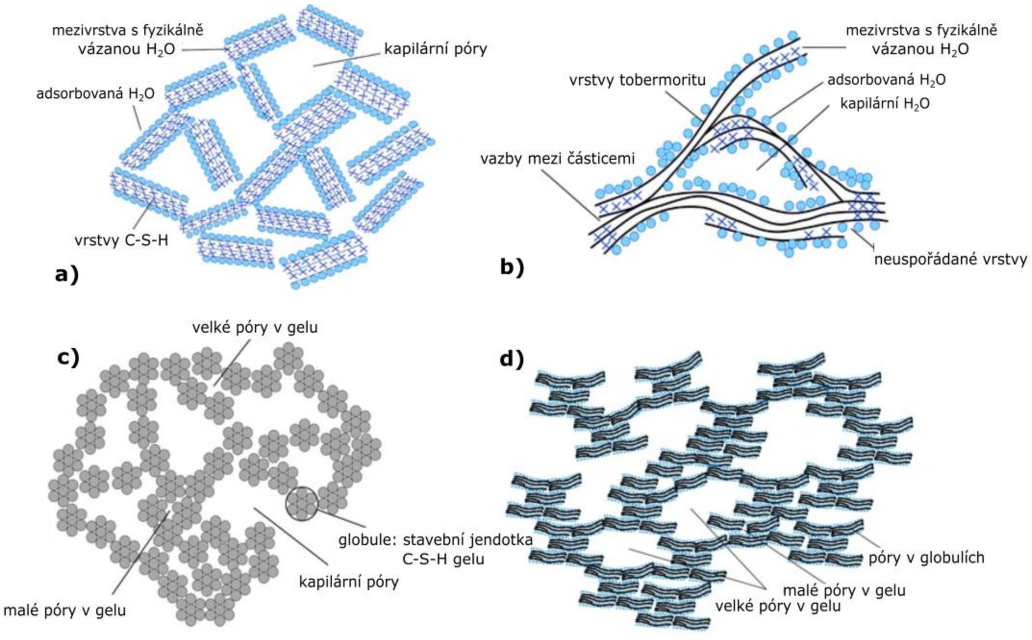

Obr. 12 Schéma nanostruktury C–S–H gelu vycházející z různých empirických modelů: a) koloidní P-B model b) vrstevnatý F-S model , c) koloidní model CM I ad) koloidní model CM II (zpracováno z [29], [68], [71], [75])

3.2.2. Numerické modely struktury C-S-H

Studium C-S-H struktur může být zkoumáno z různých pohledů od atomu přes nano a meso po mikrostrukturní měřítko, kdy každá úroveň vnáší jiné informace pro popis hydratace jako komplexního systému. Novodobějším přístupem k popisu C-S-H struktur jsou *modely využívající numerické simulace*, které využívají tzv. atomistický přístup k popisu struktury. Na Obr. 13 jsou uvedeny různé numerické metody pro výpočtové modely v závislosti na velikosti řetězce.

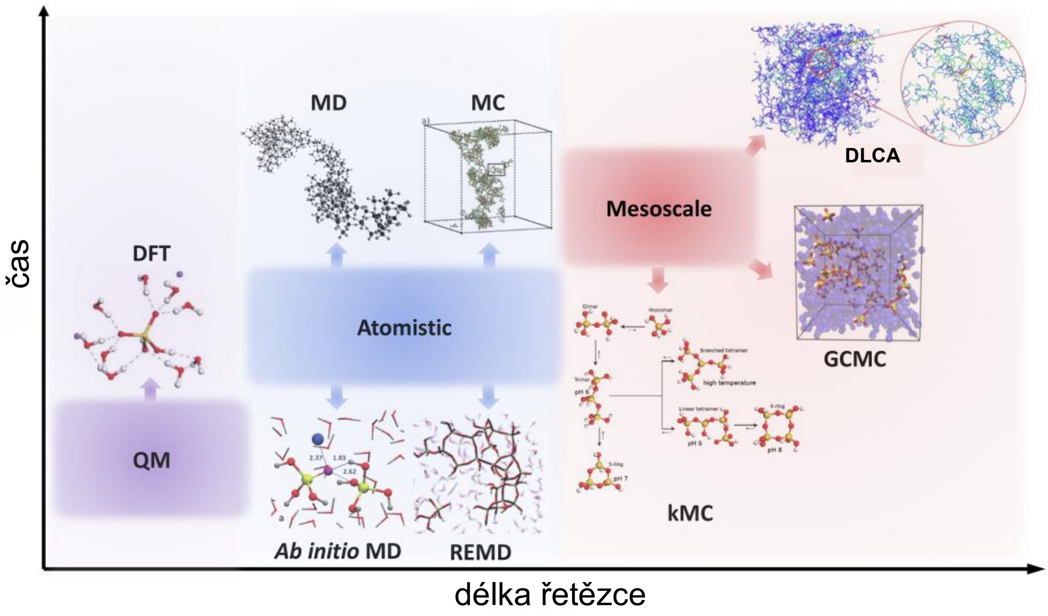

Obr. 13 Souhrn metod molekulárního modelování[4] *v souvislosti na velikosti řetězce (zpracováno z [95])*

Atomární úrovní je míněn pohled na sloučeninu z hlediska uspořádání atomů v krystalické struktuře, který je možný díky novodobým analytickým technikám jako je MAS-NMR, infračervená, Ramanova spektroskopie, či synchrotronní rentgenová difrakční analýza (XRD), rentgenový rozptyl pod malými úhly (SAXS), rentgenová fotoelektronová spektroskopie (XPS), absorpční rentgenová analýza (EXAFS), metoda rozptylu neutronů pod malými úhly (SANS) či quasi-elastický neutronový rozptyl (QENS) [42, 99-102]. Kromě poměrů C/S a C/S/H lze C-S-H strukturu popsat pomocí délky silikátového řetězce (MCL) a pomocí typů silikátového řetězce z polymerního hlediska (tzv. Q^n). Q^n jednotky označují typ SiO_4 tetraedru podle počtu kyslíkových můstků (tzv. *„bridging oxygen“,* BO), které sdílí s jinými tetraedry a nemůstkových kyslíků (tzv. *„non-bridging oxygen“,* NBO). Uspořádání jednotek Q^n v silikátovém řetězci (viz Tabulka 3) lze hodnotit jak v krystalickém, tak i amorfním systému, což právě vnáší nové poznatky v mechanismu vzniku C-S-H a jeho struktuře. Starší modely nepočítaly s morfologií gelu a nahlížely na systém jako na definovaný krystal, což už novější modely zahrnují [58].

---

[4] DFT – density functional theory, MD-molekulární dynamika, MC – Monte Carlo, REMD – „reactive exchange molecular dynamic“, kMC – kinetic Monte Carlo, GCMC - , grand canonical Monte Carlo, DLCA - diffusion-limited cluster–cluster aggregation

Tabulka 3 Přehled Q^n silikátových jednotek (zpracováno z [103, 104]

Q^n jednotka a typ	***Schéma***	***Konfigurace***	***NBO/T[5]***	***Vzorec***
Q^0 - izolovaný/monomer	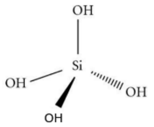		4	SiO_4^{4-}
Q^1 – pár	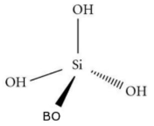	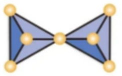	3	$Si_2O_7^{6-}$
Q^2 – kruh	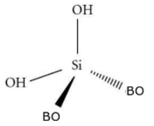	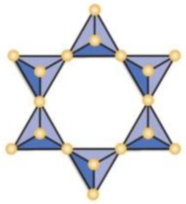	2	$Si_6O_{18}^{12-}$
Q^2 – lineární řetězec		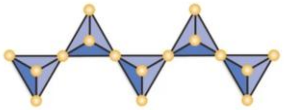	2	$Si_2O_6^{4-}$
Q^1 nebo Q^2 – dvojitý řetězec	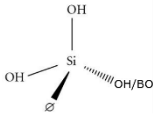	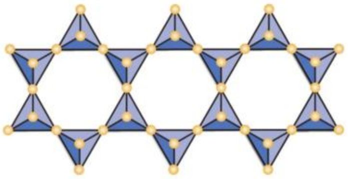	1 nebo 2	$Si_4O_{11}^{6-}$
Q^3 - vrstva	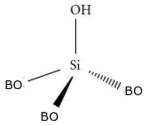	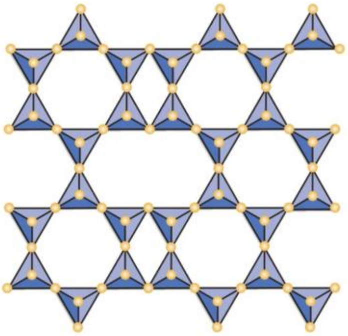	1	$Si_2O_5^{2-}$
Q^4 – 3D síť	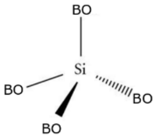	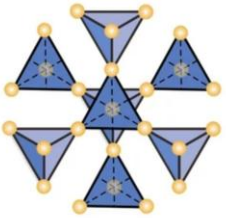	0	SiO_2

Numerické modely vycházejí z teoretických poznatků kvantové chemie na molekulové úrovni a uplatňují se zde výpočtový přístupy typu Monte Carlo, DFT či molekulové modelování (Obr. 14) a mnoho dalších. Výhodou *prediktivních modelů* vycházející z výpočtů je popis chování, struktury či jiných vlastností hydratačních produktů na atomární úrovni, jejichž experimentální potvrzení by mohlo trvat i několik let. Prof. Pelleng a jeho tým navrhli novější *model neuspořádaného C-S-H*, který koreloval s vyšší hustotou ($2{,}6\ g \cdot cm^{-3}$) a Ca/Si poměrem (1,7) v reálném C-S-H, než je u

---

[5] NBO/T = počet nemůstkových kyslíku na silikátový tetraedr.

tobermoritu /jennitu (2,23 g.cm^{-3}/0,83 a 2,32 g.cm^{-3}/1,5). Chemické složení navržené struktury bylo $(CaO)_{1,65}(SiO_2)(H_2O)_{1,75}$, což se ukázalo jako velmi podobné průměrnému složení experimentálně zjištěnému dle prof. Allena $(CaO)_{1,7}(SiO_2)(H_2O)_{1,8}$ [100]. Struktura obsahovala přibližně stejné množství vody jako u struktury 14 Å tobermoritu, ale je rozmístěna v mezivrstevném prostoru náhodně. Model byl experimentálně potvrzen pomocí XRD, EXAFS and FT-IR analýz [99, 105, 106]. Samozřejmě se během času objevila kritika navrženého modelu a nesrovnalosti v jeho výpočtu, ale i přesto je model považován za *největší milník novodobého popisu* struktury tobermoritu na molekulární bázi. Nejvýznamnější numerické modely v čase jsou shrnuty v Tabulka 4.

Tabulka 4 Významné numerické modely C-S-H struktur (zpracováno z [58] a [6])

Kdo	*Kdy*	*Co*	*Pomocný model*	*Čím*	*Reference*
Gmira	2004	Klouzavý model C-S-H vrstev	Tobermorit	Monte Carlo	[107]
Nonat	2004	Povrchový model C-S-H	Lamelární a ne zcela amorfní	Termodynamické kalkulace	[108]
Ayuela	2007	Stability silikátového řetězce	(3n-1) délka řetězce	DFT	[109]
Ayuela	2007	Mechanismus růstu	Tobermorit a jennit	Ab initio výpočty	[110]
Ayuela	2007	Polymerace silikátových řetězců v prostředí bohatém na Ca	Tobermorit a jennit	Molekulární dynamika	[111]
Pellenq	2008	Kovalentní síly mezi C-S-H vsrstvy	Nanokrystaly	Ab initio výpočty, molekulární dynamika	[112]
Skinner	2010	Nanokrystalinita v syntetickém C-S-H	11Å tobermorite	Monte Carlo, FT analýza XRD dat, párová rozdělovací funkce	[113]
González-Teresa	2010	Nepřístupnost HD C-S-H dusíkem	Nanoglobulární model	Monte Carlo	[88]
Dolado	2011	Model pro C/S vyšší než 1,7	Koloidní model	SANS, adsorpce vody, XRD, NMR	[114]
Manzano	2012	Voda v C-S-H mikropóry	Model polarizovatelného náboje	Reactive force field, ReaxFF Molekulární dynamika	[115]
Abdolhosseini Qomi	2014	Optimalizace Pellenq modelu	Nanokrystaly	Molekulární dynamika	[116]
Kovačevič	2015	3 modely C-S-H	11Å tobermorite	Molekulární dynamika	[117]
Mohamed	2018	Syntéza C-S-H při různých C/S poměrech	14Å tobermorite	DFT, molekulární dynamika	[118]

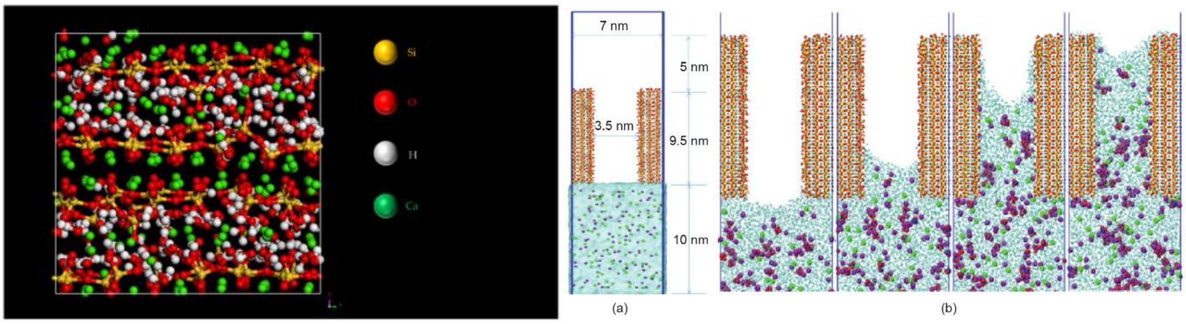

Obr. 14 Ukázky zobrazení vycházejí z a) numerického modelu na bázi modelování pomocí molekulární dynamiky (převzato z [119] a [120])

V publikaci ***Kaliny, Bartoníčkové a kol.*** [96] byla publikována data poskytující informaci o stupni polymerizovatelnosti (Q^n jednotek) v koloidních povlacích na bázi lithných silikátů před a po gelaci organickým činidlem. Na Obr. 15 je vidět znatelný nárůst Q^2 silikátových jednotek, což odpovídá pokročilé fázi gelace systému. Data jsou zcela v korelaci s publikacemi, které uvádějí vliv alkálii na C-S-H systémy [121].

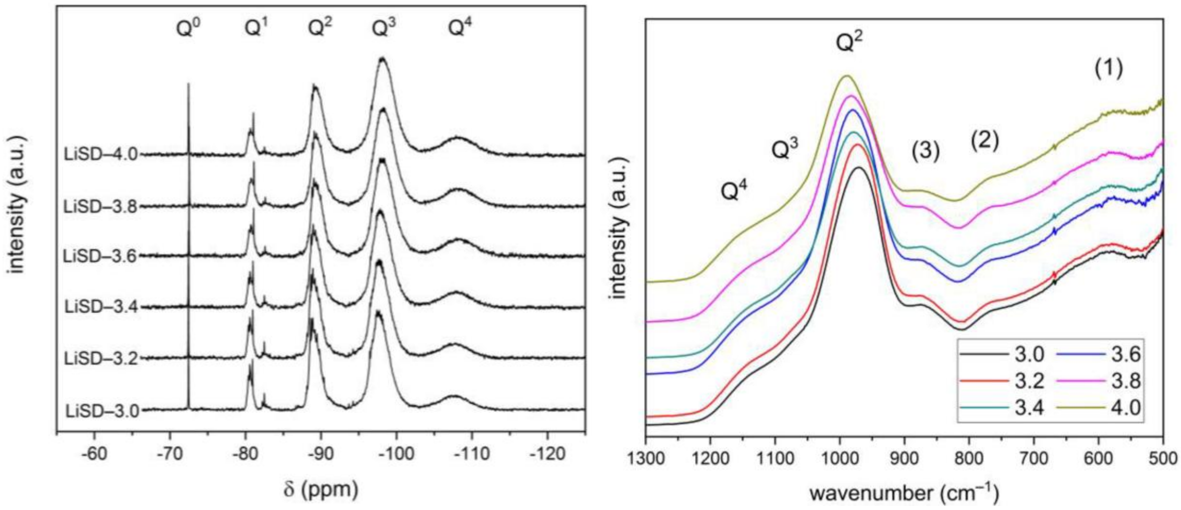

*Obr. 15 NMR (a) a FT-IR (b) analýza Q^n sealerů na bázi lithných silikátů: a) před, b) po gelaci organickým činidlem (převzato z **Kalina, Bartoníčková a kol.** [96])*

Novodobější experimenty a modelování jdou cestou syntézy C-S-H struktur za laboratorních podmínek a jejich analytického popisu. Syntéze C-S-H struktur jsou věnovány práce ***Dlabajová, Bartoníčková a kol.*** [13] a disertační práce ***Ing. Dlabajové*** [28]. Syntéza amorfních a krystalických fází a C-S-H analogů je i součástí výše zmíněných aktuálně běžících projektů (GA 23-05082S, GA 25-16766S) a aktuálně zaslaných výsledků k publikaci ***(Kunovský, Bartoníčková a kol.)*** [19]**.** Syntetický přístup k popisu mechanismu tvorby C–S–H je založen na *termodynamických modelových výpočtech* a experimentálních datech. Tématu se intenzivně věnují zejména výzkumné skupiny prof. Lothenbach [122], prof. Scrivener [123] či prof. Šiaučiūnase [124]. Využívají se pro ně různé termodynamické databáze jako je CEMDATA[6] či Nagra[7] a softwary GEM[8], μic[9] či aplikace modelů typu CSHQ [125]. Pro co nejpřesnější popis je nezbytné cílené řízení podmínek – od úvodního termodynamického modelování a kinetiky, přes návrh a řízení reaktorů, až po numerické modelování procesů a sktruktur. I přes nové přístupy a techniky je stále komplexní popis C-S-H velmi složitý.

---

[6] https://www.sciencedirect.com/science/article/pii/S0008884617312073?via%3Dihub

[7] https://www.psi.ch/en/les/database

[8] https://cemgems.org/gems/about-gems/

[9] https://micepfl.sourceforge.net/

3.3. Syntéza C-S-H struktur

Křemík jako prvek IV. A skupiny periodické tabulky, se typicky vyskytuje v konfiguraci s tetraedrickou geometrií o koordinačním čísle 4. Nejčastější formou výskytu je iont $(SiO_4)^{4-}$, jenž představuje základní stavební jednotku většiny silikátových materiálů. Vazba Si–O–Si díky iontovému a současně kovalentnímu charakteru umožňuje vznik různých uspořádání tetraedru $(SiO_4)^{4-}$, od jednoduchých řetězců po složité 3D sítě (tj. polymerizace jednotek a Q^n označení). Tato volnost konfigurace umožňuje inkorporaci široké škály kationtů díky kompenzaci záporného náboje základní Si jednotky. Struktura poskytuje i plnou substituci centrálních kationtů, typicky hliník v aluminosilikátech (tomuto tématu je věnována kapitola 4) [123, 126]. Během syntézy silikátů jsou vazebné struktury mezi silikátovými jednotkami výrazně ovlivňovány hodnotou pH, iontovou silou prostředí a přítomností různých kationtů a podléhají polykondenzačnímu mechanismu, jak již bylo zmíněno v kapitole 3.2.1. Polykondenzační reakce je katalyzovaná kationty H^+ pod pH 2 a anionty OH^- (viz rovnice (5)) při pH vyšších a postupně vznikají dimery, trimery a další oligomery. Teorie prof. Illera [127] říká, že tato reakce je prvním krokem celého procesu a je následována tvorbou koloidních zárodků a jejich růstem. V prostředí různého pH jsou i jiné formy Si struktur, rovnice (6) a Obr. 16 a popisuje jejich vzájemnou rovnovážnou závislost.

$$Si(OH)_4 \overset{K1}{\leftrightarrow} SiO(OH)_3^- + H^+ \overset{K2}{\leftrightarrow} SiO_2(OH)_2^{2-} + 2H^+ \tag{6}$$

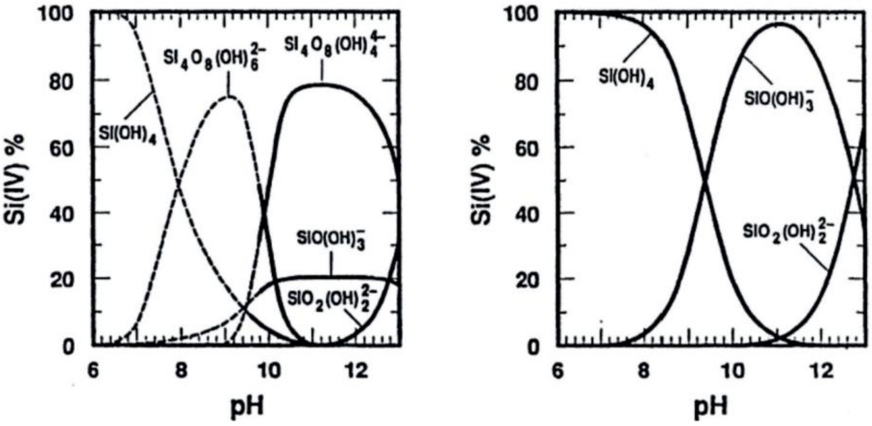

Obr. 16 Vliv pH na tvorbu silikátových jednotek (převzato z [91])

Z Obr. 16 je patrné, že $SiO(OH)_3^-$ je mírně kyselé a stabilní při pH okolo 11. $SiO_2(OH)_2^{2-}$, který se podílí na precipitaci C-S-H, může tvořit stabilní roztoky díky elektrostatickým odpuzujícím silám mezi jednotlivými Si anionty (může být viděn i zápis $H_2SiO_4^{2-}$), se tvoří nevratně až při pH nad 12. Dále se na rovnovážných reakcích podílí i koncentrace Ca^{2+} iontů ve vznikajícím C-S-H i v matečném roztoku. Za normální teploty se jedná o metastabilní rovnováhy, které však zvýšením teploty přejdou do nevratných dějů a dovolí vznikat i krystalickým C-S-H analogům [44, 63]. Na Obr. 17 je zobrazena závislost C/S poměru vznikající C-S-H struktury na koncentraci Ca^{2+} v matečném roztoku.

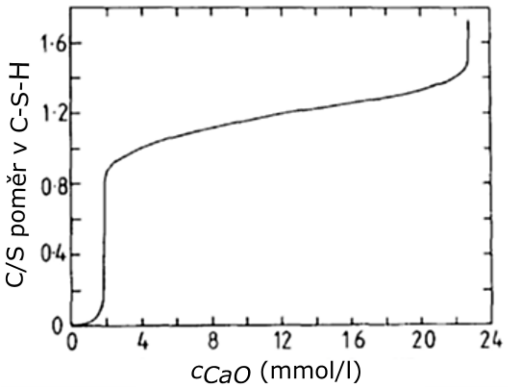

Obr. 17 Závislost C/S poměru vznikajícího metastabilního C-S-H na koncentraci CaO v matečném roztoku (zpracováno z [63])

3.3.1. Termodynamický popis nukleace a růstu

Obecná teorie nukleace a nukleace kapaliny z páry bez přímé návaznosti na CSH gel

Vlastní kapitolou je v této problematice *termodynamické modelování,* které bylo v oblasti studia hydratace směsných cementových past zavedeno již v 90. letech 20. století [128]. Z tohoto pohledu se jedná o popis reakční rovnováhy mezi produkty a výchozími látkami, přičemž směr reakce je určen změnou Gibbsovy volné energie systému ΔG, která je obecně dána rovnicí (7)[126, 129].

$$\Delta G = \Delta G^0 + RT\,ln\left(\frac{a_C^c \cdot a_D^d}{a_A^a \cdot a_{B\cdot}^b}\right), \tag{7}$$

kde *T* je absolutní teplota, *R* je molární plynová konstanta, ΔG^0je standardní Gibbsova energie systému, zlomek v logaritmu jsou aktivity *a* produktů C a D ku aktivitám výchozích látek A a B umocněné na jejich stechiometrické koeficienty. Pro popis procesů nukleace a růstu nukleí lze zjednodušeně $\Delta\hat{G}$ blížící se k nule definovat jako:

$$\Delta\hat{G} = -RT \cdot ln\left(\frac{a}{a_0}\right), \tag{8}$$

kde *a* je aktivita v daném stavu a a_0 aktivita ve stavu rovnovážném. Pokud definujeme tzv. iontovou koncentraci v čase (IAP a W = IAP/K_{sp}) a index nasycení SI neboli koeficient rozpustnosti S *(SI = log (W) nebo S = C/*C_{eq}*)* dostaneme rovnici (9) podle které můžeme odhadnout, kdy bude systém rovnovážný (SI = 0), kdy přesycený (SI > 0) nebo nenasycený (SI < 0):

$$\Delta\hat{G} = RT\,ln\left(\frac{IAP}{K_{sp}}\right) = RTln(W) = RT\,(SI) nebo = -RT \cdot ln(S). \tag{9}$$

Řídící silou precipitace nových částic je rozdíl mezi iontovou koncentrací *IAP* a součinem rozpustnosti K_{sp}. Reakční kinetika při různých teplotách a stanovení minimální aktivační energie vzniku stabilního nuklea (ΔG_c), pro vznik částic, je opět další dílkem do celkových poznatků o mechanismu vzniku C-S-H struktur.

Mechanismus precipitace (Obr. 18) je složen z dvou základních kroků, prvním je proces nukleace jemných částic z roztoku, který je následován jejich růstem. Oba procesy podléhají sobě navzájem a jejich kontrola je hlavním cestou, jak ovlivnit výsledné vlastnosti vzniklých struktur [130].

Nukleace je závislá na *aktivační energii vzniku stabilního nuklea* (ΔG_c), která se odvíjí od kritické velikosti nuklea (r_c). Pokud je velikost nuklea (*r*) menší než kritická velikost ($r < r_c$), nemohou růst a zpětně se transformují na kapalnou fázi, zatímco když je velikost nukleí větší než kritická velikost, tak mohou dále existovat a růst. Od toho se tedy odvíjí rovnice (10) a (11), kdy při platnosti d(ΔG_n)/d$_a$ = 0 můžeme říci, že:

$$r_c = \frac{2\gamma v_l}{kT\,ln(p/p_0)}\ , \tag{10}$$

$$\Delta G_C = \frac{16\pi\gamma^3 v_l^2}{3[kT\,ln(p/p_0)]^2} = \frac{4}{3}\pi v_c^2 \gamma, \tag{11}$$

kde G_n je volná energie související s utvořením nuklea kulovitého tvaru, p_0 je parciální tlak soustavy nad rovinným rozhraním, *p* je parciální tlak soustavy nad zakřivenou plochou, γ je specifická povrchová energie klastru a v_l je molární objem kapaliny, *k* je Boltzmannova konstanta, *T* je absolutní teplota a *r* je velikost vzniklého nuklea.

Dále je proces nukleace popisován pomocí tzv. stupně nukleace *I*, který udává rychlost tvorby nukleí schopných růstu. Pro přibližné vyjádření veličiny *I* je nutné vzít v úvahu, že růst nukleí bude závislý také na schopnosti atomů se shlukovat (člen exp(-$\Delta G_m/kT$) v rovnici (12)), kde *v* je charakteristická frekvence a ΔG_m je aktivační energie migrace atomů. Spojením všech členů a vztahu *v = kT/h*, kde *h* je Planckova konstanta, lze stupeň nukleace popsat pomocí rovnice [130]:

$$I \approx \frac{NkT}{h} exp\left(\frac{-G_m}{kT}\right) exp\left\{\frac{-16\pi\lambda^3 v_l^2}{3kT[kT\,ln(p/p_0)]^2}\right\}. \tag{12}$$

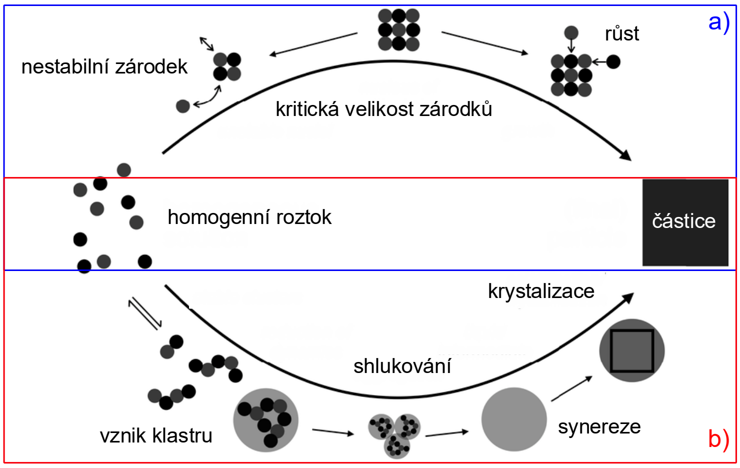

Obr. 18 Schéma procesu precipitace (zpracováno z [131])

Veličina *N* je počet atomů na jednotku objemu dané fáze procházející transformací. Při nukleaci z roztoku (fázová přeměna (*l*) – (*s*)) musíme brát v úvahu hydrataci iontů kovu. Z hydratovaných iontů se tvoří polynukleární ionty, které jsou prekursory pro tvorbu nukleí. Pro efektivní proces je potřeba mít určitou koncentraci těchto iontů (viz koeficient přesycení rovnice (10)). Na základě těchto vztahů lze stupeň nukleace částic z roztoku vyjádřit takto:

$$I \approx \frac{2Nv_S(kT\gamma)^{1/2}}{h} exp\left(\frac{-\Delta G_a}{kT}\right) exp\left(\frac{-16\pi\gamma^3 v_S^2}{3k^3T^3[ln(C_{SS}/C_S)]^2}\right), \qquad (13)$$

kde *N* je počet atomů na jednotku objemu v roztoku, v_s objem molekuly vzniklé pevné fáze, γ je specifická povrchová energie rozhraní (*l*) – (*s*), ΔG_a je aktivační energie potřebná pro migraci iontů, C_{SS} je koncentrace přesycení a C_s je koncentrace iontů v nasyceného roztoku. Proces nukleace (*l*) – (*s*) a zejména jeho rychlost je závislá na koeficientu přesycení *S* [130, 132].

Výše je popsána klasická teorie primární homogenní nukleace z přesycených roztoků (Obr. 18a), ale velkou roli zde hraje i tzv. sekundární nukleace (Obr. 18b), která je spojena z nukleací zárodků z již přítomné krystalické fáze v matečném roztoku (tzv. *Ostwaldovo zrání*, kde menší zárodky se rozpouštějí a přispívají k růstu již vzniklých zárodků).

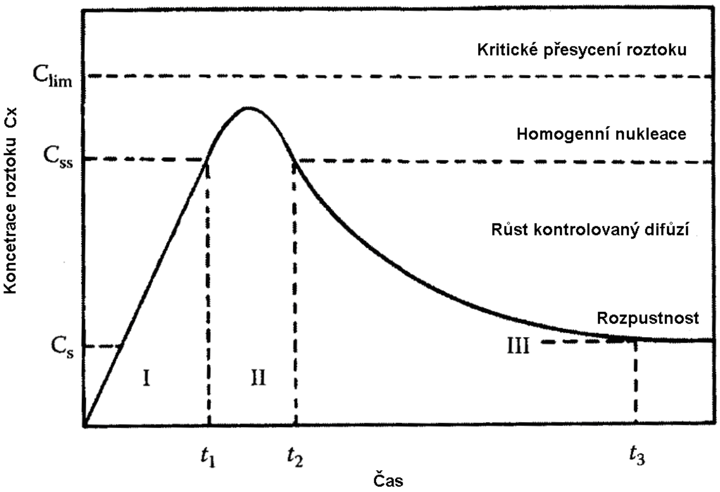

Obr. 19 Lamerův diagram nukleace a růstu (zpracováno z [133])

K procesu růstu dochází již se vznikem prvních nukleí v roztoku. Může být rozdělen a popsán na několika úrovních podle velikosti, z makroskopického hlediska je růst kontrolován hmotnostním transportem a jeho změnami. Lze mluvit i o přenosu tepla v daném roztoku, pokud je teplo krystalizace velmi velké. Pokud jsou fluktuace tepelného gradientu značné, může to způsobit nerovnoměrné shlukování, vznik dendritických struktur či jiných nežádaných struktur. Na mikroskopické úrovni je shlukování přítomno vždy, vzhledem ke klesající rychlosti difuze molekul na povrchu. Kvůli těmto shlukům dochází např. k zachycování rozpouštědla uvnitř struktury krystalu. Na molekulární úrovni difundují růstové jednotky do krystalu a atakují samy sebe, přičemž se začleňují do struktury vznikajícího krystalu nebo se opět vrací do roztoku. Rychlost růstu částice je určena jak difuzí reaktantů směrem k částici, tak i stálým přísunem nových molekul z povrchových reakcí [129]. Lamerův diagram (Obr. 19) zobrazuje tvorbu distribuce velikosti částic v souvislosti s koncentrací nukleí v roztoku.

Výsledná distribuce velikosti částic je tedy dána poměrem mezi jednotlivými růstovými mechanismy (difuzí a povrchovými reakcemi). Jak uvádějí různí autoři [134, 135], difuzně limitovaný růst vede k rovnoměrnému velikostnímu rozdělení částic, zatímco růst řízený pouze povrchovými reakcemi naopak způsobuje zvyšující se nerovnoměrnosti v distribuci velikosti částic s časem [129].

Nukleace a růst C-S-H

Termodynamické modelování řízené syntézy C-S-H gelu pomocí GEMS či μic umožňuje řídit proces tak, aby nukleace probíhala velmi krátkou dobu, kdy všechny zárodky vznikají za obdobných podmínek, což zajistí jejich uniformitu. Dosaženo toho je, pokud je růst přesně definován vytvořením dostatečné kritické koncentrace – přesycenosti, která je následně skokově snížena pod kritickou koncentraci nutnou pro vznik zárodků. Ideální stav je termodynamický model dat na vstupu do reakce → monitoring proměnných během reakce → analytická data (XRD, Raman, FT-IR, XPD, NMR, SEM-EDX, ICP, AAS) + morfologie (SEM, TEM, obrazová analýza) → atomistické numerické simulace.

Syntéza může probíhat dle obecné pucolánová reakce (rovnice (14)):

$$xCa(OH)_{2+}\, ySiO_2 + yH_2O \rightarrow xCaO \cdot ySiO_2 \cdot (x+z)H_2O. \tag{14}$$

Historicky první experimenty simulující nukleaci a růst C-S-H gelu byly založeny na kontrolované hydrataci trikalcium silikátu, která sice ukazuje na zajímavé výsledky, ale čas reakce je počítaný v měsících až rocích. Reakce je pomalá díky nízké rozpustnosti výchozích látek a většinou jsou finální produkty semikrystalické až amorfní. Zvýšení teploty a tlaku může vézt k uspokojivějším výsledkům, tj. rychlejšímu vzniku cílených struktur. Stěžejním faktorem stupně krystalinity C-S-H je teplota, tlak, C/S poměr, typ výchozí látky, atmosféra (tj. uzavřený a otevřený systém). Za pokojových podmínek vznikají fáze C-S-H I a C-S-H II. Nízká reaktivita je dána nejenom teplotou, ale vyšší koncentrací vody v systému nutnou pro dispergaci látek v suspenzi [44, 136]. Pro zvýšení reaktivity systému byly zkoušeny různé metody, zejména mechanochemická syntéza, hydrotermální (dále označováno jako HT) či sol-gel přístup.

3.3.2. Mechanochemická syntéza

Při mechanochemické úpravě se využívá mechanické energie vzniklé během mlecího procesu. Tato energie může iniciovat chemické reakce, které by za laboratorní teploty běžně neprobíhaly. Obecně platí, že mechanochemické reakce vykazují nižší závislost na vnějším tlaku a teplotě a jejich rychlost bývá často o několik řádů vyšší než u reakcí iniciovaných pouhým zvýšením teploty. Proto hovoříme i o aktivaci systému (např. zvýšení rozpustnosti SiO_2). Během mletí může docházet k širokému spektru procesů, včetně rozkladu, oxidace, redukce a syntézy nových sloučenin. Pro experimenty se používá vysokorychlostních planetových či vibračních mlýnů. Práce publikovaná týmem prof. Boldyreva [137] dokonce uvádí, že při definované koncentraci vody dochází lokálně k vzniku hydrotermálních podmínek. Autoři [138-140] při syntéze nanostrukturních C-S-H (afwilit, tobermorit) vycházeli ze silikagelu/aerosilu a hydroxidu/oxidu vápenatého ve vodném prostředí. Produkty byly charakterizovány pomocí MAS NMR, XPS či Ramanovou spektroskopií a výsledky ukázaly na nanokrystalickou fázi C-S-H, ale oproti reálnému C-S-H gelu byly více uspořádané. Nejlepších výsledků ukázala kombinace mechanochemické aktivace následovaná hydrotermální syntézou [141]. Na tyto poznatky jsme navázali v publikacích ***Galvánková, Bartoníčková a kol., Kunovský, Bartoníčková a kol.*** [13, 19] a také v aktuálně běžícím projektu GA 25-16766S.

Pro přípravu C-S-H seedů (tzn. zárodků) (***Kunovský, Bartoníčková a kol.*** [19]), které se využívají jako akcelerátory hydratace, je mechanochemická cesta také možností přípravy definované struktury. Na Obr. 20 je zobrazeno jednoduché schéma syntézy mletím [2]. Tento postup není vhodný pro velkoobjemovou přípravu C-S-H seedů, kvůli dlouhým reakčním časům a ekonomické náročnosti.

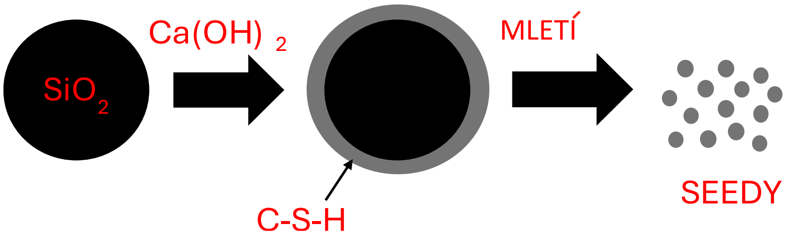

Obr. 20 Schéma syntézy C-S-H seedů pomocí mletí

Na Obr. 21-24 jsou uvedeny výsledky dvoukrokové mechanochemické syntézy s cílem připravit 11 Å tobermorit. V publikacích ***Dlabajová, Bartoníčková a kol.*** [13, 28] byly testovány různé druhy výchozích zdrojů Si (křemenná moučka, mikrosilika či hydrolyzát SiOOH). Reakční směsi byly mlety po dobu 4 h, poté vysušeny a podrobeny dalšímu hydrotermálnímu zpracování s novým matečným roztokem (1-5 d) [13, 28]. Hydrotermální syntéza je rozvedena více v následující kapitole. Na Obr. 21 je zobrazena morfologie po mechanochemické aktivaci sol-gel prekursoru SiOOH a křemenné moučky Dorsilit. Snímky ukazují výrazně odlišnou morfologii částic u sol-gel prekurzoru ve srovnání s referenčním materiálem. Pro srovnání je použita surovina Dorsilit, který se na základě minulých experimentů ukázal, že je nejvhodnější surovinou pro následující hydrotermální syntézu.

Tabulka 5 Specifický měrný povrch a velikost částic po aktivaci

Surovina	***Dorsilit***	***M_Dorsilit***	***SiOOH***	***M_SiOOH***
S_{BET} [m^2/g]	2,0	75,9	6,7	25,2
d_{50} [μm]	5,3	2,6	8,2	2,3
d_{90} [μm]	24,6	9,8	22,5	7,0

Mletím se výrazně zvýšil specifický měrný povrch u obou prekursorů (Tabulka 5). U křemenné moučky bylo mletím získáno až 3 000x většího povrchu, než měla původní surovina, což naznačuje potenciálně vyšší reaktivitu během následující reakce. U sol-gel prekursoru mletím nedocházelo až k tak vysokým změnám ve velikosti částic, ale docházelo s nejvyšší pravděpodobností už k reakci samotné a je vidět povrchová vrstva nových produktů (***Dlabajová, Bartoníčková a kol.***) [28].

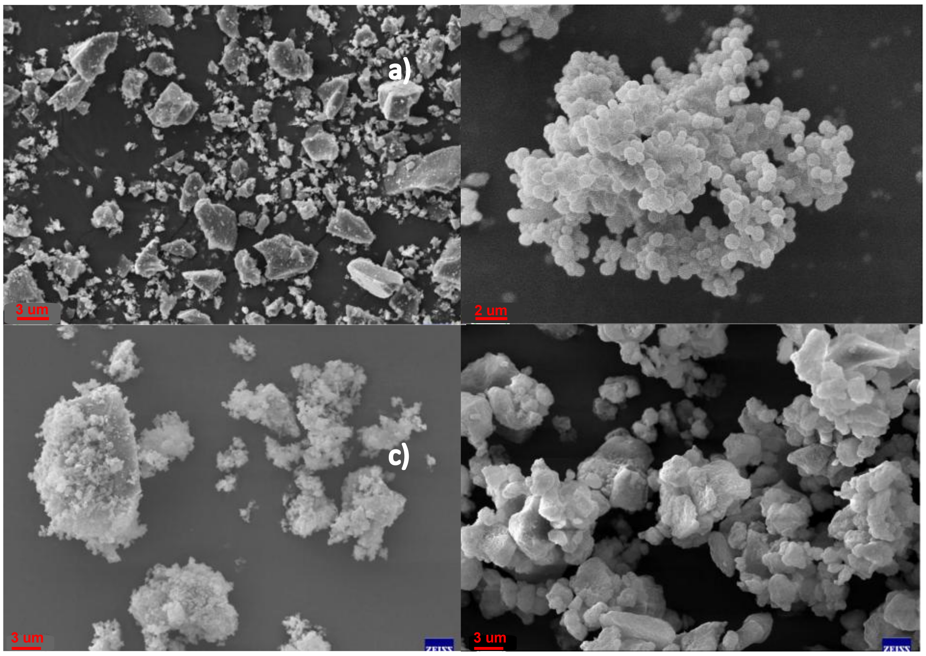

*Obr. 21 Morfologie prekursorů před a po mechanochemické aktivaci:a+c) Dorsilit, b+d) sol-gel SiOOH (převzato z DizP Dlabajová (**Bartoníčková** škol. spec.) [28])*

Po následující HT reakci se však ukázalo, že mletím se sice zvýšil povrch, ale reaktivita zůstala nízká dokonce nižší než u vzorků bez mechanochemické aktivace. Syntézou byl sice připraven cílený tobermorit, ale objevili se i sekundární produkty reakce jako gyrolit či fáze strukturně podobá C-S-H I, ale méně uspořádáná [28, 138, 142].

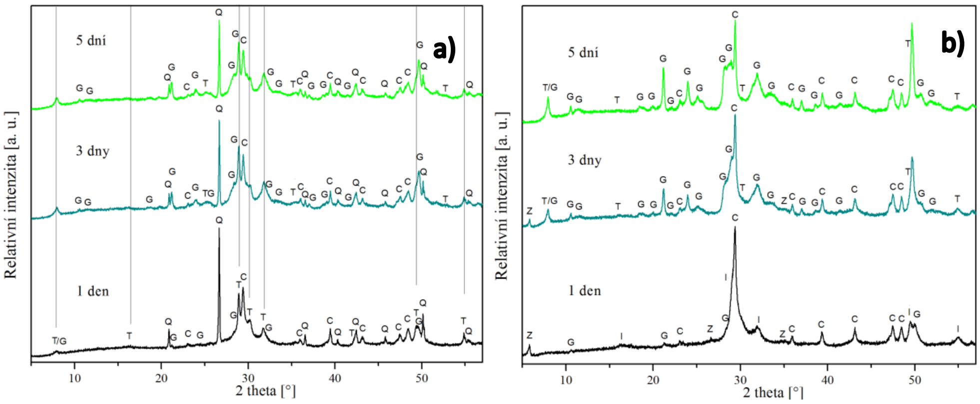

*Obr. 22 Fázové složení C-S-H synt. dvoukrokovou metodou při 180 °C, 3 mg/l: a) Dorsilit b) SiOOH, (C-kalcit, T-tobermorit, G-gyrolit, Z-Z–fáze, I-C–S–H (I)) (převzato z DizP Dlabajová (**Bartoníčková** škol. spec.) [28]*

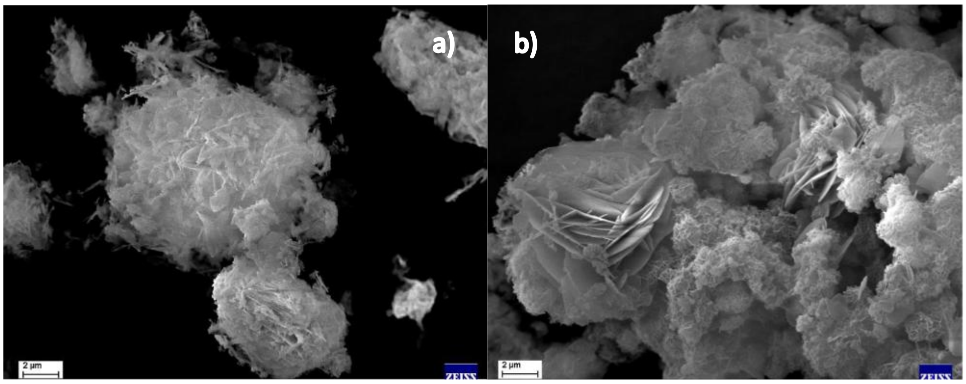

*Obr. 23 Mikrostruktura C-S-H syntetizovaných dvoukrokovou metodou při 180°C: a) Dorsilit, b) SiOOH (převzato z DizP Dlabajová (**Bartoníčková** škol. spec.) [28]*

Na Obr. 23 je vidět mikrostruktura syntézy vycházející z Dorsilitu a SiOOH. V obou případech jsou znatelné lamelární krystaly, které by zdánlivě mohly patřit C-S-H strukturám, avšak analýza prokázala přítomnost karbonatovaných fází, zejména kalcitu. Tento jev je častý a publikovaný [143, 144]. Ačkoliv pro syntézu jev nechtěný, pro cílenou karbonataci velmi výhodný. V projektu VaVal dr. Másilka (GA 24-12423S, autorka byla člen odborného týmu) týkající se cílené karbonatace pucolánových sloučenin je toto téma malou kapitolou výzkumu.

Na Obr. 24 je znatelná nanostruktura vzniklých C-S-H fází v porovnání u různého typu syntéz. Při jednoduché HT reakci vznikaly destičkovité krystaly 11 Å tobermoritu s velikostí do 5 µm společně s neuspořádanou amorfní či semikrystalickou C–S–H fází ve formě drobných lístků, zatímco u dvoukrokového procesu byla struktura nerozeznatelná a nejspíše patřila výše zmíněné neuspořádané fázi C-S-H [28].

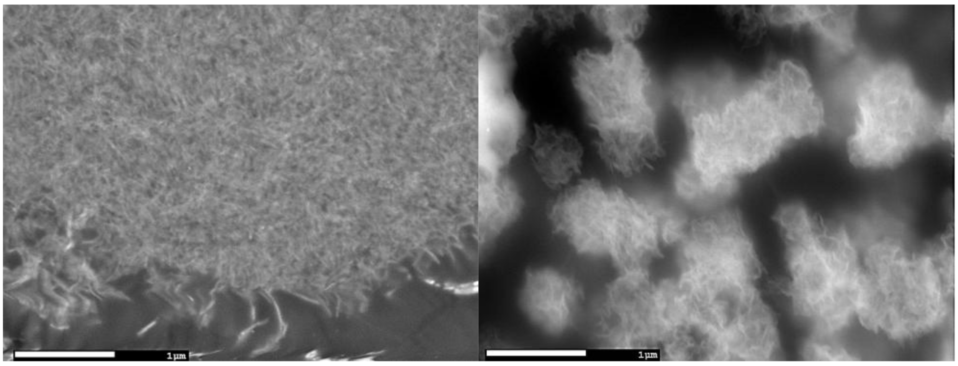

*Obr. 24 SEM snímky iontového výbrusu mikrostruktury nano C-S-H s lamelární strukturou vzniklých při dvoukrokové syntéze z křemenné moučky: a) HT syntéza, b) dvoukroková (převzato z DizP Dlabajová (**Bartoníčková** škol. spec. [28])*

3.3.3. Hydrotermální syntéza

Příprava minerálů za hydrotermálních podmínek se simuluje již od 19. stol., kdy se poprvé podařilo úspěšně připravit krystaly křemene [145]. K syntéze se využívá autoklávovatelných reaktorů, v nichž tlak odpovídá tlaku nasycených par rozpouštědla při dané teplotě. Dle rozpouštědla můžou být reakce hydrotermální (voda) či solvotermální (organické rozpouštědlo) a při subkritických či superkritických teplotách. Kromě změn fyzikálních vlastností dochází při přechodu přes kritický bod také ke změnám kinetiky chemických reakcí. Zvýšená teplota a tlak daná kritickým bodem rozpouštědla během hydrotermálních procesů vedou ke zlepšení rozpustnosti výchozích látek, a tím i ke zvýšení celkové reaktivity systému. Klíčovým rozdílem mezi reakcemi probíhajícími v pevném stavu a hydrotermálními reakcemi je mechanismus tvorby nových fází. Zatímco v pevném stavu je reakční průběh primárně řízen difuzí reaktantů k fázovému rozhraní, v případě hydrotermálních syntéz dochází k reakcím mezi ionty nebo molekulami v matečném roztoku.

Výsledná kinetika těchto procesů je proto určována především rozpustností výchozích látek a jejich aktivitou v roztoku [146, 147]. Můžeme hovořit opět o dvoukrokové syntéze – v prvním kroku dochází k rozpuštění výchozích látek a jejich homogenizaci, v druhém kroku dochází k nukleaci z nasyceného roztoku. Termodynamicky vycházíme ze stejných reakčních mechanismů nukleace a růstu podrobně popsanými již výše, přičemž vyšší teplota a tlak při reakci dovolují posunu reakční rovnováhy směrem k produktům a snížení potřebné aktivační energie vzniku nukleí. Z počátku je hlavním řídícím mechanismem rychlost rozpouštění zrn požitého zdroje křemíku (tj. křemičitanů). Po určité době dochází ke změně hlavního řídícího děje a hlavním řídícím mechanismem se stává jejich difuze skrz vrstvu produktů na povrchu zrn. V poslední fázi reakce dochází k poslední změně mechanismu, kdy je hlavním řídícím dějem reakce zbylého SiO_2 se vzniklými C–S–H fázemi [148-150]. Reakční mechanismus vychází z typu křemičitého zdroje a jeho granulometrie. Díky postupnému rozpuštění se během reakce mění rozpustnosti a tím i C/S poměr připravených látek (viz rovnice (15) [13].

$$Ca(OH)_2 + SiO_2 \xrightarrow{H_2O} C-S-H\ (II) + \alpha - C_2S\ (hydr.) \rightarrow C-S-H\ (I) \rightarrow tobermorit \rightarrow xonotlit \qquad (15)$$

Primárně vzniklý C-S-H II reaguje s dalšími rozpuštěnými ionty Si z roztoku za vzniku C-S-H I (C/S 1,25). C-S-H II dále reaguje s ionty Ca^{2+} a C/S poměr produktu klesne na 0,8, který je potřebný pro krystalizaci tobermoritu. Pokud C/S poměr klesne ještě níže může dojít k transformaci produktu na gyrolit, což není termodynamicky stabilní fáze a metastabilní tobermorit spíše přechází do formy xonotlitu [151-153].

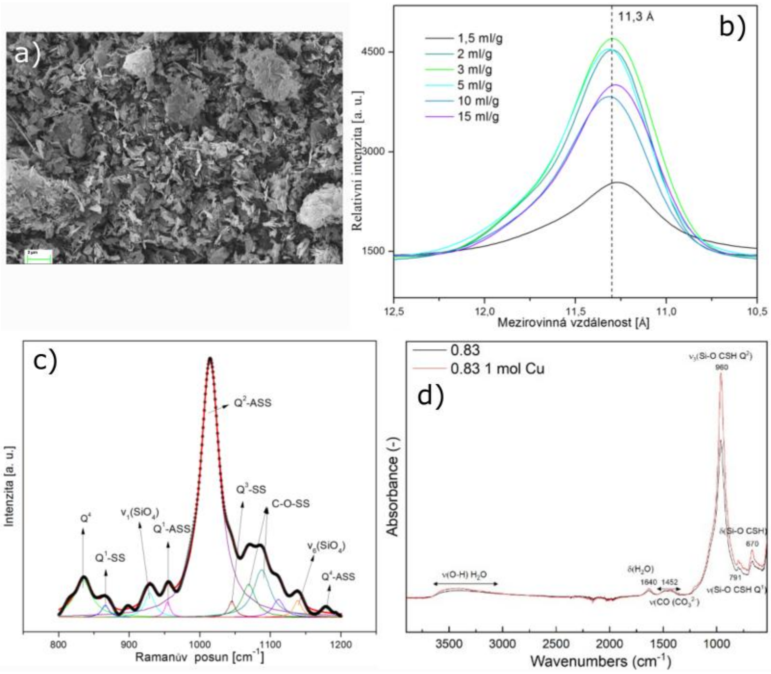

*Obr. 25 Analýza produkt HT syntézy z Dorsilitu - v/p 0,3, 1 - 3 d: a) SEM, b) XRD, c) Raman, d) FT-IR (převzato z DizP Dlabajová (Bartoníčková škol. spec. [28]) a publikace (**Galvánková, Bartoníčková a kol.** [13])*

Důležitým parametrem kromě typu výchozího zdroje a jeho granulometrie je množství vody v systému (v/p poměr = voda/prášek). V literatuře je vliv vody na přípravu tobermoritu popsán různorodě, někdo vychází z faktu, že menší velikost částic SiO_2 má vliv na v/p poměr vody a urychluje vznik tobermoritu [150], zatímco jiní uvádějí, že pod v/p poměr 1,7 tobermorit nevzniká a nad poměr 1,7 už koncentrace vody nemá na vznik vliv [154]. Experimenty *(**Dlabajová, Bartoníčková a kol.*** [13]) vycházející z jednokrokové hydrotermální syntézy a různých druhů zdrojů křemene ukázaly, že použití velmi jemné křemenné moučky Dorsilit a HT reakce podobu 1 dne již stačí pro syntézu tobermoritu s viditelnou lamelární/destičkovitou mikrostrukturou (viz Obr. 25). Provedené analýzy prokázaly krystalickou strukturu odpovídající 11 Å tobermoritu [13, 28]. Pomocí Ramanovy spektroskopie a FT-IR analýzy byla analyzována přítomnost silikátových jednotek Q^n. Obě analýzy potvrdily majoritu Q^2 uspořádání, ale také značnou míru karbonatace povrchu částic, která je bohužel nežádoucím dějem během syntézy i během dalšího uchovávání produktu (***Dlabajová*** [28], ***Kunovský, Bartoníčková a kol.*** [19]*).*

3.3.4. Sol-gel syntéza C-S-H

V kapitolách výše byl již sol-gel proces diskutován z pohledu kondenzace silikátových řetězců při vzniku C-S-H systému. V minulosti byly publikovány články věnující se sol-gel syntéze oxidů alkoxidovým mechanismem na bázi titanu či lanthanoidů (***Bruzl, Bartoníčková a kol., Cihlář, Bartoníčková a kol., Částková, Bartoníčková a kol., Bartoníčková a kol.*** [129, 155-158]). Tyto publikace nejsou součástí komentovaného souhrnu, ale jsou důležitým milníkem, neboť jsou cenným zdrojem zkušeností pro následující syntézy C-S-H struktur.

Cílená syntéza probíhá z nevodných prekursorů a jejich řízenou hydrolýzou a polykondenzací (rovnice 16 a 17) [91], tzn. použití organického alkoxidu křemíku (např. tetraethylorthosilikát, $Si(OC_2H_5)_4$ -TEOS [159]):

$$Si(OEt)_4 + nH_2O \xrightarrow{hydrolýza/esterifikace} Si(OEt)_{4-n}(OH)_n + nEtOH \tag{16}$$

$$2Si(OEt)_{4-n}(OH)_n \xrightarrow{kondenzace} (OEt)_{4-n} \boxed{-Si-O-Si-} (OEt)_{4-n} + nH_2O \tag{17}$$

Hydrolýza probíhá mechanismem nukleofilní substituce, která je závislá na pH systému. Velmi často je katalyzovaná, při bazické katalýze (OH^-) dochází k nukleofilní adici hydroxylového iontu na silikátový řetězec, ve kterém je Si kladně nabit, a zvyšuje tím jeho koordinační číslo. Dalším krokem je přenos náboje v rámci vzniklého přechodného stavu vedoucí k oddělení alkoxidového aniontu, který dále reaguje s vodou v matečném roztoku. Při kyselé katalýze dochází k protonaci kyslíkového atomu alkoxidového ligandu vedoucí ke vzniku reaktivního kationtu. Vytvořený kation následně reaguje s vodou a stejně jako při bazické katalýze je vytvořena Si–OH vazba a je uvolněn alkohol. Kyselá katalýza urychluje hydrolýzu, zatímco při bazické katalýze je reakce sice pomalejší, ale její průběh lze lépe řídit [91, 160]. Molární poměr hydrolýzy je poměr počtu molů křemíku ku počtu molů vody. Vzniká tedy komplex o obecném vzorci $[MO_NH_{2N-h}]^{(z-h)}$. Povaha komplexu závisí na náboji *z*, koordinačním čísle *N*, elektronegativitě χ_M^0 kovu (křemíku) a na pH matečného roztoku. Vliv pH na náboj *Z* a existenční oblasti výskytu ligandů OH^-, O^{2-}, H_2O jsou uvedeny na Obr. 26. V Tabulka 6 jsou uvedeny různé katalyzátory, jejich koncentrace a gelační časy. Je vidět, že rozdílné pH i iont radikálně mění poměr hydrolýzy/kondenzace systému a čas gelace.

Tabulka 6 Vliv bazických a kyselých katalyzátorů na hydrolýzu Si(OR)

Katalyzátor	Koncentrace (mol/TEOS)	pH na počátku reakce	Čas gelace (h)
HF	0,05	1,90	12
HCl	0,05	0,05	92
HNO_3	0,05	0,05	100
H_2SO_4	0,05	0,05	106
HOAc	0,05	3,70	72
NH_4OH	0,05	9,95	107
bez	-	5	1000

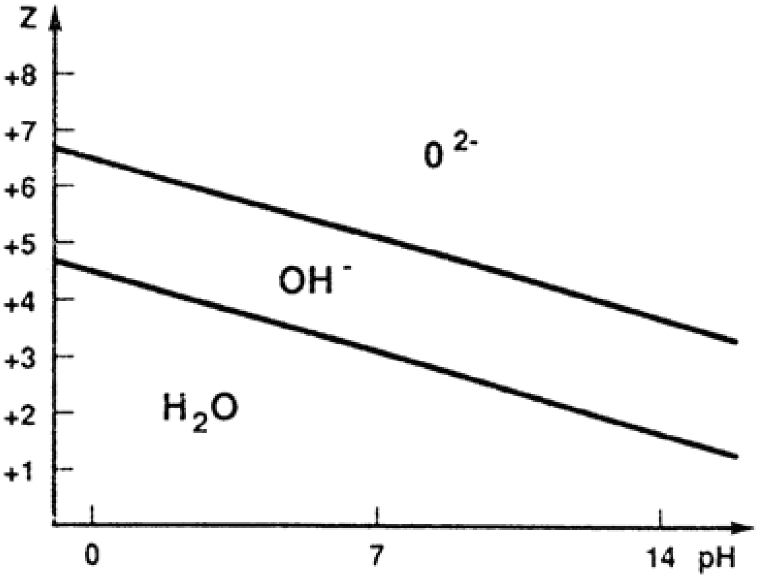

Obr. 26 Závislost náboje Z na pH, která určuje tři existenční oblasti výskytu ligandů („aqua", „hydroxo" a „oxo") (zpracováno z [32])

Současně s hydrolýzou probíhá v systému proces *polykondenzace*. Jedná se o komplexní vícestupňový proces, pro který jsou v literatuře popsány tři základní mechanismy, přičemž dominantní reakční cesta závisí na konkrétních podmínkách prostředí. Při *alkoxolaci a oxolaci* dochází ke vzniku oxo-můstku mezi dvěma atomy křemíku. Oba mechanismy probíhají obdobně: v případě *alkoxolace* je po substituci eliminována molekula alkoholu, zatímco u *oxolace* dochází k eliminaci molekuly vody. Pokud nejsou všechna koordinační místa atomu křemíku obsazena, může nastat i třetí typ kondenzační reakce – *olace*. Tato reakce vede k vytvoření hydroxo-můstku mezi atomy křemíku a je doprovázena eliminací molekuly rozpouštědla (vody nebo alkoholu). Všechny výše uvedené reakce jsou katalyzovány protony a podobně jako u hydrolýzy platí, že za zásaditých podmínek dochází ke zpomalení jejich průběhu [91, 159, 160]. V kyselém prostředí (pH < 1,5) je rychlost hydrolýzy dominantnější než kondenzace, která je ovlivněna i délkou vznikajícího silikátového řetězce. Proto v kyselém prostředí vznikají nejdříve jednoduché řetězce, které se rozvětvují až časem během stárnutí. Obecně platí, že rychlost kondenzačních reakcí je nejnižší v rozmezí pH 2–3, což odpovídá izoelektrickému bodu kyseliny křemičité. Při pH > 3 roste rychlost hydrolýzy a výsledkem je zesíťovaný gel.

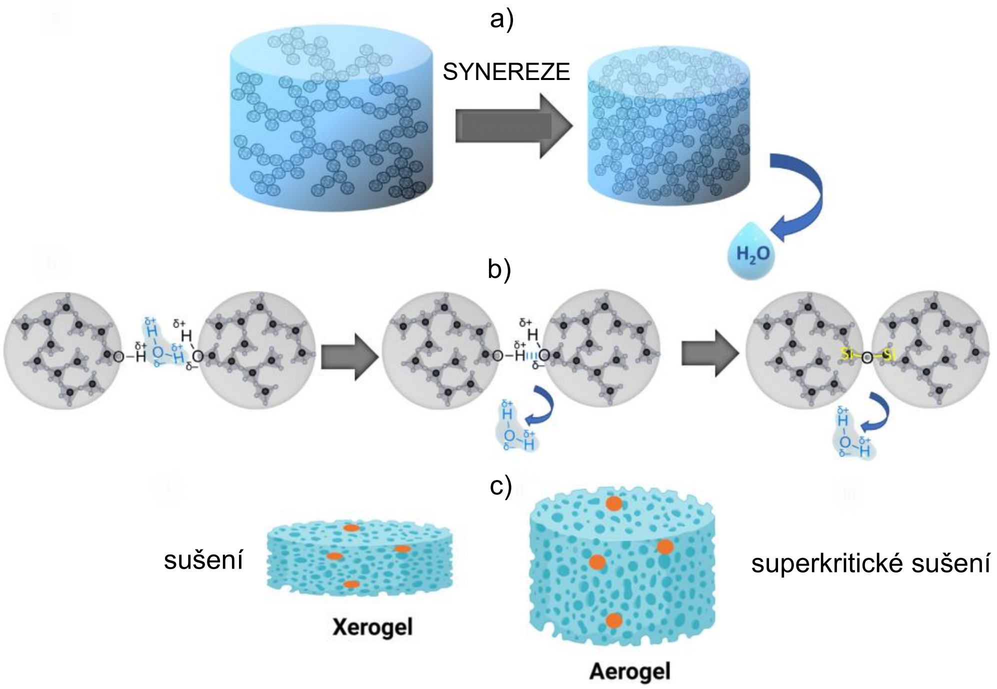

Obr. 27 Schéma synereze a vznik xero- či aero-gelu (zpracováno z [95, 161]

Struktura a morfologie výsledného gelu však nejsou ovlivňovány pouze typem katalýzy a pH reakčního prostředí, ale i celou řadou dalších parametrů. Mezi klíčové faktory patří zejména: chemická struktura prekurzoru, hydrolyzní poměr (tj. poměr vody k reaktantu), koncentrace katalyzátoru, typ použitého rozpouštědla a v neposlední řadě také teplota reakce. Tyto parametry určují nejen kinetiku, ale i mechanismus růstu a výsledné vlastnosti vzniklého silikátového gelu [159, 160]. Proces sol-gel není ukončen vznikem gelu, ale pokračuje dále. S časem dochází k synerezi gelu, již zmíněné i u popisu koloidního modelu CM II. Dochází k přeuspořádávání struktury a pokračování v polykondenzačních reakcích, vlivem toho se zvyšuje soudržnost gelu a snižuje se porozita. Gel se „vysušuje“ a po odstranění kapaliny z pórů vzniká xerogel či aerogel v závislosti na typu sušení (viz Obr. 27). Pro přípravu C-S-H seedů se sol-gel proces jeví jako vhodná technika, limitací je cena vstupních chemikálií a taktéž reprodukovatelností vlastností při velkoobjemová produkci. Touto technikou lze získat amorfní gel se strukturou obdobnou CSH I a II. V publikaci ***Kunovský, Bartoníčková a kol.*** [19] se vycházelo z alkoxidového sol-gel mechanismu pro přípravu amorfního tobermoritu.

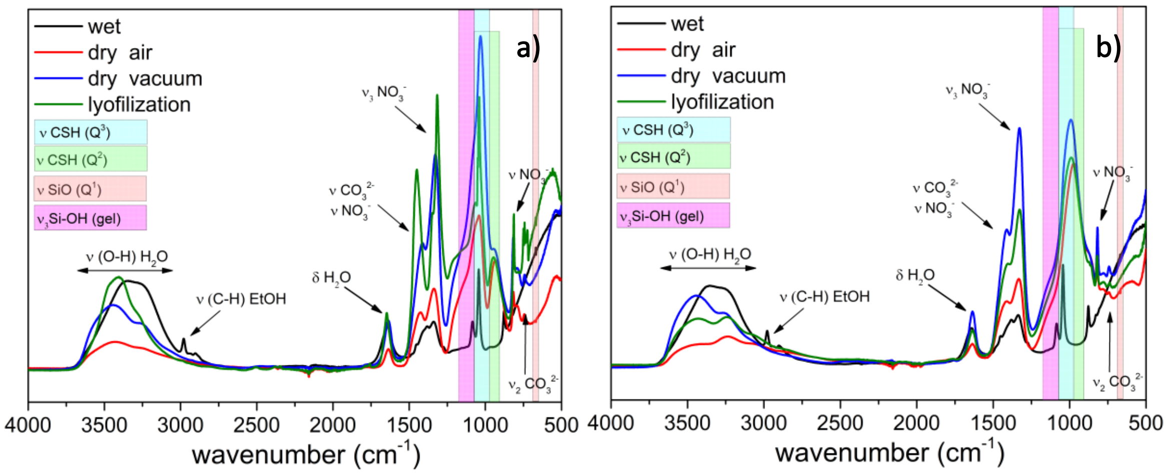

Obr. 28 FT-IR analýza gelů připravených hydrolýzou z TEOS: a) pH 3, b) pH 12 (převzato z ***Kunovský, Bartoníčková a kol.****[19])*

Na Obr. 28 je uvedena FT-IR analýza gelu připraveného alkoxidovou cestou hydrolýzy TEOSu v kyselém a zásaditém prostředí (pH upraveno pomocí HNO_3, NH_4OH) ([19]), kdy byly připraveny struktury s rozdílným Q^n složením dle počátečního pH matečného roztoku. Majoritou byla struktura s Q^3 a Q^2 silikátovými jednotkami a minoritně nezreagované výchozí látky. Dále na Obr. 29 jsou uvedeny výsledky dvoukrokové hydrotermální syntézy, kde prvním krokem byla řízená hydrolýza TEOSu v zásaditém prostředí bez (a) a v (b) přítomnosti dusičnanu vápenatého. Dle XRD analýzy se ukazuje na směs krystalických fází tobermorit, xonotlit a gyrolit. Tyto výsledky korelují s dříve publikovanými daty, kdy se zvyšujícím se povrchem amorfního prekursoru se snižuje rychlost krystalizace tobermoritu a vznikají i jiné analogy s různým C/S poměrem [162, 163].

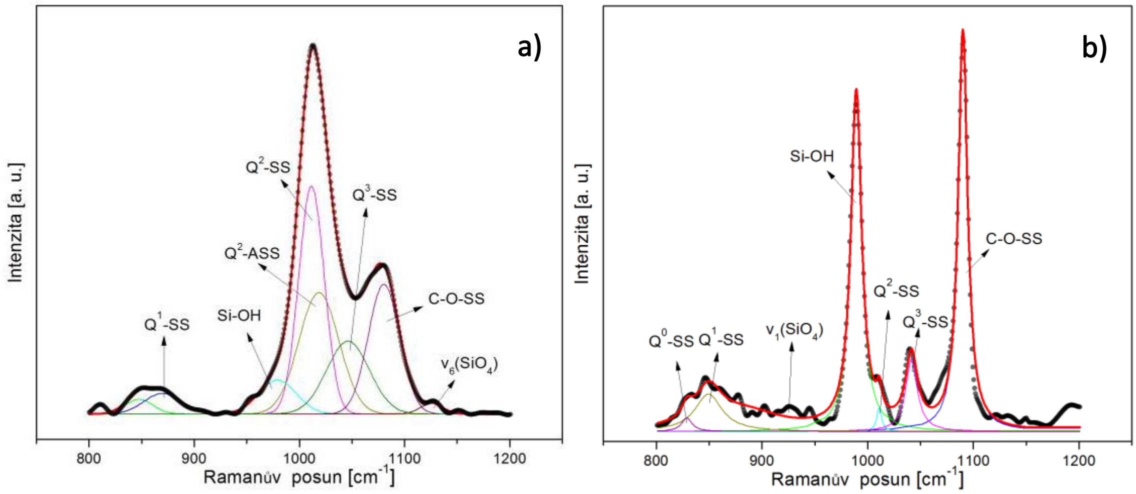

Obr. 29 Analýza silikátových jednotek Q^n pomocí Ramanovy spektroskopie: a) HT syntéza z hydrolyzátu SiOOH, b) HT syntéza z hydrolyzátu směsného Ca-SiOOH (převzato z Diz.D Dlabajová (školitel spec. Bartoníčková [28])

Jak lze vidět z uvedených výsledků (publikace ***Kunovský, Bartoníčková a kol.*** [19]), jsou analýzy pomocí FT-IR a Ramanovou spektroskopií dostatečných nástrojem pro hodnocení stupně polymerizovatelnosti systému. Pro potvrzení byla udělána i XPS analýza pro určení vazností – Ca, Si a O. Na Obr. 30 jsou zobrazeny vaznosti jednotlivých prvků vzorku, který byl pro potřebu analýzy lyofilizován. Je zde ukázáno, že metoda lyofilizace zcela zpolykondezuje Si řetězce a struktura již neodpovídá stavu gelu připraveného syntézou [19].

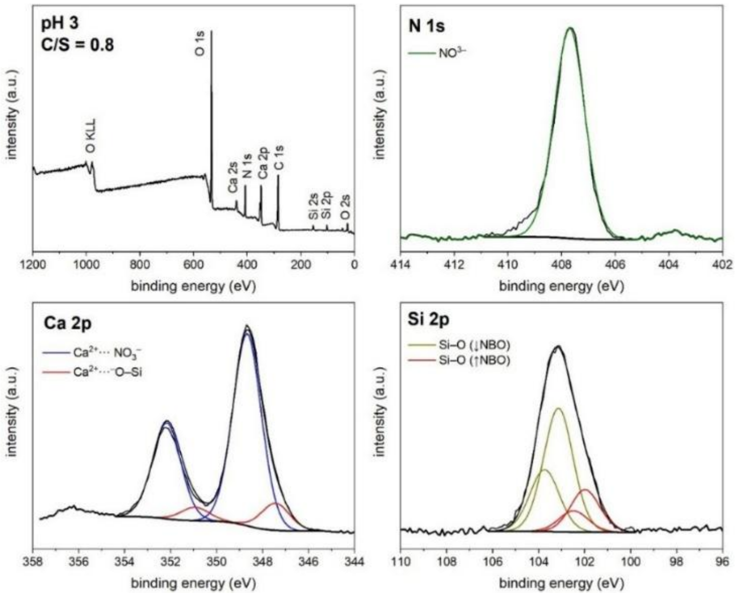

*Obr. 30 XPS analýza syntézy amorfního C-S-H alkoxidovou cestou při pH 3 (převzato z **Kunovský, Bartoníčková a kol.***[19])[10]

---

[10] NBO – „non-bridging oxygen“, který odpovídá tzv. párovému Si

3.3.5. Precipitační metoda syntéza C-S-H

Precipitační metoda, ačkoliv není žádnou novinkou má velký potenciál pro přípravu C-S-H struktur i ve velkoobjemovém měřítku, a tedy i využitelnosti jako *„seedovacího aditiva“* pro akceleraci hydratace silikátů a aluminosilikátů (aktuální téma projektu GA 25-16766S*)*. Výchozími surovinami jsou metakřemičitan sodný jako zdroj Si a dusičnan či chlorid vápenatý jako zdroj Ca. Reakční mechanismus precipitace byl v literatuře nazván jako *„double decomposition method“* [85], kdy C-S-H gel je precipitován z přesycených roztoku metakřemičitanu sodného (Na_2SiO_3) a dusičnanu vápenatého [123, 164]. Promytím produktu vzniká C-S-H gel o struktuře podobné C-S-H I a II. Pro přípravu čistých struktur neovlivněných rozkladem či karbonatací je využíváno mísících reaktorů, které jsou pod inertní atmosférou (Ar, N_2) (viz aparatura na Obr. 31 vyvinutá dr. Kumarem [123] či Harrisem [164] jejíž analogie byla použita i pro naše experimenty). Monitoring pH, vodivosti a teploty dává možnost sledovat reakci během syntézy a v budoucnu doplní kinetické křivky při sledování syntézy při různých teplotách.

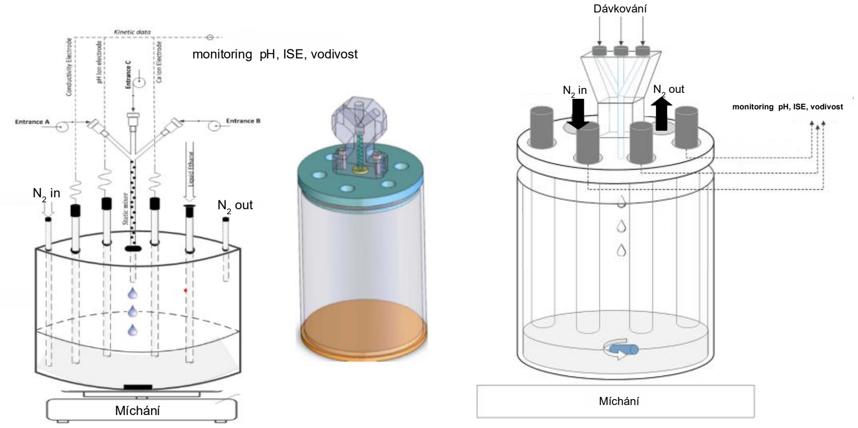

Obr. 31 Schéma reaktoru pro precipitační syntézy (zpracováno z [123] a [164])

Křemík v roztoku zhydrolyzovaného metakřemičitanu sodného je ve formě $SiO_2(OH)_2^{2-}$ (viz rovnice (6) a Obr. 16) stabilní díky vysokému pH (upraveného alkalickými hydroxidy na hodnotu 11–12). Vliv použitých typů hydroxidů je znatelný na nano struktuře připravených C-S-H, při použití KOH či NaOH a Ca/Si poměru 1 jsou výsledkem globule zatímco při Ca/Si = 2 destičky [123]. Dále byla prokázána i možná substituce Ca alkalickým kovem, a to u struktur s poměrem Ca/Si pod 1,25. V práci ***Kunovský, Bartoníčková* a kol.** [19] byly syntetizovány gely s Ca/Si poměrem 1,27 precipitační metodou, výchozími látkami byly metakřemičitan sodný a dusičnan vápenatý ve vodném roztoku o pH = 3 (HNO_3) a 12 (NH_4OH). Syntéza nebyla provedena v inertním prostředí, což se projevilo ve znatelné karbonataci připraveného gelu. Silikátové jednotky odpovídají Q^2 konfiguraci. Kvůli nedostatečnému promytí jsou viditelná i rezidua dusičnanů (Obr. 32).

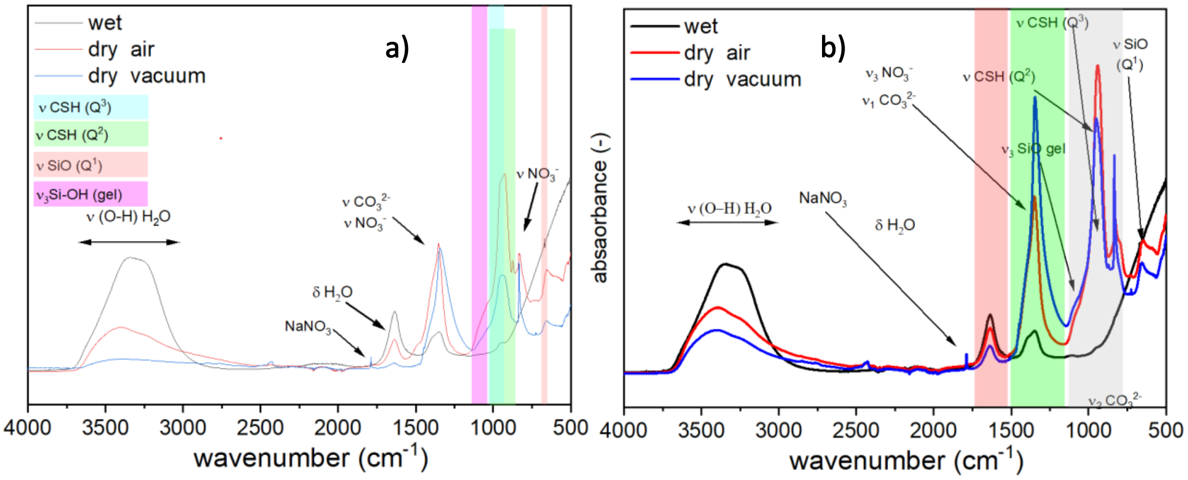

*Obr. 32 FT-IR analýza gelů připravených precipitační metodou a) pH 3 a b) pH 12 (převzato z **Kunovský, Bartoníčková a kol.** [19])*

4. Substituce C-S-H fází

V úvodní části bylo uvedeno, že cement obsahuje kromě silikátových slínkových minerálů (C_3S a C_2S) i ty aluminátové (C_3A, C_4AF). Během hydratace se rozpuštěný Al v pórovém roztoku může zabudovat do vznikajících struktur C-S-H, čímž vzniká systém CaO-yAl_2O_3-SiO_2-H_2O (neboli ve zjednodušeném zápisu C-A-S-H) i v čistém cementu bez příměsí. Typický poměr Al/Si se zde pohybuje kolem 0,05 až 0,1, což umožňuje inkorporaci až 5 at. % Al [4, 165, 166]. Na Obr. 33 je zobrazen fázový diagram systému hydrátů Ca-Si-Al se složením silikátů a aluminosilikátů (cementu a možné příměsi).

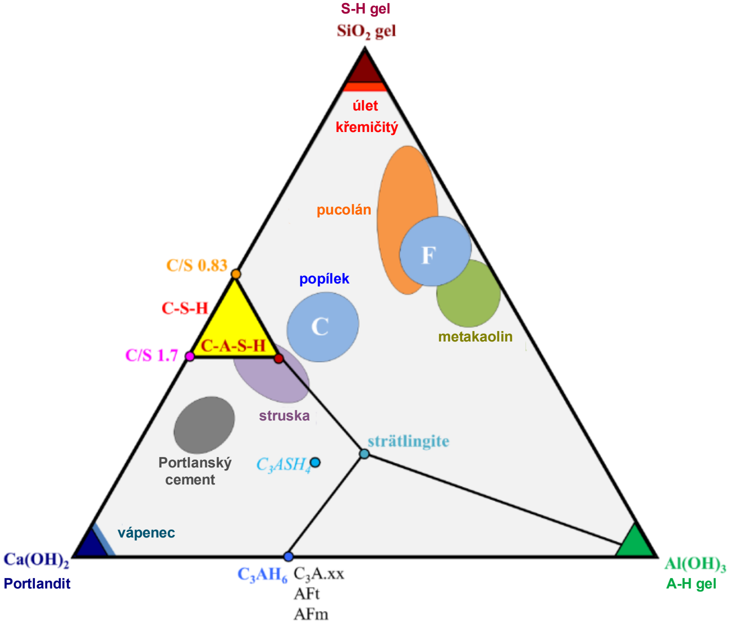

Obr. 33 Ternární fázový diagram v soustavě Ca-Si-Al (zpracováno z [67] a [4]

Výroba portlandského cementu zodpovídá za 8 % globálních emisí CO_2. Pro snížení emisí CO_2 je zásadní projít celý „*value-chain*“ řetezec od cementu, který začíná výrobou portlandského slínku, tedy obsahem slínku v pojivech a maltovinách obecně, přes přípravu betonu či tvárnic a dopravu až po konkrétní aplikaci. Při výrobě slínku je palivo zodpovědné za cca 40 % a rozklad vápence za cca 60 % souvisejících emisí CO_2. Snížení uhlíkové stopy výroby cementu má mnoho řešení. Jedním z nich je náhrada obsahu slínku v cementu použitím tzv. “*supplementary cementitious materials*” – SCM. Tradiční SCM pro směsné cementy jsou popílek, vysokopecní struska či metakaolin, které mají aluminosilikátové složení a vykazují dostatečné pucolánové vlastnosti. C-A-S-H může tedy vznikat nejenom minoritně v cementu čistém (při Al/Si poměru nižším než 0,1), ale zejména ve směsných cementech třídy CEM III, IV a V daných normou ČSN EN 197-1 [4]. Náhrada určitého množství cementu popílkem vede ke snížení množství portlanditu (CH), zvýšení obsahu C-S-H fáze s nižším poměrem Ca/Si a k nárůstu množství AFm fází, jelikož popílek často obsahuje vysoký podíl Al_2O_3. Zato při použití vysokopecní strusky má její příměs zpočátku jen malý vliv na množství portlanditu (ve srovnání s čistým slínkem), a to až do vyšších úrovní náhrady. Přesto však dochází k tvorbě většího množství C-S-H fáze s nižším poměrem Ca/Si, aby byl kompenzován nižší celkový poměr Ca/Si v celkovém systému [4]. Jak bylo zmíněno v předešlých kapitolách C-S-H při hydrataci Portlandského cementu se C/S poměr pohybuje kolem 1,5–1,9. V případě, že nahrazujeme cement za SCM o vyšší koncentraci Si docílíme, tím k vzniku C-S-H s nižším C/S poměrem a defektní strukturou podobnou tobermoritu. Se snižujícím se C/S v C-S-H se také snižuje jeho „MCL“. Vznik C-S-H s nízkým poměrem C/S vede ke zvýšené možnosti inkorporace Al^{3+} iontů do struktury [4, 85].

Možný termodynamický model mísení cementů s popílkem a struskou (viz Obr. 34) uvedla prof. Lothenbach ve své práci, kdy modelovali pomocí softwaru GEMS složení hydratačních produktů v závislosti na míře náhrady OPC[11] [4]. Využití popílků jako náhrady portladského cementu bylo téma diplomové práce autorky vedené prof. Brandštetrem, který s prof. Krivenkem patřil k průkopníkům geopolymerů a alkalicky aktivovaných materiálů v minulém století. Současně se na toto téma váže i dlouhodobá spolupráce s firmou ČEZ EP, se kterou bylo vyvinuto několik metod využití deponovaných popílků, jak vysokoteplotních i ložových, tak po SNCR procesem spojených s DENOx technologiemi.

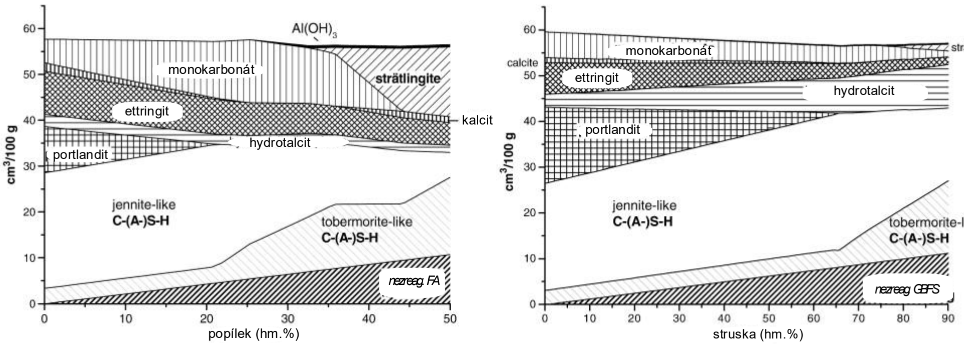

Obr. 34 Termodynamický model složení hydratovaného Portlandského cementu s příměsemi a) popílek (FA), b) vysokopecní struska (GBFS) (zpracováno z[4])

4.1.Substituované C-(A)-S-H fáze ve směsných cementech

První zmínky o možnosti modifikace struktury tobermoritu zabudováním jiných atomů kovů byly již v polovině 20. stol., kdy experimenty prof. Kalouska a potvrzeny XRD a NMR daty publikovanými Diamondem a Komarnenim [167-169]. Domněnka, že Al^{3+} může být vázáno substitučně v „*dreierketten*“ silikátovém řetězce, byla poté potvrzena mnohými autory [170, 171]. Obecně můžeme hovořit o třech možnostech, jak lze vázat kationty kovů – již zmíněnou substitucí (Obr. 35b -3), komplexací na povrchu řetězce (Obr. 35b -1) či v mezivrstvě (Obr. 35b -2). Možnosti inkorporace cizích iontů je využíváno k jejich imobilizaci, zejména se jedná o těžké kovy (Cu, Ni, Co aj.) či radiokativní prvky z odpadních elektrárenských vod (Cs, Cu, Ba, Ra, Sr, Se, Tc aj.) [172-174].

Speciální pozornost je věnována hliníku, hliník se ve struktuře neváže na všechna výše zmíněná místa, ale pouze ve formě tetraedru AlO_4. Na Obr. 35b je zobrazen model struktury s místy, kde lze Al inkorporovat do struktury v mezivrstvě formou AlO_4 tetraedru s vazbou na Q^3 a Q^2_p [38, 169, 175] silikátový řetězec. Substituce je možná pouze do molárního poměru A/(A+S) = 1,6, názorně je oblast kritických koncentrací zobrazena ve fázovém diagramu uvedeném na Obr. 33. Při substituci může docházet ke zvětšení mezivrstevného prostoru (např. u 11Å tobermoritu až na 11,5Å) a taktéž „MCL“ silikátového řetězce ([176, 177]. Substituce současně vede ke snížení množství strukturních defektů a zvyšuje stupeň polymerizace silikátového řetězce (nárůst Q^2) [175, 178]. Možnou substituci umožňuje i souvislost mezi molárními poměry Si/Ca a Al/Ca [179, 180]:

$$\frac{Si}{Ca} = 0{,}428 + 2{,}366\left(\frac{Al}{Si}\right)\cdot r^2 = 0{,}28 \tag{18}$$

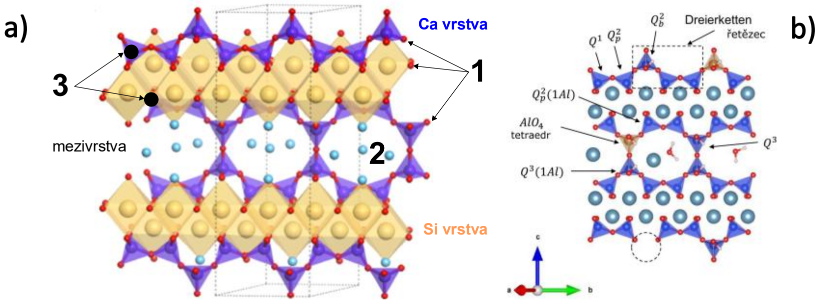

Obr. 35 Schéma teoretického začlenění jiných atomů kovů do struktury 11 Å tobermoritu (zpracováno z [58]) a b) model uspořádání C-A-S-H v propojeném tobermoritovém systémů (zpracováno z [181])

---

[11] OPC = „ordinary portland cement“, světově používáná zkratka pro portlandský cement

Se vznikem C-A-S-H se snižuje koncentrace současně vznikajícího CH [125; 148], a také se za nízkých poměrech Si/Ca a Al/Ca mění morfologie C-A-S-H struktury z destičkovité na jehličkovitou [125]. Tématem diskuse stále je, kde přesně v řetězci je opravdu kation Al^{3+} umístěn v přirozeně hydratovaných systémech.

Tématice sekundárních surovin a směsných cementů jsou věnovány tyto publikace, kde se byly studovány různé druhy příměsí jako vysokopecní struska ***Kuzielové,*** ***Bartoníčkové a kol.*** [16], popílek ***Hanisková, Bartoníčková a kol. a Kalousová, Bartoníčková a kol.*** [14, 15], aktivovaná alumina ***Novotný, Bartoníčková a kol.*** [18] nebo vápenec ***Novotný, Bartoníčková a kol.*** [17]. Např. v práci ***Kuzielové, Bartoníčkové a kol***. [16] je diskutován vliv morfologie příměsí vysokopecní strusky, křemičitých úletů či metakaolinu na vývoj porozity C-(A)-S-H gelu. Směs příměsi s OPC vedla k širšímu rozložení distribuce částic díky vyššímu stupni aglomerace jemnějších podílů (tj. křemičité úlety). U testovaných vzorků byl zaznamenám výskyt pórů (Obr. 36) menších než 4,5 nm odpovídajících gelovým pórům v C-(A)-S-H struktuře, který ale s narůstajícím časem klesal.

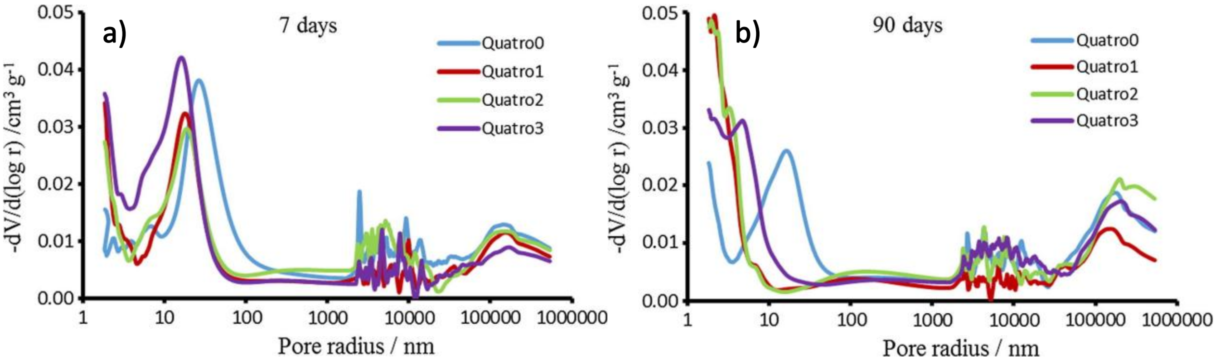

*Obr. 36 Distribuce velikosti pórů vyzrálých po 7 a 90 dnech převzato z **Kuzielová, Bartoníčková a kol.** [16])*

Na základě mechanických vlastností byla zhodnocena i pucolánová aktivita (pomocí koeficientu pucolánové aktivity vypočteného z mechanických vlastností) směsných cementů v čase. Je zde korelace s výskytem hydratačních fází na bázi C-S-H, C-(A)-S-H.

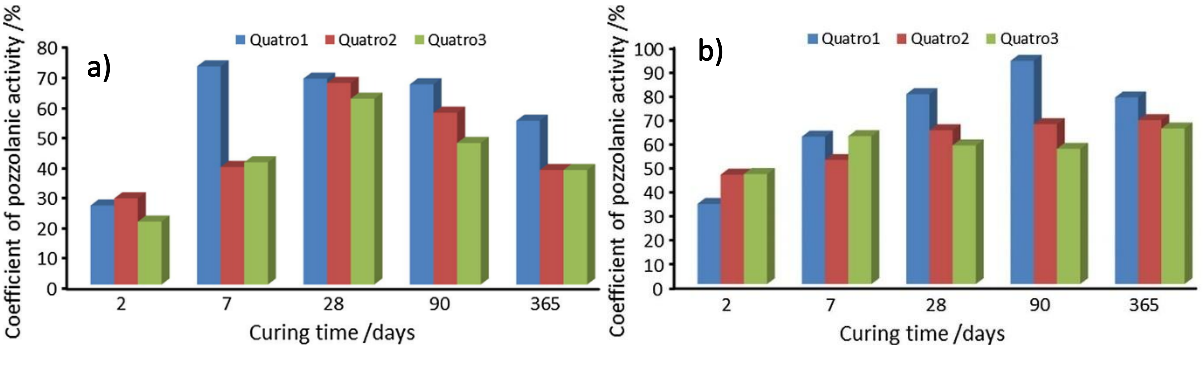

*Obr. 37 Koeficient pucolánové aktivity po 2, 5, 28, 90 a 365 dnech zrání: a) pevnost v tlaku, b) pevnost v ohybu (převzato z **Kuzielová, Bartoníčková a kol.** [16])*

4.2. C-A-S-H v alkalicky aktivovaných materiálech

Alkalicky aktivované materiály (AAM) tvoří širokou skupinu anorganických pojiv, které vznikají reakcí aluminosilikátových prekurzorů s alkalickými aktivátory, typicky hydroxidy nebo vodními skly alkalických kovů. Výsledkem těchto reakcí je tvorba hydratačních gelů, nejčastěji typu C–A–S–H (v systémech bohatých na vápník) nebo N–A–S–H (v systémech s nízkým obsahem Ca). Specifickou podmnožinou AAM jsou geopolymery [182], které vznikají výhradně z metakaolinu a alkalického aktivátoru, přičemž jejich struktura je tvořena prostorově zesíťovanou aluminosilikátovou kostrou s převahou $(SiO_4)^{4-}$ tetraedrů typu Q^4. V některých systémech dochází ke vzniku hybridních gelů typu C(N)–A–S–H, které kombinují vlastnosti obou výše uvedených typů a vznikají zejména při aktivaci směsných prekurzorů s proměnlivým obsahem Ca a alkalických kovů. Struktura C–A–S–H gelu vznikajícího v AAM je analogická C–S–H gelu známému z hydratace portlandského cementu, avšak s vyšším stupněm polymerizace silikátových řetězců a možností inkorporace hliníku do tetraedrických pozic. Reakcí alkálie s aluminosilikáty se do roztoku postupně rozpouštějí reaktivních formy SiO_2 a Al_2O_3, které zpolykondenzují do 3D sítě vzájemně propojenými tetraedry $(SiO_4)^{4-}$ (majoritně v Q^4) a AlO_4 (m_{Al}, m = 0,1–4) s alkalickými ionty (Na^+, K^+, Li^+), které kompenzují negativní náboj $(AlO_4)^{5-}$, který je s inkorporací Al spojený. V přítomností alkalických iontů v systému ochuzeném o Ca je preferovanější forma gelu N(K)-A-S-H než zmiňovaný C-A-S-H [183]. Tato kapitola se zaměřuje především na C-A-S-H gely vznikající v AAM bohatých na vápník, zejména při aktivaci vysokopecní strusky.

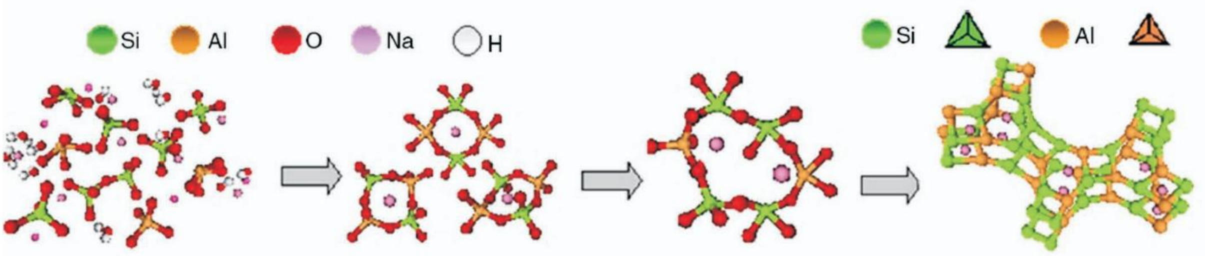

Obr. 38 Model vzniku N-A-S-H [184]

U alkalicky aktivovaných materiálů, které jsou bohaté na vápník (tj. vysokopecní struska), vzniká primárně gel na bázi C-S-H, který je strukturně podobný tomu, který vzniká při hydrataci OPC. Rozdílem mezi nimi je částečné zabudování Al do struktury C-S-H a stává se C-A-S-H formou gelu (pouze za určitých podmínek lze nalézt i hybridní C-(N)-A-S-H gel) [183, 184]. Struktura tohoto C-A-S-H gelu je velmi podobná struktuře C-A-S-H gelu vznikajícího ve směsných cementech. Al ve formě tetraedru AlO_4 se inkorporuje do struktury na pozicích Q^3 a $Q^2(1Al)$ (viz Obr. 35) [38, 169, 175, 185]. Vznikající C-(N)-A-S-H gel je strukturou podobný C-S-H I či 14Å tobermoritu, což potvrzují navržené termodynamické i atomistické numerické modely [37, 185, 186]. Detailním popisem modelů C-S-H struktur se zabývají kapitoly 3.2.1. a 3.2.2. Modely pro C-A-S-H vycházejí ze stejných teoretických základů jako u nesubstituovaného analogu, včetně těch numerických [37, 38, 166, 187]. Řídícím mechanismem tvorby nanostrukturních gelů je tedy chemické složení výchozí aluminosilikátové suroviny, typ a koncentrace alkalického aktivátoru a podmínky zrání. Přítomnost alkalického aktivátoru o vyšším pH (např. NaOH) zvyšuje rozpustnost strusky hned na počátku reakce, čímž se vytvoří hydratační produkty rychleji než u aktivátoru s nižším pH (tj.Na_2CO_3 a Na_2SiO_3) [188].

Vznikající hydratační produkty alkalicky aktivované strusky byly studovány v publikacích ***Kaliny, Bartoníčkové a kol.*** či ***Bílka, Bartoníčkové a kol.*** [20-22, 24]. Vysokopecní struska zde byla aktivována pomocí sodného vodního skla (dále AAS). Tento systém má vynikající chemickou odolnost a vysoké počáteční pevnosti, problémem je však autogenní smrštění a smrštění vysycháním. Na základě literatury, je smrštění obecně výsledkem několika na sobě nezávislých faktorů jako jsou změny ve vlhkosti materiálu, chemické reakce a fyzikální interakce na povrchů nezreagovaných zrn či hydratačních produktů s pórovým roztokem. Tyto faktory časem vedou ke vzniku deformací a trhlin. Smrštění, ať už je plastické, autogenní, dekalcifikační či způsobené vysycháním, výrazně ovlivňuje nejenom mechanické vlastnosti, ale i celkovou trvanlivost betonových kompozitů. U alkalicky aktivované strusky je smrštění výrazně vyšší než u kompozitů na bázi OPC, a to díky rozdílné distribuci pórů (zejména nano/mikro a meso, odpovídajícím gelovým pórům v C-(A)-S-H gelu), krystalické povaze hydratačních produktů a v případě aktivace koloidními křemičitými roztoky i amorfnímu křemičitému gelu [189, 190]. Teorie kapilárního a rozpojovacího tlaku je dobře známá a často využívána k vysvětlení mechanismu smrštění cementových matric. Kapilární teorie vychází z předpokladu tvorby menisků, které vznikají v důsledku působení povrchového napětí během procesu vysychání pórovité struktury.

Rozdíl mezi tlakem v kapalné fázi p_l tlakem v plynné fázi p_v, je označován jako kapilární tlak Δp_c jenž lze podle Youngovy-Laplaceovy rovnice (19) vyjádřit jako součin poloměru křivosti rozhraní kapalina–pára (κ) a povrchového napětí (γ). V případě, že chceme kapilární tlak vyjádřit v závislosti na poloměru pórů r, lze hodnotu R odvodit na základě smáčecího úhlu Θ, který charakterizuje interakci kapaliny s povrchem pevné fáze.

$$\Delta p_c = p_l - p_V = \kappa \cdot \gamma = -\frac{2\gamma}{r} \cdot \cos\theta, \qquad (19)$$

Protože smrštění může být dáno přeuspořádáním C-A-S-H struktury díky působícím kapilárními silám, byly v publikacích ***Kaliny, Bartoníčkové a kol.*** [21, 22, 24] testovány organické přísady redukující smrštění (dále SRA) na bázi fluorovaných aminoalkoholů či polypropylenglykolů. Na Obr. 39a z křivky kalorimetrie je vidět průběh hydratace AAS s a bez SRA na aminoalkoholové bázi, rozlišujeme zde fázi rozpouštění (1.pík), vznik primárního C-(A)-S-H z SiO_4 jednotek uvolněných z vodního skla a Ca^{2+} ze strusky (2 pík). Třetí pík odpovídá již vzniku C-A-S-H gelu. Z publikovaných výsledků je nanejvýš patrné, že přítomnost SRA přísad měla vliv na počáteční smrštění během tvorby C-(A)-S-H gelu, ale již nebyla tolik efektivní při objemové hydrataci, tedy vzniku hlavní pojivové fáze C-A-S-H. Z pohledu vyzrálého tělesa již po 3 dnech nebyl rozdíl, zda byly přísady SRA aplikovány či ne.

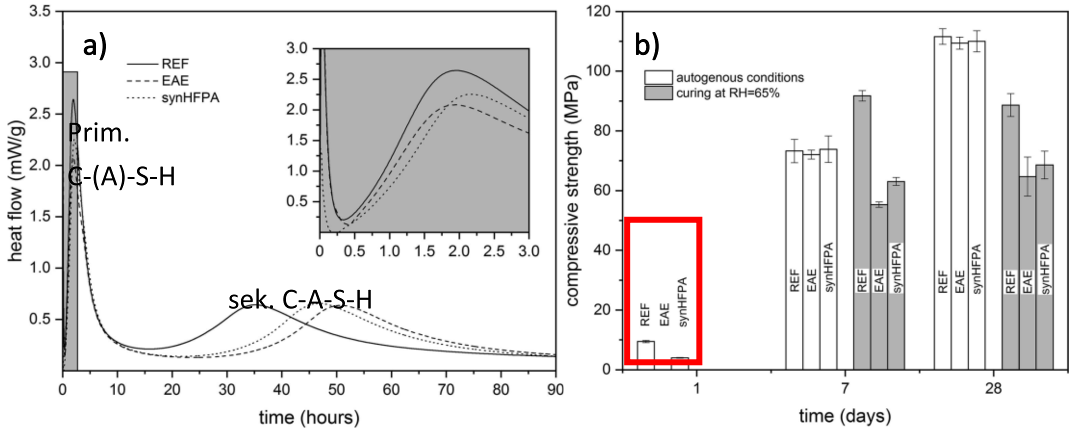

Obr. 39 Průběh hydratace AAS v prostředí SRA (a), porozimetrie AAS v prostředí SRA po 7 d zrání za různých podmínek (převzato z Kalina, Bartoníčková a kol. [24])

Výsledky korelovaly s vývojem pevností v tlaku, kdy u vzorků s SRA přídavkem byly počáteční pevnosti znatelně nižší než referenční hodnoty a odpovídá to retardovanému vývoji primárního C-S-H gelu tak i objemového C-A-S-H až o několik hodin. Struktura vzniklého pojiva je vidět na SEM snímku reference a pojiva s SRA 2-(tercbutylamino) alkoholem publikovaným ***Kalinou, Bartoníčkovou a kol.*** [21]. Ve vzorku bez přídavku SRA je struktura kompaktní bez viditelných meso a makro pórů odpovídající kompaktní struktuře C-A-S-H gelu, zatímco u vzorku s přídavkem SRA je vidět vyšší porozita a méně kompaktní struktura přisuzující se nezreagovaným výchozím látkám a odpovídající retardované hydrataci. Tyto výsledky byly v korelaci s již dříve publikovanými daty [20].

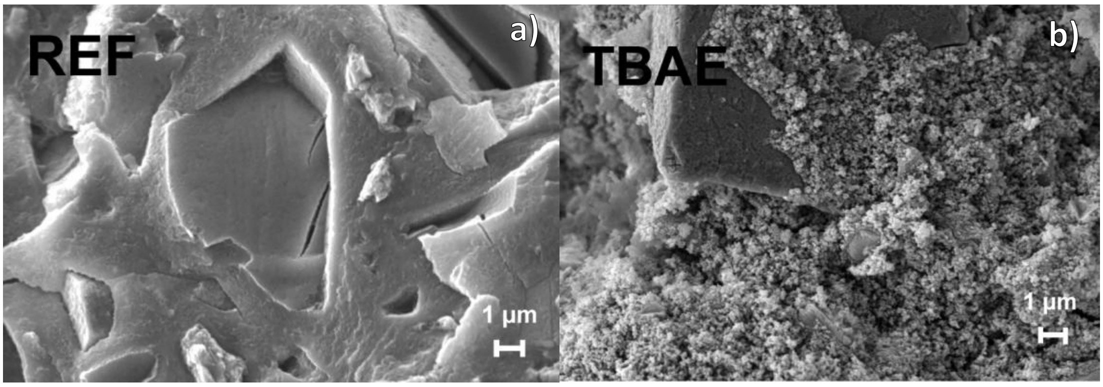

*Obr. 40 SEM mikrostruktury AAS bez (a) a s (b) 2-terc-butylaminoethanol po 7d zrání (převzato z **Kalina, Bartoníčková a kol.** [21])*

V publikaci ***Kuzielové, Bartoníčkové a kol.*** [16] byl posuzován vznik C-A-S-H gelu dle přítomnosti gelových pórů, i zde byla zaměřena pozornost na porozitu AAS ovlivněnou přídavkem SRA. Na rozdíl od směsných cementů, zde bylo zjištěno, že přídavek přísad redukujících smrštění velmi málo ovlivňuje celkovou porozitu systému během autogenního smrštění. Situace u smrštění vysycháním je zcela odlišná, vzorky s přídavkem SRA vykazovaly mnohem menší hodnoty smrštění během času oproti vzorkům referenčním. Toto zjištění koreluje s již zmíněným efektem retardace hydratace a nižší míry hydratace AAS systému. Opět lze tento jev vysvětlit oddálenou hydratací vlivem organické přísady na bázi fluorovaných aminoalkoholů. Podobná situace nastala i v případě, pokud byly použity SRA na bázi polypropylenglykolů o různé molekulové hmotnosti (práce ***Kalina, Bartoníčková a kol.*** [92]). Na kalorimetrické křivce je opět vidět druhý pík odpovídajícího primárnímu C-(A)-S-H, který je vlivem přítomnosti některých SRA přísad redukovaný oproti referenci. Zpomalení hydratace je opět velmi znatelné u třetího píku, který odpovídá vývoji hlavních hydratačních produktů. Situace je obdobná jako u použití SRA na bázi aminoalkoholů, u polypropylenglykolů s nejmenší molekulovou hmotností je viditelný posun až o 14 h a zároveň je vytvořeno nejmenší množství kapilárních pórů, které mají vliv na snížení smrštění a pokles počátečních pevností.

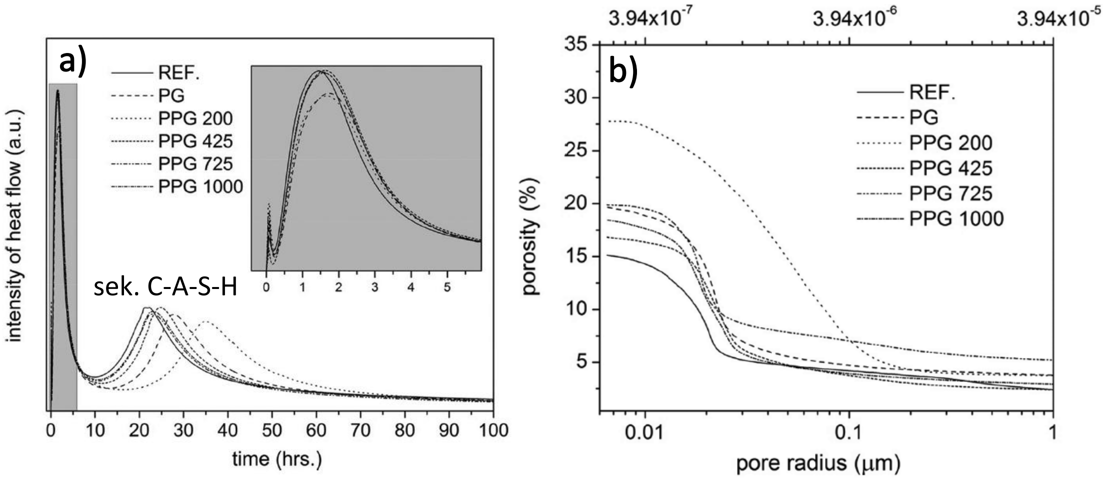

Obr. 41 Vliv PPG na hydrataci (a) a distribuci pórů v AAS (b) (převzato z ***Kalina, Bartoníčková a kol****. [22])*

.

5. Hydratace C-A fází

Aluminátové fáze patří mezi velkou skupinu minerálů ovlivňující nejenom skupinu portlandských cementů, ale i významně zasahují do žárovzdorných materiálů ve formě tzv. aluminátového cementu (dále CAC). Na ternárním i binárním fázovém diagramu (Obr. 42) vidíme všechny fáze krystalizující v soustavě $CaO\text{-}Al_2O_3$. Mezi hlavní fáze: patří kalcium aluminát - CA, kalcium dialuminát - CA_2, trikalcium aluminát – C_3A, kalcium hexaluminát - CA_6, dodekakalcium heptaaluminát - $C_{12}A_7$. Obecně platí, že reaktivita těchto aluminátových fází roste s rostoucím poměrem C/A, což odpovídá nejvyšší reaktivitě C_3A a fáze o nižším C/A jsou odolné vysokým teplotám (CA_6 – teplota tání kolem 1800 °C).

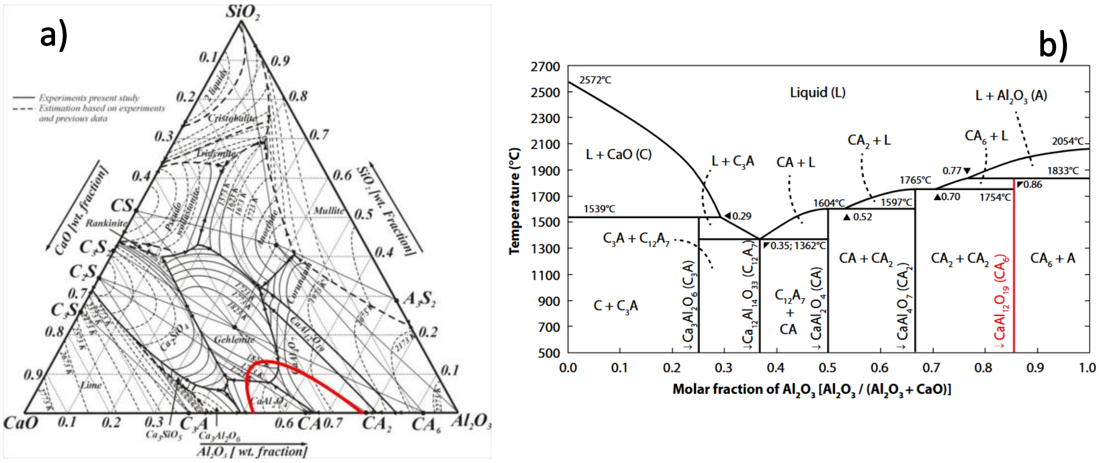

Obr. 42 Fázové digramy soustavy $Al_2O_3\text{-}CaO\text{-}SiO_2$ (a) a $CaO\text{-}Al_2O_3$ (b) (zpracováno z [191]

5.1. C-A-H: nanostrukturní hydratační produkty C_3A

Kromě trikalcium silikátu - C_3S, dikalcium silikátu - C_2S a tetrakalcium aluminátoferitu - C_4AF (nebo obecně $C_2(A_xF_y)$, kde x a y se pohybují v rozmezí 0,3 až 0,7) je běžnou složkou běžného portlandského cementu také trikalcium aluminát – C_3A [77]. Přestože se jeho obsah v OPC obvykle pohybuje mezi 5-10 %, hydratační kinetika C_3A a jeho reakční dráha zásadním způsobem ovlivňují zpracovatelnost a reologii cementových past, zejména v počátečních fázích hydratace [192]. K těmto jevům patří i dobře známý fenomén tzv. *„flash setting“* (okamžité tuhnutí), který může následně negativně ovlivnit vývoj pevnosti cementového kompozitu. C_3A velmi snadno reaguje s vodou. Z tohoto důvodu se do směsi přidává síran vápenatý ve formě dihydrátu (sádrovec, $CaSO_4{\cdot}2H_2O$, značený $C\bar{S}H_2$), aby se regulovala doba tuhnutí OPC. V přítomnosti sádrovce dochází k tvorbě ettringitu (fáze AFt, $C_6A\bar{S}_3H_{32}$) [193, 194]:

$$C_3A + 3\,C\bar{S}H_2 + 26\,H \rightarrow C_6A\bar{S}_3H_{32} \tag{20}$$

Po spotřebování veškerého síranu vápenatého pak C_3A dále reaguje s ettringitem, přičemž vzniká monosulfát (fáze AFm, $C_4A\bar{S}H_{12}$) [193, 194]

$$2\,C_3A + C_6A\bar{S}_3H_{32} + 4\,H \rightarrow 3\,C_4A\bar{S}H_{12} \tag{21}$$

Čistá fáze C_4AF hydratuje obdobně jako C_3A a přibližně stejně rychle. Oproti tomu směsné ferritové fáze s nižším poměrem Al_2O_3/Fe_2O_3 vykazují pomalejší hydratační kinetiku [27, 30]. Na rozdíl od hydratace alitu a belitu během hydratace C_3A nevzniká portlandit ($Ca(OH)_2$). Nicméně při hydrataci běžného portlandského cementu (OPC) je portlandit vždy přítomen. V takovém případě dochází ke vzniku hexagonálních hydrátů [195]:

$$C_3A + CH + 12\,H \rightarrow C_4AH_{13} \tag{22}$$

Při hydrataci čistého C_3A, tedy bez přítomnosti přísad regulujících tuhnutí, vznikají v závislosti na teplotě a relativní vlhkosti různé vápenato-aluminátové hydráty [196]:

- Termodynamicky stabilní kubický hydrogranát C_3AH_6 (katoit).
- Metastabilní hexagonální hydráty C_4AH_{13}, C_4AH_{19} a C_2AH_8.

Průběhem hydratace a faktory ovlivňujícími se zabývala publikace ***Bartoníčková a kol.***[25], kde bylo cílem popsat vliv Li, Cu a S inkorporovaných do struktury C_3A již během její syntézy na fázové složení a morfologii hydratačních produktů. C_3A krystalizuje v kubické krystalické mřížce, kdy základní jednotka je tvořena tetraedry $(AlO_4)^{5-}$ tvořících 8 kruhů $(Al_6O_{18})^{18-}$, které jsou propojeny přes kaionty Ca^{2+} s kavitou uprostřed. Struktura C_3A je schopna inkorporovat kationty v pozici Ca i Al. Strukturně velmi dobře popsaným je tuhý roztok s alkáliemi, jmenovitě s Na^+ kationty. Maximální možná koncentrace Na, kterou je bez distorze mřížka schopna zabudovat, je 1 % Na_2O. Při vyšších koncentracích dochází ke distorzi na orthorombickou až monoklinickou mřížku [197].

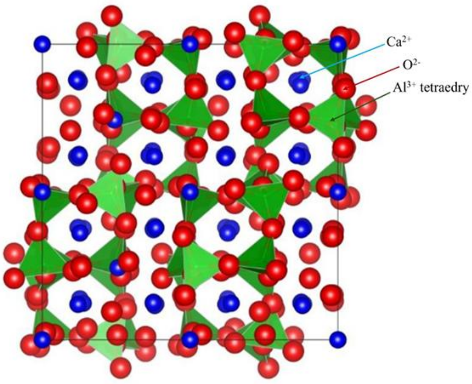

Obr. 43 Modelová struktura kubického C_3A (zpracováno z [198])

Proto byl v práci ***Bartoníčkové* a kol.** [25] studován vliv substituce 1 % Li_2O a 1°% CuO. Vliv kationtů byl sledován nejenom při syntéze (tzn. vliv na snížení tzv. „*clinkering*“ teploty) a také při hydrataci. Je známo, že hydratace C_3A v přítomnosti lithných iontů akcelerují vývin počátečních pevností, a to díky zvýšení alkality pórového roztoku reakci Li^+ na LiOH [199, 200].

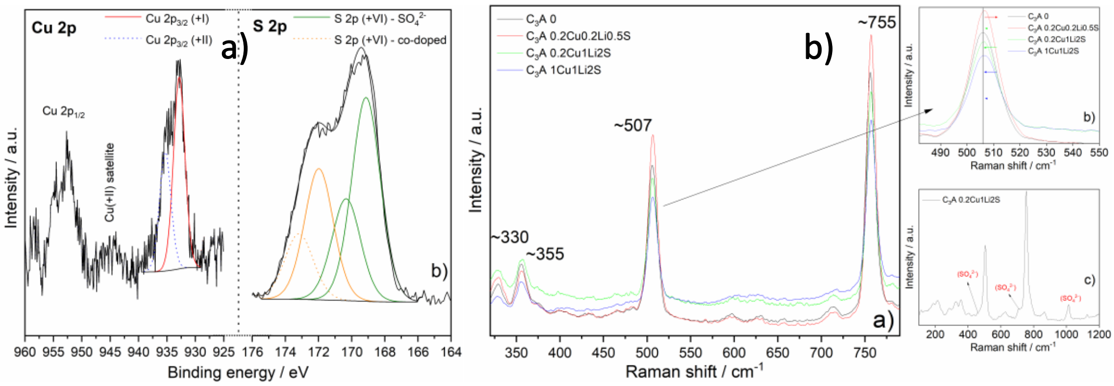

Obr. 44 Strukturní analýza inkorporace Li, Cu a S do C_3A: a) XPS analýzy, b) analýza Ramanovou spektroskopii (převzato z ***Bartoníčková* a kol***. [25])*

Byla zde použita vysokoteplotní syntéza, jejíž výsledkem byla kubická struktura C_3A a dle koncentrace dopantů vedlejší produkty (CaO, Li_2SO_4, $Ca_4AL_6O_{12}(SO_4)$ – yeelimit, $CaSO_4$ a CuO). Substituce vápenatých kationtů kationty měďnatými byla potvrzena daty z XPS analýzy, a současně také z posunu hlavní XRD difrakce C_3A či v Ramanově posunu. To, že substituovaným kationtem je Ca, potvrdil experiment se zvýšenou koncentrací nad limit možné substituce, kdy vedlejším produktem bylo CaO a poté i nezreagované CuO. Kromě Li a Cu byla k výchozím surovinám přidána i síra v reaktivní formě (síran amonný), kde bylo cíleno na sledování inkorporace S do struktury. Z XPS analýzy víme, že síra v S^{6+} byla částečně nalezena ve formě síranů Ca a Li, ale i malá část S byla ve vazebné energii podobné tuhým roztokům supravodičů $(Y_{1.4}Ce_{0.5}Sr_{0.1}Cu_{2.75}S_{0.25}O)$, což znamená zabudování do struktury C_3A. V publikaci byla dále studována kinetika hydratace za různých teplot, která se dá popsat těmito reakcemi [201]:

$$C_3A + 6\,H \overset{k_1}{\rightarrow} C_3AH_6, \tag{23}$$

$$2\,C_3A + 21\,H \overset{k_2}{\rightarrow} C_4AH_{13} + C_2AH_8 \overset{k_4}{\rightarrow} 2\,C_3AH_6 + 9\,H, \tag{24}$$

$$2\,C_3A + 27\,H \overset{k_3}{\rightarrow} C_4AH_{19} + C_2AH_8 \overset{k_4}{\rightarrow} 2\,C_3AH_6 + 15\,H, \tag{25}$$

kde *k*(*T*) představuje rychlostní konstantu reakce při dané teplotě *T* (v kelvinech). Hlavním produktem hydratace při teplotách vyšších než 21 °C je C_3AH_6 (rovnice 23). Při nižších teplotách dochází ke vzniku metastabilních hexagonálních hydrátů. Porovnáním rovnic (24) a (25) je patrné, že vyšší vodní součinitel podporuje tvorbu C_4AH_{19} namísto C_4AH_{13}. Metastabilní hydráty se spontánně transformují na termodynamicky stabilní kubickou fázi C_3AH_6, která je vždy konečným produktem hydratace. Na rozdíl od rychlé exotermní hydratace je tato transformace endotermní.

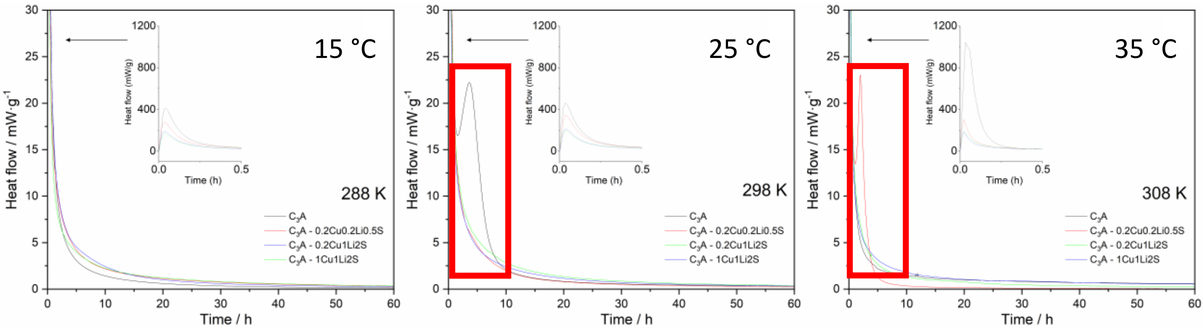

*Obr. 45 Průběh hydratace C_3A dopovaného Li, Cu a S při 15, 25 a 35 °C (převzato z publikace Bartoníčková **a kol.** [25]*

U nedopovaného systému dochází v počátku reakce (desítky minut) k zformování nanostrukturních (amorfních) metastabilních hydrátů C_4AH_{13} and C_4AH_{19}, které časem přechází do stabilnější formy C_3AH_6, tato transformace odpovídá druhému píku na kalorimetrické křivce (viz Obr. 45), který probíhá do 5 h od počátku reakce. Vliv teploty na morfologii hydratačních produktů je vidět na Obr. 46, od jemného amorfního gelu tvořeného metastabilními nanohydráty po kulovité stabilní hydráty mikrometrových rozměrů.

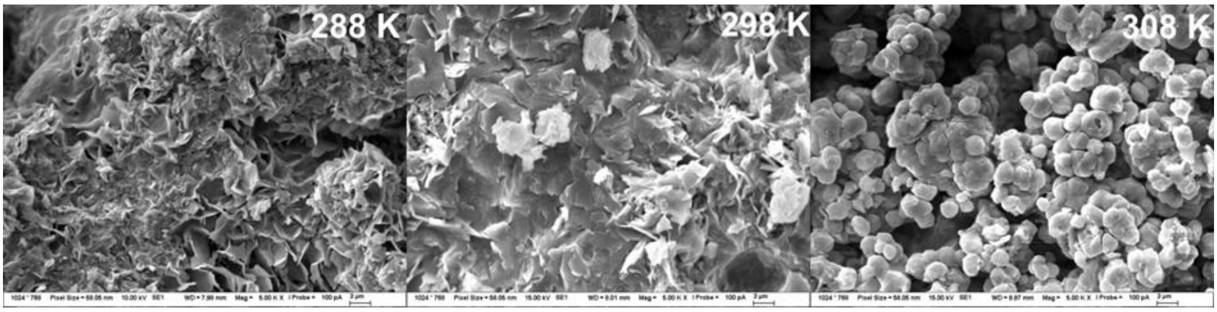

*Obr. 46 Morfologie hydratačních produktů C-A-H dopovaného C_3A (0.2 % CuO, 0.2 = Li_2O, 0.5 SO_3) (převzato z publikace Bartoníčková **a kol.** [25]*

Další práce věnovaná hydrataci dopovaných C_3A fází je dále rozpracována vnesením tzv. *„bottom-up“* přístupu, kdy za použití modifikovaných sol-gel reakcí je dosaženo syntézy fází s nanočásticovou strukturou, která je ale v konečném důsledku velmi aglomerovaná. V práci ***Koplíka, Bartoníčkové a kol.*** [26] je použito obou přístupů k syntéze – tradiční vysokoteplotní reakcí a modifikovanou sol-gel metodu. Fáze CA, $C_{12}A_7$, C_3A a CA_2 byly laboratorně připraveny a sloužily ke kontrolované hydrataci. Pro srovnání byla vybrána fáze C_3A, na které je z výsledků znatelně vidět rozdíl v použití sol-gel metody. Majoritní fází v případě hydratace fáze připravené vysokoteplotní reakcí je jediným hydratačním produktem stabilní C_3AH_6, což koreluje se zjištěními publikovanými v práci ***Bartoníčkové a kol.*** [25]. Zatímco fáze C_3A syntetizovaná modifikovanou sol-gel metodou o větším měrném povrchu hydratuje formou metastabilních hydrátů C_2AH_8, C_4AH_{11} a amorfního gelu $Al(OH)_3$ (dále AH_3). O výrazně vyšším povrchu a reaktivitě připravené fáze hovoří i výsledky z kalorimetrické analýzy (Obr. 47), kde vyvinuté teplo je mnohem vyšší (více jak 2×) u sol-gel přístupu než u tradiční metody.

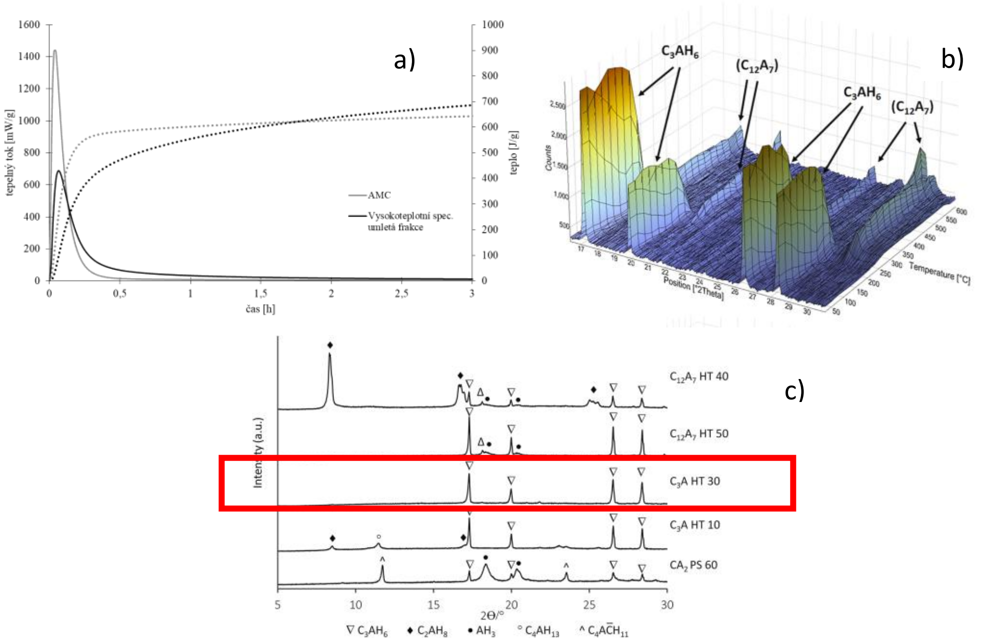

*Obr. 47 Průběh hydratace fáze C_3A připravené vysokoteplotní metodou a modifikovanou sol-gel metodou (převzato z DP Ohaňka (škol. Koplík)) b) dehydratace C_3AH_6 připraveného v C_3A sol-gel metodou a c) XRD analýza vzniklých hydrátů (převzato z **Koplíka, Bartoníčkové a kol.** [26])*

Modifikovaná sol-gel metoda byla použita i na přípravu dopovaných fází (Li, Cu i S). Tyto výsledky jsou v současné době zpracovány do publikace a budou zaslány k publikování. V případě dopovaní Cu se podařilo připravit systémy téměř bez vedlejších produktů ($C_{12}A_7$, CuO > 1 %) a XPS i Ramanova spektroskopie potvrdily dopování na atomární úrovni.

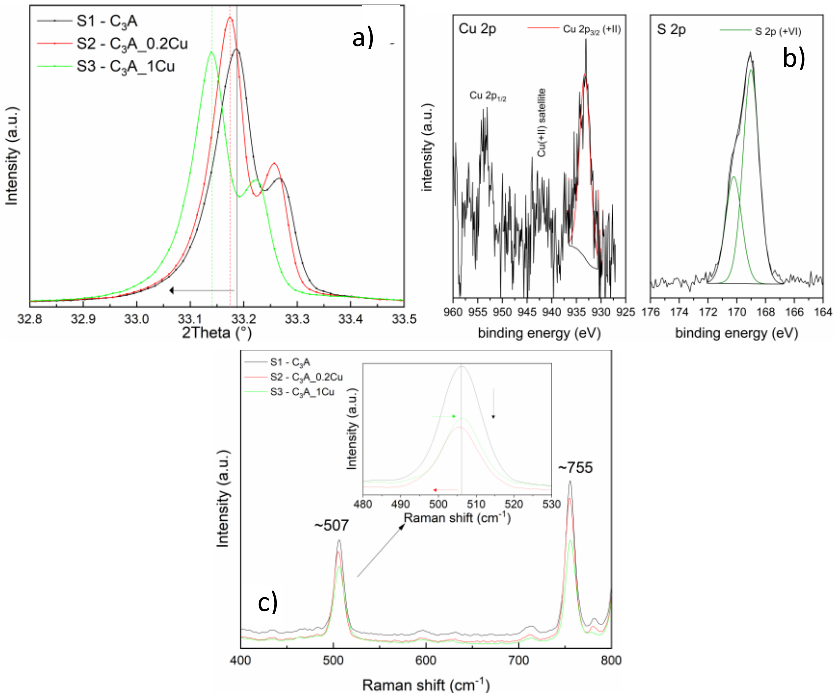

*Obr. 48 XRD (a), XPS (b) a Ramanova spektroskopická (c) analýza C_3A dopovaného Cu (převzato z BP Šmeral (škol. **Bartoníčková**) a **Bartoníčková** – nepublikovaná data)*

Kalorimetrické měření ukázalo stejný trend jako v práci **Koplíka, Bartoníčkové a kol.** [26], teplo fáze připravené *„bottom-up“* přístupem je 2× vyšší než u tradiční metody a svědčí o vysokém měrném povrchu. Morfologie hydratačních produktů C-A-H svědčí o vlivu Cu na výslednou velikost částic. V případě reference můžeme hovořit o aglomerátech složených z velmi jemných částic, zatímco u systému dopovaného mědí je struktura znatelně vyvinutější a pohybujeme se už v µm rozměrech vzniklých C-A-H fází.

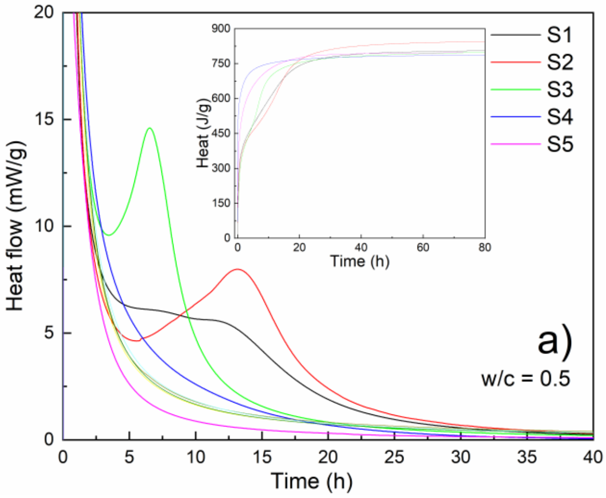

Phase	*Comp. %*
C_3A	–
C_3AH_6	++++
C_4AH_{13}	+
C_4AH_{19}	+
Heat (J/g)	806.5
Heat SSR (J/g)	450.0

*Obr. 49 Průběh hydratace dopovaného C_3A Cu připraveného pomocí modifikované sol-gel metody (**Bartoníčková** -nepublikovaná data)*

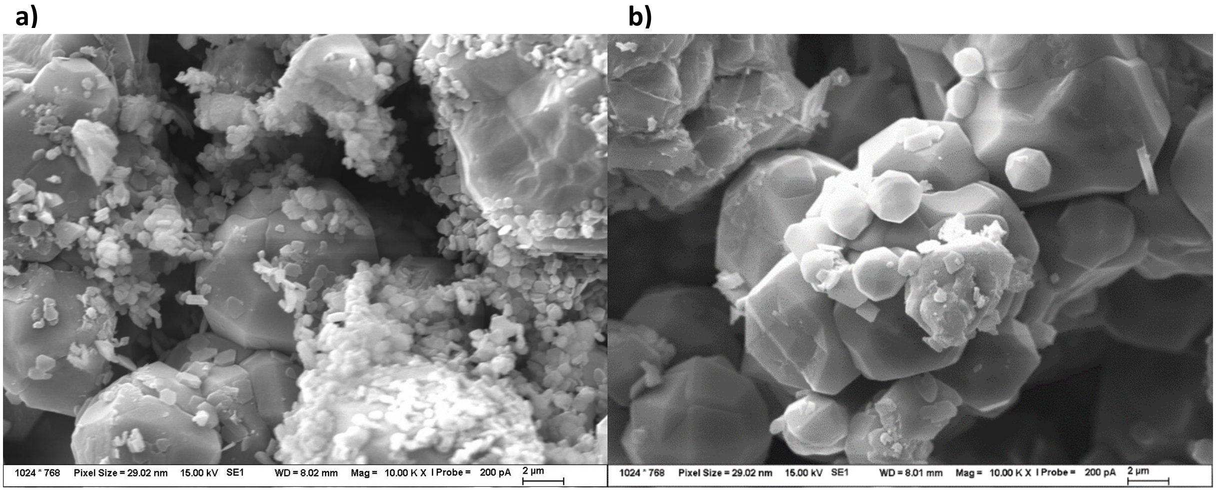

*Obr. 50 SEM snímky morfologie hydratačních produktu: a) reference C_3A, b) dopované struktury C_3A- 1% CuO (**Bartoníčková** -nepublikovaná data)*

5.2.C-A-H: hydratační produkty aluminátových cementů

Tato kapitola je věnována hydrataci kalcium aluminátových cementů, jejichž pojivové schopnosti se využívá v přípravě netvarových a izolačních žárovzdorných materiálů na bázi aluminosilikátů (dle ČSN EN ISO 1927-1). Součástí projektu aplikovaného výzkumu TA ČR TA02010995 (**Šoukal, Bartoníčková *a kol***.: člen řešitelského týmu) byl výzkum izolačních žárovzdorných materiálů pojených hydraulickou vazbou, tj. kalcium aluminátovým cementem.

Základem netvarových žárovzdorných materiálů (označovaných jako žárobeton) je pojivová fáze, kamenivo (ostřivo) a voda. Surovinová skladba se výrazně liší podle teplotní třídy finálního výrobku. Rozlišujeme několik druhů žárobetonů dle obsahu cementu:

- *normální obsah cementu RCC („regular cement castable“, 15-30 % CAC),*
- *střední obsah cementu MCC („medium cement castable“10-15 % CAC),*
- *nízký obsah cementu LCC („low cement castable“, 3 – 8 % CAC),*
- *ultranízký ULCC („ultra low cement castable“, ≈2 % CAC),*
- *bezcementový NCC („no cement castable“, sol-gel mechanismus, fosforečnanová vazby aj.)*

Standartně používané hlinitanové cementy obsahují zejména fáze CA (40–70 %), CA_2 (> 25 %) a $C_{12}A_7$ (> 25 %). Kalcium aluminát se považuje za majoritní hydratační fázi kalcium aluminátových cementů, reakce jsou obdobné jako u standardních OPC cementů. Výhodou je spotřebování velkého množství záměsové vody do hydrátů a oproti OPC rychlá hydratace (až 90 % reakce je uskutečněno do 24 h) [202]. Jak bylo zmíněno v předchozí kapitole, vývin metastabilních hydrátů v čase klesá ve prospěch jejich transformace ve stabilní C_3AH_6 (Obr. 51).

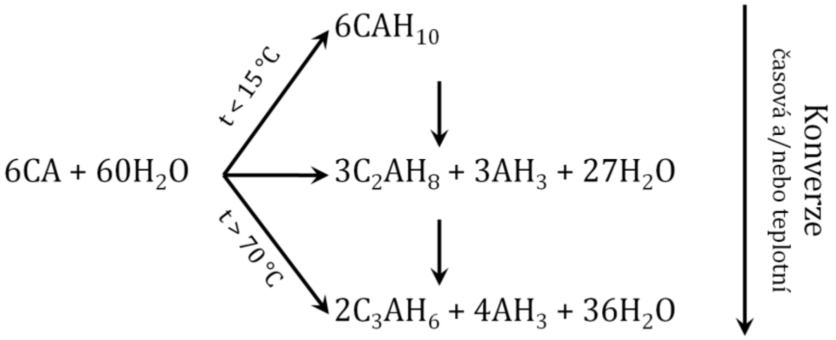

Obr. 51 Schéma hydratačních produktů kalcium aluminátu (převzato z DizP práce Novotný [203])

Publikace ***Ptáčka, Bartoníčková a kol.****[204]* navázala na předchozí publikaci věnující se přípravy vodné pěny stabilizované částicemi i povrchově aktivní látkou [205]. Pomocí hydratace kalcium aluminátového cementu byla úspěšně vytvořena pěna s velmi jemnou porozitou. Hlavními hydratačními produkty použitého komerčního kalcium aluminátového cementu byly primárně metastabilní C_2AH_8 a amorfní AH_3 gel, které sušícím procesem přešly na stabilní hydrát C_3AH_6 a hydroxid hlinitý γ-$Al(OH)_3$). Tato transformace způsobená stárnutím gelu (či jeho vysušením) je v korelaci s daty publikovanými v práci ***Bartoníčkové a kol.*** [25] diskutovanou v kapitole 5.1. Mikrostruktura připravených pěn je uvedena na Obr. 52, na rozdíl od mullitických pěn komentovanými níže na Obr. 54 a Obr. 56 je zde majoritně uzavřená pórovitost s objemovou hmotností 329 kg/m^3 a tepelnou vodivostí 0,090 W/(m.K), což jsou řádově nižší hodnoty než u pěn s otevřenou pórovitostí (práce ***Bartoníčková a kol.*** [206, 207])

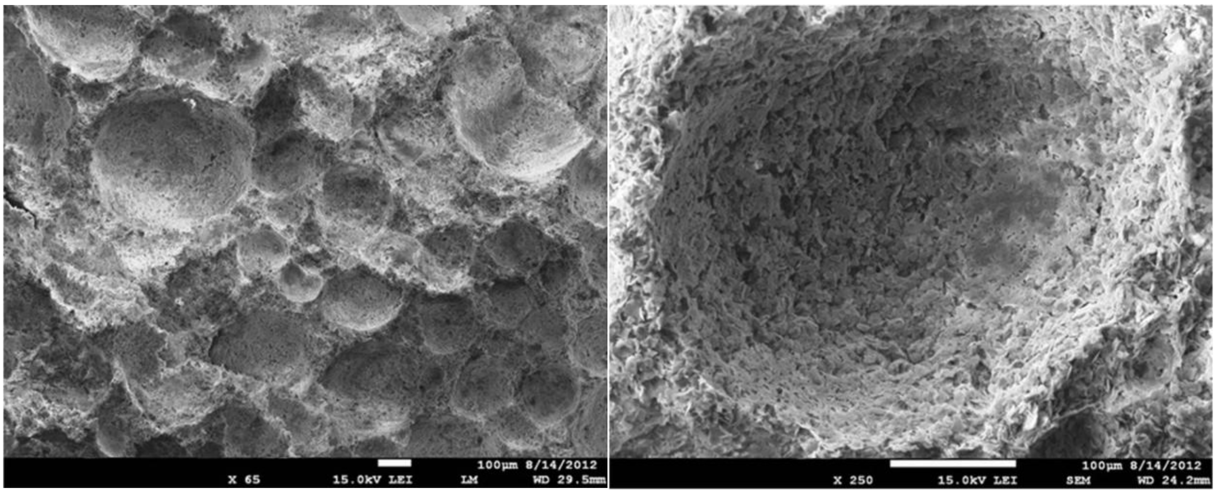

Obr. 52 Mikrostruktura NCC žárobetonu na bázi enstatitu: a) uzavřená porozita, b) detail póru (převzato z ***Ptáček, Bartoníčková a kol.*** [204]

Alternativou ke kalcium aluminátovému cementu může být cement stroncium aluminátový (dále SrA) či i barium aluminátový. V práci ***Bartoníčková a kol.***[206] bylo studováno použití SrA namísto standardního CAC v přípravě LCC netvarové hmoty (6,7 – 8,6 % CAC a SrA). Stroncium aluminátový cement má o 200 °C vyšší teplotu tání než klasický CAC, což bylo důvodem myšlenky jeho potenciální náhrady v určitých aplikacích, a tedy i téma k výzkumu. V práci bylo cíleno na přípravu materiálu z co nejmenší pórovitostí. Příprava a studium hydratace SrA bylo publikováno v dřívějších pracích ***Ptáčka, Bartoníčkové a kol.*** *[27]*, kde výchozími surovinami vysokoteplotní reakce byly uhličitan strontnatý a oxid hlinitý. V práci byla studována kinetika vysokoteplotní reakce a vývoj hydratace v čase. Výsledky ukázaly zcela odlišný průběh hydratační křivky než u CAC či OPC, není zde fáze indukční periody a jedinými hydratačními produkty, které vznikají okamžitě po smíchání s vodou, je Sr_3AH_6 (analog C_3AH_6) a amorfní aluminátový gel AH_3. V čase částečně přechází Sr_3AH_6 na $SrAH_7$ (po 7 d), ale i po 28 dnech zůstává cca 20 % primární fáze nezreagované (viz Obr. 53).

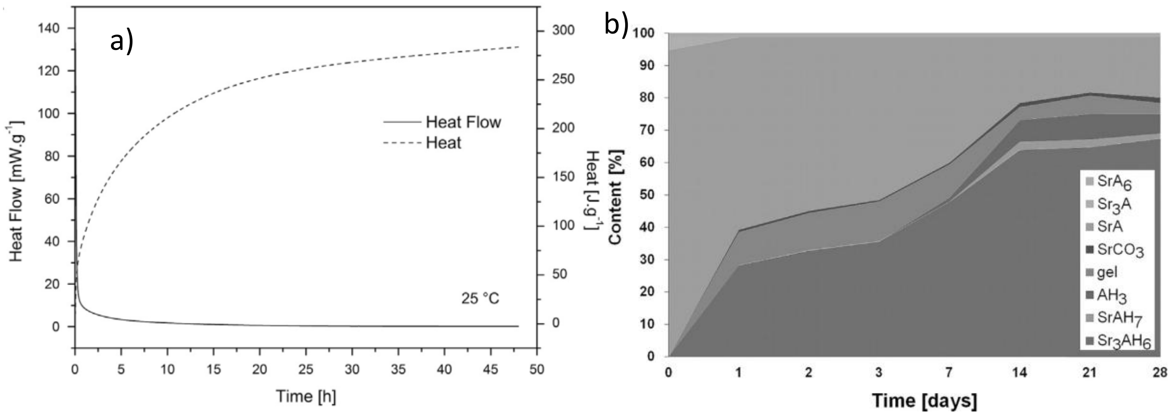

*Obr. 53 Kalorimetrická analýza SrA cementu připraveného vysokoteplotní reakcí (převzato z práce **Ptáček, Bartoníčková a kol.** [27])*

Výsledná mikrostruktura žárobetonů se odvíjí od schopnosti fixace pórů v primární pěně, což souvisí se vzniklými C-(Sr)-A-H pojivovými fázemi a tvorbě gelových pórů v ní. Typická distribuce pórů pro porézní keramické pěny je zobrazena na Obr. 54 a, bohužel z ní již nelze posoudit přítomnost gelových pórů pocházejících z nanostrukturního C-A-H gelu. Nevypálený kompozit má velmi nízkou manipulační pevnost a intruze rtutí během porozimetrické analýzy vedla ke kolapsu struktury.

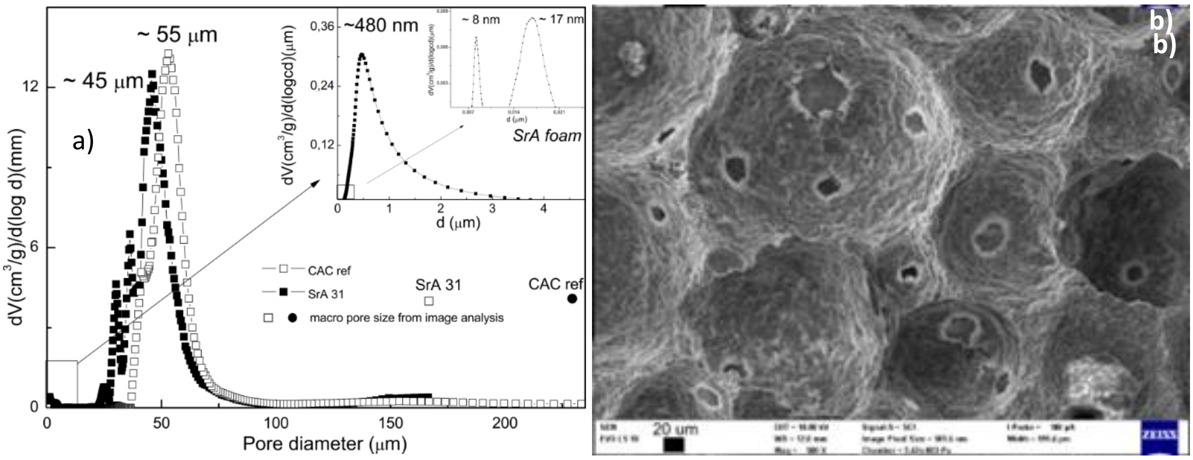

Obr. 54 Distribuce pórů (a) a mikrostruktura (b) vypálené keramické pěny SrA (převzato z ***Bartoníčková a kol.*** [204, 206]

6. Koloidní roztoky a jejich aplikace v žárovzdorných materiálech

Pokud hovoříme o nanosystémech v aluminosilikátových materiálech, nelze nezmínit koloidní systémy na bázi křemíku či hliníku – koloidní silika, alumina, aluminosilika či tzv. vodní skla - silika stabilizovaná alkalickými ionty. Jejich přínos byl znatelný zejména s nástupem HPC a UHPC[12] betonových kompozitů. Tématikou koloidních alkalických silikátů se zabývají publikace ***Kalina, Bartoníčková a kol.*** a ***Bílek, Bartoníčková a kol.***[20, 21, 23, 24], kde se využívá tzv. vodních skel pro alkalickou aktivaci vysokopecní strusky a v této kapitole nebudou diskutovány, téma nanostruktur vzniklých alkalickou reakcí je rozvedeno v kapitole věnující se C-A-S-H strukturám výše (kapitola 4.2). Komentovány budou systémy koloidní siliky využité pro sol-gel mechanismus fixace NCC žárobetonů a koloidní roztoky použité jako impregnace již vypálených žárobetonů pro zvýšení mechanických vlastností a prodloužení trvanlivosti, aplikace podobné tzv. *„vytvrzovačům“* či *„koloidním povlakům“* zmíněných v kapitole 3.3.4.

Koloidní silika je stabilní disperze nanometrických částic amorfního SiO_2 ve vodě. Velikost částic není větší než 100 nm, přičemž obsah sušiny v koloidních roztocích se pohybuje od 10 do 50 hm. %. Stabilita koloidního roztoku obsahující již částečně hydrolyzovanou siliku je zajištěna přídavkem stabilizujících iontů – v průmyslu nejčastěji Na^+, K^+ či NH_4^+. Koloidní roztok lze mimo typ stabilizace charakterizovat množstvím sušiny, velikostí částic amorfní siliky či hodnotou pH, které se nejčastěji pohybuje od 9 do 11. Tyto charakteristické vlastnosti pak výrazně ovlivňují schopnost přechodu stabilního solu v gel. Koloidní silika je využívána jak částečně v kompozitech OPC, tak mnohem výrazněji v žárovzdorných materiálech, kde plní funkci pojiva v tzv. bezcementových NCC žárobetonech [208]. Fixace gelu probíhá pomocí gelace = zesíťovaní silikátových řetězců. Interakce křemičitanového řetězce, její schopnost a míra polymerace (Q^n jednotky) byly podrobně diskutovány a shrnuty v kapitole 3.2, kdy mechanismus tvorby gelu je téměř totožný – vliv pH, koncentrace silikátových řetězců v roztoku, iontová síla matečného roztoku, přítomnost aditiv, reakční podmínky, tj. teplota a tlak [209]. Pro aplikace v žárovzdorných materiálech je proces gelace řízen použitím tzv. gelačních činidel. Projekt TA ČR FW01010077 (***Šoukal, Bartoníčková a kol.***: člen řešitelského týmu) se věnoval vývoji sol-gel vazby na bázi koloidní siliky pro NCC žárobetony, které by mohly být torkretovatelné (tj. technika nástřiku žáromateriálů na vertikální povrchy). Vedlejším výstupem tohoto projektu byla publikace ***Bartoníčkové a kol.*** [207], kde bylo využito gelačních vlastností oxidu hořečnatého pro vytvoření dostatečně pevné Si-O-Si polymerní 3D sítě pro přípravu NCC žárobetonů.

Vysoce hlinité suroviny, tj. mikrosilika a hydratovaná, reaktivní či jemně mletá alumina, byly zvoleny jako výchozí suroviny pro přípravu mullitových žáromateriálů. Skladba suroviny byla navržena na základě modifikovaného granulometrického modelu podle Andreasena, který umožňuje optimalizovat distribuci částic za účelem dosažení maximální porozity při zachování požadovaných mechanických vlastností kompozitu. Primární pěna byla připravena pomocí technologie napěňování *„in situ“* založené na povrchově aktivní látce přidané ke směsi surovin a záměsové tekutině. Při studiu stability pěny byl testován komerční roztok na bázi SiO_2 s cílem stabilizovat připravenou vodnou pěnu. Obr. 55 znázorňuje vliv přítomnosti koloidní siliky na stabilitu pěny a tvorbu xerogelu během procesu stárnutí a volného sušení. V případě pěny bez přídavku roztoku, stabilizované pouze povrchově aktivní látkou, dochází v průběhu času k postupnému kolapsu bublin. Naproti tomu pěna obsahující roztok, tedy stabilizovaná pevnými částicemi, si svou strukturu udržuje. Stabilita pěn stabilizovaných částicemi byla popsána v několika studiích [210-212]. Získané výsledky potvrdily, že gelace zajišťuje mechanickou stabilitu pěnové struktury, která zůstává zachována až po dobu 24 hodin. Během sušení však dochází k určitému smrštění a koalescenci pórů, což lze pravděpodobně přičíst gelaci pěny indukované

---

[12] HPC = *„high performance concrete“*, vysokohodnotné betony, UHP = *„ultra high performance concrete“* – ultravysocepevný beton.

procesem odpařování vody, což je na Obr. 55 patrné. Mikrostruktura vypáleného materiálu ukazuje na porézní materiál s objemovou hmotností mezi 500–900 kg/m^3 v závislosti na míře uzavřené porozity.

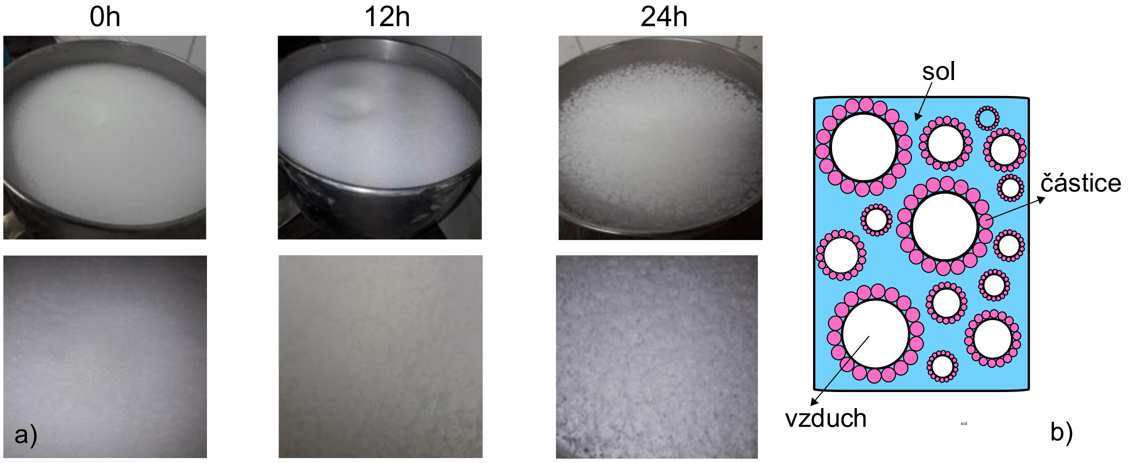

Obr. 55 Vodná pěna stabilizovaná částicemi SiO_2 *roztoku: a) stabilita v čase, b) schéma roztoku kolem částice ve vodném prostředí (převzato z* ***Bartoníčková a kol****. [207])*

Na Obr. 56 lze vidět, že se zvyšující se objemovou hmotností (tzn. snižující se porozitou) dochází k uzavírání pórů a struktura je kompaktnější. Mullit krystalizující se soustavy Al_2O_3-SiO_2 vysokoteplotní reakcí je tvarově definovaný s jehličkami okolo 10 μm, zatímco mullit krystalizující sekundární mullitizací z vakuové sol-gel impregnace vytvářející gelový povlak na celém povrchu i uvnitř pórů díky polykondenzaci Si–O–Si je mnohem jemnější a tvarově ne tolik ohraničený (viz. Obr. 58).

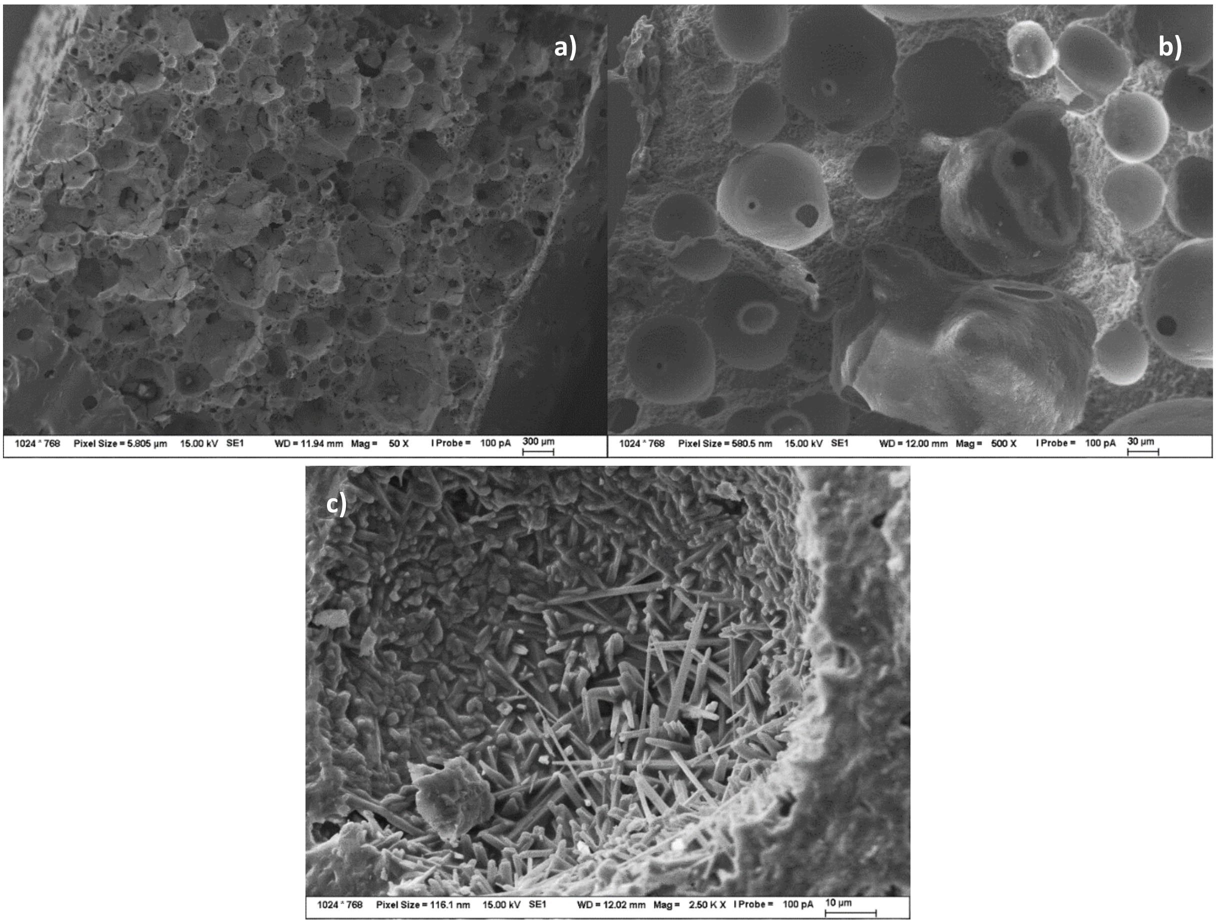

Obr. 56 Mikrostruktura NCC žárobetonu před impregnací: a) 500 kg/m^3, b) 900 kg/m^3, c) detail na krystaly vzniklého mullitu (převzato z ***Bartoníčková a kol.*** [207], ***Bartoníčková*** *- nepublikované výsledky)*

Koloidní silika byla zde použita jako primární pojivo a zároveň i jako impregnační přípravek. Na Obr. 57 je zobrazena distribuce pórů v sol-gel vytvrzeném žárobetonu, který byl následně vakuově impregnován koloidními roztoky (Si – koloidní silika, Si/silica fume – koloidní silika plněná mikrosilikou a SiAl – koloidní „aluminosilika“) a znovu podroben vysokoteplotní reakci. Na Obr. 57 lze pozorovat znatelný pokles a změnu distribuce pórů vlivem impregnace. Zaplnění pórů odpovídá sekundární mullitizaci, bohužel ale spojenou s nárustem objemové hmotnosti(z 940 na 1125 kg/m^3) a snížením porozity, což mělo vliv na tepelnou vodivost λ (vzrostla z 0,333 na 0,411 W/(m·K). Impregnace ale přinesla cílený nárůst mechanických vlastností (až o 100 %) i při relativně nízké objemové hmotnosti [207].

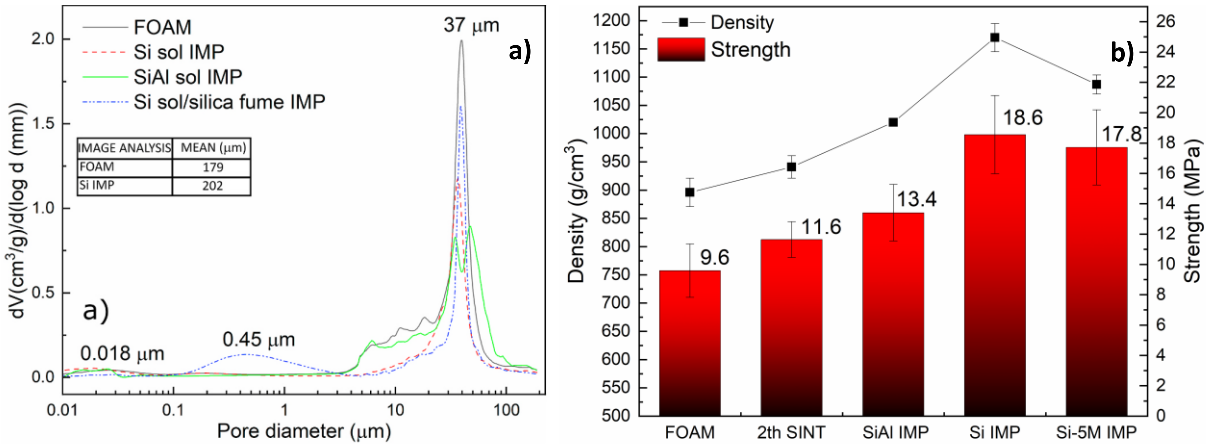

Obr. 57 Vliv impregnace koloidními roztoky na bázi Si a SiAl na distribuci pórů (a) a mechanické vlastnosti (b) žárobetonů (převzato z ***Bartoníčková a kol.*** *[207])*

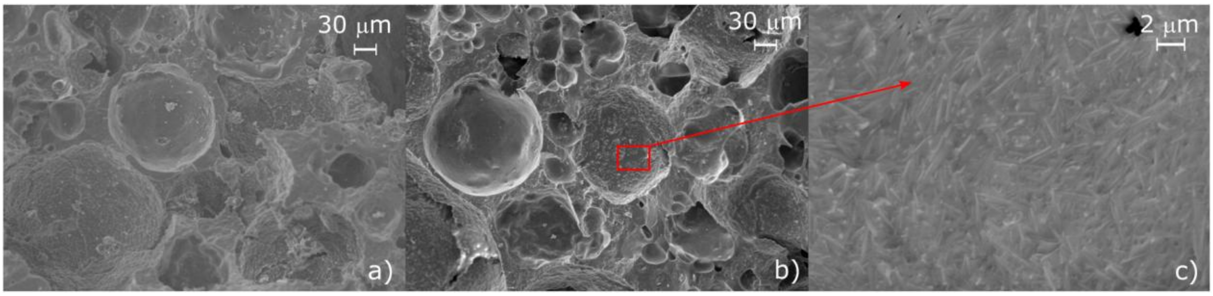

Obr. 58 Mikrostruktura pěn po Si sol-gel impregnaci: a) druhý výpal , b) po impregnaci i výpalu, c) detail stěny pěny (převzato z ***Bartoníčková a kol.*** *[207])*

Vedle koloidní siliky byl testovaný i nekomerční roztok na bázi koloidní „*aluminosiliky*“ vytvořený pro aplikaci přímo do žárobetonů. V této souvislosti bylo navázáno na dosud nepublikované experimenty impregnace aluminových pěn připravených replikační metodou, kdy po výpalu vznikne ve struktuře „díra“ po polyuretanovém templátu (tj. šablony), čímž se stane struktura velmi křehkou. Na Obr. 59 je „díra“ zaplněna vakuovou impregnací komerčním roztokem na bázi boehmitu AlOOH a sekundárním výpalem na aluminu Al_2O_3.

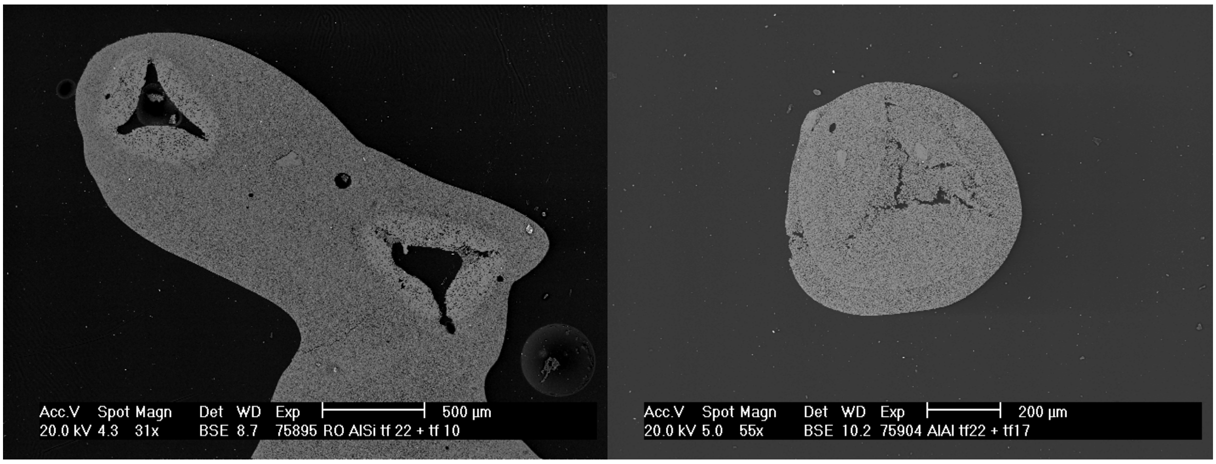

*Obr. 59 Mikrostruktura Al_2O_3 pěny před a po impregnaci (**Bartoníčková** – nepublikovaná data)*

Proto byla testována vývojová směs koloidní „*aluminosiliky*“, kde se očekával polykondenzační mechanismus jak u siliky, tak i u aluminy, tato teorie se bohužel v praxi nepotvrdila. V práci ***Bartoníčkové a kol.*** [207] kombinovaný roztok koaguloval na pseudoboehmit a výsledný gel nebyl kompaktní, tak jako u samotné koloidní siliky. Očekávaná sekundární mullitizace také neproběhla do formy jehličkovitých krystalků typických pro mullit, ale vznikaly kulovité útvary odpovídající spíše morfologii Al_2O_3 (viz Obr. 60).

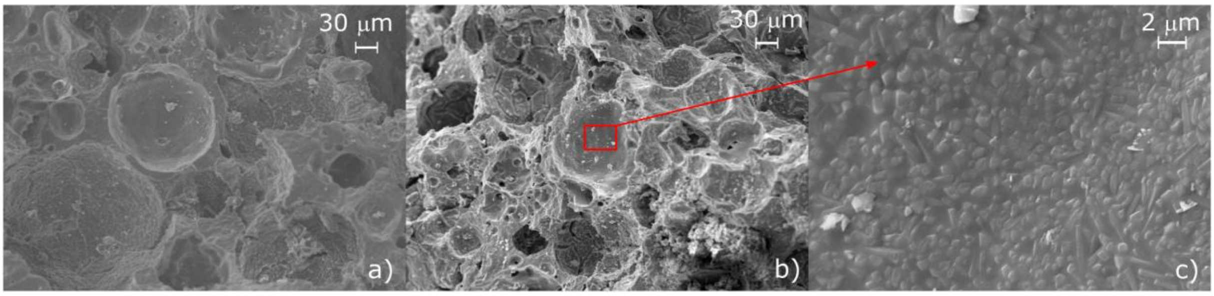

*Obr. 60 Mikrostruktura pěn po SiAl sol-gel impregnaci: a) druhý výpal , b) po impregnaci i výpalu, c) detail stěny pěny (převzato z **Bartoníčková a kol.** [207])*

7. Závěrečné shrnutí

Hydratace aluminosilikátových materiálů je stále aktuálním tématem výzkumu, ačkoliv první teorie byly uveřejněny již v 80. letech 19. století. Od té doby se nejenom teorie měnily, ale také se zároveň rozšiřovaly možnosti analýzy vznikajících sloučenin, zejména z makroskopického pohledu na atomovou/molekulární úroveň. Předkládaná práce ukazuje, jak možnosti pokročilé analýzy vznikajících struktur hrají klíčovou roli pro celkový popis mechanismu hydratace aluminosilikátových materiálů.

V práci byla popsána struktura C-S-H fází vznikajících v podmínkách přirozené hydratace jak čistého a směsných portlandských cementů, tak i krystalických či amorfních analogů C-S-H připravených za laboratorních podmínek. V systému přirozené hydratace posuzujeme C-S-H mikrostrukturu zobrazenou pomocí elektronové mikroskopie i analýzou distribuce pórů, díky nimž lze s dostatečným rozlišením lze pozorovat nano velikosti částic a pórů v nich odpovídajícím globulární struktuře C-S-H i C-A-S-H gelů. Tento systém je však velmi heterogenní a popis struktur na atomární úrovni je obtížný, proto bylo využito tzv. *„čistého“* systému na bázi syntetických C-(A)-S-H analogů, který není zatížen heterogenitou prostředí, a jehož složení a kinetiku reakce lze dobře řídit. V syntetickém modelovém systému bylo pro analýzu využito spektroskopických metod, které nám již dovolily sofistikovanější popis a doplnily makroskopické hledisko tvarové morfologie o atomární úroveň. Námi využité FT-IR, Ramanova, XPS a NMR spektroskopické analýzy poskytly nejenom informaci o uspořádání Si tetraedrů v silikátovém řetězci – jejich míře zesíťování, tj. stupni polymerizace Q^n jednotek v systému, ale i o inkorporaci či substituci doprovodných prvků (Al, Cu). Závěry plynoucí se získaných dat poskytly obdobné závěry jako ty popisované v literatuře, a to majoritu Q^2 jednotek s minimálním množstvím Q^1 a Q^4 a inkorporaci iontů do C-(Cu)-(A)-S-H struktury.

Získané poznatky o struktuře C-S-H byly využity pro přípravu tzv. *„sealerů“* a *„nanoseedů“*, kde se cíleně využilo řízené síťování vlivem aditiv (tzn. míra Q^n polymerizace), jejich uplatnění najdeme jak v cementových, tak v i žárovzdorných kompozitech.

Struktury typu C-A-H hrají zásadní roli při hydrataci portlandského slínku. Pokud slínek není smíchán se sádrovcem, dochází k preferenční hydrataci kalcium-aluminátových fází, což výrazně ovlivňuje reologii cementových kompozitů. V předkládané práci se studium zaměřilo na hydratační procesy kalcium aluminátových fází a jejich stabilitu v přítomnosti mineralizačních látek (Cu, Li a S). Obecný jev okamžitého zatuhnutí se řeší přídavkem sloučeniny se sírou, proto bylo původní myšlenkou využít síranu amonného jako mineralizátoru a zároveň vnést do struktury síru, která při hydrataci zreaguje na ettrinignit či monosulfát a oddálí hydrataci trikalcium aluminátu, což se částečně potvrdilo. Mineralizátory na bázi Li, Cu a S se ukázaly jako vhodné aditiva, které jsou schopny substituce matričních atomů (Ca a Al) v krystalické mřížce, což se potvrdilo analýzou pomocí XPS a Ramanovou spektroskopií. Analýzou procesu hydratace byl potvrzen vliv kationtů na její retardaci a vliv teploty na typ vznikajících hydratačních produktů, zejména jejich konverzi z metastabilních forem na formu stabilní. Tento jev se nese hydratačním mechanismem napříč získanými výsledky jak u čistých fází C_3A, tak i u hydratace kalcium aluminátových cementů, které jsou tvořeny majoritně CA fází.

Obecný princip hydrolýzy a polykondenzace silikátů byl v práci díky probíhajícím povrchovým interakcím pojícím můstkem mezi jednotlivými kapitolami, ať je to vznik C-S-H struktur, syntéza *„nanoseedů“* či téma koloidních roztoků.

Cílem práce bylo systematicky popsat strukturu a chování nanostrukturních hydratačních fází v aluminosilikátových pojivech, a to jak v přirozených, tak syntetických systémech. Získané poznatky mají význam nejen pro základní výzkum, ale i pro návrh nízkouhlíkových cementů, žárovzdorných kompozitů a technologií pro úpravu odpadních vod. Výsledky aktuálních našich a mezinárodních studií naznačují směr, kterým by se měl další výzkum ubírat. Současným cílem je zpřesnění strukturálního popisu materiálů s využitím moderních analytických technik, jako jsou MAS-NMR, LIBS, LA-ICP-MS či TOF-SIMS.

8. Rejstřík zkratek a symbolů

8.1.Sloučeniny a fáze

AFm – Monosulfátová fáze ($C_4A\hat{S}H_{12}$) – monosulfoaluminát
AFt – Ettringitová fáze ($C_6A\hat{S}_3H_{32}$) – ettringit
AH_3 – Hydrát hlinitý ($Al(OH)_3$) – gibbsite, boehmit, pseudoboehmit
C-(N)-A-S-H – Hybridní gel obsahující Ca, Na, Al a Si – není minerální ekvivalent, amorfní gel
$C_{12}A_7$ – Dodekakalcium heptaaluminát – mayenit
C_2AH_8 – Dikalcium aluminát oktahydrát – není běžný minerál, metastabilní fáze
C_2S – Dikalcium silikát – belit
C_3A – Trikalcium aluminát – aluminátová fáze slínku, bez přírodního ekvivalentu
C_3AH_6 – Trikalcium aluminát hexahydrát – katoit (kubický hydrogranát)
C_3S – Trikalcium silikát – alit
C_4AF – Tetrakalcium aluminoferrit – ferritová fáze slínku, často jako brownmillerit
C_4AH_{13} – Tetrakalcium aluminát trihydrát – není přírodní minerál, metastabilní fáze
C_4AH_{19} – Tetrakalcium aluminát nonadekahydráthydrát – není přírodní minerál, metastabilní fáze
$C_4A\hat{S}H_{12}$ – Monosulfát (AFm fáze) – monosulfoaluminát
$C_6A\hat{S}_3H_{32}$ – Ettringit (AFt fáze) – ettringit
CA – Monokalcium aluminát – krotit (vzácně), běžně syntetická fáze
CA_2 – Dikalcium aluminát – grossit
C-A-H – Hydrát kalcium aluminátu – soubor metastabilních fází, např. C_4AH_{13}, C_3AH_6
C-A-S-H – Hydrát kalcium aluminosilikátu – amorfní gel, bez minerálního ekvivalentu
C-S-H – Hydrát kalcium silikátu – tobermorit, jennit, afwilit (v závislosti na C/S poměru)
MC – Monokalcium silikát ($CaO{\cdot}SiO_2$) – wollastonit
Sr_3AH_6 – Tristroncium aluminát hexahydrát – analog katoitu, syntetická fáze
$SrAH_7$ – Monostroncium aluminát heptahydrát – syntetická fáze, bez přírodního ekvivalentu

8.2.Zkratky a symboly

AAM	Alkalicky aktivované materiály – anorganická pojiva vznikající reakcí aluminosilikátových prekurzorů s alkalickými aktivátory.
AAS	Atomová absorpční spektroskopie – analytická metoda pro stanovení koncentrace prvků.
FT-IR	Fourier Transform Infrared Spectroscopy –infračervená spektroskopie
BET	Brunauer–Emmett–Teller – metoda měření specifického povrchu.
BO / NBO	Bridging / Non-Bridging Oxygen – propojený / nepropojený kyslík v silikátových tetraedrech.
CEMDATA	Databáze termodynamických dat pro cementové systémy.
CM I / CM II	Koloidní model C–S–H gelu – modely struktury gelu dle Jenningsovy teorie.
DFT	Density Functional Theory – kvantově chemická metoda pro výpočty elektronové struktury.
EDX – EDS	Energy Dispersive X-ray Spectroscopy – metoda prvkové analýzy pomocí rentgenového záření, používaná v SEM.

EXAFS	Extended X-ray Absorption Fine Structure – metoda pro studium lokální struktury atomů.
FT-IR / Raman / XPS / NMR / MAS–NMR	Spektroskopické metody pro analýzu struktury a chemického složení.
GEM / GEMS	Geochemical Equilibrium Modeling Software – software pro modelování chemické rovnováhy.
HD / LD C–S–H	High / Low Density Calcium Silicate Hydrate – hustotní typy gelu dle koloidního modelu.
HPC / UHPC	High Performance Concrete / Ultra High Performance Concrete – vysokohodnotné betony.
ICP / LA–ICP–MS	Inductively Coupled Plasma / Laser Ablation ICP Mass Spectrometry – metody pro analýzu prvků.
MCL	Mean Chain Length – průměrná délka silikátového řetězce.
MAS	Magic Angle Spinning – technika rotace vzorku v NMR.
NCC / LCC / ULCC / MCC / RCC	Typy žárobetonů dle obsahu cementu: No / Low / Ultra Low / Medium / Regular Cement Castable.
Q^n	Typ silikátové jednotky – Q^0 až Q^4 podle počtu propojení s jinými tetraedry.
SANS / SAXS	Small Angle Neutron / X-ray Scattering – metody pro studium nanostruktur.
SEM / TEM	Scanning / Transmission Electron Microscopy – rastrovací / transmisní elektronová mikroskopie.
SRA	Shrinkage Reducing Admixture – přísada snižující smrštění.
TEOS	Tetraethylorthosilikát – organický prekurzor pro sol–gel syntézu silikátů.
TOF–SIMS	Time-of-Flight Secondary Ion Mass Spectrometry – hmotnostní spektrometrie sekundárních iontů.

9. Literatura

[1] H.F.W. Taylor, Nanostructure of C-S-H: Current status, 1993.

[2] E. John, T. Matschei, D. Stephan, Nucleation seeding with calcium silicate hydrate – A review, Cement and Concrete Research, 113 (2018) 74-85.

[3] J. Hlaváč, Základy technologie silikátů, SNTL – Nakladatelství technické literatur, Praha, 1988.

[4] B. Lothenbach, K. Scrivener, R.D. Hooton, Supplementary cementitious materials, Cement and Concrete Research, 41 (2011) 1244-1256.

[5] E. John, B. Lothenbach, Cement hydration mechanisms through time – a review, Journal of Materials Science, 58 (2023) 9805-9833.

[6] S. Papatzani, K. Paine, J. Calabria-Holley, A comprehensive review of the models on the nanostructure of calcium silicate hydrates, Construction and Building Materials, 74 (2015) 219-234.

[7] K. Scrivener, A. Ouzia, P. Juilland, A. Kunhi Mohamed, Advances in understanding cement hydration mechanisms, Cement and Concrete Research, 124 (2019) 105823.

[8] T. Dorn, O. Blask, D. Stephan, Acceleration of cement hydration – A review of the working mechanisms, effects on setting time, and compressive strength development of accelerating admixtures, Construction and Building Materials, 323 (2022) 126554.

[9] K.L. Scrivener, R.J. Kirkpatrick, Innovation in use and research on cementitious material, Cement and Concrete Research, 38 (2008) 128-136.

[10] H. le Chatelier, Crystalloids against colloids in the theory of cements, Transactions of the Faraday Society, 14 (1919) 8-11.

[11] W. Michaëlis, The hardening process of hydraulic cements, Cement & engineering news, Chicago, Ill., 1907.

[12] J.W. Bullard, H.M. Jennings, R.A. Livingston, A. Nonat, G.W. Scherer, J.S. Schweitzer, K.L. Scrivener, J.J. Thomas, Mechanisms of cement hydration, Cement and Concrete Research, 41 (2011) 1208-1223.

[13] L. Galvánková, E. Bartoníčková, T. Opravil, J. Tkacz, P. Ptáček, The influence of starting materials´ solubility on tobermorite structure formation under the hydrothermal conditions, IOP Conference Series: Materials Science and Engineering, 379 (2018) 012001.

[14] D. Hanisková, E. Bartoníčková, J. Koplík, T. Opravil, The Ash from Fluidized Bed Combustion as a Donor of Sulfates to the Portland Clinker, in: D. Kubatova, M. Bohac, M. Drdlova (Eds.) Procedia Engineering, Elsevier Ltd, 2016, pp. 394-401.

[15] H. Kalousová, E. Bartoníčková, T. Opravil, Influence of storage conditions on quality of fly ashes, Advanced Materials Research, Trans Tech Publications Ltd, 2014, pp. 59-62.

[16] E. Kuzielová, M. Žemlička, E. Bartoničková, M.T. Palou, The correlation between porosity and mechanical properties of multicomponent systems consisting of Portland cement–slag–silica fume–metakaolin, Construction and Building Materials, 135 (2017) 306-314.

[17] R. Novotný, E. Bartoničková, J. Kotrla, The effect of burnt lime addition on hydration of Ultra-high performance cementitious composites, IOP Conference Series: Materials Science and Engineering, Institute of Physics Publishing, 2019.

[18] R. Novotný, E. Bartoníčková, J. Švec, M. Mončeková, Influence of Active Alumina on the Hydration Process of Portland Cement, in: D. Kubatova, M. Bohac, M. Drdlova (Eds.) Procedia Engineering, Elsevier Ltd, 2016, pp. 80-86.

[19] O. Kunovský, F. Šoukal, L. Kalina, T. Opravil, E. Bartoníčková, Effect of drying on the structure of sol-gel synthesized calcium silicate hydrate gels, Acta Polytechnica CTU Proceedings, 2025.

[20] V. Bílek, L. Kalina, E. Bartonícková, J. Porízka, Evaluation of the Surfactant Leaching from Alkali-Activated Slag-Based Composites Using Surface-Tension Measurements, Mater Tehnol, 53 (2019) 33-38.

[21] L. Kalina, V. Bílek, E. Bartonícková, Effect of Amino Alcohol Admixtures on Alkali-Activated Materials, Mater Tehnol, 54 (2020) 349-353.

[22] L. Kalina, V. Bílek, E. Bartonícková, J. Krouská, Polypropylene Glycols as Effective Shrinkage-Reducing Admixtures in Alkali-Activated Materials, Aci Mater J, 115 (2018) 251-256.

[23] L. Kalina, V. Bílek, E. Bartoníčková, Effect of amino alcohol admixtures on alkali-activated materials, Mater Tehnol, 54 (2020) 349-353.

[24] L. Kalina, V. Bílek, E. Bartoníčková, M. Kalina, J. Hajzler, R. Novotný, Doubts over capillary pressure theory in context with drying and autogenous shrinkage of alkali-activated materials, Construction and Building Materials, 248 (2020).

[25] E. Bartonickova, P. Ptacek, R. Novotny, J. Palovcik, J. Masilko, J. Svec, M. Sedlacik, J. Koplik, T. Stanek, D. Hemzal, Hydration kinetics of C3A: effect of lithium, copper and sulfur-based mineralizers, Journal of Thermal Analysis and Calorimetry, (2024).

[26] J. Koplík, J. Švec, J. Másilko, M. Sedlačík, E. Bartoníčková, Synthesis of calcium aluminate hydrates, their characterization and dehydration, Ceramics International, (2024).

[27] P. Ptácek, F. Soukal, T. Opravil, E. Bartonícková, M. Zmrzly, R. Novotny, Synthesis, hydration and thermal stability of hydrates in strontium-aluminate cement, Ceramics International, 40 (2014) 9971-9979.

[28] L. Dlabajová, Příprava tobermoritu, VUT v Brně, 2020.

[29] T.C. Powers, T.L. Brownyard, Studies of the Physical Properties of Hardened Portland Cement Paste, ACI Journal Proceedings, 43.

[30] T.H.F. W, The Chemistry of Cements. , Academic Press, London, 1964.

[31] F. Ridi, E. Fratini, P. Baglioni, Cement: A two thousand year old nano-colloid, Journal of Colloid and Interface Science, 357 (2011) 255-264.

[32] J. Brouwers, Chemical Reactions in hydrated Ordinary Portland Cement based on the work by Powers and Brownyard, Proceedings 15th Ibausil (Internationale Baustofftagung), Weimar, vol 1: Proceedings 15th Ibausil (Internationale Baustofftagung), FA Finger Institut für Baustoffkunde, 2003, pp. 1-0553--0551-0566.

[33] L. Struble, G.C. Bye, Portland Cement: Composition, Production and Properties, Ice Publishing2011.

[34] I. Richardson, J.G. Cabrera, Nature of C-S-H in model slag-cements, 2000.

[35] I.G. Richardson, The nature of C-S-H in hardened cements, Cement and Concrete Research, 29 (1999) 1131-1147.

[36] I.G. Richardson, The calcium silicate hydrates, Cement and Concrete Research, 38 (2008) 137-158.

[37] I.G. Richardson, Model structures for C-(A)-S-H(I), Acta Crystallographica Section B Structural Science, Crystal Engineering and Materials, 70 (2014) 903-923.

[38] I.G. Richardson, A.R. Brough, R. Brydson, G.W. Groves, C.M. Dobson, Location of Aluminum in Substituted Calcium Silicate Hydrate (C-S-H) Gels as Determined by 29Si and 27Al NMR and EELS, Journal of the American Ceramic Society, 76 (1993) 2285-2288.

[39] I.G. Richardson, G.W. Groves, Microstructure and microanalysis of hardened cement pastes involving

ground granulated blast-furnace slag, Journal of Material Science, 27 (1992) 6204-6212.

[40] I.G. Richardson, G.W. Groves, MODELS FOR THE COMPOSITION AND STRUCTURE OF CALCIUM SILICATE HYDRATE (C-S-H) GEL IN HARDENED TRICALCIUM SILICATE PASTES, Cement and Concrete Research, 22 (1992) 1001-1010.

[41] I.G. Richardson, G.W. Groves, Microstructure and microanalysis of hardened ordinary Portland cement pastes, Journal of Materials Science, 28 (1993) 265-277.

[42] I.G. Richardson, J. Skibsted, L. Black, R.J. Kirkpatrick, Characterisation of cement hydrate phases by TEM, NMR and Raman spectroscopy, Advances in Cement Research, 22 (2010) 233-248.

[43] Z. Casar, A.K. Mohamed, P. Bowen, K. Scrivener, Atomic-Level and Surface Structure of Calcium Silicate Hydrate Nanofoils, The Journal of Physical Chemistry C, 127 (2023) 18652-18661.

[44] H.W. Taylor, Hydrated calcium silicates. Part I. Compound formation at ordinary temperatures, Journal of the Chemical Society (Resumed), (1950) 3682-3690.

[45] A. Nonat, X. Lecoq, The Structure, Stoichiometry and Properties of C-S-H Prepared by C3S Hydration Under Controlled Condition, (1998) 197-207.

[46] R.J. Kirkpatrick, J.L. Yarger, P.F. McMillan, Y. Ping, X. Cong, Raman spectroscopy of C-S-H, tobermorite, and jennite, Advanced Cement Based Materials, 5 (1997) 93-99.

[47] H.F.W. TAYLOR, Proposed Structure for Calcium Silicate Hydrate Gel, Journal of the American Ceramic Society, 69 (1986) 464-467.

[48] S. Grangeon, F. Claret, C. Lerouge, F. Warmont, T. Sato, S. Anraku, C. Numako, Y. Linard, B. Lanson, On the nature of structural disorder in calcium silicate hydrates with a calcium/silicon ratio similar to tobermorite, Cement and Concrete Research, 52 (2013) 31-37.

[49] A. Cuesta, J.D. Zea-Garcia, D. Londono-Zuluaga, A.G. De la Torre, I. Santacruz, O. Vallcorba, M. Dapiaggi, S.G. Sanfélix, M.A. Aranda, Multiscale understanding of tricalcium silicate hydration reactions, Scientific reports, 8 (2018) 8544.

[50] P. Rejmak, J.S. Dolado, M.J. Stott, A. Ayuela, 29Si NMR in Cement: A Theoretical Study on Calcium Silicate Hydrates, The Journal of Physical Chemistry C, 116 (2012) 9755-9761.

[51] C. Biagioni, S. Merlino, E. Bonaccorsi, The tobermorite supergroup: a new nomenclature, Mineralogical Magazine, 79 (2015) 485-495.

[52] M.C. Day, F.C. Hawthorne, A structure hierarchy for silicate minerals: chain, ribbon, and tube silicates, Mineralogical Magazine, 84 (2020) 165-244.

[53] S.A. Hamid, The crystal structure of the 11 Ä natural tobermorite Ca2.25[Si3O7.5(OH)1.5]·1H2O, Zeitschrift für Kristallographie - Crystalline Materials, 154 (1981) 189-198.

[54] S. Merlino, E. Bonaccorsi, T. Armbruster, Tobermorites: Their real structure and order-disorder (OD) character, American Mineralogist, 84 (1999) 1613-1621.

[55] D. Tunega, A. Zaoui, Understanding of bonding and mechanical characteristics of cementitious mineral tobermorite from first principles, Journal of Computational Chemistry, 32 (2011) 306-314.

[56] E. Bonaccorsi, S. Merlino, Modular microporous minerals: cancrinite-davyne group and CSH phases, Reviews in Mineralogy and Geochemistry, 57 (2005) 241-290.

[57] R.J.M. Pellenq, N. Lequeux, H. van Damme, Engineering the bonding scheme in C-S-H: The iono-covalent framework, Cement and Concrete Research, 38 (2008) 159-174.

[58] E. Duque-Redondo, P.A. Bonnaud, H. Manzano, A comprehensive review of C-S-H empirical and computational models, their applications, and practical aspects, Cement and Concrete Research, 156 (2022) 106784.

[59] S. Merlino, E. Bonacorsi, T. Armbuster, The real structure of tobermorite 11Å : normal and anomalous forms, OD character and polytypic modifications, European Journal of Mineralogy, 13 (2001) 577-590.

[60] R. Dupuis, J. Moon, Y. Jeong, R. Taylor, S.H. Kang, H. Manzano, A. Ayuela, P.J.M. Monteiro, J.S. Dolado, Normal and anomalous self-healing mechanism of crystalline calcium silicate hydrates, Cement and Concrete Research, 142 (2021).

[61] E. Bonaccorsi, S. Merlino, A.R. Kampf, The Crystal Structure of Tobermorite 14 Å (Plombierite), a C–S–H Phase, Journal of the American Ceramic Society, 88 (2005) 505-512.

[62] S. Merlino, E. Bonaccorsi, T. Armbruster, The Real Structures of Clinotobermorite and Tobermorite 9 Å: OD Character, Polytypes, and Structural Relationships, 2000.

[63] H.F.W. Taylor, Cement Chemistry, Emerald Publishing Limited1997.

[64] I.G. Richardson, Tobermorite/jennite- and tobermorite/calcium hydroxide-based models for the structure of C-S-H: Applicability to hardened pastes of tricalcium silicate, β-dicalcium silicate, Portland cement, and blends of Portland cement with blast-furnace slag, metakaolin, or silica fume, Cement and Concrete Research, 34 (2004) 1733-1777.

[65] I.L. Moudrakovski, R. Alizadeh, J.J. Beaudoin, Natural abundance high field 43Ca solid state NMR in cement science, Physical Chemistry Chemical Physics, 12 (2010) 6961-6969.

[66] S. Grangeon, A. Fernandez-Martinez, A. Baronnet, N. Marty, A. Poulain, E. Elkaim, C. Roosz, S. Gaboreau, P. Henocq, F. Claret, Quantitative X-ray pair distribution function analysis of nanocrystalline calcium silicate hydrates: a contribution to the understanding of cement chemistry, Applied Crystallography, 50 (2017) 14-21.

[67] J. Rossen, Composition and morphology of C-A-S-H in pastes of alite and cement blended with supplementary cementitious materials, 2014.

[68] R.F. Feldman, P.J. Sereda, A model for hydrated Portland cement paste as deduced from sorption-length change and mechanical properties, Matériaux et Construction, 1 (1968) 509-520.

[69] P.D. Tennis, H.M. Jennings, A model for two types of calcium silicate hydrate in the microstructure of Portland cement pastes, Cement and Concrete Research, 30 (2000) 855-863.

[70] H.M. Jennings, Colloid model of C-S-H and implications to the problem of creep and shrinkage, Materials and Structures/Materiaux et Constructions, 37 (2004) 59-70.

[71] H.M. Jennings, A model for the microstructure of calcium silicate hydrate in cement paste, Cement and Concrete Research, 30 (2000) 101-116.

[72] G. Constantinides, F.-J. Ulm, The effect of two types of C-S-H on the elasticity of cement-based materials: Results from nanoindentation and micromechanical modeling, Cement and Concrete Research, 34 (2004) 67-80.

[73] J.J. Thomas, H.M. Jennings, A colloidal interpretation of chemical aging of the C-S-H gel and its effects on the properties of cement paste, Cement and Concrete Research, 36 (2006) 30-38.

[74] H.M. Jennings, J.J. Thomas, J.S. Gevrenov, G. Constantinides, F.-J. Ulm, A multi-technique investigation of the nanoporosity of cement paste, Cement and Concrete Research, 37 (2007) 329-336.

[75] H.M. Jennings, Refinements to colloid model of C-S-H in cement: CM-II, Cement and Concrete Research, 38 (2008) 275-289.

[76] J.D. Bernal, J.W. Jeffery, H.F.W. Taylor, Crystallographic research on the hydration of Portland cement. A first report on investigations in progress, Magazine of Concrete Research, 4 (1952) 49-54.

[77] H. Taylor, J. Howison, Relationships between calcium silicates and clay minerals, Clay Minerals Bulletin, 3 (1956) 98-111.

[78] H. Kurczyk, H. Schwiete, Paper III-S13. Concerning the Hydration Products of CS and B-C2S, Chemistry of Cement: Proceedings of the Fourth International Symposium, Washington, 1960, Symposium Held October 2-7, 1960 at the National Bureau of Standards, Washington, DC, US Government Printing Office, 1962, pp. 349.

[79] S. Brunauer, R.S. Mikhail, E.E. Bodor, Some remarks about capillary condensation and pore structure analysis, Journal of Colloid and Interface Science, 25 (1967) 353-358.

[80] F. Wittmann, The structure of hardened cement paste-a basis for a better understanding of the materials properties, Proc. Hydraulic cement pastes: their structure and properties, (1976) 96-117.

[81] H. Stade, W. Wieker, Zum Aufbau schlecht geordneter Calciumhydrogensilicate. I. Bildung und Eigenschaften einer schlecht geordneten Calciumhydrogendisilicatphase, Zeitschrift für anorganische und allgemeine Chemie, 466 (1980) 55-70.

[82] F.P. GLASSER, E.E. LACHOWSKI, D.E. MACPHEE, Compositional Model for Calcium Silicate Hydrate (C-S-H) Gels, Their Solubilities, and Free Energies of Formation, Journal of the American Ceramic Society, 70 (1987) 481-485.

[83] I.G. Richardson, G.W. Groves, Models for the composition and structure of calcium silicate hydrate (C・S・H) gel in hardened tricalcium silicate pastes, Cement and Concrete Research, 22 (1992) 1001-1010.

[84] A. Nonat, X. Lecoq, The Structure, Stoichiometry and Properties of C-S-H Prepared by C3S Hydration Under Controlled Condition, in: P. Colombet, H. Zanni, A.-R. Grimmer, P. Sozzani (Eds.) Nuclear Magnetic Resonance Spectroscopy of Cement-Based Materials, Springer Berlin Heidelberg, Berlin, Heidelberg, 1998, pp. 197-207.

[85] J.J. Chen, J.J. Thomas, H.F.W. Taylor, H.M. Jennings, Solubility and structure of calcium silicate hydrate, Cement and Concrete Research, 34 (2004) 1499-1519.

[86] C. Plassard, E. Lesniewska, I. Pochard, A. Nonat, Investigation of the surface structure and elastic properties of calcium silicate hydrates at the nanoscale, Ultramicroscopy, 100 (2004) 331-338.

[87] A.J. Allen, R.C. Oberthur, D. Pearson, P. Schofield, C.R. Wilding, Development of the fine porosity and gel structure of hydrating cement systems, Philosophical Magazine B, 56 (1987) 263-288.

[88] R. González-Teresa, V. Morales-Florez, H. Manzano, J.S. Dolado, Structural models of randomly packed Tobermorite-like spherical particles: A simple computational approach, Materiales de Construcción, 60 (2010) 7-15.

[89] G. Constantinides, F.-J. Ulm, The nanogranular nature of C–S–H, Journal of the Mechanics and Physics of Solids, 55 (2007) 64-90.

[90] J.J. Thomas, H.M. Jennings, Effect of Heat Treatment on the Pore Structure and Drying Shrinkage Behavior of Hydrated Cement Paste, Journal of the American Ceramic Society, 85 (2002) 2293-2298.

[91] C.J. Brinker, G.W. Scherer, CHAPTER 3 - Hydrolysis and Condensation II: Silicates, in: C.J. Brinker, G.W. Scherer (Eds.) Sol-Gel Science, Academic Press, San Diego, 1990, pp. 96-233.

[92] X. Yang, P. Roonasi, A. Holmgren, A study of sodium silicate in aqueous solution and sorbed by synthetic magnetite using in situ ATR-FTIR spectroscopy, Journal of Colloid and Interface Science, 328 (2008) 41-47.

[93] G.W. Scherer, Structure and properties of gels, Cement and Concrete Research, 29 (1999) 1149-1157.

[94] H.M. Jennings, Colloid model of C− S− H and implications to the problem of creep and shrinkage, Materials and structures, 37 (2004) 59-70.

[95] M. Matinfar, J.A. Nychka, A review of sodium silicate solutions: Structure, gelation, and syneresis, Adv Colloid Interface Sci, 322 (2023) 103036.

[96] L. Kalina, V. Bílek, M. Sedlačík, V. Cába, J. Smilek, J. Švec, E. Bartoníčková, P. Rovnaník, J. Fládr, Physico-Chemical Properties of Lithium Silicates Related to Their Utilization for Concrete Densifiers, Materials, 16 (2023).

[97] G. Constantinides, F.-J. Ulm, K. Van Vliet, On the use of nanoindentation for cementitious materials, Materials and structures, 36 (2003) 191-196.

[98] F. Ridi, P. Luciani, E. Fratini, P. Baglioni, Water Confined in Cement Pastes as a Probe of Cement Microstructure Evolution, The Journal of Physical Chemistry B, 113 (2009) 3080-3087.

[99] P. Yu, R.J. Kirkpatrick, B. Poe, P.F. McMillan, X. Cong, Structure of Calcium Silicate Hydrate (C-S-H): Near-, Mid-, and Far-Infrared Spectroscopy, Journal of the American Ceramic Society, 82 (1999) 742-748.

[100] A.J. Allen, J.J. Thomas, H.M. Jennings, Composition and density of nanoscale calcium–silicate–hydrate in cement, Nature Materials, 6 (2007) 311-316.

[101] P.J.M. Monteiro, G. Geng, D. Marchon, J. Li, P. Alapati, K.E. Kurtis, M.J.A. Qomi, Advances in characterizing and understanding the microstructure of cementitious materials, Cement and Concrete Research, 124 (2019).

[102] V.K. Peterson, D.A. Neumann, R.A. Livingston, Hydration of Tricalcium and Dicalcium Silicate Mixtures Studied Using Quasielastic Neutron Scattering, The Journal of Physical Chemistry B, 109 (2005) 14449-14453.

[103] K. Chassapis, M. Roulia, E. Vrettou, D. Fili, M. Zervaki, Biofunctional Characteristics of Lignite Fly Ash Modified by Humates: A New Soil Conditioner, Bioinorganic Chemistry and Applications, 2010 (2010) 457964.

[104] W. Yan, M. Lv, M. He, X. Liu, Effect of second Si–O vibrational overtones/combinations on quantifying water in silicate and silica minerals using infrared spectroscopy, and an experimental method for its removal, Physics and Chemistry of Minerals, 49 (2022) 5.

[105] J. Janik, W. Kurdowski, R. Podsiadły, J. Samseth, Fractal structure of CSH and tobermorite phases, Acta Physica Polonica A, 100 (2001) 529-537.

[106] N. Lequeux, A. Morau, S. Philippot, P. Boch, Extended X-ray Absorption Fine Structure Investigation of Calcium Silicate Hydrates, Journal of the American Ceramic Society, 82 (1999) 1299-1306.

[107] A. Gmira, M. Zabat, R.-M. Pellenq, H. Van Damme, Microscopic physical basis of the poromechanical behavior of cement-based materials, Materials and Structures, 37 (2004) 3-14.

[108] A. Nonat, The structure and stoichiometry of C-S-H, Cement and Concrete Research, 34 (2004) 1521-1528.

[109] A. Ayuela, J.S. Dolado, I. Campillo, Y. De Miguel, E. Erkizia, D. Sánchez-Portal, A. Rubio, A. Porro, P.M. Echenique, Silicate chain formation in the nanostructure of cement-based materials, The Journal of chemical physics, 127 (2007).

[110] H. Manzano, A. Ayuela, J.S. Dolado, On the formation of cementitious C–S–H nanoparticles, Journal of Computer-Aided Materials Design, 14 (2007) 45-51.

[111] J.S. Dolado, M. Griebel, J. Hamaekers, A Molecular Dynamic Study of Cementitious Calcium Silicate Hydrate (C–S–H) Gels, Journal of the American Ceramic Society, 90 (2007) 3938-3942.

[112] R.J.M. Pellenq, N. Lequeux, H. van Damme, Engineering the bonding scheme in C–S–H: The iono-covalent framework, Cement and Concrete Research, 38 (2008) 159-174.

[113] L.B. Skinner, S.R. Chae, C.J. Benmore, H.R. Wenk, P.J.M. Monteiro, Nanostructure of Calcium Silicate Hydrates in Cements, Physical Review Letters, 104 (2010) 195502.

[114] J.S. Dolado, M. Griebel, J. Hamaekers, F. Heber, The nano-branched structure of cementitious calcium–silicate–hydrate gel, Journal of Materials Chemistry, 21 (2011) 4445-4449.

[115] H. Manzano, R.J.M. Pellenq, F.-J. Ulm, M.J. Buehler, A.C.T. van Duin, Hydration of Calcium Oxide Surface Predicted by Reactive Force Field Molecular Dynamics, Langmuir, 28 (2012) 4187-4197.

[116] M.A. Qomi, K. Krakowiak, M. Bauchy, K. Stewart, R. Shahsavari, D. Jagannathan, D. Brommer, A. Baronnet, M. Buehler, S. Yip, Combinatorial molecular optimization of cement hydrates, Nat. Commun. 5 (2014) 4960.

[117] G. Kovačević, B. Persson, L. Nicoleau, A. Nonat, V. Veryazov, Atomistic modeling of crystal structure of Ca1.67SiHx, Cement and Concrete Research, 67 (2015) 197-203.

[118] A. Kunhi Mohamed, S.C. Parker, P. Bowen, S. Galmarini, An atomistic building block description of C-S-H - Towards a realistic C-S-H model, Cement and Concrete Research, 107 (2018) 221-235.

[119] S. Tang, Y. Wang, Z. Geng, X. Xu, W. Yu, H. A, J. Chen, Structure, Fractality, Mechanics and Durability of Calcium Silicate Hydrates, Fractal and Fractional, 5 (2021) 47.

[120] A.A. Bahraq, M.A. Al-Osta, O.S. Baghabra Al-Amoudi, I.B. Obot, M. Maslehuddin, H.-u.-R. Ahmed, T.A. Saleh, Molecular Simulation of Cement-Based Materials and Their Properties, Engineering, 15 (2022) 165-178.

[121] I. García Lodeiro, D.E. Macphee, A. Palomo, A. Fernández-Jiménez, Effect of alkalis on fresh C–S–H gels. FTIR analysis, Cement and Concrete Research, 39 (2009) 147-153.

[122] B. Lothenbach, A. Nonat, Calcium silicate hydrates: Solid and liquid phase composition, Cement and Concrete Research, 78 (2015) 57-70.

[123] A. Kumar, B.J. Walder, A. Kunhi Mohamed, A. Hofstetter, B. Srinivasan, A.J. Rossini, K. Scrivener, L. Emsley, P. Bowen, The Atomic-Level Structure of Cementitious Calcium Silicate Hydrate, The Journal of Physical Chemistry C, 121 (2017) 17188-17196.

[124] R. Siauciunas, K. Baltakys, Formation of gyrolite during hydrothermal synthesis in the mixtures of CaO and amorphous SiO2 or quartz, CEMENT AND CONCRETE RESEARCH, 34 (2004) 2029-2036.

[125] N. Holmes, C. Walker, M. Tyrer, D. Kelliher, Deriving discrete solid phases from CSH-3T and CSHQ end-members to model cement hydration in PHREEQC, 2022.

[126] A. Kumar, Synthetic Calcium Silicate Hydrates, EPFL, Lausanne, 2017.

[127] I.R. K., The Chemistry of Silica, Wiley, New York, 1979.

[128] S. Garrault-Gauffinet, A. Nonat, Experimental investigation of calcium silicate hydrate (C-S-H) nucleation, Journal of Crystal Growth, 200 (1999) 565-574.

[129] E. Bartoníčková, Syntéza a analýza kompozitních oxidových keramik v přítomnosti nekonvenčních energetických polí, Brno university of technology, Brno, 2010.

[130] Walton A.G., Nucleation in liquids, and solutions, Zettlemoyer A.C. Ed.,1962.

[131] D. Gebauer, P. Raiteri, J. Gale, H. Cölfen, On classical and non-classical views on nucleation, American Journal of Science, 318 (2018) 969-988.

[132] J.W. Christian, The theory of transformations in metals and alloys, Pergamon Press Inc, Oxford, (1975).

[133] V.K. Lamer, R.H. Dinegar, Theory, Production and Mechanism of Formation of Monodispersed Hydrosols, Journal of the American Chemical Society, 72 (1950) 4847-4854.

[134] J.A. Dirksen, T.A. Ring, Fundamentals of crystallization: Kinetic effects on particle size distributions and morphology, Chemical Engineering Science, 46 (1991) 2389-2427.

[135] J. Mullin, Crystallization (Fourth Edition), Butterworth-Heinemann, Oxford, 2001.

[136] R. Alizadeh, L. Raki, J.M. Makar, J.J. Beaudoin, I. Moudrakovski, Hydration of tricalcium silicate in the presence of synthetic calcium–silicate–hydrate, Journal of Materials Chemistry, 19 (2009) 7937-7946.

[137] V.V. Boldyrev, Hydrothermal reactions under mechanochemical action, Powder Technology, 122 (2002) 247-254.

[138] F. Saito, G. Mi, M. Hanada, Mechanochemical synthesis of hydrated calcium silicates by room temperature grinding, Solid State Ionics, 101-103 (1997) 37-43.

[139] G. Mi, F. Saito, M. Hanada, Mechanochemical synthesis of tobermorite by wet grinding in a planetary ball mill, Powder Technology, 93 (1997) 77-81.

[140] K. Garbev, G. Beuchle, M. Bornefeld, L. Black, P. Stemmermann, Cell Dimensions and Composition of Nanocrystalline Calcium Silicate Hydrate Solid Solutions. Part 1: Synchrotron-Based X-Ray Diffraction, Journal of the American Ceramic Society, 91 (2008) 3005-3014.

[141] L. Black, K. Garbev, P. Stemmermann, K.R. Hallam, G.C. Allen, Characterisation of crystalline C-S-H phases by X-ray photoelectron spectroscopy, Cement and Concrete Research, 33 (2003) 899-911.

[142] E. Tajuelo Rodriguez, K. Garbev, D. Merz, L. Black, I.G. Richardson, Thermal stability of C-S-H phases and applicability of Richardson and Groves' and Richardson C-(A)-S-H(I) models to synthetic C-S-H, Cement and Concrete Research, 93 (2017) 45-56.

[143] A. Niedermayr, S.J. Köhler, M. Dietzel, Impacts of aqueous carbonate accumulation rate, magnesium and polyaspartic acid on calcium carbonate formation (6–40°C), Chemical Geology, 340 (2013) 105-120.

[144] Ç.M. Oral, B. Ercan, Influence of pH on morphology, size and polymorph of room temperature synthesized calcium carbonate particles, Powder Technology, 339 (2018) 781-788.

[145] K. Schaufthaoul, Gelehrten Anzeigen [online], Bayerische Akademie,, 20 (1845) 557.

[146] K. Byrrapa, M. Yoshimura, Handbook of hydrothermal technology: a technology for crystal growth and materials processing, Noyes Publications, Norwich, N.Y., 2001.

[147] G. Brunner, Hydrothermal and supercritical water processes, Elsevier, Amsterdam, 2014.

[148] C.F. Chan, M. Sakiyama, T. Mitsuda, Kinetics of the CaO ・ quartz ・ H2O reaction at 120° to 180°C in suspensions, Cement and Concrete Research, 8 (1978) 1-5.

[149] C.F. Dickinson, G.R. Heal, Solid–liquid diffusion controlled rate equations, Thermochimica Acta, 340-341 (1999) 89-103.

[150] S. Bernstein, K.T. Fehr, The formation of 1.13 nm tobermorite under hydrothermal conditions: 1. The influence of quartz grain size within the system CaO–SiO2–D2O, Progress in Crystal Growth and Characterization of Materials, 58 (2012) 84-91.

[151] A. Hartmann, D. Schulenberg, J. Buhl, Synthesis and Structural Characterization of CSH-Phases in the Range of C/S = 0.41 - 1.66 at Temperatures of the Tobermorite Xonotlite Crossover, Journal of Materials Science and Chemical Engineering, 3 (2015) 39-55.

[152] S.Y. Hong, F.P. Glasser, Phase relations in the CaO–SiO2–H2O system to 200 °C at saturated steam pressure, Cement and Concrete Research, 34 (2004) 1529-1534.

[153] J. Brandštetr, Z. Šauman, Teorie struktury stavebních látek., Vysoké učení technické v Brně, Brno, 1979.

[154] J. Kikuma, M. Tsunashima, T. Ishikawa, S. Matsuno, A. Ogawa, K. Matsui, M. Sato, Effects of quartz particle size and water-to-solid ratio on hydrothermal synthesis of tobermorite studied by in-situ time-resolved X-ray diffraction, Journal of Solid State Chemistry, 184 (2011) 2066-2074.

[155] D. Bruzl, L. Bocian, P. Sokola, J. Másilko, M. Sedlačík, J. Švec, E. Bartoníčková, F. Šoukal, Sol gel synthesis of TiO2@ZnO composites for self-cleaning and antimicrobial coating, in: M. Bohac, M. Drdlova, D. Kubatova, A. Zezulova (Eds.) Journal of Physics: Conference Series, Institute of Physics, 2024.

[156] K. Castkova, A. Matousek, E. Bartonickova, J. Cihlar, P. Vanysek, Sintering of Ce, Sm, and Pr Oxide Nanorods, Journal of the American Ceramic Society, 99 (2016) 1155-1163.

[157] J. Cihlar, J. Cihlar Jr, E. Bartonickova, Low-temperature sol-gel synthesis of anatase nanoparticles modified by Au, Pd and Pt and activity of TiO2/Au, Pd, Pt photocatalysts in water splitting, J Sol-Gel Sci Techn, 65 (2013) 430-442.

[158] E. Bartonickova, K. Wiik, K. Maca, H.L. Lein, E.A. Rudberg, Synthesis and oxygen transport properties of LaSrFeTiO (=0.2, 0.4) intended for syn-gas production, Journal of the European Ceramic Society, 30 (2010) 605-611.

[159] J. Cihlář, Hydrolysis and polycondensation of ethyl silicates. 1. Effect of pH and catalyst on the hydrolysis and polycondensation of tetraethoxysilane (TEOS), Colloids and Surfaces A: Physicochemical and Engineering Aspects, 70 (1993) 239-251.

[160] V.G. Kessler, G.I. Spijksma, G.A. Seisenbaeva, S. Håkansson, D.H.A. Blank, H.J.M. Bouwmeester, New insight in the role of modifying ligands in the sol-gel processing of metal alkoxide precursors: A possibility to approach new classes of materials, J Sol-Gel Sci Techn, 40 (2006) 163-179.

[161] M. Neagu, F. Grisi, A. Pulvirenti, R. Simón-Vázquez, C.A. García-González, A.C. Boccia, Aerogel Compounds., Encyclopedia., (2025).

[162] T. Hayashi, H. Saito, Preparation of CaO-SiO2 glasses by the gel method, Journal of Materials Science, 15 (1980) 1971-1977.

[163] I. García-Lodeiro, A. Fernández-Jiménez, M.T. Blanco, A. Palomo, FTIR study of the sol–gel synthesis of cementitious gels: C–S–H and N–A–S–H, J Sol-Gel Sci Techn, 45 (2008) 63-72.

[164] M. Harris, G. Simpson, K. Scrivener, P. Bowen, A method for the reliable and reproducible precipitation of phase pure high Ca/Si ratio (>1.5) synthetic calcium silicate hydrates (CSH), Cement and Concrete Research, 151 (2022) 106623.

[165] C.A. Love, I.G. Richardson, A.R. Brough, Composition and structure of C–S–H in white Portland cement–20% metakaolin pastes hydrated at 25 °C, Cement and Concrete Research, 37 (2007) 109-117.

[166] E. L'Hôpital, B. Lothenbach, G. Le Saout, D. Kulik, K. Scrivener, Incorporation of aluminium in calcium-silicate-hydrates, Cement and Concrete Research, 75 (2015) 91-103.

[167] G.L. KALOUSEK, Crystal Chemistry of Hydrous Calcium Silicates: I, Substitution of Aluminum in Lattice of Tobermorite, Journal of the American Ceramic Society, 40 (1957) 74-80.

[168] S. Diamond, J.L. White, W.L. Dolch, EFFECTS OF ISOMORPHOUS SUBSTITUTION IN HYDROTHERMALLY-SYNTHESIZED TOBERMORITE, AMERICAN MINERALOGIST, 51 (1966) 388-&.

[169] S. Komarneni, R. Roy, D.M. Roy, C.A. Fyfe, G.J. Kennedy, Al-substituted tobermorite—The coordination of aluminum as revealed by solid-state 27Al magic angle spinning (MAS) NMR, Cement and Concrete Research, 15 (1985) 723-728.

[170] M. Tsuji, S. Komarneni, P. Malla, Substituted Tobermorites: 27Al and 29Si MASNMR, Cation Exchange, and Water Sorption Studies, Journal of the American Ceramic Society, 74 (1991) 274-279.

[171] I. García Lodeiro, A. Fernández-Jimenez, A. Palomo, D.E. Macphee, Effect on fresh C-S-H gels of the simultaneous addition of alkali and aluminium, Cement and Concrete Research, 40 (2010) 27-32.

[172] Q. Liu, P. Feng, L. Shao, C. Chen, X. Liu, Y. Ma, L. Zhang, G. Geng, Quantifying the immobilization mechanisms of heavy metals by Calcium Silicate Hydrate (C-S-H): The case of Cu2+, Cement and Concrete Research, 186 (2024) 107695.

[173] J. Park, S. Cho, H. Suh, S. Her, J. Yang, S. Bae, Immobilization and leaching behavior of cobalt in alkali-activated fly ash/dehydrated cement paste fine blends, Cement and Concrete Research, 195 (2025) 107921.

[174] J.-M. Wolter, K. Schmeide, N. Huittinen, T. Stumpf, Cm(III) retention by calcium silicate hydrate (C-S-H) gel and secondary alteration phases in carbonate solutions with high ionic strength: A site-selective TRLFS study, Scientific Reports, 9 (2019) 14255.

[175] X. Pardal, I. Pochard, A. Nonat, Experimental study of Si–Al substitution in calcium-silicate-hydrate (C-S-H) prepared under equilibrium conditions, Cement and Concrete Research, 39 (2009) 637-643.

[176] J. Skibsted, C. Hall, Characterization of cement minerals, cements and their reaction products at the atomic and nano scale, Cement and Concrete Research, 38 (2008) 205-225.

[177] L. Black, A. Stumm, K. Garbev, P. Stemmermann, K.R. Hallam, G.C. Allen, X-ray photoelectron spectroscopy of aluminium-substituted tobermorite, Cement and Concrete Research, 35 (2005) 51-55.

[178] E. L'Hôpital, B. Lothenbach, D.A. Kulik, K. Scrivener, Influence of calcium to silica ratio on aluminium uptake in calcium silicate hydrate, Cement and Concrete Research, 85 (2016) 111-121.

[179] I.G. Richardson, A.V. Girão, R. Taylor, S. Jia, Hydration of water- and alkali-activated white Portland cement pastes and blends with low-calcium pulverized fuel ash, Cement and Concrete Research, 83 (2016) 1-18.

[180] R. Taylor, I.G. Richardson, R.M.D. Brydson, Composition and microstructure of 20-year-old ordinary Portland cement–ground granulated blast-furnace slag blends containing 0 to 100% slag, Cement and Concrete Research, 40 (2010) 971-983.

[181] B. Lothenbach, D. Jansen, Y. Yan, J. Schreiner, Solubility and characterization of synthesized 11 Å Al-tobermorite, Cement and Concrete Research, 159 (2022) 106871.

[182] J. Davidovits, Mineral polymers and methods of making them., 1982b.

[183] P. Kryvenko, Why Alkaline Activation – 60 Years of the Theory and Practice of Alkali-Activated Materials, Journal of Ceramic Science and Technology, 8 (2017) 323-334.

[184] A. Palomo, P. Krivenko, I. Garcia-Lodeiro, E. Kavalerova, O. Maltseva, A. Fernández-Jiménez, A review on alkaline activation: new analytical perspectives, Materiales de Construcción, 64 (2014) e022.

[185] R.J. Myers, S.A. Bernal, R. San Nicolas, J.L. Provis, Generalized Structural Description of Calcium–Sodium Aluminosilicate Hydrate Gels: The Cross-Linked Substituted Tobermorite Model, Langmuir, 29 (2013) 5294-5306.

[186] I.G. Richardson, G.W. Groves, The incorporation of minor and trace elements into calcium silicate hydrate (C・S・H) gel in hardened cement pastes, Cement and Concrete Research, 23 (1993) 131-138.

[187] A. Kunhi Mohamed, P. Moutzouri, P. Berruyer, B.J. Walder, J. Siramanont, M. Harris, M. Negroni, S.C. Galmarini, S.C. Parker, K.L. Scrivener, L. Emsley, P. Bowen, The Atomic-Level Structure of Cementitious Calcium Aluminate Silicate Hydrate, J Am Chem Soc, 142 (2020) 11060-11071.

[188] Q. Fu, M. Bu, Z. Zhang, W. Xu, Q. Yuan, D. Niu, Hydration Characteristics and Microstructure of Alkali-Activated Slag Concrete: A Review, Engineering, 20 (2023) 162-179.

[189] L.Y. Yang, Z.J. Jia, Y.M. Zhang, J.G. Dai, Effects of nano-TiO2 on strength, shrinkage and microstructure of alkali activated slag pastes, Cement and Concrete Composites, 57 (2015) 1-7.

[190] F. Collins, J.G. Sanjayan, Effect of pore size distribution on drying shrinking of alkali-activated slag concrete, Cement and Concrete Research, 30 (2000) 1401-1406.

[191] E. Haccuria, T. Crivits, P. Hayes, E. Jak, Selected phase equilibria studies in the Al2O3-CaO-SiO2 system, Journal of the American Ceramic Society, Online (2015).

[192] J.S. Andrade Neto, P.R. de Matos, A.G. De la Torre, C.E.M. Campos, P.J.P. Gleize, P.J.M. Monteiro, A.P. Kirchheim, The role of sodium and sulfate sources on the rheology and hydration of C3A polymorphs, Cement and Concrete Research, 151 (2022) 106639.

[193] P. Padilla-Encinas, A. Palomo, M.T. Blanco-Varela, A. Fernández-Jiménez, Calcium sulfoaluminate clinker hydration at different alkali concentrations, Cement and Concrete Research, 138 (2020) 106251.

[194] J. Havlica, D. Roztocká, S. Sahu, Hydration kinetics of calciumaluminate phases in the presence of various ratios of Ca2+ and SO42− ions in liquid phase, Cement and Concrete Research, 23 (1993) 294-300.

[195] K. Meinhard, R. Lackner, Multi-phase hydration model for prediction of hydration-heat release of blended cements, Cement and Concrete Research, 38 (2008) 794-802.

[196] B. Lothenbach, L. Pelletier-Chaignat, F. Winnefeld, Stability in the system CaO–Al2O3–H2O, Cement and Concrete Research, 42 (2012) 1621-1634.

[197] L. Gobbo, L.l. Sant'Agostino, L. Garcez, C3A polymorphs related to industrial clinker alkalies content, Cement and Concrete Research, 34 (2004) 657-664.

[198] N. Garg, Structure, Reactivity, and Dissolution of Calcined Clays by Solid-state NMR, 2015.

[199] W. Han, T. Sun, X. Li, Z. Shui, Y. Chen, M. Sun, Influence of Lithium Carbonate on C3A Hydration, Advances in Materials Science and Engineering, 2018 (2018) 6120269.

[200] J. Wang, C. Qian, J. Qu, J. Guo, Effect of lithium salt and nano nucleating agent on early hydration of cement based materials, Construction and Building Materials, 174 (2018) 24-29.

[201] P. Mondal, J.W. Jeffery, The crystal structure of tricalcium aluminate, Ca3Al2O6, Acta Crystallographica Section B, 31 (1975) 689-697.

[202] K. Scrivener, Advanced concrete technology, Elsevier, Amsterdam, 2003.

[203] R. Novotný, Tepelně izolační lité žárovzdorné materiály, VUT, Brno, 2016.

[204] P. Ptáček, K. Lang, F. Šoukal, T. Opravil, E. Bartoníčková, L. Tvrdík, Preparation and properties of enstatite ceramic foam from talc, Journal of the European Ceramic Society, 34 (2014) 515-522.

[205] P. Ptáček, K. Lang, F. Šoukal, T. Opravil, L. Tvrdík, R. Novotný, Preparation and properties of nanostructured ceramic foam from kaolinite, Powder Technology, 253 (2014) 29-34.

[206] E. Bartonickova, P. Ptacek, T. Opravil, F. Soukal, J. Masilko, R. Novotny, J. Svec, J. Havlica, Mullite-based refractories fabricated by foam casting, Ceramics International, 41 (2015) 14116-14123.

[207] E. Bartonickova, J. Svec, L. Dlabajova, P. Hruby, V. Caba, M. Sedlacik, L. Kalina, J. Koplik, F. Soukal, L. Kersnerova, J. Zach, V. Novak, K. Dvorak, Tailoring microstructure and properties of porous mullite-based ceramics via sol-gel impregnation, Ceramics International, 51 (2025) 5505-5513.

[208] M. Ismael, R.D. Anjos, R. Salomão, V. Pandolfelli, Colloidal silica as a nanostructured binder for refractory castables, Refract. Appl. News, 11 (2015) 16-20.

[209] R.D. dos Anjos, M.R. Ismael, I.R. de Oliveira, V.C. Pandolfelli, Workability and setting parameters evaluation of colloidal silica bonded refractory suspensions, Ceramics International, 34 (2008) 165-171.

[210] A.R. Studart, U.T. Gonzenbach, E. Tervoort, L.J. Gauckler, Processing Routes to Macroporous Ceramics: A Review, Journal of the American Ceramic Society, 89 (2006) 1771-1789.

[211] L. Wang, Y. Liang, Y. Yin, L. Zhao, M. Cai, J. Nie, Enhancing the green mechanical strength of colloidal silica-bonded alumina castables using a silane coupling agent, Ceramics International, 42 (2016) 11496-11499.

[212] C. Chuanuwatanakul, C. Tallon, D.E. Dunstan, G.V. Franks, Producing Large Complex-Shaped Ceramic Particle Stabilized Foams, Journal of the American Ceramic Society, 96 (2013) 1407-1413.

10. Seznam komentovaných publikací

A: Skupina publikací týkající se C-S-H a C-A-S-H struktur

B: Skupina publikací týkajícíc se C-A-H hydrátů z C_3A fáze

C: Skupina publikací týkající se hydratace CAC cemetů a koloidních roztoků

A: Skupina publikací týkající se C-S-H a C-A-S-H struktur

1. *L. Galvánková, E. **Bartoníčková**, T. Opravil, J. Tkacz, P. Ptáček*, The influence of starting materials´ solubility on tobermorite structure formation under the hydrothermal conditions, IOP Conference Series: Materials Science and Engineering 379 (2018) 012001.
2. *D. Hanisková, E. **Bartoníčková**, J. Koplík, T. Opravil*, The Ash from Fluidized Bed Combustion as a Donor of Sulfates to the Portland Clinker, in: D. Kubatova, M. Bohac, M. Drdlova (Eds.) Procedia Engineering, Elsevier Ltd, 2016, pp. 394-401.
3. *H. Kalousová, E. **Bartoníčková**, T. Opravil*, Influence of storage conditions on quality of fly ashes, Advanced Materials Research, Trans Tech Publications Ltd, 2014, pp. 59-62.
4. *E. Kuzielová, M. Žemlička, E. Bartoničková, M.T. Palou*, The correlation between porosity and mechanical properties of multicomponent systems consisting of Portland cement–slag–silica fume–metakaolin, Construction and Building Materials 135 (2017) 306-314.
5. *R. Novotný, E. **Bartoníčková**, J. Kotrla*, The effect of burnt lime addition on hydration of Ultra-high performance cementitious composites, IOP Conference Series: Materials Science and Engineering, Institute of Physics Publishing, 2019.
6. *R. Novotný, E. **Bartoníčková**, J. Švec, M. Mončeková*, Influence of Active Alumina on the Hydration Process of Portland Cement, in: D. Kubatova, M. Bohac, M. Drdlova (Eds.) Procedia Engineering, Elsevier Ltd, 2016, pp. 80-86.
7. *L. Kalina, V. Bílek, M. Sedlačík, V. Cába, J. Smilek, J. Švec, E. **Bartoníčková**, P. Rovnaník, J. Fládr*, Physico-Chemical Properties of Lithium Silicates Related to Their Utilization for Concrete Densifiers, Materials, 16 (2023).
8. *O. Kunovský, F. Šoukal, L. Kalina, T. Opravil, E. **Bartoníčková**:* Effect of drying on the structure of sol-gel synthesized calcium silicate hydrate gels, Acta Polytechnica CTU Proceedings, under review
9. *L. Kalina, V. Bílek, E. **Bartoníčková,** M. Kalina, J. Hajzler, R. Novotný,* Doubts over capillary pressure theory in context with drying and autogenous shrinkage of alkali-activated materials, Construction and Building Materials, 248 (2020).
10. *L. Kalina, V. Bílek, E. **Bartoníčková***, Effect of amino alcohol admixtures on alkali-activated materials, Mater Tehnol, 54 (2020) 349-353.
11. *V. Bílek, L. Kalina, E. **Bartoníčková**, J. Pořízka*, Evaluation of the Surfactant Leaching from Alkali-Activated Slag-Based Composites Using Surface-Tension Measurements, Mater Tehnol, 53 (2019) 33-38.
12. *L. Kalina, V. Bílek, E. **Bartoníčková,** J. Krouská*, Polypropylene Glycols as Effective Shrinkage-Reducing Admixtures in Alkali-Activated Materials, Aci Mater J, 115 (2018) 251-256.

The influence of starting materials´ solubility on tobermorite structure formation under the hydrothermal conditions

L Galvánková[1]**, E Bartoníčková**[1]**, T Opravil**[1]**, J Tkacz**[1] **and P Ptáček**[1]

[1] Brno University of Technology, Faculty of Chemistry, Institute of Material Chemistry, Purkyňova 118, 612 00, Brno, Czech Republic

Email: xcgalvankova@fch.vut.cz

Abstract. Overall, the tobermorite mineral crystallises under the hydrothermal conditions from the CaO-SiO_2-H_2O system. The system of calcium hydrosilicates species is extremely complex and many factors play an important role. The solubility of starting materials belongs to one of the most important factors. Dissolution rates of SiO_2 source are significantly affected by their particle size distribution. Also the starting cation´s concentration in the aqueous solution affects the yield of the hydrothermal reaction. The main aim of this contribution is to study the influence of water-to-solid ratio on tobermorite crystallization. The effect of particle size of various sources of SiO_2 was also studied. The cost effective Ca and Si sources was primarily favoured. The C/S ratio of the experiments was set to 0.83. All syntheses were performed at 180 °C in laboratory steel autoclaves. The prepared powdered samples were characterized in order to determine the phase composition by using of X-Ray diffractometry. The thermal behaviour of prepared samples was studied by TG-DTA analyser. Morphology and particle size of synthetized powdered products was studied by scanning electron microscopy.

1. Introduction

Tobermorite, a mineral belonging to a group of calcium silicate hydrates (C–S–H), is very rare in nature but plays an important role in several technical applications in building chemistry, mainly in hydration processes of Portland cement and production of autoclaved aerated concrete.

Tobermorite was firstly described by Heddle in 1880 [1]. The natural samples were found in three different localities near towns Tobermory and Dunvegan in Scotland. Generally the mineral could be formed in places with possible hydrothermal activity (i.e. in cavities in alkaline rocks, where was formed by hydrothermal alteration or in places where the hydrothermal fluids react with calcium silicate minerals) [2]. Till now, three main different phases of crystal structure have been described. The type of the structure is associated with the different degree of hydration, 9 Å tobermorite also called riversideite ($Ca_5Si_6O_{16}(OH)_2$), 11 Å tobermorite ($Ca_5Si_6O_{17}\cdot 5H_2O$) and 14 Å tobermorite also called plombierite ($Ca_5Si_6O_{16}(OH)_2\cdot 7H_2O$). The denomination of phases is related to characteristic d_{002} values in the powder diffraction pattern, 9.3 Å, 11.3 Å and 14.0 Å from the least to the most hydrated form [3]. The most important phase is 11 Å tobermorite which crystallizes in orthorhombic or monoclinic form. The monoclinic form was found by Henmi and Kusachi [4] and was named clinotobermorite. The crystal structure of natural 11 Å tobermorite structure was firstly described by Megaw and Kelsey [5] and then by Hamid [6]. However, the detailed description of the real structure of both orthorhombic and monoclinic form was solved by Merlino et al. [7, 8] using order-disorder theory. The basic structure is build up by central CaO-octahedra layer attached from both sides with infinite silicate double chains composed of condensed dreierketten units along the *b* axis. Each dreierketten unit consists of two paired tetrahedra pointing towards to Ca-layer and one bridging tetrahedron oriented to the interlayer. The composite layers consist of one calcium layer and two silicate layers bounded together by the interlayer containing mainly calcium ions and water molecules. Depending on the dehydration behaviour, the two types of 11 Å tobermorite, normal and anomalous type, can be distinguished. During the dehydration process the normal 11 Å form loses its interlayer water and transforms to a 9 Å tobermorite, while the anomalous one is affected by the dehydration process, but the formed crystalline structure is not 9 Å tobermorite [9]. At the temperatures above 800°C, both types recrystallize to new phase called wollastonite ($CaSiO_3$) [2].

The hydrothermal synthesis of tobermorite in various laboratory conditions has been extensively studied [10-14]. Generally, $Ca(OH)_2$ and SiO_2 react to form C–S–H phases under hydrothermal conditions. At the beginning of the reaction, the solution is saturated with lime so the Ca-rich phases like C–S–H (II) (C/S ratio around 1.5) and α–C_2S hydrate are formed. Whereas the temperature in the system start increases, the solubility of CaO decrease and the increase of SiO_2 solubility occur simultaneously. The next step of the hydrothermal reaction is the reduction of the C/S ratio to 1.25 and the creation of C–S–H (I) phase. In the final stage of the reaction, the C/S ratio drops to the optimal value for tobermorite formation (i.e. between 0.8–1) and the C–S–H (I) phase recrystallize to 11 Å tobermorite [15]. The whole reaction is schematically shown in equation (1). The course of the reaction is affected by many factors. The reaction temperature and pressure are one of the most important factors, temperatures between 120°C and 200°C and saturated steam pressure has been reported as the optimal. The reaction temperature and the reaction time are strongly depended on the particle size of SiO_2 [13, 15]. Generally, with higher temperature and longer reaction time the recrystallization of tobermorite to other calcium silicate hydrate, xonotlite ($Ca_6Si_6O_{17}(OH)_2$), is favoured. Besides mentioned factors, the amount of added water to reaction system plays also an important role in the final yield of the hydrothermal reaction [16].

$$Ca(OH)_2 + SiO_2 \rightarrow C-S-H(II) + \alpha - C_2S\ hydr. \rightarrow C-S-H(I) \rightarrow tobermorite \rightarrow xonotlite \quad (1)$$

The formation of tobermorite under the hydrothermal conditions is beside shown the strong dependence on the reaction temperature, time and especially on the solubility of SiO_2 source. Therefore, the main aim of the present work was to study the influence of SiO_2 particle size distribution together with the starting concentration in the aqueous solution. The influence of reaction time was also examined.

2. Experimental

2.1. Materials and synthesis

For the synthesis of a mineral tobermorite under the hydrothermal conditions, two types of silica sources, silica sand Dorsilit and specially crushed quartz sand, were chosen as starting materials. The average particle size (d_{50}) of silica sources is 5.29 μm for silica sand Dorsilit and 20.24 μm for specially crushed quartz sand. As the source of calcium oxide, the grounded $CaCO_3$ calcinated at 1000°C for 1 hour was used. The amount of CaO in calcinated limestone was determined to be higher than 97%. All the starting mixtures were mixed using the same C/S ratio equal to 0.83. The method of synthesis used in this study was inspired by Diamond et al. [17]. Required quantity of CaO was mixed with freshly-boiled distilled water (to supress the undesirable carbonization) and stirred for 3 minutes. Then the calculated amount of SiO_2 was added to the mixture and was mixed for 5 more minutes. Used water-to-solid (w/s) ratio was set in a range from 1.5 to 15 ml/g. Hydrothermal reactions were carried out in a Teflon-lined laboratory autoclave placed in a conventional dryer. Prepared slurries were hydrothermally treated at 180°C and autogenous pressure for 1 and 5 days. Synthesized products were dried at 50°C for 12 hours.

2.2. Characterization of synthesized products

The phase composition of synthesized products was determined by X-ray diffraction analysis (XRD). Data were collected by X-ray diffractometer Empyrean (Pananalytical) using Cu Kα radiation. For selected samples, a thermogravimetric and differential thermal analysis was performed using TG-DTA instrument Q 600 (TA Instruments). Analyses was run in Pt crucibles and were heated with the rate of 10°C/min from 20°C to 1000°C under the Ar atmosphere. The morphology of these chosen samples was observed by scanning electron microscopy (SEM) using microscope ZEISS EVO LS 10.

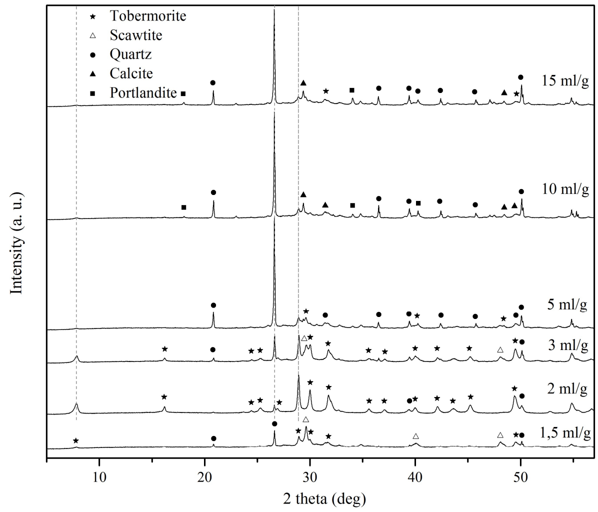

Figure 1. XRD patterns of samples synthesised for 1 day using specially crushed quartz sand and different w/s ratios (1.5–15 ml/g).

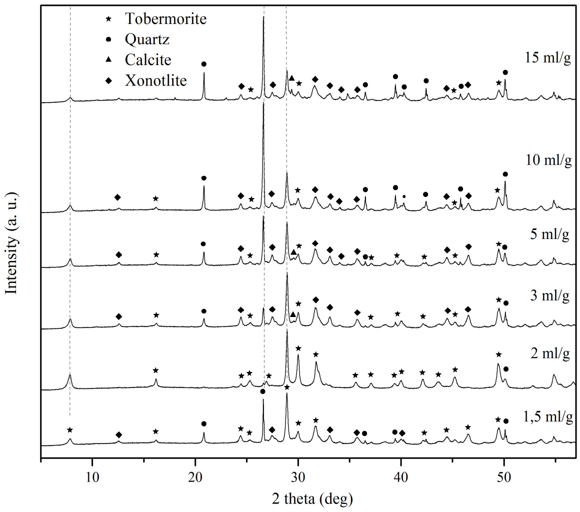

Figure 2. XRD patterns of samples synthesised for 5 days using specially crushed quartz sand and different w/s ratios (1.5–15 ml/g).

3. Results

3.1. Synthesis of tobermorite using specially crushed quartz sand

The solubility of silica source is affected by the amount of added water to the reaction system. For the examination of the influence of w/s ratio on tobermorite formation, six samples with different w/s ratio were used (1.5, 2, 3, 5, 10 and 15 ml/g). Figure 1 shows the XRD patterns of samples prepared from the mixture of specially crushed sand and calcinated $CaCO_3$ hydrothermally treated for 1 day. It is obvious that after a one day of hydrothermal reaction the different w/s ratio strongly affects the phase composition of prepared samples. With the increasing amount of water in the system the amount of prepared tobermorite strongly decrease. The XRD results show the presence of crystalline tobermorite only in samples prepared with w/s ratio between 1.5–3 ml/g. The highest yield of tobermorite formation after 1 day of hydrothermal treatment was observed with the use of w/s ratio of 2 ml/g. In samples with higher w/s ratio, the starting materials are the only detected. If the reaction time is prolonged from one to five days, the amount of tobermorite in samples is increased. The highest amount of tobermorite is still found in the sample prepared with w/s ratio of 2 ml/g. In some samples, part of crystalline tobermorite was transformed into xonotlite. The unreacted SiO_2 is still the main phase even after five days of the treatment. Except the unreacted starting materials, the CO_2 bearing compounds like calcite and scawtite ($Ca_7(Si_6O_{18})(CO_3)\cdot 2H_2O$) were presented in some samples. The contamination is caused by the reaction of wet samples with air containing CO_2 during the preparing process and mainly during the drying of prepared products [18].

The influence of reaction time on morphology of formed tobermorite particles was observed on samples with the highest amount of tobermorite determined from XRD analysis. Therefore, the samples prepared with the used w/s ratio 2 ml/g were analysed by SEM and the images are given in Figure 3 and Figure 4. It could be seen, that the SiO_2 particles from the starting material are covered with tobermorite platelet-like crystals. The crystals in sample hydrothermally treated for 1 day are longer and could be better distinguished than the crystals in sample that was autoclaved for 5 days. The higher degree of agglomeration of platelet tobermorite particles could be here also observed. The various length of the hydrothermal reaction showed the differences in the morphology of prepared tobermorite crystals. No other significant phases could be detected from the SEM images.

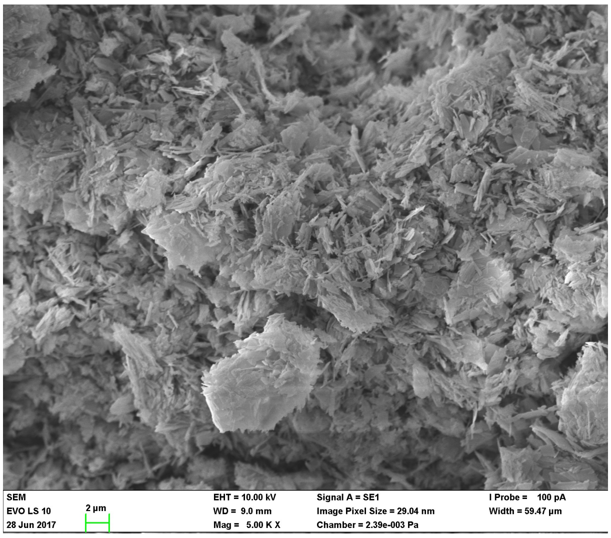

Figure 3. SEM images of samples synthesised for 1 day using specially crushed quartz sand and w/s ratio 2 ml/g.

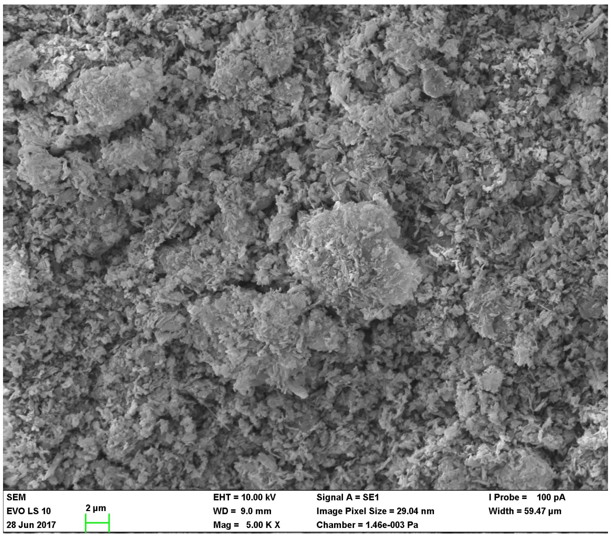

Figure 4. SEM images of samples synthesised for 5 days using specially crushed quartz sand and w/s ratio 2 ml/g.

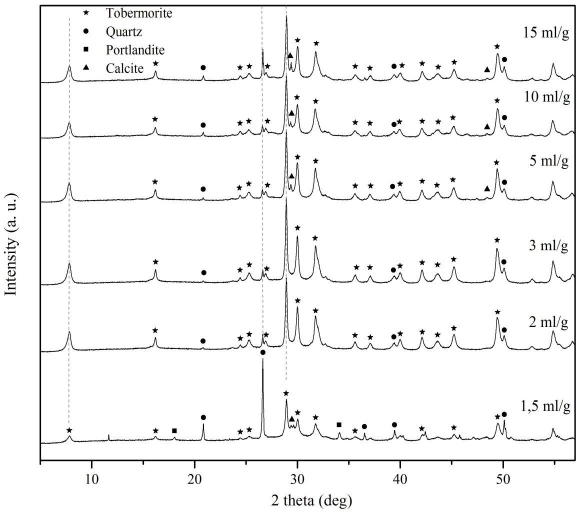

Figure 5. XRD patterns of samples synthesised for 1 day using silica sand Dorsilit and different w/s ratios (1.5–15 ml/g).

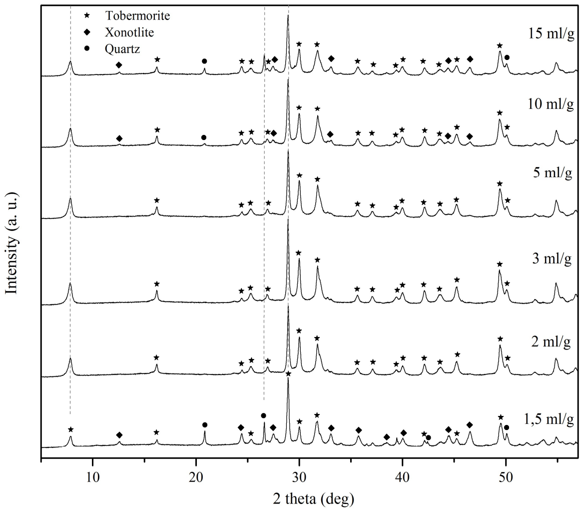

Figure 6. XRD patterns of samples synthesised for 5 days using silica sand Dorsilit and different w/s ratios (1.5–15 ml/g).

3.2. Synthesis of tobermorite using silica sand Dorsilit

Results of the XRD analysis on samples prepared using silica sand Dorsilit are shown in Figure 5 and Figure 6. After one day of hydrothermal reaction, tobermorite is present in all samples. The influence of w/s ratio is consistent with the trend observed in the samples prepared using specially crushed silica sand. It was also determined that with the increasing w/s ratio the amount of prepared tobermorite phase decreased. None of the prepared samples is phase pure and the presence of the starting materials is determined. Prolonging the reaction time from one to five days allowed the reaction to proceed, so the amount of tobermorite phase is higher in all samples independently of the w/s ratio. The only detected crystalline phase, in samples with w/s ratio from 2 to 5 ml/g, was tobermorite. Conversion to xonotlite appears only in samples with higher w/s ratio, but the amount of crystallized xonotlite is almost negligible. No CO_2 bearing phases were detected after five days of hydrothermal reaction.

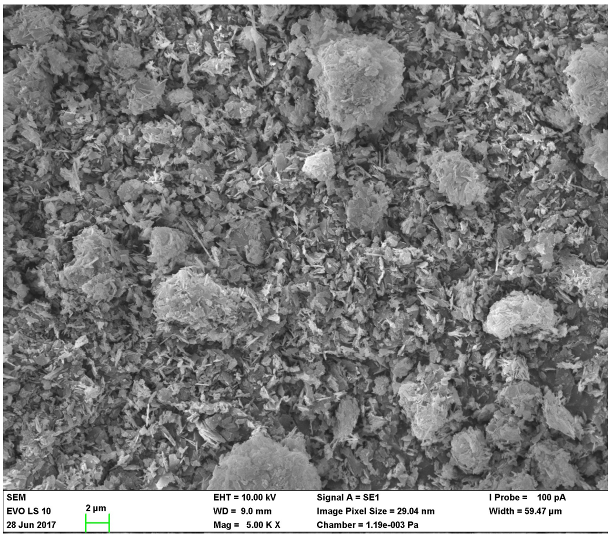

Figure 7. SEM images of samples synthesised for 1 day using silica sand Dorsilit and w/s ratio 3 ml/g.

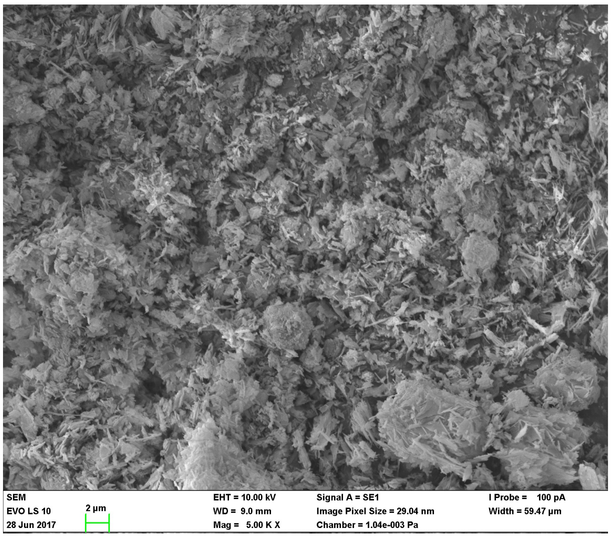

Figure 8. SEM images of samples synthesised for 5 days using silica sand Dorsilit and w/s ratio 3 ml/g.

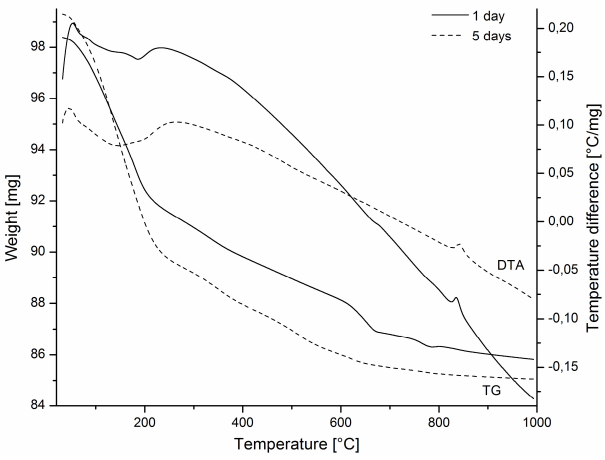

Figure 9. TG-DTA curves of samples synthesised for 1 and 5 days using specially crushed quartz sand and w/s ratio 2 ml/g.

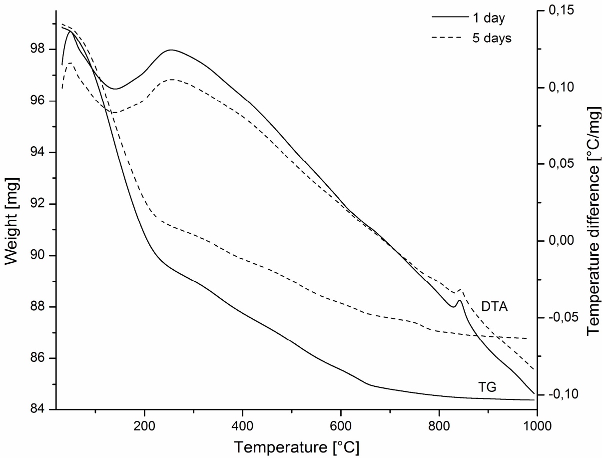

Figure 10. TG-DTA curves of samples synthesised for 1 and 5 days using silica sand Dorsilit and w/s ratio 3 ml/g.

The morphology of prepared tobermorite using silica sand Dorsilit as a starting source of SiO_2 were studied on the samples with the w/s ratio 3 ml/g. It was found that the prepared tobermorite phases crystalized in the platelet form particles independently of the reaction time (Figure 7 and 8). Observed morphology is almost the same as in case of the synthesis with specially milled quartz sand after five days of hydrothermal reaction.

3.3. TG-DTA analysis

For confirmation of the results from XRD analysis, TG-DTA measurements on samples with the highest yield of tobermorite (detected by XRD) were performed. The influence of particle size on thermal processes was also studied. The main weight loss on a TG curve occurs between 50°C and 250°C. The weight decrease is accompanied by the broad endothermic hump on a DTA curve presumably resulting from the loss of the loosely bound molecular water from tobermorite structure. The weight decrease is comparable in all four samples. In samples prepared using specially crushed silica sand, it is obvious that the amount of tobermorite increases with prolonged reaction time (Figure 9). This confirms the XRD analysis, whilst the results for the samples prepared using silica sand Dorsilit is opposite (Figure 10). The amount of tobermorite phase is lower in sample hydrothermally treated for 5 days. This difference could be caused by the additional carbonation of tobermorite during the sample storage. Between 250°C and 800°C, any remaining molecular water from tobermorite is lost. At about 850°C a sharp exothermic peak is detected indicating the recrystallization of tobermorite into wollastonite. Besides the changes connected with the presence of tobermorite, the presence of calcite is detected by the weight loss between 600°C and 650°C, where the decomposition of calcite takes place. Mentioned weight loss is most obvious in the sample prepared using specially crushed silica sand synthesised for one day.

4. Discussion

The formation of tobermorite in hydrothermal conditions is strongly affected by the average particle size of the used source of SiO_2. Two sources differing in particle size were used to prove this fact. The experiments reveal that if the particle size is smaller the formation of tobermorite is easier and the yield of the reaction is higher. This result corresponds with previously reported studies [16, 19–21]. The rate of dissolution of quartz particles corresponds to particle size and it is time dependent, the finer particles have quicker dissolution, whilst the coarser one has the slower. So, the overall reaction is accelerated due to an increase in reactivity depending on particle size. According to the literature [21], when the SiO_2 source with the particle size higher than 10 μm is used as a starting material, synthesized tobermorite decomposes to xonotlite. The result in this work is basically in good agreement with those found in the literature. Kikuma et al. [16] had proposed an explanation of this phenomenon. During the hydrothermal reaction non-crystalline C–S–H is formed as an intermediate phase before the crystalline calcium silicate hydrates occur. When the less soluble SiO_2 source is used, the C/S ratio in the non-crystalline C–S–H is higher and the reaction equation (1) proceeds towards xonotlite instead of tobermorite.

Another not negligible factor for all hydrothermal synthesis, including the formation of tobermorite, is the water-to-solid ratio. The obtained results indicate that the amount of prepared tobermorite significantly decreases with the increasing value of w/s ratio. The calcium and silicate ions concentration in the reaction solution probably plays an important role in tobermorite formation. Thess results ties well with previous study published by Kikuma et al. [16]. They have done an examination on the samples prepared from fine quartz with particle size 2 μm and quicklime. The used w/s ratio was 1.7, 3, 6 and 9 ml/g and the measurements were done by in-situ time-resolved XRD. Based on the obtained results they suggested that the silicate ion concentration is differing according to the w/s ratio. They showed that the lower silicate ion concentration in the solution phase is important for the tobermorite formation under the hydrothermal conditions.

The influence of the particle size of SiO_2 source and reaction time on the morphology of prepared tobermorite was also observed. Tobermorite crystallises into the platelet-like crystals. The size of formed crystals decreases with the increasing reaction time and they have a tendency to form aggregates after five days of hydrothermal reaction. The reaction of the coarser SiO_2 particles is slower so the aggregates are created after a longer reaction time. The formation of platelets crystals of tobermorite throw the heterogeneous nucleation was also described by Bell and Adair [22].

5. Conclusions

Hydrothermal formation of mineral tobermorite in system $CaO–SiO_2–H_2O$ was studied. Two important factors were mainly examined – the average particle size of SiO_2 source and the water-to-solid ratio. Based on experiments conducted at 180°C and an autogenous pressure with two different particle size of SiO_2 source, it can be shown that the SiO_2 source containing smaller particles accelerating the reaction. These could be attributed to a better solubility of finer quartz particles in a hydrothermal system. The formation of tobermorite is also significantly influenced by the changes in w/s ratio. The increase in the w/s ratio probably influences the calcium and silicate ions concentration in a solution, which plays an important role in a process of tobermorite formation. The ideal w/s ratio was almost independent of the used SiO_2 sources and lies in a range of 2 to 3 ml/g. Using the optimal w/s ratio and the prolonged reaction time from one to five days resulted in a preparation of samples containing phase pure tobermorite. In samples prepared with higher w/s ratio and longer reaction times the unfavourable formation of xonotlite occurs. This trend was more like observed in samples prepared from coarser SiO_2 source, which is probably caused by the higher C/S ratio in a system thanks to its lower solubility.

Acknowledgements

This study was supported by the project of Materials Research Centre on Faculty of Chemistry, Brno University of Technology - sustainability and development REG LO1211 with the financial support of National program of sustainability I (The Ministry of Education, Youth, and Sports).

References

[1] Heddle M F 1880 *Mineral. Mag.* **4** pp 119-123
[2] Bonaccorsi E and Merlino S 2005 *Rev. Mineral. Geochem.* **57** pp 241-90
[3] Biagioni C, Merlino S and Bonaccorsi E 2015 *Mineral. Mag.* **79**(2) pp 485-95
[4] Henmi C and Kusachi I 1995 *Mineral. Mag.* **56**(384) pp 353-58
[5] Megaw H and Kelsey C 1956 *Nature* **177** pp 390-91
[6] Hamid S *Z. Kristallogr. Cryst. Mater.* **154** pp 189-98
[7] Merlino S, Bonnacorsi E and Armbruster T 2001 *Eur. J. Mineral.* **13** pp 577-90
[8] Merlino S, Bonnacorsi E and Armbruster T 2000 *Eur. J. Mineral.* **12** pp 411-29
[9] Mitsuda T and Taylor H F W 1978 *Mineral. Mag.* **42** pp 229-35
[10] Hong S Y and Glasser F P 2004 *Cem. Concr. Res.* **34** pp 1529-34
[11] Hartmann A, Schulenberg D and Buhl J Ch 2015 *J. Mater. Sci. Eng.* **3** pp 39-55
[12] Shaw S, Clark S M and Henderson C M B 2000 *Chem. Comp.* **167** pp 129-40
[13] Snell D S 1975 *J. AM. Ceram. Soc.* **58**(7-8) pp 292-95
[14] Trankle S, Jahn D, Neumann T, Nicoleau L, Husing N and Volkmer D 2013 *J. Mater. Chem. A* **1** pp 10318-26
[15] Taylor H F W 1964 *The Chemistry of Cements* (London: Academic Press)
[16] Kikuma J, Tsunashima M, Ishikawa T, Matsuno S, Ogawa A, Matsui K and Sato M 2011 *J. Solid State Chem.* **184** pp 2066-74
[17] Diamons S, White J L and Dolch W L 1966 *Amer. Mineral.* **51**(3-4) pp 388-401
[18] Siauciunas R, Rupsyté E, Kitrys S and Galeckas V 2004 *Colloids Surf. A* **244** pp 197-204
[19] Sato H and Grutzeck M 1992 *Mat. Res. Soc. Symp. Proc.* **245** pp 235-240
[20] Bernstein S and Fehr K T 2012 *Prog. Cryst. Growth Charact. Mater.* **58** pp 84-91
[21] El-Hemaly S A S, Mitsuda T and Taylor H F W *Cem. Concr. Res.* **7** pp 429-438
[22] Bell N S and Adair J H 1996 *J. AM. Ceram. Soc.* **79** pp 2175-78

Available online at www.sciencedirect.com

ScienceDirect

Procedia Engineering 151 (2016) 394 – 401

Procedia Engineering

www.elsevier.com/locate/procedia

International Conference on Ecology and new Building materials and products, ICEBMP 2016

The ash from fluidized bed combustion as a donor of sulfates to the Portland clinker

Denisa Hanisková*, Eva Bartoníčková, Jan Koplík, Tomáš Opravil

Brno University of Technology, Faculty of Chemistry, Materials Research Centre, Purkyňova 464/118, Brno 612 00, Czech Republic

---

Abstract

The paper deals with possibilities of using solid residues from fluidized bed combustion of coal, bed and filter ash in the production of composite Portland cements. The ash from fluidized bed combustion contains a high amount of CaO, in the form of free lime or $CaSO_4$ (anhydrite), so it could be used as a possible donor of sulfates to the Portland clinker instead of usually used gypsum. At first, the chemical composition of collected ashes was determined by X-Ray Fluorescence and the ongoing hydration process was monitored by isoperibolic calorimetry. Then samples containing mixtures of Portland clinker and ash were prepared. Their respective compressive strength and flexural strength were analyzed and observations were made on the hydration and composition of products of the hydration reaction detected by X-Ray diffraction. Finally, the results of selected mixtures were verified with prepared standardized mortars.

Peer-review under responsibility of the organizing committee of ICEBMP 2016

Keywords: Portland clinker; fluidized bed combustion ash; compressive strength; flexural strength; reaction of hydration.

---

1. Introduction

The main fossil fuel for production of the electric energy in thermal power plants is coal. During a combustion process, a high amount of solid residues is formed. Chemical, physical and mineralogical properties of the residues differ depending on a type of coal and a type of combustion process [1,2,3]. There are two main types of the combustion process, a high-temperature combustion and a fluidized bed combustion [4]. The advantage

---

* Corresponding author.
E-mail address: xchaniskova@fch.vutbr.cz

Peer-review under responsibility of the organizing committee of ICEBMP 2016
doi:10.1016/j.proeng.2016.07.392

of the fluidized bed combustion is that the desulfurization process is situated in a boiler. On the other hand at high-temperature combustion special technological equipment is needed, because desulfurization is situated after the combustion process [5,6,7,8]. Limestone ($CaCO_3$) is added directly to the boiler as a desulfurization additive. The calcium sulfate ($CaSO_4$) is formed by the reaction of the limestone particles with sulfur dioxide (SO_2). The solid residues from the fluidized bed combustion contain noncombustible constituents of coal and products of desulfurization, so particles of $CaSO_4$ [9]. The high amounts of SO_3 and CaO are the reason why fluidized bed combustion ashes differ from high-temperature combustion ashes. For that matter fluidized bed combustion ashes should not be used as an additive to concrete [10].

There are some studies where hydration behavior and properties of mixtures prepared from cement and fluidized bed combustion fly ash were observed [11,12]. Ash was added in small amounts and as a replacement of high temperature fly ash. In both cases the addition of ash caused the increase in mechanical properties.

The main additive, which is mixed with Portland clinker to make Portland cement, is gypsum ($CaSO_4{\cdot}2H_2O$). It retards hydration of C_3A ($3CaO{\cdot}Al_2O_3$, tricalcium aluminate), one of the main phases of cement, and allows workability of Portland cement. In this work, the fluidized bed combustion ash is added to the Portland clinker as a donor of sulfates and also as partially substituent of the clinker. Using the secondary raw materials in the production of cement has ecological and economic advantages [13]. In mixtures presented in this work mass ratio between the clinker and the ash from 90:10 to 10:90 was applied. Fluidized bed combustion ashes, bed and filter ashes, from two thermal power plants in The Czech Republic, was used. The mechanical properties and the process of hydration reaction were monitored on the prepared mixtures.

2. Experimental

2.1. Methods

Saccharate method was used to determine a content of free lime in collected ashes. A sample of ash was mixed with saccharose and water. The mixture was filtered and a filtrate was titrated by hydrochloric acid solution on phenolphthalein. The content of free lime (CaO) was calculated according to the formula:

$$\%\ CaO = \frac{c \cdot V \cdot M}{m \cdot v} \tag{1}$$

where c is a concentration of hydrochloric acid solution ($mol{\cdot}dm^{-3}$), V is a volume of the hydrochloric acid solution (dm^3), M is a molar weight of CaO ($g{\cdot}mol^{-1}$), m is a weight of the sample of ash (g), v is a stoichiometric ratio of reaction.

Mechanical properties, compressive and flexural strength, were measured on the complex device for strength tests on building materials DESTTEST 3310 (Betonsystem). Flexural and compressive strength were measured on each testing prism. Dimensions of prisms from pastes were 20×20×100 mm, and from mortars 40×40×160 mm. Prisms were preserved in a humid environment. Strengths were measured after 1, 7 and 28 days.

The process of hydration reaction was observed by isoperibolic calorimetry, on a device constructed and placed in FCH BUT (Faculty of chemistry, Brno University of technology). Immediately after stirring the mixture, 300 g of it were placed in a polystyrene cup, which was enclosed in thermo-insulation foam container and a thermocouple for measuring temperature during hydration reaction was embedded into the testing mixture. The measurements were ended after 30 hours when the temperature was almost constant.

2.2. Material

Bed and filter ashes from fluidized bed combustion (power plants Tisová and Poříčí K8, The Czech republic) and the Portland clinker (Mokrá, HeidelbergCement, The Czech republic) were used for preparation pastes and standardized mortars. Bed ashes and Portland clinker were fine grounded. To mortars, the standardized fine, medium and coarse sand (ČSN 196-1) was used.

The chemical composition of used ashes was examined by X-Ray fluorescence on the device Xenemetric EX-6600 SSD and is given in Table 1. The content of free lime (CaO) in ashes was determined by saccharate method and is given in Table 2.

Table 1. The chemical composition of used ashes.

Major oxides (%)	Tisová		Poříčí K8	
	Bed ash	Filter ash	Bed ash	Filter ash
SiO_2	31.1	33.9	30.0	31.2
Al_2O_3	21.7	22.4	15.1	16.5
CaO	28.1	22.8	29.1	31.2
Na_2O	0.34	0.66	0.26	0.40
K_2O	0.81	0.67	1.48	1.38
MgO	0.47	0.85	0.82	0.90
SO_3	7.77	5.19	16.10	8.80
Fe_2O_3	3.46	7.17	5.41	7.48
TiO_2	5.45	5.41	1.21	1.53
P_2O_5	0.26	0.31	0.14	0.19

Table 2. The content of free lime in used ashes.

	Tisová		Poříčí K8	
	Bed ash	Filter ash	Bed ash	Filter ash
Content of free lime (*wt.%*)	22.94	9.68	9.57	13.54

2.3. Samples composition

Four series of mixtures were prepared. The composition of mixtures in each series was the same (Table 3), they differ in a type of ash added. Following ashes were used: bed ash from fluidized bed combustion from power plant Tisová (TB), filter ash from power plant Tisová (TF), bed ash from power plant Poříčí K8 (PB), filter ash from power plant Poříčí K8 (PF). The amount of water added to various mixtures was determined from consistency of the paste, made from clinker and water with water to binder ratio 0.35. The water to binder ratio (w/b) is the ratio between the total amount of water (*g*) and the total amount of binder (*g*), which is the sum of an amount of the ash and the clinker used in pastes or mortars.

Table 3. The composition of mixtures.

Sample	CL	A	B	C	D	E	F	G	H	I
Ash (*wt.%*)	0	10	20	30	40	50	60	70	80	90
Clinker (*wt.%*)	100	90	80	70	60	50	40	30	20	10

The clinker to ash ratio in mortars was same as in pastes. Fine, medium and coarse sand was used to prepare mortars. The types of sand were in ratio 1:1:1. The sand to binder ratio in mortars was 3:1.

3. Results and discussion

The time dependence of compressive and flexural strengths of the pastes prepared from the Portland clinker and fluidized bed combustion ashes measured on testing prisms after 1, 7 and 28 days are presented in Fig. 1, Fig. 2, Fig. 3 and Fig. 4.

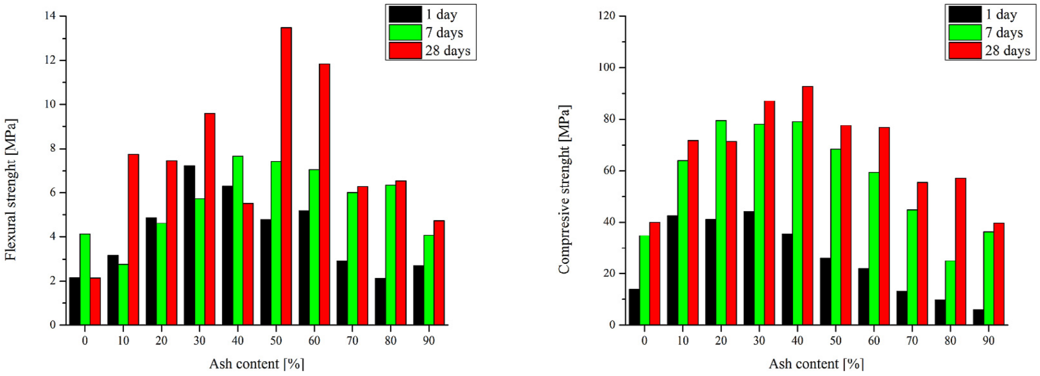

(a) (b)

Fig. 1. Dependence of flexural (a) and compressive (b) strength of pastes with TB on time.

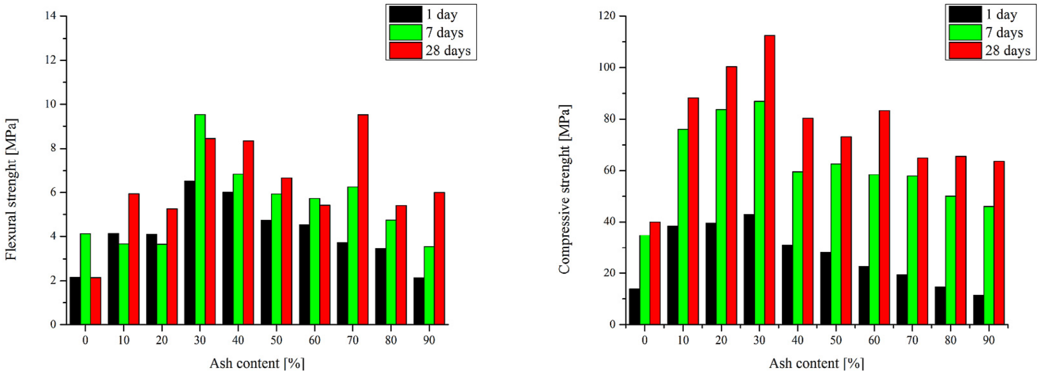

(a) (b)

Fig. 2. Dependence of flexural (a) and compressive (b) strength of pastes with PB on time.

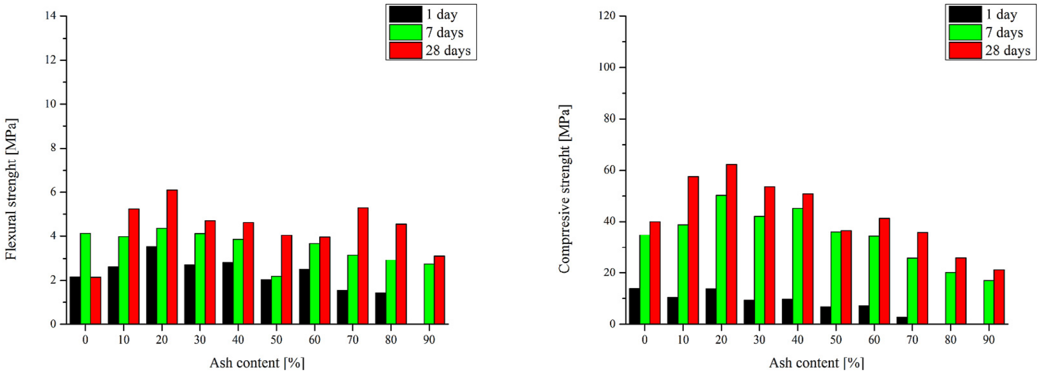

(a) (b)

Fig. 3. Dependence of flexural (a) and compressive (b) strength of pastes with TF on time.

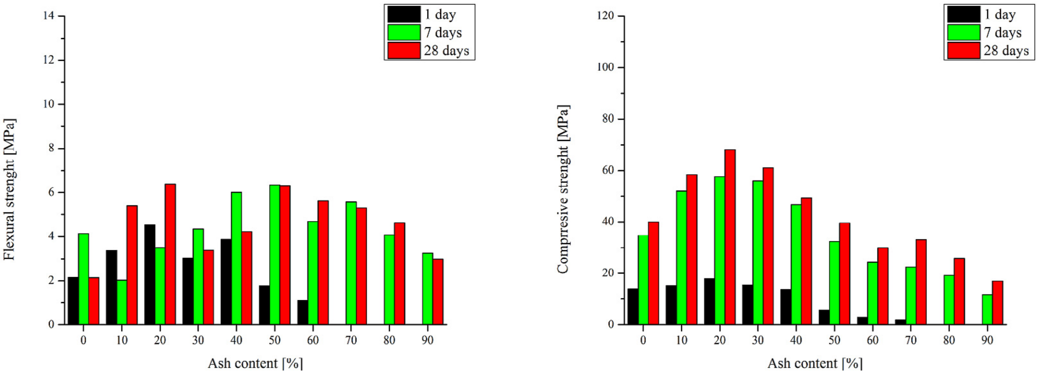

(a) (b)

Fig. 4. Dependence of flexural (a) and compressive (b) strength of pastes with the PF on time.

Generally, we can say, that reached strengths increase with increasing time of curing and the highest values reached the pastes with a content of ash from 10–50 wt.%.

Flexural strengths of all pastes made with bed ash from Tisová (Fig. 1) after 28 days exceeded value 6 MPa. The highest value was measured on the mixture with the content of ash 50 wt.% and it is almost 14 MPa. The compressive strengths (Fig. 1) of all pastes after 28 days were higher than the compressive strength of clinker itself. This fact is due to an absence of sulfate ions, which are needed to form ettringite, as is also described in work of Quennoz,et al. [14]. The values of the compressive strength of all pastes after 28 days were higher than 40 MPa, the highest values exceeded 80 MPa. The strengths increased with growing quantity of ash, but after they exceeded the 40 wt.% content of ash the strengths were decreasing. The amount of added ash is equal to 3% content of sulfates in the mixture, what is the optimal quantity which positively influenced the compressive strength of cement paste prisms, as also published Lerch [15]. So we suggest the similar mechanism in the strength development due to the addition of fluidized bed combustion fly ash to the clinker in corresponding amounts.

Navazze et al. [16] also deals with an addition of fluidized bed combustion ash to the Portland cement. They observed that the strengths of pastes made with the addition of ash were after 91 days higher than the cement itself. The increase was caused by added amount of free lime. Our experiments show higher strengths for pastes with addition of ash with lower amount of free lime (Poříčí), so the effect of addition of free lime to clinker is probably opposite compared to the cement.

The values of flexural strengths of the pastes made with bed ash from Poříčí K8 (Fig. 2) were after 28 days between 5 and 10 MPa. So they were slightly lower compared to the pastes with ash from Tisová. The values of compressive strengths (Fig. 2) were for all pastes higher than 60 MPa, and the highest measured value was 112 MPa, i.e. for paste with 30% content of ash. In comparison to bed ash from Tisová, Poříčí bed ash has higher content of sulfates (Table 1) so the quantity of added ash needed to reach an optimum amount of sulfates and the highest strengths is lower. Again, strengths of all pastes are significantly higher than the strength of the clinker, which is caused by the absence of sulfate ions [15].

The usage of filter ash to prepare pastes entails lower values of strengths. Pastes made with fluidized bed combustion filter ash from power plant Tisová (Fig. 3) had after 28 days flexural strengths about 4–5 MPa, the highest value was 6 MPa, for paste with the content of ash 20 wt.%. The same paste has the highest value of the compressive strength, 62 MPa after 28 days.

Pastes made from filter ash from power plant Poříčí K8 (Fig. 4) had comparable values of the flexural strength to pastes with filter ash from Tisová. The compressive strengths are comparable too. Lower strengths then clinker had pastes with the content of ash higher than 50 wt.%.

The lower values of strengths of mixtures with filter ashes are probably due to slightly different chemical composition and the higher amount of water needed to prepare the mixture with demanded consistence.

Mixtures with the highest content of bed ash and the highest strength were selected for tests on mortars. The measured values showed the same trends as in pastes. Flexural strengths of mortars after 28 days were about 7 MPa. Compressive strengths were about 40 MPa, what is due to the high content of fly ash satisfactorily.

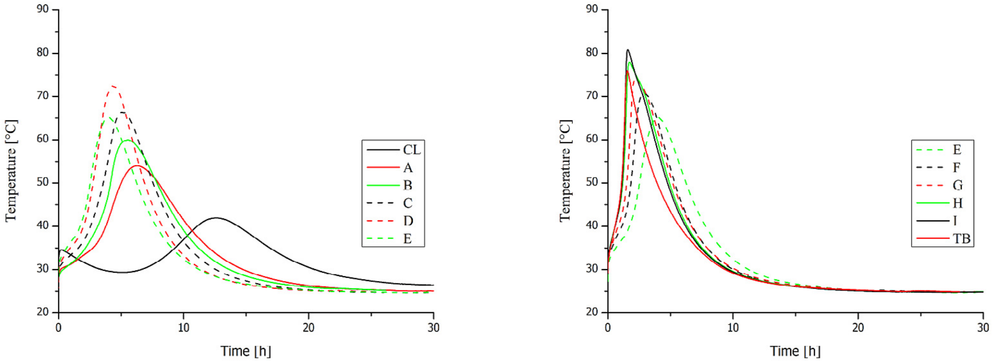

(a) (b)

Fig. 5. Differential calorimetric curves of pastes with 0–50% (a) and 50–100% (b) content of the TB.

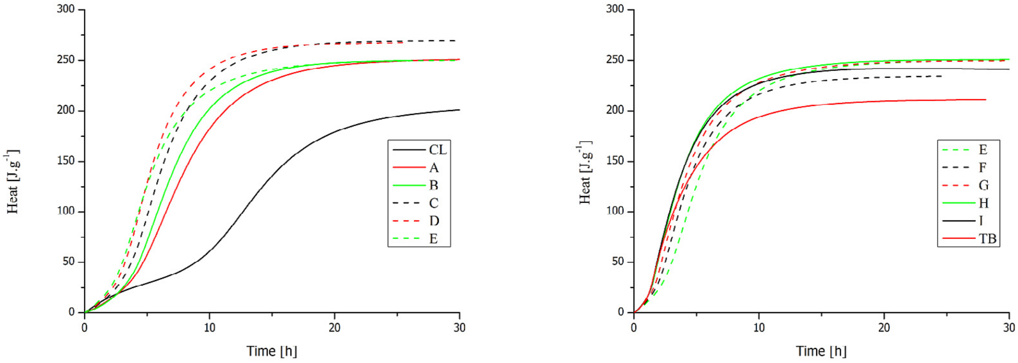

(a) (b)

Fig. 6. Integral calorimetric curves of pastes with 0–50% (a) and 50–100% (b) content of the TB.

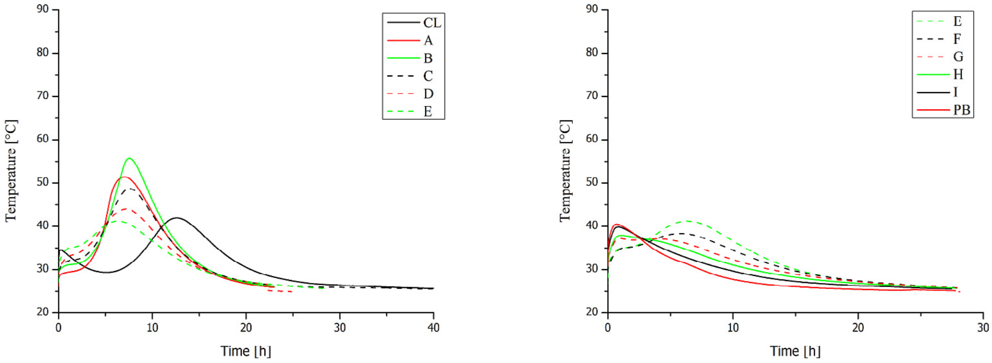

(a) (b)

Fig. 7. Differential calorimetric curves of pastes with 0–50% (a) and 50–100% (b) content of the PB.

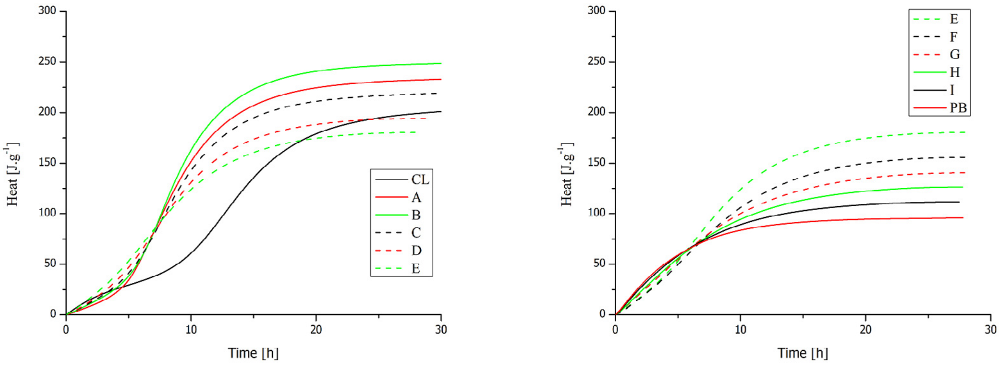

(a) (b)

Fig. 8. Integral calorimetric curves of pastes with 0–50% (a) and 50–100% (b) content of the PB.

The calorimetric curves presented on Fig. 6 and Fig. 8 show, that process of hydration of ashes is dependent on the content of free lime, which exothermally reacts with water. The experimental data were in good agreement with data published here [17]. The temperature and the heat of hydration increase with the increasing content of free lime. So, the bed ash from power plant Tisová (TB) achieved during hydration reaction higher temperature and higher amount of heat in comparison to bed ash from Poříčí K8 (PB).

The maximum reached temperature (Fig. 5) increases with the increasing amount of the fly ash in the mixture. For the mixture with 90% content of fly ash the temperature was higher than for the pure fly ash. The total released heat for all pastes made with bed ash from Tisová (Fig. 6) was similar and was higher than for the pure ash and the pure clinker.

The behavior of cement mixtures was published elsewhere [17,18,19]. They studied hydration reaction of mixtures made from cement and fluidized bed combustion ash and observed that the increasing addition of ash conversely caused the retardation of hydration.

The Fig. 7 and Fig. 8 show that the maximum reached temperature and the total released heat for pastes made with bed ash from Poříčí K8 decrease with increasing amount of the bed ash. It is due to the fact, that the total released heat for the pure bed is about two times lower than for the pure clinker.

4. Conclusion

The work was focused on the utilization of fluidized bed combustion fly ash from two thermal power plants in The Czech republic as a donor of sulfates.

From the experimental observations, the highest values of compressive strengths were measured on pastes with the ash content from 20 to 60 wt. %. Inconsiderable high values of strength reached mixtures with a higher ash content. The strengths were more than 60 MPa. These values were measured on the mixtures containing 80 wt.% of ash, too. The highest value of compressive strength was measured on pastes with 30% content of fluidized bed combustion fly ash from power plant Poříčí K8 and it reached 112 MPa after 28 days.

When the filter ash was used, the highest values of compressive strength reached mixtures with the content of ash from 20 to 40 wt.%. The compressive and flexural strengths measured on the pastes with filter ashes were lower in comparison with the mixtures with bed ashes. The larger surface area of filter ash caused need of higher volumes of mixing water, which could be a possible disadvantage of their application.

From measured calorimetric curves, we can see the affected process of hydration reaction of ashes by the content of free lime. Mixtures made using bed ash from Tisová reached the similar values of total released heat. The released heat of bed ash from Poříčí was about two times lower than released heat for the Portland clinker. We can also see the dependence of ash content on the calorimetric measurements. So the released heat and the maximum reached temperature decreased when the content of ash increased.

Acknowledgement

This work was supported by the project “Materials Research Centre at FCH BUT - Sustainability and Development, REG LO1211, with financial support from National Programme for Sustainability I (Ministry of Education, Youth and Sports)”.

References

[1] M. Ahmaruzzaman, A review on the utilization of fly ash, Prog. Energy Combust. Sci. 36 (2010) 327–363.
[2] S.V. Vassilev, R. Menendez, M. Diaz-Somoano, M.R. Martinez-Tarazona, Phase-mineral and chemical composition of coal fly ashes as a basis for their multicomponent utilization. 2. Characterization of ceramic cenosphere and salt concentrates, Fuel 83 (2004) 585–603.
[3] R. Siddique, Utilization of coal combustion by-products in sustainable construction materials, Resour. Conserv. Recycl. 54 (2010) 1060–1066.
[4] J. Koornneef, M. Junginger, A. Faaij, Development of fluidized bed combustion - An overview of trends, performance and cost, Prog. Energy Combust. Sci. 33 (2007) 19–55.
[5] A. Baba, G. Gurdal, F. Sengunalp, Leaching characteristics of fly ash from fluidized bed combustion thermal power plant: Case study, Fuel Process. Technol. 91 (2010) 1073–1080.
[6] J. Havlica, J. Brandstetr, I. Odler. Possibilities of utilizing solid residues from pressured fluidized bed coal combustion (PSBC) for the production of blended cements, Cement Concrete Res. 28 (1998) 299–307.
[7] J. Kaminski, Technologies and costs of SO2-emissions reduction for the energy sector, Appl. Energy 75 (2003) 165–172.
[8] L.E. Kallinikos, E.I. Farsari, D.N. Spartinos, N.G. Papayannakos, Simulation of the operation of an industrial wet flue gas desulfurization system, Fuel Process. Technol. 91 (2010) 1794–1802.
[9] X. Fu, Q. Li, J. Zhai, G. Sheng, F. Li, The physical–chemical characterization of mechanically-treated CFBC fly ash, Cement Concrete Comp. 30 (2008) 220–226.
[10] European Committee for Standardization. European standard: Fly ash for concrete. Definition, specifications and conformity criteria. EN 450-1:2005 E. 2005.
[11] P. Šiler, P. Bayer, T. Sehnal, I. Kolářová, T. Opravil, F. Šoukal, Effects of high-temperature fly ash and fluidized bed combustion ash on the hydration of Portland cement, Constr. Build. Mater. 78 (2015) 181–188.
[12] J. Havlica, J. Brandštetr, I. Odler, Possibilities of utilizing solid residues from pressured fluidized bed coal combustion (PSBC) for the production of blended cements, Cement Concrete Res. 28 (1998) 299–307.
[13] A.A. Usón, A.M. López-Sabirón, G. Ferreira, E.L. Sastresa, Uses of alternative fuels and raw materials in the cement industry as sustainable waste management options, Renew. Sust. Energ. Rev. 23 (2013) 242–260.
[14] A. Quennoz, K.L. Scrivener, Hydration of C3A–gypsum systems, Cement Concrete Res. 42 (2012) 1032–1041.
[15] W. Lerch, The influence of gypsum on the hydration and properties of portland cement pastes, Chicago, 1946.
[16] A. Nawaz, P. Julnipitawong, P. Krammart, S. Tangtermsirikul, Effect and limitation of free lime content in cement-fly ash mixtures, Constr. Build. Mater. 102 (2016) 515–530.
[17] B. Pacewska, G. Blonkowski, I. Wilińska, Studies on the pozzolanic and hydraulic properties of fly ashes in model systems, J. Therm. Anal. Calorim. 94 (2008) 469–476.
[18] W. Nocuń-Wczelik, A. Łagosz, B. Kowalski, M. Gawlicki, Calorimetry in testing waste materials from the brown coal combustion, J. Therm. Anal. Calorim. 118 (2014) 123–131.
[19] B. Pacewska, G. Blonkowski, I. Wilińska, Investigationsof the influence of different fly ashes on cement hydration, J. Therm. Anal. Calorim. 86 (2006) 179–186.

Advanced Materials Research
ISSN: 1662-8985, Vol. 1000, pp 59-62
doi:10.4028/www.scientific.net/AMR.1000.59

Submitted: 2014-05-29
Accepted: 2014-06-02
Online: 2014-08-11

Influence of storage conditions on quality of fly ashes

Hana Kalousová[1, a], Eva Bartoníčková [1, b], Tomáš Opravil [1, c]

[1]Brno University of Technology, Faculty of Chemistry, Department of Materials Science, Purkyňova 118, 61200, Brno, Czech Republic

[a] xckalousova@fch.vutbr.cz, [b] bartonickova@fch.vutbr.cz, [c] opravil@fch.vutbr.cz

Keywords: Fly ash, fly ash stock-piles, quality evaluation in time.

Abstract

The presented paper deals with the issue of influence of storage conditions on the quality of conventional fly ashes which are produced by combustion of lignite. These ashes were stockpiled for long time. A borehole for sampling was made in the fly ash stock-pile. Total depth of the borehole was 20 m. Samples of fly ashes taken from every single meter were analyzed and next mechanical properties and the volume stability of materials containing these fly ashes were tested.

The quality of fly ashes especially with respect to the possibility to use them as components of pastes, mortars and concretes as pozzolanic admixture or fine filler was evaluated.

Introduction

Fly ash is an industrial by-product which if not used in beneficial way, is recognized as environmental pollutant. It is generated during the coal combustion at the production of energy. Coal fly ashes are generated at 1200–1700 °C from various inorganic and organic constituents of the feed coal. Because of the scale of variety of the components, coal fly ashes are one of the most complex anthropogenic materials which can be characterized. It is a heterogeneous mixture, with amorphous and reactive glass phase and inert crystalline phases such as quartz and mullite. Fly ash reacts with $Ca(OH)_2$, the byproduct of cementitious reactions, to improve concrete's strength and durability. [1]

The presented research is devoted to the investigation of the influence of storage conditions on the quality of stockpiled ash from the power plant located in the north-west part of the Czech Republic. This coal fly ash was stockpiled for very long time without any protection from weathering – changing temperature, humidity, etc. A borehole with total depth of 20 m was made for the investigation and sampling. Samples of fly ash taken from every single meter were collected and next analyzed. The research contains the determination of mechanical properties and volume stability of building materials in which a part of cement was replaced by fly ash. The replacement of cement is very important for the reduction of environmental impact and for achieving economic and energy savings.

Cement is in many ways an essential material that is used worldwide, mainly as a component of concrete, but cement production and usage are highly energy and material demanding and of high environmental impact. More than 5% of global anthropogenic CO_2 emissions and substantial emissions of SO_2, NO_x and other pollutants are formed during cement fabrication. [2]

The most common type of cement is Portland cement which consists of a clinker. This is formed when raw material burns at high temperature in a cement kiln. In this process calcium carbonate decomposes and CO_2 is produced. This process is called calcination and it is very important from the viewpoint of greenhouse gas emissions, since in the process carbon bound in mineral is transformed into CO_2. The calcination typically causes more than 50 % of total CO_2 emissions from cement production. Another part of remaining emissions originates from the combustion of fuels in the kiln.

In this paper, the utilization of fly ash in the production of building materials, as a low-cost material is discussed, because it is important for two aspects – ecological and economic. Partial replacement of cement by fly ash can positively affect the CO_2 emissions and purposeful use of fly ash is a solution to the ecological problem with stockpiling of secondary raw materials. [3,4]

Analysis of stockpiled fly ash

Collected samples were subjected to the series of several analyses to determine the properties of fly ashes. Particularly it was the determination of moisture, the determination of bulk and tapped density, the determination of particles size, the determination of pH and conductivity of extract, X-ray diffraction (XRD) analysis, and the loss on ignition (LOI) test. Testing was carried out according to CSN EN 72 2072 (Fly ash for building industry purposes) and CSN EN 450 (Fly ash for concrete).
Chemical properties of coal fly ashes are highly dependent on what kind of coal was burned and on the combustion system as well. Tested fly ash originated from one power plant, so the combustion system was unchanged.
The XRD analysis showed the most interesting results. All samples contained amorphous phase, Quartz and Mullit in large quantities. The results also revealed the presence of Magnetite, Hematite and Anatase. The XRD analysis showed that there were no big differences among individual samples. This fact is very positive - because there are probably no phase changes in time and it is possible to use this secondary raw material as a component in building materials.

Mechanical properties of pastes and mortars containing fly ash

For the tests of mechanical properties the specimens containing 65 – 70 % fly ash, 25 % cement CEM 42, 5 R (according to the European cement standard EN 197-1), water and superplasticizer (0,8 % of quantity of cement) were prepared. The amount of water was chosen according to consistency (all mixtures were prepared with the same consistency).
The specimens for testing the tensile strength and compressive strength had the dimension of 40×40×160 mm. Strengths were measured after 1, 7, 28 and 90 days. For the comparison the reference sample containing sand, cement, water and superplasticizer was prepared. The results are given in Table 1.

Table 1: Tensile strength (Tens.) and compressive strength (Comp.) after 1, 7, 28 and 90 days

Specimen	Strength after 24 hours [MPa]		Strength after 7 days [MPa]		Strength after 28 days [MPa]		Strength after 90 days [MPa]	
	Tens.	Comp.	Tens.	Comp.	Tens.	Comp.	Tens.	Comp.
Sand	7,34	38,69	10,36	72,26	11,73	86,69	10,32	91,49
0-1 m	0,13	0,99	2,66	10,82	3,54	16,79	4,71	34,35
1-2 m	0,51	2,01	3,75	19,37	4,93	30,46	5,86	37,89
2-3 m	0,99	4,08	4,18	22,57	5,14	26,03	4,39	35,04
3-4 m	0,39	1,68	2,63	11,79	4,66	25,24	4,39	26,03
4-5 m	0,88	3,27	3,57	17,02	4,89	28,69	5,49	35,63
5-6 m	0,80	3,78	4,03	18,90	4,87	27,97	3,94	31,86
6-7 m	1,02	4,04	3,98	18,11	4,77	27,76	5,01	31,16
7-8 m	0,67	2,34	2,99	18,28	4,06	24,12	5,28	29,56
8-9 m	1,15	4,85	4,13	19,84	5,42	28,30	6,03	33,25
9-10 m	1,19	3,58	3,97	18,23	5,85	32,05	6,13	40,69
10-11 m	1,31	5,36	3,71	22,66	4,8	37,24	5,86	40,83
11-12 m	1,76	6,56	4,35	27,65	4,56	35,79	7,19	43,62
12-13 m	1,69	6,20	3,98	22,83	4,86	37,23	4,47	37,14

13-14 m	1,16	5,05	5,36	30,46	5,84	38,78	5,53	35,91
14-15 m	1,69	6,15	4,63	25,30	6,64	35,92	6,18	49,68
15-16 m	1,31	6,07	4,41	26,85	5,33	36,78	6,16	44,34
16-17 m	1,20	4,04	4,04	21,29	1,09	30,58	5,51	34,78
17-18 m	1,02	3,73	3,38	17,51	4,18	25,80	5,28	31,44
18-19 m	1,24	5,69	3,68	24,18	4,55	34,41	5,35	36,77
19-20 m	0,83	2,05	1,78	9,66	3,26	13,20	3,89	18,21

In Table 1 we can see, that the compressive strengths after 28 and 90 have the values around 35 – 40 MPa. These values are totally sufficient for use as a part of cement. The specimen with fly ash from the depth of 19-20 m has significantly lower values. The XRD analysis of this sample showed the presence of Kaolinite. So we can assume that the sample from the depth of 19-20 m was a blend of fly ash and soil which caused the decrease of strength.

Fly ashes from the depth of 0-1 m, 10-11 m, 13-14 m and 19-20 m were chosen for the tests in mixtures in which 25 % of cement was replaced by fly ash. The results are given in Table 2.

Table 2: Tensile strength and compressive strength after 1, 7, 28 in mixtures with 25 % cement replaced by fly ash

Specimen	Strength after 24 hours [MPa]		Strength after 7 days [MPa]		Strength after 28 days [MPa]	
	Tensile	Compressive	Tensile	Compressive	Tensile	Compressive
0-1 m	5,19	36,76	10,76	66,79	7,51	76,93
10-11 m	4,38	38,75	7,28	66,91	5,71	73,40
13-14 m	5,84	38,60	9,01	71,24	6,37	75,89
19-20 m	3,26	29,89	6,54	51,73	4,61	50,35

The strength development is similar as in previous case. Mortars with cement replacement of 25, 30, 35 and 65 % by sample 13-14 m were prepared. The strengths are given in Table 3.

Table 3: Tensile strength and compressive strength of mortars

Specimen	Strength after 24 hours [MPa]		Strength after 7 days [MPa]		Strength after 28 days [MPa]	
	Tensile	Compressive	Tensile	Compressive	Tensile	Compressive
Without fly ash	1,57	5,60	1,88	7,94	2,77	11,97
25 % fly ash	1,37	3,14	2,81	14,24	3,62	19,50
30 % fly ash	0,94	2,84	2,75	13,27	13,27	13,98
35 % fly ash	0,52	1,76	2,65	11,67	11,67	15,19
65 % fly ash	0,14	0,01	0,84	2,51	1,16	4,16

The results from Table 3 show that optimal content of fly ash is around 25 %, but very good strength was obtained as well when replacing cement by 35 %.

Volume stability

Volume stability was measured as a dilatation of testing specimens of cement pastes which contained 65-70 % of fly ash. The dilatations of individual specimens converted to mm · m^{-1} are shown in Table 4.

Table 4: Dilatations of cement mortars

Specimen	Dilatation [mm · m^{-1}]	Specimen	Dilatation [mm · m^{-1}]	Specimen	Dilatation [mm · m^{-1}]	Specimen	Dilatation [mm · m^{-1}]
Sand	0,006	**5-6 m**	0,313	**10-11 m**	0,013	**15-16 m**	0,325
0-1 m	0,144	**6-7 m**	0,338	**11-12 m**	0,344	**16-17 m**	0,313
1-2 m	0,238	**7-8 m**	0,006	**12-13 m**	0,513	**17-18 m**	0,275
2-3 m	0,225	**8-9 m**	0,319	**13-14 m**	0,506	**18-19 m**	0,213
3-4 m	0,013	**9-10 m**	0,475	**14-15 m**	0,288	**19-20 m**	0,819
4-5 m	0,019						

Summary

The presented paper shows the results of research which studies the influence of storage conditions on the quality of fly ashes. Based on the results we can see, that there are neither the phase changes in time nor different mechanical properties and volume instability. This fact is very positive for the application of these fly ashes as components of building materials.

Acknowledgements

The authors also gratefully acknowledge the funding provided from the project “Excellent Teams” No. CZ.1.07/2.3.00/30.0005.

References

[1] AHMARUZZAMAN M. A review on the utilization of fly ash. In: *Progress in Energy and Combustion Science*, 2010, Vol. 36, Issue 3, p. 327 – 363.

[2] BLISSETT R.S., ROWSON N.A. A review of the multi-component utilisation of coal fly ash. In: *Fuel*, 2012, Vol. 97, p. 1 – 23.

[3] FEIZ R., AMMENBERG J., BAAS L., EKLUND M., HELGSTRAND A., MARSHALL R.: Improving the CO2 performance of cement, part I: utilizing life-cycle assessment and key performance indicators to assess development within the cement industry. In: *Journal of Cleaner Production*, 2014, In Press

[4] SCRIVENER K.L., KIRKPATRICK R.J.: Innovation in use and research on cementitious materials. In: *Cement and Concrete research*, 2008, Vol. 38, Issue 2, p. 128 – 136.

Construction and Building Materials 135 (2017) 306–314

Contents lists available at ScienceDirect

Construction and Building Materials

journal homepage: www.elsevier.com/locate/conbuildmat

The correlation between porosity and mechanical properties of multicomponent systems consisting of Portland cement–slag–silica fume–metakaolin

Eva Kuzielová [a,b,*], Matúš Žemlička [a,b], Eva Bartoničková [c], Martin T. Palou [a,b,c]

[a] Institute of Construction and Architecture, Slovak Academy of Sciences, Dúbravská cesta 9, SK-845 03 Bratislava, Slovak Republic
[b] Faculty of Chemical and Food Technology, Slovak University of Technology, Radlinského 9, SK-812 37 Bratislava, Slovak Republic
[c] Materials Research Centre, Faculty of Chemistry, Brno University of Technology, Purkyňova 118, CZ-612 00 Brno, Czech Republic

HIGHLIGHTS

- Refinement of the structure as a result of applied SCMs (BFS, SF and MK).
- Synergic effect of SCMs ensured high strengths in every curing time.
- Improvement of strength in comparison with numerous reported binary or ternary systems.
- Determination of relationship between strengths and porosities.

ARTICLE INFO

Article history:
Received 15 July 2016
Received in revised form 25 October 2016
Accepted 21 December 2016
Available online 10 January 2017

Keywords:
Blended cements
Metakaolin
Silica fume
Ground granulated blast-furnace slag
Porosity

ABSTRACT

Pore structure and mechanical strength of quaternary systems consisting of ordinary Portland cement (PC) replaced in 25, 30 and 35 wt% by ground granulated blast-furnace slag (BFS), silica fume (SF) and metakaolin (MK) were evaluated up to 365 days. Refinement of the structure as a result of cement supplementary materials (SCMs) demonstrated mainly by the rise of gel pores portion, whereas the portion of middle capillary pores decreased. Despite dilution effect in blended samples, both the compressive (CS) and flexural strength (FS) increased throughout all the curing time and reached the values higher than that of referential sample. Development of strength in time reflected different activity of SCMs. The highest values of strength corresponding to the lowest total porosities were determined in the samples containing the most SF (CS = 125 MPa, FS = 18 MPa after 365 days), whilst the highest amount of BFS together with the highest substitution level led to the lowest strengths among blended samples (CS = 99 MPa, FS = 15 MPa).

1. Introduction

Even though the blended cements are in the center of attention for a relatively long time, their possibilities are not still exhausted. Continue improvement of their properties is based on the combined effect of various binders' materials and allowed e.g. the development of self-compacting concrete or high performance cements [1–5].

Performance of multicomponent materials depends on the variety of initial factors, such as chemical and mineralogical composition, selected preparation conditions (e.g. water content, initial and curing temperature, dosage of plasticizer) [6]. Many preparation parameters (workability, water to binder ratio, bleeding and drying shrinkage) are affected by fineness of initial materials. The rate by which cement and supplementary materials react with water also considerably depends on their fineness. Higher fineness increases reaction kinetics owing to the corresponding increase of surface area [7] and ensures mainly the early age strength acquirement [8,9].

The fineness characteristics of materials include particle morphology, particle size, particle size distribution and specific surface [10]. It is necessary to be aware that characterization of material fineness only by average particle size or specific surface area is not sufficient. Two cements with the same average particle size but different distributions will exhibit dissimilar rate of early hydration. A better parameter for describing the fineness of the

---

* Corresponding author at: Institute of Construction and Architecture, Slovak Academy of Sciences, Dúbravská cesta 9, SK-845 03 Bratislava, Slovak Republic.

E-mail address: eva.kuzielova@savba.sk (E. Kuzielová).

http://dx.doi.org/10.1016/j.conbuildmat.2016.12.105
0950-0618/

material (at least in terms of knowing the early times reactivity) is the specific surface area. However, specific surface area does not depose about the size of the largest particles and about the breadth of the particle size distribution. Both of these parameters affect the workability at a given water to binder ratio, the degree of reaction and correspondingly the strength development over long periods of time. Different particle size distribution of materials possessing the same specific surface area will lead to the different water demands. Wider size distribution increases the packing density of the system and thus effectively reduces water demand [11]. Consequently, it is expected that increasing of the packing density would have a positive contribution to strength gain potential.

Besides the fineness of initial materials, the curing procedure has an important impact on the porosity and the related final material properties. According to Ramezanianpour and Malhotra [12], the continuous moist curing of concrete is essential to achieve the lowest porosity and the highest compressive strength. They reported that the use of BFS produces a very poor permeable concrete however it is more sensitive to curing process than the use of SF or pure PC and this sensitivity increases with slag content in the particular mixtures.

It is well known that also incorporation of MK up to 20 wt% leads to the decrease of total porosity [13,14]. On the contrary, the substitution of more than 30 wt% of PC by MK results in the increase of porosity, which was attributed to its fineness and corresponding increase of water to binder ratios. The flowability of fresh cement mixtures deteriorated due to the MK content can be improved by addition of BFS. In the same manner, the presence of BFS helps to decrease the water demand and the need of plasticizer use in blended cements with SF [15]. Accordingly, it helps to prevent from the resulting decrease of the compressive strength.

In general, the contribution of SCMs to concrete strength can be divided into three elementary factors associated with fineness: the filler effect, the acceleration of PC hydration (nucleation sites) and the pozzolanic reaction of admixtures with $Ca(OH)_2$ [16–18]. SCMs can produce more efficient packing at the cement paste-aggregate particle interface, reduce the amount of bleeding and form a denser, more homogeneous initial transition zone microstructure and also a narrower transition zone. The acceleration of PC hydration in the presence of substitution materials is apparent from the higher rates of heat evolution but also from nearly the same or even higher content of $Ca(OH)_2$ determined at very early times of hydration than the expected amounts due to the consummation of arising hydroxide by pozzolanic reactions [16]. Pozzolanic reactions improve material strength by the formation of additional binding phases (C-S-H, C_4AH_{13}, C_3AH_6 and C_2ASH_8) [19–22]. The contribution of particular factors differs according to the activity of the used substitution materials, their replacement level but also the curing time. For example according to [16] dealing with MK blended cements, whilst the filler effect shows immediately, the acceleration of PC has its major impact within the first 24 h and the maximum effect of the pozzolanic reaction occurs between 7 and 14 days. The main contribution of SF as highly active pozzolan to concrete strength at normal curing temperature takes place from about 3 to 28 days. After this time, the effect of SF on strength development becomes negligible. Unlike the MK and SF, reactivity of BFS is much lower and its contribution to the strength gain was demonstrated at medium and later ages of hydration.

Majority of published studies focus on the binary or ternary systems, whereas only few researches deal with the replacement of cement by three supplementary materials together. The reason why we have studied the four compound systems is the synergic effect of materials that can moves the barriers and bring other improvement of final material properties. The following SCMs with different reaction activity have been selected to this goal: BFS, SF and MK.

In our previously published paper [23], evaluation of pozzolanic activity and heat profiles of 2 days samples from the referred four compounds systems using isothermal calorimetry and thermal analysis were already discussed. It was proved that the suitable combination of SF, BFS and MK can prevent from the decrease of strength due to the partial replacement of PC. On the contrary, significantly higher values of compressive strength than the values announced in the number of studies devoted to binary or ternary systems may be attained, which makes these materials promising for the use as e.g. high performance cements. In addition, the formation of phases resistant to higher temperatures (such as tobermorite, C-A-S-H) indicates their possible applications in hydrothermal conditions of deep geothermal wells. Present article continues to study referred systems up to 365 days and investigates the correlation of porosity, compressive and flexural strength.

2. Experimental

The following initial materials were used to prepare the samples: Portland cement (CEM I 52.5 N, Holcim (Slovensko), a.s., Slovakia,), ground granulated blast-furnace slag (Kotouč Štramberk, spol. s r.o., Czech Republic), silica fume (Oravské ferozliatinárske závody, a.s., Slovakia) and metakaolin L_{05} (Mefisto, České lupkové závody, Czech Republic). Composition of particular samples is listed in Table 1. The concept was based on STN-EN 197-1 that limits the content of Portland clinker to 65 wt% for binary blended cements in order to assure necessary $Ca(OH)_2$ quantity for alkali activation or pozzolanic reactions. Keeping into mind, the combination of SCMs to replace PC up to 35 wt% was used. As both, MK and SF, are very reactive since the initial stage of hydration, the decreasing proportion of SF with increasing proportion of MK was chosen in order to establish their influences on the hydration and relating properties of final materials. On the contrary, BFS acts after longer period and its effect does not overlap to the significant extent with those of MK and SF. Its amount was chosen to be the same as MK. The results of chemical analysis and physical characteristic of the used Portland cement and supplementary cementitious materials are shown in Table 2. Chemical analysis of cement was done according to EN 196-2. Mineral composition of the used cement is displayed in Table 3.

The whole experimental procedure of mortar preparation, storage and measurement of flexural and compressive strength was done in accordance with STN EN-196-1. Standard sand satisfying the tests for CEN Reference sand was added to binders in the weight ratio of 3/1. The amount of sulphate ions consumed by metakaolin to form additional ettringite was compensated by gypsum addition [24]. Except referential sample, gypsum was added to each mixture in the amount corresponding to 1.25 wt% of metakaolin content. According to our preliminary results it should assure necessary quantity of gypsum needed for the formation of both ettringites (from C_3A and MK) and also the formation of C-S-H and C-A-S-H from MK by pozzolanic reaction.

Prepared mixtures were homogenized along with the gradual adding of water using the cement mixer. Quantity of water was adjusted to achieve suitable workability of pastes (Table 1). The demand for water was reduced by Plasticizer Stachement® 2353 (Stachema Bratislava, Slovakia). Plasticizer concentration in water of 0.05 vol% was kept constant. After the whole amount of water was added, 10 min of additional homogenization followed. Three prisms with the dimensions of 160 × 40 × 40 mm were prepared from the mortar of each composition. Prisms were covered with moist tissue and foil and kept at laboratory temperature of 20 ± 0.5 °C for 24 h. Demolded samples were immersed in the water and stored at laboratory temperature until the strength

Table 1
Composition of prepared samples (in wt%) and used water to binder ratio (*w*/*b*).

Sample	w_{PC}/%	w_{BFS}/%	w_{SF}/%	w_{MK}/%	*w*/*b*
Quatro0	100	–	–	–	0.42
Quatro1	75	5	15	5	0.33
Quatro2	70	10	10	10	0.34
Quatro3	65	15	5	15	0.36

Table 2
Oxide composition (in wt%) and specific surface (in $m^2\ kg^{-1}$) of the used Portland cement and supplementary cementitious materials. All depicted values of specific surface areas determined using Blaine represent the average of three measurements.

	Oxide composition/wt%						Specific surface/$m^2\ kg^{-1}$	
	CaO	SiO_2	Al_2O_3	Fe_2O_3	MgO	SO_3		
CEM I 52.5 N	64.01	20.39	4.85	2.88	2.06	2.85	Blaine	464.3 ± 0.9
SF	0.50	97.10	0.21	–	0.40	–	BET	15000
MK	0.24	49.70	42.36	0.79	0.22	0.08	Blaine	2586 ± 38
BFS	36.53	35.76	9.39	0.24	14.0	0.03	Blaine	469.9 ± 0.5

Table 3
Mineral composition (in wt%) of CEM I 52.5 N given by producer. C_3A is present in orthorhombic and cubic form, MgO as periclase (cubic form).

Mineral composition/wt%							
CEM I 52.5 N	C_3S	C_2S	C_3A (ort.)	C_3A (cub.)	C_4AF	Free lime	MgO
	61.49	15.44	3.85	5.48	8.76	0.93	1.35

measurements and the mercury porosimetry were carried out. Flexural and compressive strength of hardened composites were determined using WPM WEB Thuringer Industriwerk Rauestein 11/2612 (up to 25,000 N). The three-point bending flexural test was used for determination of flexural strength. The compressive strength was measured using the broken pieces of the prism samples obtained from flexural strength measurements. Each displayed data of the flexural and the compressive strength thus represents arithmetic mean of 3 or 6 experimental measurements, respectively.

MIP Quantachrome Poremaster 60GT (Quantachrome, UK) was used for the determination of the pore structure parameters of the samples. Pieces of the dried samples (24 h at 105 °C) taken from their different parts, with diameter less than 10 mm and total mass max. 2 g, were used for the tests. The maximum applied pressure of mercury was 414 MPa, equivalent to a Washburn pore radius of 1.8 nm.

The particle size analysis of prepared dry mixtures was carried out on the laser granulometer Helos with dry dispersion unit Rodos (Sympatec, Germany). Displayed results represent the average of three measurements.

3. Results and discussion

3.1. Laser diffraction analysis

As can be seen from Table 4, median of particle size in blended mixtures is due to the substitution of PC by finer materials approximately by half less than in referential mixture. By reason of large differences among specific surfaces of particular cementitious materials (Table 2), the refinement of structure was not affected primarily by the total level of PC replacement, but mainly by the substitution level of particular components and their synergic effect. Accordingly, the lowest value of x_{50} and correspondingly the highest specific surface were determined for mixture Quatro1 prepared with the highest content of SF.

Whilst the density distribution curve of Quatro0 showed the main from the two well distinguished peaks at approximately 15 μm, the size of particles occurring the mostly in the blended mixtures Quatro1 and Quatro2 was shifted to the much lower values (between 1 and 2 μm) (Fig. 1). The refinement of blended samples manifested also by higher occurrence of particles with the size below 0.5 μm. Particles with sizes between approximately 5 μm and 20 μm that came chiefly from PC represented the second frequent size region. The composition of Quatro3 (mainly higher content of coarser BFS with specific surface comparable with that of PC (Table 2)) caused that the presence of these particle sizes became again more frequent than the previously mentioned lower size one.

Blending of SF, BFS and MK in PC resulted in broader particle size distribution of particular mixtures even though the specific surface of all the used cementitious materials is higher or similar to that of PC. Whereas the values of x_{90} roughly equaled 23 μm for all the mixtures, x_{99} values of Quatro1, Quatro2 and Quatro3 increased to 70.76 μm, 71.11 μm and 67.71 μm, respectively. 99th percentile of referential mixture attained the value of 40.95 μm. The presence of particles larger than 40 μm causing

Table 4
Particle size analysis of dry mixtures; x_{50} – median of particle size, x_{90} – 90th percentile of particle size, x_{99} – 99th percentile of particle size, a_s – specific surface. Each shown result is the average of three individual measurements; corrected sample standard deviations are presented for each value. By reason of the different principles of measurements were used to assess the values of specific surface of referential sample in Tables 2 (Blaine) and 4 (laser diffraction technique), they cannot be compared each other.

Mixtures	Quatro0	Quatro1	Quatro2	Quatro3
x_{50}/μm	6.75 ± 0.11	2.67 ± 0.11	3.40 ± 0.05	3.27 ± 0.05
x_{90}/μm	23.47 ± 0.47	22.85 ± 1.27	23.42 ± 0.57	21.42 ± 0.17
x_{99}/μm	40.95 ± 2.84	70.76 ± 1.84	71.11 ± 0.64	67.71 ± 0.50
a_s/$cm^2\ g^{-1}$	16,059 ± 212	22,421 ± 563	19,604 ± 432	21,293 ± 452

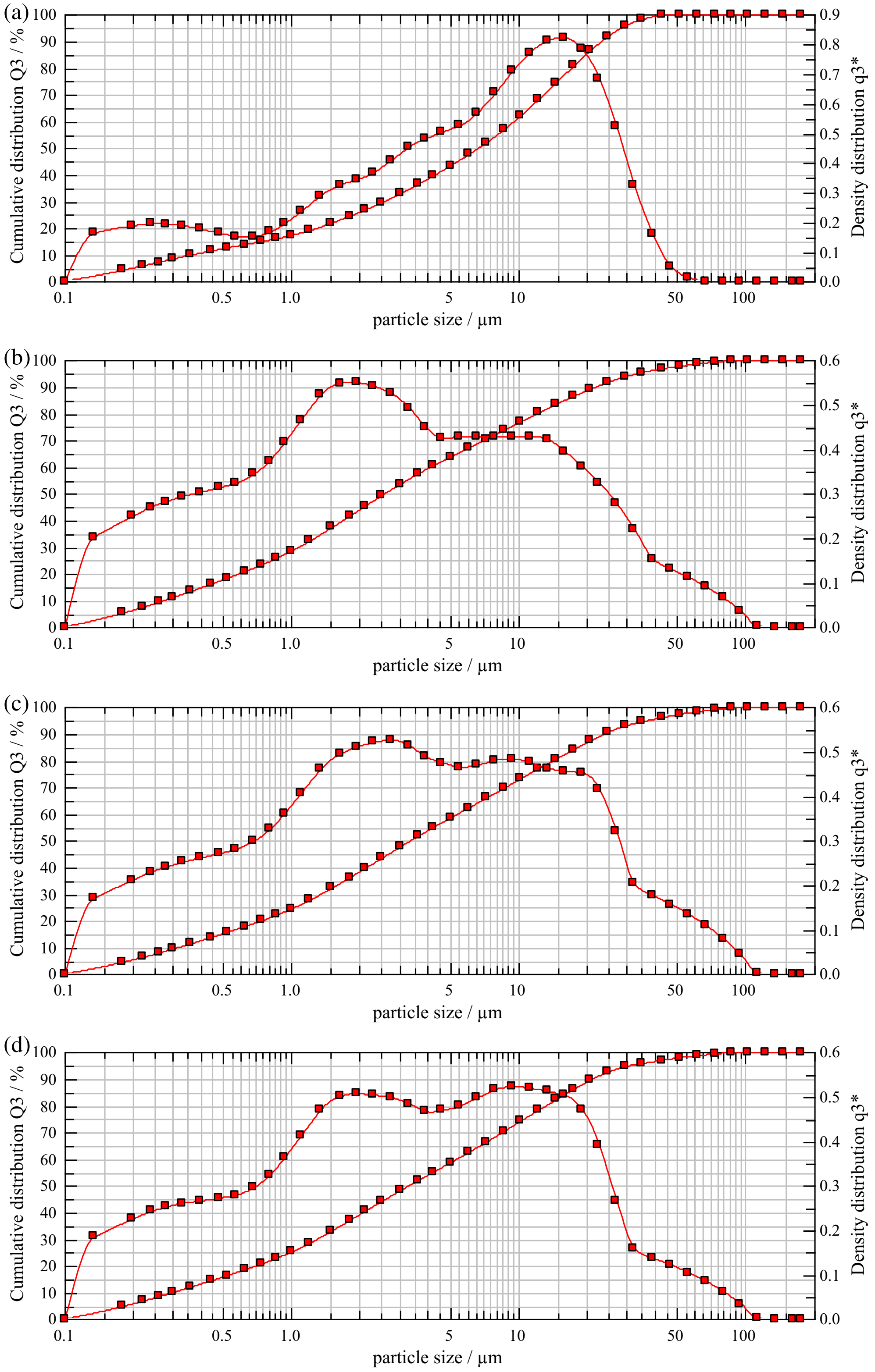

Fig. 1. Particle size analyses of prepared dry mixtures: (a) Quatro0, (b) Quatro1, (c) Quatro2 and (d) Quatro3.

the increase of x_{99} can be according to the particle size analysis of individual supplementary materials explained by agglomeration of finer supplementary material particles mostly of silica fume. It can be assumed that agglomerates were disintegrated already during mixing and homogenization process. Indeed, the nanometer-sized particles tend to agglomerate due to the effect of electrostatic forces and thus generate a complex structure that makes their particle size analysis seem to be broader. However, it can be assumed that during mixing with water and hydration process agglomerates will disintegrate.

Table 5
"Pore size distribution" (portion of pores in the given area of pore diameter) of samples cured from 2 up to 365 days.

Series	Curing time/days	Pore size distribution/vol%					Total porosity/%
		<4.5 nm	4.5–50 nm	50–10^2 nm	10^2–10^4 nm	>10^4 nm	
Quatro0	2	1.41	24.38	17.73	17.91	38.57	15.96
	7	1.33	25.08	18.80	21.92	32.87	12.64
	28	3.34	31.55	11.63	13.19	40.29	11.28
	90	3.52	32.44	5.69	18.20	40.15	11.20
	365	2.55	32.21	3.35	16.49	45.40	11.76
Quatro1	2	1.87	26.06	19.14	20.60	32.33	14.57
	7	5.23	39.56	8.65	14.85	31.71	9.75
	28	5.98	31.70	1.55	15.09	45.68	9.60
	90	11.29	33.22	1.93	17.43	36.13	8.36
	365	8.21	24.53	1.20	14.38	51.68	9.70
Quatro2	2	1.67	33.68	16.70	18.19	29.76	14.83
	7	3.86	33.80	8.23	21.93	32.18	11.19
	28	6.74	39.89	1.35	16.03	35.99	10.58
	90	8.01	26.07	1.58	19.87	44.47	11.07
	365	9.90	26.43	1.08	18.87	43.72	10.85
Quatro3	2	0.39	23.78	16.17	20.59	39.07	16.05
	7	5.49	52.50	6.92	12.38	22.71	11.71
	28	4.79	41.27	1.91	16.12	35.91	10.90
	90	5.34	35.66	1.63	16.23	41.14	11.36
	365	7.11	41.30	1.17	14.20	36.22	9.96

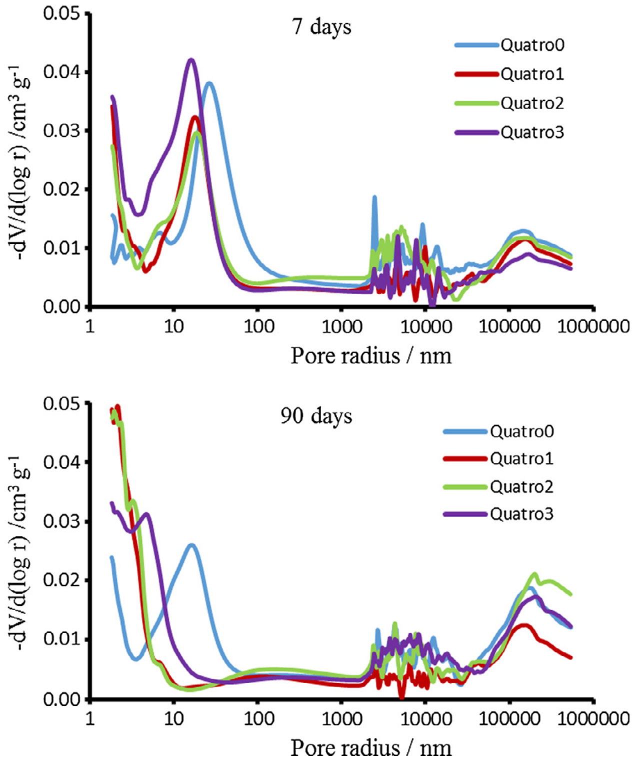

Fig. 2. Pore size distribution curves of the samples cured for 7 and 90 days, respectively.

3.2. Mercury porosimetry

The results of mercury porosimetry performed on the samples cured for 2, 7, 28, 90 and 365 days are summarized in Table 5 and Fig. 2. It must be mentioned that referred pore sizes are interpreted only in the terms of mercury intrusion context. Correspondingly, the term "pore sizes" relates the percolation size of pores corresponding to the intruded pressure. Vočka et al. [25] have reported the existence of two types of porosity in a cement paste: the porosity of the hydration product (C-S-H porosity), the so-called gel porosity, and the capillary porosity. In general, a more detailed dividing of pores into particular categories and relevant classification of their sizes is not strict [25,26]. In the present study, pores are divided into the particular types according to Metha and Monteirio [27]. In the case of series Quatro2 and Quatro3, the percentage (expressed as volume percentage of mercury intruded) of pores with size lower than 4.5 nm increased with increasing curing time. Quatro1 as well as Quatro0 displayed the decrease in the percentage of gel pores after 365 days in comparison with the samples of the same composition cured for 90 days, whereby the more significant drop was determined for Quatro1. Nevertheless, except the 2 days samples, the percentage of these pores is in all the blended samples and in all the times higher than in referential one.

Unlike the gel pores, mesopores with the size ranging between 4.5 nm and 50 nm affect permeability of the samples. Their percentage did not show clear dependence neither on the curing time nor on the composition of the samples. Nevertheless, in accordance with the results presented in [28], the presence of additives created a larger amount of pores of this size up to 28 days of curing. Longer curing times in the case of Quatro1 and 2 led to the more pronounced creation of gel pores.

The portion of middle capillary pores (50–100 nm) decreased with curing time and their percentage is the lowest among the capillary ones regardless of the curing time. Except 7 days samples, substitution of PC by SCMs led to the significant decrease of these pores in comparison with referential samples. Accordingly, the refinement of structure as a result of PC replacement as well as due to increasing amount of reaction products in time can be besides gel pores mainly attributed to the changes of middle capillary porosity.

On the contrary, the fraction of large capillaries (above 100 nm) and macropores occupied in most cases approximately the half or higher proportion of total porosity of all the samples. Except Quatro2, when the lowest percentage of large pores was determined in 2 days samples, other blended samples displayed the lowest percentage of these pores in 7 days samples. Series Quatro1 plus referential Quatro0 contained the highest portion of large pores after 365 days of curing. The greatest portion of large pores in Quatro3 and Quatro2 was measured after 90 days of curing. At this place it should be aware that high pressures produced by the used technique of MIP could possibly induce cracks. In addition, e.g.

Gallé [23] evidenced that also oven-drying at 105 °C leads to an overestimation of total porosity. Hydrates like ettringite and C-S-H lose a significant amount of non-evaporable water and desiccate, microcracks and capillary stress can be generated which results in the large capillary porosity.

The mechanisms of transport processes in the pores of different size categories are different [29]. In the case of mesopores, electrostatic interactions between the pore walls and the pore liquid can hinder transport processes, whereas in the pores of greater size electrostatic effects do not happen. Capillary pores sized from 50 to 10,000 nm have the main effect on the transport processes and correspondingly the detrimental influence on the durability of composites. On the contrary, they have only a minor effect on hydration rates [30]. In all the studied systems, the percentage of these pores decreased with increasing curing time, however did not change significantly in comparison with referential samples. Nevertheless, as clearly evidenced by Fig. 2, the main peaks of PSD localized especially in the area of pores radius below 1000 nm significantly moved toward lower sizes. The shift is more pronounced in the later times of curing and in the case of lower substitution levels (Quatro1 and 2). SCMs additions reduced the size of capillary pores and probably caused the partial segmentation of pore system.

Bentz et al. [31] in their study dealing with the influence of SF on the diffusivity of cement based materials mentioned that at higher capillary porosities (above 20%), the transport of liquids is dominated by the percolated pathways through the capillary porosity phase. However in the systems with lower capillary porosities (below 20%), the capillary pores become discontinuous and transport is controlled by the properties of the nanoporous C-S-H phase. In present blended systems, the percentage of pores between 50 and 10,000 nm moved around or below 20%, especially in the case of Quatro1 and 3 after 28 days of curing.

The refinement of capillary porosity after the substitution of PC by all the used supplementary materials in this study was referred by many researchers [32–35]. Some authors [28,36] reported that besides refinement also the fraction of capillary pores decreased with increasing content of additives. In our case, not only substitution level of PC was increased, but also the composition of samples was changed which complicates the explanations. However, as it can be seen from the comparison among the series, the largest drop of capillary pores occurrence with curing time appeared in Quatro1, followed by Quatro3, referential series and Quatro2 thus reflecting different reactivity of SCMs and their mutual interactions. The effect of mutual interaction depends on the composition, surface area, particle size and particle size distribution as well as on the shape of individual particle of each SCM.

Total porosity of the samples from series Quatro0 and Quatro1 decreased with increasing curing time except 365 days samples that showed slight increase. Values for Quatro2 and Quatro3 decreased up to 28 days of curing, followed by the slight increase determined for 90 days samples. In general, porosity decreased the most rapidly within the first 7 days of curing as a result of filling effect of the used additives and arising hydrates filling the pores.

Higher substitution levels of PC in blended series resulted in the decreased amount of primary cement hydration products, C-S-H and $Ca(OH)_2$ (portlandite). Portlandite was in addition consumed in pozzolanic reactions, which, however, in turn led to the formation of additional binding phases (C-S-H, C-A-H, C-A-S-H). Among them, the presence of gehlenite hydrate (C_2ASH_8), especially in the samples with higher amount of MK and BFS, was detected on DTG curves [23].

As mentioned above, the most markedly was the development of total porosity demonstrated by the decrease of middle capillary pores portion. With regard to just gentle progress of subsequent reactions, no significant changes were observed after this time. Limited reactions in later curing periods can be explained by the lack of water-filled capillary pores [37,38] as well as by the dilution effect and the depletion of faster reacting SF and MK in blended samples. Not surprisingly, the most obvious was the drop of porosity in the case of Quatro1 owing to the highest amount SF. This series demonstrated the lowest values of total porosity regardless of the curing time. Thermal analysis revealed the formation of phases with $C/S \cong 1$ (such as tobermorite), demonstrated by wollastonite crystallization at higher temperatures, already after 2 days of curing [23]. On the contrary, the highest values among the blended samples showed Quatro3 prepared with the lowest amount of PC and the highest content of BFS as the slowest reactive SCM. Higher presence of aluminium ions in this series (and also in Quatro2) manifested by mullite formation during coupled TGA/DSC [23]. Reactivity of particular SCMs reflected their fineness determined by Laser diffraction analysis (Fig. 1). Contrary to the referential sample, the most particles in dry mixtures Quatro1 and 2 belonged to the values below 2 μm. As a result of the highest BFS content, as material with the surface area similar to that of PC, PSD of Quatro3 shifted back to the higher particle size area. The majority of particles belonged to the size of approximately 9 μm.

Besides the composition, higher total porosities of Quatro3 series can be explained also by the highest PC replacement level. At this point it is necessary to emphasize that despite the relatively high substitution levels of PC in the studied blended systems (ranging from 25% to 35% by weight), no increase in porosity (except 2 and 90 days Quatro3) was observed when compared with referential Quatro0. Unlike some reported studies [39,40], it seems that the amount of PC was still sufficient to produce enough $Ca(OH)_2$ that could be consumed in pozzolanic reactions leading to the refinement of structure.

Higher total porosity of 2 days Quatro3 in comparison with Quatro0 can be explained by slower pozzolanic reactions of BFS together with the highest replacement level of PC. In accordance with the results of Berodier et al. [37], higher porosity of 90 days Quatro3 may be assigned also to the lower solid volume increase produced by slag reactions when compared with Portland clinker.

From the comparison among the blended samples it is obvious that the higher w/b (Table 1), the higher values of total porosities were determined (Table 5). For the same composition of mixture and degree of hydration, the volume of hydration products would remain constant irrespective of the water content (assuming that it is sufficient to run the reactions). Consequently, unfilled spaces would increase with the increase of water to binder ratio and cause the rise of porosity [41]. On the other hand, when the insufficient amount of water is taken into account, because higher w/b should provide higher content of water available for hydration and consequent pozzolanic reactions, the opposite dependence can be expected [42]. Considering this and above mentioned, the stronger influence of replacement level and reactivity of SCMs than w/b ratio on porosity was demonstrated in these samples.

3.3. Compressive and flexural strength

Even though it is not expected that progressing reactions bring significant changes in phase compositions of samples at later periods, increasing amount of reaction products led to the gradual increase of strength values. Correspondingly, compressive strength of all the samples increased with increasing curing time regardless of their composition (Table 6). Except 2 days Quatro2 and Quatro3, all blended samples attained higher values of compressive strength than corresponding referential samples cured for the same time. As portlandite is not considered to be a strength bringing phase, its consummation in pozzolanic reactions and consequent formation of new binding phases caused enhancement of blended series

Table 6
Compressive (CS; MPa) and flexural strength (FS; MPa) of samples cured from 2 up to 365 days together with the corrected sample standard deviations.

Series	Quatro0		Quatro1		Quatro2		Quatro3	
curing	CS/MPa	FS/MPa	CS/MPa	FS/MPa	CS/MPa	FS/MPa	CS/MPa	FS/MPa
2	56.0 ± 3.2	8.4 ± 0.1	56.7 ± 1.2	9.1 ± 0.6	55.2 ± 2.2	9.7 ± 0.4	48.1 ± 2.3	9.3 ± 1.0
7	62.8 ± 9.9	10.2 ± 0.2	92.5 ± 13.9	13.9 ± 0.5	68.4 ± 2.0	12.4 ± 0.8	66.3 ± 1.7	12.9 ± 0.2
28	75.7 ± 4.6	11.5 ± 0.6	108.4 ± 6.4	17.7 ± 0.7	103.5 ± 3.0	15.4 ± 1.0	95.8 ± 3.8	14.1 ± 0.2
90	85.8 ± 2.7	11.8 ± 0.9	121.2 ± 2.8	19.8 ± 1.5	108.9 ± 2.5	16.1 ± 2.0	96.0 ± 7.5	14.3 ± 0.2
365	96.4 ± 2.2	11.8 ± 0.2	124.6 ± 2.9	18.0 ± 1.1	107.6 ± 7.7	16.3 ± 0.9	99.2 ± 5.5	15.3 ± 0.7

strength. The lowest substitution level together with the highest amount of SF in Quatro1 led to the best values of compressive strength. High pozzolanic activity of SF was well demonstrated particularly in earlier times. The most significant difference between this and other series, especially in comparison with Quatro0, was observed after 7 days of curing. This corresponds well with the results of mercury porosimetry (Table 5). Significant decrease of total porosity was the consequence of middle capillaries drop and larger pores portion, whilst the portion of gel pores increased at this time. The strength was 47% higher than corresponding value of referential sample, whilst 29% difference was attained after 365 days. Longer curing times permitted also the demonstration of MK and BFS activity and compressive strength of relevant samples increased even though it was considerably influenced by higher dilution effect. It can be expected that mainly the content of C-A-S-H increased in particular periods.

As mentioned above, the initial 2 days compressive strengths of Quatro2 and Quatro3 attained lower values than that of referential Quatro0. Some authors [43,44] reported that there is an optimal replacement of SCMs above which the refinement and the reduction of the pore volume are not occurring, which leads to the slower improvement of mechanical properties. From chemical point of view, the lower rate strength gain of Quatro2 and Quatro3 can be explained by lower reactivity of BFS, but also by the cement substitution level responsible for CH generation. Indeed, the amount of CH production, which is a result of cement hydration, is lower in the case of Quatro2 and Quatro3. Other development of mechanical properties implied that the refinement of structure and corresponding gain of strength needed longer time due to delayed reactions of BFS, which is supported also by our previously reported results [23].

In general, the influence of both, the dilution effect and the faster reactions of SF and MK, in blended series caused that increase of strengths in later periods was not so pronounced as in the case of referential samples.

The development of flexural strength showed the same dependencies on the curing time and the composition of samples as the course of compressive strength (Table 6). It can be noticed that long curing for 90 or 365 days did not lead to the following distinguished or any increase of flexural strength. Flexural strength of 365 days Quatro1 even attained lower value than corresponding sample cured for 90 days, however it is still within the error of measurement.

Because both, the dilution effect and the pozzolanic activity, influence compressive strength of final samples, we established the so called Coefficient of pozzolanic activity (*CPA*; in %) [23]. The CPA allows us to distinguish between their contributions and can be considered as a qualitative criteria which indicates the effective contribution of SCMs to the strength generation. Synergic effect of more effective SF and MK in equivalent amounts resulted in the highest *CPA* of two days Quatro2. The strongest demonstration of pozzolanic activity showed for all other curing times Quatro1, mostly due to the best effectiveness of very fine SF in the highest quantity. Whereas Quatro1 displayed the most pronounced influence of pozzolanic activity on compressive strength in 7 days samples, maximum in the case of Quatro2 and Quatro3 was observed after 28 days of curing (Fig. 3). At this time, the smallest difference among *CPA* of particular series could be observed. Contribution of pozzolanic activity decreased with following prolongation of curing time which was caused by decreasing amount of CH available to participate in pozzolanic reaction.

As can be seen from Fig. 4, *CPA* calculated from the values of flexural strength differed from that estimated from compressive strengths. Whilst *CPA* of Quatro1 reached the maximum in 90 days samples (68% increase of flexural strength in comparison with the strength of Quatro0), *CPA* of Quatro2 increased with time and attained the highest value after 365 days of curing (38% increase when compared with Quatro0). The effect of pozzolanic activity on flexural strength of Quatro3 seemed to be unclear. *CPA* estimated for 7 days samples was higher than that of 2 days and after following decrease it obtained the maximum value in 365 days samples. Besides small amount of measurements, it must be taken into account that flexural tests are very sensitive not only to own properties of samples but also to specimen preparation and handling. Inhomogeneity in material arising also from these reasons can significantly influence measured values of flexural strength.

It is also necessary to consider that although *CPA* was calculated by separation of OPC contribution to the development of strength,

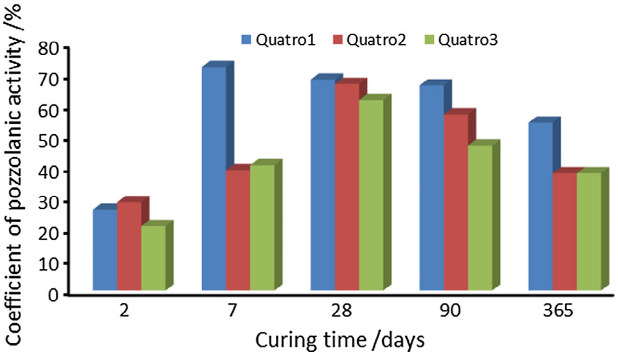

Fig. 3. Coefficient of pozzolanic activity (%) calculated from the values of compressive strength determined after 2, 7, 28, 90 and 365 days of curing.

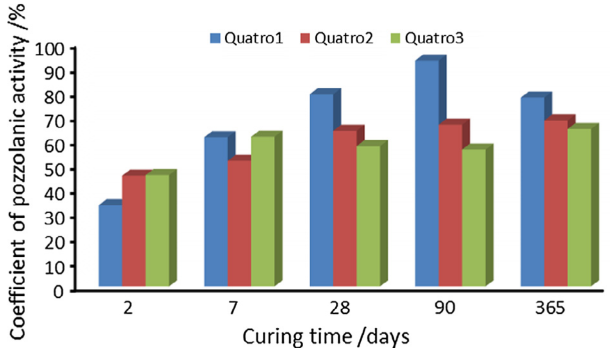

Fig. 4. Coefficient of pozzolanic activity (%) calculated from the values of flexural strength determined after 2, 7, 28, 90 and 365 days of curing.

CPA of series was influenced by lower amount of CH formed when higher substitution level of OPC was used.

In general, it can be assumed that attained values of compressive the same as flexural strength are considerably higher than values reported in numerous studies treating binary or ternary systems [45–47]. Appropriate combination of various substitution materials manifesting activity in different times led to the development of high strengths from early to later times of curing. The early strength gain was in the case of blended samples caused by the strong and soon pozzolanic effect of SF and MK together with filler effect of SCMs. As discussed in particular section, median particle size of blended mixtures was at least by half lower than that of Quatro0 which resulted in better packing of the initial material mixtures. The most promising structure and strength values were attained in the mixtures with the highest SF content as a result of its the most distinctive pozzolanic reactions and fineness which verified our previously published results [23]. Besides additional binding phases (instead of CH that does not contribute to the development of the strength) that are formed by pozzolanic reaction, addition of SCMs strengthens the transition zone between the paste and the aggregate (due to the improved bond between these two phases). The physical action of pozzolans thus provided a denser, more homogenous and uniform pastes suggesting increased synergetic performance between SF and MK or BFS.

4. Conclusion

Present work continued to study quaternary systems comprising of PC and three SCMs: MK, BFS and SF. The development of porous structure as well as its influence on compressive and flexural strength were evaluated up to 365 days of curing. Despite the relatively high substitution levels, up to 35 wt%, the amount of PC was still sufficient to initialize pozzolanic reactions of SCMs that led to the decrease of total porosity. The refinement of structure depended on both the reactivity of the used SCMs and the substitution level of PC. In accordance with the fineness, the reactivity of particular SCMs was proved in order: SF > MK > BFS. Correspondingly, the highest content of SF in the samples together with the lowest replacement level of PC resulted in the most pronounced drop of porosity. The composition of blended samples influenced the porosity especially in the area of middle capillary pores, the portion of which decreased significantly in comparison with referential PC samples in all the curing times. On the contrary, the presence of SCMs led to the increase of gel pores percentage. Strength characteristics of blended samples increased as a result of total porosity decrease. The most significant rise was in the case of samples initially containing the highest amount of SF determined in 7 days samples, after which further although moderate increase was demonstrated as the reactions in the systems slowed down. On the contrary, the higher quantity of MK and BFS led to the most notable increase of strengths after 28 days. The combination of SCMs disposing of different reactivity allowed the enhancement of porosity as well as strengths of the samples also in later times of curing.

Acknowledgement

This work was supported by courtesy of APVV-15-0631, Slovak Grant Agency VEGA No. 1/0696/15 and by Project Sustainability and Development REG LO1211 addressed to the Materials Research Center at FCH VUT.

References

[1] Z. Li, Z. Ding, Property improvement of Portland cement by incorporating with metakaolin and slag, Cem. Concr. Res. 33 (2003) 579–584.
[2] F. Curcio, B.A. Deangelis, S. Pagliolico, Metakaolin as a pozzolanic microfiller for high-performance mortars, Cem. Concr. Res. 28 (6) (1998) 803–809.
[3] S. Maheswaran, N.R. Iyer, G.S. Palani, R. Alagu Pandi, D. Divina Dikar, S. Kalaiselvam, Effect of high temperature on the properties of ternary blended cement pastes and mortars, J. Therm. Anal. Calorim. 122 (2015) 775–786.
[4] D. Torréns-Martín, L. Fernández-Carrasco, M.T. Blanco-Varela, Thermal analysis of blended cements, J. Therm. Anal. Calorim. 121 (2015) 1197–1204.
[5] Y. Chen, D. Gu, Selection of superplasticizer for high performance concrete, Concrete 5 (1997) 28–31.
[6] T. Zhang, O. Yu, J. Wei, P. Gao, P. Zhang, Study on optimization of hydration process of blended cement, J. Therm. Anal. Calorim. 107 (2012) 489–498.
[7] K. Maekawa, R. Chaube, T. Kishi, Modeling of Concrete Performance, Hydration, Microstructure Formation, and Mass Transport, E & FN Spon, London, 1999.
[8] S. Mindess, J.F. Young, D. Darwin, Concrete, second ed., Prentice-Hall, Upper Saddle River, NJ, 2003.
[9] P. Mehta, P. Monteiro, Concrete: Structure, Properties, and Materials, second ed., Prentice-Hall International Series in Civil Engineering and Engineering Mechanics, Englewood Cliffs, NJ, 1993.
[10] L. Huajian, Y. Lu, X. Yongjiang, Effect of fineness on the properties of cement paste, Key Eng. Mater. 629–630 (2015) 366–370.
[11] A. Wang, C. Zhang, Z. Ningsheng, The theoretic analysis of the influence of the particle size distribution of cement system on the property of cement, Cem. Concr. Res. 29 (11) (1999) 1721–1726.
[12] A.A. Ramezanianpour, V.M. Malhotra, Effect of curing on the compressive strength, resistance to chloride-ion penetration and porosity of concretes incorporating slag, fly ash or silica fume, Cem. Concr. Compos. 17 (2) (1995) 125–133.
[13] C.S. Poona, L. Lama, S.C. Koua, Y.L. Wonga, R. Wong, Rate of pozzolanic reaction of metakaolin in high-performance cement pastes, Cem. Concr. Res. 31 (2001) 1301–1306.
[14] Z. Li, Advanced Concrete Technology, Wiley, Hoboken, NJ, USA, 2011, ISBN 978-0-470- 43743-8. 14, 34.
[15] L. Bágel', Strength and pore structure of ternary blended cement mortars containing blast furnace slag and silica fume, Cem. Concr. Res. 28 (7) (1998) 1011–1020.
[16] S. Wild, J.M. Khatib, A. Jones, Relative strength, pozzolanic activity and cement hydration in superplasticised metakaolin concrete, Cem. Concr. Res. 26 (10) (1996) 1537–1544.
[17] M. El-Shahate, I. Saraya, Study physico-chemical properties of blended cements containing fixed amount of silica fume, blast furnace slag, basalt and limestone, a comparative study, Constr. Build. Mater. 72 (2014) 104–112.
[18] J. Guang, R. Zhidan, S. Wei, Effects of metakaolin on mechanical properties, pore structure and hydration heat of mortars at 0.17 w/b ratio, Constr. Build. Mater. 93 (2015) 564–572.
[19] I. Janotka, Hydration of the cement paste with Na_2CO_3 addition, Ceram. Silik 45 (1) (2001) 16–23.
[20] Ľ. Krajči, I. Janotka, F. Puertas, M. Palacios, M. Kuliffayová, Long – term properties of cement composites with various metakaolinite content, Ceram. Silik. 57 (1) (2013) 74–81.
[21] N.J. Coleman, W.R. McWhinnie, The solid state chemistry of metakaolin-blended ordinary Portland cement, J. Mater. Sci. 35 (11) (2000) 2701–2710.
[22] H. Changling, B. Osbaeck, E. Makovicky, Pozzolanic reaction of six principal clay minerals: activation reactivity assessments and technological effects, Cem. Concr. Res. 25 (8) (1995) 1691–1702.
[23] M.T. Palou, E. Kuzielova, R. Novotný, F. Šoukal, M. Žemlička, Blended cements consisting of Portland cement–slag–silica fume–metakaolin system, J. Therm. Anal. Calorim. (2016), http://dx.doi.org/10.1007/s10973-016-5399-5.
[24] M. Žemlička, E. Kuzielová, M. Kuliffayová, J. Tkacz, M. Palou, Study of hydration products in the model systems metakaolin-lime and metakaolin-lime-gypsum, Ceram. Silik. 59 (4) (2015) 283–291.
[25] R. Vočka, C.h. Gallé, M. Dubois, P. Lovera, Mercury intrusion porosimetry and hierarchical structure of cement pastes: theory and experiment, Cem. Concr. Res. 30 (4) (2000) 521–527.
[26] J. Rouquerol, G. Baron, R. Denoyel, H. Giesche, J. Groen, P. Klobes, P. Levitz, A.V. Neimark, S. Rigby, R. Skudas, K. Sing, M. Thommes, K. Unger, Liquid intrusion and alternative methods for the characterization of macroporous materials (IUPAC technical report), Pure Appl. Chem. 84 (1) (2012) 107–136.
[27] P.K. Metha, P.J.M. Monterio, Concrete, Microstructure, Properties and Materials, McGraw-Hill, London, 2006.
[28] P. Pipilikaki, M. Katsioti, Study of the hydration process of quaternary blended cements and durability of the produced mortars and concretes, Constr. Build. Mater. 23 (2009) 2246–2250.
[29] K.K. Aligizaki, Pore Structure of Cement-based Materials, Taylor & Francis, Abington, 2006, ISBN 0-419-22800-4.
[30] P.W. Brown, D. Shi, Porosity/permeability relationships, in: J. Scalny, S. Mindess (Eds.), Materials Science of Concrete II, The American Ceramic Society, Westerville, 1991, pp. 83–109.
[31] D.P. Bentz, C.J. Haecker, An argument for using coarse cements in high performance concretes, Cem. Concr. Res. 29 (4) (1999) 615–618.
[32] L. Courard, F. Michel, Limestone fillers cement based composites: effects of blast furnace slags on fresh and hardened properties, Constr. Build. Mater. 31 (51) (2014) 439–445.
[33] A. Arora, G. Sant, N. Neithalath, Ternary blends containing slag and interground/blended limestone: hydration, strength, and pore structure, Constr. Build. Mater. 102 (2016) 113–124.

[34] Y. Senhadji, G. Escadeillas, M. Mouli, H. Khelafi, Benosman, Influence of natural pozzolan, silica fume and limestone fine on strength, acid resistance and microstructure of mortar, Powder Technol. 254 (2014) 314–323.

[35] H.-W. Song, S.-W. Pack, J.-C. Jang, V. Saraswathy, Estimation of the permeability of silica fume cement concrete, Constr. Build. Mater. 24 (2010) 315–321.

[36] R. Loser, B. Lothenbach, A. Leemann, M. Tuchscnmid, Chloride resistance of concrete and its binding capacity-comparison between experimental results and thermodynamic modeling, Cem. Concr. Compos. 32 (1) (2010) 34–42.

[37] E. Berodier, K. Scrivener, Evolution of pore structure in blended systems, Cem. Concr. Res. 73 (2015) 25–35.

[38] H.M. Jennings, J.W. Bullard, J.J. Thomas, J.E. Andrade, J.J. Chen, G.W. Scherer, Characterization and modeling of pores and surfaces in cement paste: correlations to processing and properties, J. Adv. Concr. Technol. 6 (1) (2008) 5–29.

[39] H. Sun, Z. Li, J. Bai, S.A. Memon, B. Dong, Y. Fang, W. Xu, F. Xing, Properties of chemically combusted calcium carbide residue and its influence on cement properties, Materials 8 (2015) 638–651.

[40] P. Chindaprasirt, S. Rukzon, Strength, porosity and corrosion resistance of ternary blend Portland cement, rice husk ash and fly ash mortar, Constr. Build. Mater. 22 (8) (2008) 1601–1606.

[41] T.R. Naik, Concrete durability as influenced by density and/or porosity, in: Presented and Published at the Cement and Concrete Institute of Mexico Symposium ‘‘World of Concrete – Mexico”, Guadalajara, Mexico, June 4–7, 1997.

[42] G.A. Rao, Role of water-binder ratio on the strength development in mortars incorporated with silica fume, Cem. Concr. Res. 31 (2001) 443–447.

[43] A. Oner, S. Akyuz, An experimental study on optimum usage of GGBS for the compressive strength of concrete, Cem. Concr. Compos. 29 (2007) 505–514.

[44] A. Oner, S. Akyuz, R. Yildiz, An experimental study on strength development of concrete containing fly ash and optimum usage of fly ash in concrete, Cem. Concr. Res. 35 (2005) 1165–1171.

[45] M. Ghrici, S. Kenai, M. Said-Mansour, Mechanical properties and durability of mortar and concrete containing natural pozzolana and limestone blended cements, Cem. Concr. Compos. 29 (2007) 542–549.

[46] L. Mo, M. Liu, A. Al-Tabbaa, M. Deng, W.Y. Lau, Deformation and mechanical properties of quaternary blended cements containing ground granulated blast furnace slag, fly ash and magnesia, Cem. Concr. Res. 71 (2015) 7–13.

[47] T. Zhang, Q. Yu, J. Wei, P. Zhang, Efficient utilization of cementitious materials to produce sustainable blended cement, Cem. Concr. Compos. 34 (2012) 692–699.

IOP Conf. Series: Materials Science and Engineering **583** (2019) 012004 doi:10.1088/1757-899X/583/1/012004

The effect of burnt lime addition on hydration of Ultra-high performance cementitious composites

R Novotný[1], E Bartoníčková[1] and J Kotrla[1]

[1] Institute of Materials Chemistry, Brno University of Technology,
Purkyňova 464/118, Brno 61200, Czech Republic

EmaiL: xcnovotny2@fch.vut.cz

Abstract. The paper deals with the burnt lime utilization as a source of calcium ions participated during hydration process of ultra-high performance cementitious composites. These type of ultra-high performance cementitious composites are based on the high content of silica fume that together with calcium ions form the binder phase. In the case of ordinary Portland cement, the hydration during induction period supposed to be too slow for dissolution of required amount of calcium ions necessary for the pozzolanic reaction of presented silica fume. The low addition of the lime should be a sufficient calcium source that allow the starting of the pozzolanic reaction before the acceleration period occurs. The calcium ions content from the beginning of the reaction was controlled by an addition of soft-burnt and dead-burnt lime. Its influence was studied in terms of hydration process by isothermal calorimetry. Based on the experimental data, the hydration reaction mechanism was proposed.

1. Introduction

Commonly used types of concretes could be typically characterized by their low homogeneity closely related to low tensile flexural strengths. The possible solution to solve this problem is to substitute coarse aggregates with fine sand, to increase content of Portland cement (OPC), addition of extremely fine reactive components (i.e. silica fume, precipitated silica, metakaolin, ground blast furnace slag) and to reduce the water to cement ratio by superplasticizer application [1]. These types of concretes are generally named as ultra-high performance cementitious composites (UHPC). High content of cement, reactive components and low water to cement ratio, typical for this type of composite system, cause volume changes that result in formation of micro-cracks due to plastic and autogenous shrinkage and self-exsiccation [2]. Due to the shrinkage phenomena, it is necessary to apply water curing during hydration and further hardening of prepared composites [2, 3].

High silica fume content, which in dispersion may behave as an aggregate causing less friction between cement particles, is also typical for UHPC [4]. Silica fume and calcium cations, coming from OPC hydration as a secondary product, react together and form binder phases which are beneficiary to mechanical properties of binder species [5]. Nevertheless, the velocity of calcium ions formation for pozzolanic reaction is directly connected with the cement hydration rate [6]. During the first hours of hydration, the induction period occurs and the hydration process is slowed down. Induction period can be prolonged due to the higher content of superplasticizers [7]. High bulk density also reduces the ionic transport, therefore the binders with high content of silica fumes against OPC demonstrate slower strength development [8].

Paper deals with the possibility of calcium oxide usage as a source of calcium cations for silica fume (SF) hydration during the cement induction period. The advantages of calcium oxide is its high reactivity, no other ion contaminations and signs of exhibit the undesirable plastic behavior as it is in case of calcium hydroxide [9]. The utilization of soft-burnt (SBL) and dead-burnt lime (DBL) and curing conditions with respect to the reactivity and long term stability were studied. Srinivasan et al. studied the effect of lime water on OPC-SF binders [10].

2. Materials and methods

The white OPC CEM I 52.5 R (Aalborg Portland A/S, Denmark), white undensified silica fume RW-Füller Q1 (RW silicium GmbH, Germany), SBL CL 90-Q (Kotouč Štramberk, spol. s r. o., Czech Republic) sieved under the 63 µm, dead-burnt lime CL 90-Q (Vápenka Vitošov s.r.o., Czech Republic) sieved under the 63 µm, superplasticizer Master Glenium ACE 446 (BASF Stavební hmoty Česká republika s.r.o., Czech Republic), coarse aggregate (Filtrační písky, spol. s r.o., Czech Republic) and deionised water were used for UHPC preparation.

All the components were gradually mixed for 1 min, and then the ¾ of gauge water with the superplasticiser dosage was added and mixed for 5 min. The ¼ of the missing gauge water was added and mixed for other 5 min. The homogenized mixture was moulded to moulds with the dimensions 4 × 4 × 16 cm intended for mechanical testing. After 24 h the experimental specimens were demoulded and the dry or water curing conditions were applied under the controlled temperature of 25°C. Hydration process of binder was analysed by using of isothermal calorimeter TAMair (TA Instruments) under the 25°C. All of the used components were storage before using under the same conditions for 24 hours, i.e. controlled 25°C. Analysed samples were prepared by hand mixing of bath contents of 40 g of binder, deionized water and additives for 2 min, and then 5 g of this mixture was placed into lockable plastic ampules. The measurements were performed against to reference sample (i.e. water) with similar heating capacity. The studied hydration process was precisely stopped by acetone washing [11]. Formed hydration products (50 mg) were observed by TG-DTA analysis (Q600, TA Instruments) up to 1000°C with heating rate 10°C/min under the dried air atmosphere. Table 1 summarizes the composition and designation of studied samples.

Table 1. Composition (g) of measured samples.

Sample	OPC	SF	SBL	DBL	SP	Sand	H_2O
R	188	62.0	0	0	7.5	750	67
1.a	186	61.5	2.5	0	7.5	750	67
1.b	184	61.0	5	0	7.5	750	67
1.c	180	60.0	10	0	7.5	750	67
1.d	176	59.0	15	0	7.5	750	67
1.e	169	56.0	25	0	7.5	750	67
1.f	0	0	250	0	7.5	0	67
2.a	186	61.5	0	2.5	7.5	750	67
2.b	184	61.0	0	5	7.5	750	67
2.c	180	60.0	0	10	7.5	750	67
2.d	176	59.0	0	15	7.5	750	67
2.e	169	56.0	0	25	7.5	750	67
2.f	0	0	0	250	7.5	0	67

3. Results and discussion

3.1. Setting of UHPC

With the increasing content of the SBL (see figure 1.a), the heat flow in pre-induction period was gradually increased, the difference between R and 1.e sample was 12.2 mW/g. If the un-influenced hydration process of SBL in UHPC occurs the difference in heat values supposed to be 35.7 mW/g. In case of DBL addition (see figure 1.b), the increase of the heat flow between R and 2.e samples was determined to 2.1 mW/g. From the obtained results is obvious that in the UHPC system the retardation of the CaO hydration occurred which was more substantial when the DBL was applied.

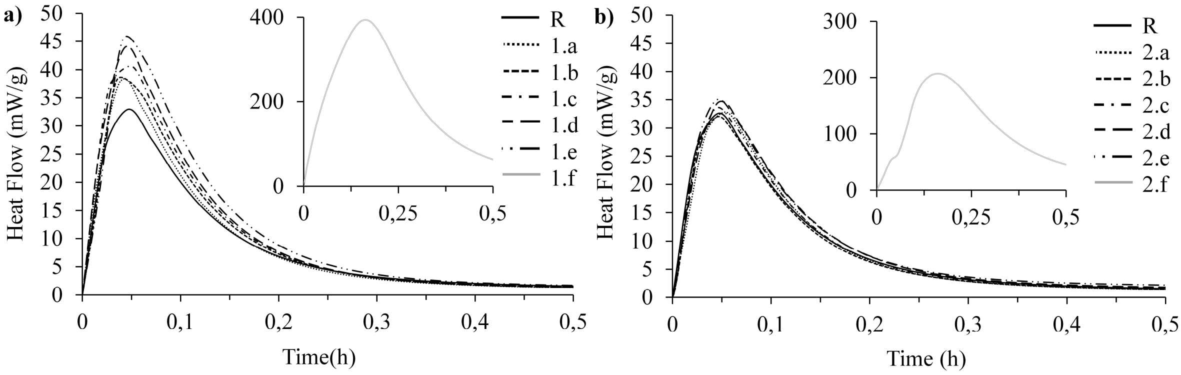

Figure 1. Heat flow in the pre-induction period a) SBL, b) DBL.

Figure 2 shows the retardation of main hydration peak when the SBL was applied. The retardation of the peak in the case of the sample 1.c is almost 1 hour against the R one. The hydration of samples with SBL addition was not significantly retarded too. Sample 1.e reached the maximum of main hydration peak in the same time as the reference R one. Without the dependence on the weight of the addition of SBL, the heat flow value of the main peak maximum was increased of 0.4 mW/g. The significant influence of soft-burned lime to hydration process was observed in part of induction period. The lowest heat flow 0.4 mW/g was determined in the case f R sample, with the increasing amount of lime addition the heat flow gradually increased to 2.3 mW/g in the case of 1.e sample. Samples 1.d and 1.e showed local minimum of heat flow after 1 hour of hydration. From this point the hydration rate was accelerated to the end of induction period. This phenomenon is clearly visible on the figure 2.b, where during first hour of hydration process the difference in total hydration heat, as well as the amount of formed hydrates, was between particular samples minimal. The total hydration heat increased proportionally with increasing lime content and proved the reaction of silica fume during the induction period and cement hydration process. Sample R reached for 60 mW/g heat more than the sample 1.e after 30 hours of hydration.

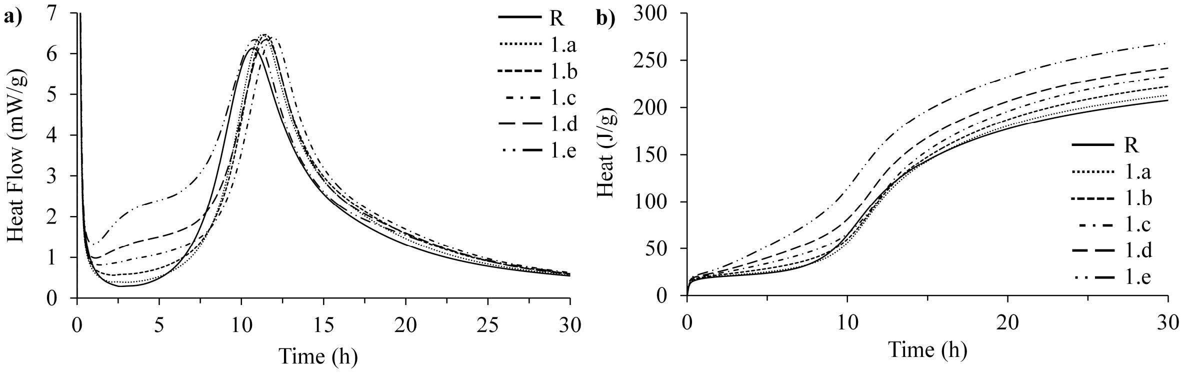

Figure 2. Calorimetric measurement of the UHPC with SBL a) heat flow, b) heat.

Samples with DBL addition showed similar hydration coarse as the one with SBL (see figure 3.a). However, during the first hour of the induction period the almost depletion of the previously observed local minimum occurred and the hydration rate after this minimum to the end of induction period was approximately constant. The retardation of the main hydration peak was similar in case of both types of the limes. Nevertheless, the maximum of the main hydration peak was with the DBL addition slightly decreased. Also the course of the main hydration heat was for the both types of the lime similar (see figure 3). The total hydration heat produced by sample R after 30 hours was or 57 mW/g less than the sample 2.e.

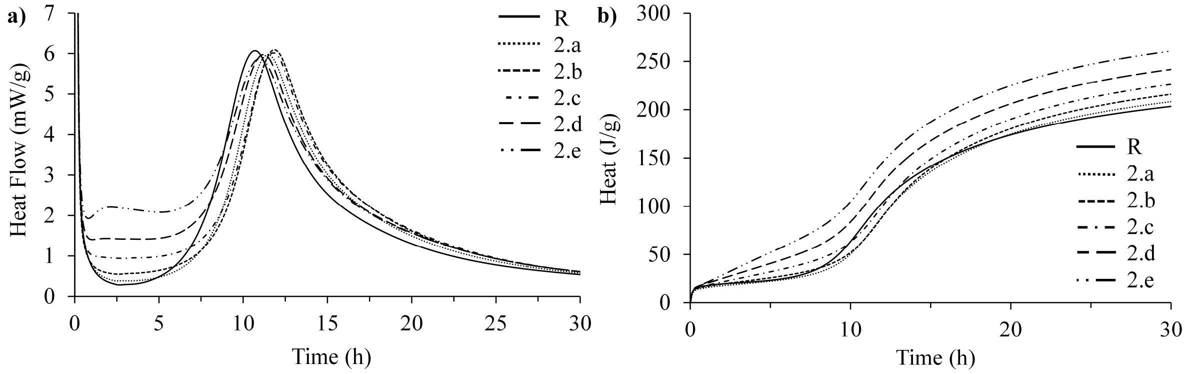

Figure 3. Calorimetric measurement of the UHPC with DBL a) heat flow, b) heat.

3.2. Testing of mechanical parameters

Tensile and compressive strengths for samples stored under the dry and water curing condition for hydration after 1 day were almost similar due to demoulding after 24 hours and subsequently set up of the different curing conditions for 24 hours. After 1 day of hydration (figure 1.a) the increase of tensile strengths values for 1 MPa was observed for the samples with low content of SBL. On the contrary the higher content of SBL caused the decrease of tensile strength values for 1 MPa against reference sample R. After 7 days of dry curing conditions the gradual increase of tensile strengths with increasing soft-lime content was observed from 9.5 MPa for sample R to 13.2. MPa for sample 1.d. Higher soft-lime content again caused the decrease of the tensile strength values. After 28 days of dry curing conditions the tendency in mechanical behaviour was identical as was observed after 7 days. The tensile strength value of sample R under the water curing conditions was 19 MPa, but the any addition of SBL caused the decrease in tensile strength values. Also the similar tendency after 28 days of water curing was observed, the value for reference sample R was even decreased to 17.5 MPa.

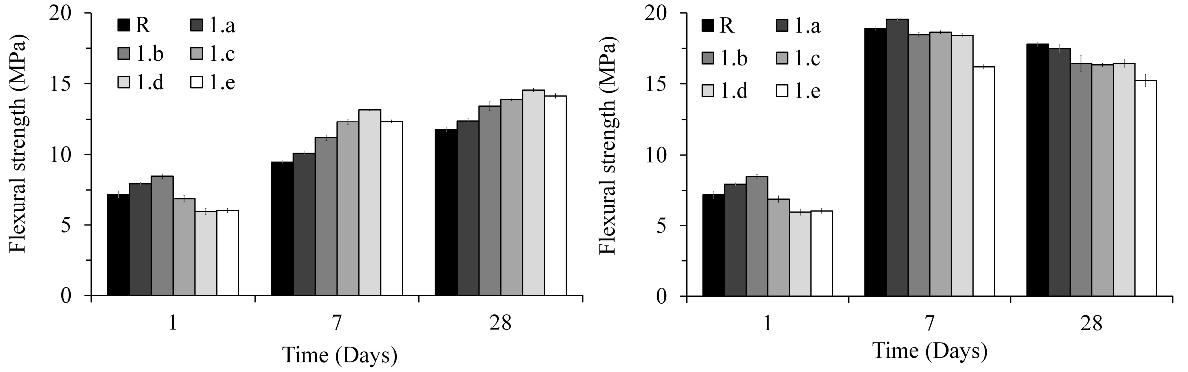

Figure 4. Flexural strength of the specimens with soft b. lime a) dry curing, b) water curing.

The compressive strength behaviour (figure 4.a) of the samples with the addition of SBL (R-1.d) and cured under the dry conditions was not significantly influenced and for 1.e the value even decreased. After 7 days of the water curing conditions (see figure 1.b) the compressive strength values decreased with the increasing lime content. The maximum was reached for sample 1.e. After 28 days of water curing, the values of compressive strength slightly increased for samples 1.a and 1.b with SBL addition. Sample 1.b reached the total maximum compressive strength's value of 131.3 MPa. On the contrary sample 1.e reached the maximum decrease against the reference R one.

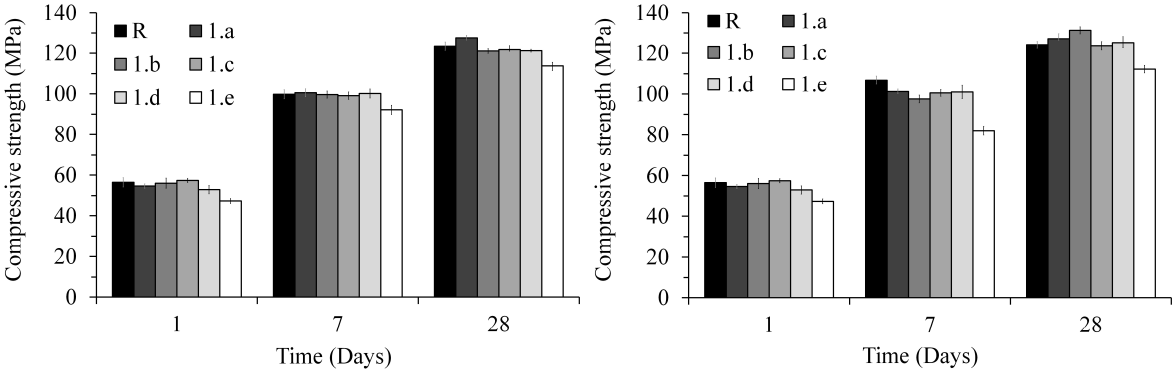

Figure 5. Compressive strength of the specimens with soft b. lime a) dry curing, b) water curing.

After 1 day of dry curing, the tensile strengths of the samples with dead-lime content reached the similar or higher values than the reference R one. In the case of the sample 2.a and 2.b (dead-burnt) the tensile strength increase was substantial then in the case of 1.a and 1.b (soft-burnt) after 1 day of the dry curing. The increasing tendency in tensile strength values with the increasing content of the lime was observed after 7 and 28 days of dry curing (see figure 6.a). The behaviour of the samples under the water curing conditions and dead-lime addition is given on the figure 6.b. The samples showed the minimal decreasing tendency after 7 and 28 days. Sample 2.d under the 28 day of the water curing conditions reached maximum value of tensile strength 19.3 MPa. The significant defects were observed for samples 2.e after the 7 and 28 day of water curing and the values were not able to determine. The compressive strength behaviour of the samples with DBL addition under dry and water curing conditions (figure 7) showed the identical tendency as the samples with soft-burnt one.

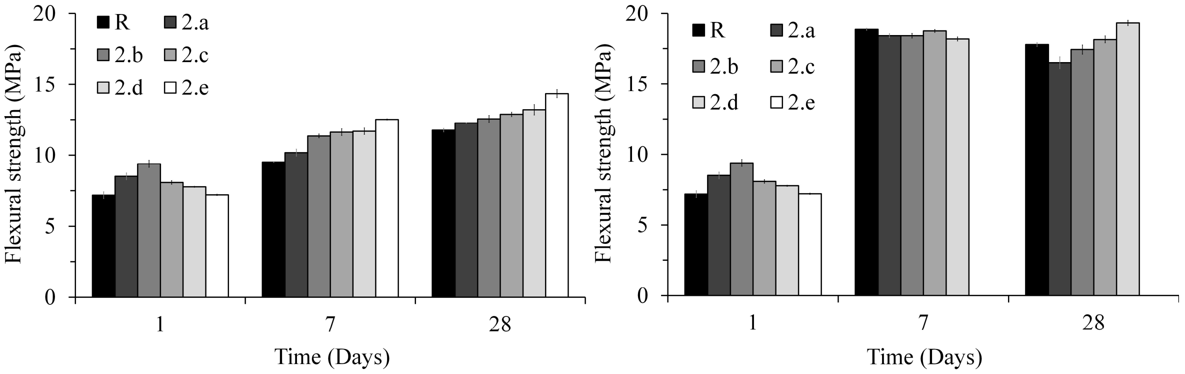

Figure 6. Flexural strength of the specimens with dead b. lime a) dry curing, b) water curing.

3.3. DTA analysis of hydration products in time

The thermal study of the hydration products formed after 1, 5 and 24 hours is given on figure 8. The mass loss visible on the TG curve in the region of 100°C can be assigned to free water content, decomposition of amorphous hydration products and ettringite. In the case of reference sample R the mass loss after 1 and 5 hours of hydration was minimal, however in the case of 1.d sample with the lime content was substantial. This finding proved the formation of hydration products in the presence of the lime even in induction period of cement hydration what was also proposed from the calorimetric data. Mass loss around 120°C can be assigned to gypsum decomposition, which was gradually depleted to the 5 hours of hydration and explain the absence of sulphate depletion peak in calorimetric curves with high intensity of heat flow within the main hydration peak [12]. Strong exothermic effect with low mass loss in the region from 250 to 300°C can be assigned to superplasticisers decomposition.

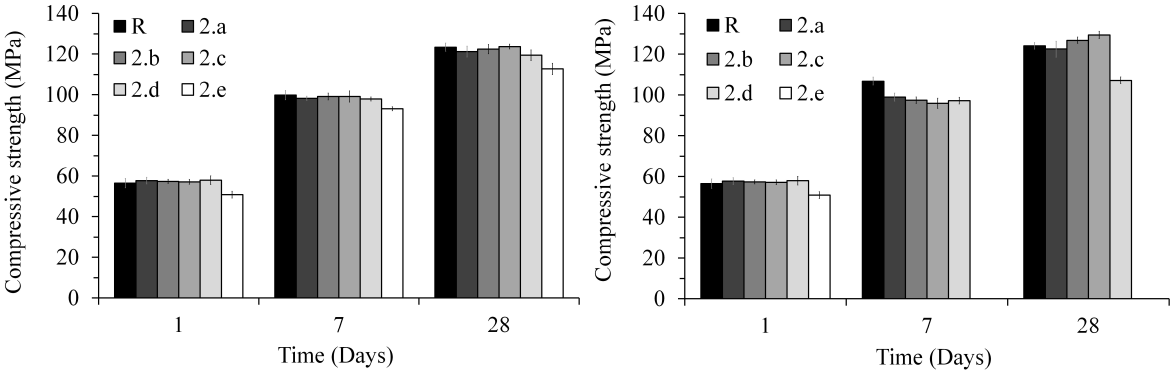

Figure 7. Compressive strength of the specimens with DBL a) dry curing, b) water curing.

This effect was not visible in the samples R and 1.d 0 h where the SP was not added. In the region around 450°C the decomposition of $Ca(OH)_2$ took place, which belonged to early stage hydration products.[13] In the case of reference sample R the portlandite peak was firstly depleted due to the portlandite consumption in reaction with silica fume species and afterwards formed due to the ongoing hydration process. In the case of sample 1.d the portlandite seemed to be slightly consumed within the first hour of hydration, further its content was increased due to the higher formation from the lime addition than the reaction rate with the silica fume. Decomposition of calcium carbonates took place above 650°C [14]. The addition of the lime to the system increased also the carbonate content even before the hydration process due to the not precise its firing and also carbonation process. During the hydration of the sample R the carbonate content was constant up to 5 hours of hydration, the significant increase was observed after the 24 hours of hydration. In the case of 1.d sample the content of carbonates during the whole hydration process was only slightly increased. Reaction of calcium ions with silica fume was observed by gradual depletion of portlandite in the end of cement induction period. In the case of the sample 1.d the significantly higher formation of hydration products during and also after induction period was observed.

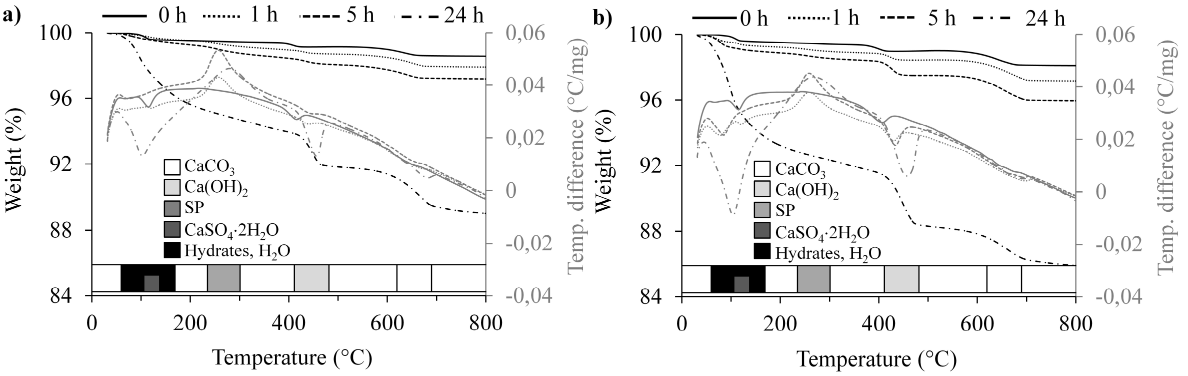

Figure 8. TG-DTA analysis of hydration products by means of time a) sample R, b) sample 1.d.

4. Conclusion

The presented data proved that the lime content can improve the silica fume hydration in binder systems even during the induction period of OPC hydration regardless the lime burning conditions. In the case of the content of dead-burnt lime followed by water curing conditions, mechanical strengths were not significantly affected, but there is high risk of product destruction with the high content of this lime.

The dry curing conditions applied to samples with both types of the lime remarkably enhanced the flexural strengths with minimal influence to compressive ones.

Acknowledgements

This outcome has been achieved with the financial support by the project: GA19-16646S "The elimination of the negative impact of zinc in Portland cement by accelerating concrete admixtures", with financial support from the Czech science foundation.

References

[1] Metha P K and Monteiro P J M 2014 *Concrete: Microstructure, Properties, and Materials* (New York: McGraw-Hill Education)
[2] AÏtcin P C 2005 *High-Performance Concrete* (New York)
[3] Neville A M 2011 *Properties of Concrete* (New York: Pearson) chapter 6 pp 271–313
[4] Sounthararajan V M (2013) Micro filler effects of silica-fume on the setting and hardened properties of concrete *Research Journal of Applied Sciences, Engineering and Technology*
[5] Köksal F, Altun F, Yiğit İ and Şahin Y 2008 Combined effect of silica fume and steel fiber on the mechanical properties of high strength concretes *Con. Build. Mat.* **22** pp 1874-1880
[6] Kolani B, Buffo-lacarrière L, Sellier A, Scadeillas G, Boutillon L and Linger L 2012 Hydration of slag-blended cements *Cem. Concr. Com.* **34** pp 1009-1018
[7] Zhang Y, Kong X, Sellier A, Escadeillas G, Boutillon L and Linger L 2015 Correlations of the dispersing capability of NSF and PCE types of superplasticizer and their impacts on cement hydration with the adsorption in fresh cement pastes *Cem. Concr. Res.* **69** pp 1-9
[8] Wong H S and Razak H A 2005 Efficiency of calcined kaolin and silica fume as cement replacement material for strength performance. *Cem. Concr. Res.* **35** pp 696-702
[9] Ruiz-Agudo E, Rodriguez-Navarro C, Sellier A, Escadeillas G, Boutillon L and Linger L 2010 Microstructure and Rheology of Lime Putty. *Lang.* **26** pp 3868-3877
[10] Srinivasan M, Kumar V R, Saffiq R M, Gopinath S, Murthy A, Iyer N 2017 Effect of lime water on the properties of silica fume blended cementitious composite *I. J. E. Mat. Sci.* **24** pp 491-498
[11] Luz A P and Pandolfelli V C 2011 Halting the calcium aluminate cement hydration process. *Cer. Int.* **37** pp 3789-3793
[12] Novotný R, Bartoníčková E, Švec J and Mončeková M 2016 Influence of Active Alumina on the Hydration Process of Portland Cement *Pro. Eng*. **151** pp 80-86
[13] Esteves L P 2011 On the hydration of water-entrained cement–silica systems: Combined SEM, XRD and thermal analysis in cement pastes *Ter. Acta* **518** pp 27-35
[14] Boháč M, Palou M, Novotný R, Másilko J, Šoukal F and Opravil T 2017 Influence of temperature on early hydration of Portland cement–metakaolin–slag system. *J. Therm. Anal. Cal.* **127** pp 309-318

Available online at www.sciencedirect.com

ScienceDirect

Procedia Engineering 151 (2016) 80 – 86

Procedia Engineering

www.elsevier.com/locate/procedia

International Conference on Ecology and new Building materials and products, ICEBMP 2016

Influence of active alumina on the hydration process of Portland cement

Radoslav Novotný*, Eva Bartoníčková, Jiří Švec, Miroslava Mončeková

Brno university of technology, Faculty of Chemistry, Materials Research Centre, Purkyňova 464/118, Brno Cz-612 00, Czech Republic

---

Abstract

The work is interested in the study of the hydration process by means of the isothermal calorimetry method. The Portland cement hydration process led to gradual consumption of contained calcium sulfate. This sulfate depletion is observed on the calorimetry curve as a shoulder of main silicate peak. The addition of hydratable alumina to Portland cement was studied in order to determine its influence on hydration process. Experimental results showed the shifted position of this shoulder according to alumina and calcium sulfate content. It was also observed that the overall hydration process was almost unaffected by alumina addition.

Peer-review under responsibility of the organizing committee of ICEBMP 2016

Keywords: Cement; isothermal calorimetry; hydratable alumina; sulfate depletion

---

1. Introduction

Hydration of Portland cement is complex process of the reactions which lead to setting and hardening of cement paste. The water addition to cement starts contemporary dissolution reaction of some cement components and formation of the insoluble hydrated products. The main part of Portland cement, alite (C_3S), reacts with water to form the C-S-H gel and portlandite. The same hydration products are also formed during the hydration of other cement component, belite (C_2S). Portland cement is produced by continuous milling of Portland clinker with gypsum. The final properties of cement are strongly influenced by this milling process [1].

Ettringite ($C_6A\overline{S}_3H_{32}$, AFt) as a hydration product, is a result of the reaction between tricalcium aluminate phase

---

* Corresponding author.
E-mail address: xcnovotny2@fch.vutbr.cz

Peer-review under responsibility of the organizing committee of ICEBMP 2016
doi:10.1016/j.proeng.2016.07.383

(C_3A) and gypsum in aqueous conditions. C_3A phase dissolves immediately after the first contact of cement with water and its dissolution is stopped when the minimal heat flow in the induction period is reached. During hydration reaction of alite, the dissolution of C_3A phase is retarded. The re-dissolution of C_3A phase occurs after the all present sulfates are consumed. This process causes the rapid AFt precipitation [2].

The required sulfates for rapid AFt precipitation are released to the solution from the C-S-H gel after sulfate depletion [3]. The source of C_3A necessary for AFt formation during the time between induction period and the sulfate consumption are amorphous hydroaluminates. These hydroaluminates are formed from C_3A phase in the beginning of the overall hydration reaction [4]. The retardation of C_3A phase should be caused by sorption of sulfate ions to its surface. The peak position assigned to sulfate depletion is dependent on the sulfate content in the cement [5]. The occurred retardation also influences the strength of hardened paste [6]. The cement particle size strongly affects the velocity of the sulfate depletion. The fine particles cause rapid sulfate consumption which can be seen on the calorimetry curve as a strong sharp peak. While, the coarse particles need more time for consumption reaction and can be seen as a weak broad peak. Nevertheless the hydration heat of both processes is identical [7]. Some cement admixtures can be considered as a source of reactive aluminates. For example, the high furnace slag (as a typical cement admixture) is not involved to the aluminate reaction but influences the reaction by filler effect [8].

2. Materials and methods

Portland cement was prepared by ball milling of Portland clinker (Českomoravský cement a.s., plant Mokrá, CZ) with resulted specific surface area 400 m^2/kg (determined via Blaine method). Gypsum (commercially purchased; phase composition – 73.6 wt. % of gypsum and 26.4 wt. % of bassanite; Penta, CZ) was used as setting regulator. Alphabond 300 (commercially purchased; phase composition - boehmite and ρ-alumina; Almatis, factory Leetsdale, USA) was used as substitute of clinker and gypsum species. Samples for calorimetry measurements were mixed and homogenized in vibrational mill in stainless steel bowl for 10 s. Samples for mechanical properties determination were ball milled for 10 min. The clinker composition is summarized in Table 1. The composition of the measured samples is shown in Table 2. The particle size of the samples was assessed by laser diffractometry (Helos KR, Sympatec) and is shown on Fig. 1a.

Table 1. Chemical and phase composition of the clinker.

Chemical composition	(%)	Phase composition	(%)
CaO	70.6	C_3S	76.6
SiO_2	19.2	C_2S	8.5
Al_2O_3	3.9	C_3A	3.0
Fe_2O_3	5.1	C_4AF	11.9

Table 2. Composition of measured samples.

Sample	Clinker (%)	Gypsum (%)	AB300 (%)	Sample	Clinker (%)	Gypsum (%)	AB300 (%)
1.a	95.25	4.75	0	2.c	94.00	6.00	0.50
1.b	95.00	5.00	0	2.d	94.00	6.00	0.75
1.c	94.75	5.25	0	2.e	94.00	6.00	1.00
1.d	94.50	5.50	0	3.a	92.50	7.50	1.00
1.e	94.25	5.75	0	3.b	90.50	9.50	2.00
1.f	94.00	6.00	0	3.c	93.25	6.75	1.50
2.a	94.00	6.00	0.10	3.d	92.50	7.50	2.00
2.b	94.00	6.00	0.25				

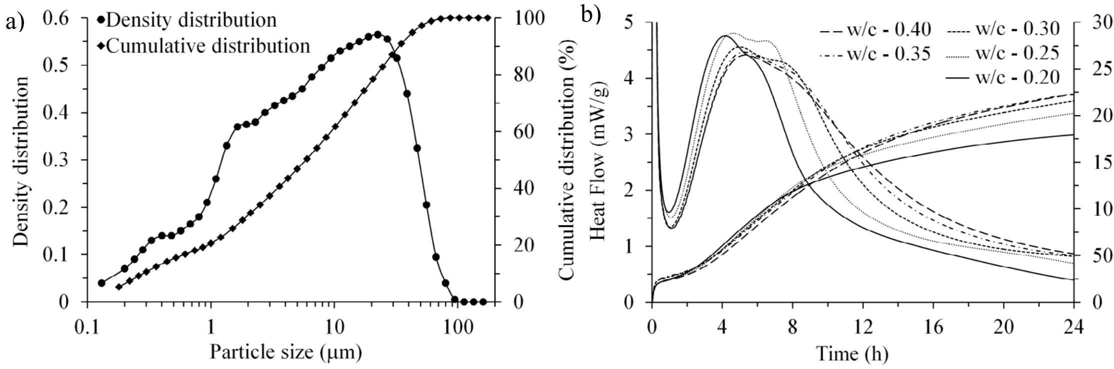

Fig. 1. (a) Particle size distribution of clinker (b) Adjustment of water to cement ratio (composition 1.f).

The hydration process was analyzed by isothermal calorimeter TAM air (TA Instruments) at the isothermal temperature of 25 °C. The temperation of the source material under the constant climatic condition took place for 24 h. The samples were prepared by mixing of 30 g of cement with 9 ml of deionized water (w/c ratio = 0.3) for 1 min. The 6.5 g of mixture was placed into closed glass ampoule for calorimetry analysis. The analysis was measured against to the reference sample (quartz) with the same heat capacity as the measured sample. The samples for DTA analysis (Q600; TA Instruments) were crashed and the hydration process was stopped by immersing them in acetone. Residual acetone was removed by evaporating at the 50 °C. The mechanical properties were assessed on the prisms with the dimensions 2 × 2 × 10 cm (4 pieces for each sample).

3. Results and discussion

The water to cement ratio was adjusted to 0.3 (see Fig. 1b). The influence of different w/c ratio can be clearly seen from the Fig. 1b. Insufficient homogenization of samples was observed at w/c ratios lower than 0.3 and on the other hand the third hydration peak is not distinguishable at higher values of w/c.

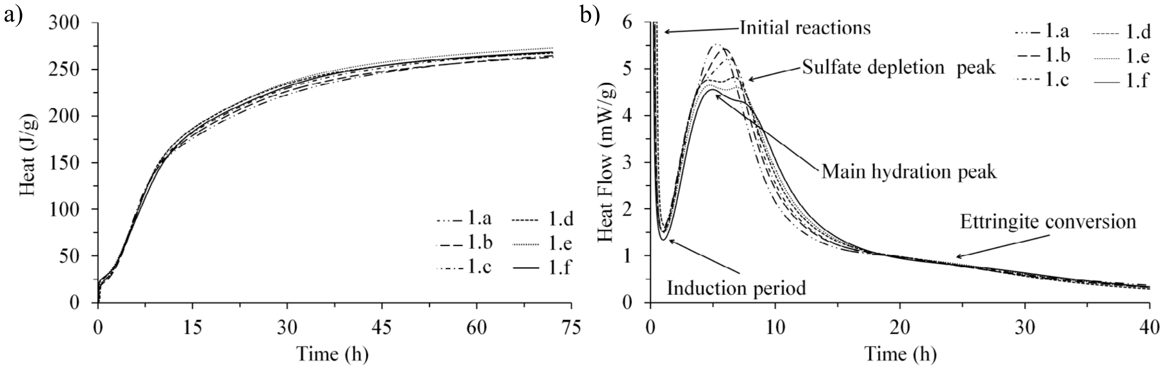

Fig. 2. Clinker with gypsum (a) Total heat of hydration (b) Heat flow.

The substitution of 4.75 – 6 wt. % of clinker with gypsum did not influence the overall hydration process, what was confirmed by analysis of the total hydration heat after 72 h with the values 257 – 274 J·g^{-1} (see Fig. 2a). The values of total hydration heat were increased with the increasing amount of the gypsum content. Sample 1.f reached the minimal heat flow value in induction period. In the Fig. 2b there can be seen the influence of the gypsum content on the main hydration peak. The gypsum content slightly delayed the silicate phase hydration. The main dynamic response on the calorimetric curve connected with the clinker substitution is characterized by the shift of the peak position related to sulfate depletion. The gypsum content of 6 wt. % in the reference sample 1.f was adjusted to be able to observe this peak at 2.5 h after the main hydration peak. This position (optimal) was defined by Lerch [6]. The decreasing content of the gypsum in the system was resulted in the shift of the depletion peak towards earlier times, i.e. closer to maximum of the main hydration peak. This shift is coupled with an increase heat flow of this process. When the gypsum content is lower than 5 wt. % the peak of sulfate depletion was monitored before the main hydration one and found to be merged with him. The increasing of the sulfate depletion peak mentioned above is probably negatively influenced by the diffusion process as a main driving force of the overall hydration process [1,6].

Sample 1.a with the 4.75 wt. % of the gypsum achieved 21.5 % higher maximum heat flow during main silicate phase hydration compared to reference sample. This finding (i.e. lack of the gypsum content in cement) can explain the technological problems with concreting of massive constructions. Weak peak observed at around 22.5 h was assigned to the decomposition of AFt to monosulfate (AFm). The varying of the gypsum content in the cement-gypsum mixture did not have the influence on the AFt to AFm decomposition process (see Fig. 2b).

From the current knowledge, Alphabond 300 (further AB300) is the source of AlO_4^- ions and should be involved in AFt hydration. AB300 addition should not influence the main silicate hydration process. The obtained experimental data (see Fig. 3a) showed the total hydration heat released during 72 h in the range from 259 to 269 $J{\cdot}g^{-1}$. Nevertheless the first distinction occurred in the place of induction period (see Fig. 4a), where the minimal content of AB300 caused appearance of the peak which should be assigned to portlandite formation in accordance with [9]. The presence of this peak was not confirmed in the analyses of the samples without AB300. The cement admixtures, with low content of Ca^{2+} ions and taking place in hydration process, have decreasing tendency of portlandite formation [1]. AB300 consumes Ca^{2+} ions from other hydraulic phases present in the hydration process and accelerate their dissolution. The consumption of all aluminates coming from AB300 can cause saturation of the solution with Ca^{2+} ions and consequently lead to portlandite precipitation. The peak assigned to portlandite formation was varied from 0.7 h to 1.3 h in the range of AB300 0.1 – 1 wt. %, resp. With the increasing content of AB300 in the mixture the heat flow values during dormant period were increased. The increase should be explained with the presence of aluminates from AB300, which also play a role in quantification of hydration process. AB300 did not influence the main silicate peak, but strongly influenced the peak of sulfate depletion. With the increasing amount of AB300 up to the 1 wt. %; the sulfate depletion process in the cement is accelerated. In comparison of analyses, the behaviour of samples with gypsum or AB300 addition by means of the peak position shift is similar.

From obtained data (comparison Fig. 2b with Fig. 3b), it can be assumed that 1 wt. % of AB300 was compensated by addition of 1.25 to 1.5 wt. % of gypsum (factor of gypsum / AB300 compensation). Position and intensity of the 4th peak of the conversion AFt to AFm was stable until the sample 2.d, but the AFt to AFm decomposition is strongly accelerated for sample 2.e.

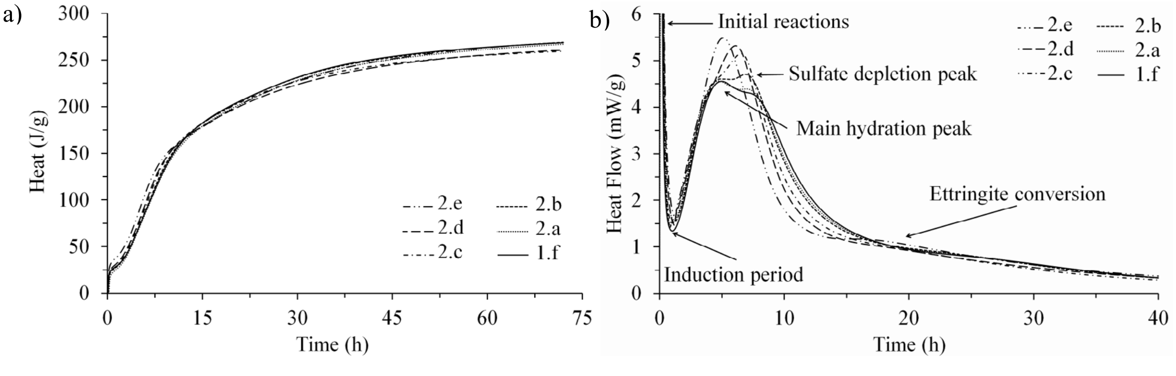

Fig. 3. PC with AB300 (a) Total heat of hydration (b) Heat flow.

From the experimentally determined factor of gypsum / AB300 compensation, the series of samples with designed position of sulfate depletion peak were prepared. Two series of samples with adjusted position of the sulfate depletion peak were prepared. In first samples series (2.e, 3.c, 3.d) the sulfate depletion peak was adjusted before, the second series (1.f, 3.a, 3.b) approximately 2.5 h after the main silicate peak. The calorimetry analyses showed in the Fig. 4b confirmed the apparent behaviour of these samples. The minimal heat flow during induction period was increased with the increasing gypsum / AB300 compensation factor. The sample prepared with the various gypsum / AB300 compensation factor influenced the portlandite precipitation. In the case of sample 3.c the peak assigned to portlandite formation was observed around 1 h after the beginning of hydration process. Position of this peak for the other ones was observed around 90 min. The position of the main silicate peak was almost not influenced by the various amounts of AB300 and gypsum.

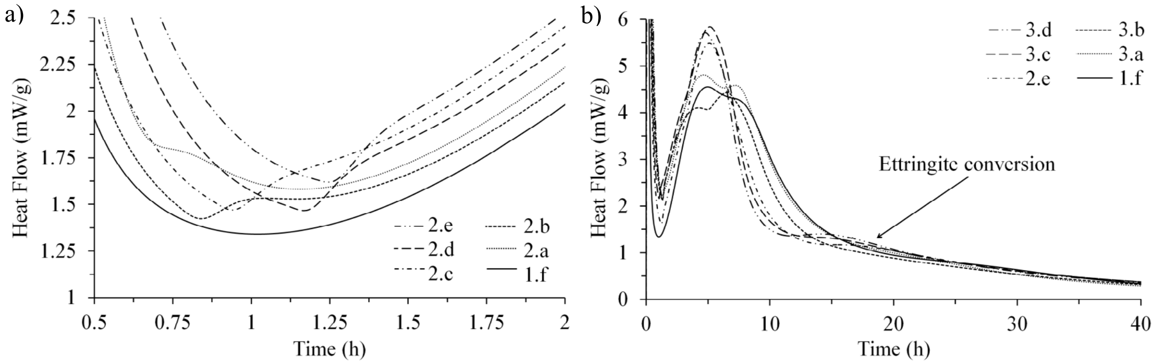

Fig. 4. (a) Induction period with peak of portlandite precipitation (b) Alphabond 300 compensation by gypsum.

The apparent dependence between decomposition of AFt to AFm and position of sulfate depletion peak can be clearly distinguished in Fig. 4b. When the sulfate depletion occurred before appearance of the main silicate peak, then the 4th peak was intensive. In some cases the plot regression reached the positive values. On the other hand when the sulfate depletion occurred after the main silicate peak the 4th peak was observed only as a weak shoulder of the main silicate peak. The intensity of the 4th peak is strongly dependent of the AB300 content and on occurred sulfate depletion before maximum of the main silicate peak. The sulfate depletion before maximum of the main silicate peak also influenced the C-S-H gel structure (higher porosity). This finding was also confirmed in work of Lerch et al [6]. In the model system of C_3A-gypsum the velocity of AFt to AFm decomposition is forced by remaining C_3A surface, where the nucleation takes place [7]. The presence of AB300 in the system caused more amount of remaining C_3A and therefore more amount of C_3A that can react with AFt to AFm.

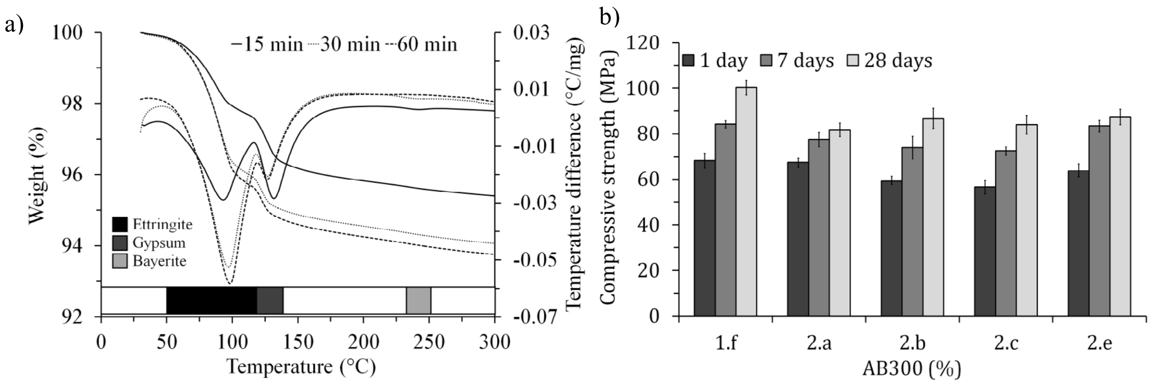

Fig. 5. (a) DTA curve of the hydration product 3.c in time (b) Mechanical testing of binder with AB 300.

The provided DTA analyses (see Fig. 5) of the samples clarified the mechanism of AB300 in the presence of Portland cement. AB300 hydrated through formation of amorphous products to crystalline bayerite was published elsewhere [10,11]. On the DTA curve, peak around 90 – 96 °C can be observed which can be assigned to Aft formation. The peak area corresponding to amount of formed AFt was enlarged with the increasing time of hydration. The size of formed crystallites influenced the peak position; peak is shifted towards higher temperatures with increasing crystallite size. Peak observed around 124 – 126 °C can be assigned to gypsum dehydration [1] and it is also influenced by the time of hydration and gypsum crystallite size (i.e. decreasing size connected with its dissolution). Third weak peak observed on the DTA curve (238 – 234 °C) is related to dehydration of bayerite, this process was observed [12]. Peak was observed after 15 and 30 min of the hydration. The peak disappeared after 60 min. of the hydration. This effect can be explained as a consumption of all present bayerite crystals to AFt formation. This finding should be closely connected with the observation from experimental calorimetry data. The relationship between bayerite consumption and portlandite precipitation is the subject of further investigation.

4. Conclusion

The partial substitution of cement by hydratable alumina showed acceleration of sulfate depletion during hydration process. This reaction should be predicated as a gypsum deficiency in the binder specie. This lack can be solved by another gypsum addition which can influence overall hydration process. It was found that the hydration process of modified samples was unchanged.

The addition of hydratable alumina is shown on the calorimetric curve as clearly detected peak of precipitated portlandite. The portlandite peak is shifted to higher reaction time with increasing content of hydratable alumina.

If the sulfates were depleted before the main silicate peak occurred (in samples with hydratable alumina content), the conversion of AFt to AFm was rapidly accelerated.

It was found that the minimal addition of hydratable alumina without gypsum compensation led to decrease of mechanical properties with no influence of the aging time.

Acknowledgements

This work was supported by the project “Materials Research Centre at FCH BUT - Sustainability and Development, REG LO1211, with financial support from National Programme for Sustainability I (Ministry of Education, Youth and Sports).”

References

[1] H. Taylor, Cement chemistry, 2nd ed. London: T. Telford, 1997.

[2] Ch. Hesse, F. Goetz-Neunhoeffer, J. Neunbauer, A new approach in quantitative in-situ XRD of cement pastes: Correlation of heat flow curves with early hydration reactions, Cement Concrete Res. 41 (2011) 123–128.

[3] A. Quennoz, K. L. Scrivener, L. Regnaud, A. Nonat, Interactions between alite and C3A-gypsum hydrations in model cements: Correlation of heat flow curves with early hydration reactions, Cement Concrete Res. 44 (2013) 46–54.

[4] D. Jansen, F. Goetz-Neunhoeffer, B. Lothenbach, J. Neunbauer, The early hydration of Ordinary Portland Cement (OPC): An approach comparing measured heat flow with calculated heat flow from QXRD, Cement Concrete Res. 42 (2012) 134–138.

[5] H. Minard, S. Garrault, L. Regnaud, A. Nonat, Mechanisms and parameters controlling the tricalcium aluminate reactivity in the presence of gypsum: Correlation of heat flow curves with early hydration reactions, Cement Concrete Res. 37 (2007) 1418–1426.

[6] W. Lerch, The influence of gypsum on the hydration and properties of Portland cementpastes, Am. Soc. Test. Mater. 46 (1946) 1252–1297.

[7] A. Quennoz, K. L. Scrivener, Hydration of C_3A–gypsum systems: Correlation of heat flow curves with early hydration reactions, Cement Concrete Res. 42 (2012) 1032–1041.

[8] V. Kocaba, Development and evaluation of methods to follow microstructural development of cementitious systems including slags, Laussane, 2009.

[9] P.-C. Aitcin, High-Performance Concrete, 1st Czech Ed., Prague, 2005.

[10] W. Mišta, J. Wrzyszcz, Rehydration of transition aluminas obtained by flash calcination of gibbsite, Thermochem. Ac. 331 (1999) 67–72.

[11] F.A. Cardoso, M.D.M. Innocentini, M.F.S. Miranda, F.A.O. Valenzuela, V.C. Pandolfelli, Drying behavior of hydratable aluminabonded refractory castables, J. Eur. Ceram. Soc. 24 (2004) 797–802.

[12] J. Szczerba, D. Madej, E. Śniezek, R. Prorok, The application of DTA and TG methods to investigate the non-crystalline hydration products of CaAl2O4 and Ca7ZrAl6O18 compounds, Thermochim. Acta 567 (2013) 40–45.

materials

MDPI

Article

Physico-Chemical Properties of Lithium Silicates Related to Their Utilization for Concrete Densifiers

Lukáš Kalina [1,*], Vlastimil Bílek [1], Martin Sedlačík [1], Vladislav Cába [1], Jiří Smilek [1], Jiří Švec [1], Eva Bartoníčková [1], Pavel Rovnaník [2] and Josef Fládr [3]

[1] Faculty of Chemistry, Brno University of Technology, 612 00 Brno, Czech Republic
[2] Faculty of Civil Engineering, Brno University of Technology, 612 00 Brno, Czech Republic
[3] Faculty of Civil Engineering, Czech Technical University in Prague, 166 36 Prague, Czech Republic
* Correspondence: kalina@fch.vut.cz; Tel.: +42-054-114-9366

Abstract: Protection of concrete against aggressive influences from the surrounding environment becomes an important step to increase its durability. Today, alkali silicate solutions are advantageously used as pore-blocking treatments that increase the hardness and impermeability of the concrete's surface layer. Among these chemical substances, known as concrete densifiers, lithium silicate solutions are growing in popularity. In the present study, the chemical composition of the lithium silicate densifiers is put into context with the properties of the newly created insoluble inorganic gel responsible for the micro-filling effect. Fourier-transform infrared spectroscopy was used as a key method to describe the structure of the formed gel. In this context, the gelation process was studied through the evolution of viscoelastic properties over time using oscillatory measurements. It was found that the gelation process is fundamentally controlled by the molar ratio of SiO_2 and Li_2O in the densifier. The low SiO_2 to Li_2O ratio promotes the gelling process, resulting in a rapidly formed gel structure that affects macro characteristics, such as water permeability, directly related to the durability of treated concretes.

Keywords: concrete densifier; lithium silicate; surface treatment; gelation process

check for updates

Citation: Kalina, L.; Bílek, V.; Sedlačík, M.; Cába, V.; Smilek, J.; Švec, J.; Bartoníčková, E.; Rovnaník, P.; Fládr, J. Physico-Chemical Properties of Lithium Silicates Related to Their Utilization for Concrete Densifiers. *Materials* **2023**, *16*, 2173. https://doi.org/10.3390/ma16062173

Academic Editor: Jean-Marc Tulliani

Received: 26 January 2023
Revised: 3 March 2023
Accepted: 7 March 2023
Published: 8 March 2023

1. Introduction

Alkali silicate solutions are widely used in various applications. One of them is their utilization in the building industry as concrete densifiers. They can effectively block the capillaries existing in the concrete surface, resulting in an increase in the hardness and impermeability of the concrete's surface layer [1]. In addition to the traditional use of sodium and potassium silicate solutions, densifiers based on lithium silicates have been growing in market share. Among the main advantages of lithium densifiers are lower alkalinity [2], higher water resistance, prevention of alkali-silica reaction [3,4], as well as a potentially lower tendency to efflorescence compared to sodium and potassium alternatives [5].

The widely accepted working mechanism of alkali silicate densifiers lies in their reaction with calcium ions in the surface layer of the concrete to form an inorganic gel [6]. The formed insoluble silicate gel acts as a micro-filler, generating a compact and dense microstructure on the treated concrete surface. Subsequently, this affects many characteristics of concrete, such as a decrease in water absorption [7,8], chloride permeability [6,9], and carbonation depth [6,10]. Simultaneously, a noticeable increase in abrasion [11,12] and frost resistance [6] has been reported.

In addition to the quality and properties of the concrete substrate or ambient conditions, the chemical composition of the used alkali silicate is of great importance. The main factors are primarily the cation nature, the total SiO_2 content, and the silicate modulus (molar ratio between SiO_2 and alkali oxide). These main chemical parameters play an important role in gel formation induced by the addition of calcium ions. The effect of the ion type is fundamentally connected to their ion radius. The increase in cation size results in a more efficient structural disorder, which is then responsible for a long gelation process [13]. Moreover, according to the hydration rule, the small cation binds water more strongly and has a smaller effective charge than a large cation with the same valence. Thus, large potassium ions are more effective in compensating the charge of the silicate anions than sodium or lithium ions, which cause gelation to be slower [14]. Hence, in the case of lithium silicates, polycondensation reactions are more preferred. The effect of the total SiO_2 content is subject to the following trend. The time of gelation increases with decreasing silicon concentration in the solution due to the dilution of the reactional medium. In such a system, the silanol tetrahedra units are strongly dispersed and the polycondensation reactions become difficult, inducing a long gelation time [15]. On the other hand, a silicate concentration that is too high is responsible for the increase in viscosity of the used densifier, which affects the ability of the molecules of alkali silicate to make adequate contact with calcium ions, causing a prolongation of gelation times [8]. Finally, the effect of the silicate modulus can significantly influence the point of gelation. The concentration of alkali ions has a direct impact on the electrostatic repulsion forces among the silica units. When the concentration of cations increases (reducing the silicate modulus), the zeta potential value of the originally negatively charged silica species becomes less negative and approaches the isoelectric point, which is related to the aggregation and acceleration of gelling [16].

The time of gelation determines the correct function of the used densifier. As previously stated, a gelation time that is too short results in a low penetration of the densifier into the sample, because its pores are blocked quite fast [8], while a gelation time that is too long is not desirable from a technological point of view. Previous studies have mainly solved the effect of the cation nature [13,17], pH [15], temperature [18], or the amount of dissolved silicate species [17] on the gelation mechanism. In addition, they have not focused on relating the gelation time to the densifying properties of a lithium silicate densifier. For these reasons, this study investigates the influence of the silicate modulus of the used lithium silicate on the gelation process, while keeping the amount of dissolved SiO_2 the same. Subsequently, the physico-chemical properties of formed gels were put into context with the quality of the surface treatment, which was verified by means of water permeability tests.

2. Materials and Methods

2.1. Preparation of the Lithium Silicate Densifiers

Lithium silicate solutions (densifiers) with different silicate moduli (M_S = 3.0; 3.2; 3.4; 3.6; 3.8; 4.0) were prepared by mixing commercially available lithium water glass (M_S = 4.51) with the appropriate amount of lithium hydroxide monohydrate to obtain the corresponding modules. An example of the preparation of lithium silicate densifiers (LiSD) is presented in Table 1. The total SiO_2 content in all lithium densifiers was held at 18 wt%. The chemical composition of lithium waterglass (SChem, a.s., Ústí nad Labem, Czech Republic) as well as lithium hydroxide monohydrate of analytical grade purity (Penta, s.r.o., Prague, Czech Republic) was determined using conductometry titration and is included in Table 1.

Table 1. Preparation proposal of 100 mL lithium silicate densifiers.

	Quantity (g)		
	Commercial Lithium Waterglass (Li_2O = 2.1 wt%; SiO_2 = 19.04 wt%)	**$LiOH{\cdot}H_2O$ (Li_2O = 35.61 wt%)**	**H_2O**
LiSD–3.0	111.55	3.31	3.14
LiSD–3.2	111.55	2.69	3.75
LiSD–3.4	111.55	2.15	4.30
LiSD–3.6	111.55	1.66	4.78
LiSD–3.8	111.55	1.23	5.22
LiSD–4.0	111.55	0.84	5.61

2.2. Preparation and Surface Treatment of Cement Mortar Samples

Ordinary Portland cement (OPC CEM I 42.5 R) mortar samples with dimensions of $4 \times 4 \times 16$ cm^3 were prepared for their subsequent surface treatment using lithium silicate densifiers. The preparation process was inspired by the EN 196-1 standard [19]. The sand-to-OPC ratio was 3:1 using three different fractions of standard siliceous sand, and the water-to-OPC ratio was set at 0.50. A laboratory mixer was used for the mixing. The prepared mixtures were cast into steel molds and moistly (RH~99%) cured at laboratory temperature (25 °C) for 24 h. After the demolding process, the specimens were stored in water at 25 °C for 28 days.

After 28 days, the mortar samples were left in laboratory conditions for 24 h. Subsequently, they were immersed in the lithium silicate densifier for 24 h, ensuring penetration to its maximum amount. At the same time, the reference samples were not put in a densifier, but into water. Thereafter, the samples were removed from the treatment bath and the surface was freed of excess densifiers. After 24 h, the treated and untreated (reference) samples were subjected to a water permeability test.

2.3. Chemical Characterization

2.3.1. FT-IR Measurement

Fourier transform infrared spectroscopy (FT-IR) spectra were obtained using a Nicolet iS10 FTIR spectrometer (Thermo Fisher Scientific, Middleton, WI, USA) using the attenuated total reflection method (ATR). Spectra were recorded in the 400–4000 cm^{-1} range with a resolution of 2 cm^{-1}. Five separate measurements were carried out for each sample, where every obtained spectrum was the average of 64 scans. The analyses were carried out in an air atmosphere. The background spectrum was measured using the same parameters and was subtracted from the sample spectra. FT-IR was chosen as a suitable analytical technique for the chemical characterization of lithium silicate densifiers. Moreover, the chemical nature of silanol tetrahedra units in lithium silicate solutions was revealed using NMR spectroscopy, which had a significant impact on the evaluation of FT-IR spectra.

In addition, FT-IR was also used to monitor the evolution of the gelation process as a result of the presence of calcium ions. These gels were prepared based on JC/T 1018-2006 standard, where 0.593 g of $Ca(OH)_2$ was mixed with 18 mL of deionized water, and then 25 mL of lithium silicate densifiers (the samples varied in silicate moduli–M_S = 3.0; 3.2; 3.4; 3.6; 3.8; 4.0) were added to the solution. This mixture was homogenized by manually shaking for 1 min. In this way, the gelation process was initiated and the samples were measured first, shortly before the gelation point, determined according to rheological investigations, and then the gels were measured after 24, 48, 96, and 168 h.

2.3.2. NMR Measurement

NMR spectra were measured on a Bruker Avance III HD 700 MHz spectrometer operating at 139.2 MHz for ^{29}Si using a 5 mm dual broad-band probe. To improve the base line and allow signal quantification, the ring-down elimination pulse sequence was used as described by Schraml et al. [20]. Prior to the reading pulse, a 500 µs adiabatic inversion Chirp pulse over 60 kHz was applied. To eliminate the signal originating from the glass in the NMR tube and probe parts, the FID measured with a sample containing 100 mL solution of KCl in D_2O was subtracted from the data after the Fourier transform. All spectra were recorded at 298.2 K. The spectra were measured using a spectral width of 200 ppm (27.8 kHz); WALTZ16 proton decoupling was applied during acquisition, but not during the relaxation delay. The relaxation delay was set to 10 s and the number of acquired points was set to 64 k. Altogether, 2048 or 4096 scans were collected, resulting in measuring times six and a half or thirteen hours per spectrum, respectively. A mild line broadening of 3 Hz was used in data processing.

2.4. Rheological Investigation

Rheological measurements were performed using a rotational rheometer DHR-2 (TA Instruments, New Castle, DE, USA). Samples were prepared as outlined in Section 2.3.1. All measurements, including sample preparation, were carried out at a temperature of 25 °C. The gel point was determined using vane-in-cup geometry. The vane had a diameter of 20.0 mm and a height of 19.5 mm, while the cup diameter was 30.4 mm. The operating gap was 30.0 mm. The measurement was carried out within the range of small-amplitude oscillatory shear (SAOS), i.e., within the linear viscoelastic region (LVR), using a time sweep measurement. The strain amplitude and frequency were kept constant at 0.1% and 10 rad/s, respectively; five cycles per each point. The gel point was evaluated as the crossover of the storage modulus (G') and the loss modulus (G''), i.e., the point of change in the viscoelastic character of the sample from liquid-like ($G' < G''$) to solid-like ($G' > G''$). In this case, only one sample of each composition was tested due to high time requirements for measurements.

To avoid the ineffective continuous occupation of the rheometer by repeating the whole gelation process inside the rheometer, the gels were externally prepared in a plastic vial of approximately the same shape as the rheometer cup. The viscoelastic properties of the externally prepared gel samples were determined using amplitude strain sweep measurements in the chosen time intervals (24 and 48 h from the start of gelation). A plate-like sample of each gel was cut off with a scalpel and immediately inserted into the rheometer. A cross-hatched steel parallel plate geometry system 20 mm in diameter was used as a suitable sensor for these types of samples. The advantage of cross-hatched geometry lies in the prevention of wall slip during rheological tests. The frequency of oscillation was maintained at a constant value (1 Hz), while the amplitude of deformation was logarithmically increased from 0.01% until 1000% (logarithmic sweep, 20 points per decade). Before each individual measurement, a conditioning step was included (2 min of sample relaxation at constant temperature 25 °C). The axial force during the squeezing of the gel sample to the geometry gap did not exceed 8 N. The measuring gap was maintained at a constant value (1000 µm). The crucial viscoelastic parameters (elastic moduli in strain independent part, the end of linear viscoelastic region) were calculated as the average (with standard deviation) of at least two to four individual measurements.

2.5. Water Permeability Measurement

The water permeability test was performed on the basis of the EN 1062-3 standard [21]. The treated and reference samples were weighed to the nearest 0.1 g. The specimens were inserted into a plastic rack, which ensured maximum contact with the test medium, and immersed in the container with deionized water. The specimens were removed from the container in time intervals of 10 min, 30 min, 1 h, 2 h, 3 h, and 24 h. They were always carefully wiped, weighed, and returned back to the water bath. Water permeability was determined by the change in mass and compared in percentage terms to the reference samples.

3. Results and Discussion

3.1. Characterization of Lithium Silicate Densifiers

The lithium silicate densifiers prepared according to Table 1 were first characterized by FT-IR in ATR mode to identify different vibration bands. Figure 1a shows their FT-IR spectra having a similar nature. The broad band located from 2500 to 3700 cm^{-1} corresponds to both the contribution of OH vibrations in the Si–OH bonds and in water molecules [22]. For water, an intense band at 1638 cm^{-1} as a result of O–H–O scissors-bending is also typical [23]. The asymmetric stretching of the Si–O–Si bonds falls within the area of the extended band from 950 to 1250 cm^{-1} [17]. This broad band with a sharp peak at 1012–1020 cm^{-1} has its origin in the presence of Q^2 silicate tetrahedra units [24]. The peak is shifted to a lower wavenumber with decreasing silicate modulus relating to the bond strength between the alkali cation and non-bridging oxygen ($Si–O^{-}M^{+}$) [13,17].

This statement was also confirmed by the NMR results (Figure 1b, Table 2), where the portion of Q^2 units representing Si–O–Si and/or Si–O^-M^+ connections decreased with increasing silicate modulus at the expense of Q^3 and Q^4 cross-linking silica tetrahedra. In addition, the asymmetric stretching broad band is characterized by a distinctive tail at high wavenumbers (1060–1250 cm^{-1}), exactly identifying the presence of Q^3 and Q^4 tetrahedra [24,25].

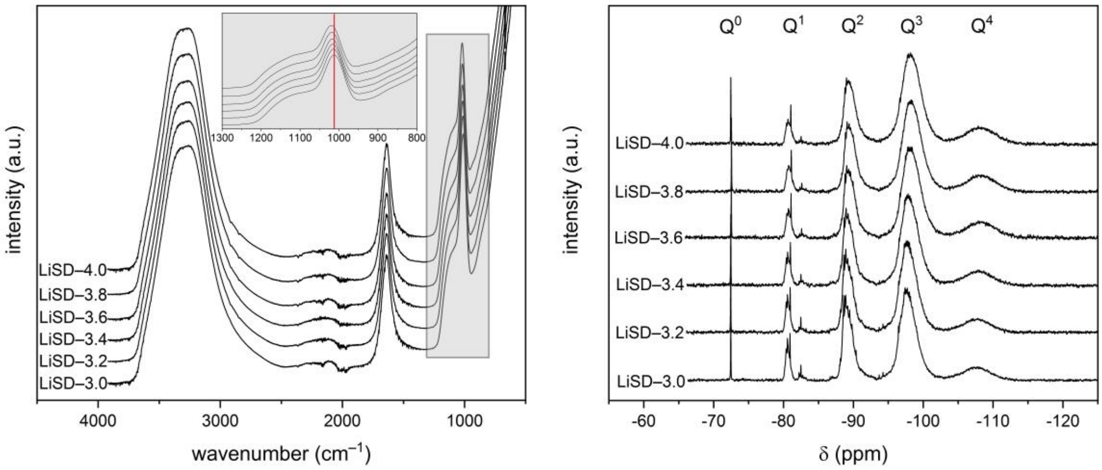

(**a**) (**b**)

Figure 1. (**a**) FT-IR spectra; (**b**) NMR spectra of studied lithium silicate densifiers.

Table 2. Distribution of Q^n silicate units determined by ^{29}Si-NMR spectra in lithium silicate densifiers.

Sample/(mol%)	Q^0	Q^1	Q^2	Q^3	Q^4
LiSD–3.0	0.90	6.10	28.44	52.74	11.81
LiSD–3.2	0.87	5.77	27.96	53.84	11.56
LiSD–3.4	0.83	5.45	26.37	54.70	12.66
LiSD–3.6	0.83	4.90	25.13	54.98	14.16
LiSD–3.8	0.82	4.70	24.72	55.58	14.17
LiSD–4.0	0.80	4.53	24.23	55.33	15.10

3.2. Monitoring of Gelation Process by FT-IR

During the gelation process initiated by the presence of Ca^{2+} ions (prepared according to the JC/T 1018-2006 standard), polycondensation reactions occur, and thus the final structure of the silicate gels is formed. These gels are created by the similar chemical mechanism that is given by the cementitious environment, and therefore this approach can simulate the situation inside the treated samples. The main goal of this procedure was to reveal the changes in the chemical composition of gels prepared by the use of lithium silicate densifiers with various Li_2O contents (silicate modulus).

The FT-IR results of all studied lithium silicate gels are very similar to those of lithium silicate densifiers, including the contributions of water and Si–OH bonds in higher wavenumbers. However, they differ in the region of low wavenumbers, as shown in Figure 2a. The appearance of three new bands is observed. The less noticeable band (**1**) at 577 cm^{-1} is attributed to the O–Si–O bending vibrations. Several studies have reported [13,24,26] that this band is related to the ring structure of silica units, as well as the second more visible band (**2**) of Si–O–Si symmetric stretching vibration at 771 cm^{-1}. Finally, the band (**3**), forming a shoulder at 869 cm^{-1}, is assigned to the stretching vibration of Si–O^-M^+ contributions. While in the case of lithium silicate solutions this type of bonding only affects the shift of the sharp peak associated with Q^2 silicate units, a noticeable band is observed in the gel spectra. This may be related to the fact that due to the increase in OH^- concentration in aqueous solution caused by the addition of $Ca(OH)_2$, the hydrolysis of

Si–O–Si bonds takes place [27]. As a result, the Si–O^-M^+ contributions increase with the appropriate band in the FT-IR spectra, and, at the same time, the wavenumber of the peak representing the Q^2 entities is strongly affected. Whereas the previous FT-IR measurements of lithium silicate solutions ranged this sharp peak in a broad band from 1012 to 1020 cm^{-1}, in the case of lithium silicate gels, it is situated in the area of 963–990 cm^{-1} depending on the different modules. The shift of this band to lower wavenumbers is therefore a consequence of the alkaline cations incorporation (Ca^{2+}, Li^+) into the gel structure, inducing a weakening of the covalent bond for the benefit of the ionic bond, as was previously reported [28,29]. However, during the gelation process, polycondensation reactions take place that increase the number of Si–O–Si bonds and the shift of this band gradually returns back to higher wavenumbers, as shown in Figure 2b. The asymmetric stretching of the Si–O–Si bonds due to Q^2 and Q^3 silicate units is located in areas with higher wavenumbers of this broad band, as was previously mentioned for the solutions of lithium silicate densifiers.

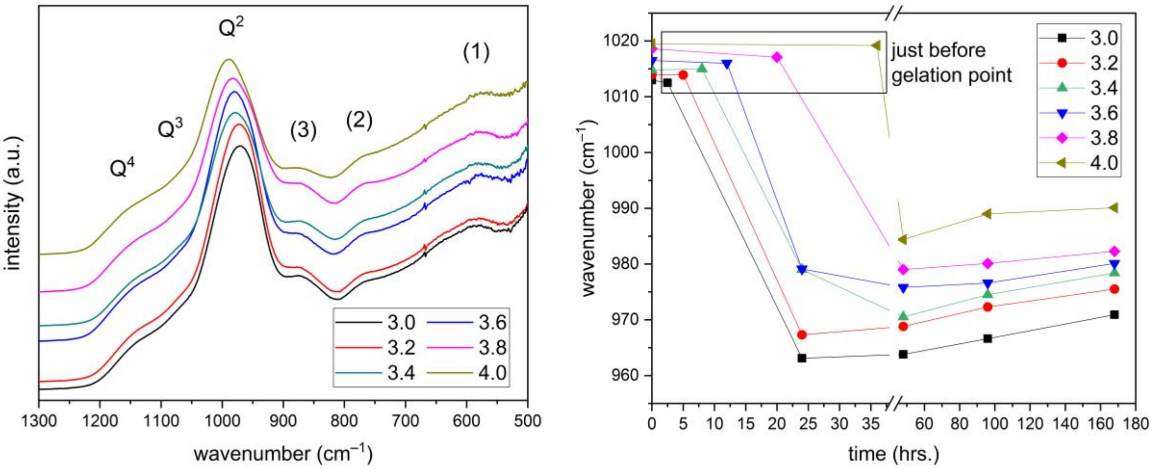

(**a**) (**b**)

Figure 2. (**a**) Asymmetric stretching vibration bands of silicate entities in lithium silicate gels at the age of 48 h; (**b**) The shift of asymmetric vibration band belonging to Q^2 silicate units as a function of time.

3.3. Monitoring of Gelation Process by Rheological Approach

The gelation process of the investigated lithium silicate densifiers was monitored using continuous SAOS measurements over time (Figure 3), and discontinuously using strain amplitude sweeps at the selected times (24 and 48 h), from which the storage modulus in the LVR was evaluated (Figure 4). The former approach is advantageous in terms of the continuous monitoring of the change from liquid-like to solid-like behavior, and further subsequent stiffening of the gel. All without the additional need for care regarding the sample and without altering its structure during preparation for the rheometer. On the other hand, continuous measurement is highly impractical in terms of long-term device occupation and unavoidable partial drying, even though the solvent trap is used. Therefore, the combination of these two rheological approaches provides valuable information from the perspective of the gelation process, but also the possibilities of the gel characterization. Figure 3a clearly shows that the gradual increase in the silicate modulus of the lithium densifier from 3.0 to 4.0 greatly prolongs the gel time and also affects the overall evolution of the gel stiffness. As further shown in Figure 3b, the dependence of the gel time on the silicate modulus can be fitted by the simple exponential curve. The relatively low dependence of gel time in the range of relatively low silicate moduli is in agreement with the study by Gaboriaud et al. [30]. In addition, Figure 3a shows similar values of the viscoelastic moduli during their crossover point, regardless of the silicate modulus of the tested densifier. This is likely due to the same mechanism of the gelation process, as already illustrated in Section 3.2. Because the only difference in the compositions of the used densifiers is the content of Li^+, changes in the dependence of the gel time are likely related to the differences in the ionic strength, pH, and overall capability of Li^+ to stabilize the silicates. It is worth noting that the long-term stability of the densifiers also increases with increasing silicate modulus.

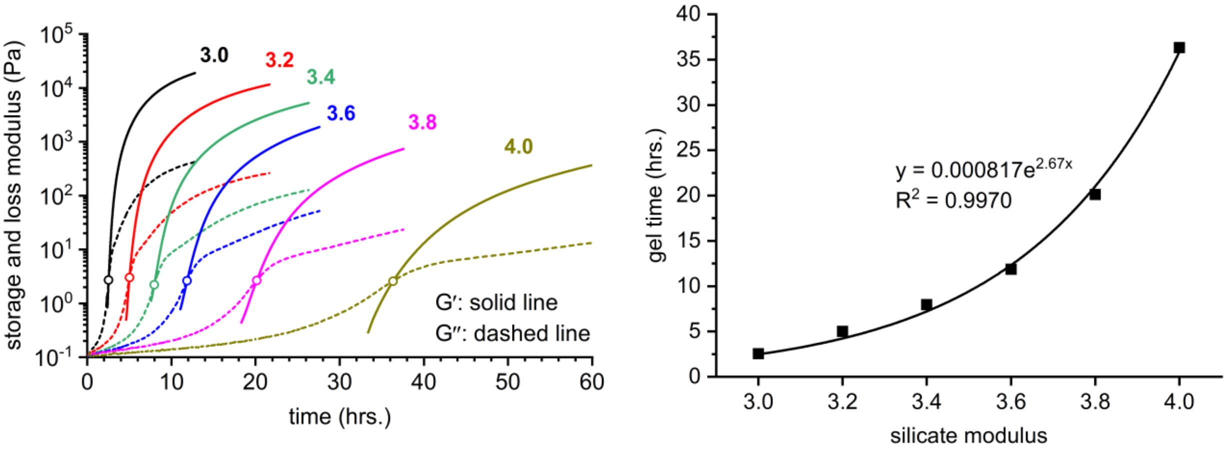

(**a**) (**b**)

Figure 3. (**a**) Continuous monitoring of the gelation process of lithium silicate densifiers with different silicate moduli. The open circles highlight the gel point, in which G′ = G″; (**b**) Exponential fit of the time needed to reach the gel point plotted against the silicate modulus of densifiers.

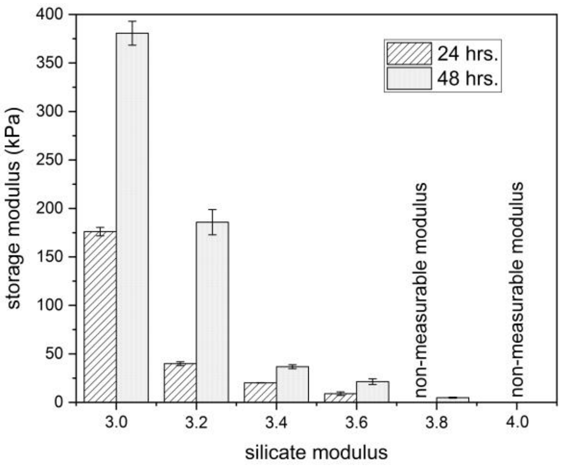

Figure 4. Values of the storage modulus of lithium silicate densifiers with different silicate moduli determined using discontinuous rheological experiments after 24 and 48 h.

Figure 4 shows that the mechanical properties of the gels increase over time beyond the timescale of the measurement in Figure 3a. In addition, a clear trend of decreasing the storage modulus with an increase in the silicate modulus of the densifier was verified after both 24 and 48 h. The absolute values of the storage modulus after 24 h seem slightly different for both rheological approaches, which could be mainly related to the sample preparation of the gels for the discontinuous measurements. Nevertheless, these results are well-reproducible, which indicates the suitability of this approach for the long-term characterization of the gels. Finally, it should be noted that both the gel time and the evolution of the mechanical properties correlate well with the trend in the FT-IR results (Section 3.2).

3.4. Water Permeability

Since water is essential for many forms of concrete deterioration, resistance to water penetration is a fundamental criterion by which to determine the efficiency of surface treatment [31]. The results of the water penetration test of the treated samples are shown in Figure 5. It can be seen that the rate of reduction in water absorption is highest for samples treated with lithium densifiers, having a low silicate modulus. This fact may seem to go against general theories on how silicates act to improve the performance of concrete. The most often accepted theory on the formation of insoluble calcium-silicate hydrates was mentioned in the introduction. Another theory is based on the precipitation of SiO_2 from alkali silicate in the pores, and a third standpoint is that the silicates form an expansive gel to fill the concrete voids by swelling [9,12,32]. The important factor in all of them is the presence of SiO_2 units in the treating medium, and therefore, with their higher amount, its effectiveness should increase, as reported by Jiang et al. [8]. However, this study is focused on the effect of the alkali ion. Thanks to the fact that the SiO_2 portion is the same for all lithium densifiers (18 wt%), the key parameter is the Li_2O content controlling the silicate modulus. As already shown in Section 3.3, the Li_2O amount determines the point of gelation, which is delayed with the use of a higher silicate modulus. One can say that the gelation process, associated with the formation of the gel structure, affects its compactness. Quickly formed structures composed of an amorphous network of silica species significantly slow down the travel of the water molecules passing through the gel, resulting in the water permeability reduction mainly in the initial stages of the test. After a long immersion time (more than 2 h), the molecules of water gradually penetrate into the material and the differences among the samples begin to be marginal. It is important to point out that all lithium silicate densifiers show about 20% better results in comparison with untreated samples after the 24-h water permeability test. This demonstrates the beneficial use of lithium silicate densifiers in the process of concrete surface treatment.

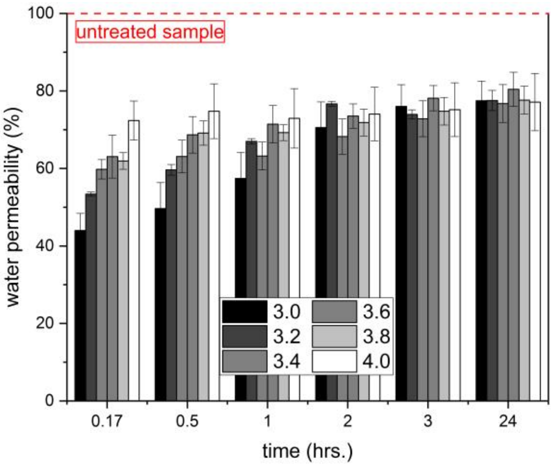

Figure 5. Water absorption of treated samples after applying the lithium silicate densifiers.

4. Conclusions

In this paper, the effect of the silicate modulus of the lithium silicate densifier on its gelation process was investigated. The obtained results were further correlated with the water permeability of the hardened cementitious mortars treated with the densifiers. Based on the obtained results, the following conclusions can be drawn.

- For the constant content of SiO_2 (18 wt%), the gelation time of the lithium silicate densifiers exponentially increased as the molar SiO_2 to Li_2O ratio decreased from 4.0 to 3.0. It follows that the lithium silicate solution with a silicate modulus of 4.0 shows a delay of up to 14.5 times in gelation time compared to a solution with $M_S = 3.0$.
- The storage modulus of the obtained gels also considerably increased with the decrease in the silicate modulus. This trend was observed for both continuous rheological

measurements of the gelation process in situ and the measurements of the samples taken from externally prepared gel after 24 and 48 h.

- The gelation process was accompanied by the shift in the FT-IR band related to Q^2 units from the wavenumbers of 1010–1020 cm^{-1} to the wavenumbers of 960–980 cm^{-1}. The magnitude of this change increased with the decrease in silicate modulus, which correlates with the viscoelastic properties of the gels.
- The surface treatment of the hardened cementitious mortars with the investigated densifiers led to a decrease in water permeability by 20% after 24 h of the test duration. During the first 60 min, the amount of absorbed water considerably decreased with decreasing silicate modulus, and thus with the gelation time of the used densifiers.

These results emphasize that gelation time is a key aspect of the use of lithium silicates as densifiers for OPC-based materials. To verify it, further research will be focused on the in-depth assessment of the action of the densifiers in a concrete surface, along with their impact on durability.

Author Contributions: Conceptualization, L.K. and V.B.; investigation, writing—original draft preparation, project administration, L.K.; writing—original draft preparation, V.B.; methodology, formal analysis, V.C. and M.S.; investigation, formal analysis, J.S.; data curation, investigation, J.Š. and E.B.; data curation, visualization, P.R.; validation, funding acquisition, J.F. All authors have read and agreed to the published version of the manuscript.

Funding: This outcome was achieved with financial support within the project: GA22-04828S "Advanced lithium silicate sealers: on the way to sustainable building materials".

Institutional Review Board Statement: Not applicable.

Informed Consent Statement: Not applicable.

Data Availability Statement: The data presented in this study are available on request from the corresponding author. The data are not publicly available due to ongoing research.

Acknowledgments: We acknowledge CF NMR of CIISB, Instruct-CZ Centre, supported by MEYS CR (LM2018127) and European Regional Development Fund-Project "UP CIISB" (No. CZ.02.1.01/0.0/0.0/18_046/0015974).

Conflicts of Interest: The authors declare no conflict of interest.

References

1. Pan, X.Y.; Shi, Z.G.; Shi, C.J.; Ling, T.C.; Li, N. A review on concrete surface treatment Part I: Types and mechanisms. *Constr. Build Mater.* **2017**, *132*, 578–590. [CrossRef]
2. Berube, M.A.; Tremblay, C.; Fournier, B.; Thomas, M.D.; Stokes, D.B. Influence of lithium-based products proposed for counteracting ASR on the chemistry of pore solution and cement hydrates. *Cement Concrete Res.* **2004**, *34*, 1645–1660. [CrossRef]
3. Wang, W.C. Effects of fly ash and lithium compounds on the water-soluble alkali and lithium content of cement specimens. *Constr. Build Mater.* **2014**, *50*, 727–735. [CrossRef]
4. Souza, L.M.S.; Polder, R.B.; Copuroglu, O. Lithium migration in a two-chamber set-up as treatment against expansion due to alkali-silica reaction. *Constr. Build Mater.* **2017**, *134*, 324–335. [CrossRef]
5. Veinot, D.E.; Langille, K.B.; Nguyen, D.T.; Bernt, J.O. Efflorescence of soluble silicate coatings. *J. Non-Cryst. Solids* **1991**, *127*, 221–226. [CrossRef]
6. Moon, H.Y.; Shin, D.G.; Choi, D.S. Evaluation of the durability of mortar and concrete applied with inorganic coating material and surface treatment system. *Constr. Build Mater.* **2007**, *21*, 362–369. [CrossRef]
7. Park, S.S.; Kim, Y.Y.; Lee, B.J.; Kwon, S.J. Evaluation of concrete durability performance with sodium silicate impregnants. *Adv. Mater. Sci. Eng.* **2014**, *2014*, 1–11. [CrossRef]
8. Jiang, L.H.; Xue, X.; Zhang, W.D.; Yang, J.N.; Zhang, H.Q.; Li, Y.W.; Zhang, R.P.; Zhang, Z.Y.; Xu, L.J.; Qu, J.; et al. The investigation of factors affecting the water impermeability of inorganic sodium silicate-based concrete sealers. *Constr. Build Mater.* **2015**, *93*, 729–736. [CrossRef]
9. Medeiros, M.H.F.; Castro-Borges, P.; Aleixo, D.M.; Quarcioni, V.A.; Marcondes, C.G.N.; Helene, P. Reducing water and chloride penetration through silicate treatments for concrete as a mean to control corrosion kinetics. *Int. J. Electrochem. Sci.* **2012**, *7*, 9682–9696.
10. Ibrahim, M.; Al-Gahtani, A.S.; Maslehuddin, M.; Dakhil, F.H. Use of surface treatment materials to improve concrete durability. *J. Mater. Civil. Eng.* **1999**, *11*, 36–40. [CrossRef]

11. Baltazar, L.; Santana, J.; Lopes, B.; Rodrigues, M.P.; Correia, J.R. Surface skin protection of concrete with silicate-based impregnations: Influence of the substrate roughness and moisture. *Constr. Build Mater.* **2014**, *70*, 191–200. [CrossRef]
12. Thompson, J.L.; Silsbee, M.R.; Gill, P.M.; Scheetz, B.E. Characterization of silicate sealers on concrete. *Cement Concrete Res.* **1997**, *27*, 1561–1567. [CrossRef]
13. Tognonvi, M.T.; Rossignol, S.; Bonnet, J.P. Effect of alkali cation on irreversible gel formation in basic medium. *J. Non-Cryst. Solids* **2011**, *357*, 43–49. [CrossRef]
14. Visser, J.H.M. Fundamentals of alkali-silica gel formation and swelling: Condensation under influence of dissolved salts. *Cement Concrete Res.* **2018**, *105*, 18–30. [CrossRef]
15. MunozAguado, M.J.; Gregorkiewitz, M. Sol-gel synthesis of microporous amorphous silica from purely inorganic precursors. *J. Colloid Interfaces Sci.* **1997**, *185*, 459–465. [CrossRef] [PubMed]
16. Sogaard, C.; Funehag, J.; Abbas, Z. Silica sol as grouting material: A physio-chemical analysis. *Nano Converg.* **2018**, *5*, 1–15. [CrossRef]
17. Tognonvi, M.T.; Soro, J.; Rossignol, S. Physical-chemistry of silica/alkaline silicate interactions during consolidation. Part 1: Effect of cation size. *J. Non-Cryst. Solids* **2012**, *358*, 81–87. [CrossRef]
18. Tamar, Y.; Sasson, Y. Examination of the regime controlling sol-gel based colloidal silica aggregation. *J. Non-Cryst. Solids* **2013**, *380*, 35–41. [CrossRef]
19. British Standards, I. *Methods of Testing Cement*; British Standards Institution: London, UK, 2010.
20. Schraml, J.; Sandor, P.; Korec, S.; Krump, M.; Foller, B. Improved baseline in 29si nmr spectra of water glasses. *Magn. Reson. Chem.* **2013**, *51*, 403–406. [CrossRef]
21. British Standards, I. *Paints and Varnishes. Coating Materials and Coating Systems for Exterior Masonry and Concrete*; British Standards Institution: London, UK, 1997.
22. Innocenzi, P. Infrared spectroscopy of sol-gel derived silica-based films: A spectra-microstructure overview. *J. Non-Cryst. Solids* **2003**, *316*, 309–319. [CrossRef]
23. Mojet, B.L.; Ebbesen, S.D.; Lefferts, L. Light at the interface: The potential of attenuated total reflection infrared spectroscopy for understanding heterogeneous catalysis in water. *Chem. Soc. Rev.* **2010**, *39*, 4643–4655. [CrossRef]
24. MacDonald, S.A.; Schardt, C.R.; Masiello, D.J.; Simmons, J.H. Dispersion analysis of ftir reflection measurements in silicate glasses. *J. Non-Cryst. Solids* **2000**, *275*, 72–82. [CrossRef]
25. Brew, D.R.M.; Glasser, F.P. Synthesis and characterisation of magnesium silicate hydrate gels. *Cement Concrete Res.* **2005**, *35*, 85–98. [CrossRef]
26. Aouissi, A.; Aldhayan, D.; Abduh, N.A.Y.; Al Kahtani, A. Propylene carbonate synthesis from propylene oxide and CO_2 over Ga-Silicate-1 catalyst. *Green Proc. Synth.* **2020**, *9*, 440–450. [CrossRef]
27. Armelao, L.; Bassan, A.; Bertoncello, R.; Biscontin, G.; Daolio, S.; Glisenti, A. Silica glass interaction with calcium hydroxide: A surface chemistry approach. *J. Cult. Herit.* **2000**, *1*, 375–384. [CrossRef]
28. Garcia-Lodeiro, I.; Fernandez-Jimenez, A.; Blanco, M.T.; Palomo, A. FTIR study of the sol-gel synthesis of cementitious gels: C-S-H and N-A-S-H. *J. Sol. Gel. Sci. Technol.* **2008**, *45*, 63–72. [CrossRef]
29. Schneider, J.F.; Hasparyk, N.P.; Silva, D.A.; Monteiro, P.J.M. Effect of lithium nitrate on the alkali-silica reaction gel. *J. Am. Ceram. Soc.* **2008**, *91*, 3370–3374. [CrossRef]
30. Gaboriaud, F.; Chaumont, D.; Nonat, A.; Hanquet, B.; Craeivich, A. Study of the influence of alkaline ions (Li, Na and K) on the structure of the silicate entities in silico-alkaline sol and on the formation of the silico-calco-alkaline gel. *J. Sol. Gel. Sci. Technol.* **1998**, *13*, 353–358. [CrossRef]
31. Pan, X.Y.; Shi, Z.G.; Shi, C.J.; Ling, T.C.; Li, N. A review on surface treatment for concrete—Part 2: Performance. *Constr. Build Mater.* **2017**, *133*, 81–90. [CrossRef]
32. Song, Z.N.; Xue, X.; Li, Y.W.; Yang, J.N.; He, Z.Y.; Shen, S.Z.; Jiang, L.H.; Zhang, W.D.; Xu, L.J.; Zhang, H.Q.; et al. Experimental exploration of the waterproofing mechanism of inorganic sodium silicate-based concrete sealers. *Constr. Build Mater.* **2016**, *104*, 276–283. [CrossRef]

EFFECT OF DRYING ON THE STRUCTURE OF SOL-GEL SYNTHESIZED CALCIUM SILICATE HYDRATE GELS

Ondřej Kunovský [a], František Šoukal[a], Lukáš Kalina[a], Tomáš Opravil[a], Eva Bartoníčková[a]

[a] Brno University of Technology, Faculty of Chemistry, Institute of Materials Science, Purkyňova 464, 612 00 Brno, Czech Republic,

∗ corresponding author: Ondrej.Kunovsky@vut.cz

Abstract

This article investigates the effect of lyophilization, air drying, and vacuum drying on the structural changes of synthetized calcium-silicate-hydrate (C-S-H) gel. X-ray photoelectron Spectroscopy (XPS) and Fourier-Transform infrared (FT-IR) spectroscopy were employed to analyze the structural changes induced by each drying method. Our findings reveal that lyophilization most significantly affects the C-S-H gel structure, leading to its substantial decomposition, particularly affecting samples prepared under acidic and alkaline conditions. In contrast, air drying and vacuum drying proved to be gentler alternatives, effectively preserving the inherent C-S-H gel structure. Among the methods tested, vacuum drying emerged as the most suitable technique for preparing C-S-H gel samples, primarily due to its superior control over drying conditions. These results underscore the critical importance of selecting an appropriate drying method for accurate and reproducible characterization of synthetized C-S-H gel, providing valuable insights to C-S-H gel formation mechanism.

Keywords: sol gel, C-S-H gel, drying, Si–O–Si polymerization, XPS, FT-IR

1. Introduction

Cement-based binders remain the most widely used materials in modern construction. Most important product of hydration reaction is calcium-silicate-hydrate (C-S-H) gel. Formation of various C-S-H gels is crucial for the development of strength and durability of concrete composites during hydration of cementitious materials. Advances in synthetic approaches open new ways for preparing C-S-H analogues with controlled morphology and composition, thereby enabling structural optimization and providing deeper insight into the hydration mechanism [1].

In the initial phase of Portland cement hydration, C-S-H I with a fibrillar structure is formed. This type of C-S-H gel typically has a lower C/S ratio, ranging from 1.5 to 1.7. In contrast, v gel formed in later phases of hydration has a higher C/S ratio, typically ranging from 1.5 to 2.0, and exhibits a foliated structure. The formation of a specific type depends on several factors, such as the concentration of Ca^{2+} ions in the solution, the available space for nucleation and growth, the temperature, and the quantity of water [1, 2].

Crystalline analogues of calcium silicate hydrates exist in various compositions with different C/S/H ratios, e.g. tobermorite, xonotlite, jennite and others. Crystalline structure can be achieved by using hydrothermal synthetic conditions. In this study, a C/S ratio of 0.8 [3], typical for tobermorite analogues, was used to synthesize calcium silicate hydrates.

The sol-gel synthesis of amorphous C-S-H gel was here employed, using various precursors such as sodium metasilicate or tetraethoxysilane (TEOS) as a silicon source and calcium salts, like calcium nitrate, as a source of calcium. With the sol-gel process, it is possible to form materials with high purity and specific structures, what was difficult to achieve through traditional hydration reactions between Portland cement and water [4, 5].

The characterization techniques commonly used to analyze the structure of synthesized calcium silicate hydrates and the Si–O–Si polymerization rate (Q^n) are X-ray powder diffraction to determine phase composition and crystallographic structure, vibrational spectroscopy as Fourier-transform infrared (FT-IR) spectroscopy and Raman spectroscopy to observe chemical composition and finally X-ray photoelectron spectroscopy (XPS) to analyze elemental chemical state. The origin of synthetized C-S-H samples, amorphous or crystalline state, is crucial for the analytical measurements [6, 7, 8].

XPS technique has a fundamental requirement for complete dryness of the measured samples. Also, for FT-IR a completely dry sample is beneficial due to the strong response of water in measured spectra [9, 10]. Lyophilization, widely employed drying technique for its ability to preserve sample morphology and porosity by avoiding liquid-vapor interfaces, is typically the method of choice for drying such types of materials [11]. However, the 'gentle' reputation of lyophilization can be misleading. The rapid freezing and subsequent sublimation steps can induce irreversible changes, including the decomposition of the target material into its more stable compounds [12].

To address this problem effectively, this study focuses on other gentler drying techniques, such as vacuum drying or open-air drying, to prepare dry samples of C-S-H gels for analyses where the presence of unbound water is undesirable. FT-IR analysis is well-suited for comparing these types of drying, as it enables the assessment of Si–O bonding vibrations and, unlike XPS, does not require a strictly high-vacuum environment.

2. Experimental

2.1 Materials

Tetraethyl orthosilicate (TEOS) (Sigma-Aldrich, USA), $Ca(NO_3)_2 \cdot 4\ H_2O$ (Penta, Czech Republic), HNO_3 65 % solution (Lachner, Czech Republic), NH_4OH 24 % solution (Penta, Czech Republic)

2.2 Methods

Sample preparation

In the first step, an environmental solution (0.003M HNO_3 or 3.7M NH_4OH) was added to a three-neck flask. Solutions with reagents were then dropped through dropping flasks, containing TEOS (diluted with ethanol) and a saturated solution of calcium nitrate, respectively. The quantity of calcium nitrate was chosen to maintain C/S ratios of 0.8. During the dropping process, the mixture was stirred at 550 RPM on a magnetic stirrer. After the complete addition of both solutions to the environmental solution, the mixture was stirred for another hour. Subsequently, the mixture was transferred to a large vial and left to age for 24 hours at 25 °C.

Sample treatment before analysis

FT-IR analysis was performed on samples prepared under different drying conditions: as-synthesized (wet), air-dried, vacuum-dried and lyophilized. Wet samples were immediately subjected to FT-IR measurement. Air-dried samples were prepared in situ in the spectrometer by using an airflow for 0.5 hours before measurement. For vacuum-dried conditions, samples were drying in a vacuum chamber at 25 °C for 24 hours. Lyophilized samples were prepared in two steps. In the first step, samples were frozen in a freezer at −18 °C for 24 hours. In the second step, samples were dried in a lyophilizer (SP VirTis AdVantage Pro with Intellitronics) down to −40 °C.

FT-IR analysis

FT-IR analysis was performed with ATR diamond crystal in range of wavenumbers from 400 cm^{-1} to 4000 cm^{-1} with 64 scans for sample on Thermo Scientific Nicolet iS10 FTIR Spectrometer.

XPS analysis

X-ray photoelectron spectroscopy (XPS) analyses were carried out with an Axis Ultra DLD spectrometer using a monochromatic Al Kα (hν = 1486.7 eV) X-ray source operating at 75 W (5 mA, 15 kV). The spectra were obtained using an analysis area of ~300 × 700 μm^2. The Kratos charge neutralizer system was used for all analyses. High-resolution spectra were measured with a step size of 0.1 eV and 20 eV pass energy. The instrument base pressure was $2 \cdot 10^{-8}$ Pa. Spectra were analyzed using CasaXPS software (version 2.3.15) and have been charge corrected to the main line of the carbon C 1s spectral component (C–C, C–H) set to 284.80 eV. A standard Shirley background was used for all sample spectra.

3. Results and discussion

Lyophilization (or freeze-drying) is commonly considered the standard pre-preparation technique applied to synthesized C-S-H gels. According to the literature [11], these processes are believed to preserve the C-S-H gel structure prior to analysis. Synthesized C-S-H gels were therefore subjected to lyophilization and subsequently analyzed using XPS to observe the Si–O–Si polymerization rate (Q^n) and assess Ca^{2+} binding within the C-S-H structure. However, the analysis performed, as detailed below, revealed unexpected results.

The chemical composition and binding states of lyophilized C-S-H gels were analyzed using X-ray photoelectron spectroscopy (XPS). The functional groups identified in the gels are summarized in Table 1, and the corresponding XPS results are presented in Figure 1. Due to the similarity of the XPS spectra for both C-S-H gels prepared at initial pH values of 3 and 12, only the sample with an initial pH of 3 is shown in Figure 1 (survey spectra and high-resolution spectra for N, Si and Ca). The survey spectra provided information on the elemental composition of the samples (i.e. O, Ca, N, C, and Si), while the high-resolution spectra (N 1s, Ca 2p, and Si 2p) revealed the chemical states of the relevant elements. As expected, the N 1s spectrum consisted of a single peak, whereas the Ca 2p and Si 2p spectra were characterized by spin-orbit doublets. The area ratio of the spin-orbit peaks ($2p_{3/2}$:$2p_{1/2}$) was fixed at 2:1, and the full width at half maximum (FWHM) was constrained to be identical for both peaks in each doublet [13].

The high-resolution N 1s spectrum exhibits a sharp peak centered at 407.7 eV, attributed to nitrate groups. The presence of nitrates originating from calcium nitrate is further supported by the Ca $2p_{3/2}$ peak at 348.7 eV [14]. A second component in the Ca 2p spectrum, located at 347.4 eV, corresponds to calcium incorporated into the C-S-H gel. However, since the binding energy of Ca $2p_{3/2}$ in potential calcium carbonate phases closely overlaps with that in the C-S-H phase [15], the presence of the inorganic gel is more definitively confirmed by the Si 2p spectrum.

The Si 2p core-level spectrum reveals two distinct components. The main peak, located at 103.1 eV (Si $2p_{3/2}$), is attributed to a highly polymerized silicate structure originating from the TEOS precursor. The second component, with a Si $2p_{3/2}$ binding energy of 101.9 eV, corresponds to silicate species with a higher proportion of non-bridging oxygen (NBO), resulting in a shift to lower binding energies [16, 17]. This structure is characteristic of the tobermorite mineral group with a close relationship to the amorphous C-S-H gel, as previously reported by Black et al. [15].

Table 1. Binding energies of functional groups in amorphous C-S-H gel synthesized at initial pH values of 3 and 12 after lyophilization

pH 3			pH 12		
	functional groups	binding energy (eV)		functional groups	binding energy (eV)
N 1s	NO_3^-	407.7	N 1s	NO_3^-	407.5
Ca $2p_{3/2}$	$Ca^{2+}\cdots NO_3^-$	348.7	Ca $2p_{3/2}$	$Ca^{2+}\cdots NO_3^-$	348.2
	$Ca^{2+}\cdots{}^-O–Si$	347.4		$Ca^{2+}\cdots{}^-O–Si$	347.3
Si $2p_{3/2}$	Si–O (↓NBO)	103.1	Si $2p_{3/2}$	Si–O (↓NBO)	103.1
	Si–O (↑NBO)	101.9		Si–O (↑NBO)	102.1

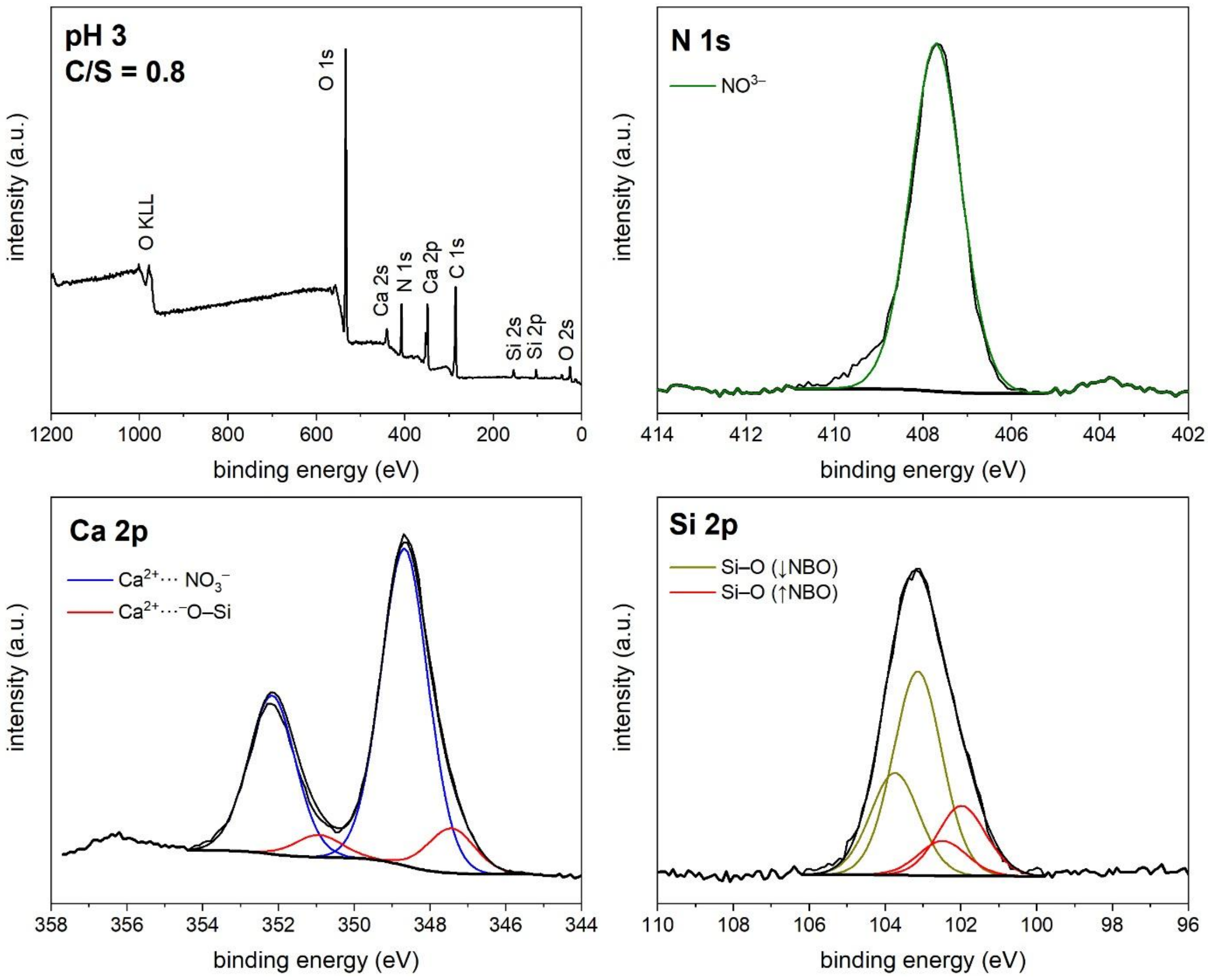

Figure 1. XPS spectra of C-S-H gel with C/S ratio of 0.8 synthetized from TEOS and $Ca(NO_3)_2$ at an initial pH of 3 after lyophilization

Figures 2–4 depict the FT-IR spectra of C-S-H gel prepared from TEOS and calcium nitrate with C/S ratio of 0.8. Figures 2 and 4 show a consistent trend of decreasing intensity in the O–H in H_2O peak within the 3800-3100 cm^{-1} wavenumber range. This effect is expected, as the samples were dried. However, samples dried in air exhibited a lower peak intensity than those dried in an airflow. This is attributed to differences in evaporation rates, as drying under airflow creates a more stable environment, thereby reducing disruption of the C-S-H structure, as reported by Ma et al. [18]. All FT-IR spectra also exhibit two peaks around 2980 cm^{-1} originated from ethanol, a by-product of TEOS hydrolysis.

Figure 2 represents the FT-IR spectrum of C-S-H gel synthetized with an initial pH of 3. Figure 4 represents spectra at an initial pH of 12. Both spectra are exhibited a pair of peaks at 1420 and 1330 cm^{-1}. Both of these peaks represent N–O vibrations from nitrates, which were used as a calcium source. The peak at 1420 cm^{-1} [19, 20] also represents carbonate, as C-S-H gel was subject to carbonation, as described by Lu et al. [21].

Characteristic peaks of C-S-H gels are highlighted by rectangles. A discrete peak of the Si–OH bond on Figure 2 is visible only in the wet spectrum at 1085 cm^{-1} [22], with no shift at different pH values. This peak became shoulder during the drying process because the intensity of neighboring peaks is increased. The region around 1050 cm^{-1} is also associated with the siloxane group, which can be attributed to unreacted TEOS precursor. These findings are also supported by the XPS results presented in Figure 1 and discussed in the corresponding section.

The maximum of the overlapping peaks at pH 3 is shifted only for vacuum drying from 1043 cm^{-1} to 1034 cm^{-1}. This could indicate a small change in the structure or be a side effect of the coupling of neighboring peaks. According to other publications, this peak did not correspond to a single vibration. Instead, there was a Si–O vibration (Q^3) at 930 cm^{-1} by Simonsen [23]. Additionally, there was a Q^2 vibration, which according to the study by Yu [20] is connected with a sharp peak at 940 cm^{-1}. Here, however, there could be a summation of these peaks, which corresponded to what is observed in the wet spectrum. The positions of characteristic group peaks are listed in Table 2.

The effect of lyophilization is visible on Figure 3. After the drying process, the intensity of the nitrate and carbonate peaks increased; however, for the peak at about 1330 cm^{-1}, a shift is indicated a change in chemical structure, whereas the peaks from vacuum drying and air drying only show an increase in intensity [24].

The same trend is visible on a small, focused peak at approximately 1760 cm^{-1}. This focused figure shows that the peak decomposes into two discrete peaks, which also indicates a change in the structure of C-S-H gel [24]. For other types of drying, only an intensity change is observed compared to the wet sample.

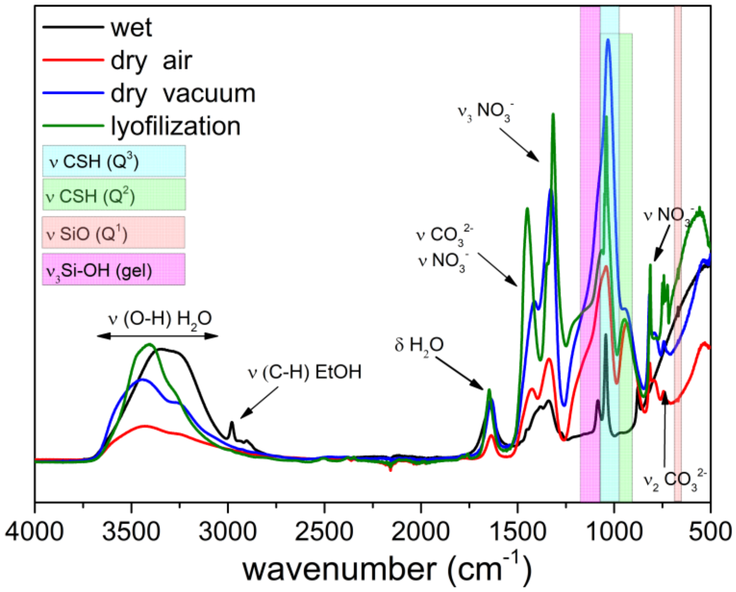

Figure 2. FT-IR spectra of C-S-H gels with C/S 0.8 synthetized from TEOS and Ca(NO_3)$_2$ at initial pH 3

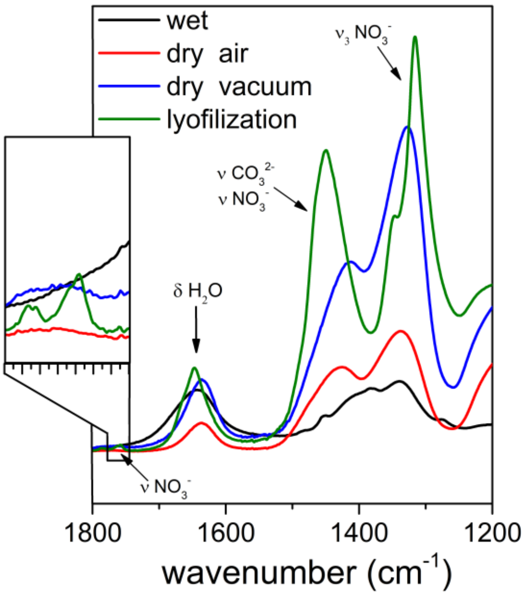

Figure 3. Focus on wavenumber range 1200-1800 cm^{-1} from Fig. 2

Table 2. Wavenumbers of groups and bonds measured in spectra of C-S-H gels

Bond/group	Wavenumber [cm^{-1}]	Reference	Bond/group	Wavenumber [cm^{-1}]	Reference
Si–O (Q^1)	800	25	Si–O (Q^3)	1030	27
Si–O	946	26	Si–O (Q^4)	1100	28
(TEOS)	1050-1100	22	N–O (NO_3^-)	1312-1340	19
Si–OH				818-833	
Si–O (Q^2)	940	20	CO_3^{2-}	1400-1500	20
Si–O (Q^{2}b)	1060	20	–OH (H_2O)	3100-380	29
				1600	

The situation is different with samples prepared at pH 12, due to the incorporation of calcium ions into the C-S-H gel structure, as discussed by Zhang et al. and Matsuyama et al. [30, 31]. This change in the structure is reflected in the shift of the Si–O peaks, as shown in Figure 4 and discussed in a study by Smith [24]. The shift is from 1043 cm^{-1} at pH 3 to 990 cm^{-1} at pH 12. This indicates higher incorporation of calcium into the structure, which agrees with the publication by Zhang et al. and Matsuyama et al. [30, 31].

Decomposition of C-S-H gel prepared at pH 12 during lyophilization is discussable by FT-IR analysis, as shown in Figure 5. XPS analysis revealed the same results as was determined for samples synthetized at pH 3. The positions of peaks at 1330 cm^{-1} and 1420 cm^{-1} are the same for all types of drying, but for samples regardless of the type of drying, peaks with a maximum of 1760 cm^{-1} appear, indicates the content of nitrates in these samples.

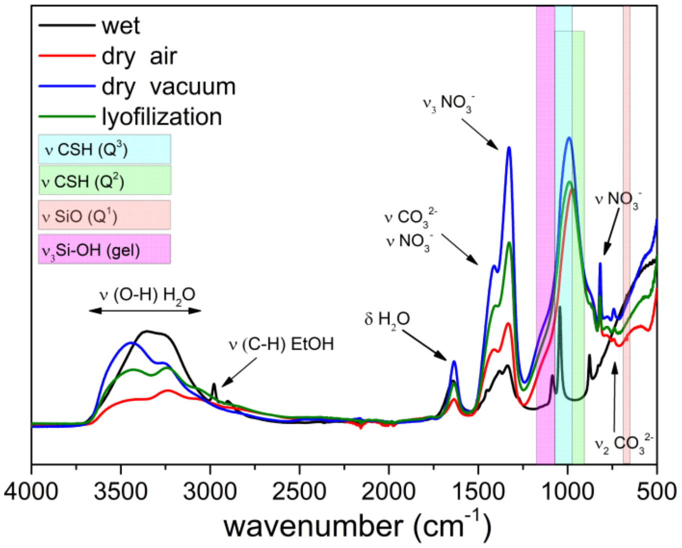

Figure 4. FT-IR spectra of C-S-H gels with C/S 0.8 synthesized from TEOS and $Ca(NO_3)_2$ at initial pH 12

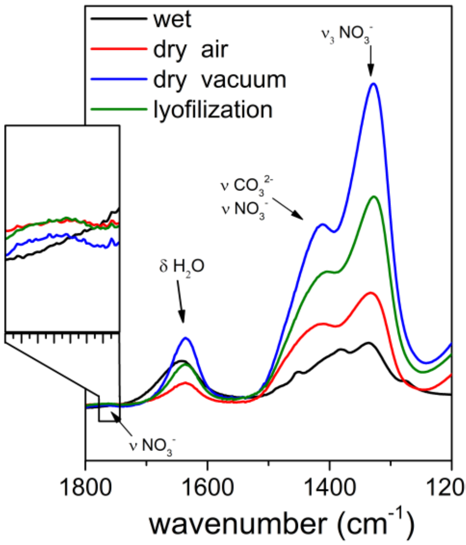

Figure 5. Focus on wavenumber range 1200-1800 cm^{-1} from Fig. 4

4. Conclusions

In this study, the effects of various drying techniques on the structural integrity of calcium-silicate-hydrate (C-S-H) gel, were investigated. Our findings undoubtedly demonstrated that the choice of drying method significantly impacts the preserved microstructure and chemical state of C-S-H gel, particularly highlighting the detrimental effect of lyophilization on samples prepared under both, acidic and alkaline, conditions. Other gentler drying approaches, such as ambient air drying and vacuum drying, proved to be more suitable alternatives, effectively preserving the inherent structure of the C-S-H gel. Our results suggest that these gentler drying methods minimize structural changes often introduced by harsher drying processes. Among these, vacuum drying emerged as the preferred method, offering superior control over drying conditions and ensuring sample stability, which is crucial for reproducible analytical measurements.

Acknowledgment

This research was funded by the Czech Science Foundation under the project number GA25-16766S: "*Engineering spatial distribution of hydrates in low-carbon cements* ".

References

[1] Taylor, H. F. W. *Cement chemistry* (2nd ed). Telford.

[2] Scrivener, K. L., Juilland, P., & Monteiro, P. J. M. Advances in understanding hydration of Portland cement. *Cement and Concrete Research*, *78*, 38-56. https://doi.org/10.1016/j.cemconres.2015.05.025

[3] Siauciunas, R., Smalakys, G., Eisinas, A., & Prichockiene, E. Synthesis of High Crystallinity 1.13 nm Tobermorite and Xonotlite from Natural Rocks, Their Properties and Application for Heat-Resistant Products. *Materials*, *15*(10). https://doi.org/10.3390/ma15103474

[4] Murari, B. M., & Chauhan, S. S. Characterisation of TEOS-Based Sol–Gel-Hydroxyapatite Composite Coating on Titanium Implants. *Biomedical Materials & Devices*, *3*(1), 496-503. https://doi.org/10.1007/s44174-024-00182-4

[5] Zhu, K., Wang, L., Liao, L., Bai, Y., & Hu, J. Study on Synthesis of CSH Gel and Its Immobilization of Heavy Metals. *Crystals*, *14*(10). https://doi.org/10.3390/cryst14100864

[6] Madadi, A., & Wei, J. Characterization of Calcium Silicate Hydrate Gels with Different Calcium to Silica Ratios and Polymer Modifications. *Gels*, *8*(2). https://doi.org/10.3390/gels8020075

[7] Verma, H. R. *Atomic and nuclear analytical methods: XRF, Mössbauer, XPS, NAA and ion-beam spectroscopic techniques*. Springer-Verlag. https://ebookcentral.proquest.com/lib/techlib-ebooks/detail.action?docID=301781

[8] Luke, K., & Quercia, G. Formation of tobermorite and xonotlite fiber matrices in well cementing and impact on mechanical properties. *Journal of Sustainable Cement-Based Materials*, *5*(1-2), 91-105. https://doi.org/10.1080/21650373.2015.1077752

[9] A. Madadi, J. Wei. Characterization of Calcium Silicate Hydrate Gels with Different Calcium to Silica Ratios and Polymer Modifications. *Gels* 8(2):75, 2022. https://doi.org/10.3390/gels8020075

[10] Simonsen, M. E., Sønderby, C., Li, Z., & Søgaard, E. G. XPS and FT-IR investigation of silicate polymers. *Journal of Materials Science*, *44*(8), 2079-2088. https://doi.org/10.1007/s10853-009-3270-9

[11] Hoppe Filho, J., Rodrigues, C. S., Ribeiro, L. S. O. P., & Medeiros, M. H. F. Evaluation of sample drying methods to determine the apparent porosity and estimation of degree of hydration of portland cement pastes. *Journal of Building Pathology and Rehabilitation*, *6*(1). https://doi.org/10.1007/s41024-020-00095-x

[12] Korpa, A., & Trettin, R.The influence of different drying methods on cement paste microstructures as reflected by gas adsorption: Comparison between freeze-drying (F-drying), D-drying, P-drying and oven-drying methods. *Cement and Concrete Research*, *36*(4), 634-649. https://doi.org/10.1016/j.cemconres.2005.11.021

[13] D. Briggs, XPS: Basic Principles, Spectral Features and Qualitative Analysis, in: D. Briggs, J.T. Grant (Eds.), Surface Analysis by Auger and X-ray Photoelectron Spectroscopy, IM Publications, Chichester, 2003, pp. 31-56

[14] Christie, A. B., Lee, J., Sutherland, I., & Walls, J. M. An XPS study of ion-induced compositional changes with group II and group IV compounds. *Applications of Surface Science*, *15*(1-4), 224-237. https://doi.org/10.1016/0378-5963(83)90018-1

[15] Black, L., Stumm, A., Garbev, K., Stemmermann, P., Hallam, K. R., & Allen, G. C. (2005). X-ray photoelectron spectroscopy of aluminium-substituted tobermorite. *Cement and Concrete Research*, *35*(1), 51-55. https://doi.org/10.1016/j.cemconres.2004.08.005

[16] Black, L., Garbev, K., & Gee, I. Surface carbonation of synthetic C-S-H samples: A comparison between fresh and aged C-S-H using X-ray photoelectron spectroscopy. *Cement and Concrete Research*, *38*(6), 745-750. https://doi.org/10.1016/j.cemconres.2008.02.003

[17] Nesbitt, H. W., Bancroft, G. M., Henderson, G. S., Ho, R., Dalby, K. N., Huang, Y., & Yan, Z. Bridging, non-bridging and free (O2–) oxygen in Na2O–SiO2 glasses: An X-ray

Photoelectron Spectroscopic (XPS) and Nuclear Magnetic Resonance (NMR) study. *Journal of Non-Crystalline Solids*, *357*(1), 170-180. https://doi.org/10.1016/j.jnoncrysol.2010.09.031

[18] Ma, Y., Jin, M., Li, W., Zhang, J., Huang, J., Shen, X., Liu, Z., Zeng, H., & Liu, J. Effect of drying method on calcium silicate hydrate (C-S-H): Experiments and molecular dynamics simulations study. *Construction and Building Materials*, *411*. https://doi.org/10.1016/j.conbuildmat.2023.134367

[19] Alemán Espinosa, E., Escobar-Barrios, V., Palestino Escobedo, G., & Waldo Mendoza, M. A. Thermal and mechanical properties of UHMWPE / HDPE / PCL and bioglass filler: Effect of polycaprolactone. *Journal of Applied Polymer Science*, *138*(19). https://doi.org/10.1002/app.50374

[20] Yu, P., Kirkpatrick, R. J., Poe, B., McMillan, P. F., & Cong, X. Structure of Calcium Silicate Hydrate (C-S-H): Near-, Mid-, and Far-Infrared Spectroscopy. *Journal of the American Ceramic Society*, *82*(3), 742-748. https://doi.org/10.1111/j.1151-2916.1999.tb01826.x

[21] Lu, B., Huo, Z., Xu, Q., Hou, G., Wang, X., Liu, J., & Hu, X. Characteristics of CSH under carbonation and its effects on the hydration and microstructure of cement paste. *Construction and Building Materials*, *364*. https://doi.org/10.1016/j.conbuildmat.2022.129952

[22] Ribicki, A. C., Chemin, B. G., Van Haandel, V. J., Winiarski, J. P., de Castro Rozada, T., Pessoa, C. A., Estrada, R. A., Fiorin, B. C., & Fujiwara, S. T. Sol gel synthesis of 3-n-propyl(4-aminomethyl)pyridinium silsesquioxane chloride and the enhanced electrocatalytic activity of LbL films. *Journal of Sol-Gel Science and Technology*, *87*(1), 216-229. https://doi.org/10.1007/s10971-018-4706-y

[23] Simonsen, M. E., Sønderby, C., Li, Z., & Søgaard, E. G. XPS and FT-IR investigation of silicate polymers. *Journal of Materials Science*, *44*(8), 2079-2088. https://doi.org/10.1007/s10853-009-3270-9

[24] Smith, Z. J., Chang, C. -W., Lawson, L. S., Lane, S. M., & Wachsmann-Hogiu, S. Precise Monitoring of Chemical Changes through Localization Analysis of Dynamic Spectra (LADS). *Applied Spectroscopy*, *67*(2), 187-195. https://doi.org/10.1366/12-06770

[25] Mojet, B. L., Ebbesen, S. D., & Lefferts, L. Light at the interface: the potential of attenuated total reflection infrared spectroscopy for understanding heterogeneous catalysis in water. *Chemical Society Reviews*, *39*(12). https://doi.org/10.1039/c0cs00014k

[26] Wencel, D., Lenehan, C. E., & McDonagh, C. Synthesis, tailoring and characterization of silica nanoparticles containing a highly stable ruthenium complex. *Nanotechnology*, *24*(36), 365705.

[27] Yan, Y., Yang, S. -Y., Miron, G. D., Collings, I. E., L'Hôpital, E., Skibsted, J., Winnefeld, F., Scrivener, K., & Lothenbach, B. Effect of alkali hydroxide on calcium silicate hydrate (C-S-H). *Cement and Concrete Research*, *151*. https://doi.org/10.1016/j.cemconres.2021.106636

[28] Mozgawa, W., Sitarz, M., & Król, M. Spectroscopic Characterization of Silicate Amorphous Materials. In A. Koleżyński & M. Król (Eds.), *Molecular Spectroscopy—Experiment and Theory* (pp. 457-481). Springer International Publishing. https://doi.org/10.1007/978-3-030-01355-4_15

[29] Mojet, B. L., Ebbesen, S. D., & Lefferts, L. Light at the interface: the potential of attenuated total reflection infrared spectroscopy for understanding heterogeneous catalysis in water. *Chemical Society Reviews*, *39*(12). https://doi.org/10.1039/c0cs00014k

[30] Zhang, W., Hou, D., Wang, P., Xu, J., & Li, Z. Mesoscale Simulation of the Effect of pH on the Hydration Rate, Morphology, and Mechanical Performance of a Calcium-Silicate-Hydrate Gel. *Journal of Materials in Civil Engineering*, *35*(9). https://doi.org/10.1061/JMCEE7.MTENG-15044

[31] Matsuyama, H., & Young, J. F. Effects of pH on precipitation of quasi-crystalline calcium silicate hydrate in aqueous solution. *Advances in Cement Research*, *12*(1), 29-33. https://doi.org/10.1680/adcr.2000.12.1.29

Construction and Building Materials 248 (2020) 118620

Contents lists available at ScienceDirect

Construction and Building Materials

journal homepage: www.elsevier.com/locate/conbuildmat

Doubts over capillary pressure theory in context with drying and autogenous shrinkage of alkali-activated materials

Lukáš Kalina *, Vlastimil Bílek Jr., Eva Bartoníčková, Michal Kalina, Jan Hajzler, Radoslav Novotný

Brno University of Technology, Faculty of Chemistry, Materials Research Centre, Purkyňova 464/118, Brno CZ-612 00, Czech Republic

HIGHLIGHTS

- Amino alcohol surfactants reduced the surface tension of AAS pore solutions.
- Surfactants had a minor effect on autogenous shrinkage.
- Drying shrinkage was reduced mainly thanks to hydration retardation caused by surfactants.
- Decrease in surface tension does not necessarily lead to decrease in shrinkage.
- Adsorption of surfactants on slag particles were observed.

ARTICLE INFO

Article history:
Received 10 September 2019
Received in revised form 27 February 2020
Accepted 28 February 2020
Available online 6 March 2020

Keywords:
Alkali-activated slag
Shrinkage
Admixture
Hydration
Capillary pressure
Surface tension

ABSTRACT

One of the most important technological problems associated with alkali-activated materials is high shrinkage. In this study, shrinkage reducing admixtures (SRAs) based on amino alcohols were used in alkali-activated slag (AAS) as strong surfactants that should, in terms of capillary pressure theory, decrease shrinkage via the decrease in surface tension. Although the surface tension of the pore solution was reduced by SRAs, autogenous shrinkage was not affected in the long run, while drying shrinkage was noticeably reduced and simultaneous weight changes were dramatically increased. The expected retardation effect of SRAs on hydration was confirmed using isothermal calorimetry, strength development, mercury intrusion porosimetry and scanning electron microscopy. The obtained results suggest that the observed effect of SRAs on drying shrinkage was caused by coarser pore structure rather than by a decrease in surface tension of the pore solution. Since the decrease in surface tension does not necessarily lead to decrease in shrinkage, the application of capillary pressure theory in AAS can sometimes be an issue.

1. Introduction

Alkali-activated materials (AAM) are non-traditional cementitious materials, the research and subsequent practical applications of which are currently undergoing an unprecedented development. The increased interest in these materials is primarily related to the revelation of their potential options, which are in many cases crucial in comparison with the conventional way represented by the usage of ordinary Portland cement (OPC). The main reason why AAM are gaining increased recognition and interest is connected with the reduction of CO_2 emissions which are lower compared to the emissions coming from Portland cement-based materials [1]. It should also be noted that most AAM are based on industrial waste and secondary raw materials which significantly contribute to the saving of natural resources.

Generally AAM show very good chemical [2] and high-temperature [3] resistance. High early strength is also an advantageous property typical for alkaline activated blast furnace slag-based systems (AAS) cured under ambient conditions [4]. Nevertheless, these materials also have some disadvantages considerably limiting their practical applications, especially their high autogenous and drying shrinkage [5].

The capillary pressure theory and disjoining pressure theory are known and abundantly used to explain the origin of shrinkage phenomena [6]. The former theory was based on the formation of menisci which arise during the drying of cementitious matrix as a consequence of surface tension forces. The difference between the pressures in liquid and vapour phase Δp comprises a menisci curvature. For a spherical liquid/vapour interfaces the Laplace equation can be used:

---

* Corresponding author.
E-mail address: kalina@fch.vut.cz (L. Kalina).

https://doi.org/10.1016/j.conbuildmat.2020.118620
0950-0618/© 2020 Elsevier Ltd. All rights reserved.

$$\Delta p = \frac{2\gamma}{r} \quad (1)$$

where r is the radius of the largest solution-filled cylindrical pore and γ is the surface tension at the liquid/vapour interface.

However, there are some doubts about the applicability of this theory to the cementitious systems with very fine pores (below 10 nm) regarding the pore shape, the existence of menisci and also the relative humidity lower than 50% [7,8]. According to these authors, disjoining forces play the main role in the shrinkage mechanism, particularly in mature hydrated cement paste. The term "disjoining pressure" represents the complex interactions between water and two solid surfaces, which may be written in simplified version as a superposition of the contribution of dispersive attractive or molecular forces (predominantly van der Waals forces), repulsive electric double layer components and structural components. When the solid surfaces are close to each other in a vacuum or in dry air, the attractive contributions dominate, and the solid surfaces are in close contact. As the relative humidity increases, water that is adsorbed and condensed within the capillaries forms a film separating the solid surfaces. This theory is applicable throughout the whole range of relative humidity [6].

Additionally, recent investigations [9,10] also showed that extensive shrinkage of AAS is created by the contribution of visco-elastic/visco-plastic behaviour during drying related to the rearrangement of C-(A)-S-H under capillary stresses. This could be more pronounced by the presence of alkalis and results in chemical and physical changes in AAS.

With respect to the capillary model described above, one of the ways to effectively reduce the shrinkage phenomenon is by using the organic surfactants-based shrinkage reducing admixtures (SRAs). The basic premise of the SRAs function is the reduction of surface tension of the capillary fluid, i.e. pore solution, which also decreases the capillary forces described by the Laplace equation (Eq. (1)). This results in the mitigation of drying [11] as well as autogenous [12] shrinkage. According to certain studies [13,14], the correlations between the shrinkage reduction and the reduction of surface tension of pore solution exhibit direct dependence. Thus, the assumption of good efficiency of SRAs according to the previous studies should particularly lie on the ability to decrease the surface tension of pore solution in alkali-activated systems as well.

Contrary to the above mentioned well-established findings regarding the Portland cement-based systems and also to some studies in AAS [15,16] we have observed some problems when using SRAs in waterglass-activated slag [17]. During the drying of porous immature AAS with delayed hydration, very low drying shrinkage was observed, while after prolonged curing, SRAs lost its efficiency. Similar observations of other SRAs and other related organic substances of various types led us to a more in-depth analysis including the context of the surface tension of the pore solution, i.e. in relation to original working mechanism of SRAs. Therefore, this paper provides information about the efficiency of non-ionic amino alcohol surfactants upon the ability to reduce both drying and autogenous shrinkage in alkali-activated blast furnace slag. The presented results discussed are regarding surface tension of the pore solution, hydration process and physical-mechanical properties of AAS, and suggest that the decrease in surface tension by SRAs does not necessarily lead to expected shrinkage reduction.

2. Experimental part

2.1. Materials

Commercial blast furnace slag (BFS) (ArcellorMittal Ostrava, a.s.) with the Blaine fineness of 400 m^2/kg was the main aluminosilicate material for alkaline activation. The phase composition was determined using X-Ray powder diffraction (XRD) analyser EMPYREAN (PANalytical, Netherland) in a central focusing arrangement using CuKα radiation with step 0.013 °2θ. The method of internal standard (calcium fluorite) for the amorphous part determination was applied. The XRD analysis showed the content of an amorphous phase of about 90%. The evaluation of the crystallographic structure and quantitative analysis was done by a Highscore programme using the Rietveld method. The crystal phases identified in BFS were melilite, calcite and merwinite. The chemical composition of BFS determined by X-ray fluorescence (XRF) is given in Table 1 and was performed with the spectrometer VANTA VRC (BAS, CZE). Quantification of elements was calculated via the internal mode in Geochem and represented as oxides. Sodium waterglass (Vodní sklo, a.s.) with the silicate modulus of 1.96 was used as an alkaline activator. Silicate modulus was determined by conductometry analysis.

2-(Ethylamino)ethanol (non-fluorinated secondary amine, further EAE) obtained from Sigma-Aldrich (per analysis grade) and self-synthetized N-ethyl,N-hydroxyethyl-heptafluoropropylamid (fluorinated secondary amide further synHFPA) were used as the SRA additives with assumed potential to reduce the surface tension of a pore solution. SynHFPA was prepared according to the patent CN106831504 by nucleophile acylation of 2-(Ethanolamino) ethanol with perfluoroester of carboxylic acid, i.e Methyl heptafluorobutyrate (99%, Sigma-Aldrich). The concentration of added surfactants was set to 0.5 wt% (by weight of BFS).

2.2. Testing methods

2.2.1. Physical-mechanical properties

Testing samples for the measurements of compressive strength as well as drying and autogenous shrinkage evolution were prepared as follows. BFS was activated by using sodium waterglass in an automatic mortar mixer set to exact mixing cycle in compliance with EN 196-1. The mass ratio Na_2O/BFS was set to 0.04 and water to BFS ratio was adjusted to 0.35 including the water presented in the alkaline activator. Prepared alkali-activated pastes were cast into steel moulds with the dimensions of 25 × 25 × 285 mm, which were moistly cured for the next 24 h. Both, mixing and curing were performed at laboratory temperature of 25 °C. Two different curing conditions after demoulding the samples were chosen for the strength and shrinkage measurements. One set of species was placed in the curing chamber with a defined relative humidity (65%, humidity chamber HC 105 Memmert), whereas the other one was wrapped into plastic foil to ensure autogenous conditions. Compressive strength measurements were carried out by a compressive and bending tester Desttest 3310 (Betonsystem, CZE) at 1, 7 and 28 days. Observed data were statistically processes (standard average and deviation from 6 samples). The length changes were measured in short time intervals using the ASTM C490 apparatus until the age of 28 days. Observed data were also statistically processed as standard average from three separately measurements.

To observe the autogenous volume changes during the first 24 h, Archimedes principle measurements were carried out. The mixtures of AAS were placed into the elastic membranes of commercially available non-lubricated, non-reservoir condoms. The condoms were then tied by a thin fishing line and hung to an analytical balance (Metler Toledo ME 204, USA). The sample weight of air (w_{air}) was obtained. Subsequently, the condom was submerged into a beaker filled with paraffin oil and the weight of the sample (w_{is}) in the initial setting time was determined. The initial setting time was identified simultaneously using the Vicat needle. Thereafter the weights (w_t) were monitored during the setting and hardening of the binder every minute. The change of sample volume ΔV

Table 1
Chemical compositions of blast furnace slag.

Raw material	Chemical composition/wt.%									
	SiO_2	Al_2O_3	CaO	MgO	SO_3	Na_2O	K_2O	TiO_2	MnO	Fe_2O_3
Blast furnace slag	34.7	9.1	41.1	10.5	1.4	0.4	0.9	1.0	0.6	0.3

at a constant laboratory temperature T (25 °C) was calculated as follows:

$$-\Delta V(T) = \frac{w_{is-}w_t}{w_{air} - w_{is}}(\%) \tag{2}$$

2.2.2. Isothermal calorimetry

The evolution of hydration heat was measured using the TAM Air isothermal microcalorimeter (TA instruments, USA). The measurements of heat evolution were performed at constant temperature of 25 °C. BFS and alkaline activator were mixed together by injecting the solution into a 15 mL Admix® vial and stirring it for 3 min, immediately after the thermal equilibrium of placed BFS was reached. Water/BFS (0.35) as well as the Na_2O/BFS (0.04) ratios were the same as in the preparation process of testing samples. The heat evolution was immediately recorded as the heat flow. These measurements were performed against a reference sample which has a similar heating capacity (i.e. water).

2.2.3. Porosimetry

The total porosity and the pore size distribution were determined by mercury intrusion porosimeter Poremaster (Quantachrome Instruments, USA). The working pressure range was from 0.14 to 231 MPa which covered the pore diameter range from 6.5 to 1000 nm. These measurements were carried out using Hg with the surface tension of 0.480 N/m and the contact angle of 140°. The contact angle value was selected according to Collins and Sanjayan study [18] focused on the measurement of pore size distribution of AAS-based systems. Nevertheless, the contact angle is dependent on several factors [19] which can affect the value of calculated pore diameter. The scan mode was chosen to average from 11 points. Obtained intrusion data were processed by the Poremaster program and normalized by sample weight and volume. Observed experimental data were presented as standard averaged values from three measurements. The chosen experimental parameters should provide information about the trend of porosity evolution due to the different mechanism of hydration in the presence of different SRA and not determine the exact pore distribution which could be given by the innovative MIP methods [19].

2.2.4. Surface tension

The dynamic surface tensions of pore solutions as well as pure amino alcohol admixtures were measured by the tensiometer BPA-800P (KSV Instruments, Finland) with the maximum bubble pressure method. Measurements were carried out at a constant temperature of 25 °C. Pore solutions were obtained from hardened samples stored in autogenous conditions in different time periods (1 and 7 days) using the steel die-and-piston system subjected to a pressure of 300 kN.

2.2.5. Zeta potential

The effect of surfactant addition on the values of zeta potential of slag suspension was investigated by the method of electrophoretic light scattering using Zetasizer Nano ZS (Malvern Panalytical Ltd., UK). Our main goal in this part of measurement was mainly to confirm the relative effect of used SRAs on surface chemistry of BFS grains in comparison with the sample without admixture. For this purpose, 10 mL of slag suspension (1 g BFS/ 100 mL H_2O) with alkaline activator (4 wt% Na_2O/BFS) was titrated with the surfactants solutions using the MPT-2 titration unit (Malvern Panalytical Ltd., UK) in the concentration range 0-5 wt% by mass of BFS. The surfactant addition was performed stepwise with defined concentration steps (0.25 wt%). After each step, the pH, the conductivity, the average scattered light intensity and the zeta potential of the suspension were measured. The above described titrations were performed for all investigated surfactants under a controlled temperature (25.0 ± 0.2 °C) in three independently prepared replicates. Electrophoretic light scattering (ELS) was done for each of these replicates after individual surfactant additions in three repeated scans (results are presented in the form of mean values ± SD, n = 9 (three repeated measurements of three sample replicates)). The obtained data from ELS titration were processed using the Zetasizer software (version 7.11; Malvern Panalytical Ltd., UK). It should be noted that the values of zeta potential determined by electrophoretic light scattering for colloidal particles are also influenced by the concentration and by the size of analysed particles. The measurement of zeta potential in concentrated suspensions such as AAS suspensions with SRAs admixtures is generally a great technological challenge, due to the high sample turbidity. As a consequence the measurable concentrations using this method must be in comparison with real used concentrations in formulations significantly lower. On the other hand, the dilution can be beneficial for the measurement because of suppressing the changes in particle size thanks to slowed down hydration, i.e. dissolution of slag particles and growth of hydration products.

3. Results and discussion

3.1. Surface activity of amino alcohols

Surface activity is an essential property of surface-active agents (surfactants) and can be evaluated by means of the surface tension measurements. Fig. 1 shows the values of surface tension of pure amino alcohol admixtures, as well as pore solutions. The solution of alkaline activator exhibited relatively high surface tension (71.4 mN/m at 25 °C), very similar to distilled water (72.0 mN/m at 25 °C) and the surface tension of EAE and synHFPA showed more than halved values, 33.2 and 28.7 mN/m respectively. The addition of surfactants into the activated BFS sample resulted in a decrease of surface tension in pore solution, especially when the synthesized fluorocarbon surfactant was used. In the case of EAE addition, a 15% reduction was achieved. The synthesized fluorocarbon (synHFPA) admixture decreased surface tension by about 30%. From Fig. 1 it is evident that the surface tension of pore solution did not change during the hydration process, although the bulk concentration of SRA should be increased due to the chemical bonding of water into the hydration products. Similar values and trends of surface tension of AAS pore solution without SRAs, where the surface tension increased only very slightly from 24 h to seven days have previously been published [20].

3.2. Autogenous shrinkage

It is well known that capillary stress occurs due to internal drying during autogenous conditions. The consumption of water for

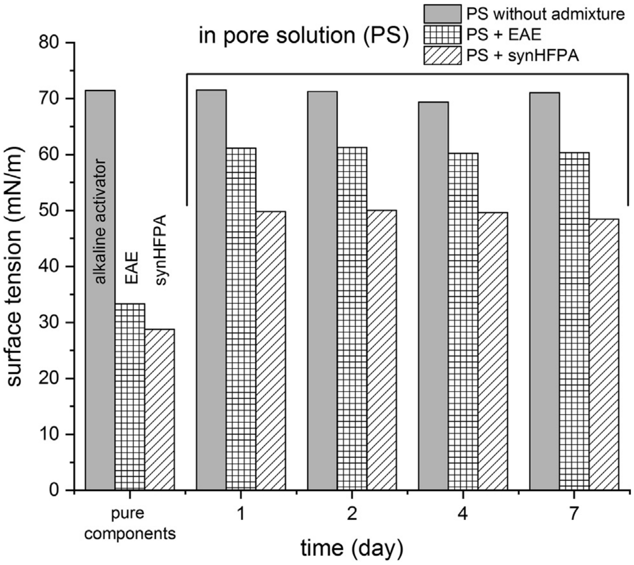

Fig. 1. Surface tension of pure amino alcohol admixtures and pore solutions.

the hydration products formation, i.e. self-desiccation, results in a decrease in relative humidity in the whole system and therefore curved menisci are created. Weiss et al. [21] and Bentz et al. [22] confirmed that the presence of SRAs in autogenous conditions leads to lower development of shrinkage. The utilization of some types of commercial SRAs can even lead to an initial expansion which decreases a part of the autogenous shrinkage later on. Sant et al. [23] explained that this behaviour should be connected with the amplification in portlandite oversaturation and its precipitation causes an early-age expansion. Several studies also confirm that the addition of the SRAs causes high internal relative humidity retention [21,24,25]. For this reason, the main mechanism controlling the shrinkage is attributed primarily to the capillary stress while disjoining pressure or another mechanism may dominate the shrinkage response at lower relative humidity [26]. Nevertheless, it should be noted that previous studies were mainly focused on cementitious systems based on Portland cement. The situation in the case of AAS seems to be different which is shown in Fig. 2.

From a long-term point of view, the autogenous shrinkage evolution exhibits very similar progress whether the systems contain SRAs or not. The distinction among the samples was observed only during the early timeframes of the hydration process. The samples containing SRAs showed a lower shrinkage rate up to 72 h from the start of alkaline activation, which can be related to the changes of hydration in the presence of SRAs. Therefore, microcalorimetry measurements were implemented. Fig. 3 shows two peaks appearing in the first minutes and hours of hydration process and one peak occurring after tens of hours. Typologically the same shape of the calorimetric curve for waterglass-activated BFS was reported by Shi and Day [27]. According to them, the initial peak is attributed to the wetting and dissolution of slag grains and adsorption of ions onto them while the additional initial peak is connected with the formation of a primary binder phase resulting mainly from the reaction of $(SiO_4)^{4-}$ ions from sodium waterglass and Ca^{2+} ions dissolved from the surface of BFS. The third hydration peak is the main one where the bulk hydration of the slag takes place [28] resulting in the fast evolution of the gel-like interstitial matrix among the slag grains [29]. C-(A)-S-H gel is a typical binder phase which occurs during alkaline activation of BFS [30]. It is evident that the presence of SRAs somewhat decreased the content of the binder phase formed during the initial hydration phase and noticeably retarded the peak corresponding to bulk hydration. It can be seen that once the C-(A)-S-H gel started to form, the autogenous shrinkage increased sharply. After 3 days, all samples behaved the same way, despite the different shapes of testing samples and the beginning of autogenous shrinkage measurement, i.e. 1 day from the start of mixing (Fig. 2A) or the time of initial settings (Fig. 2B). The calorimetry measurements were also in accordance with the compressive strength development (Fig. 4). After 1 day, the samples containing an SRA showed significantly lower values of compressive strengths in comparison with the reference samples. The retardation effect of SRAs was undoubtedly manifested. After 7 and 28 days, the compressive strength values of all samples were very similar.

An important factor that controls the capillary pressure is also the pore size distribution. The magnitude of shrinkage predominantly depends on the loss of water from mesopores (2–50 nm) [31]. In the case of AAS, the proportion of pores in the mentioned region is higher compared to hydrated OPC which is the main reason for its higher shrinkage [18]. The effect of SRAs addition on the change of porosity is one of the crucial factors which influence the shrinkage phenomena. Shah et al. [32] revealed a minor influence of SRAs on the pore size distribution of hydrated OPC. However, Kalina and Bilek [17,33] showed that some surfactants increase the porosity of AAS very strongly. Therefore, the differences in pore size distribution and total porosity of hardened samples were examined. Fig. 5A shows that MIP response under the autogenous treatment is very similar up to the pore diameter of 50 nm for all samples after just 7 days. Simultaneously, it is evident that all samples have a high concentration of pores within the mesopore size range, responsible for magnification of capillary tensile forces set up at the menisci. Therefore, the effect of surface tension should play the key role for the reduction of capillary pressure. However, the autogenous shrinkage rate remains unchanged with or without the SRA addition, even though the surface tension of the pore solution seems to be effectively reduced.

3.3. Drying shrinkage

According to the Wittmann and Splittgerber studies [34,35], a relative humidity above 55% of the surrounding air ensures that the capillary pressure outweighs the disjoining pressure because the van der Waals attractive forces among the pore walls are minimized. Therefore, the verification of the capillary force shrinkage model was further based on the measurements of length change during the curing process with controlled relative humidity (65%). The results in Fig. 6A show that the usage of SRAs decreased the drying shrinkage by about 35% compared to the reference samples. Consequently, one fundamental question arises: Does the decrease of surface tension by the addition of SRAs affect the drying shrinkage reduction? The combination of several measurements suggests that a different explanation should be offered.

During the drying shrinkage measurement, the weight changes of tested specimens were also obtained (Fig. 6B). A significant weight loss was observed in the case of samples with SRAs, especially when EAE was used. This can be related to the reduced surface tension of the pore solution, but also to the porosity and pore size distribution. The latter is supported by the comparison of the weight loss and drying shrinkage development. It can be seen that for the reference paste both drying and shrinkage rate is the highest at the beginning of drying while for both pastes with SRAs, extensive initial drying is not accompanied by rapid shrinking. The highest shrinkage rate is somewhat delayed and can be seen after around two days. This suggests that after 24 h, SRA-containing specimens had much larger pores whose emptying does not lead to severe shrinkage. Coarser porosity is related to the retardation of hydration by SRAs, particularly to the delay of the third peak on the calorimetric curve (Fig. 4), which was also

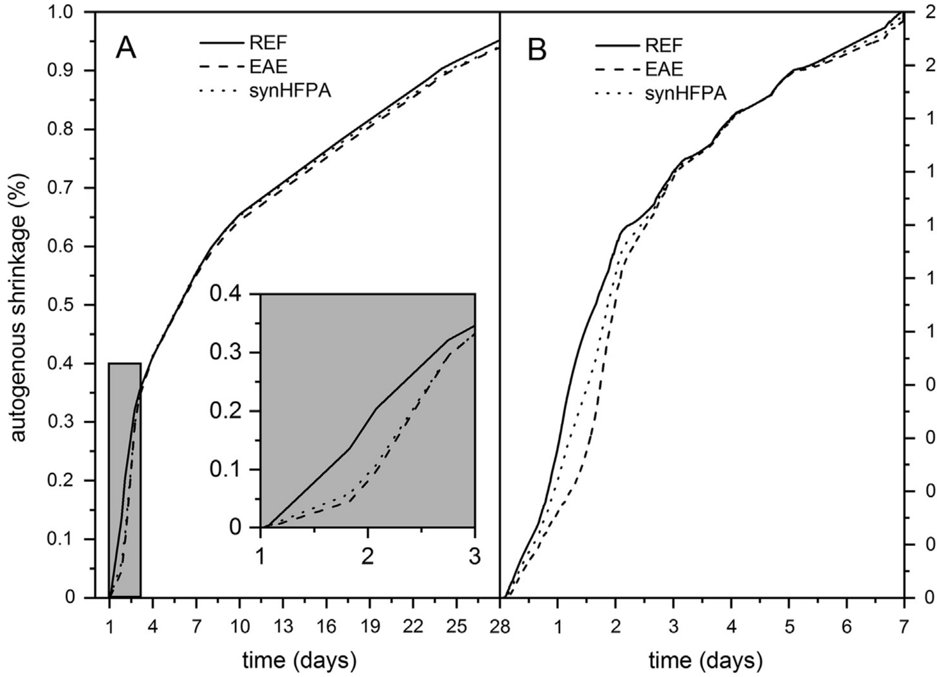

Fig. 2. Autogenous shrinkage of alkali-activated blast furnace slag samples measured on the test beams (A) and in the elastic membrane (B).

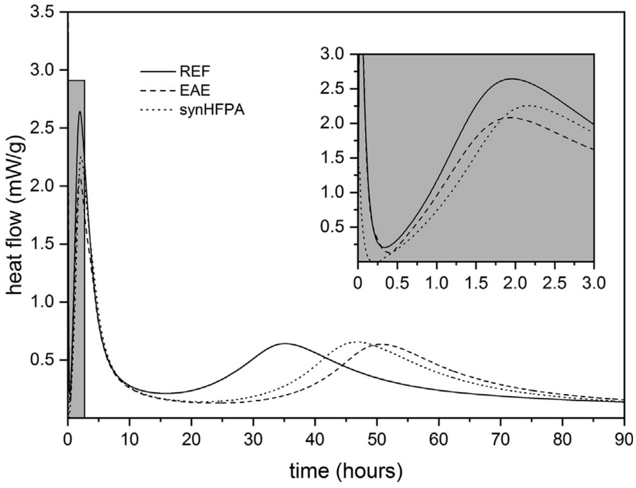

Fig. 3. Effect of surfactants on hydration process of alkali-activated blast furnace slag.

reported in the Bilek et al. study [17]. Simultaneously, due to a lower degree of hydration at the start of drying (24 h), a lower amount of water is bound in the hydration products and thus more water can freely evaporate out which increases total weight loss during drying. Consequently, less water is available for the creation of hydration products which is the main difference between autogenous conditions and controlled curing at RH = 65%. The lower amount of formed binder phase has a direct impact on total porosity and mechanical properties as well. Fig. 5B shows that the porosity is greatly influenced. After 7 days; the total porosity of the samples with SRA addition was more than five times higher than that of the reference ones. This porosity and the slowing down of the hydration process also reduced strength development. Fig. 4 shows that the compressive strength of samples with SRA cured at 65% of relative humidity was always noticeably lower compared to the reference samples. It is obvious that a lower degree of hydration also results in a lower extent of drying shrinkage. For this reason, it is difficult to conclude whether the decline in drying shrinkage is related to the reduction of surface tension of the pore solution or the creation of a coarser microstructure (Fig. 7) with a lower proportion of mesopores.

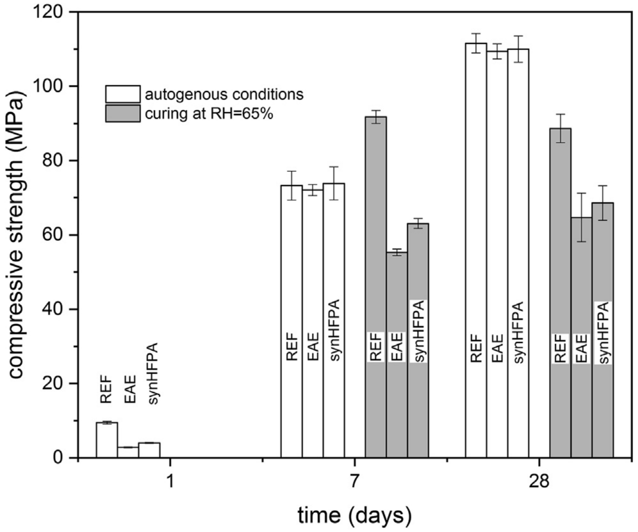

Fig. 4. Effect of surfactants on compressive strength development of alkali-activated blast furnace slag.

It should be noted that the usage of SRAs in improving the drying shrinkage performance of OPC systems shows a somewhat different effect. Namely, it has been observed that the cement binders containing SRAs exhibit the reduction in the rate of cement hydration and strength development. Nevertheless, the reduction takes place mainly in the early-age compressive and tensile strength [32,36] but a noticeable strength improvement was later confirmed with simultaneous reduction of drying shrinkage [36,37]. It is obvious that the behaviour of AAS with the addition of SRAs is quite different. The reason may be related to the AAS pore

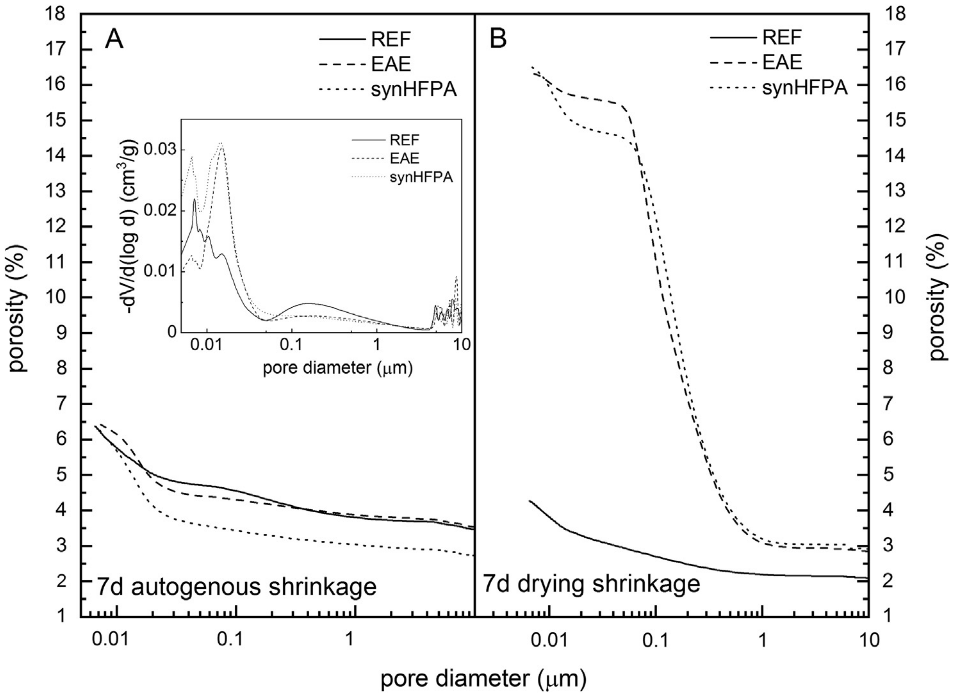

Fig. 5. Porosity of alkali-activated blast furnace slag in autogenous conditions (A) and cured at RH = 65% (B).

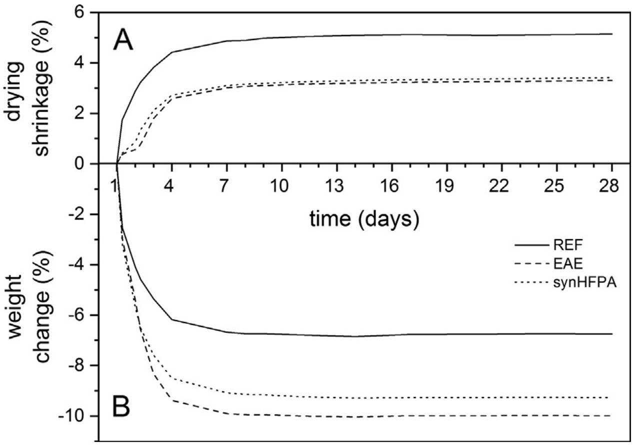

Fig. 6. Drying shrinkage (A) and weight changes (B) of alkali-activated blast furnace slag samples.

structure being generally more refined when compared to Portland cement. This implies that the lack of SRA molecules at the liquid-vapour interface can occur at a higher relative humidity compared to Portland cement and thus SRA loses its efficiency during the earlier drying stages. This can be partially slowed down by an increased dose of the SRA beyond its critical micelle concentration (CMC). Although it does not lead to a further decrease of the bulk pore solution surface tension, micelles can serve as a buffer for later stages of drying and interfacial area increase [6]. In this context, the issues of immobilization of SRA molecules by interactions with AAS through adsorption on slag particles and hydration products, as well as their consumption by hydration product may occur. Our recent study [38] showed that depending on the structure of SRAs, only a relatively small fraction of SRA remains in the pore solution in the mobile form, capable of migrating to the interfacial area to reduce surface tension. If the portion of the immobilized SRA is so high that its concentration in the pore solution is below CMC, the above described buffering effect is lost resulting in an earlier decrease of SRA efficiency.

Initially high but subsequently decreasing SRA efficiency can be seen in previous research by Bilim et al. [16], while work by

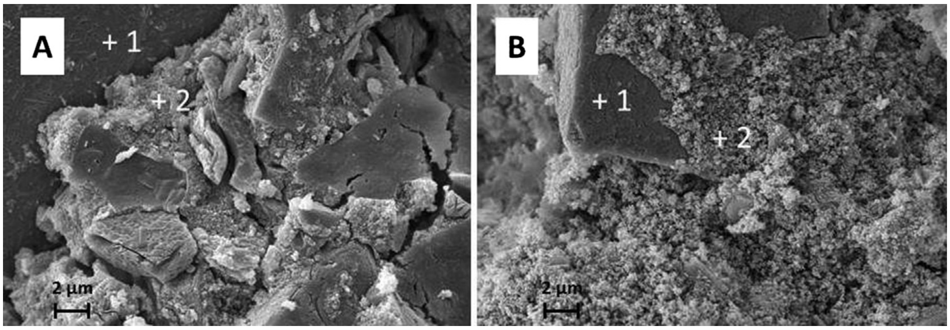

Fig. 7. SEM images of alkali-activated blast furnace slag with (B) and without (A) SRA addition after 7 days of hydration; RH = 65%; 1 – blast furnace slag particle, 2 – binder phase.

Palacios and Puertas [15] reported much higher SRA efficiency at the relative humidity of 99% compared to 50%. These results correlate well with the increase interfacial area during drying discussed above. However, findings presented in this study are rather opposite due to unaffected autogenous shrinkage and reduced drying shrinkage. It is true that during initial stages of autogenous shrinkage both SRAs seem to be efficient, but the decrease in shrinkage correlates better with the retardation of hydration than with the decrease in surface tension. The same stands for the initial stages of drying shrinkage and for weight loss during drying. These results, therefore suggest that at least in some cases of AAS, the effects of hydration degree and related pore structure or surface area on shrinkage prevail over the (bulk) pore solution surface tension.

3.4. Action of amino alcohols in alkali-activated systems

The efficiency of SRAs can be affected if they adsorb at the solid/liquid interfaces. The adsorption of non-ionic surfactants was observed in various studies focused on different silicate solid materials such as precipitated silica [39], ground quartz [40], soils [41] or clays [42]. The consequence of adsorption closely related to the development of undesired properties of mortar or concrete and changed working mechanism of SRA at the liquid/air interface. Therefore, the examination of how the molecular nature of used surfactants affects the adsorption at the solid/liquid interfaces is critical for their utilization in alkali-activated systems.

This paper provided an investigation of SRAs adsorption based on the zeta potential measurement which gives information about the electrokinetic potential in the interfacial double layer of BFS grains. Several factors such as different pH, the nature of used alkaline activator or the addition of some admixture can fundamentally change the charge on BFS grain surface. If the BFS particles are in contact with water, the Si–O, Al–O and Ca–O bonds on their surface are broken under the polarization effect of OH^- [43]. The strength of Ca–O bonds is weaker than that of Si–O or Al–O bonds resulting in a higher concentration of Ca^{2+} ions in the solution [44] and very quick Si-Al-rich layer creation on the surface of BFS particles [45]. The Si-Al-rich layer can adsorb H_3O^+ ions causing the increase of OH^- concentration and consequently increasing the pH of the solution. An alkaline pH means that some silanol groups on wetted particle surface deprotonate and a negative charge is induced [46]. When alkaline activator (sodium waterglass) was added into the BFS suspension, a higher negative value of zeta potential was observed (Fig. 8). Kashani et al. [47] explained negative zeta potential through the presence of additional silicate species from the alkaline activator which can be adsorbed or can precipitate on the BFS particle surface. However, the situation will quickly change if an SRA is added to the alkaline suspension. Fig. 8 shows that a higher content of amino alcohol surfactants decreased the zeta potential values, as well as the surface charge. The effect of particle size variation on actual determined values of zeta potentials after individual SRA addition was neglected due to the minimal observed changes in average scattered light intensity during the performed experiments. It should follow that used surfactants were adsorbed on the BFS surface. The adsorption mechanism of surfactants may be explained by the hydrogen bonding between the polar hydrophilic head of SRAs (C–OH) and the silanol groups on the slag surface [48]. Due to the amphiphilic nature of the most used SRAs for which the non-ionic character is typical, the tendency to adsorb onto hydrophilic surfaces is always expected. The adsorption is more accelerated if a fluorinated surfactant with a longer hydrophobic tail is used. Similar results were achieved in the Partyka et al. [39] study. Moreover, the authors observed that the CMC of surfactant with longer hydrophobic chain was drastically decreased which is related to the maximum degree of adsorption. The dissolution of BFS is then negatively affected and the hydration process slows down as was shown in the formation of a primary C-(A)-S-H gel in the previous results (see Fig. 3). The delay in the creation of the secondary C-(A)-S-H gel probably also depends on the length of the hydrophobic tail and molecular structure of SRAs in general as was showed by Bilek et al. [49]. However, further and deeper investigation between the character of organic admixtures and the hydration mechanism of AAM is necessary.

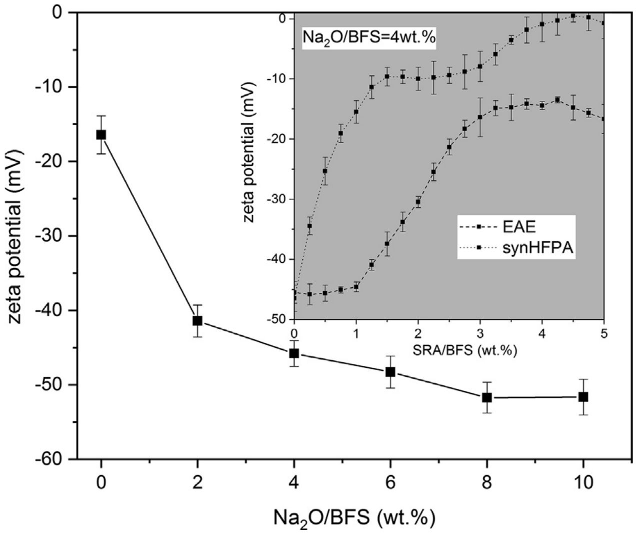

Fig. 8. Zeta potential of slag suspensions with different sodium waterglass dosage and after the addition of amino alcohol admixtures.

4. Conclusion

Based on obtained results, the essential conclusions may be summarized as follows:

- The addition of surfactants with a higher potential to reduce the surface tension of pore solution does not have any influence on the autogenous shrinkage or on the hydration process of AAS from a long-term point of view. The decrease in capillary pressure does not lead to the shrinkage reduction. Therefore, the basic principle of the working mechanism of SRAs in alkali-activated systems ceases to be applicable.
- The effect of SRAs on the drying shrinkage reduction is also speculative. Observed shrinkage reduction with the SRAs content is caused by the smaller amount of binder phase formation, rather than by the effective action of used admixtures.
- A great influence on the hydration process of AAS in the presence of SRAs was shown. The molecular character of used non-ionic surfactants causes a noticeable adsorption on slag particles during the alkaline activation resulting in the retardation of the hydration process. Due to similar nature of the most commercially used SRAs, the analogous behaviour can be expected. Therefore, the development of specific admixtures designed exclusively for AAM will be necessary for the future.

CRediT authorship contribution statement

Lukáš Kalina: Conceptualization, Investigation, Writing - original draft, Writing - review & editing, Methodology. **Vlastimil Bílek:** Validation, Methodology, Writing - review & editing. **Eva Bartoníčková:** Visualization. **Michal Kalina:** Formal analysis. **Jan Hajzler:** Formal analysis. **Radoslav Novotný:** Formal analysis.

Acknowledgements

This work was financially supported by the project: GA17-03670S, "Development of shrinkage reducing agents designed for alkali activated systems," with financial support from the Czech science foundation.

References

[1] J.L. Provis, Geopolymers and other alkali activated materials: why, how, and what?, Mater. Struct. 47 (2014) 11–25, https://doi.org/10.1617/s11527-013-0211-5.

[2] A. Palomo, M.T. Blanco-Varela, M.L. Granizo, F. Puertas, T. Vazquez, M.W. Grutzeck, Chemical stability of cementitious materials based on metakaolin, Cement Concrete Res 29 (1999) 997–1004, https://doi.org/10.1016/S0008-8846(99)00074-5.

[3] J. Davidovits, Geopolymers – inorganic polymeric new materials, J. Therm. Anal. 37 (1991) 1633–1656, https://doi.org/10.1007/Bf01912193.

[4] W.K.W. Lee, J.S.J. van Deventer, The effect of ionic contaminants on the early-age properties of alkali-activated fly ash-based cements, Cem. Concr. Res. 32 (2002) 577–584, https://doi.org/10.1016/S0008-8846(01)00724-4.

[5] A.A.M. Neto, M.A. Cincotto, W. Repette, Drying and autogenous shrinkage of pastes and mortars with activated slag cement, Cem. Concr. Res. 38 (2008) 565–574, https://doi.org/10.1016/j.cemconres.2007.11.002.

[6] P.C. Aïtcin, R.J. Flatt, Science and Technology of Concrete Admixtures, Woodhead Publishing, Cambridge, 2015.

[7] F. Beltzung, F.H. Wittmann, Role of disjoining pressure in cement based materials, Cem. Concr. Res 35 (2005) 2364–2370, https://doi.org/10.1016/j.cemconres.2005.04.004.

[8] G.W. Scherer, Drying, shrinkage, and cracking of cementitious materials, Transport Porous Med. 110 (2015) 311–331, https://doi.org/10.1007/s11242-015-0518-5.

[9] H.L. Ye, A. Radlinska, Shrinkage mechanisms of alkali-activated slag, Cem. Concr. Res 88 (2016) 126–135, https://doi.org/10.1016/j.cemconres.2016.07.001.

[10] H.L. Ye, C. Cartwright, F. Rajabipour, A. Radlinska, Understanding the drying shrinkage performance of alkali-activated slag mortars, Cem. Concr. Comp. 76 (2017) 13–24, https://doi.org/10.1016/j.cemconcomp.2016.11.010.

[11] P.K. Mehta, P.J.M. Monteiro, Concrete: Microstructure, Properties, and Materials, third ed., McGraw-Hill, New York, 2006.

[12] G. Sant, The influence of temperature on autogenous volume changes in cementitious materials containing shrinkage reducing admixtures, Cem. Concr. Comp. 34 (2012) 855–865, https://doi.org/10.1016/j.cemconcomp.2012.04.003.

[13] P. Lura, B. Pease, G.B. Mazzotta, F. Rajabipour, J. Weiss, Influence of shrinkage-reducing admixtures on development of plastic shrinkage cracks, ACI Mater. J. 104 (2007) 187–194. https://doi.org/10.14359/18582.

[14] D.P. Bentz, Influence of shrinkage-reducing admixtures on early-age properties of cement pastes, J. Adv. Concr. Technol. 4 (2006) 423–429, https://doi.org/10.3151/Jact.4.423.

[15] M. Palacios, F. Puertas, Effect of shrinkage-reducing admixtures on the properties of alkali-activated slag mortars and pastes, Cem. Concr. Res. 37 (2007) 691–702, https://doi.org/10.1016/j.cemconres.2006.11.021.

[16] C. Bilim, O. Karahan, C.D. Atis, S. Ilkentapar, Influence of admixtures on the properties of alkali-activated slag mortars subjected to different curing conditions, Mater Des. 44 (2013) 540–547, https://doi.org/10.1016/j.matdes.2012.08.049.

[17] V. Bilek, L. Kalina, R. Novotny, J. Tkacz, L. Parizek, Some issues of shrinkage-reducing admixtures application in alkali-activated slag systems, Materials 9 (2016), https://doi.org/10.3390/Ma9060462.

[18] F. Collins, J.G. Sanjayan, Effect of pore size distribution on drying shrinkage of alkali-activated slag concrete, Cem. Concr. Res. 30 (2000) 1401–1406, https://doi.org/10.1016/S0008-8846(00)00327-6.

[19] J.A. Zhou, G.A. Ye, K. van Breugel, Characterization of pore structure in cement-based materials using pressurization-depressurization cycling mercury intrusion porosimetry (PDC-MIP), Cem. Concr. Res. 40 (2010) 1120–1128, https://doi.org/10.1016/j.cemconres.2010.02.011.

[20] D.B. Kumarappa, S. Peethamparan, M. Ngami, Autogenous shrinkage of alkali activated slag mortars: basic mechanisms and mitigation methods, Cem. Concr. Res. 109 (2018) 1–9, https://doi.org/10.1016/j.cemconres.2018.04.004.

[21] J. Weiss, P. Lura, F. Rajabipour, G. Sant, Performance of shrinkage-reducing admixtures at different humidities and at early ages 638-638, ACI Mater. J. 105 (2008). https://doi.org/10.14359/19977.

[22] D.P. Bentz, M.R. Geiker, K.K. Hansen, Shrinkage-reducing admixtures and early-age desiccation in cement pastes and mortars, Cem. Concr. Res. 31 (2001) 1075–1085, https://doi.org/10.1016/S0008-8846(01)00519-1.

[23] G. Sant, B. Lothenbach, P. Juilland, G. Le Saout, J. Weiss, K. Scrivener, The origin of early age expansions induced in cementitious materials containing shrinkage reducing admixtures, Cem. Concr. Res. 41 (2011) 218–229, https://doi.org/10.1016/j.cemconres.2010.12.004.

[24] S. Chen, H. Zhao, Y. Chen, D. Huang, Y. Chen, X. Chen, Experimental study on interior relative humidity development in early-age concrete mixed with shrinkage-reducing and expansive admixtures, Constr. Build. Mater. 232 (2020), https://doi.org/10.1016/j.conbuildmat.2019.117204.

[25] Z.H. He, C.X. Qian, Internal relative humidity and creep of concrete with modified admixtures, Prog. Nat. Sci.-Mater. 21 (2011) 426–432, https://doi.org/10.1016/S1002-0071(12)60079-3.

[26] F.H. Wittmann, F. Beltzung, Fundamental aspects of the interaction between hardened cement paste and water applied to improve prediction of shrinkage and creep of concrete: a critical review, J. Sustain. Cem.-Based 5 (2016) 106–116, https://doi.org/10.1080/21650373.2015.1091998.

[27] C.J. Shi, R.L. Day, A calorimetric study of early hydration of alkali-slag cements, Cem. Concr. Res. 25 (1995) 1333–1346, https://doi.org/10.1016/0008-8846(95)00126-W.

[28] A.R. Brough, M. Holloway, J. Sykes, A. Atkinson, Sodium silicate-based alkali-activated slag mortars Part II. The retarding effect of additions of sodium chloride or malic acid, Cem. Concr. Res. 30 (2000) 1375–1379, https://doi.org/10.1016/S0008-8846(00)00356-2.

[29] A. Gruskovnjak, B. Lothenbach, L. Holzer, R. Figi, F. Winnefeld, Hydration of alkali-activated slag: comparison with ordinary Portland cement, Adv. Cem. Res. 18 (2006) 119–128, https://doi.org/10.1680/adcr.2006.18.3.119.

[30] A. Fernandez-Jimenez, F. Puertas, I. Sobrados, J. Sanz, Structure of calcium silicate hydrates formed in alkaline-activated slag: influence of the type of alkaline activator, J. Am. Ceram. Soc. 86 (2003) 1389–1394, https://doi.org/10.1111/j.1151-2916.2003.tb03481.x.

[31] S. Mindess, J.F. Young, Concrete, Prentice-Hall, Englewood Cliffs, N.J., 1981.

[32] S.P. Shah, M.E. Karaguler, M. Sarigaphuti, Effects of shrinkage-reducing admixtures on restrained shrinkage cracking of concrete, ACI Mater. J. 89 (1992) 289–295. https://doi.org/10.14359/2593.

[33] L. Kalina, V. Bilek, E. Bartonickova, J. Krouska, Polypropylene glycols as effective shrinkage-reducing admixtures in alkali-activated materials, ACI Mater. J. 115 (2018) 251–256. https://doi.org/10.14359/51701099.

[34] F. Wittmann, H. Splittgerber, K. Ebert, Vanderwaals force at small distances, Z. Phys. 245 (1971) 354, https://doi.org/10.1007/Bf01400699.

[35] H. Splittgerber, F. Wittmann, Influence of adsorbed water films on vanderwaals forces between quartz glass surfaces, Surf. Sci. 41 (1974) 504–514, https://doi.org/10.1016/0039-6028(74)90066-1.

[36] K.J. Folliard, N.S. Berke, Properties of high-performance concrete containing shrinkage-reducing admixture, Cem. Concr. Res. 27 (1997) 1357–1364, https://doi.org/10.1016/S0008-8846(97)00135-X.

[37] V. Corinaldesi, Combined effect of expansive, shrinkage reducing and hydrophobic admixtures for durable self compacting concrete, Constr. Build. Mater. 36 (2012) 758–764, https://doi.org/10.1016/j.conbuildmat.2012.04.129.

[38] V. Bilek, L. Kalina, E. Bartonickova, J. Porizka, Evaluation of the surfactant leaching from alkali-activated slag-based composites using surface-tension measurements, Mater. Technol. 53 (2019) 33–38. https://doi.org/10.17222/mit.2018.148.

[39] S. Partyka, S. Zaini, M. Lindheimer, B. Brun, The adsorption of non-ionic surfactants on a silica-gel, Colloid Surf. 12 (1984) 255–270, https://doi.org/10.1016/0166-6622(84)80104-3.

[40] R. Denoyel, J. Rouquerol, Thermodynamic (including microcalorimetry) study of the adsorption of nonionic and anionic surfactants onto silica, kaolin, and alumina, J. Colloid Interf. Sci. 143 (1991) 555–572, https://doi.org/10.1016/0021-9797(91)90287-I.

[41] Z.B. Liu, D.A. Edwards, R.G. Luthy, Sorption of nonionic surfactants onto soil, Water Res. 26 (1992) 1337–1345, https://doi.org/10.1016/0043-1354(92)90128-Q.

[42] N. Narkis, B. Bendavid, Adsorption of non-ionic surfactants on activated carbon and mineral clay, Water Res. 19 (1985) 815–824, https://doi.org/10.1016/0043-1354(85)90138-1.

[43] C. Shi, P.V. Krivenko, D.M. Roy, Alkali-Activated Cements and Concretes, Taylor & Francis, London, New York, 2006.

[44] S.J. Song, H.M. Jennings, Pore solution chemistry of alkali-activated ground granulated blast-furnace slag, Cem. Concr. Res. 29 (1999) 159–170, https://doi.org/10.1016/S0008-8846(98)00212-9.

[45] Z. Rajaokarivonyandriambololona, J.H. Thomassin, P. Baillif, J.C. Touray, Experimental Hydration of 2 Synthetic Glassy Blast-Furnace Slags in Water and Alkaline-Solutions (Naoh and Koh0.1n) at 40-Degrees-C – Structure, Composition and Origin of the Hydrated Layer, J. Mater. Sci. 25 (1990) 2399–2410, https://doi.org/10.1007/Bf00638034.

[46] C. Labbez, B. Jonsson, I. Pochard, A. Nonat, B. Cabane, Surface charge density and electrokinetic potential of highly charged minerals: experiments and Monte Carlo simulations on calcium silicate hydrate, J. Phys. Chem. B 110 (2006) 9219–9230, https://doi.org/10.1021/jp057096+.

[47] A. Kashani, J.L. Provis, G.G. Qiao, J.S.J. van Deventer, The interrelationship between surface chemistry and rheology in alkali activated slag paste, Constr. Build. Mater. 65 (2014) 583–591, https://doi.org/10.1016/j.conbuildmat.2014.04.127.

[48] P. Somasundaran, S. Krishnakumar, Adsorption of surfactants and polymers at the solid-liquid interface, Colloid Surface A 123 (1997) 491–513, https://doi.org/10.1016/S0927-7757(96)03829-0.

[49] V. Bilek, L. Kalina, R. Novotny, J. Porizka, O. Opravil, F. Soukal, Effect of alcohol structure on hydration of alkali-activated slag, 10th ACI/RILEM International Conference on Cementitious Materials and Alternative Binders for Sustainable Concrete, 2017.

UDK 620.1:661.725.844
Original scientific article/Izvirni znanstveni članek

ISSN 1580-2949
MTAEC9, 54(3)349(2020)

EFFECT OF AMINO ALCOHOL ADMIXTURES ON ALKALI-ACTIVATED MATERIALS

VPLIV AMINO-ALKOHOLNIH DODATKOV NA ALKALNO AKTIVIRANE MATERIALE

Lukáš Kalina[*], **Vlastimil Bílek Jr.**, **Eva Bartoníčková**

Brno University of Technology, Faculty of Chemistry, Purkyňova 118, 612 00 Brno, Czech Republic

Prejem rokopisa – received: 2019-07-15; sprejem za objavo – accepted for publication: 2020-01-29

doi:10.17222/mit.2019.150

One of the most important technological problems associated with alkali-activated materials (AAM) is large shrinkage. A possible solution to decrease the extensive drying shrinkage of these materials is the use of shrinkage-reducing admixtures (SRAs). The promising group of SRAs, from the perspective of using in AAMs, are amino alcohols. However, the efficiency of reducing the drying shrinkage strongly depends on their chemical structure. Hence, the study is focused on the molecular architecture of amino alcohol surfactants and its relation to the affected properties of alkali-activated blast-furnace slag systems. Selected amino alcohols were tested in terms of the ability to reduce the surface tension of pore solution as well as to influence the drying shrinkage, hydration mechanism and mechanical properties of AAMs. The study confirms that the length and branching of the alkyl chain linked to the amino group play the key role in SRA efficiency. Amino alcohol surfactants with a high-carbon alkyl chain decreased dramatically both the surface tension and the drying shrinkage, but simultaneously negatively affected the process of alkali activation, resulting in a deterioration of the mechanical properties. Conversely, the addition of 0.5 *w*/ % of the surfactants with a low molecular weight, such as 2-(Methylamino)ethanol, showed a slight improvement of the compressive strength after 7 d and 28 d, and at the same time reduced the drying shrinkage by 30 % compared to the reference sample.

Keywords: amino alcohols, admixture, drying shrinkage, alkali-activated materials

Eden od najpomembnejših tehnoloških problemov, ki se nanaša na alkalno aktivirane materiale (AAM) je njihov skrček. Možna rešitev za zmanjšanje znatnega krčenja med sušenjem teh materialov je uporaba dodatkov (SRAs) za njegovo zmanjšanje. Obetajoča skupina SRA dodatkov s stališča njihove uporabe za AAM so amino-alkoholi. Vendar je učinkovitost zmanjšanja krčenja med sušenjem močno odvisna od njihove kemijske strukture. Zato so se avtorji tega prispevka osredotočili na študij arhitekture snovi (surfaktantov), ki aktivno vplivajo na površino amino-alkoholov in njihovo povezavo z vzročnimi lastnostmi alkalno aktiviranih sistemov plavžnih žlinder. Izbrane amino-alkohole so avtorji testirali glede na sposobnost zmanjšanja površinske napetosti porozne (mehurčaste) raztopine, kakor tudi vpliv na krčenje med sušenjem, hidracijske mehanizme in mehanske lastnosti AAM. Študija je potrdila da dolge in razvejane vezi alkalnih verig igrajo ključno vlogo pri dodatkih, ki učinkovito zmanjšujejo krčenje. Amino-alkoholni surfaktanti z visoko vsebnostjo ogljiko-alkilnih vezi močno zmanjšujejo tako površinsko napetost kot tudi krčenje med sušenjem, ki pa žal istočasno negativno vpliva na proces alkalne aktivacije, kar posledično vodi do poslabšanja mehanskih lastnosti. Nasprotno temu pa dodatek 0,5 masnih % površinsko aktivne snovi z majhno molekularno maso kot je 2-(metilamino)etanol kaže rahlo izboljšanje tlačne trdnosti po 7 in 28 dneh in istočasno zmanjšanje skrčka med sušenjem za 30 % v primerjavi z referenčnimi vzorci.

Ključne besede: amino-alkoholi, mešanice, skrček po sušenju, alkalno aktivirani materiali

1 INTRODUCTION

From the general point of view, shrinkage-reducing admixtures (SRAs) are organic surfactants that reduce the surface tension of the pore solution of water films that cover the solid surfaces in cementitious materials.[1] The utilization of SRAs was introduced in 1983 in the study by T. Sato,[2] where chemical admixtures based on polyoxyalkylene glycol alkyl ether were used. Nowadays, the SRAs are characteristic for their non-ionic nature preventing the adsorption of the additive to the hydration products. The typical chemical compounds used for SRAs belong to the groups of mono-alcohols, glycols, alkylether oxyalkylene glycols and polymeric surfactants or their mutual combination, having a synergic effect in enhancing the shrinkage reduction. The vast majority of commercial SRAs are designed for ordinary Portland cements (OPCs); therefore, their efficiency in other inorganic binders may vary significantly.

Alkali-activated materials (AAMs) represent a group of inorganic materials characterized by a pore solution with a high pH;[3] therefore, the molecular design of any organic admixture plays a key role. The same applies to SRAs. The searching for a suitable type of SRA designed especially for AAMs turned out to be complicated, despite the fact that shrinkage is one of the most important technological problems related to many alkali-activated systems. Until now, only several studies have been focused on the organic admixtures affecting the shrinkage of AAMs.[4]

M. Palacios and F. Puertas[5] studied the effect of polypropylene glycol-based SRA on the shrinkage and other properties of water-glass-activated slag (4 % Na_2O). At a

---

*Corresponding author's e-mail:
kalina@fch.vut.cz (Lukáš Kalina)

relative humidity of 50 % the drying shrinkage of alkali-activated slag mortars was reduced by approximately 7 % and 35 % for doses of SRA of 1 % and 2 %, respectively, while the shrinkage reduction at the relative humidity of 99 % was considerably greater: about 50 % and 75 % for the same doses. Also, C. Bilim et al.[6,7] used SRA based on polypropylene glycol to mitigate the shrinkage of alkali-activated slag mortars. Again, the drying shrinkage as well as the shrinkage during the moist curing was significantly reduced (up to about 40 % after 180 days) for either liquid sodium silicate or solid sodium metasilicate. The SRA based on polypropylene glycols with different molecular weights was the subject of an investigation by L. Kalina et al.[8] as well. The study demonstrated that increasing the length of the polymeric chain decreases the surface tension, but also fundamentally changes the pore size distribution, affecting the total shrinkage of alkali-activated blast-furnace slag. The effect of polyethylene glycols on the drying shrinkage of water-glass-activated slag was studied by V. Bilek et al.[9] The results showed that the efficiency of the shrinkage reduction increased with the increasing molecular weight of the tested glycols.

It is evident that the research in this area was primarily focused on the surfactants based on alkylene glycols. Another alternative may be amino alcohols. These surfactants provide an essential benefit in comparison with alkylene glycols. One of the important properties regarding the SRA's action is the dispersion of used surfactants within the alkaline solution. Amino alcohols show a high dispersibility range in the pore solution because they contain hydrophilic groups, which increase their hydrophile lipophile balance (HLB) value.[10]

Therefore, this study deals with the efficiency assessment of amino alcohol-based SRAs in alkali-activated blast-furnace slag systems. The molecular structure of the used surfactants is evaluated in terms of affecting the character and properties of the prepared alkali-activated materials.

2 EXPERIMENTAL PART

2.1 Materials and sample preparation

Blast-furnace slag (BFS) with a Blaine fineness of 400 m^2/kg and the chemical composition given in **Table 1** was chosen as the primary aluminosilicate material for the preparation of the alkali-activated samples. The XRD analysis determined more than 90 % of amorphous phase with the content of crystals such as melilite, calcite and merwinite. Sodium water-glass with a silicate module of

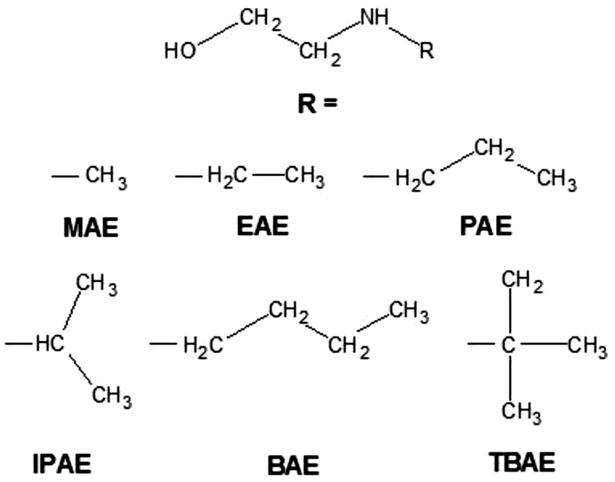

Figure 1: Molecular structure of used amino ethanol surfactants (**MAE**: 2-(Methylamino)ethanol; **EAE**: 2-(Ethylamino)ethanol; **PAE**: 2-(Propylamino)ethanol; **IPAE**: 2-(Isopropylamino)ethanol; **BAE**: 2-(Butylamino)ethanol; **TBAE:** 2-(*tert*-Butylamino)ethanol)

1.98 was used as the alkaline activator. The Na_2O/BFS ratio was adjusted to 4 *w*/%. Amino alcohols with different alkyl chains (summarized in **Figure 1)** were added in the dosage of 0.5 *w*/% by mass of BFS.

2.2 Preparation and physical-mechanical testing of samples

Alkali-activated BFS mortars were prepared as follows. The sand-to-BFS ratio was 3:1 using three different fractions of siliceous sand specified according to the EN-196-1 standard and the water-to-BFS ratio was adjusted to 0.50. The mixing and curing processes were carried out at laboratory temperature (25 °C). Mortar samples with the dimensions of (40 × 40 × 160) mm were cast and further cured under a defined relative humidity (50 %) and then subjected to compressive strength measurements using the strength tester Betonsystem Desttest 3310 after 1, 7 and 28 d. The same process of preparation was applied for (25 × 25 × 285) mm samples. These species were subjected to the shrinkage measurements based on ASTM C596 (25 °C; RH = 50 %). The dynamic surface tension of synthetic pore solutions with 128

different amino alcohol admixtures was measured by the tensiometer BPA-800P (KSV Instruments company) using the maximum-bubble-pressure method. The synthetic pore solution was prepared based on the chemical composition of the real pore solution obtained 24 hours after mixing and determined by ICP-OES. It

Table 1: Chemical compositions of blast furnace slag by XRF analysis

Raw material	Chemical composition / *w*/%									
	SiO_2	Al_2O_3	CaO	MgO	SO_3	Na_2O	K_2O	TiO_2	MnO	Fe_2O_3
blast furnace slag	34.7	9.1	41.1	10.5	1.4	0.4	0.9	1.0	0.6	0.3

means the same time as the drying shrinkage measurement was started.

2.3 Isothermal calorimetry

The evolution of hydration heat was monitored using the TAM Air isothermal microcalorimeter (TA instruments). The measurements of heat evolution were performed at a constant surrounding temperature of 25 °C. When the thermal equilibrium was achieved, the BFS and alkaline activator with a specific SRA were mixed together by injecting the solution into the 15-mL vial and stirring it for 3 min. The samples were made of alkali-activated paste without the standard sand; however, with the same water/BFS and Na_2O/BFS mass ratios that were used for the preparation process of the mortars. The heat evolution was recorded as the heat flow immediately after mixing.

2.4 Microstructure characterization

Microstructure characterization was performed using scanning electron microscopy (Zeiss EVO LS 10) in secondary-electron mode. The working distance during the observation was 9.5 mm and the accelerating voltage was set to 10 kV. All the samples were sputtered with gold before the measurements.

2.5 Mercury-intrusion porosimetry

The total porosity of the samples was determined with a mercury porosimeter (Poremaster Quantachrome Instruments). The working pressure range was from 0.14 MPa to 231 MPa, which covered a pore diameter range from 0.007 µm to 10 µm. The measurements were performed with the following conditions: Hg surface tension was 0.480 N/m, Hg contact angle was 140° and scan mode was chosen to average from 11 points. The intrusion data were normalized by sample weight and volume.

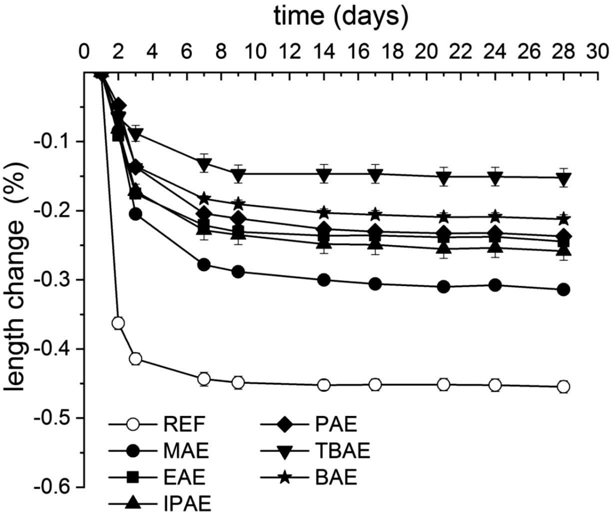

Figure 3: Effect of amino alcohols (0.5 % by weight of BFS) on the drying shrinkage

3 RESULTS AND DISCUSSION

The mechanism of action of SRA was introduced in the study of Sato et al.[2] in 1983. They suggested that the decrease of the surface tension of a cement pore solution tends to reduce the shrinkage due to the elimination of capillary forces. Therefore, the effect of quantity and molecular structure of the used amino alcohols on the surface tension of pore solution were tested. **Figure 2** shows that the surface tension decreases with both a large amount of surfactant and the presence of long or branched alkyl substituents. Moreover, the surface-tension measurement provides information about the effective bulk concentration of surface-active admixtures in AAM. In terms of a good ability to decrease the

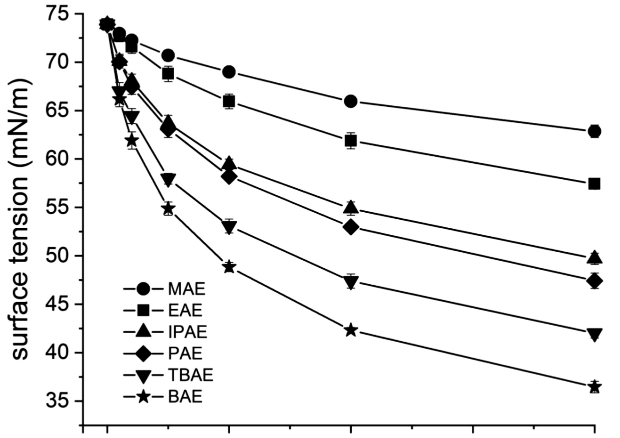

Figure 2: Effect of amino alcohols on the surface tension of the pore solution

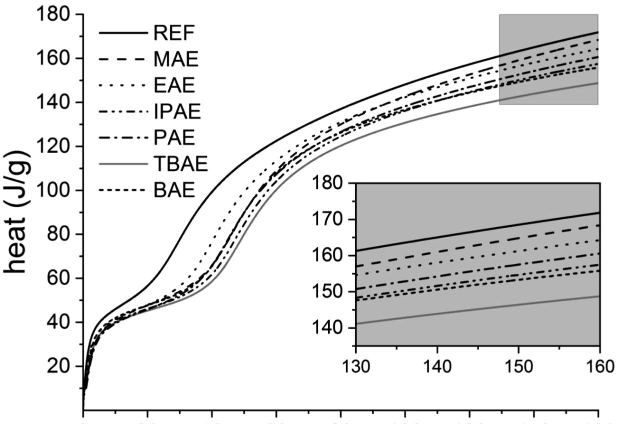

Figure 4: Effect of amino alcohols (0.5 % by weight of BFS) on the total heat evolution

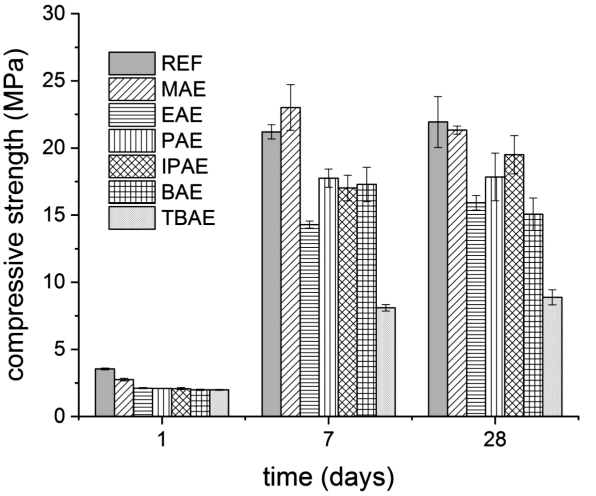

Figure 5: Effect of amino alcohols (0.5 % by weight of BFS) on the compressive-strength development

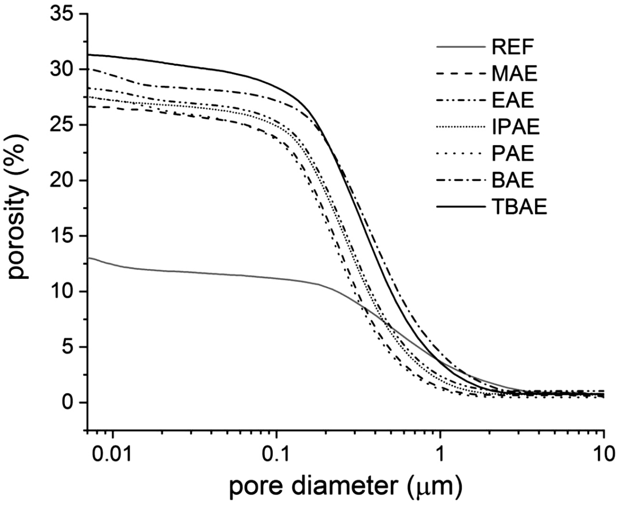

Figure 7: Total porosity measurement of alkali-activated blast-furnace slag with and without amino alcohol admixtures (0.5 % by weight of BFS) after 7 d

surface tension, the addition of 0.5 *w*/% by mass of BFS was used for the preparation of the mortar samples.

The effect of amino alcohol SRA on the reduction of the drying shrinkage is clear from **Figure 3**. It can be seen that the surfactants with a long alkyl chain bonded to the amino group tended to decrease the drying shrinkage. Branched chains of substituents also play an important role. It is evident that 2-(*tert*-Butylamino)alcohol has a higher ability to reduce the drying shrinkage compared to 2-(Butylamino)alcohol. However, we can see that the surface-tension measurement does not fully correlate with the drying shrinkage evolution. Therefore, the fundamental question arises. Are these two parameters directly dependent on each other? The answer can be suggested by the monitoring of the hydration process. The measurement of the total heat evolution (**Figure 4**) during the alkaline activation clearly indicates the negative effect of the SRA content, especially during the early ages of the hydration process. This is also confirmed by the development of compressive strengths (**Figure 5**). The results from the isothermal calorimetry also show that amino alcohols with a low molecular weight such as 2-(Methylamino)alcohol exhibit almost the same total heat evolution as the reference sample without any admixture after 7 d.

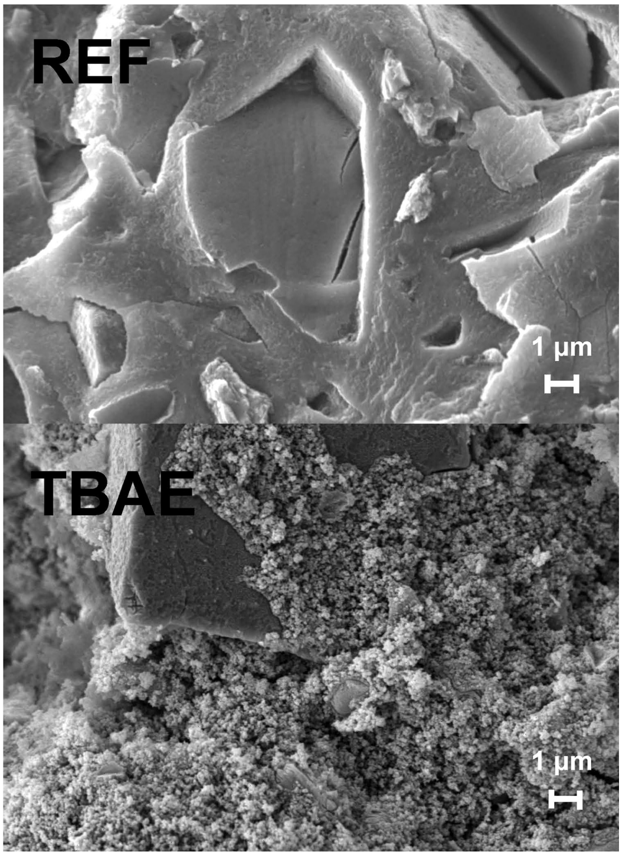

Figure 6: Microstructure of alkali-activated blast-furnace slag without (top) and with 2-(*tert*-Butylamino)alcohol (bottom) after 7 d

It is well known that the total heat evolution is directly related to the binder phase's formation. CASH (calcium-aluminium-silicate-hydrate) gel is the main hydration product in the systems based on the alkaline activation of BFS, which was confirmed by several studies.[11] The amount of formed CASH gel strongly influences the porosity of the a AAM. The materials with higher content of CSH or CASH gels create denser structures with small pores. Such systems contain mainly pores with a diameter lower than 10 nm, which greatly affects the magnitude of the drying shrinkage.[12] Since alkali-activated BFS without SRA has a typical structure, as mentioned above, one would expect the shrinkage strain to be larger than in a material with a coarser microstructure, such as in the case of AAM with TBAE (**Figure 6**). A similar relationship between the adverse effect of the SRA on the AAM hydration resulting in a lower amount of CASH and a more porous microstructure was also observed in previous studies[8,13] where

SRAs-based glycols were used. The changes in total porosity were confirmed by mercury-intrusion porosimetry (**Figure 7**). The samples with the addition of SRA had a significantly higher porosity compared to the reference sample after 7 d. The direct relationship between drying-shrinkage development and the porosity of samples caused by the addition of specific amino alcohol surfactants was clearly observed.

4 CONCLUSIONS

The results suggest that the extent of the drying shrinkage of AAM is mainly controlled by the porosity of the formed structure. In other words, by the quantity of created binder phase, rather than by the decrease of surface tension of the pore solution. Despite the non-ionic character of the used amino alcohol surfactants, the adsorption on the BFS particles, causing the reduction of their solubility in an alkaline environment could be assumed. Promising results indicate the usage of 2-(Methylamino)alcohol. This surface-active admixture in the amount of 0.5 *w*/% by mass of BFS did not negatively influence the mechanical properties after 7 d and 28 d and reduced the drying shrinkage by 30 % compared to the reference sample.

Acknowledgement

This outcome has been achieved with the financial support by the project: GA17-03670S, "Development of shrinkage reducing agents designed for alkali activated systems," with financial support from the Czech science foundation.

5 REFERENCES

[1] P. C. Aïtcin, R. J. Flatt, Science and Technology of Concrete Admixtures, 1st ed., Elsevier, Cambridge 2015, 613

[2] T. Sato, T. Goto, K. Sakai, Mechanism for reducing drying shrinkage of hardened cement by organic additives, Cement Association of Japan Review, **1983**, 52–54

[3] R. R. Lloyd, J. L. Provis, J. S. J. van Deventer, Pore solution composition and alkali diffusion in inorganic polymer cement. Cement and Concrete Research, 40 (**2010**), 1386–1392, doi:10.1016/j.cemconres.2010.04.008

[4] J. L. Provis, J. S. J. van Deventer, Alkali Activated Materials, 1st ed., Springer, London 2014, 388, doi:10.1007/978-94-007-7672-2

[5] M. Palacios, F. Puertas, Effect of shrinkage-reducing admixtures on the properties of alkali-activated slag mortars and pastes, Cement and Concrete Research, 37 (**2007**), 691–702, doi:10.1016/j.cemconres.2006.11.021

[6] C. Bilim, O. Karahan, C. D. Atis, S. Ilkentapar, Influence of admixtures on the properties of alkali-activated slag mortars subjected to different curing conditions, Materials & Design, 44 (**2013**), 540–547, doi:10.1016/j.matdes.2012.08.049

[7] C. Bilim, O. Karahan, C. D. Atis, S. Ilkentapar, Effects of chemical admixtures and curing conditions on some properties of alkali-activated cementless slag mixtures, KSCE Journal of Civil Engineering, 19 (**2015**), 733–741, doi:10.1007/s12205-015-0629-0

[8] L. Kalina, V. Bilek, E. Bartonickova, J. Krouska, Polypropylene Glycols as Effective Shrinkage-Reducing Admixtures in Alkali-Activated Materials, ACI Materials Journal, 115 (**2018**), 251–256, doi:10.14359/51701099

[9] V. Bilek, L. Kalina, R. Novotny, Polyethylene glycol molecular weight as an important parameter affecting drying shrinkage and hydration of alkali-activated slag mortars and pastes, Construction and Building Materials, 166 (**2018**), 564–571, doi:10.1016/j.conbuildmat.2018.01.176

[10] X. W. Guo, Z. M. Rong, X. G. Ying, Calculation of hydrophile-lipophile balance for polyethoxylated surfactants by group contribution method, Journal of Colloid and Interface Science, 298 (**2006**), 441–450, doi:10.1016/j.jcis.2005.12.009

[11] C. Shi, P. V. Krivenko, D. Roy, Alkali-Activated Cements and Concretes, 1st ed., Taylor&Francis, Oxon 2006, 376.

[12] S. Mindess, J. F. Young, D. Darwin, Concrete, 2nd ed., Prentice Hall, NJ 2003, 644

[13] V. Bílek Jr., L. Kalina, R. Novotný, J. Tkacz, L. Pařízek, Some Issues of Shrinkage-Reducing Admixtures Application in Alkali-Activated Slag Systems, Materials 9, 462 (**2016**), doi:10.3390/ma9060462

UDK 620.1:532.612:66.063.4:620.168
Original scientific article/Izvirni znanstveni članek

ISSN 1580-2949
MTAEC9, 53(1)33(2019)

EVALUATION OF THE SURFACTANT LEACHING FROM ALKALI-ACTIVATED SLAG-BASED COMPOSITES USING SURFACE-TENSION MEASUREMENTS

UPORABA MERITEV POVRŠINSKE NAPETOSTI ZA OCENO IZLUŽEVANJA POVRŠINSKO AKTIVNE SNOVI IZ KOMPOZITOV NA OSNOVI ALKALNO AKTIVIRANE ŽLINDRE

Vlastimil Bílek Jr., Lukáš Kalina, Eva Bartoníčková, Jaromír Pořízka
Brno University of Technology, Faculty of Chemistry, Materials Research Centre, Purkyňova 118, 612 00 Brno, Czech Republic

Prejem rokopisa – received: 2018-07-13; sprejem za objavo – accepted for publication: 2018-09-06

doi:10.17222/mit.2018.148

Nowadays, there are many efforts to reduce CO_2 emissions in the building industry, particularly through the use of some alternative binders to those based on Portland cement. One promising group of such binders includes binders based on alkali-activated slag (AAS). However, extensive drying, autogenous shrinkage and the associated cracking prevent AAS from being widely utilized in practice. A possible solution could be the application of shrinkage-reducing admixtures, whose molecules present in the pore solution reduce its surface tension and thus mitigate the AAS shrinkage. However, if AAS comes into contact with water, shrinkage-reducing admixtures can be leached and its effectiveness reduced. This work tries to evaluate the amount of surfactant leached from the AAS-based mortars using a very simple surface-tension (ST) measuring technique. Mortars based on AAS with and without 2 % of PEG varying in molecular weight (MW) were prepared. Waterglass with a SiO_2-to-Na_2O ratio equal to 2.0 was used at a dose corresponding to 8 % Na_2O with respect to the slag weight. Mortar specimens were prepared and sealed for 24 h, 3 d and 7 d. Then they were demolded and immersed in demineralized water, whose ST was monitored over time. During the early stages (from minutes to a few hours) the ST dropped rapidly, while it remained approximately constant after a few days, which indicates that organic molecules are leached from the AAS specimens very quickly. It was observed that a relatively small fraction of PEGs can be leached out, which indicates that organic molecules are rather bound in the matrix, unable to reduce the ST of the pore solution.

Keywords: Alkali-activated slag, polyethylene glycol, leaching, surface tension

Dandanes v gradbeništvu vlagajo velike napore za zmanjšanje emisij CO_2, še posebej z uporabo nekaterih Portland cementu alternativnih veziv. Ena od takšnih obetajočih skupin so veziva na osnovi alkalno aktiviranih žlinder (AAS; angl.: alkali-activated slag). Vendar hitro sušenje, avtogeno krčenje, ter s tem povezano pokanje preprečujejo široko uporabo AAS v praksi. Možna rešitev bi lahko bila uporaba dodatkov, ki zmanjšujejo krčenje AAS. Molekule teh dodatkov v porah raztopine zmanjšajo njeno površinsko napetost in tako zmanjšajo krčenje AAS. Če pa je AAS v stiku z vodo, pride do izluževanja dodatkov za zmanjševanje krčenja, pri čemer se zmanjša njihova učinkovitost. V tej raziskavi so avtorji poizkušali oceniti vsebnost izluženega surfaktanta (površinsko aktivne snovi) iz malt na osnovi AAS z uporabo zelo enostavne merilne tehnike merjenja površinske napetosti (ST; angl.: surface tension). Pripravili so malte s spreminjajočo se molekularno maso (MW, angl.: molecular weight) na osnovi AAS brez in z dodatkom 2-% polietilenglikola (PEG). Uporabili so vodno steklo z razmerjem SiO_2:Na_2O=2, kar odgovarja vsebnosti 8 % Na_2O glede na maso žlindre. Pripravili so vzorce malt in jih zapečatili oz. jih za 24 h, 3 d in 7 d zaprli v modele. Nato so modele odprli in malte potopili v destilirano vodo, ter ves čas merili njeno površinsko napetost. V začetnih stadijih opazovanja (nekaj minut do nekaj ur) je površinska napetost vode hitro padala, medtem ko se je po nekaj dneh ustalila, kar pomeni, da so se organske molekule iz vzorcev AAS izlužile zelo hitro. Na osnovi opazovanja so ugotovili, da se lahko izluži le relativno majhen delež PEG. To nakazuje na to, da so organske molekule precej vezane na matrico in niso sposobne zmanjšati površinske napetosti porozne raztopine.

Ključne besede: alkalno aktivirana žlindra, polietilen glikol, izluževanje, površinska napetost

1 INTRODUCTION

Alkali-activated materials (AAMs) belong to the group of alternative binders with the potential to enhance the sustainability of the building industry, since they are usually based on secondary raw materials or waste materials, and thus can decrease greenhouse-gas emissions, save energy, etc. The most common sources of aluminosilicate precursors for AAMs are metakaolin, fly ash and granulated blast-furnace slag. The latter, particularly when a waterglass is used for activation, often achieves excellent mechanical properties, even at room temperature, that are similar or even better compared to those of Portland-cement-based materials.[1] However, extensive drying and autogenous shrinkage, resulting in cracking and deterioration of the material properties in general, limit the use of AAS in practice.

Several possible approaches to reduce AAS shrinkage can be found in literature, e.g., the use of mineral admixtures,[2,3] curing at elevated temperatures[4,5] or internal curing.[6] Also, the use of shrinkage-reducing admixtures (SRAs) or generally surface-active substances was reported as being an effective method for AAS shrinkage reduction.[7–10] In these studies, the beneficial effects of

---

*Corresponding author e-mail:
bilek@fch.vut.cz

SRAs were usually attributed to the changes in pore structure and a reduction of the surface tension, which is, according to capillary-pressure theory, closely related to shrinkage-inducing forces in desiccating (of self-desiccating) material.

These effects can be, in terms of capillary-pressure theory, illustrated by the Young-Laplace equation (Equation (1)), according to which, for the spherical meniscus inside the pore partially filled with liquid, the pressure difference Δp between the liquid and the vapor phase is proportional to the surface tension γ and inversely proportional to the pore radius r; $\cos\theta$ is the wetting angle. Nevertheless, it was summarized[11] that capillary-pressure theory can explain the drying shrinkage only for pores larger than approximately 10 nm and a relative humidity higher than 40–50 %. Some authors[12,13] contest the role of capillary action itself and emphasize that the disjoining pressure is at the origin of the shrinkage. The disjoining pressure is a superposition of attractive van der Waals forces, repulsive electric forces and structural forces.

$$\Delta p = -\frac{2\gamma}{r}\cos\theta \tag{1}$$

It is clear (Equation (1)) that if SRAs would act against AAS shrinkage in accordance with the capillary-pressure theory, they have to be present in a pore solution and able to adsorb at the liquid-air interface to reduce its energy (surface tension). However, this also means that at least part of this portion of the SRAs can be leached either during the water curing or in contact with the surrounding water in practice, and its effectiveness consequently reduced. These issues were widely studied by Eberhardt[14] on Portland-cement-based specimens, who observed that 40 % of the studied SRA was associated with hydration products. Such an immobile fraction of the SRA would only be released with the dissolution of the solid matrix itself. Although it cannot reduce the shrinkage via a reduction of the surface-tension decrease, its beneficial effect on the shrinkage can be explained by the disjoining-pressure theory. On the other hand, the mobile fraction of SRA can be removed from the specimen, particularly by diffusion.

Therefore, the purpose of this paper is to pioneer SRA leaching issues for AAS-based mortars. More specifically, the influence of polyethylene glycol's molecular weight, as well as the time of curing before immersion of the specimens in water, on the leaching extent and rate was investigated. The amount of leached PEG was determined using a dynamic surface-tension measurement. Additionally, this study follows our previous one,[10] where the effect of PEG MW on the drying shrinkage and other properties of AAS mortars and pastes was investigated. In that case, the specimens for drying shrinkage and mechanical properties testing were cured in water for 3 d and thus the study of the impact of leaching on the obtained results is at hand.

2 EXPERIMENTAL PART

2.1 Materials and mortar composition

Common ground granulated blast-furnace slag from the Czech production (Kotouč Štramberk, spol. s r.o) with a Blaine fineness of 400 m^2/kg was activated by sodium waterglass (Vodní sklo, a.s.) with a silicate modulus, i.e., SiO_2-to-Na_2O molar ratio, equal to 2.0. Siliceous sand with a maximum grain size of 2 mm was used as a fine aggregate. The Na_2O (introduced into the system by waterglass) to slag ratio, water-to-slag ratio and sand-to-slag ratio were the same for all the prepared mortars: 0.08, 0.46 and 3.0 by weight, respectively. The mortars differed in the organic admixture used. One mortar type was the reference without any other additive (Ref.), while the other five types were modified by polyethylene glycol in the wide range of MW from monomer (ethylene glycol, EG) up to polyethylene glycol of 35,000 g/mole, namely, PEG400, PEG2000, PEG10000 and PEG35000. Their doses were 2 % with respect to the slag weight.

2.2 Specimen preparation and curing

The mixing procedure was the same as that prescribed for Portland-cement testing in EN 196-1. After the mixing, mortars were cast into a polypropylene cylindrical container with a diameter of 33 mm and a height of 70 mm. Then the containers were sealed and kept at 25 °C until the start of the leaching experiments, i.e., 24 h, 3 d or 7 d. After the desired time, the specimens were demolded and immersed in demineralized water for 7 d, during which time the dynamic surface tension of the leachate was measured. After the 7 d of leaching, water was exchanged and the ST of the renewed leachate determined after 24 h. The weight of

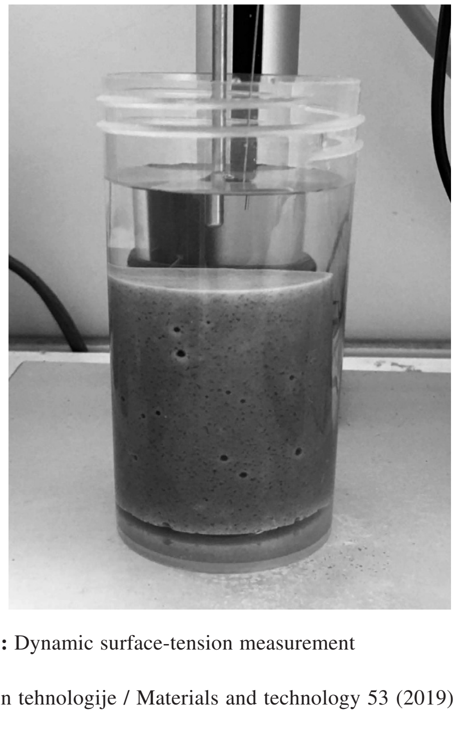

Figure 1: Dynamic surface-tension measurement

water was the same as the weight of the sample in both cases. One or two specimens for the reference mortar and two or three specimens for the PEG-modified mortars were used for each test series.

2.3 Dynamic surface-tension measurement

Before the start of the dynamic ST measurement (**Figure 1**), leachate in a container containing the specimen was homogenized by gentle gyration. The dynamic ST was determined using a bubble pressure tensiometer BPA 800P (KSV Instruments, Ltd.) after (0.5, 2.5, 5 and 24) h of leaching, and during the following days, as was mentioned above. A capillary with a diameter of 0.130 mm was immersed 5 mm under the leachate surface and the bubble life time was set to 0.1 s. For each time of the test, the values of the ST were recorded every 20 s during the several minutes and then averaged. Synthetic leachates (see following section) used for the determination of the amount of leached PEG were tested with the same settings.

2.4 Evaluation of the amount of leached PEG

The amount of leached PEG was calculated using calibration curves obtained from the dynamic ST measurement of the synthetic leachates containing various amounts of the desired PEG. The synthetic leachates were prepared on the basis of the silicon and sodium content in the leaching water after the first 7 days of leaching, determined using inductively coupled plasma optical emission spectroscopy (ICP-OES). The presence of other elements was neglected due to their very low content in the leachate. Synthetic leachates were prepared by the dilution of waterglass and sodium hydroxide by demineralized water in a volumetric flask, according to **Table 1**.

Table 1: Average Si and Na contents in the leachates after each curing time and the amounts of waterglass and 50 % NaOH used for the synthetic leachates' preparation

curing series	Si (mg/L)	Na (mg/L)	waterglass (g/L)	50 % NaOH (g/L)
24 h	158.6	4254	1.07	11.28
3 d	126.8	3461	0.857	9.19
7 d	118.2	2845	0.799	7.51

3 RESULTS

The development of the ST of the leachates is given in **Figure 2**. It can be seen that except for their monomer, all the PEGs decreased the dynamic ST rapidly within the first 30 min, while this did not change markedly during the following hours and days. On the other hand, all the leachates after the exchange of water reached the same ST values. To assess the amount of leached PEG, calibration curves were determined using synthetic leachate and known additions of PEG. The obtained results are in **Figure 3**. The amount of leached PEG was determined as its concentration (*w*/%) in between the two neighboring points using an interpolation with the assumption that the dependence of ST on the weight concentration is linear between each two measured points and compared with the maximum theoretical PEG concentration (0.42 %). Using this approach, the mass fraction of easily leachable PEG from the total PEG amount was evaluated (**Figure 4**). It is clear that an

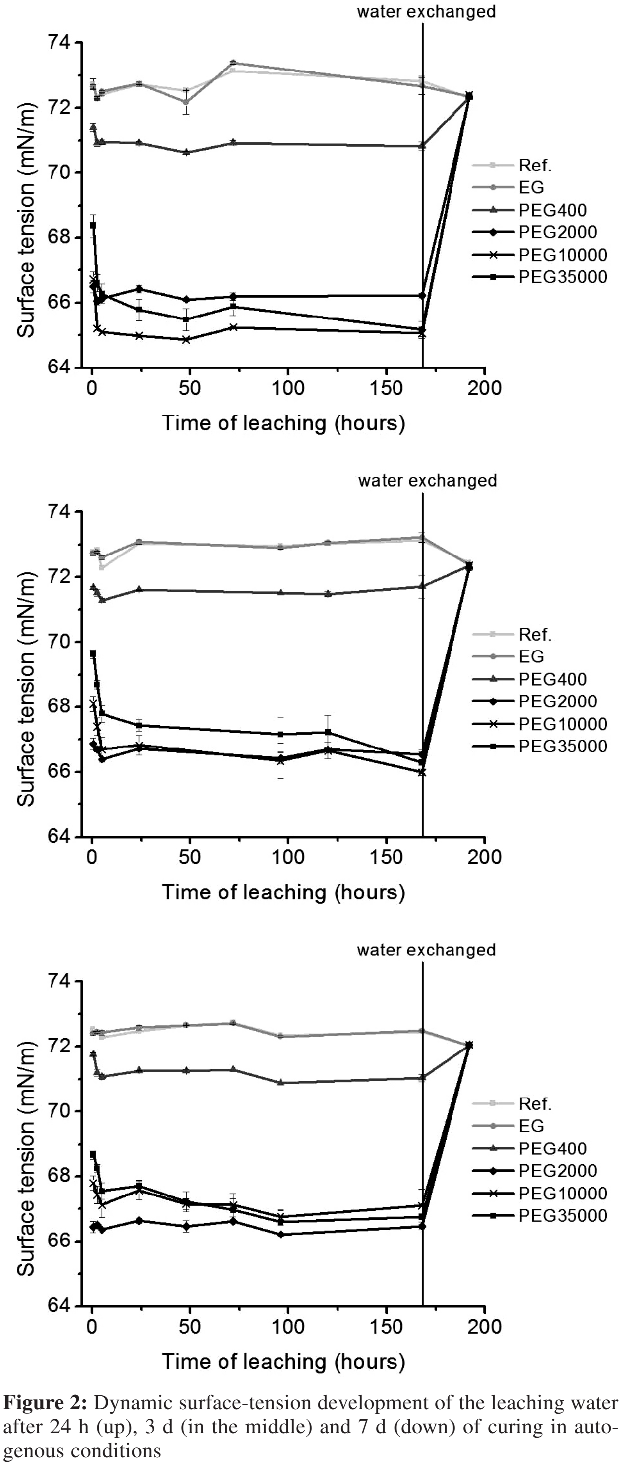

Figure 2: Dynamic surface-tension development of the leaching water after 24 h (up), 3 d (in the middle) and 7 d (down) of curing in autogenous conditions

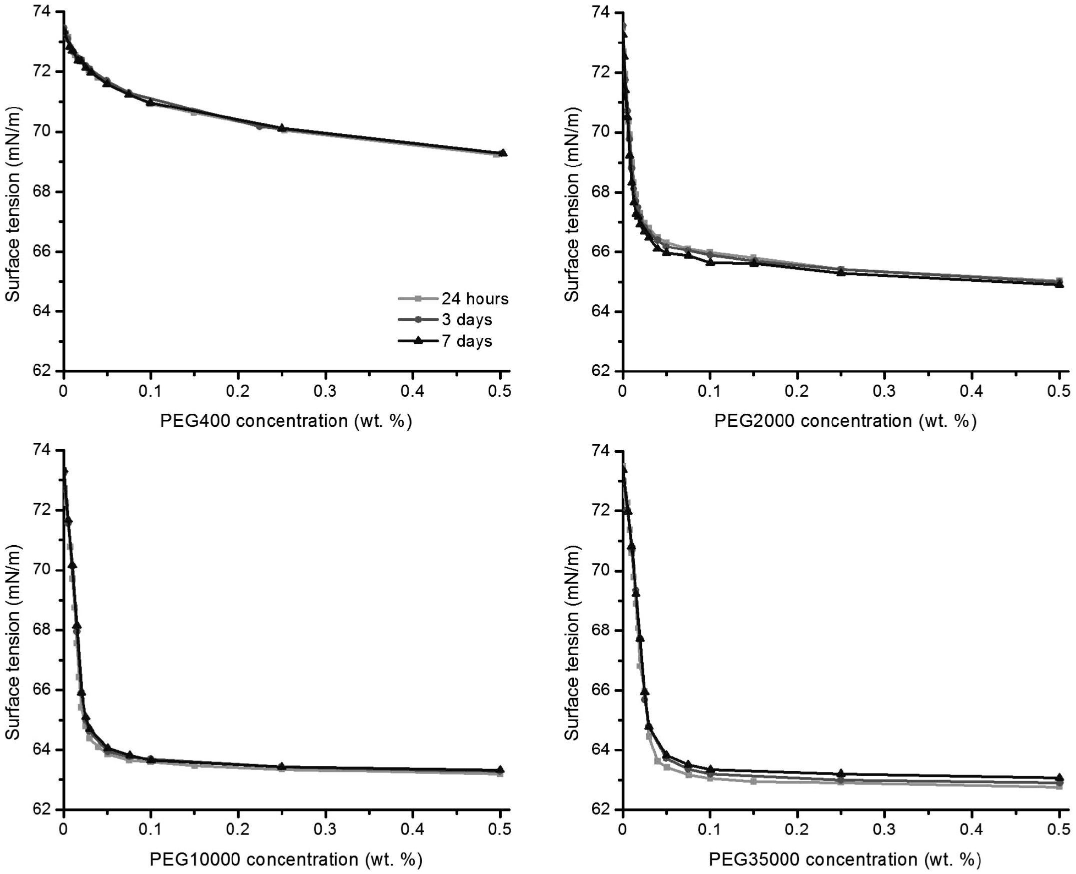

Figure 3: Calibration curves determined using synthetic leachates for each curing time

increase in PEG MW resulted in a decrease of its leachable portion, as it was, e.g., for 24 h of sealed curing calculated to be (28, 14, 5.4 and 6.3) % for PEG400, 2000, 10000 and 35000, respectively. Also, a prolonged time of curing before the leaching experiment, particularly between 24 h and 3 d, resulted in an increased immobilization of the PEGs. The higher leached amount of PEG400 after 7 d compared to 3 d is probably a random error. It also, together with the lengths of the error bars, shows a general disadvantage of the use of ST measurements for a determination of the leached amount of an organic substance. If the ST concentration dependence is flat, i.e., if the substance is not effective in reducing the ST (such as PEG400) or at high surfactant concentrations (above approximately 0.05 % in our cases), even a slight change in the measured ST means a large change in the calculated surfactant concentration. In contrast, the more steep the ST change is, the more precise the results are.

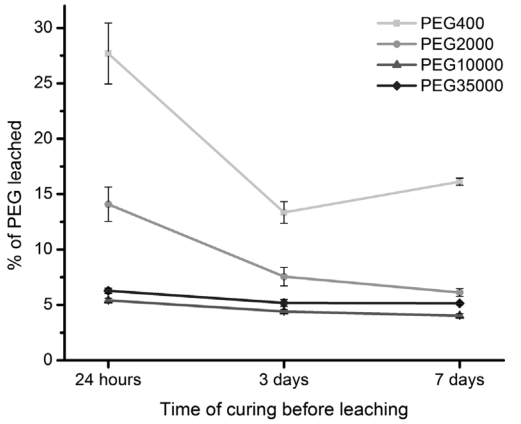

Figure 4: Effect of PEG's molecular weight and time of curing on the amount of PEG leached during the first 7 d of leaching

4 DISCUSSION

As is well known and as we also reported earlier,[10] the ST-reducing ability of surfactants depends on their molecular weight. Therefore, it is not possible to estimate the amount of leached PEG only from the ST of the leachate (**Figure 2**), but the use of calibration curves (**Figure 3**) is necessary. However, the presence of other ions in the leachate can affect its ST as well as the performance of organic admixtures, and hence synthetic leachates instead of pure water should be used. In our case, the gradual leaching of ions from the specimens, particularly silicon and sodium (**Table 1**), plays an important role and can also affect the ST's development. This is probably the reason why the ST of the reference and EG leachate rather increased during ongoing leaching and was usually a few tenths higher than those determined for demineralized water. On the other hand, the ST of the second leachate from the Ref and EG specimens was lower compared to that of the first leachate and very close to that of demineralized water, since most of the Si and Na leached during the first cycle. The same ST values of the second leachates as for the Ref and EG were observed for all the other PEG specimens, regardless of the time of curing before the start of leaching, which indicates that the total or at least the vast majority of the leachable fraction of PEG had already been leached at the end of the first leaching cycle.

Eberhardt[14] summarized that the following three mechanisms of leaching can be distinguished: washing out, diffusion and a dissolution process. The very high rate of leaching during its early stages observed in **Figure 2** suggests that washing out is the dominating factor in our case. The diffusion at later leaching stages cannot be excluded, since there is likely a competition between the leaching of ions like Si or Na and surfactant molecules. Therefore, it can be expected that if the latter is of very limited rate, the former prevails and hence the leaching of the surfactant does not lead to a noticeable ST reduction. To investigate this in more detail, some other methods of organic-matter detection could be used, e.g., chromatography.

According to **Figure 2** and **4**, the molecular weight of the used PEG also affected its leaching rate, as well as the amount of leached PEG. While PEG400 and PEG2000 were mostly leached within the first 30 min or 150 min, the longer PEGs (PEG10000 and PEG35000) gradually decreased the ST up to 5 h. This is likely related to their longer chains, which cannot be transported through the specimen as easily as their shorter analogues. Moreover, the longer molecules are more prone to immobilization in the hydration products, which again contributes to a reduction of their mobile fraction. These issues can also explain the decrease in the amount of mobile fraction with increasing molecular weight and the time of curing before the start of the leaching (**Figure 4**). Slightly higher leached amounts of PEG35000 compared to PEG10000 would probably be due to their lower and slower solubility in water and activating solution and the consequent lower homogeneity of the specimens, despite efforts to dissolve and homogenize them as well as possible before the slag and sand addition.

The presented findings have a significant impact on the shrinkage behavior. As we have already presented,[10] MW plays an important role in the shrinkage-reducing ability since EG did not noticeably reduce the drying shrinkage of the AAS mortar, while a further increase in PEG MW had a beneficial effect, particularly up to a molecular weight of 2000 g/mole. The determination of the amount of SRA that can be leached from the specimen and also the SRA ST-reducing ability allows us to support the discussion from the previous paper and even distinguish between the dominating mechanisms of shrinkage reduction. For shorter molecules like PEG400, only a slight ST-reducing ability, together with a relatively high leaching extent, indicate that neither the reduction of the ST by the mobile phase nor the reduction of the disjoining pressure by the presence of immobile PEG molecules, particularly when water curing is applied, can explain the quite high shrinkage reduction by PEG400. This supports our findings that the shrinkage-reducing ability of the PEG400 lies rather in the changes of the pore structure. On the other hand, the presence of longer PEG molecules, which cannot be easily leached, can act against shrinking via a disjoining-pressure mechanism and thus can be more effective in practical applications. However, a too high MW would also be impractical due to solubility and miscibility issues. For the case of PEGs, a MW of around 2000 g/mole (and not more than 10,000 g/mole) would be optimal due to the combination of its relatively high shrinkage-reducing ability and good solubility.

5 CONCLUSIONS

This paper investigated the leaching issues associated with AAS-based fine-grained composites. The amount of leached PEGs, depending on their molecular weight and time of curing before the start of the leaching, was determined using dynamic ST measurements.

Both the leaching rate and particularly the leaching extent of the PEGs decrease with their increasing molecular weight. This has a significant impact on the AAS shrinkage performance.

The leaching rate and extent also decrease with a prolonged time of curing.

For practical applications, the use of SRAs based on rather longer polymeric surfactants can be recommended, since they are more effective in reducing the ST, which favors shrinkage reduction according to the capillary-pressure theory, while its increased immobile fraction can act against shrinkage in terms of the disjoining-pressure theory. Moreover, a reduced leaching extent is important from the environmental viewpoint. On the other hand, for molecules that are too long, miscibility or solubility issues should also be kept in mind.

Acknowledgment

This outcome was achieved with the financial support within the project: Materials Research Centre at FCH BUT- Sustainability and Development, REG LO1211, with financial support from the National Program for Sustainability I (Ministry of Education, Youth and Sports) and GA17-03670S "Development of shrinkage reducing agents designed for alkali activated systems", with financial support from the Czech science foundation.

6 REFERENCES

[1] F. G. Collins, J. G. Sanjayan, Workability and mechanical properties of alkali activated slag concrete, Cem. Concr. Res., 29 (**1999**) 3, 455–458, doi:10.1016/S0008-8846(98)00236-1

[2] N. K. Lee, J. G. Jang, H. K. Lee, Shrinkage characteristics of alkali-activated fly ash/slag paste and mortar at early ages, Cem. Concr. Compos., 53 (**2014**), 239–248, doi:10.1016/j.cemconcomp.2014.07.007

[3] S. Aydin, A ternary optimisation of mineral additives of alkali activated cement mortars, Constr. Build. Mater., 43 (**2013**), 131–138, doi:10.1016/j.conbuildmat.2013.02.005

[4] N. Marjanovic, M. Komljenovic, Z. Bascarevic, V. Nikolic, R. Petrovic, Physical-mechanical and microstructural properties of alkali-activated fly ash-blast furnace slag blends, Ceram. Int., 41 (**2015**) 1, 1421–1435, doi:10.1016/j.ceramint.2014.09.075

[5] T. Bakharev, J. G. Sanjayan, Y. B. Cheng, Effect of elevated temperature curing on properties of alkali-activated slag concrete, Cem. Concr, Res., 29 (**1999**) 10, 1619–1625, doi:10.1016/S0008-8846(99)00143-X

[6] A. R. Sakulich, D. P. Bentz, Mitigation of autogenous shrinkage in alkali activated slag mortars by internal curing, Mater. Struct., 46 (**2013**) 8, 1355–1367, doi:10.1617/s11527-012-9978-z

[7] M. Palacios, F. Puertas, Effect of shrinkage-reducing admixtures on the properties of alkali-activated slag mortars and pastes, Cem. Concr. Res., 37 (**2007**) 5, 691–702, doi:10.1016/j.cemconres.2006.11.021

[8] C. Bilim, O. Karahan, C. D. Atis, S. Ilkentapar, Influence of admixtures on the properties of alkali-activated slag mortars subjected to different curing conditions, Mater. Des., 44 (**2013**), 540–547, doi:10.1016/j.matdes.2012.08.049

[9] L. Kalina, V. Bilek, E. Bartonickova, J. Krouska, Polypropylene glycols as effective shrinkage-reducing admixtures in alkali-activated materials, ACI Mater. J., 115 (**2018**) 2, 251–256, doi:10.14359/51701099

[10] V. Bilek, L. Kalina, R. Novotny, Polyethylene glycol molecular weight as an important parameter affecting drying shrinkage and hydration of alkali-activated slag mortars and pastes, Constr. Build. Mater., 166 (**2018**), 564–671, doi:10.1016/j.conbuildmat.2018.01.176

[11] P. C. Aïtcin, R. J. Flatt, Science and Technology of Concrete Admixtures, 1st ed., Woodhead Publishing: Sawston, Cambridge, UK 2015

[12] F. H. Wittman, Heresies on shrinkage and creep mechanisms, Proc. of the 8th Inter. Conf. on Creep, Shrinkage and Durability of Concrete and Concrete Structures, Japan 2009

[13] F. Beltzung, F. H.Wittmann, Role of disjoining pressure in cement based materials, Cem. Concr. Res., 35 (**2005**) 12, 2364–2370, doi:10.1016/j.cemconres.2005.04.004

[14] A. B. Eberhardt, On the Mechanisms of Shrinkage Reducing Admixtures in Self Consolidating Mortars and Concretes, Ph.D. Thesis, Bauhaus Universität Weimar, Weimar, Germany 2011

ACI MATERIALS JOURNAL TECHNICAL PAPER

Title No. 115-M23

Polypropylene Glycols as Effective Shrinkage-Reducing Admixtures in Alkali-Activated Materials

by Lukáš Kalina, Vlastimil Bílek Jr., Eva Bartoníčková, and Jitka Krouská

In recent years, the use of various nontraditional cements and composites has increased. Alkali-activated materials, especially those based on alkali activation of blast-furnace slag, have considerable potential in construction industry. However, alkali-activated slag binders exhibit significant shrinkage, in some circumstances several times greater than portland cement-based materials, which hinders wider use of these materials in numerous applications. Therefore, the use of specific admixtures suitable for alkali-activated systems is necessary. This paper is consequently focused on testing the efficiency of shrinkage-reducing additives based on polypropylene glycols, as well as their influence on the hydration mechanism and mechanical properties of prepared alkali-activated materials.

Keywords: alkali-activated materials; chemical admixtures; shrinkage reduction.

INTRODUCTION

Whether 50 years ago or nowadays, concrete based on ordinary portland cement (OPC) has been by far the most widely used construction material around the world. It is versatile and durable, but also widely available and cheap.[1] Nevertheless, the process of OPC production is associated with a high rate of carbon dioxide emissions, alterations of the landscape due to the exploitation of quarries, and high energy consumption required for the clinkerization process.[2] Because concrete production continuously increases, it is necessary to search for some alternative non-clinker binders. Alkali-activated materials is a file of a wider mosaic towards sustainable solutions.

From the wide group of these materials, alkali-activated slag (AAS) is probably the most prospective for construction purposes because it generates superior mechanical performance even at room temperature, particularly when it is activated by waterglass.[3] This phenomenon is a consequence of the presence of dissolved silicates in waterglass, which lead to the formation of calcium silicate hydrate (CSH) with a lower Ca/Si ratio and a more cross-linked structure.[4] Last but not least, AAS was reported to be equal or even better than portland cement in terms of durability in aggressive environments,[5] behavior at elevated temperatures,[6] and interfacial transition zone.[7]

On the other hand, AAS has some disadvantages considerably limiting its practical application, particularly its rapid set time[8] and high autogenous and drying shrinkage.[9] The significantly higher shrinkage of AAS compared to portland cement is attributed to its more refined pore structure,[10] the formation of shrinkage-prone silicate gel,[11] and lower creep modulus of its solid skeleton.[12] Previous studies suggest[13-15] that the extensive shrinkage could be solved with the addition of shrinkage reducing admixtures (SRAs) commonly used in concrete technology. For more than 30 years, SRAs have been used to reduce shrinkage of cementitious systems. They generally belong to group of organic compounds called surfactants, which are chemical species with amphiphilic character; that is, they are composed of a hydrophilic head and hydrophobic chain. The main effect in shrinkage reduction consists of a decrease in pore solution surface tension.[16] Due to the very distinct chemistry of the alkali activation process compared with the hydration of portland cement, the efficiency of common SRAs differs. Bílek et al.[17] found that one of the typical chemical compounds (2-methyl-2,4-pentanediol) used in SRAs designed for OPC binders reduces shrinkage only with a high dosage, which negatively influences the mechanical properties of AAS concretes. Very similar results were published by Kalina et al.[18] when they tested commercial SRA based on oxyalkylene glycols. The shrinkage was considerably reduced by half with 1.25 wt.% addition of SRA; however, the same reduction was obtained in compressive strength development. From the wide range of non-ionic surfactants, the SRAs with the structure of polymeric glycols show promising results for their use in alkali-activated materials. Palacios and Puertas[14] reported that SRAs based on polypropylene glycol reduced both autogenous and drying shrinkage significantly. Moreover, the mechanical properties of the specimens with admixture were even better in comparison with reference AAS samples. Therefore, the effect of different polypropylene glycols in terms of chemical structure on the shrinkage behavior, hydration process, and mechanical properties of AAS samples is essential to study.

RESEARCH SIGNIFICANCE

The main obstacle for wider practical use of alkali-activated materials is its significant autogenous and drying shrinkage, which may cause cracks, resulting in decrease of mechanical properties and durability. The use of SRAs has been suggested to reduce both drying and autogenous shrinkage. Unfortunately, these admixtures are designed mainly for binders based on OPC. Therefore, the authors believe that the research focused on the specific chemical

---

ACI Materials Journal, V. 115, No. 2, March 2018.
MS No. M-2017-122.R1, doi: 10.14359/51701099, was received April 24, 2017, and reviewed under Institute publication policies. Pertinent discussion including author's closure, if any, will be published ten months from this journal's date if the discussion is received within four months of the paper's print publication.

additives designed especially for alkali-activated systems could be very helpful for their potential practical applications.

EXPERIMENTAL INVESTIGATION

Alkali-activated blast-furnace slag (BFS) mortars with different kinds of chemical admixtures (polypropylene glycols) and three different fractions of siliceous sand were prepared based on ČSN EN 196-1 standard. The mass ratio between sand and binder was set as 3:1, while the water-BFS ratio was calculated to be 0.40. The amount of sodium waterglass was adjusted to maintain the mass ratio Na_2O/BFS at 0.04. Mixing and curing processes were carried out at a laboratory temperature 77°F (25°C) and the specimens were then stored in the curing chamber with defined relative humidity (50%). Thus, prepared samples were subjected to compressive strength determination and shrinkage measurements.

Materials

The main material used for alkali activation was blast-furnace slag with Blaine fineness of 1953 ft^2/lb (400 m^2/kg). The XRD analysis of BFS indicated the presence of a great amount of amorphous phase. The main mineral phases identified in BFS were melilite and merwinite. The chemical composition of slag determined by X-ray fluorescence (XRF) is given in Table 1. The particle size distribution D50 of BFS determined by laser granulometry in dry state was 2.8×10^{-4} in. (~7.0 μm). BFS was activated by sodium waterglass with a silica modulus of 1.93. The surfactants used as SRAs were propylene (PG) and polypropylene glycols (PPG) with different molar weights (PPG 200; PPG 425; PPG 725; PPG 1000) in addition to 0.5% by weight of BFS.

Specimens

For the compressive strength development, specimens of dimension 1.57 x 1.57 x 6.30 in. (40 x 40 x 160 mm), based on ČSN EN 196-1 standard, were prepared. Each value was supported by the average of four measurements. The shrinkage evolution was determined based on ASTM C596. Three mortars bars 0.98 x 0.98 x 11.22 in. (25 x 25 x 285 mm) of each mixture were prepared and measured until the age of 28 days. Each value was supported by the average of three measurements.

Items of investigation

At the age of 1, 7, and 28 days, specimens were tested for mechanical properties through the compressive and bending strength tester Betonsystem Desttset 3310. Length changes for obtaining the shrinkage evolution were measured in short time intervals using the ASTM C490 apparatus. Evolution of hydration heat was monitored by using of an air isothermal microcalorimeter. Measurements of heat evolution were performed at constant temperature of 77 ± 0.02°F (25 ± 0.04°C). When thermal equilibrium was achieved, the BFS and the alkali liquid created by waterglass, water, and SRA were mixed together by injecting the solution into the 5.3×10^{-4} ft^3 (15 mL) vial and stirred for 3 minutes. The water/BFS, as well as the mass Na_2O/BFS, were the same as in the preparation process of the mortars. The heat evolution was recorded as heat flow immediately.

Table 1—Physical and chemical compositions of blast-furnace slag

	BFS
Specific gravity	2.95
Blaine fineness, ft^2/lb	1953
SiO_2, %	34.7
Al_2O_3, %	9.1
CaO, %	41.1
MgO, %	10.5
SO_3, %	1.4
Na_2O, %	0.4
K_2O, %	0.9
TiO_2, %	1.0
MnO, %	0.6
Fe_2O_3, %	0.3

The total porosity and pore size distribution was determined by mercury porosimeter. The working pressure range was from 0.2 to 33 000 psi (0.14 to 231 MPa) which covered a pore diameter range from 2.56×10^{-7} to 3.94×10^{-5} in. (6.5 to 1000 nm). The measurements were performed with the following conditions: Hg surface tension was 2.74×10^{-3} lbf/in. (0.480 N/m); Hg contact angle was 140; and scan mode was chosen to average from 11 points. Obtained intrusion data were normalized by sample weight and volume.

ANALYTICAL INVESTIGATION

It was previously stated that the beneficial effect of SRAs on shrinkage lies in the reduction of surface tension at the pore solution/air interface. The surface tension arises thanks to the aqueous character of the pore solution, where the molecules interact mutually through the hydrogen bonds and form a loose three-dimensional network. Molecules at the surface cannot achieve the same level of molecular interactions compared to the molecules in the bulk and therefore have an energy excess. The consequence of this effect is that the liquid squeezes itself together to minimize surface area. This process is termed surface tension (γ) and was determined through a bubble pressure tensiometer. This analytical instrument measures the maximum internal pressure of a gas bubble which is formed in a liquid. According to the Young-Laplace equation, the internal pressure (p) of a spherical gas bubble depends on the radius of curvature (r) and surface tension

$$p = \frac{2\gamma}{r} \quad \text{(Pa)} \tag{1}$$

When a gas bubble is produced in a liquid at the tip of a capillary, the maximum internal pressure (p_{max}) is measured. This greatest pressure occurs when the radius of a gas bubble is equal to the radius of the capillary (r_c). As the capillary is immersed in the liquid, the hydrostatic pressure (p_0) resulting from the immersion depth and the density of the

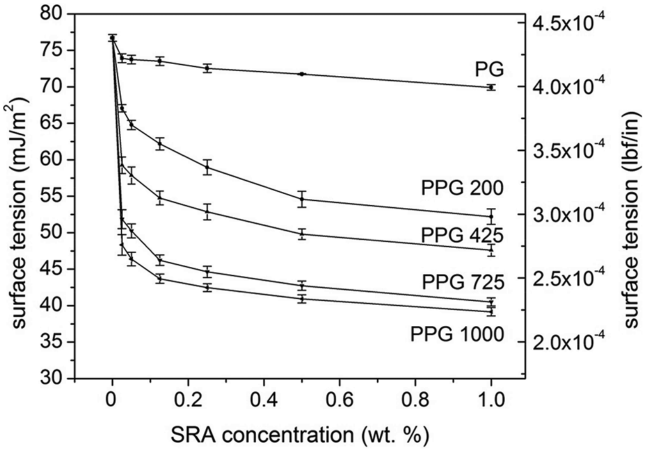

Fig. 1—Effect of surfactants on surface tension of pore solution (PG is propylene glycol; PPG is polypropylene glycol).

liquid must be subtracted from the measured pressure. The resulting surface tension is then calculated

$$\gamma = \frac{(p_{max} - p_0)\cdot r_c}{2} \ (\text{mJ/m}^2) \qquad (2)$$

COMPARISON OF PREDICTIONS AND EXPERIMENTAL RESULTS

According to the theoretical background, the analytical calculations predict the relationship between the tail length of surfactants and surface tension.[19] The molecular dynamic simulation clearly demonstrates that increasing the chain length makes the surfactants more effective. This model is also supported by the study of Szleifer et al.,[20] which supposed dependence of lateral pressure among hydrophobic chains and their length. The theory could be simplified and explained as follows. If the chain length is increased, the lateral pressure arises and therefore the surface tension decreases, which is described in the following equation

$$\gamma = \int (p_n - p_l(z))dz \qquad (3)$$

The surface is oriented in the *z*-direction, where p_n is the normal pressure and $p_l(z)$ is the lateral pressure.[21]

The experimental data show (Fig. 1) that the surfactants with higher molar weight, consequently with a longer hydrophobic chain, generally show a higher efficiency at low concentrations. Therefore, a smaller amount of surfactants is needed to achieve the same reduction of surface tension. The measured data are completely in agreement with presented theoretical predictions.

EXPERIMENTAL RESULTS AND DISCUSSION

Surface tension of pore solution

The action of a specific surfactant depends strongly on the chemical composition of the solution in which it is situated. In the other words, the aqueous solution may contain ions that promote the solubilisation and miscibility of surfactants or decrease critical micellation concentration (CMC). This phenomenon describes Hofmeister series relating in the ability of ions to increase or decrease the solubility of non-ionic surfactants in electrolyte solution.[22] Therefore, the nature of a pore solution of alkali-activated BFS is crucial for SRA efficiency. Its chemical composition was obtained by ICP-OES 24 hours after from mixing, thus the same time as shrinkage measurement was started.

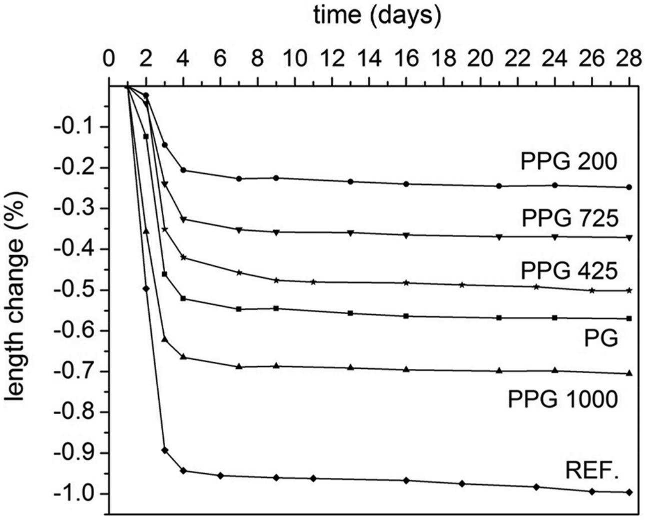

Fig. 2—Effect of surfactant addition (0.5% by weight of BFS) on shrinkage evolution.

The surface tension of synthetic pore solutions with different glycols is shown in Fig. 1. The higher content of surfactants in the solution causes a decrease in surface tension until reaching a plateau. In the case of polypropylene glycols, the critical micellation concentrations correspond to surface tension in the range of 2.28×10^{-4} to 3.14×10^{-4} lbf/in. (40 to 55 mJ/m^2). The presented results suggest that the surfactant PPG 1000 reduces the surface tension the most because its molecular weight is the highest. The other glycols achieved worse results in surface tension reduction as was expected, based on the theoretical background.

Factors affecting shrinkage evolution

Figure 2 shows that all the used surfactants, dosed at 0.5% by weight of BFS, are more effective in decreasing shrinkage evolution compared with the reference sample. However, the molecular character of the used glycols does play a significant role on the drying shrinkage evolution. Surprisingly, the length change measurements demonstrate the highest shrinkage reduction using PPG 200 and the lowest in the case of PPG 1000. These results clearly indicate that the ability to effectively decreasing the surface tension may not be correlated to the shrinkage reduction. There are other factors that must be taken into consideration.

One of the important things is the miscibility of used surfactants with aqueous alkali solution, because it is generally accepted that the critical surfactant concentrations are formed from the surfactant molecules' adsorption on interfaces and thus, further surface tension reduction is negligible.[23] In the case of glycols, the micellation related to total miscibility is controlled by molecular weight, as reported by Seguin et al.[24] Higher effective volume of micelles causes irregular distribution of surfactant in the pore solution, thus

Fig. 3—Miscibility of surfactants in alkali activator solution (sodium waterglass).

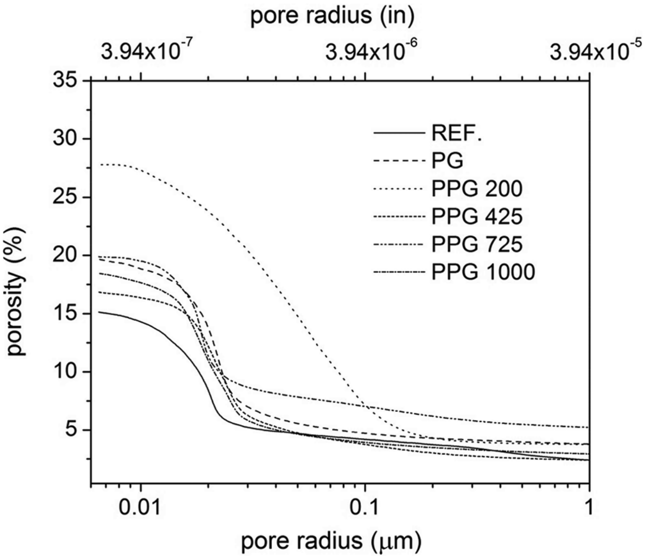

Fig. 4—Pore size distribution of alkali-activated samples.

resulting in higher shrinkage in certain areas of the alkali activated system. Figure 3 shows the 0.5 wt.% addition of used surfactants in alkali activator (sodium waterglass with a silica modulus of 1.93), where the higher molecular weight tends to increase the segregation of polypropylene glycols. To highlight this effect, a drop of phenolphthalein was added to the solutions. However, during the AAS hydration especially, silicate ions from activating solution are consumed to form CSH phase, which leads to increased miscibility of longer PPGs with pore solution, making them more effective in pore fluid surface tension reduction as was shown in Fig. 1.

Another impact of SRA is the ability to change the pore size distribution, which can significantly influence the drying shrinkage. During the ongoing drying process of AAS, the diameter of the pores partially filled with water (that is, with the presence of menisci) decreases until the equilibrium for a given relative humidity is reached, and thus capillary stress according to the Young-Laplace equation (Eq. (1)) increases, which results in higher shrinkage. The magnitude of drying shrinkage strongly depends on the loss of water from small (9.84×10^{-8} to 3.93×10^{-7} in. [2.5 to 10 nm]) and medium (3.93×10^{-7} to 1.97×10^{-6} in. [10 to 50 nm]) capillaries.[25] Previous studies[10,26] suggest that the alkali-activated BFS binders contain mainly pores in the mentioned regions, which is probably one of the main reasons for higher shrinkage of AAS compared to OPC.

Table 2—Porosity of alkali-activated samples

Sample (0.5% surfactant by weight of BFS)	Total porosity, %	Pores in small and medium capillaries, %
REF.[*]	15.08	69.89
PG	19.59	73.10
PPG 200	27.81	54.36
PPG 425	16.83	73.02
PPG 725	19.80	61.26
PPG 1000	18.43	76.18

[*] Reference sample (REF.) did not contain any surfactant.

Bílek et al.[17] showed that some surfactants strongly retard the hydration of AAS, which leads to its increased porosity and coarser the pore size distribution. Similar results were also observed in the case of the tested glycols (Fig. 4). The samples with surfactants indicated higher porosity in comparison with the reference sample, particularly in the case of PPG 200 sample, which was the most porous and had a coarser pore structure as a consequence of the strong retardation of hydration. The essential factor for the drying shrinkage behavior is the content of small and medium capillaries in the total porosity of materials. Table 2 summarizes the percentage portion of pore sizes within the critical 2.56×10^{-7} to 1.97×10^{-6} in. (6.5 to 50 nm) range. If the samples are ordered according to increasing content of pores in that region, the following dependence will be achieved: PPG 200 < PPG 725 < REF. < PPG 425 < PG < PPG 1000. This trend is similar with the extent of shrinkage of measured samples (Fig. 2) except the reference sample, which did not contain any admixture reducing surface tension of pore solution. It can be said that PPG additions influence surface tension reduction and also possibility their air-entraining effects, which could contribute to the increased total porosity of PPG containing mixtures.

From the presented shrinkage evolution results follow that the surfactant action influencing surface tension, pore size distribution, and miscibility, plays a crucial role in final shrinkage reduction.

Hydration process

The hydration process of alkali-activated systems with different kinds of glycols was measured using isothermal

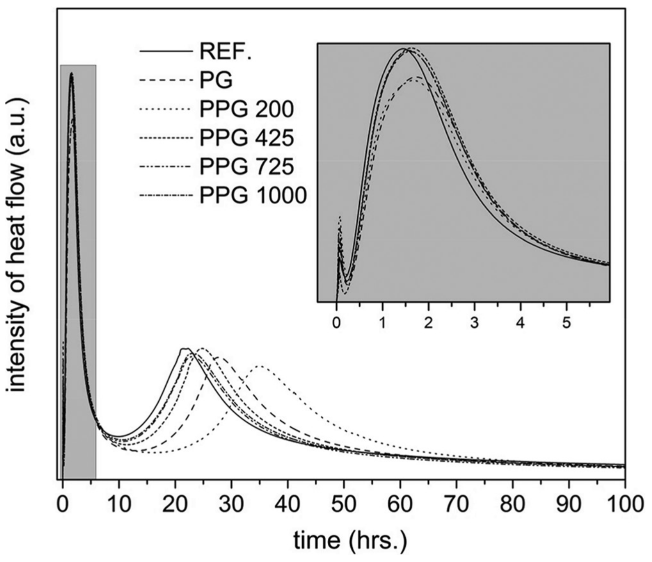

Fig. 5—Effect of surfactant addition (0.5% by weight of BFS) on hydration process.

microcalorimetry (Fig. 5). Typical calorimetric curves for waterglass-activated slag with three peaks as described by Shi and Day[27] were observed. The first peak occurring during the first 10 minutes of hydration is always associated with wetting and dissolution of BFS. From the zoomed area, it is clear that the second peak, starting after 15 minutes, which is connected with the gelation of dissolved silica to formation of primary CSH gel,[28] is reduced with the use of propylene (PG) and polypropylene (PPG 200) glycols, respectively. The slowing of hydration in case of these glycols is also well observed on the third peak, associated with the secondary formation of CSH gel. For the reference sample, the maximum of this peak occurred after 22 hours of hydration, but in presence of 0.5% of PG and PPG 200, was delayed by 6 and 14 hours, respectively. The other surfactants did not affect the alkali activation process significantly. These results suggest that the polypropylene glycols with a shorter chain length (for example, PPG 200) are responsible for the lower binder phase creation and create a smaller amount of capillary pores, resulting in shrinkage reduction. However, this effect leads to the deterioration of mechanical properties, which is further discussed.

Mechanical properties

Compressive strength evolution of samples with different kinds of surfactants is shown in Fig. 6. The measured data are fully in accordance with previous calorimetry measurements. After 24 hours, there is a decrease in the compressive strength of samples with the addition of PG and PPG 200. This difference is enhanced after 7 days of curing. The noticeable negative influence of PG and PPG 200 on compressive strength is probably related to the combination of their retardation effect and drying after the demolding process, followed by exposure to dry conditions (50% relative humidity). This influence started after 24 hours of hydration—that is, beyond the maximum of the reference main hydration peak, but significantly earlier than its maximum for PG and PPG 200 occurred, as can be seen from Fig. 5. Due to drying, further hydration was limited and thus, the hydration degree was lower in these mortars compared to those without significant retardation effect. The question about the efficiency of shrinkage reducing admixtures is well answered after 28 days. Similar to the reference specimens, the compressive strength of PG and PPG 425 samples remained almost the same between 7 and 28 days. On the other hand, the specimens with PPG 200, PPG 725, and surprisingly in the case of PPG 1000 showed a progressive increase in strength. Additionally, the surface of reference samples without any glycols was covered with small visible cracks, which only confirm the importance of the surfactants use.

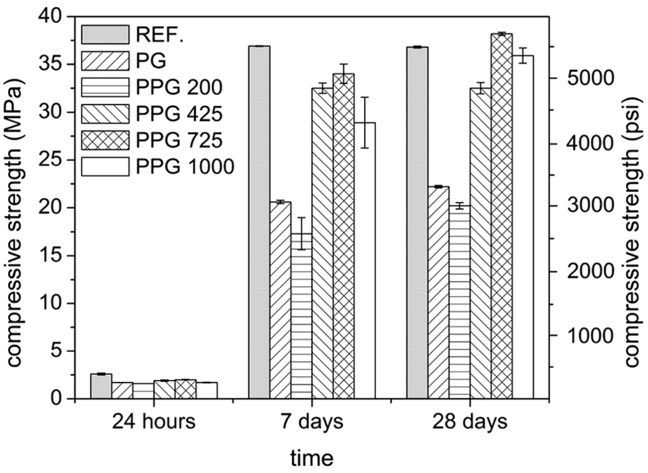

Fig. 6—Effect of surfactants (0.5% by weight of BFS) on compressive strength evolution.

FURTHER RESEARCH

The presented results show that the effect of surfactants in alkali-activated binders depends on various factors. Therefore, further research will be focused on the detailed study of microstructure with different kinds of SRAs. Moreover, the effort to enhance their efficiency through the synthesis of specific organic groups into polymeric structure will be another possible solution. Long-term testing (months and years) of alkali-activated materials with SRAs within the meaning of mechanical properties and durability will also take place.

CONCLUSIONS

In general, polypropylene glycols significantly reduce surface tension and seem to be suitable for SRAs. The measured data connected several factors which must be taken into account:

1. The significant reduction of surface tension leads not only to effective reduction of shrinkage. Other factors play an important role, such as the effect of surfactants on the pore size distribution and miscibility of used shrinkage reducing admixtures in the alkali activator solution.
2. The microcalorimetry results demonstrate that surfactants with low molecular weight (for example, PG and PPG 200) delay the hydration of BFS, which negatively influence their compressive strength development.

3. The behavior of polypropylene glycols investigated in this study greatly affects shrinkage reduction as well as compressive strength development.

The presented results suggest that the most usable polypropylene surfactant is PPG 725, which exhibits good ability to reduce shrinkage, does not affect negatively the alkali activation process, and increases the 28 days compressive strength compared with reference sample.

AUTHOR BIOS

Lukáš Kalina *is a Senior Researcher at the Materials Research Centre, Faculty of Chemistry, Brno University of Technology, Brno, Czech Republic. He received his MS and PhD in chemistry and materials technology. His interests include inorganic binders, especially alkali-activated materials.*

Vlastimil Bílek Jr. *is a Junior Researcher at Materials Research Centre, Faculty of Chemistry, Brno University of Technology. He received his MS in chemistry and materials technology. His research interests include alkali-activated materials and cementitious admixtures.*

Eva Bartoníčková *is a Senior Researcher at Materials Research Centre, Faculty of Chemistry, Brno University of Technology. She received her PhD from the Institute of Physical and Applied Chemistry at Brno University of Technology. Her research interests include ceramic materials.*

Jitka Krouská *is a Junior Researcher at Materials Research Centre, Brno University of Technology, Faculty of Chemistry. She received her PhD from the Institute of Physical and Applied Chemistry. Her research interests include colloid chemistry.*

ACKNOWLEDGMENTS

This outcome has been achieved with the financial support by the project: Materials Research Centre at FCH BUT- Sustainability and Development, REG LO1211, with financial support from the National Programme for Sustainability I (Ministry of Education, Youth and Sports) and GA17-03670S, "Development of shrinkage reducing agents designed for alkali activated systems," with financial support from the Czech science foundation.

REFERENCES

1. Mehta, P. K., and Monteiro, P. J. M., *Concrete: Microstructure, Properties, and Materials*, McGraw-Hill Education, New York, 2013, 704 pp.

2. Puertas, F.; Gutiérrez, R.; Fernández-Jiménez, A.; Delvasto, S.; and Maldonado, J., "Alkaline Cement Mortars. Chemical Resistance to Sulfate and Seawater Attack," *Materiales de Construcción*, V. 52, No. 267, 2002, pp. 55-71. (in Spanish) doi: 10.3989/mc.2002.v52.i267.326

3. Fernández-Jiménez, A.; Palomo, J. G.; and Puertas, F., "Alkali-Activated Slag Mortars," *Cement and Concrete Research*, V. 29, No. 8, 1999, pp. 1313-1321. doi: 10.1016/S0008-8846(99)00154-4

4. Fernández-Jiménez, A.; Puertas, F.; Sobrados, I.; and Sanz, J., "Structure of Calcium Silicate Hydrates Formed in Alkaline-Activated Slag: Influence of the Type of Alkaline Activator," *Journal of the American Ceramic Society*, V. 86, No. 8, 2003, pp. 1389-1394. doi: 10.1111/j.1151-2916.2003.tb03481.x

5. Bernal, S. A., and Provis, J. L., "Durability of Alkali-Activated Materials: Progress and Perspectives," *Journal of the American Ceramic Society*, V. 97, No. 4, 2014, pp. 997-1008. doi: 10.1111/jace.12831

6. Wang, W. C.; Wang, H. Y.; and Lo, M. H., "The Engineering Properties of Alkali-Activated Slag Pastes Exposed to High Temperatures," *Construction and Building Materials*, V. 68, 2014, pp. 409-415. doi: 10.1016/j.conbuildmat.2014.06.016

7. San Nicolas, R.; Bernal, S. A.; Mejía de Gutiérrez, R.; van Deventer, J. S. J.; and Provis, J. L., "Distinctive Microstructural Features of Aged Sodium Silicate-Activated Slag Concretes," *Cement and Concrete Research*, V. 65, Nov, 2014, pp. 41-51. doi: 10.1016/j.cemconres.2014.07.008

8. Kalina, L.; Bilek, V.; Novotny, R.; Moncekova, M.; Masilko, J.; and Koplik, J., "Effect of Na3PO4 on the Hydration Process of Alkali-Activated Blast Furnace Slag," *Materials (Basel)*, V. 9, No. 12, 2016, p. 395 doi: 10.3390/ma9050395

9. Melo Neto, A. A.; Cincotto, M. A.; and Repette, W., "Drying and Autogenous Shrinkage of Pastes and Mortars with Activated Slag Cement," *Cement and Concrete Research*, V. 38, No. 4, 2008, pp. 565-574. doi: 10.1016/j.cemconres.2007.11.002

10. Collins, F., and Sanjayan, J. G., "Effect of Pore Size Distribution on Drying Shrinkage of Alkali-Activated Slag Concrete," *Cement and Concrete Research*, V. 30, No. 9, 2000, pp. 1401-1406. doi: 10.1016/S0008-8846(00)00327-6

11. Krizan, D., and Zivanovic, B., "Effects of Dosage and Modulus of Water Glass on Early Hydration of Alkali-Slag Cements," *Cement and Concrete Research*, V. 32, No. 8, 2002, pp. 1181-1188. doi: 10.1016/S0008-8846(01)00717-7

12. Ye, H. L.; Cartwright, C.; Rajabipour, F.; and Radlinska, A., "Understanding the Drying Shrinkage Performance of Alkali-Activated Slag Mortars," *Cement and Concrete Composites*, V. 76, Feb. 2017, pp. 13-24. doi: 10.1016/j.cemconcomp.2016.11.010

13. Bakharev, T.; Sanjayan, J. G.; and Cheng, Y. B., "Effect of Admixtures on Properties of Alkali-Activated Slag Concrete," *Cement and Concrete Research*, V. 30, No. 9, 2000, pp. 1367-1374. doi: 10.1016/S0008-8846(00)00349-5

14. Palacios, M., and Puertas, F., "Effect of Shrinkage-Reducing Admixtures on the Properties of Alkali-Activated Slag Mortars and Pastes," *Cement and Concrete Research*, V. 37, No. 5, 2007, pp. 691-702. doi: 10.1016/j.cemconres.2006.11.021

15. Bilim, C.; Karahan, O.; Atis, C. D.; and Ilkentapar, S., "Effects of Chemical Admixtures and Curing Conditions on Some Properties of Alkali-Activated Cementless Slag Mixtures," *KSCE Journal of Civil Engineering*, V. 19, No. 3, 2015, pp. 733-741. doi: 10.1007/s12205-015-0629-0

16. Aïtcin, P. C., and Flatt, R. J., *Science and Technology of Concrete Admixtures*, Elsevier Science, Amsterdam, the Netherlands, 2015, 666 pp.

17. Bílek, V.; Kalina, L.; Novotny, R.; Tkacz, J.; and Parizek, L., "Some Issues of Shrinkage-Reducing Admixtures Application in Alkali-Activated Slag Systems," *Materials (Basel)*, V. 9, No. 12, 2016, p. 462 doi: 10.3390/ma9060462

18. Kalina, L.; Bílek, V.; Šoukal, F.; and Opravil, T., "Recycling of Waste Technological Sludge in Alkali-Activated Concretes," *Recycling of Waste Technological Sludge in Alkali-Activated Concretes*, fédération internationale du béton, Lausanne, Switzerland, 2016, 635 pp.

19. Smit, B.; Schlijper, A. G.; Rupert, L. A. M.; and Vanos, N. M., "Effects of Chain-Length of Surfactants on the Interfacial-Tension—Molecular Dynamics Simulations and Experiments," *Journal of Physical Chemistry*, V. 94, No. 18, 1990, pp. 6933-6935. doi: 10.1021/j100381a003

20. Szleifer, I.; Benshaul, A.; and Gelbart, W. M., "Chain Packing Statistics and Thermodynamics of Amphiphile Monolayers," *Journal of Physical Chemistry*, V. 94, No. 12, 1990, pp. 5081-5089. doi: 10.1021/j100375a060

21. Lundberg, L., and Edholm, O., "Dispersion Corrections to the Surface Tension at Planar Surfaces," *Journal of Chemical Theory and Computation*, V. 12, No. 8, 2016, pp. 4025-4032. doi: 10.1021/acs.jctc.6b00182

22. Kunz, W.; Henle, J.; and Ninham, B. W., "Zur Lehre von der Wirkung der Salze (About the Science of the Effect of Salts): Franz Hofmeister's Historical Papers," *Current Opinion in Colloid & Interface Science*, V. 9, No. 1-2, 2004, pp. 19-37. doi: 10.1016/j.cocis.2004.05.005

23. Rajabipour, F.; Sant, G.; and Weiss, J., "Interactions between Shrinkage Reducing Admixtures (SRA) and Cement Paste's Pore Solution," *Cement and Concrete Research*, V. 38, No. 5, 2008, pp. 606-615. doi: 10.1016/j.cemconres.2007.12.005

24. Seguin, C.; Eastoe, J.; Clapperton, R.; Heenan, R. K.; and Grillo, I., "Alternative Non-Aqueous Water-Miscible Solvents for Surfactants," *Colloids and Surfaces a-Physicochemical and Engineering Aspects*, V. 282, July 2006, pp. 134-142.

25. Mindess, S., and Young, J. F., *Concrete*, Prentice-Hall, Upper Saddle River, NJ, 1981, 671 pp.

26. Shi, C. J.; Day, R. L.; Wu, X. Q.; and Tang, M. S., "Uptake of Metal Ions by Autoclaved Cement Pastes," *Advanced Cementitious Systems: Mechanisms and Properties*, V. 245, 1992, pp. 141-149.

27. Shi, C. J., and Day, R. L., "A Calorimetric Study of Early Hydration of Alkali-Slag Cements," *Cement and Concrete Research*, V. 25, No. 6, 1995, pp. 1333-1346. doi: 10.1016/0008-8846(95)00126-W

28. Brough, A. R., and Atkinson, A., "Sodium Silicate-Based, Alkali-Activated Slag Mortars," *Cement and Concrete Research*, V. 32, No. 6, 2002, pp. 865-879. doi: 10.1016/S0008-8846(02)00717-2

B: Skupina publikací týkající se C-A-H hydrátů z C_3A fáze

13. *E.* ***Bartoníčková****, P. Ptáček, R. Novotný, J. Palovčíkk, J. Másilko, J. Švec, M. Sedlačík, J. Koplíik, T. Staněk, D. Hemzal*, Hydration kinetics of C_3A: effect of lithium, copper and sulfur-based mineralizers, Journal of Thermal Analysis and Calorimetry (2024).
14. *J. Koplík, J. Švec, J. Másilko, M. Sedlačík, E.* ***Bartoníčková****,* Synthesis of calcium aluminate hydrates, their characterization and dehydration, Ceramics International (2024).

Journal of Thermal Analysis and Calorimetry (2025) 150:1119–1135
https://doi.org/10.1007/s10973-024-13525-6

Hydration kinetics of C_3A: effect of lithium, copper and sulfur-based mineralizers

Eva Bartonickova[1] · **Petr Ptacek**[1] · **Radoslav Novotny**[1] · **Jakub Palovcik**[1] · **Jiri Masilko**[1] · **Jiri Svec**[1] · **Martin Sedlacik**[1] · **Jan Koplik**[1] · **Theodor Stanek**[2] · **Dusan Hemzal**[3]

Received: 1 February 2024 / Accepted: 19 July 2024

Abstract

Calcium aluminate phases have a particular effect on the early heat release during setting initiation and have a substantial influence on the further workability of ordinary Portland cement. The nature of the calcium aluminate hydration products and its kinetics strongly depends on sulfate content and humidity. The effect of mineralisers on melt formation and viscosity is well described for calcium silicate systems, but information is still lacking for calcium aluminates. Therefore, the synergistic effect on the crystal structure and hydration mechanism of the tricalcium aluminate phase of the addition of mineralizers, i.e. Li_2O, CuO, SO_3 to the raw meal is here investigated. Co-doped calcium aluminate structures were formed during high-temperature treatment. Thermal analysis (TG–DTA and heating microscopy) was used to describe the ongoing high-temperature reaction. Resulting phase composition was dependent on the concentration of the mineralizer. While phase pure system was prepared with low mineralizer concentrations, with increasing mineralizer content the secondary phases were formed. Raman spectroscopy and XPS analysis were used to investigate the cation substitution and to help describe the cations bonding in co-doped calcium aluminate system. Prepared powders have been hydrated in a controlled manner at different temperatures (288, 298, 308 K). The resulting calorimetric data have been used to investigate the hydration kinetics and determine the rate constant of hydration reaction. First-order reaction (FOR) model was here applied for the activation energy and frequency factor calculations. The metastable and stable calcium aluminate hydrates were formed according to initial phase composition. In phase pure systems with low S content, the formation of stable and metastable hydrates was depended on the reaction temperature. Conversely, in systems with secondary phases and higher S content, the hydration mechanism resembled that which appears in calcium sulfoaluminates.

Keywords C_3A · Synthesis · Hydration · Isothermal calorimetry · Kinetics · Activation energy

Introduction

With 7 percent of global CO_2 emissions, cement industry is one of the major sources of greenhouse gasses in the world. Annual worldwide production of cement reached 4.4 billion tonnes as of 2021 and is projected to further increase [1]. Due to the ongoing efforts on lowering the environmental footprint of the cement industry, recently emphasized in the CEMBUREAU Roadmap [2], two major approaches are employed in order to achieve this goal. First being the lowering of the clinker content in cement by use of supplementary cementitious materials [3, 4, 5] and second being the use of alternative low energy clinkers [6, 7, 8, 9] Both approaches serve the common goal in the reduction of the greenhouse gas emissions and the consumption of raw materials [1, 2]. Alternative clinkers generally have lower burning temperatures by at least 423 K compared to ordinary Portland clinker and therefore lower energy consumption [1, 6, 9]. Most promising alternatives to ordinary Portland clinker are *Reactive Belite-rich Portland clinkers* [10, 11] and various *sulfoaluminate*

✉ Eva Bartonickova
bartonickova@fch.vutbr.cz

[1] Institute of Material Science, Faculty of Chemistry, Brno University of Technology, Purkynova 464/118, Brno 612 00, Czech Republic

[2] Research Institute for Building Materials, Hnevkovského 30/65, Brno 617 00, Czech Republic

[3] Department of Condensed Matter Physics, Faculty of Science, Masaryk University, Kotlarska 267/2, Brno 611 37, Czech Republic

or belite-sulfoaluminate clinkers [9, 12, 13, 14]. The possibility of using various dopant elements is also often employed with the alternative clinkers [15, 16, 17]. Main reasons for adding dopants to a raw meal are stabilization of more reactive polymorphs of clinker phases, altering the course of hydration [18, 19, 20, 21] and increasing the efficiency of the burning process by using fluxes and mineralizers and promoting melt formation or altering the surface tension of the melt [22, 23].

Besides alite (C_3S), belite (C_2S) and tetracalcium aluminoferrite (ferrite phase, C_4AF, or $C_2(A_xF_y)$ where x, y ranges from 0.3 to 0.7), tricalcium aluminate (aluminate phase, C_3A) is a common component of Ordinary Portland Cement (OPC) [24]. Even though OPC usually contains typically between 5 and 10% of C_3A, its hydration kinetics and reaction path critically influence the workability and rheology of cement pastes, especially in the early hydration stages [25]. This includes the well-established phenomenon of flash setting, which in turn can have a significant effect on overall strength development [24, 26].

C_3A readily reacts with water. Therefore, gypsum ($CaSO_4 \cdot 2H_2O, C\overline{S}H_2$) is used to control the setting time of OPC. In its presence, ettringite (trisulfate, AFt, $C_6A\overline{S}_3H_{32}$) is formed [27, 28, 29].

$$C_3A + 3C\overline{S}H_2 + 26H \rightarrow C_6A\overline{S}_3H_{32} \tag{1}$$

After consumption of gypsum, the reaction C_3A with AFt takes place. It leads to the monosulfate (AFm, $C_4A\overline{S}H_{12}$) phase [27, 28, 29].

$$2C_3A + C_6A\overline{S}_3H_{32} + 4H \rightarrow 3C_4A\overline{S}H_{12} \tag{2}$$

Without gypsum, then the setting occurs too quickly, and the cement does not develop strength. Unlike the hydration of alite and belite, portlandite is not formed during the hydration of C_3A. However, during hydration of OPC, portlandite is always present. In that case, hexagonal hydrates are formed [30]:

$$C_3A + CH + 12\ H \rightarrow C_4AH_{13} \tag{3}$$

During hydration of pure C_3A, i.e., without setting additives, depending on the temperature and relative humidity, calcium aluminate hydrates are formed. There are known [31, 32]:

(a) Thermodynamically stable cubic hydrogarnet C_3AH_6 (katoite)
(b) Metastable hexagonal hydrates C_4AH_{13}, C_4AH_{19} and C_2AH_8

In dependence on the temperature, the course of hydration of C_3A as pure phase can be described as follows [33]:

$$C_3A + 6H \xrightarrow{k_1} C_3AH_6, \tag{4}$$

$$2C_3A + 21H \xrightarrow{k_2} C_4AH_{13} + C_2AH_8 \xrightarrow{k_4} 2C_3AH_6 + 9H, \tag{5}$$

$$2C_3A + 27H \xrightarrow{k_3} C_4AH_{19} + C_2AH_8 \xrightarrow{k_4} 2C_3AH_6 + 15H, \tag{6}$$

where $k(T)$ is the rate constant at temperature T [K]. The applied rate constants indexing was used in chapter 2.3.3 dealing with investigation of the kinetics of hydration. C_3AH_6 is the main product of hydration at temperatures higher than 294 K (Eq. 4). At lower temperatures, hexagonal hydrates are formed. By comparing Eqs. 5 and 6, it is obvious that formation of C_4AH_{19} instead of C_4AH_{13} is promoted by higher humidity. Because metastable hydrates are spontaneously transformed to stable cubic phase, the final product of hydration is C_3AH_6. Unlike rapid exothermic hydration, this transformation is endothermic.

Tricalcium aluminate usually exists as cubic crystals. However, if the amount of alkalies in OPC is high, orthorhombic or monoclinic polymorphs of C_3A can be formed [34]. The basic structural unit of cubic C_3A is twelve-membered ring $\left[Al_6O_{18}\right]^{18-}$, which is formed from AlO_4 tetrahedra [24]. The elementary cell of C_3A contains eight of these cycles. These cycles form the central cavity with diameter of 147 pm [35]. This, together with a certain tension in the grid, enables a rapid course of hydration. The substitution of Ca^{2+} by different ions (MgO, SiO_2, Fe_2O_3, Na_2O, etc.) can therefore take place and have an influence on the type of calcium aluminates and their subsequent reaction activity. [36]. Sodium substitution was the most commonly investigated. Here one Na^+ ion can enter the structure in position of Ca^{2+} and second one in center of $(Al_{16}O_{18})^{18-}$ ring [36, 37] with no crystal structure distortion. The no structure distortion limit is 1% of Na_2O, with higher level the structure transforms to orthorhombic (3.7–4.6% Na_2O) and monoclinic (4.6–5.7 Na_2O) [34]. Therefore, the maximum ion substitution in Ca^{2+} position is supposed to be 1% and was applied in this work (i.e. Li_2O, CuO). The elements chosen for this study were Sulfur, Lithium and Copper which should play significant role as mineralizers during clinkering reactions and their separate effect was previously very well-described. In general, compounds with Li, Na, Mg, Cu or S are commonly added to raw meal material in order to lower the melt formation temperature and decrease the clinkering temperature [38]. Lithium in the form of lithium carbonate added to clinker raw meal reacted during the high temperature reaction with calcium aluminate and formed solid solution. The incorporation of Li^+ ion into the cubic structure could be similar to Na^+ one [34, 36, 39]. Lithium should act here as a flux and lower melt formation [40]. The influence of Li_2CO_3 on the hydration of C_3A was also previously investigated. The addition can accelerate early-stage hydration through increased alkalinity in the system [41, 42]:

$$Li_2CO_3 + Ca(OH)_2 \rightarrow 2LiOH + CaCO_3 \quad (7)$$

Different situation is the hydration in the presence of gypsum, where the following reaction takes place, and the hydration is retarded due to the lower solubility of calcium carbonate. The more alkaline environment due to Li^+ ions give as a slightly higher course of hydration in comparison with the system without $LiCO_3$ [41].

$$Li_2CO_3 + CaSO_4 \rightarrow Li_2SO_4 + CaCO_3 \quad (8)$$

CuO acts as a strong flux during clinker formation [20]. In moderate amounts no higher than 1%, Cu doping can have a positive effect on the overall hydration. However, in larger quantities it can cause significantly prolonged induction period and strength decrease in the early hydration stages [43, 44]. The effects of sulfur in clinker formation and on the properties of OPC have been extensively studied by many authors [18, 19, 21, 23, 43]. The amount of C_3A formed is influenced by the sulfur present during clinker formation [43]. Furthermore, sulfate content is of special interest in the context of C_3A hydration, as the course of hydration changes drastically in the presence of sulfur containing compounds [22], strongly depending on the sulfate source [25]. In previous research the alite modifications have been the center of attention. It was proven that SO_3 present in raw clinker meal should significantly promote the formation of monoclinic M_1 alite prior to monoclinic modification M_3 and strongly influences hydraulic activity and strength development [45].

To our knowledge, no research has been devoted to synergistic effect of Li, Cu and S-based mineralizer on calcium aluminate system and its hydration. The presented findings provide a comprehensive study how combined mineralizers could affect both the structural composition and hydration behavior of tricalcium aluminate phase assemblage. The course of hydration was observed using isothermal calorimetry, which served as the basis for investigating hydration kinetics and determining the rate constant of the hydration reaction. A first-order reaction (FOR) model was applied to calculate the activation energy and frequency factor.

Experimental

Sample preparations

Tricalcium aluminate samples for this study were synthetized by high temperature solid state reaction. Firstly, $CaCO_3$ (PENTA, lab grade) and Al_2O_3 (PENTA, lab grade) powders were mixed with a molar ratio 3:1, homogenized in vibrational mill and burned at the temperature of 1673 K. Reagent grade Li_2CO_3 (Lach-Ner, lab grade), $(NH_4)_2SO_4$ (PENTA, lab grade) and CuO (PENTA, lab grade) were used as dopant sources for subsequent high temperature treatment. Selected dopant levels were 0.2 and 1% of mass for CuO and Li_2O and 0.5 and 2% of mass for SO_3. Reaction mixture, containing as-prepared calcium aluminate phase and dopant sources, was homogenized in vibrational mill and pelletized. Pellets with 40 mm in diameter were prepared using maximal pressure of 20 MPa and then burned at the temperature of 1723 K for 1 h. After cooling to laboratory temperature, the specimens were finally ground in vibrational mill for 2 min. The composition and notation of prepared samples are listed in Table 1.

Sample characterization

Phase composition of synthetized powders was determined by X-Ray diffraction analyses (XRD). The XRD analyses were carried out with diffractometer Empyrean from Malwern-PANalytical corporation. The measurement parameters were following tube current 30 mA and voltage 40 kV; anode material Cu (Kα1 = 1.540598 Å); scan axis gonio; scan range 5–90°2 Theta; step size 0.01313 Å; time per step 96 s. The results were evaluated using the software HighScore plus. The lattice parameters were fitted using the Rietveld refinement.

Crystal structure was investigated by Raman scattering spectroscopy. Measurements were performed using a NanoFinder S confocal micro-Raman microscope (SOL instruments) and Renishaw inVia spectrometer. The Raman scattering spectra were excited at 633 nm with 10 mW power and 532 nm, respectively. The system was calibrated on silicon (520.8 cm^{-1}). The beam was focused on the samples with a 50 × microscope objective with a numerical aperture of 0.8 and 0.7. The exposure time was 120 s with a grating with 2.7 cm^{-1} and 1.5 cm^{-1} resolution. All measurements were performed at room temperature in an ambient atmosphere.

XPS analyses were carried out with Axis Ultra DLD spectrometer using a monochromatic Al Kα (hν = 1486.7 eV) X-ray source operating at 150 W (10 mA, 15 kV). The spectra were obtained using an analysis area of ~ 300 × 700 µm. The Kratos charge neutralizer system was used for all

Table 1 Raw meal compositions used for the preparation of doped C_3A. samples

Sample designation		CuO/g	Li_2CO_3/g	$(NH_4)_2SO_4$/g	C_3A/g
S1	C_3A	0	0	0	40
S2	C_3A 0.2Cu0.2Li0.5S	0.08	0.20	0.33	
S3	C_3A 0.2Cu1Li2S		0.99	1.32	
S4	C_3A 1Cu1Li2S	0.40			

analyses. The high-resolution spectra were measured with the step size 0.1 eV and a pass energy of 20 eV. Instrument base pressure was 2 10−8 Pa. Spectra were analyzed using CasaXPS software and have been charge-corrected to the main line of the carbon C 1 s spectral component (C–C, C–H) set to 284.80 eV. A standard Shirley background was used for all sample spectra.

Thermal analyses were carried out using a heating microscope and TG–DTA analysis. Heating microscopy measurements were carried out using EMI2 heating microscope (Hesse Instruments) on pressed 2.5 × 3 mm cylindrical powdered samples at a heating rate of 1 °K.min^{-1} up to 1923 K, with an image taken at least every 10 K or when the shape or area of the sample silhouette changed. TG–DTA analyses were performed on SDT Q650 TA instrument in alumina crucible and dried air atmosphere at a heating rate of 10 K/min to 1273 K. The loaded sample mass was approximately 50 mg.

Microstructure and chemical composition were characterized by electron scanning microscope ZEISS EVO LS10 coupled with EDS analysis (OXFORD X-Max 80 mm^2). Images of hydrated and unhydrated samples were taken under 10 or 15 kV acceleration voltage. Samples for analyses were cut, ground and polished under non-aqueous medium and for EDS analyses sputtered by gold nanoparticles. Hydrated samples were cut into appropriate dimensions and sputtered.

The hydration process of the synthesized C_3A samples was analyzed by isothermal calorimetry using a TAMAir instrument (TA Instruments). The external mixing method was used. All raw materials and equipment were tempered together for approximately 16 h in an air-conditioned laboratory to a temperature close to the measurement temperature. Samples were measured in glass vials with ground-in bottoms for better contact with the thermocouple and heat transfer from the sample to the calorimeter body. The loading was 1 g of dry sample. The water to binder ratio was 0.5. Demineralized water was used. Standard sand was measured simultaneously as a reference sample.

Results and discussion

High-temperature behavior of C_3A in presence of Li, Cu and S

The formation temperature of the C_3A phase is 1812 K according to the phase diagram. Analysis of the reaction mixture for undoped C_3A using a heating microscope showed that the temperature sufficient for the reaction, without the occurrence of melt formation, is 1723 K (Fig. 1a). This temperature is slightly lower than literature-based one. The reaction proceeds in several steps. Around 873 K, carbonates decompose into CaO, which then reacts stepwise with Al_2O_3 to form the intermediate Mayenite ($C_{12}A_7$) [46]. Around 1373 K, $C_{12}A_7$ reacts with unreacted CaO and forms the targeted C_3A phase. This process has been published by many authors, and the obtained data are consistent with it [46, 47, 48].

In terms of standard firing cycle temperatures for OPC clinkers, this temperature can be further reduced by incorporating various dopants, particularly alkalis [42, 49]. The TG–DTA analysis (Fig. 1b) reveals the impact of the introduced ions. Region I is connected to the decomposition of surface adsorbed water and ammonium sulfate (~ 500 K) [50]. Region II is connected to lithium carbonate decomposition [51]. At higher Li and S concentrations (i.e.1 and 2%

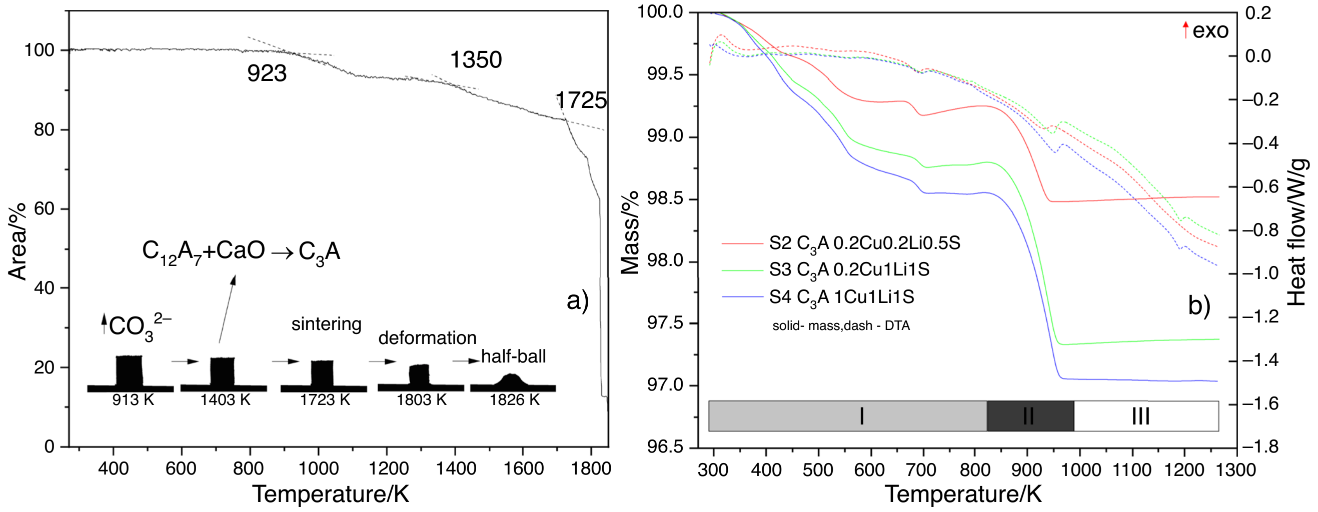

Fig. 1 **a** Heating microscope analysis of C_3A high temperature synthesis, **b** TG–DTA analysis of raw mixtures

Table 2 Phase composition of synthesized products

Sample		C_3A cub	CaO	Li_2SO_4	$Ca_4Al_6O_{12}(SO_4)$	$CaSO_4$	Cu_2O
		Composition/% of mass					
S1	C_3A	99.9	0.1				
S2	C_3A 0.2Cu0.2Li0.5S	99.9	0.1				
S3	C_3A 0.2Cu1Li2S	98.4	0.3	0.4	0.4	0.5	
S4	C_3A 1Cu1Li2S	98.3	0.6	0.2	0.3	0.7	<0.1

of mass resp.), an endothermic peak appears in the region around 1173 K which is most likely related to the melting of as-formed lithium sulfate detected by the XRD analysis (Table 2) [52]. The selected burning temperature was also found to be optimal in relation to the resulting phase composition of the synthesized doped products. It was determined that the majority of the synthesized samples (up to 99.99%) exhibited a cubic structure of C_3A without distortion (see Table 2).

Examination of the phase composition of the doped $CaO–Li_2O–CuO–Al_2O_3\_SO_3$ system revealed the formation of a cubic C_3A structure was affected by ion substitution, resulting in a diffraction shift towards higher angles (see Fig. 2). The ionic radius of Ca^{2+} is 100 pm whereas the Li^+ and Cu^{2+} ions are smaller (Cu^{2+} is 73 pm and Li^+ is 76 pm). Sulfur can occur in 3 oxidative states—S^{6+} ion is with 29 pm or S^{4+} with 37 pm or as an anion S^{-2} with 184 pm ionic radius [53]. Thus, resulting in variation of the interfacial d-spacing (see Table 3). The general idea was that Cu^{2+} ion with lower diameter can intercorporate into the C_3A structure in Ca position and shift the angles to lower values, while 2 molecules of Li^+ can shifted towards higher values. The content of free lime (CaO) in samples was subsequently increased with increasing levels of Li^+ and Cu^{2+} and the possible incorporation of ions into the structure [54]. Copper incorporation can be discussed according to performed XPS analysis given on Fig. 2b. The Cu 2p core level spectrum was deconvoluted with two components. The first peak of Cu 2p3/2 at 932.9 eV is related to Cu−O, where Copper occurs in the + I oxidation number. Diffractions of Cuprite was observed in traces by XRD analysis in sample S4 with 1% mineralizer dosage. The second peak of Cu

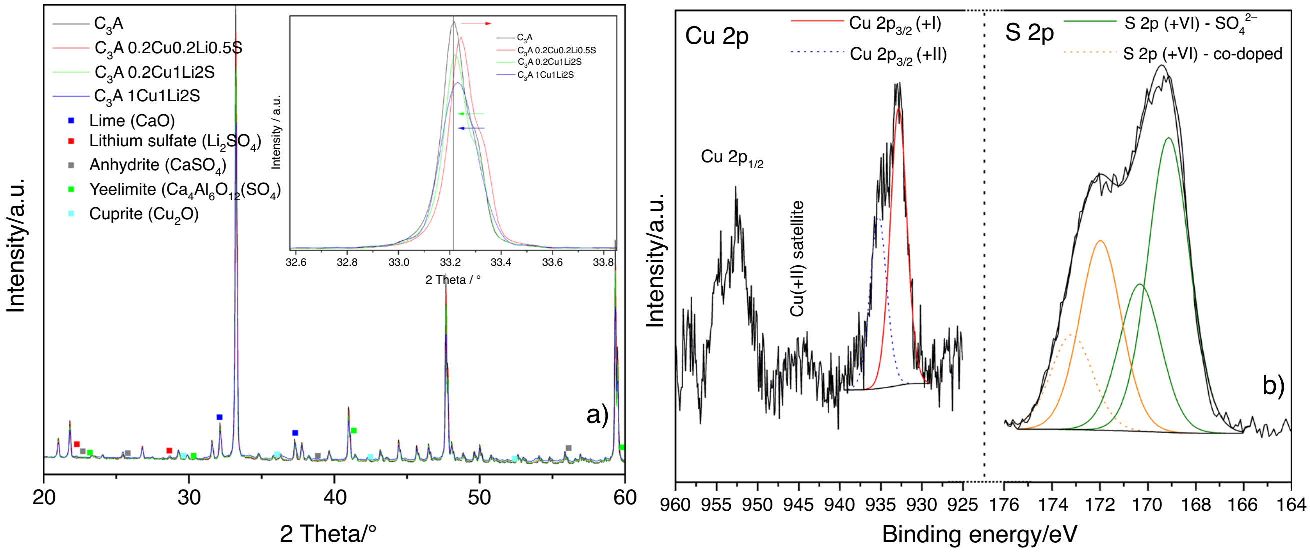

Fig. 2 XRD (**a**) analysis of as-synthetized products and XPS analysis of sample S4—C_3A 1Cu1Li2S (**b**)

Table 3 Lattice parameters of C_3A phase prepared with various doping

Sample		Cell parameters/Å	Position/°2θ	d-spacing	FWHM
S1	C_3A	15.25808	33.2076	2.69569	0.0768
S2	C_3A 0.2Cu0.2Li0.5S	15.25271	33.234	2.69361	0.0797
S3	C_3A 0.2Cu1Li2S	15.25127	33.2131	2.69526	0.0784
S4	C_3A 1Cu1Li2S	15.25239	33.2118	2.69536	0.0787

2p3/2 at 935.3 eV is corresponded to the Copper appears to be found in $CuSiO_2(OH)$ or $CuAl_2O_4$, according to NIST XPS database [55, 56, 57]. The confirmation of the + II oxidation state was associated with a strong shake-up satellite located between binding energies of 941–949 eV. Similar findings about Copper entrance into the clinker system were also recently published [55, 58]. Lithium even at content of 1% was not detectable. Lithium doping behavior is expected similar to sodium one in valence but not in ion diameter. Na^+ ion radius is much higher, so the increasing doping caused the structural distortion (Na^+—102 pm) [36]. The crystal structure of the $Na_{2x}Ca_{3-x}Al_2O_6$ system is strongly influenced by the Na content. As the Na content increases, the cubic structure is distorted to orthorhombic one. In solid solution, the replacement of one Ca^{2+} cation by two Na^+ cations occurred, where one is in position of original Ca^{2+} and the second is placed in the middle of $(Al_6O_{18})^{18-}$ ring [34, 36]. Replacement of Ca^{2+} ion prior to Al^{3+} ion was also reported by other studies with different cations and valences as Na^+ or Eu^{3+} [39, 59]. Synergistic effect of Li^+ and Cu^{2+} ions incorporation should compensate charges and resulting in small shift to higher values and did not cause the cell distortion [39]. Therefore, sulfur exists in calcium aluminates in two oxidative S^{2-} and S^{6+}. Sulfur in S^{2-} oxidative state can replace Al^{3+} or O^{2-} in tetrahedral $(AlO_4)^{5-}$ respectively with no shift. This suggestion is coming from the solid solution´s studies of system $CaO–Al_2O_3–CaS$ which are formed as an inclusion in Al-killed steel [60]. Sulfur in S^{2-} will appear only in reducing atmosphere, we can assume that we were working in oxidative environment, so the sulfide presence is not possible. Performed XPS analysis confirmed sulfur in oxidative state S^{6+} in S2p (169.12 eV(+ VI)) probably in $CaSO_4$ or Li_2SO_4 compounds according to NIST database [56] and S2p (171.98 eV (+ VI)) most likely coming from co-doped structure Ca–Cu–Al–S–O, similar binding energies has been published in substituted superconducting oxide ($Y_{1.4}Ce_{0.5}Sr_{0.1}Cu_{2.75}S_{0.25}O$) [61]. With an increase in dopant content, particularly Sulfur and Copper ones, an unfavorable reaction occurred, and secondary phases were formed. The phase composition analysis revealed the presence of lithium sulfate ($LiSO_4$), Ye´elimite ($Ca_4Al_6O_{12}(SO_4)$), Anhydrite ($CaSO_4$) and Cuprite (Cu_2O). We assume that ammonium sulfate in the starting mixture reacted with Ca^{2+} ions to form anhydrite, which subsequently reacted with the C_3A phase around 1573 K, leading to the formation of Ye´elimite and free lime (CaO) see Eq. 9)). Li et al. [62] a El Khessaimi et al. [63] have published data with the same findings.

$$3Ca_3Al_2O_6 + CaSO_4 \rightarrow Ca_4Al_6O_{12}(SO_4) + 6CaO \tag{9}$$

The findings obtained from XRD analysis were confirmed by Raman spectroscopy analysis (refer to Fig. 3). The peak corresponding to the position of the asymmetric vibration $\nu_1(AlO_4^{5-})$—757 cm^{-1} [22, 64], was shifted towards higher values due to the presence of low concentrations of Li^+, Cu^{2+} and S^{6+} ions (i.e. sample S2 C_3A–0.2Cu0.2Li0.5S). Whereas for higher concentrations (i. e. samples S3 C_3A–0.2Cu1L2S and S4 C_3A–Cu1Li2S) was shifted much less due to the formation of intermediate phases (lithium sulfate, Ye´elimite, Anhydrite and Cuprite), indicating only partial Ca^{2+} substitution. Vibrations corresponding to sulfate group inside products such as sulfates and Ye´elimite are visible as a shoulder at 460 cm^{-1} and strong peak at 1012 cm^{-1} ($\nu_1(SO_4^{2-})$) or as a shoulder visible at 607 cm^{-1} (ν_4 (SO_4^{2-}) [64, 65, 66] (see inset Fig. 3c).

Figure 4 shows the cross section of the tablet after the high temperature reaction. At first sight, the difference in size of the phases formed is obvious. In the case of undoped system the grain size distribution is too wide (20 to 120 μm).

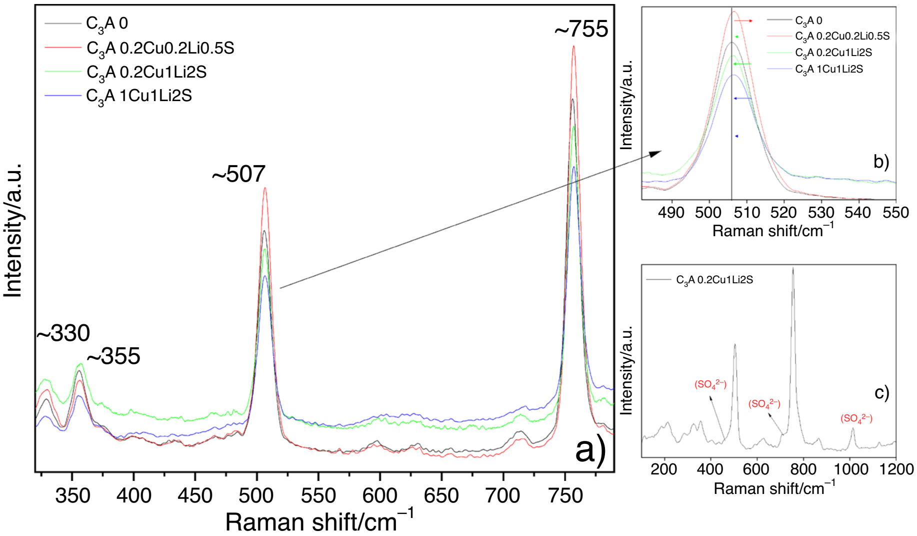

Fig. 3 Raman spectral analysis of synthesized products: **a** +, **b** Raman spectra of doped C_3A structure, **c** S3—C_3A 0.2Cu1Li2S

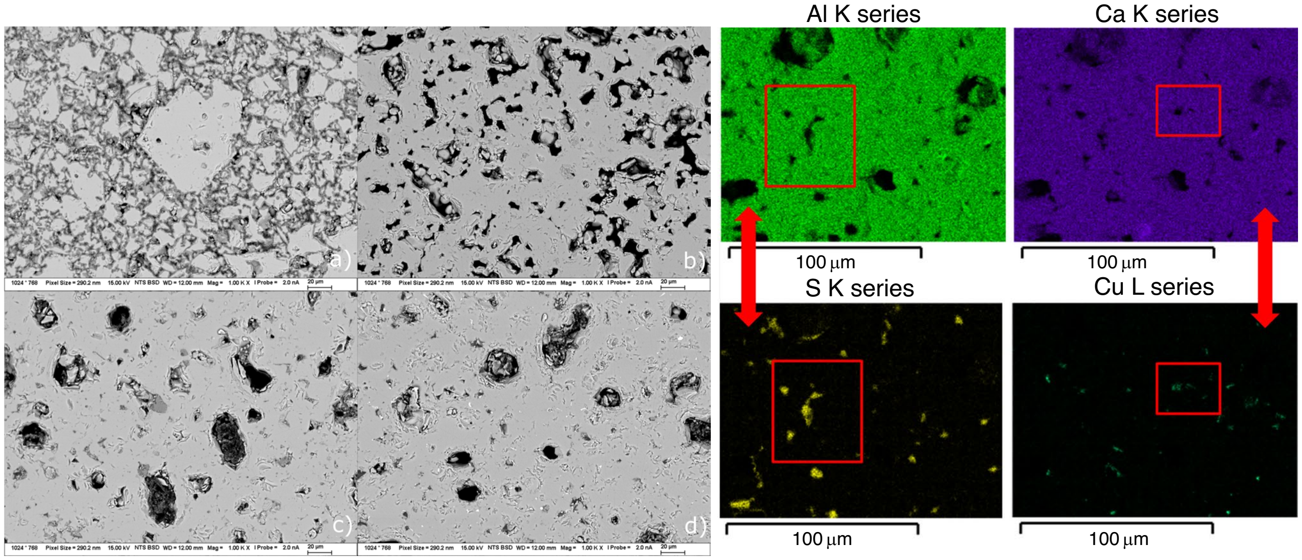

a) b)

Fig. 4 **a** Microstructure of doped C_3A system: (a) S1, (b) S2, (c) S3 and (d) S4; **b** SEM–EDS doped C_3A system: sample S4—C_3A 1Cu1Li2S

The distribution was significantly narrower (10 to 30 µm) with the increasing concentration of doped species (Li^+, Cu^{2+} a SO_3). This phenomenon has been described by several authors in the combined $CaO–Al_2O_3–SiO_2–Fe_2O_3$ system [49, 58, 67]. For the pure C_3A system, only the influence of doped elements on the formation of hydration products was discussed [58, 68]. Considering the chemical composition shown in Fig. 4b, there is a visible presence or absence of cations in combination Ca-Cu and S-Al (see highlighted areas), where the Cu is present the Ca is absent and where the S is present Al is absent. Raman spectroscopy and XRD analysis revealed the doping caused peak shifts to higher values, i.e. Raman shift (cm^{-1}) and 2Theta (°) respectively, and XPS analysis with defined binding energies. We can assume that the crystal structure has been modified by the incorporation of Ca^{2+} ion probably in position of Cu^{2+} ions and S^{6+} instead of 2 Al^{3+}. The observed results indicate that Li^+ ions should be incorporated, as can be inferred from the formation of lithium sulfate when the doping concentrations were increased, leading to a shift back to lower values. The introduced sulfate anions reacted with Li^+ and as well as with C_3A matrix to form secondary phases (lithium sulfate and Ye´elimite) [62, 63]. Introduced Cu^{2+} ions did not form any secondary phases.

Hydration

Hydration products

In the case of undoped sample S1 (Fig. 5), the hydration peak at 288 K and the first peak at 298 K are attributed to the formation of amorphous and irregular flakes of C_4AH_{13} and C_4AH_{19} hydrates. At 288 K, the further transformation of these hydrates is outside the measured hydration interval and is therefore very slow. The second hydration peak at 298 K is due to the conversion of hydrates from the first peak to cubic C_3AH_6. This conversion is very fast at 308 K and the formation of amorphous and irregular flakes and their subsequent conversion to cubic C_3AH_6 combine to form one intense peak on the calorimetric curve [31]. Therefore, at 288 and 298 K a heat flux of approximately 450 mW/g is achieved in the first peak, however, at 308 K a heat flux of 1050 mW/g was achieved in which the majority of the total hydration heat is generated within the first few minutes. A similar progression of undoped C_3A was observed by [69]. Axthammer et al. [70] measured a one-step hydration process, which took place at 290 K, but the amount of hydration heat was generated as in 2-step hydration. For doped sample S2 (Fig. 6), C_3A hydration proceeds in a one-step process at 288 and 298 K. The 2-step hydration shifts to higher temperatures and is evident at 308 K. Doping with different elements generally results in the disappearance of the second hydration peak in the temperature interval 293–298 K, accompanied by a decrease in the total hydration heat [71, 72]. For sample S3 (Fig. 7), at all measured temperatures,

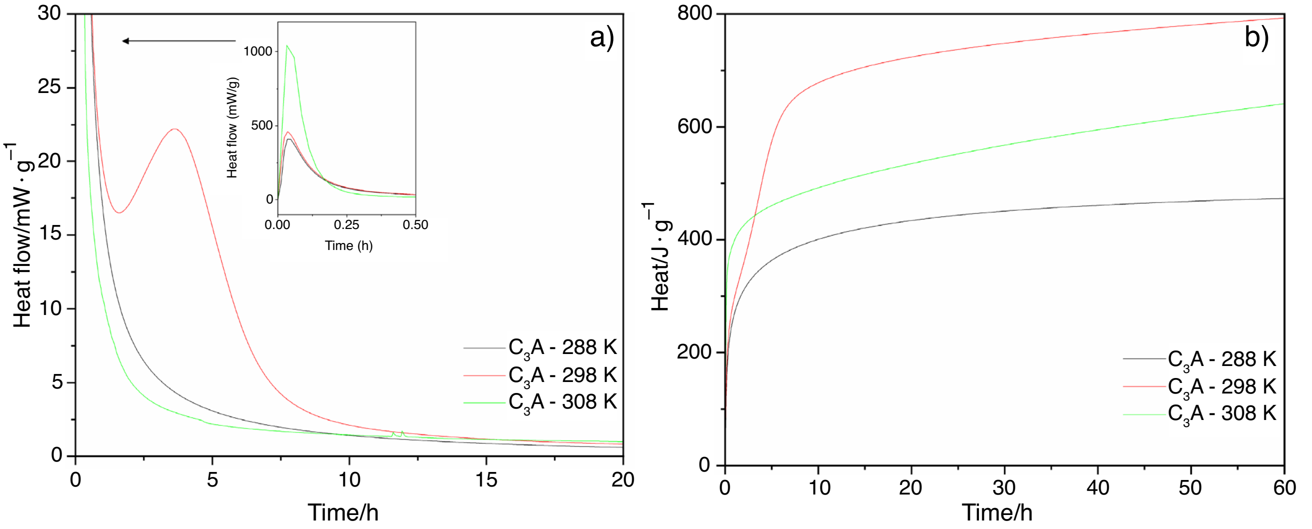

Fig. 5 Isothermal analysis of undoped C_3A: **a** heat flow, **b** release heat

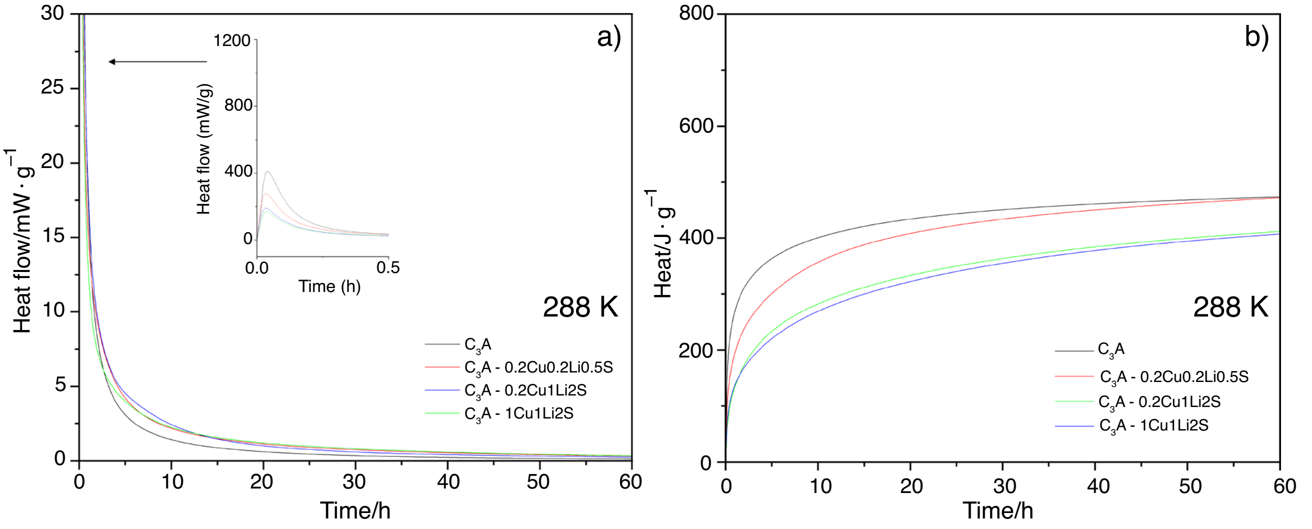

Fig. 6 Isothermal calorimetry of doped C_3A at 288 K: **a** heat flow, **b** release heat

hydration proceeds in a single-peaked manner with a concomitant decrease in the hydration heat developed. This is due to Cu^{2+} doping, which limits the formation of C_3AH_6 in the hydrates and promotes the formation of monocarbonate [73]. Further increase in the amounts of dopants in sample S4 (Fig. 8) had minimal effect on the hydration process. However, if the ions are not doped but added to the pure C_3A solution, the heat flux during hydration usually increases [36]. Samples S3 and S4 contain soluble sulfates due to doping, so they do not have the standard retarding effect on the hydration progress, probably due to the fact that this small sulfate content is additionally overgrown in C_3A and cannot saturate as when sulfates are added as a chemical [68, 74].

Phase composition of formed hydrates (Table 4) correlates with the calorimetric curves given above. For undoped C_3A, the formation of C_3AH_6 increased with increasing temperature, while C_4AH_{13} decreased. Figure 9 shows the change from platelet-like hexagonal particles of metastable hydrates to spherical cubic one. This phenomenon has been published by many authors [31, 32, 33, 48, 69]. The hydration process was affected when dopants were incorporated into the structure. At lower Li, Cu and S contents, where no secondary phases were present according to the phase composition analysis, the system behaved quite differently than undoped one. At lower temperatures, in the presence of even small amounts of S, the formation of C_4AH_{13} and C_4AH_{19}

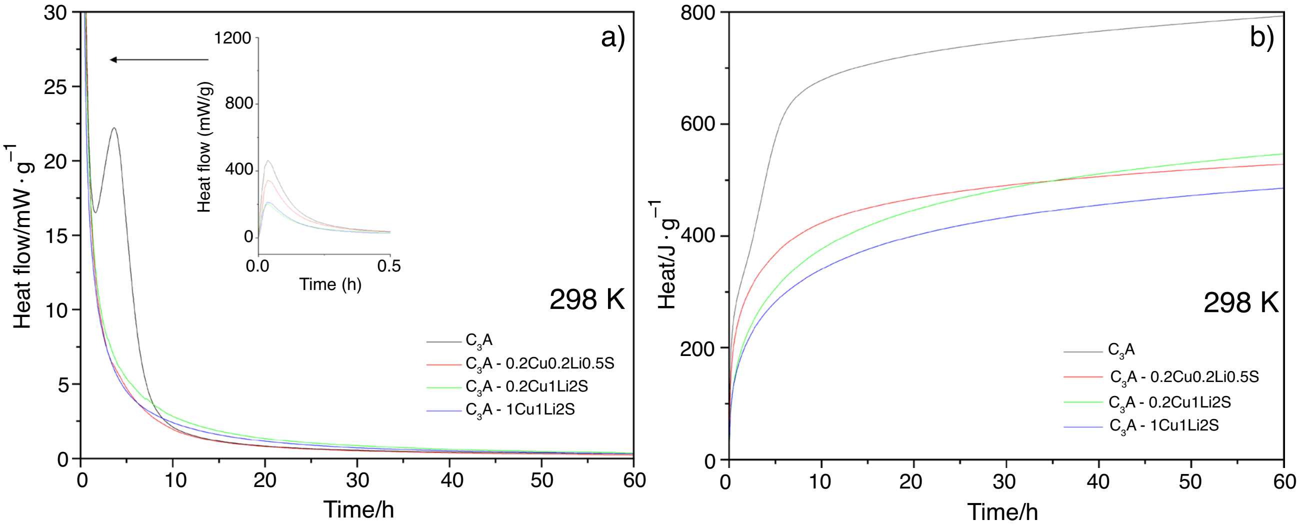

Fig. 7 Isothermal calorimetry of doped C_3A at 298 K: **a** heat flow, **b** release heat

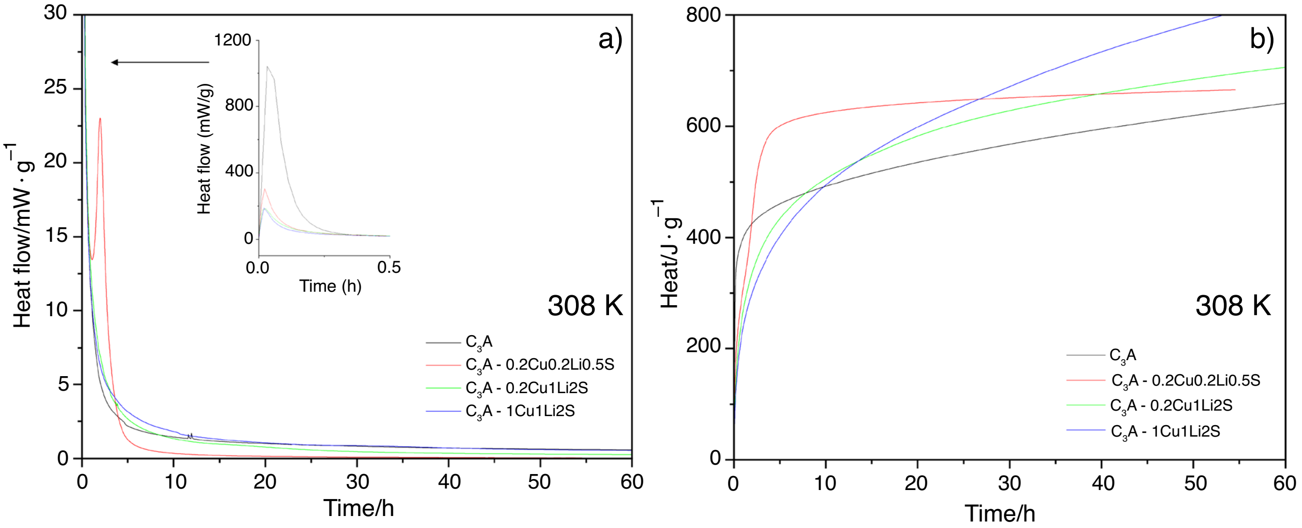

Fig. 8 Isothermal calorimetry of doped C_3A at 308 K: **a** heat flow, **b** release heat

hydrates dominated, while at 308 K the cubic C_3AH_6 was the dominant phase. These results also correlate nicely with the SEM images below (Fig. 10). As the S content increases, the trend is again changed (see Figs. 11 and 12). At lower temperatures C_4AH_{13} hydrates were dominant, but C_4AH_{19} did not form. In addition to the hydrates formed from the doped C_3A phase, there were also hydrates associated with the reaction of secondary phases nonstoichiometric monosulfate (C–A–(CO_3;SO_4;OH;H_2O)), monocarbonate (Mc) and also portlandite (CH).

Kinetics of hydration

Figure 13a shows the heat evolution during hydration of undoped tricalcium aluminate (S1, refer to Table 1) measured by isothermal calorimetry. In order to evaluate the hydration kinetics, the time dependence of the degree of conversion ($\alpha = f(t)$) was calculated (b) from these data as follows:

$$\alpha = \frac{H_t}{H_\infty - H_t}[0 - 1], \qquad (10)$$

where H_t and H_∞ is the heat of the hydration measured in the general time t a $t \to \infty$, respectively. The value of H_∞ was

Table 4 Phase composition of hydration products treated at different temperatures

Sample	T /K	C_3A cub	C_3AH_6	C_4AH_{13}	C_4AH_{19}	$C_3A\cdot C\bar{C}$ 11H_2O (Mc)	C-A-(CO_3;SO_4;OH;H_2O)	CH
S1	288	++++	+	++	++	–	–	–
	298	++	++++	+	–	–	–	–
	308	++	++++	+	–	–	–	–
S2	288	++++	–	++	++	–	–	–
	298	++++	–	+++	++	–	–	–
	308	++	++++	+	–	–	–	–
S3	288	++++	–	++	–	++	++	–
	298	++++	++	++	–	++	++	+
	308	+++	+++	+	–	++	+	++
S4	288	++++	–	++	–	++	++	–
	298	++++	+	++	–	++	++	–
	308	+++	+++	++	–	++	++	+

++++ = >40%, +++ = 10–40%, ++ = 5–10%, + = 0–5%, – = 0%

determined by fitting the experimental data (Fig. 13a). The R^2 value of the fit is higher than 0.99 in all cases.

Hydration of C_3A has a very specific nature. Depending on the temperature, hexagonal or cubic hydration products are formed. Alternatively, the primarily formed hexagonal hydration products are converted to cubic hydrate (see Eqs. 5–8). As a result, the calculated activation energy values are strongly dependent on the degree of conversion. This means that very similar values can only be obtained in a certain, relatively narrow area of α (Fig. 13c). For these reasons, this interval has been designated as the "kinetic window". The activation energy can be determined, i.e., the kinetic graph (Fig. 14) will provide a straight line ($R^2 \rightarrow 1$), only in this region.

For the above-mentioned facts, the usually applied kinetic method, which is based on the search for most probable mechanism, i.e., kinetic equations:

$$g(\alpha) = k(T)t, \tag{11}$$

does not lead to the desired result. And this despite the fact that for a given temperature such an equation can be found, as will be discussed below.

Within the range of the kinetic window (Fig. 13c), these difficulties can be circumvented to a large extent by determination of the apparent activation energy (E_a^{ap}) by using a kinetic model (mechanism)-free method. One of these approaches is the kinetic graph shown in Fig. 14 where the natural logarithm of the time required to reach a certain degree of conversion ($\ln t_\alpha$) is plotted at the reciprocal temperature (T^{-1}). The average apparent activation energy (E_{av}^{ap}) of the process can then be calculated from the slope of the straight line to 67.7 kJ mol^{-1}.

This obtained value of the apparent activation energy is very helpful in deciding on the most probable mechanism of hydration of tricalcium aluminate. When searching for a suitable kinetic equation, it is otherwise difficult to decide between the two most likely reaction mechanisms (Fig. 15b), which are:

1. KJMA in the form:

$$\alpha = 1 - \exp\left(-k(T)t^{5/2}\right), \tag{12}$$

which points to the process driven by the diffusion when homogeneous nucleation of the new phase with constant rate takes place. Nuclei grow in all directions at the same rate. For and in the range of the kinetic window, the value of the rate constant can then be calculated according to the equation:

$$k(T) = -\frac{\ln(1-\alpha)}{t^{5/2}}. \tag{13}$$

2. First-order kinetic equation (FOR):

$$k(T)t = \frac{1}{(1-\alpha)} - 1, \tag{14}$$

where in the range of the kinetic window:

$$k(T) = \frac{\frac{1}{1-\alpha} - 1}{t}. \tag{15}$$

By plotting of $\ln k$ versus $1/T$ in, e.g. for $\alpha = 0.7$ (Fig. 15b), the Arrhenius plot shows the activation energy of 167.7kJ mol^{-1} for the KJMA equation and 67kJ mol^{-1} for the first-order equation can be obtained. Comparing these values with the results of the method (Fig. 14), which does not depend on the choice of reaction mechanism, it can be

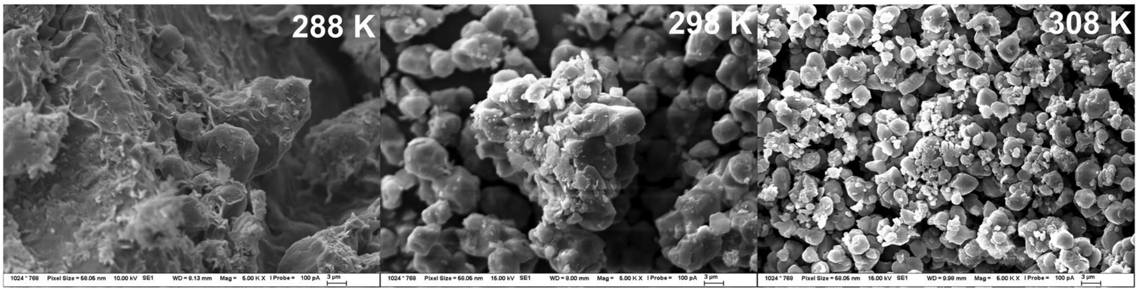

Fig. 9 SEM analysis of products hydrated at different temperatures– S1 C_3A

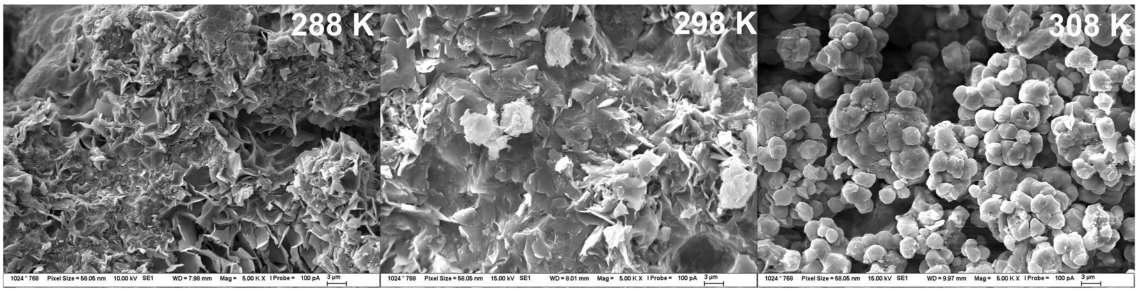

Fig. 10 SEM analysis of products hydrated at different temperatures—S2 C_3A 0.2Cu0.2Li0.5S

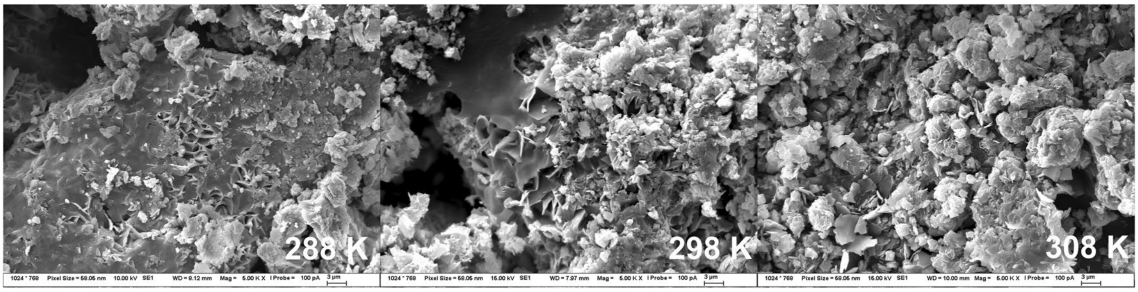

Fig. 11 SEM analysis of products hydrated at different temperatures—S3 C_3A 0.2Cu1Li1S

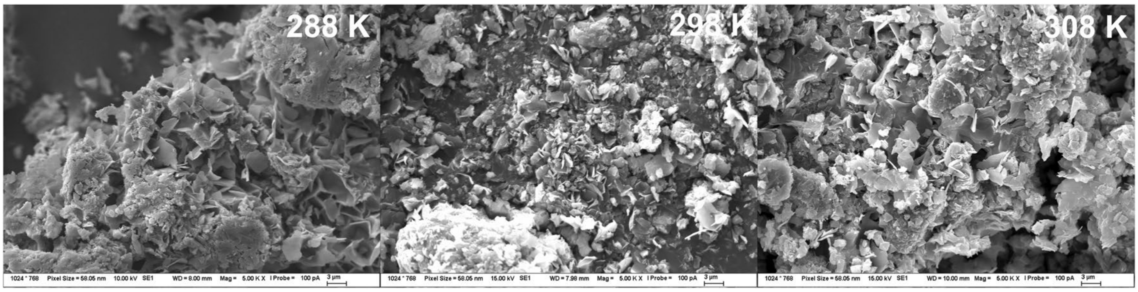

Fig. 12 SEM analysis of products hydrated at different temperatures – S4 C_3A 1Cu1Li2S

Table 5 Estimation of the average activation energy of hydration of sample S3

S3	Degree of conversion									
	0.3	0.4	0.5	0.55	0.6	0.65	0.68	0.7	0.8	0.9
R^2	0.863	0.873	0.872	0.846	0.815	0.800	0.823	0.775	0.776	0.792
$E_a^{ap}\left(\mathrm{k\ mol^{-1}}\right)$	21.9	23.2	26.5	29	31.7	34.5	36.2	36.9	41.2	43.9
$E_{av}^{ap}\left(\mathrm{k\ mol^{-1}}\right)$	29.0±4							Not included		

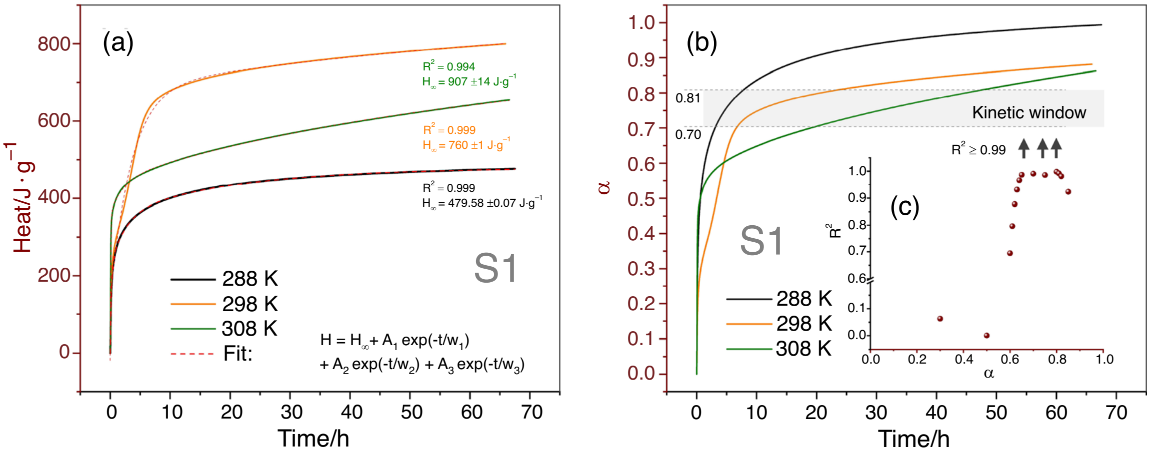

Fig. 13 Hydration of undoped C_3A (S1): Heat of the hydration measured by isothermal calorimetry (**a**) and the time dependence of the degree of the conversion (**b**). The dependence of R^2 on the degree of conversion (**c**), which defines the range of the "kinetic window", where the kinetics of the hydration process can be evaluated

decided that the mechanism based on the kinetics of the first-order reaction is more probable ($E_a(\mathrm{FOR}) \cong E_{ap}^{av}$). And this regardless of the fact that R^2 is slightly higher in the case of the second mechanism.

The presence of the dopants has a significant effect on the hydration kinetics of tricalcium aluminate. Pure C_3A produces much more heat than is released during hydration of doped samples—compare Fig. 13(S1) and Fig. 16(S2). Furthermore, the kinetic window is significantly reduced by dopants (S2, Fig. 16c) or even absent (S3 and S4). For example, for sample S3, the highest value of $R^2 = 0.873$, which was found for $\alpha = 0.4$ (Table 5). It can therefore be stated that the kinetic window narrows with increasing dopant concentration and moves towards lower conversions degree. A serious consequence of this fact is that it is very difficult to determine the activation energy of hydration for samples with a higher contents or more complex combinations of dopants.

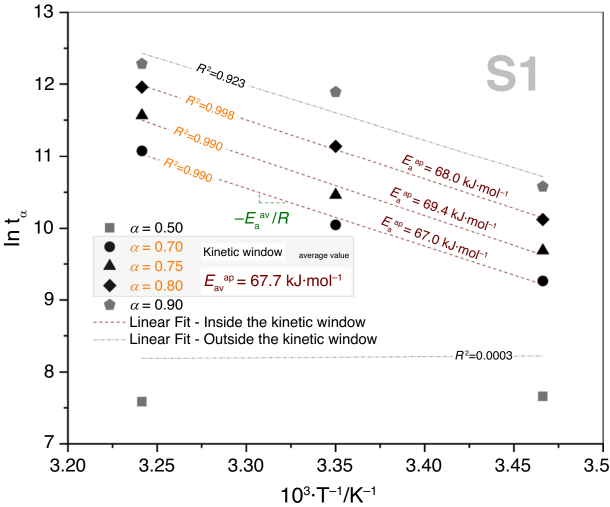

Fig. 14 Kinetic plot for undoped C_3A (S1)—reaction mechanism-free method showing dependence of $\ln t_{\alpha}(T)$ on reciprocal temperature

The presence of additives will also affect the stability of hexagonal hydrates. As results, the kinetic graphs then gain the usual slope sign (Fig. 17). The probable reason for such behavior is the different influence and its temperature dependence of the individual components of the mixture on the stability of the hydrates. Within the range of the kinetic window (Fig. 16c), the average apparent activation energy determined for S2 hydration is 19.2kJ mol^{-1} (Fig. 18).

With regard to the above facts, the problem of determining the activation energy for the hydration of the S3 (C_3A 0.2Cu1Li2S) and S4 (C_3A 1Cu1Li2S) lies mainly in the fact that the kinetic window is completely missing. However, if the course of hydration of sample S3 (C_3A 0.2Cu1Li2S) is treated analogously to sample S2 (C_3A 0.2Cu0.2Li0.5S) and

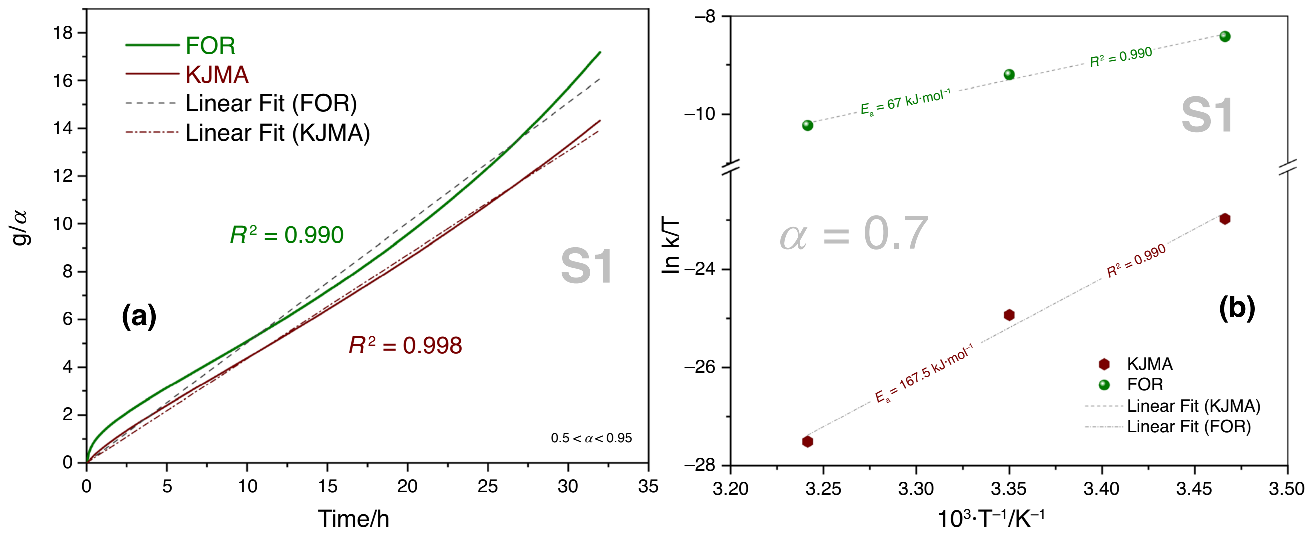

Fig. 15 By comparing the activation energy (**b**) of the two most likely kinetic equations (**a**), i.e., FOR and KJMA, with the results of the mechanism-independent model, FOR can be determined as the most propable reaction mechanism. The selected α value is located in the area of kinetic window (Fig. 13c)

only kinetic data for $R^2 > 0.8$ are used (Table 5), then the average value of the activation energy can be estimated at 29 ± 4 kJ mol^{-1}. However, for sample S4 (C_3A 1Cu1Li2S), where the content of additives is the largest, even this method fails, and no relevant conclusions can be drawn about the activation energy of their hydration.

In other words, the overall result of the combination of a greater number of ingredients at different temperatures is different. However, based on the results for S3 (C_3A 0.2Cu1Li2S), it can be concluded that the additives used have the opposite effect on the course of hydration. Among other things, this will be manifested by the fact that the activation energy of C_3A (S1) hydration will increase by one-third compared to sample S2 (C_3A 0.2Cu0.2Li0.5S). By comparing the apparent activation energy for the hydration of pure C_3A (S1) and the doped S2 (C_3A 0.2Cu0.2Li0.5S) and S3 (C_3A 0.2Cu1Li2S) (Fig. 18), it is obvious that the $E_{\mathrm{ap}}^{\mathrm{av}}$ decreases with doping. If the composition of the additive is expressed in the form of a dimensionless modulus:

$$M_D = \frac{\mathrm{Cu} + \mathrm{Li}}{\mathrm{S}} \tag{16}$$

For example, the value of M_D for the S3 (C_3A 0.2Cu1Li2S) is 0.6. Obtained dependence can be reliably described as linear. This also explains why the activation energy of S3 is higher than that of sample S2. The extrapolation of this dependence on the composition corresponding to S4 (C_3A 1Cu1Li2S) was used in this work to estimate the activation energy (6kJ mol^{-1}), which in the case of this sample cannot be determined experimentally.

The decrease in the activation energy of C_3A hydration with the increasing concentration of cationic dopants, especially Li, is fully consistent with research that points to the fact that lithium accelerates the hydration of tricalcium aluminate (see discussion of Eqs. 7 and 8). Considering the following facts:

a. Apparent activation energy decreases with increasing value of modulus M_D (Fig. 18).
b. Depending on the condition, the hydration of C_3A leads to different hydrates, i.e. cubic or hexagonal hydrates. In other words, this means that at ambient temperature the hexagonal hydrates (C_2AH_8, C_4AH_{13}…) form faster, but cubic hydrate (C_3AH_6) is thermodynamically more stable. Formation of C_4AH_{13} is also supported via free lime, which is present in the prepared samples.
c. Hydration of clinker phases are generally long chemical processes that take place on the order of days to weeks. The slow progress of the process generally supports the tasks of the thermodynamic point of view to control the speed of the process.

It can be concluded that with increasing value of the modulus $M_\mathrm{D} \gtrsim 1$, the energy barrier is lowered enough that hydration reaction is not controlled kinetically but becomes more and more thermodynamically (non-kinetically) controlled process. In other words, this means that the higher thermodynamic stability of the cubic hydrate becomes more and more apparent during the course of C_3A hydration. It can be also seen from Fig. 17 that apparent activation energy for hydration of S3 (C_3A 0.2Cu1Li2S) and S2 (C_3A

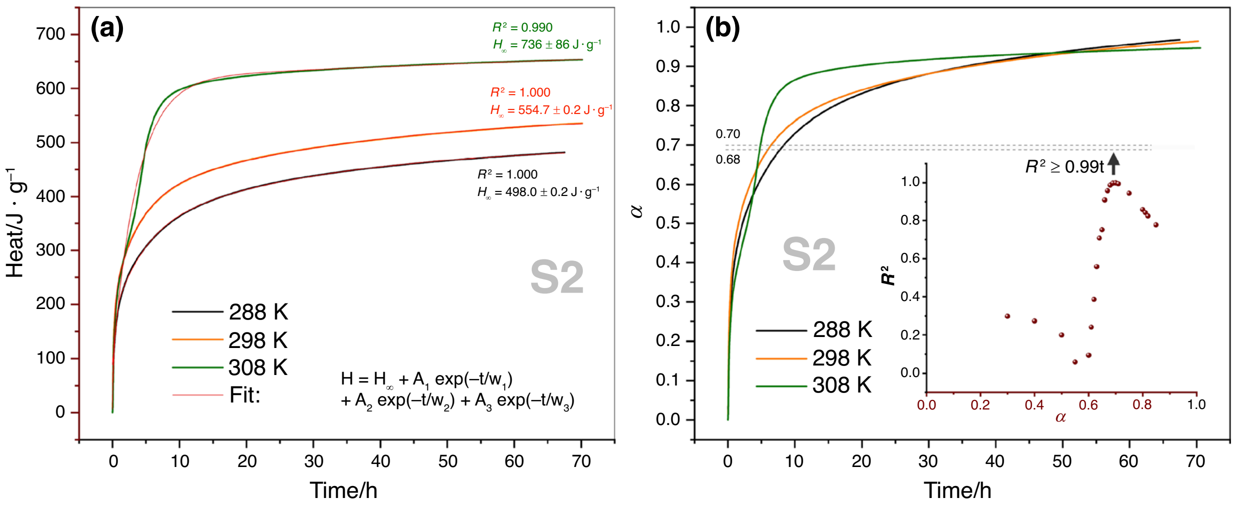

Fig. 16 Hydration of S2 (C_3A 0.2Cu0.2Li0.5S): Heat of the hydration measured by isothermal calorimetry (**a**) and degree of the conversion (**b**). The dependence of R.^{2} on the degree of conversion (**c**), which defines the range of the "kinetic window"

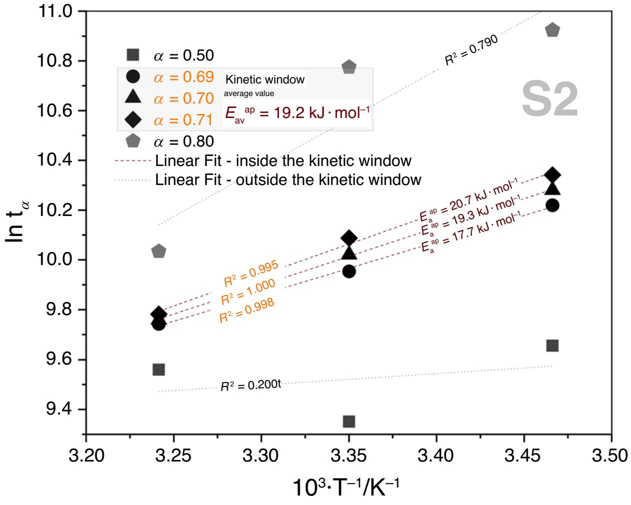

Fig. 17 Kinetic plot for S2—reaction mechanism-free method showing dependence of $\ln t_{\alpha}(T)$ on reciprocal temperature

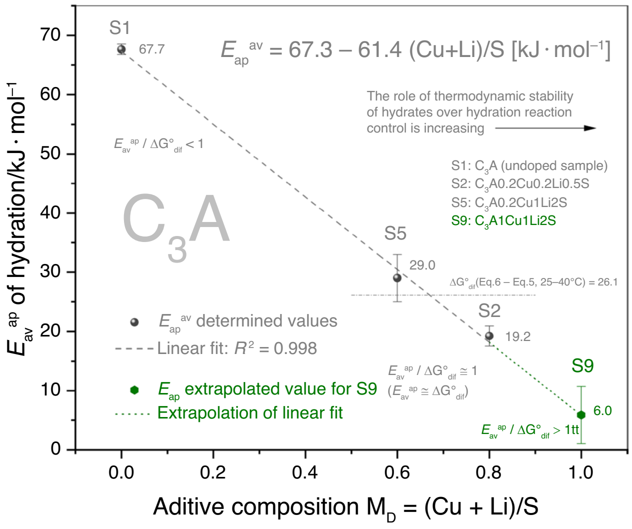

Fig. 18 Effect of doping on tricalcium aluminate hydration kinetics

0.2Cu0.2Li0.5S) is comparable to average difference of ΔG° for reaction Eq. 4 (formation of C_3AH_6) and Eq. 3 (formation of C_4AH_{13}) that is 26 kJ mol^{-1} (298–313 K). In general, this difference is higher at lower temperatures. This can be generalized as follows:

1. Doping of C_3A leads to presence of free lime and causes decrease in activation energy of hydration. As results, the reaction becomes thermodynamically controlled. This causes that formation of hexagonal hydrates.
2. Formation of C_4AH_{13} is preferred over C_4AH_{19}.
3. Increasing temperature support formation of cubic hydrate (C_3AH_6) instead of C_4AH_{13}.

Conclusions

- Investigation of the hydration kinetics revealed the differences in the influence of dopants on the hydration mechanism of C_3A:
    - System containing lower amount of S follows standard behavior expected during the hydration of tricalcium aluminate phase.

  - Higher sulfur content changes the hydration behavior significantly more resembling that of sulfoaluminate cements.

- Lithium and Copper doping lower the activation energy of C_3A hydration.
- Sulfate doping increases the activation energy of C_3A hydration, so its effect is opposite to that of cationic dopants.
- The increasing value of MD leads to the fact that role of thermodynamic control over the C_3A hydration increases while role of kinetic reaction control is decreasing.

Acknowledgements This research was funded by the Czech Science Foundation under the project number GA23-05082S: The research on the combined effect of sulfur, copper and lithium oxides on the formation and properties of Portland cement clinker.

Author contributions *Eva Bartonickova* contributed to conceptualization, investigation, methodology, resources, supervision, validation, visualization, writing—original draft, writing—review and editing. *Petr Ptacek* done investigation, methodology, resources, writing—original draft writing—review and editing. *Radoslav Novotny*, *Jiri Svec*, and *Jakub Palovcik* done investigation and methodology. *Jiri Masilko* done investigation and visualization. *Martin Sedlacik* done investigation and writing—review and editing. *Jan Koplik*, *Theodor Stanek*, and *Dusan Hemzal* done investigation.

Funding Open access publishing supported by the National Technical Library in Prague.

Declarations

Conflict of interest The authors declare that they have no known competing financial interests or personal relationships that could have appeared to influence the work reported in this paper.

References

1. Supriya CR, Sharma U, Thapliyal PC, Singh LP. Low-CO_2 emission strategies to achieve net zero target in cement sector. J Clean Prod. 2023;417:137466. https://doi.org/10.1016/j.jclepro.2023.137466.
2. CEMBUREAU. The European Cement Association. The role of cement the 2050 Low carbon economy
3. Juenger MCG, Siddique R. Recent advances in understanding the role of supplementary cementitious materials in concrete. Cem Concr Res. 2015;78:71–80. https://doi.org/10.1016/j.cemconres.2015.03.018.
4. Jhatial A, Nováková I, Gjerløw E. A Review on Emerging Cementitious Materials, Reactivity Evaluation and Treatment Methods. Buildings. 2023;13:526. https://doi.org/10.3390/buildings13020526.
5. Raghav M, Park T, Yang H-M, Lee S-Y, Karthick S, Lee H-S. Review of the effects of supplementary cementitious materials and chemical additives on the physical, mechanical and durability properties of hydraulic concrete. Materials. 2021;14(23):7270.
6. Gartner E, Sui T. Alternative cement clinkers. Cem Concr Res. 2018;114:27–39. https://doi.org/10.1016/j.cemconres.2017.02.002.
7. Nie S, Zhou J, Yang F, Lan M, Li J, Zhang Z, et al. Analysis of theoretical carbon dioxide emissions from cement production: methodology and application. J Clean Prod. 2022;334:130270. https://doi.org/10.1016/j.jclepro.2021.130270.
8. Antunes M, Santos RL, Pereira J, Rocha P, Horta RB, Colaço R. Alternative clinker technologies for reducing carbon emissions in cement industry: a critical review. Materials. 2022;15(1):209.
9. Paul G, Boccaleri E, Marchese L, Buzzi L, Canonico F, Gastaldi D. Low temperature sulfoaluminate clinkers: the role of sulfates and silicates on the different hydration behavior. Constr Build Mater. 2021;268:121111. https://doi.org/10.1016/j.conbuildmat.2020.121111.
10. Cuesta A, Ayuela A, Aranda MAG. Belite cements and their activation. Cem Concr Res. 2021;140:106319. https://doi.org/10.1016/j.cemconres.2020.106319.
11. Kacimi L, Simon-Masseron A, Salem S, Ghomari A, Derriche Z. Synthesis of belite cement clinker of high hydraulic reactivity. Cem Concr Res. 2009;39(7):559–65. https://doi.org/10.1016/j.cemconres.2009.02.004.
12. Hanein T, Galan I, Glasser FP, Skalamprinos S, Elhoweris A, Imbabi MS, et al. Stability of ternesite and the production at scale of ternesite-based clinkers. Cem Concr Res. 2017;98:91–100. https://doi.org/10.1016/j.cemconres.2017.04.010.
13. Pimraksa K, Chindaprasirt P. 14–Sulfoaluminate cement-based concrete. In: Pacheco-Torgal F, Melchers RE, Shi X, Belie ND, Tittelboom KV, Sáez A, editors. eco-efficient repair and rehabilitation of concrete infrastructures. Woodhead Publishing; 2018. p. 355–85.
14. Tao Y, Rahul AV, Mohan MK, De Schutter G, Van Tittelboom K. Recent progress and technical challenges in using calcium sulfoaluminate (CSA) cement. Cement Concr Compos. 2023;137:104908. https://doi.org/10.1016/j.cemconcomp.2022.104908.
15. Li C, Wu M, Yao W. Effect of coupled B/Na and B/Ba doping on hydraulic properties of belite-ye'elimite-ferrite cement. Constr Build Mater. 2019;208:23–35. https://doi.org/10.1016/j.conbuildmat.2019.02.163.
16. Zhao J, Huang J, Yu C, Cui C. Synthesis and formation process of a typical doped solid-solution ye'elimite ($Ca_{3.8}Na_{0.2}Al_{5.6}Fe_{0.2}Si_{0.2}SO_{1.6}$): experiments and kinetic analysis. Appl Sci. 2021;11(17):8015.
17. Morsli K, de la Torre ÁG, Zahir M, Aranda MAG. Mineralogical phase analysis of alkali and sulfate bearing belite rich laboratory clinkers. Cem Concr Res. 2007;37(5):639–46. https://doi.org/10.1016/j.cemconres.2007.01.012.
18. Fortsch DS (ed.) (2004) The effects of excess sulfur on clinker properties. In: *IEEE-IAS/PCA 2004 cement industry technical conference (IEEE Cat No04CH37518)*, pp 25–30

19. Kolovos KG, Tsivilis S, Kakali G. Study of clinker dopped with P and S compounds. J Therm Anal Calorim. 2004;77(3):759–66. https://doi.org/10.1023/B:JTAN.0000041655.82776.09.
20. Ma X-W, Chen H-X, Wang P-M. Effect of CuO on the formation of clinker minerals and the hydration properties. Cem Concr Res. 2010;40(12):1681–7. https://doi.org/10.1016/j.cemconres.2010.08.009.
21. Yamashita M, Harada T, Sakai E, Tsuchiya K. Influence of sulfur trioxide in clinker on the hydration heat and physical properties of Portland cement. Constr Build Mater. 2020;250:118844. https://doi.org/10.1016/j.conbuildmat.2020.118844.
22. Black L, Breen C, Yarwood J, Deng CS, Phipps J, Maitland G. Hydration of tricalcium aluminate (C_3A) in the presence and absence of gypsum—studied by Raman spectroscopy and X-ray diffraction. J Mater Chem. 2006;16(13):1263–72. https://doi.org/10.1039/B509904H.
23. Jin Q, Chen L. A Review of the Influence of Copper Slag on the Properties of Cement-Based Materials. Materials. 2022;15(23):8594.
24. Taylor HFW. Cement Chemistry. Thomas Telford Publishing; 1997. https://doi.org/10.1680/cc.25929.
25. Andrade Neto JS, de Matos PR, De la Torre AG, Campos CEM, Gleize PJP, Monteiro PJM, et al. The role of sodium and sulfate sources on the rheology and hydration of C_3A polymorphs. Cem Concr Res. 2022;151:106639. https://doi.org/10.1016/j.cemconres.2021.106639.
26. Andrade Neto JdS, De la Torre AG, Kirchheim AP. Effects of sulfates on the hydration of Portland cement—A review. Constr Build Mater. 2021;279:122428. https://doi.org/10.1016/j.conbuildmat.2021.122428.
27. Padilla-Encinas P, Palomo A, Blanco-Varela MT, Fernández-Jiménez A. Calcium sulfoaluminate clinker hydration at different alkali concentrations. Cem Conc Res. 2020. https://doi.org/10.1016/j.cemconres.2020.106251.
28. Tokyay M. Cement and Concrete Mineral Admixtures. 1st ed. Boca Raton: CRC Press; 2016.
29. Havlica J, Roztocka D, Sahu S. Hydration kinetics of calcium-aluminate phases in the presence of various ratios of Ca^{2+} and SO_4^{2-} ions in liquid-phase. Cem Concr Res. 1993;23(2):294–300. https://doi.org/10.1016/0008-8846(93)90094-p.
30. Meinhard K, Lackner R. Multi-phase hydration model for prediction of hydration-heat release of blended cements. Cem Concr Res. 2008;38(6):794–802. https://doi.org/10.1016/j.cemconres.2008.01.008.
31. Breval E. C3A hydration. Cem Concr Res. 1976;6(1):129–37. https://doi.org/10.1016/0008-8846(76)90057-0.
32. Lothenbach B, Pelletier-Chaignat L, Winnefeld F. Stability in the system $CaO–Al_2O_3–H_2O$. Cem Concr Res. 2012;42(12):1621–34. https://doi.org/10.1016/j.cemconres.2012.09.002.
33. Joseph S, Skibsted J, Cizer Ö. A quantitative study of the C_3A hydration. Cem Concr Res. 2019;115:145–59. https://doi.org/10.1016/j.cemconres.2018.10.017.
34. Gobbo L, Ll Sant'Agostino, Garcez L. C3A polymorphs related to industrial clinker alkalies content. Cem Concr Res. 2004;34(4):657–64. https://doi.org/10.1016/j.cemconres.2003.10.020.
35. Mondal P, Jeffery JW. The crystal structure of tricalcium aluminate, $Ca_3Al_2O_6$. Acta Crystallogr B. 1975;31(3):689–97. https://doi.org/10.1107/S0567740875003639.
36. Stephan D, Wistuba S. Crystal structure refinement and hydration behaviour of doped tricalcium aluminate. Cem Concr Res. 2006;36(11):2011–20. https://doi.org/10.1016/j.cemconres.2006.06.001.
37. Yu H-y, Pan X-l, Wang B, Zhang W, Sun H-l, Bi S-w. Effect of Na_2O on formation of calcium aluminates in $CaO–Al_2O_3–SiO_2$ system. Trans Nonferrous Metals Soc China. 2012;22(12):3108–12. https://doi.org/10.1016/S1003-6326(11)61578-1.
38. Segata M, Marinoni N, Galimberti M, Marchi M, Cantaluppi M, Pavese A, et al. The effects of MgO, Na_2O and SO_3 on industrial clinkering process: phase composition, polymorphism, microstructure and hydration, using a multidisciplinary approach. Mater Charact. 2019;155:109809. https://doi.org/10.1016/j.matchar.2019.109809.
39. Tian Y-p, Pan X-l, Yu H-y, Tu G-f. Formation mechanism and crystal simulation of Na_2O-doped calcium aluminate compounds. Trans Nonferrous Metals Soc China. 2016;26(3):849–58. https://doi.org/10.1016/S1003-6326(16)64176-6.
40. Boháč M, Kubátová D, Krejčí Kotlánová M, Khongová I, Zezulová A, Novotný R, et al. The role of Li_2O, MgO and CuO on SO_3 activated clinkers. Cem Concr Res. 2022;152:106672. https://doi.org/10.1016/j.cemconres.2021.106672.
41. Han WW, Sun T, Li XP, Shui ZH, Chen YZ, Sun MA. Influence of lithium carbonate on CA hydration. Adv Mater Sci Eng. 2018;2018:1–8. https://doi.org/10.1155/2018/6120269.
42. Wang J, Qian C, Qu J, Guo J. Effect of lithium salt and nano nucleating agent on early hydration of cement based materials. Constr Build Mater. 2018;174:24–9. https://doi.org/10.1016/j.conbuildmat.2018.04.073.
43. Horkoss S, Lteif R, Rizk T. Calculation of the C_3A percentage in high sulfur clinker. Int J Anal Chem. 2010;2010:102146. https://doi.org/10.1155/2010/102146.
44. Deng Q, Zhao M, Rao M, Wang F. Effect of CuO-doping on the hydration mechanism and the chloride-binding capacity of C4AF and high ferrite Portland clinker. Constr Build Mater. 2020;252:119119. https://doi.org/10.1016/j.conbuildmat.2020.119119.
45. Staněk T, Sulovský P. The influence of the alite polymorphism on the strength of the Portland cement. Cem Concr Res. 2002;32(7):1169–75. https://doi.org/10.1016/S0008-8846(02)00756-1.
46. Ghoroi C, Suresh AK. Solid–solid reaction kinetics: Formation of tricalcium aluminate. AIChE J. 2007;53(2):502–13. https://doi.org/10.1002/aic.11086.
47. Lazău I, Păcurariu C, Băbuţă R. The use of thermal analysis in the study of $Ca_3Al_2O_6$ formation by the polymeric precursor method. J Therm Anal Calorim. 2011;105(2):427–34. https://doi.org/10.1007/s10973-010-1246-2.
48. Mohamed BM, Sharp JH. Kinetics and mechanism of formation of tricalcium aluminate, $Ca_3Al_2O_6$. Thermochim Acta. 2002;388(1):105–14. https://doi.org/10.1016/S0040-6031(02)00035-7.
49. Kolovos K, Tsivilis S, Kakali G. The effect of foreign ions on the reactivity of the $CaO–SiO_2–Al_2O_3–Fe_2O_3$ system: Part II: Cations. Cem Concr Res. 2002;32(3):463–9. https://doi.org/10.1016/S0008-8846(01)00705-0.
50. Tizzoni A, Corsaro N, D'Ottavi C, Licoccia S, Sau S, Tarquini P. Oxygen production by intermediate metal sulphates in sulphur based thermochemical water splitting cycles. Int J Hydrog Energy. 2015. https://doi.org/10.1016/j.ijhydene.2015.01.147.
51. Yasnó J, Conconi S, Visintin A, Suárez G. Non-isothermal reaction mechanism and kinetic analysis for the synthesis of monoclinic lithium zirconate (m-Li_2ZrO_3) during solid-state reaction. J Anal Sci Technol. 2021. https://doi.org/10.1186/s40543-021-00267-5.
52. Varghese S, Hariharan K. Influence of quenching on the structural and conduction characteristics of lithium sulfate. Ionics. 2018. https://doi.org/10.1007/s11581-017-2395-0.
53. Shannon RD. Revised Effective Ionic Radii and Systematic Studies of Interatomic Distances in Halides and Chalcogenides. Acta Crystalographica. 1976;A32:751–67.

54. Saraswat IP, Mathur VK, Ahluwalia SC. Thermal studies of the $CaCO_3$: SiO_2 (2:1) system containing lithium as dopant. Thermochim Acta. 1986;97:313–20. https://doi.org/10.1016/0040-6031(86)87033-2.
55. Nakai I, Sugitani Y, Nagashima K, Niwa Y. X-ray photoelectron spectroscopic study of copper minerals. J Inorg Nucl Chem. 1978;40(5):789–91. https://doi.org/10.1016/0022-1902(78)80152-3.
56. NIST X-ray Photoelectron Spectroscopy Database [database on the Internet] 2000. Accessed
57. Ertl G, Hierl R, Knözinger H, Thiele N, Urbach HP. XPS study of copper aluminate catalysts. Appl Surf Sci. 1980;5(1):49–64. https://doi.org/10.1016/0378-5963(80)90117-8.
58. Da YQ, He TS, Shi C, Lin YK, Feng Y. Revealing the co-doping effects of fluorine and copper on the formation and hydration of cement clinker. Constr Build Mater. 2022. https://doi.org/10.1016/j.conbuildmat.2022.127516.
59. Rao J, Wang Y, Wang W, Ke H, Li Y, Zhao Y, et al. Mechanism of superior luminescent and high-efficiency photocatalytic properties of Eu-doped calcium aluminate by low-cost self-propagating combustion synthesis technique. Sci Rep. 2017;7(1):2906. https://doi.org/10.1038/s41598-017-03099-9.
60. Kim S-j, Kageyama M, Gao X, Ueda S, Kitamura S-y. Solubility of sulfur in the solid oxide of the calcium-aluminate system. ISIJ Int. 2019;59(10):1752–5. https://doi.org/10.2355/isijinternational.ISIJINT-2019-127.
61. Kurmaev EZ, Fedorenko VV, Galakhov VR, Bartkowski S, Uhlenbrock S, Neumann M, et al. Analysis of oxyanion (BO_3^{3-}, CO_3^{2-}, SO_4^{2-}, PO_4^{3-}, SeO_4^{4-}) substitution in Y123 compounds studied by X-ray photoelectron spectroscopy. J Supercond. 1996;9(1):97–100. https://doi.org/10.1007/BF00728433.
62. Li X, Zhang Y, Shen X, Wang Q, Pan Z. Kinetics of calcium sulfoaluminate formation from tricalcium aluminate, calcium sulfate and calcium oxide. Cem Concr Res. 2014;55:79–87. https://doi.org/10.1016/j.cemconres.2013.10.006.
63. El Khessaimi Y, El Hafiane Y, Smith A. Examination of ye'elimite formation mechanisms. J Eur Ceram Soc. 2019;39(15):5086–95. https://doi.org/10.1016/j.jeurceramsoc.2019.07.042.
64. Brahim M-N, Mechling J-M, Janvier-Badosa S, Marchetti M. Early stage ettringite and monosulfoaluminate carbonation investigated by in situ Raman spectroscopy coupled with principal component analysis. Mater Today Commun. 2023;35:105539. https://doi.org/10.1016/j.mtcomm.2023.105539.
65. Black L, Breen C, Yarwood J, Phipps J, Maitland G. In situ Raman analysis of hydrating C3A and C4AF pastes in presence and absence of sulphate. Adv Appl Ceram. 2006;105(4):209–16. https://doi.org/10.1179/174367606X120179.
66. Jing G, Ye Z, Cui J, Li C, Liu S, Wu J, et al. Effects of graphene oxide on the hydration behavior of ye'elimite. J Mater Sci. 2019;54(19):12582–91. https://doi.org/10.1007/s10853-019-03801-4.
67. Kolovos K, Tsivilis S, Kakali G. SEM examination of clinkers containing foreign elements. Cement Concr Compos. 2005;27(2):163–70. https://doi.org/10.1016/j.cemconcomp.2004.02.003.
68. Neto JSA, de Matos PR, De la Torre AG, Campos CEM, Gleize PJP, Monteiro PJM, et al. The role of sodium and sulfate sources on the rheology and hydration of CA polymorphs. C Concr Res. 2022. https://doi.org/10.1016/j.cemconres.2021.106639.
69. Myers RJ, Geng G, Rodriguez ED, da Rosa P, Kirchheim AP, Monteiro PJM. Solution chemistry of cubic and orthorhombic tricalcium aluminate hydration. Cem Concr Res. 2017;100:176–85. https://doi.org/10.1016/j.cemconres.2017.06.008.
70. Axthammer D, Lange T, Dengler J, Gädt T. Kilogram scale synthesis of C_3A polymorphs and their hydration reactions. CEMENT. 2023;12:100064. https://doi.org/10.1016/j.cement.2023.100064.
71. Li S, Wei Y, Li B, Wang X, Chen J. Effect of MgO on microstructure evolution and exothermic characteristics of tricalcium aluminate during hydration. Ceram Int. 2024;50(2055):61. https://doi.org/10.1016/j.ceramint.2023.10.313.
72. Saikia DN, Kato S, Kojima T. Influence of Sn on the hydration of tricalcium aluminate, $Ca_3Al_2O_6$. J Therm Anal Calorim. 2011;109:1–14. https://doi.org/10.1007/s10973-011-1750-z.
73. Chen Q, Hills C, Tyrer M, Slipper I. The Hydration and Carbonation of Tricalcium Aluminate (C_3A) in the Presence of Heavy Metals. China's Refract. 2005;14:27–42.
74. Pourchet S, Regnaud L, Perez JP, Nonat A. Early C_3A hydration in the presence of different kinds of calcium sulfate. Cem Concr Res. 2009;39(11):989–96. https://doi.org/10.1016/j.cemconres.2009.07.019.

Ceramics International 51 (2025) 5536–5543

Contents lists available at ScienceDirect

Ceramics International

journal homepage: www.elsevier.com/locate/ceramint

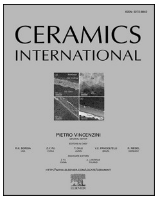

Synthesis of calcium aluminate hydrates, their characterization and dehydration

Jan Koplík [*], Jiří Švec, Jiří Másilko, Martin Sedlačík, Eva Bartoníčková

Institute of Material Science, Faculty of Chemistry, Brno University of Technology, Purkyňova 464/118, 612 00, Brno, Czech Republic

ARTICLE INFO

Handling Editor: Dr P. Vincenzini

Keywords:
Calcium aluminate hydrates
Thermal analysis
High-temperature X-ray diffraction
Dehydration
Calcium aluminate phases

ABSTRACT

This study is focused on the description of the dehydration of calcium aluminate hydrates (CAHs) and their identification. Four calcium aluminates (CA, $C_{12}A_7$, C_3A, CA_2) prepared by high temperature solid-state synthesis or modified Pechini synthesis served as precursors for CAHs. Hydration was carried out at the various temperatures in a range of 5–60 °C for 48 h. CAHs were identified by X-ray diffraction analysis (XRD) and their dehydration was characterized by Thermogravimetry and effluent gas analysis (TG/EGA) and high temperature XRD. Pure C_3AH_6 and CAH_{10} were successfully prepared, other CAHs (C_2AH_8, C_4AH_{19}, AH_3, $C_4A\bar{C}H_{11}$) were present in the mixtures. The results indicate that dehydration of C_3AH_6 takes place at a temperature of about 300 °C, followed by the formation of a new product with a structure similar to $C_{12}A_7$. C_2AH_8 dehydration can be described in three steps. The dehydration is accompanied by the formation of crystalline intermediate products. CAH_{10} dehydration can be assigned to a broad peak on the DTG curve with a maximum at approximately 100 °C. The decomposition of $C_4A\bar{C}H_{11}$ takes place in two steps, with CO_2 evolving in the temperature range 500–700 °C.

1. Introduction

Monocalcium aluminate (CA), monocalcium dialuminate (CA_2), dodecacalcium heptaaluminate ($C_{12}A_7$) and tricalcium aluminate (C_3A) are the most common stable compounds in the system $CaO–Al_2O_3$. C_3A is an indispensable component of the Ordinary Portland Cement. CA and CA_2 are the main components of Calcium Aluminate Cement (CAC), so far what $C_{12}A_7$ is the minor component of CAC [1].

Calcium aluminates can be prepared in various ways. The most common is high temperature solid-state synthesis. This method is based on high-temperature sintering of a stochiometric mixture of raw materials [2]. Another often used method is the modified Pechini technique, which is based on the ability of some hydroxycarboxylic acids to form chelates with metallic ions. The most common raw materials are nitrate salts (source of metal ions) and citric acid (chelating agent). The advantage of this method is the lower temperature of sintering. Calcium aluminates prepared by this method contain finer particles [3,4]. The alternative method is combustion synthesis or mechanochemical activation synthesis [5,6].

During the hydration of CAC or pure calcium aluminate phases, different calcium aluminate hydrates (CAHs) originate. The course of hydration can be influenced by various conditions such as particle size, pH, or admixtures [7]. The most significant is the influence of temperature. At low temperatures, metastable hydrates prevail, whereas at high temperatures stable hydrates originate. The only stable hydrate in the system is C_3AH_6. This stable hydrate can be formed directly during hydration at temperatures higher than 30 °C or as a result of the conversion of metastable hydrates. Depending essentially on the temperature and humidity, the conversion can take minutes to years. The most abundant metastable hydrates are CAH_{10} and C_2AH_8. CAH_{10} has prevailed at hydration below 20 °C, whereas C_2AH_8 dominates at hydration at 20–30 °C [8,9]. The formation of other metastable hydrates C_4AH_{19} and C_4AH_{13} is less frequent [10]. Instead of pure hydrates, in the presence of CO_2, various calcium aluminate carbonate hydrates can be formed. The predominant one is $C_4A\bar{C}H_{11}$ [11]. During the hydration of calcium aluminates with CaO/Al_2O_3 molar ratio below 2, AH_3 originates as a minor hydration product.

The CAHs can be described and characterized by various analytical methods. The most used analytical technique is X-ray diffraction analysis (XRD) [12,13]. Fourier Transform Infrared spectroscopy (FTIR) is another possible analytical technique for the characterization of CAHs and mainly FTIR bands of C_3A hydrates are well described [14]. Rarely

---

[*] Corresponding author.
E-mail address: koplik@fch.vut.cz (J. Koplík).

https://doi.org/10.1016/j.ceramint.2024.05.071
Received 2 January 2024; Received in revised form 30 April 2024; Accepted 6 May 2024

have been used Raman spectroscopy [15] or Nuclear magnetic resonance (^{27}Al NMR) yet [16]. The microstructural differences between cubic hydrates [17] and hexagonal hydrates [18] can be well distinguished by Scanning electron microscopy (SEM) or Transmitted light microscopy (TML) [19]. In the literature, CAHs are mostly described independently and an overall review of the characterization of all CAHs together is missing.

Due to the crystalline nature of CAHs, the most suitable method for their identification is XRD. The identification of C_3AH_6 and CAH_{10} is fairly straight forward, since both phases show a high degree of crystallinity and their main diffraction patterns do not overlap with those of other CAHs [20]. However, there is only a small shift between the main diffraction patterns of C_2AH_8 and C_4AH_{19}, and these hydrates can hardly be distinguished [21]. In previous works [22,23], C_2AH_8 was identified as the most common hydration product of calcium aluminates, while the formation of C_4AH_{19} was rarely mentioned [24]. The similar problem is with the precise identification of $C_4A\,\overline{C}H_{11}$ and C_4AH_{13} by XRD. Both have the main diffraction patterns near each other, which makes it difficult to characterize them. Different kind of difficulties is related to the characterization of AH_3. AH_3 in crystalline form occurs after hydration at high temperatures, whereas hydration at low temperatures leads to the formation of an amorphous or semicrystalline alumina gel, and in these states can not be identified by XRD analysis [11].

The dehydration of CAHs can be observed by thermal analysis methods such as differential thermal analysis and thermogravimetry (DTA/TG) or differential scanning calorimetry (DSC). Individual steps of dehydration are represented by endotherms by both methods. Although the dehydration of CAHs has already been widely investigated, significant differences and contradictory information in the description of characteristic endotherms can be found in the literature. The dehydration of C_3AH_6 is generally described as a one step process with a minimum at a temperature of 270–300 °C [25,26]. Some studies refer to another step of decomposition of C_3AH_6 with a minimum at 430–450 °C [27,28]. CAH_{10} dehydration is described in a wide temperature interval with a minimum of 100–200 °C [29,30]. Guirado et al. [31] and Szczerba et al. [32] also identified the second dehydration step of CAH_{10} with a minimum at 260 °C, respectively 165 °C. The wide temperature range is probably caused by overlaps with another hexagonal CAHs and incorrect attribution. The description of C_2AH_8 dehydration is quite unclear. Endotherms with minimum in the temperature range of 125–285 °C are assigned as the main step of the decomposition of C_2AH_8 [32,33]. Ukrainczyk et al. [34] characterized the dehydration of C_2AH_8 in the three main steps with a minimum at 110, 170 and 300 °C. The decomposition of calcium aluminate carbonate hydrates is generally reported by endotherm with a minimum at 150–200 °C, which can lead to confusion with another CAHs [35,36]. AH_3 dehydration can take place in more steps. If the AH_3 is present in an amorphous or semicrystalline form, the decomposition occurs at a temperature of about 100 °C. Crystalline AH_3 dehydrates in single step with endotherm with a minimum at 260–270 °C or in two steps with a minimum of 270 °C and 290 °C [37,38].

The main goal of this work is to create a concise and comprehensive interpretation of the TG/DTG curves and assign each dehydration step to the particular CAH and contribute to clearing up the confusing and contradictory results, which can often be found in the literature. To allow for unambiguous identification of the dehydration steps, pure CAHs were prepared, if it was possible, and the TG/DTA analysis was supplemented by XRD high-temperature measurement. Another aim of this work is to characterize all of the prepared hydrates by suitable analytical methods such as XRD.

2. Experimental procedure

2.1. Synthesis

2.1.1. Calcium aluminates

As precursors for calcium aluminate hydrates pure CA, CA_2, $C_{12}A_7$ and C_3A were synthesized in two ways: by high temperature solid-state synthesis [2] and modified Pechini synthesis [3,4]. $CaCO_3$ (ACS reagent) and Al_2O_3 (ACS reagent) served as raw materials for high temperature solid-state synthesis. Raw materials were mixed in a stochiometric ratio. The homogenized mixture was heated to 900 °C with 1 h delay to allow the decomposition of $CaCO_3$. Then the heating continued up to the sintering temperature (1360 °C–$C_{12}A_7$; 1450 °C–C_3A, CA; 1600 °C – CA_2) with 5 h delay.

$Al(NO_3)_3{\cdot}9H_2O$ (ACS reagent), $Ca(NO_3)_2{\cdot}4H_2O$ (ACS reagent) and $C_6H_8O_7$ (ACS reagent) were used for modified Pechini synthesis. The nitrate salts were dissolved in demineralized water in a stochiometric ratio. Citric acid was added as the complexation agent in the 1:1 M ratio (citric acid:total cations) and the mixture was stirred until all compounds dissolved. The superabundant water was evaporated, until a yellow viscose gel was formed. The prepared gel was dried for 24 h at 200 °C. The originated xerogel was grinded and heated at 400 °C for 2 h to remove organic compounds and to form the powder. The powder was then calcined for 3 h at a suitable temperature to form the final calcium aluminate (900 °C – CA, CA_2; 1200 °C–C_3A, $C_{12}A_7$). The purity of the prepared phases was determined by XRD (Table 1, Figure 1).

In general, the calcium aluminates prepared by modified Pechini synthesis (PS) contained particles with smaller diameters than those of the calcium aluminates prepared by solid state synthesis (HT). This led to increased reactivity of PS calcium aluminates, which caused the occurrence of C_3AH_6 (C_2AH_8) at lower hydration temperatures compared to HT calcium aluminates. Similar results reported Liu et al. in their study [39]. Moreover, PS calcium aluminates encourage the formation of calcium aluminate carbonate hydrates.

2.1.2. Calcium aluminate hydrates

CAHs were prepared by hydration of prepared calcium aluminates in demineralized water with a water/solid ratio of 2.0. Hydration took place at the various temperatures in a range of 5–60 °C and each one took 48 h. The hydration was then arrested by rinsing with isopropyl alcohol and diethyl ether and dried at 40 °C for 30 min.

A total of 72 samples were prepared, which differed in the temperature of hydration or in the used precursor. For the following characterization only samples containing pure hydrate (2 samples) or a unique mixture of hydrates (8 samples) were selected based on the XRD analysis. The rest of the samples contained the same pure hydrates or the same combinations of hydrates and were not characterized. The selected samples with their abbreviations are listed in Table 2. Each abbreviation consists of three parts – CA HT 5. The first part indicates the precursor of hydrate (CA, CA_2, C_3A, $C_{12}A_7$); the second one indicates how the precursor was prepared (HT – high temperature solid-state synthesis, PS – modified Pechini synthesis); the last part indicates the hydration temperature.

Table 1

The purity of prepared calcium aluminates.

Sample	Purity (wt.%)	Minor phases
C_3A HT	98	$C_{12}A_7$
CA HT	99	CA_2
$C_{12}A_7$ HT	97	CA
CA_2 HT	97	C_3A
C_3A PS	100	–
CA PS	97	CA_2
$C_{12}A_7$ PS	96	CA
CA_2 PS	100	–

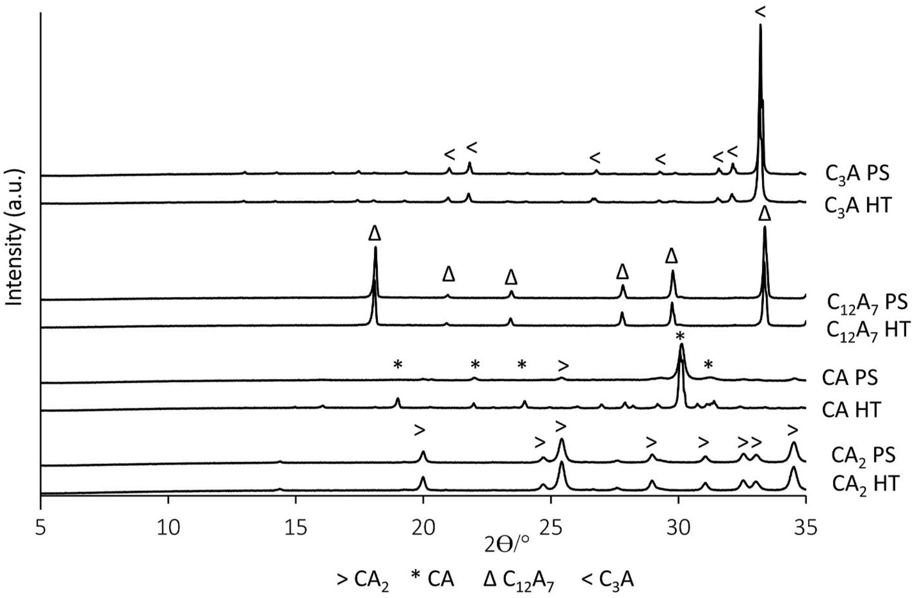

Fig. 1. XRD patterns of pure calcium aluminates.

Table 2
Selected samples.

Sample	Major hydrate	Minor hydrate	Sample	Major hydrate	Minor hydrate
CA_2 PS 60	AH_3, $C_4A\overline{C}H_{11}$	C_3AH_6	**CA PS 10**	CAH_{10}, AH_3	$C_4A\overline{C}H_{11}$
C_3A HT 10	C_3AH_6, C_2AH_8	C_4AH_{13}	**CA PS 30**	C_2AH_8, $C_4A\overline{C}H_{11}$	AH_3
C_3A HT 30	C_3AH_6	–	**CA HT 5**	CAH_{10}	–
$C_{12}A_7$ HT 50	C_3AH_6	AH_3	**$C_{12}A_7$ HT 10**	CAH_{10}, C_2AH_8	–
$C_{12}A_7$ HT 40	C_3AH_6, C_2AH_8	AH_3	**$C_{12}A_7$ HT 30**	C_2AH_8	AH_3, C_4AH_{13}

2.2. Methods

XRD analysis was carried out using Empyrean diffractometr (Malvern Panalytical Ltd., UK) with CuKα radiation in Bragg-Brentano configuration. A voltage of 40 kV and a current of 30 mA were used. Measurements were taken at the range 5–90° 2θ with step 0,013° 2θ. Data was evaluated using the HighScore Plus program. For high-temperature measurements, the HTK-16 N chamber (Anton Paar, Austria) was used. The measurements were made on a platinum strip with a heating rate of 10 °C/min.

CAHs dehydration was analyzed using the combined thermal analysis technique – TG/DTA using SDT Q650 (TA Instruments, USA) and effluent gas analysis (EGA) using Nicolet IS 10 (Thermo Fisher Scientific, USA). Measurements were carried out up to 800 °C using a heating rate of 10 °C.min^{-1} under a dried air atmosphere. The gas chamber and the transfer capillary were heated to 200 °C and the FTIR spectra of evolved gases were collected in the spectral range 450–4000 cm^{-1}, spectral resolution 4 cm^{-1} and spectra measurement interval 50 s.

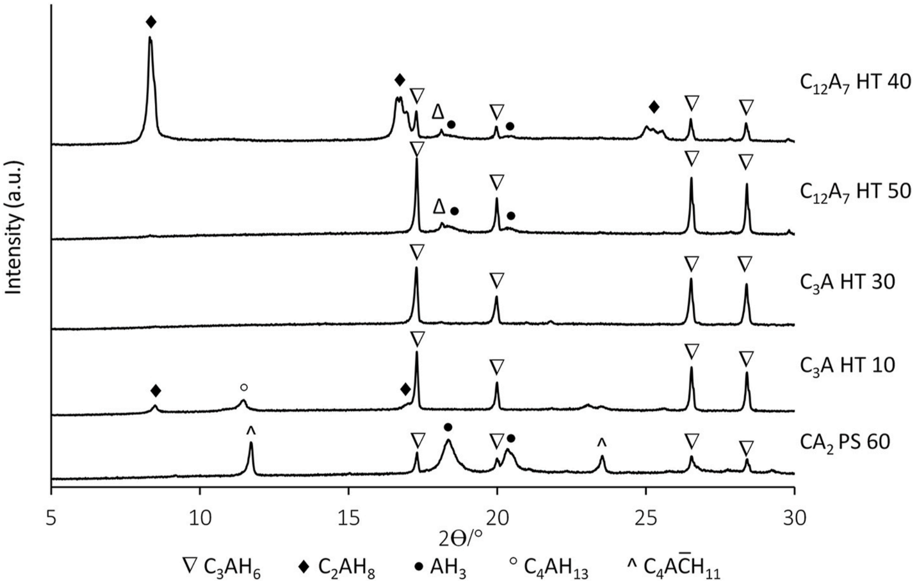

Fig. 2. XRD patterns of mixtures with cubic hydrates.

3. Results and discussion

3.1. XRD

The results of XRD analysis are summarized in Figs. 2 and 3. The analysis proved, that C_3AH_6 (C_3A HT 30) and CAH_{10} (CA HT 5) were prepared themselves without the presence of any other polluting CAHs. Pure CAH_{10} was successfully prepared by hydration of CA at temperatures below 20 °C. In general, pure C_3AH_6 can be prepared from C_3A by hydration at higher temperatures. Other calcium aluminates by hydration at high temperatures form the mixture of C_3AH_6 and AH_3 (ex. $C_{12}A_7$ HT 50), which is caused by a higher A/C stoichiometric ratio [40,41]. The main diffractions of AH_3 are broad and less distinct. This is caused by the structure of AH_3 with small size of crystallite and incomplete periodicity. After hydration at low temperatures, AH_3 is often present in the amorphous state as an alumina gel [22]. The remaining CAHs were not successfully prepared in a pure state and occur in a mixtures. The difficulty was in identifying of $C_4AH_{13,}$ because the main diffraction pattern at about 11 °2Θ overlaps with the diffraction of $C_4A\,\overline{C}H_{11}$. These two hexagonal products had to be distinguished by the comparison of the following diffraction patterns.

The results of high-temperature XRD are displayed in Fig. 4. Dehydration of C_3AH_6 (Fig. 4a) occurs in the temperature interval 265–290 °C in one step. This corresponds to the perceptible weight change with the maximum at about 300 °C observable on the DTG curves of samples containing C_3AH_6 (Fig. 5). The dehydration is followed by the formation of a new crystalline phase. This phase can be described as a structural analogue of $C_{12}A_7$, because of the nearly the same diffraction patterns. $C_{12}A_7$ was reported as the product of C_3AH_6 decomposition by Wang et al. [25]. Other works mentioned $C_{12}A_7$ as the remaining crystalline phase, into which other calcium aluminates and CAHs convert, when exposed to high temperatures [32,34].

CAH_{10} dehydration (Fig. 4b) took place in single step in the temperature range of 80–140 °C. Such a broad interval corresponds to the broad peak on the DTG curves with a maximum at 100–110 °C (Fig. 6). Compared to other CAHs, CAH_{10} dehydration was slow and occurred in the broadest temperature interval.

The dehydration of $C_4A\,\overline{C}H_{11}$ and AH_3 is described in Fig. 4c. $C_4A\,\overline{C}H_{11}$ dehydrated in the temperature interval 100–130 °C and none new crystalline product was formed. This result can be assigned to the peak on the DTG curve with maximum at 130–145 °C, which appeared in all samples containing $C_4A\,\overline{C}H_{11}$. AH_3 dehydration took place in one step in the temperature range of 210–250 °C. It can be linked with the peaks on the DTG curve with a maximum at 215–220 °C and 260–270 °C. This peak was prevailing in the samples with a major content of AH_3 (e.g., CA_2 PS 60).

The dehydration of C_2AH_8 (Fig. 4d) differed significantly from previously described hydrates. Dehydration took place in three steps, followed by the formation of crystalline intermediate products. The first dehydration step occurred in the temperature interval 60–70 °C, second in the interval 100–120 °C and the last one in the interval 260–300 °C. The identification of intermediate crystalline products, which were formed after the first and second dehydration steps, was not successful. Ukrainczyk et al. [34] attributed the formed intermediate dehydration products to C_2AH_5 and C_2AH_4. C_2AH_5 was reported as metastable hydration product of C_2AH_8 by Heueller et al. too [42]. After the last dehydration step, no stable crystalline product was formed. The comparison of high-temperature XRD of C_2AH_8 with the TG measurements was not unambiguous. The C_2AH_8 in the samples was present in the mixture with other CAHs, which caused overlaps on the DTG curves. However, in mixtures containing C_2AH_8 the peaks on the DTG curves with maximum at 70–80 °C, 125–145 °C and 260–290 °C appeared, which corresponded to the XRD measurement.

3.2. TG/DTG/EGA

For description of CAHs dehydration, TG analysis was used. The measurement of CAHs represented by DTG curves is summarized in Figs. 5 and 6. The DTG curves of all samples with C_3AH_6 contained two peaks with maximum at 290–300 °C and 430–440 °C. The first one was described in the previous section. The second one had much lower intensity and in the case of low C_3AH_6 content in the sample, it could be indistinct. Since XRD measurement did not identify any new phase at this temperature interval, the second peak can be attributed to the dehydration of the C_3AH_6 residues [32]. Phrompet et al. Reported, that C_3AH_6 residues can be identified as $C_3AH_{1.5}$ [43]. The presence of C_3AH_6 in the mixture with other CAHs can lead to overlaps of the peak on the DTG curves, namely the overlap with the last step of dehydration of C_2AH_8 and dehydration of AH_3.

The sample C_3A HT 10 represented the mixture of C_3AH_6, C_2AH_8 and C_4AH_{13}. Four areas of weight changes are noticeable on the DTG curve. The first one with maximum at 58 °C resulted from the dehydration of

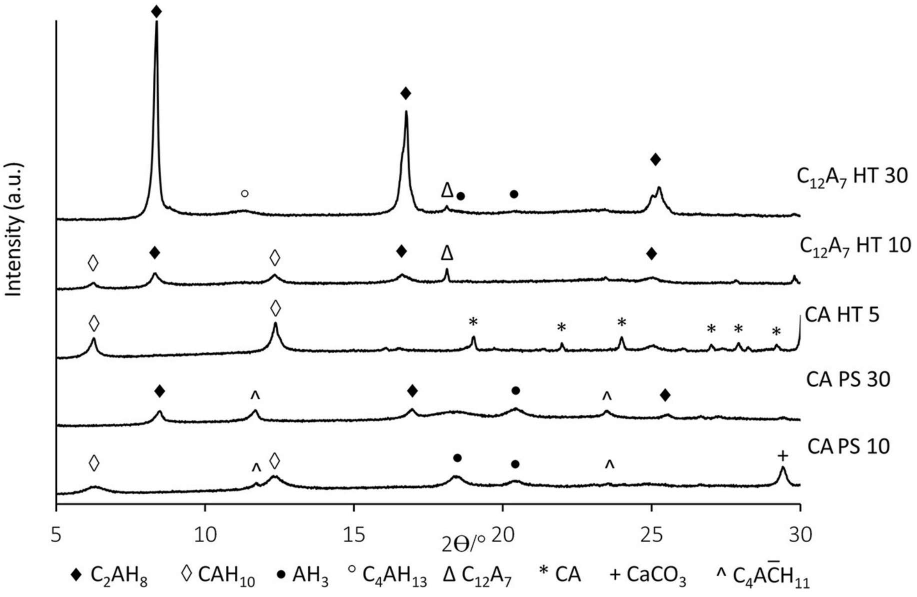

Fig. 3. XRD patterns of mixtures with hexagonal hydrates.

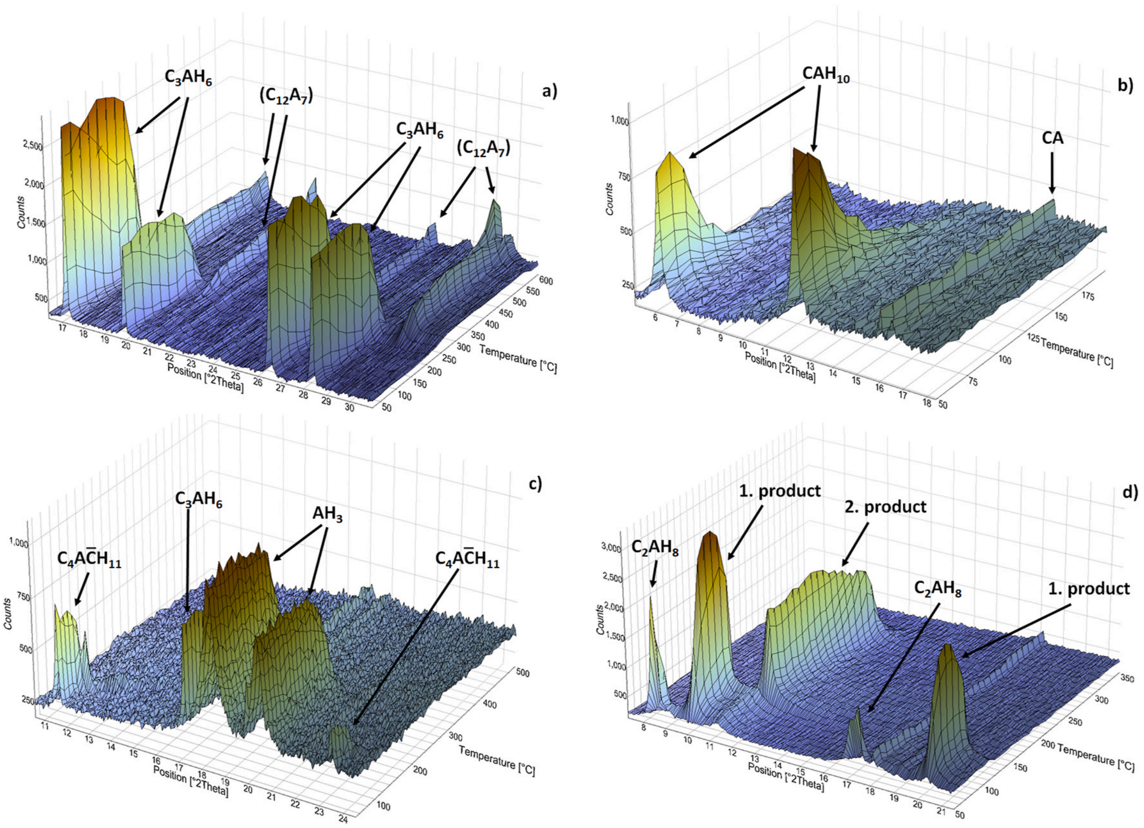

Fig. 4. (a) Dehydration of C_3AH_6; (b) dehydration of CAH_{10}; (c) dehydration of AH_3 and $C_4A\bar{C}H_{11}$; (d) dehydration of C_2AH_8.

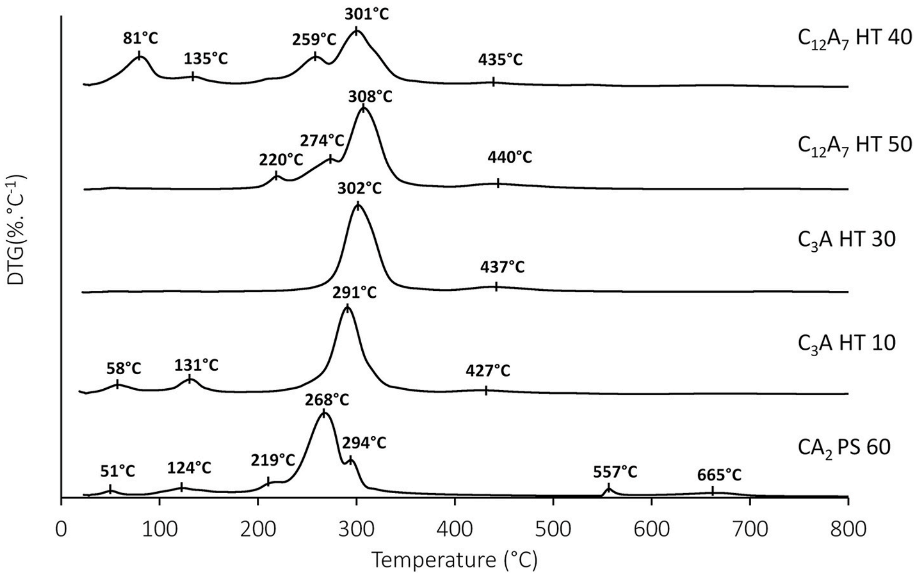

Fig. 5. DTG curves of mixtures with cubic hydrates.

C_2AH_8. The position of the peak at such a low temperature can also be influenced by residual humidity in the measured sample. The peak with maximum at 132 °C can be assigned to the second dehydration step of C_2AH_8 or to the dehydration of C_4AH_{13} [27]. The peak with the maximum at 291 °C can be attributed to the last step of C_2AH_8 dehydration and C_3AH_6 decomposition. The last peak with maximum at 427 °C represented the decomposition of C_3AH_6 as previously mentioned. The mixture of C_3AH_6, AH_3 and C_2AH_8 ($C_{12}A_7$ HT 40) showed five peaks on the DTG curve. The peaks with maximums at 301 °C and 435 °C represent the decomposition of C_3AH_6, the peaks with maximum at 81 °C, 135 °C and 301 °C represent the dehydration of C_2AH_8. The peak with maximum at 259 °C can be attributed to AH_3 dehydration [38]. The mixture of C_3AH_6 and AH_3 was represented by $C_{12}A_7$ HT 50. Unlike the previous mixtures, the peak with maximum at 220 °C on the DTG curve appeared representing AH_3 dehydration. This corresponded to high-temperature XRD measurements, which identified AH_3 dehydration in the temperature interval 210–250 °C. On the DTG curve of the mixture of C_3AH_6, AH_3 and $C_4A\bar{C}H_{11}$ (CA_2 PS 60), six areas

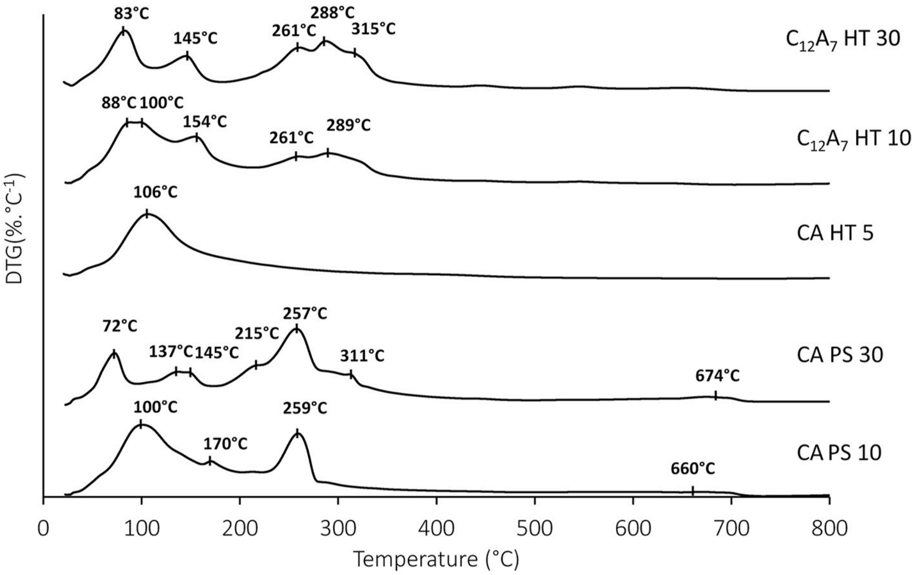

Fig. 6. DTG curves of mixtures with hexagonal hydrates.

of major weight changes can be observed. The first one with maximum at 50 °C can possibly be related to the loss of residual free water from incomplete drying of the sample prior the measurement. The peak with maximum at 137 °C can be assigned to the dehydration of $C_4A\overline{C}H_{11}$, which correlated to the XRD measurements. The area at 500–700 °C can be linked to the weight change resulting from the decomposition of $C_4A\overline{C}H_{11}$ and the evolving of CO_2. This was proved by EGA analysis, which results are showed at Fig. 7. The remaining peaks on the DTG curve can be attributed to the dehydration of C_3AH_6 and AH_3, as was described previously.

The major weight change of the sample CA HT 5 and the corresponding peak on the DTG curve with the maximum at 110 °C (Fig. 6) resulting from CAH_{10} dehydration. In the presence of other CAHs, the maximum can shift to lower temperatures up to 100 °C (CA PS 10, $C_{12}A_7$ HT 10). The CAH_{10} dehydration took place in a broader temperature interval, which can cause overlaps and shifting of the dehydration peaks of other hexagonal CAHs. It concerns the first two steps of decomposition of C_2AH_8 and dehydration of $C_4A\overline{C}H_{11}$. The mixture of CAH_{10} and C_2AH_8 was represented by the sample $C_{12}A_7$ HT 10. The broad peak with two maximums at 83 and 100 °C can be assigned to the first step of C_2AH_8 dehydration and CAH_{10} dehydration respectively. The remaining peaks with maximums at 154, 261 and 289 °C can be attributed to the dehydration of C_2AH_8. The sample CA PS 10 represented the mixture of CAH_{10}, AH_3 and $C_4A\overline{C}H_{11}$. The peak located at 100 °C resulting from the dehydration of CAH_{10}. The peak with maximum at 259 °C represented the AH_3 dehydration. The peak with maximum at 170 °C can be assigned to dehydration of $C_4A\overline{C}H_{11}$ as was mentioned in previous works [35, 36]. The mixture of C_2AH_8, AH_3 and C_4AH_{13} was represented by the sample $C_{12}A_7$ HT 30. The dehydration of C_4AH_{13} could be hidden in the peak on the DTG curve with maximum at 145 °C, which belongs to the second dehydration step of C_2AH_8. The broad peak with three maximums at 261, 288 and 315 °C represented the dehydration of C_2AH_8 and AH_3. As a result of the similar dehydration temperatures, these two hydrates cannot be distinguished clearly. Quite similar course of the DTG curve had the mixture C_2AH_8, AH_3 and $C_4A\overline{C}H_{11}$ (CA PS 30). The difference is in the broad peak with two maximums at 137 and 147 °C, which can be attributed to the dehydration of C_2AH_8 and $C_4A\overline{C}H_{11}$ and in the presence peak with maximum at 675 °C resulting from the evolving of CO_2 from $C_4A\overline{C}H_{11}$.

In general, the dehydration of C_3AH_6 is represented by two peaks on the DTG curve with maximum at about 300 °C and 440 °C. The first one corresponds to the major decomposition of C_3AH_6 resulting in the formation of a new crystalline product with the similar structure as $C_{12}A_7$. The second one can be assigned to the dehydration of the C_3AH_6 residues. The dehydration of CAH_{10} is characterized by a broad peak on the DTG curve with a maximum at about 100 °C. The dehydration of C_2AH_8 takes place in three steps resulting in the formation of crystalline intermediate products. This can be attributed to the peaks on the DTG curve with the maximums at about 80, 130 and 260–290 °C. The decomposition of $C_4A\overline{C}H_{11}$ is represented by two areas of weight change on the DTG curve. The first peak with the maximum at about 140 °C is related to the dehydration process, the second area can be linked to the CO_2 evolving, which corresponds with EGA analysis (Fig. 7). The peaks on the DTG curve with maximums at about 220, 260 and 300 °C can be attributed to the dehydration of AH_3. The presence of CAHs in the mixture causes shifting of the peaks on the DTG curve and their overlapping. Furthermore, in the temperature range of 70–170 °C the area of the dehydration of the alumina gel can be found, which can make it

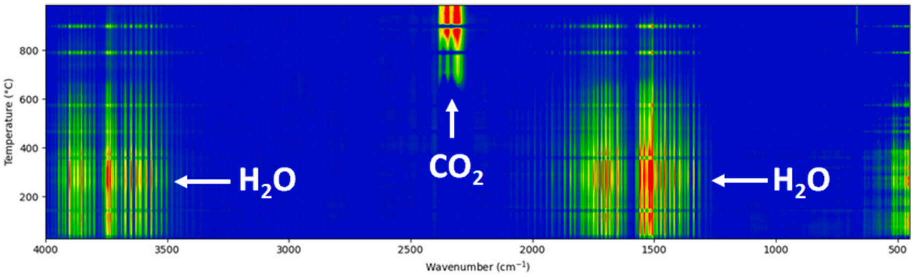

Fig. 7. EGA analysis of CA2 PS 60.

difficult to assign peaks on the DTG curve to each CAH [44,45].

4. Conclusions

Due to the hydration of various calcium aluminates at different temperatures in the range of 5–60 °C pure C_3AH_6 and CAH_{10} were prepared. Other CAHs occurred as mixtures. The CAHs were identified by XRD and their dehydration was characterized by TG analysis and high-temperature XRD and the following findings can be concluded:

- Because of crystalline structure of CAHs, XRD analysis proved to be a suitable method for their identification. The distinguishing between C_4AH_{13} and $C_4A\,\overline{C}H_{11}$ proved to be challenging, due to the overlaps of their major diffraction patterns. The identification of AH_3 can be unclear due to its possible amorphous or semicrystalline character.
- The dehydration of C_3AH_6 is represented by two peaks on the DTG curve. The first one with a maximum at about 300 °C is connected with the formation of a crystalline product structurally similar to $C_{12}A_7$. The second one with a maximum at about 440 °C can be attributed to the decomposition of the C_3AH_6 residues.
- The dehydration of C_2AH_8 takes place in three steps, which are represented by peaks on the DTG curve with maximums at about 80, 130 and 260–290 °C. The dehydration is accompanied by the formation of crystalline intermediate products.
- The dehydration of CAH_{10} is represented by a broad peak on the DTG curve with a maximum at approximately 100 °C.
- The peak with maximum at about 140 °C can be assigned to the dehydration of $C_4A\,\overline{C}H_{11}$. The evolving of CO_2 from this structure is related to the weight change on the DTG curve at 500–700 °C, which corresponds to the EGA measurement.

Using both TG/DTA and high-temperature XRD analysis enabled better characterization of the CAHs dehydration process. The results can help to describe the thermal effects linked with dehydration on the DTA/DTG curves of more complex systems such as CAC.

CRediT authorship contribution statement

Jan Koplík: Conceptualization, Data curation, Investigation, Methodology, Supervision, Validation, Writing – original draft, Writing – review & editing. **Jiří Švec:** Formal analysis, Validation. **Jiří Másilko:** Formal analysis. **Martin Sedlačík:** Formal analysis, Validation. **Eva Bartoníčková:** Formal analysis, Supervision.

Declaration of competing interest

The authors declare that they have no known competing financial interests or personal relationships that could have appeared to influence the work reported in this paper.

Acknowledgements

This paper was prepared within the framework of the work on the project no. 23-05082S financed by the Grant Agency of the Czech Republic.

References

[1] I. Odler, Special Inorganic Cements, first ed., Taylor & Francis, New York, 2000.

[2] F. Šoukal, J. Koplík, P. Ptáček, J. Havlica, M.T. Palou, L. Kalina, The influence of pH buffers on hydration of hydraulic phases in system CaO-Al_2O_3, J. Therm. Anal. Calorim. 124 (2016) 629–638, https://doi.org/10.1016/j.proeng.2016.07.392.

[3] G. Voicu, C.D. Chitulica, E. Andronescu, Modified Pechini synthesis of tricalcium aluminate powder, Mater. Char. 73 (2012) 89–95, https://doi.org/10.1016/j.matchar.2012.08.002.

[4] A. Gaki, R. Chrysafi, G. Kakali, Chemical synthesis of hydraulic calcium aluminate compounds using the Pechini technique, J. Eur. Ceram. Soc. 27 (2007) 1781–1784, https://doi.org/10.1016/j.jeurceramsoc.2006.05.002.

[5] D.A. Fumo, M.R. Moreli, A.M. Segadaes, Combustion synthesis of calcium aluminates, Mater. Res. Bull. 31 (1996) 1243–1255, https://doi.org/10.1016/0025-5408(96)00112-2.

[6] S. Kumar, A. Bandopadhyay, T.C. Alex, R. Kumar, Influence of mechanical activation on the synthesis and hydraulic aktivity of calcium dialuminate, Ceram. Int. 32 (2006) 555–560, https://doi.org/10.1016/j.ceramint.2005.04.017.

[7] P. Garces, E.G. Alcocel, S. Chinchon, C.G. Andreu, J. Alcaide, Effect of curing temperature in some hydration characteristics of calcium aluminate cement compared with those of portland cement, Cement Concr. Res. 27 (1997) 1343–1355, https://doi.org/10.1016/S0008-8846(97)00136-1.

[8] S.R. Klaus, J. Neubauer, F. Goetz-Neunhoeffer, Hydration kinetics of CA_2 and CA—investigations performed on a synthetic calcium aluminate cement, Cement Concr. Res. 43 (2013) 62–69, https://doi.org/10.1016/j.cemconres.2012.09.005.

[9] M. Nowacka, B. Pacewska, Effect of structurally different aluminosilicates on early-age hydration of calcium aluminate cement depending on temperature, Construct. Build. Mater. 235 (2020) 117404, https://doi.org/10.1016/j.conbuildmat.2019.117404.

[10] A.P. Luz, V.C. Pandolfelli, Halting the calcium aluminate cement hydration proces, Ceram. Int. 37 (2011) 3789–3793, https://doi.org/10.1016/j.ceramint.2011.06.034.

[11] E. Litwinek, M. Madej, Structure, microstructure and thermal stability characterizations of C_3AH_6 synthesized from different precursors through hydration, J. Therm. Anal. Calorim. 139 (2020) 1693–1706, https://doi.org/10.1007/s10973-019-08656-0.

[12] W. Ding, Y. He, L. Lu, F. Wang, S. Hu, Comparative study of hydration of monocalcium aluminate and quaternary phase and the amorphous AH_3 phase in their hydrates, J. Therm. Anal. Calorim. 141 (2020) 707–716, https://doi.org/10.1007/s10973-019-09069-9.

[13] C.-K. Park, Characteristics and hydration of $C_{12\text{-}x}A_7{\cdot}x(CaF_2)$ ($x = 0 \sim 1.5$) minerals, Cement Concr. Res. 28 (1998) 1357–1362, https://doi.org/10.1016/S0008-8846(98)00105-7.

[14] D. Torréns-Martín, L. Fernández-Carrasco, M.T. Blanco-Varela, Conduction calorimetric studies of ternary binders based on Portland cement, calcium aluminate cement and calcium sulphate, J. Therm. Anal. Calorim. 114 (2013), https://doi.org/10.1007/s10973-013-3003-9, 799-807.

[15] D. Torréns-Martín, L. Fernández-Carrasco, S. Martínez-Ramírez, Hydration of calcium aluminates and calcium sulfoaluminate studied by Raman spectroscopy, Cement Concr. Res. 47 (2013) 43–50, https://doi.org/10.1016/j.cemconres.2013.01.015.

[16] J. Shiju, J. Skibstead, O. Cizer, A quantitative study of the C_3A hydration, Cement Concr. Res. 115 (2019) 145–159, https://doi.org/10.1016/j.cemconres.2018.10.017.

[17] A. Solanki, L.P. Singh, S.R. Karade, U. Sharma, Functionality of silica nanoparticles on hydration mechanism and microstructure of tricalcium aluminate, Construct. Build. Mater. 299 (2021) 124238, https://doi.org/10.1016/j.conbuildmat.2021.124238.

[18] E. García Alcocel, P. Garcés, S. Chinchón, General study of alkaline hydrolysis in calcium aluminate cement mortars under a broad range of experimental conditions, Cement Concr. Res. 30 (2000) 1689–1699, https://doi.org/10.1016/S0008-8846(00)00396-3.

[19] García del Cura, P. Garcés, E. García Alcocel, Petrographical analysis of calcium aluminate cement mortars Scanning electron microscopy and transmitted light microscopy, Cement Concr. Res. 29 (1999) 1881–1885, https://doi.org/10.1016/S0008-8846(99)00184-2.

[20] C. Pastor, A. Fernandez-Jimenez, T. Vazquez, A. Palomo, Calcium aluminate cement hydration in a high alkalinity environment, Mater Construct 59 (2009) 21–34, https://doi.org/10.3989/mc.2009.42407.

[21] A. Jupe, X. Turrillas, P. Barnes, S.L. Colson, Fast in situ X-ray-diffraction studies of chemical reactions: a synchrotron view of the hydration of tricalcium aluminate, Phys. Rev. B 53 (1996) 14967, https://doi.org/10.1103/PhysRevB.53.R14697, 14700.

[22] B. Pacewska, M. Nowacka, Studies of conversion progress of calcium aluminate cement hydrates by thermal analysis method, J. Therm. Anal. Calorim. 117 (2014) 653–660, https://doi.org/10.1007/s10973-014-3804-5.

[23] S. Rashid, X. Turrilas, Hydration kinetics of $CaAl_2O_4$ using synchrotron energy-dispersive diffraction, Thermochim. Acta 302 (1997) 25–34, https://doi.org/10.1002/chin.199804015.

[24] T.R. Jensen, A.N. Christensen, J.C. Hanson, Hydrothermal transformation of the calcium aluminum oxide hydrates $CaAl_2O_4.10H_2O$ and $Ca_2Al_2O_5.8H_2O$ to $Ca_3Al_2(OH)_{12}$ investigated by in situ synchrotron X-ray powder diffraction, Cement Concr. Res. 35 (2005) 2300–2309, https://doi.org/10.1016/j.cemconres.2004.10.034.

[25] Y. Wang, X. Li, B. Zhu, P. Chen, Microstructure evolution during the heating proces and its effect on the elastic properties of CAC-bonded alumina castables, Ceram. Int. 42 (2016) 11355–11362, https://doi.org/10.1016/j.ceramint.2016.04.058.

[26] V.S. Ramachandran, R.F. Feldman, Hydration characteristics of monocalcium aluminate at a low water/solid ration, Cement Concr. Res. 3 (1973) 729–750, https://doi.org/10.1016/0008-8846(73)90008-2.

[27] V. Zivivca, M.T. Palou, M. Krizma, Low-porosity tricalcium aluminate paste, Construct. Build. Mater. 38 (2013) 1191–1198, https://doi.org/10.1016/j.conbuildmat.2012.09.025.

[28] M.M. Radwan, M. Heikal, Hydration characteristics of tricalcium aluminate phase in mixes containing β-hemihydate and phosphogypsum, Cement Concr. Res. 35 (2005) 1061–1608, https://doi.org/10.1016/j.cemconres.2004.06.037.

[29] A. Smith, T. Chotard, N. Gimet-Breart, D. Fargeot, Correlation between hydration mechanism and ultrasonic measurements in an aluminous cement: effect of setting

time and temperature on the early hydration, J. Eur. Ceram. Soc. 22 (2002) 1947–1958, https://doi.org/10.1016/S0955-2219(01)00530-1.

[30] A. Hidalgo, J.L. García, M. Cruz Alonso, L. Fernández, C. Andrade, Microstructure development in mixes of calcium aluminate cement with silica fume or fly ash, J. Therm. Anal. Calorim. 96 (2009) 335–345, https://doi.org/10.1007/s10973-007-8439-3.

[31] F. Guirado, S. Gali, J.S. Chinchón, Thermal decomposition of hydrated alumina cement ($CAHS_{10}$), Cement Concr. Res. 28 (1998) 381–390, https://doi.org/10.1016/S0008-8846(98)00007-6.

[32] J. Szczerba, D. Madej, E. Sniezek, R. Prorok, The application of DTA and TG methods to invest igate the non-crystalline hydration products of $CaAl_2O_4$ and $Ca_7ZrAl_6O_{18}$ compounds, Thermochim. Acta.

[33] S.K. Das, A. Mitra, P.K. Das Poddar, Thermal analysis of hydrated calcium aluminates, J. Therm. Anal. 47 (1996) 765–774, https://doi.org/10.1007/BF01981812.

[34] N. Ukrainczyk, T. Matusinovic, S. Kurajica, B. Zimmermann, J. Sipusic, Dehydration of a layered double hydroxide – C_2AH_8, Thermnochim, Acta 464 (2007) 7–15.

[35] J. Keriené, V. Antonovič, R. Stonys, R. Boris, The influence of the ageing of calcium aluminate cement on the properties of mortar, Construct. Build. Mater. 205 (2019) 387–397, https://doi.org/10.1016/j.conbuildmat.2019.02.039.

[36] S.M. Bushnell-Watson, J.H. Sharp, The detection of the carboaluminate phase in hydrated high alumina cements by differential thermal analysis, Thermochim. Acta 90 (1985) 613–616, https://doi.org/10.1016/0040-6031(85)85154-6.

[37] N.M. Reza, T. Nasrien, The hydration products of a refractory calcium aluminate cement at low temperatures, Iran, J. Chem. Eng. 26 (2007), https://doi.org/10.30492/ijcce.2007.7655, 71-76.

[38] E.R. Cantrill, M.G. Stevens, A. Ray, L. Aldridge, The use of DTA to determine the effects of mineralizers on the cement-quartz autoclave reactions. Gibbsite addition, Themochim, Acta 224 (1993) 241–246, https://doi.org/10.1016/0040-6031(93)80174-9.

[39] K. Liu, A. Chen X. Shang, L. Chen, L. Zheng, S. Gao, Y. Zhou, Q. Wang, G. Ye, The impact of mechanical grinding on calcium aluminate cement hydration at 30 °C, Cerarm. Inter. 11 (2019) 14121–14125, https://doi.org/10.1016/j.ceramint.2019.04.112.

[40] I.R. Oliveira, V.C. Pandolfelli, Castable matrix, additives and their role on hydraulic binder hydration, Ceram. Int. 35 (2009) 1453–1460, https://doi.org/10.1016/j.ceramint.2008.07.024.

[41] B. Raab, H. Poellmann, Heat flow calorimetry and SEM investigations to characterize the hydration at different temperatures of different $12CaO{\cdot}Al_2O_3$ ($C_{12}A_7$) samples synthesized by solid state reaction, polymer precursor process and glycine nitrate process, Thermochim. Acta 513 (2011) 106–111, https://doi.org/10.1016/j.tca.2010.11.019.

[42] F. Hueller, J. Neubauer, S. Kaessner, F. Gietz-Neunhoeffer, Hydration of calcium aluminates at 60°C – development paths of C_2AH_x in dependence on the content of free water, J. Am. Ceram. Soc. 102 (2019) 4376–7387, https://doi.org/10.1111/jace.16314.

[43] Ch. Phrompet, Ch. Sriwong, S. Maensiri, P. Chondaprasirt, Ch. Ruttanapun, Optical and dielectric properties of nano-sized tricalcium aluminate hexahydrate (C_3AH_6) cement, Construct. Build. Mater. 179 (2018) 57–65, https://doi.org/10.1016/j.conbuildmat.2018.05.180.

[44] J.L. Szetu, R.L. Frost, J.T. Kloprogge, S.C. Russel, W. Martens, Dehydration and dehydroxylation of alumina gels prepared from tri-sec-butoxyaluminium modified with short chain aliphatic acids, Thermochim. Acta 362 (2000) 37–48, https://doi.org/10.1016/S0040-6031(00)00572-4.

[45] Y. Wang, S. Xing, Y. Zhang, Z. Li, Y. Ma, Z. Zhang, Mineralogical and thermal characteristics of low-grade Jinlong bauxite sourced from Guangxi Province, China, J. Therm. Anal. Calorim. 122 (2015) 917–927, https://doi.org/10.1007/s10973-015-4742-6.

C: Skupina publikací týkající se hydratace CAC cementů a koloidních roztoků

15. *P. Ptáček, F. Šoukal, T. Opravil, E.* ***Bartoníčková****, M. Zmrzlý, R. Novotný*, Synthesis, hydration and thermal stability of hydrates in strontium-aluminate cement, Ceramics International, 40 (2014) 9971-9979.
16. *E.* ***Bartoníčková,*** *P. Ptáček, T. Opravil, F. Šoukal, J. Másilko, R. Novotný, J. Švec, J. Havlica*, Mullite-based refractories fabricated by foam casting, Ceramics International 41(10) (2015) 14116-14123.
17. *P. Ptáček, K. Lang, F. Šoukal, T. Opravil, E.* ***Bartoníčková****, L. Tvrdík,* Preparation and properties of enstatite ceramic foam from talc, Journal of the European Ceramic Society 34(2) (2014) 515-522.
18. *E.* ***Bartonickov****a, J. Svec, L. Dlabajova, P. Hruby, V. Caba, M. Sedlacik, L. Kalina, J. Koplik, F. Soukal, L. Kersnerova, J. Zach, V. Novak, K. Dvorak*, Tailoring microstructure and properties of porous mullite-based ceramics via sol-gel impregnation, Ceramics International 51(5) (2025) 5505-5513.

Available online at www.sciencedirect.com

ScienceDirect

Ceramics International 40 (2014) 9971–9979

CERAMICS INTERNATIONAL

www.elsevier.com/locate/ceramint

Synthesis, hydration and thermal stability of hydrates in strontium-aluminate cement[☆]

Petr Ptáček*, František Šoukal, Tomáš Opravil, Eva Bartoníčková, Martin Zmrzlý, Radoslav Novotný

Brno University of Technology, Faculty of Chemistry, Centre for Materials Research CZ.1.05/2.1.00/01.0012, Purkyňova 464/118, Brno CZ-612 00, Czech Republic

Received 22 January 2014; accepted 21 February 2014
Available online 28 February 2014

Abstract

The synthesis of strontium aluminate cement, the course of hydration and the thermal stability of hydrates are described in this work. The activation energy of the process of $SrAl_2O_4$ formation was calculated using the model-free Kissinger kinetic equation. The synthesis of the main clinker phase required the activation energy of 218 kJ mol^{-1}. The value of kinetic exponent was corresponded to the process controlled by increasing nucleation rate of a new phase. For the hydration of strontium aluminate cement an immediate and intensive evolution of heat without any measurable induction period is typical. The cubic tri-strontium aluminate hexahydrate (Sr_3AH_6) and alumina gel (AH_3) phases were formed as the first and also the main hydration products. The formations of strontium aluminate heptahydrate ($SrAH_7$) and gibbsite (γ-AH_3) were recognized after 7th day of hydration process.

Keywords: $SrAl_2O_4$; Strontium-aluminate cement; Hydration; Kinetics; Thermal analysis

1. Introduction

Strontium aluminates have a potential utilization as aluminous hydraulic binders for the production of basic refractory materials. As SrO formally replaces CaO in calcium aluminate cement, the strontium aluminate binder belongs to the family of aluminous cements based on the system of CaO–SrO–BaO–Al_2O_3–ZrO_2–HfO [1–4]. Furthermore, strontium aluminate ($SrAl_2O_4$ or $SrO \cdot Al_2O_3$) attracts the attention of materials scientists as photoluminiscent or thermoluminescent pigments, anodes for oxide fuel cells and highly conductive electrolytes. Doped with rare-earth metal ions ($SrAl_2O_4$:M, where M=Eu^{2+}, Gd^{3+}, Yb^{3+}, Dy^{3+}, Sm^{3+}, Tb^{3+}, etc.) it exhibits high quantum efficiency and phosphorescence [1,5–9]. $SrAl_2O_4$ was previously successfully synthesized by the solid-state reaction [10], the combustion method [7], the self-propagating high temperature synthesis [11], the hydrothermal synthesis [12], the co-precipitation method [13], the sol-gel process [8,9] and the mechano-chemical synthesis [14].

The tetra-strontium aluminate ($Sr_4Al_2O_7$, Sr_4A), cubic tri-strontium aluminate ($Sr_3Al_2O_6$, Sr_3A), monoclinic strontium aluminate ($SrAl_2O_4$, SrA), strontium di-aluminate ($SrAl_4O_7$, SrA_2) and strontium hexa-aluminate phases ($SrAl_{12}O_{19}$, SrA_6) occur in the phase diagram (Fig. 1) of the system of SrO–Al_2O_3. The high temperature modification of α-Sr_4A is stable in the temperature range from 1320 to 1690 °C. The transformation into low temperature β-Sr_4A phase takes place below 1320 °C. Under the temperature of 1125 °C α-phase of Sr_4A is decomposed to Sr_3A and SrO. The phase diagram shows that the low temperature phase of Sr_4A forms a solid solution with Sr_3A [15,16]. These methods enable to prepare other strontium-aluminate

---

[☆] Notation: The following notations and abbreviations are used in this work: CaO = C, SrO = Sr, CO_2 = *C*, Al_2O_3 = A, H = H_2O, *w/c* = water to cement ratio.

*Corresponding author.

E-mail address: ptacek@fch.vutbr.cz (P. Ptáček).

http://dx.doi.org/10.1016/j.ceramint.2014.02.095

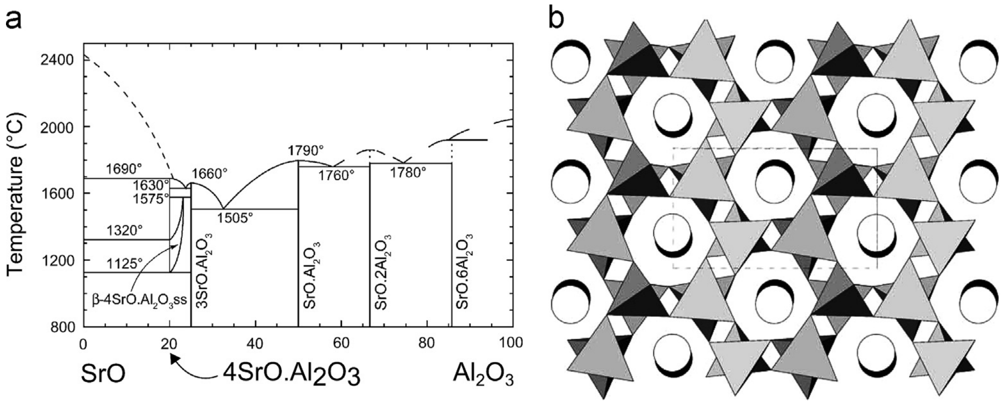

Fig. 1. Equilibrium phase diagram (a) of SrO–Al_2O_3 system [15] and structure (b) of $SrAl_2O_4$ [18].

phases with the stoichiometry corresponding to $Sr_3Al_{32}O_{51}$ [14] or $Sr_2Al_2O_5$ [9].

The structure of strontium aluminate (Fig. 1(b)) is composed of six corner-shared $[AlO_4]^{5-}$ tetrahedrons connected into so called "*zigzag strings*" or "*stuffed tridymite structure*". Ions of Sr^{2+} are accommodated in the cavities of the structure [17,18]. During heating this compound undergoes a phase transformation from monoclinic to hexagonal modification at the temperature of 650 °C [10,19,20]. The structure of $SrAl_2O_4$ is similar but not isostructural to $CaAl_2O_4$ [21,22].

The paper deals with the synthesis and the hydration of strontium-aluminate cement prepared by the thermal treatment of the mixture of $SrCO_3$ and Al_2O_3 powder. The behavior during the thermal treatment, the mechanism and the kinetics of formation of strontium aluminate is described. The course of hydration of prepared strontium aluminate cement was investigated by the calorimetric experiments and followed by thermal analysis, infrared spectroscopy, x-ray diffraction analysis and scanning electron microscopy of the cement stone. The thermal stability and the kinetics of dehydration of formed hydrates were assessed by the Kissinger method.

2. Experimental

2.1. Synthesis of strontium aluminate cement

Strontium aluminate cement was prepared using the equimolar mixture of $SrCO_3$ and Al_2O_3 powders (both in the analytical purity grade). The composition was corresponded to the weight ratio of 1:0.69. After 10 min of milling in laboratory ball-mill, the raw mixture was introduced into the alumina cup and calcined at the temperature of 1600 °C for the time of 2 h. Sintered pellets were then ground, milled in the laboratory stain-less steel vibration mill and fired again using the same conditions as previously. $SrAl_2O_4$ clinker was prepared by fine ball-milling of pre-milled cement product. The particle size analyzer Helos (Sympatec) was used to investigate the particle size distribution in prepared strontium aluminate cement.

The process which took place during the synthesis was investigated by simultaneous TG-DTA and EGA analyses (Q600, TA Instruments connected to infrared spectrometer iS10, Thermo Scientific). Sample (50 mg) was introduced into Pt cup and heated under the heating rate of 10 °C to the temperature of 1450 °C under the flow of CO_2-free dry air (100 ml min^{-1}). The phase composition and in situ crystallization under various temperatures were studied by means of x-ray diffraction analysis (HT-XRD, X´pert Empyrean, PANanalytical) coupled with high temperature chamber HTK 16 (Anton Paar). The horizontal type of heating microscope EM 201 (Leitz) was used to determine the temperature of the points of sintering (*SP*). The cylinder shaped specimen of the diameter and the height of 3 mm was pressed out and insert to the sample holder. The sample was heated under the heating rate of 5 °C min^{-1} up to the temperature of 1600 °C. The behavior of the specimen during the thermal treatment was investigated by relative change of the specimen area. The infrared spectra were collected using the spectrometer iS10 (Thermo Scientific) and applying the KBr technique with the mass ratio of sample to KBr of 1:100.

2.2. Hydration of strontium aluminate cement

The cement slurry was prepared from the mixture of strontium aluminate cement with water using the water to cement ratio (*w*/*c*) of 0.5 at the temperature of 25 °C. The course of hydration of strontium aluminate cement was investigated via isothermal microcalorimeter TAM Air (TA Instruments). The hydration products and the thermal stability of hydrates were investigated by thermal analysis, infrared spectroscopy, x-ray diffraction analysis (mentioned above) and scanning electron microscopy (SEM) performed with Field emission microscope JSM-7600F (Jeol).

2.3. Kinetics and mechanism

The apparent activation energy (E_a) and the frequency factor (A) related to the formation of strontium aluminate during the treatment of raw mixture of $SrCO_3$ and Al_2O_3 as well as the thermal decomposition of strontium aluminate hexahydrate were investigated by the mechanism-free method based on the

Kissinger kinetic approach [23,24]:

$$\ln\left[\frac{\Theta}{T_m^2}\right] = \ln\left[\frac{AR}{E_a}n(1-\alpha_m)^{n-1}\right] - \frac{E_a}{RT_m} = \text{const.} - \frac{E_a}{RT_m}; \quad (1)$$

where T_m is the peak temperature measured under applied heating rate Θ, n is the empirical reaction order (kinetic exponent), α_m is the fractional conversion reached for the temperature T_m and R is the universal gas constant.

The non-isothermal kinetics experiments were performed using TG-DTA analyzer SDT Q600 (TA Instruments). Sample (30 mg) was heated under the heating rate (Θ) of 3, 5, 8, 10, 15 and 20 °C min^{-1} up to 1250 °C. The points on the plot of ln (AR/E_a) versus T_m^{-1} were fitted by the straight line with the slope equal to $-E_a/R$ whereas the intercept yielded to the constant term of Eq. (1).

The mechanism was estimated from the shape of DTG peak via the value of kinetic exponent (n) which was related to the empirical order of reaction [23]. The exponent can be calculated from the equation [25,26]:

$$n = \frac{2.5RT_m^2}{w_{1/2}E_a}; \quad (2)$$

where $w_{1/2}$ is the half-width (width at a half high) of peak. The value of kinetic exponent is typical for various mechanisms of investigated process [27].

3. Results and discussion

3.1. Synthesis of the strontium aluminate cement

Simultaneous TG-DTA and EGA analyses of the mixture of strontium carbonate and alumina (Fig. 2) showed that the formation of strontium aluminate as the main clinker phase proceeded via the solid-state reaction of equimolar amount of SrO (formed via the thermal decomposition of $SrCO_3$) and Al_2O_3. The process should be described by general reaction scheme as follows:

$$SrCO_3 + Al_2O_3 \rightarrow SrAl_2O_4 + CO_2(g). \quad (3)$$

The process showed sharp exothermic peak at the temperature of 967 °C which divided the huge endothermic effect of thermal decomposition of strontium carbonate which occurred within the temperature range from 810 to 1020 °C. Formed $SrAl_2O_4$ phase covered the surface of decomposed $SrCO_3$ particle and this layer slowed down the diffusion of CO_2 from the reaction interface of disappearing $SrCO_3$ core. Therefore the thermal decomposition of $SrCO_3$ was suppressed. The volume changes caused by the decarbonation and recrystallization of products led to the formation of cracks which enabled easy diffusion of CO_2 through the layer of product. The simplified idea about the process is shown in Fig. 2. The mass of the sample was reduced by 17.7 wt% during this process.

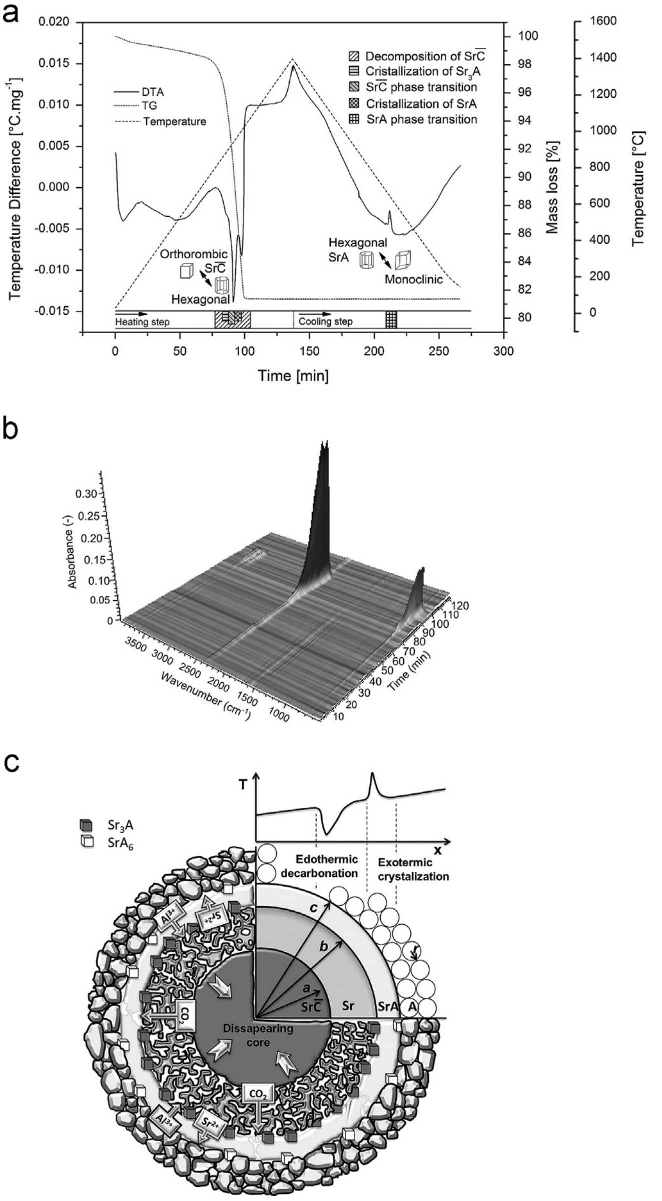

Fig. 2. TG-DTA of mixture of strontium carbonate and alumina (a), EGA plot for the heating zone (b), and simplified process schema (c).

The reaction interface abundance of SrO (outer side of formed strontium aluminate layer) or Al_2O_3 (inner side) component led to the formation of tri-strontium aluminate (Sr_3A) and strontium hexa-aluminate (SrA_6). The equilibrium composition of strontium aluminate was then established via the opposite direction diffusion of Sr^{2+} and Al^{3+} ions. The opposite model, i.e. Al_2O_3 particle surrounded by $SrCO_3$, where the formation of strontium aluminate is limited by the diffusion of Sr^{2+} ions into the disappearing alumina core cannot explain the observed behavior.

Heating microscopy (Fig. 3) showed the expansion of specimen to 113% of its original height. For the temperatures higher than 1050 °C the height of specimen decreased. The initial temperatures of solid-state and liquid state sintering were determined to be 1450 and 1550 °C, respectively. The cooling zone of Fig. 2 shows an exothermic effect of reversible transformation of hexagonal high-temperature modification of $SrAl_2O_4$ to low-temperature monoclinic phase at the temperature of 650 °C. During repeated cycle of heating, the exothermic transformation took place at

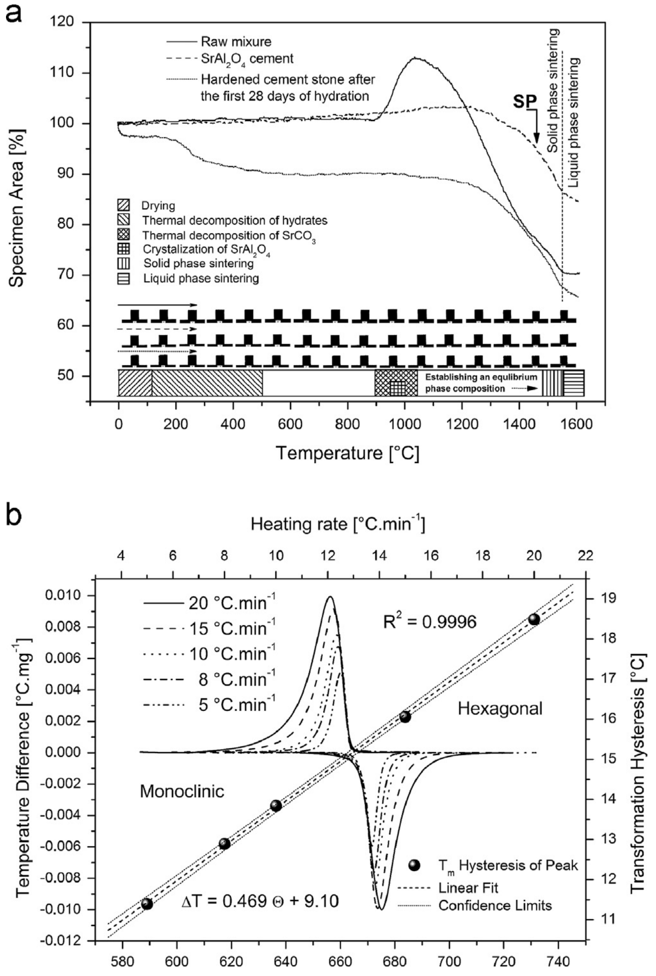

Fig. 3. Heating microscopy of the mixture of strontium carbonate and alumina (a) and the temperature hysteresis in polymorphic transformation of $SrAl_2O_4$ (b).

higher temperature. The temperature hysteresis of this transformation increased linearly with the heating rate (Fig. 3(b)). Therefore the limit value of 9.10 ± 0.07 °C should be estimated from the linear fit for $\Theta \rightarrow 0$.

The solid-state character led to local abundances of SrO or Al_2O_3 components and to the formation of $Sr_3Al_2O_6$ (Sr_3A) or $SrAl_{12}O_{19}$ (SrA_6). Therefore high temperatures and the time of thermal treatment are necessary to reach the equilibrium composition. Therefore the first eutectic melt was formed at the temperature of 1550 °C (Fig. 3(a)) and a certain amount of glassy phase was necessary to improve the hydraulic behavior of clinker. The firing temperature necessary for the preparation of strontium aluminate cement was 1600 °C.

The changes in the phase composition during the thermal treatment of strontium aluminate clinker were investigated by high-temperature X-ray diffraction analysis (Fig. 4(a)). The diffraction lines of $SrCO_3$ started disappearing at the temperature of 800 °C. At the temperature of 825 °C SrO, formed via the thermal decomposition of $SrCO_3$, reacted with Al_2O_3 to form tri-strontium aluminate (Sr_3A) and therefore the intensity of Al_2O_3 diffractions decreased at the same time. The diffraction lines of hexagonal strontium aluminate as the

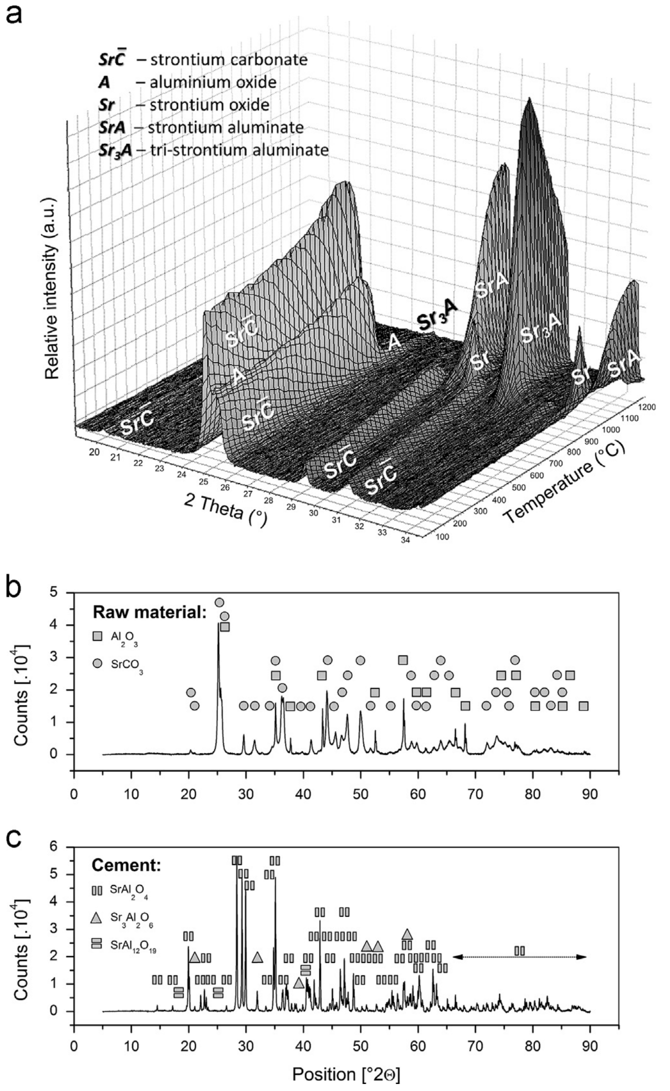

Fig. 4. HT-XRD of mixture of strontium carbonate and alumina up to 1400 °C (a) and XRD analysis of initial (b) and final composition of calcium aluminate clinker (c).

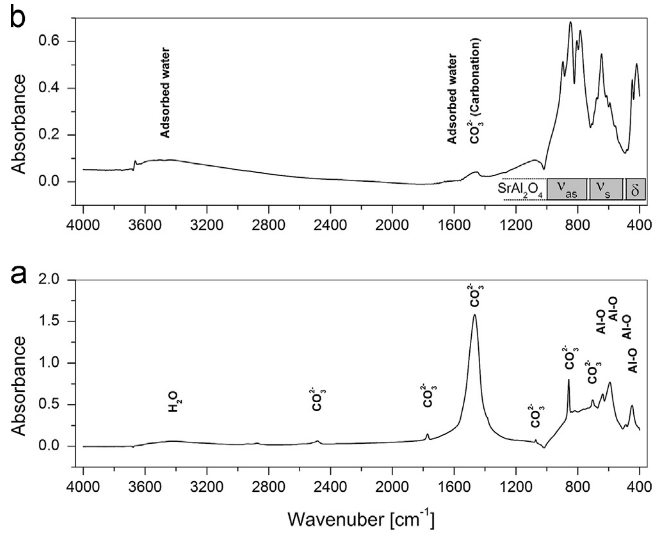

Fig. 5. Infrared spectroscopy of clinker before (a) and after the thermal treatment (b).

main clinker phase appeared at the temperature of 875 °C. In accordance with the results of TG-DTA (Fig. 2(a)) the material still contained un-decomposed strontium aluminate. The local abundance of Al_2O_3 led to the formation of SrA_6 phase. At the temperature of 1000 °C the thermal decomposition of $SrCO_3$ was almost completed but the clinker still contained free strontium oxide, the diffraction lines of which gradually disappeared up to the temperature of 1250 °C.

X-ray diffraction analyses of the mixture of raw materials and of clinker prepared by calcination at the temperature of 1600 °C are shown in Fig. 4(b) and (c), respectively. Under applied firing conditions, the prepared strontium aluminate cement contains 96% of strontium aluminate phase (SrA) and 4% of tri-strontium aluminate (Sr_3A).

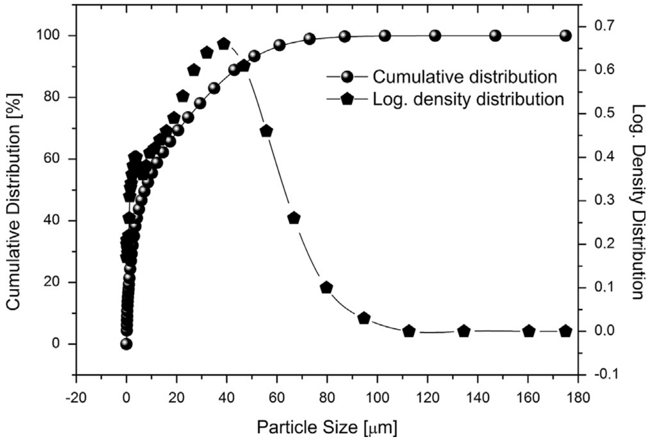

Fig. 6. Distribution of the particle sizes in strontium aluminate cement.

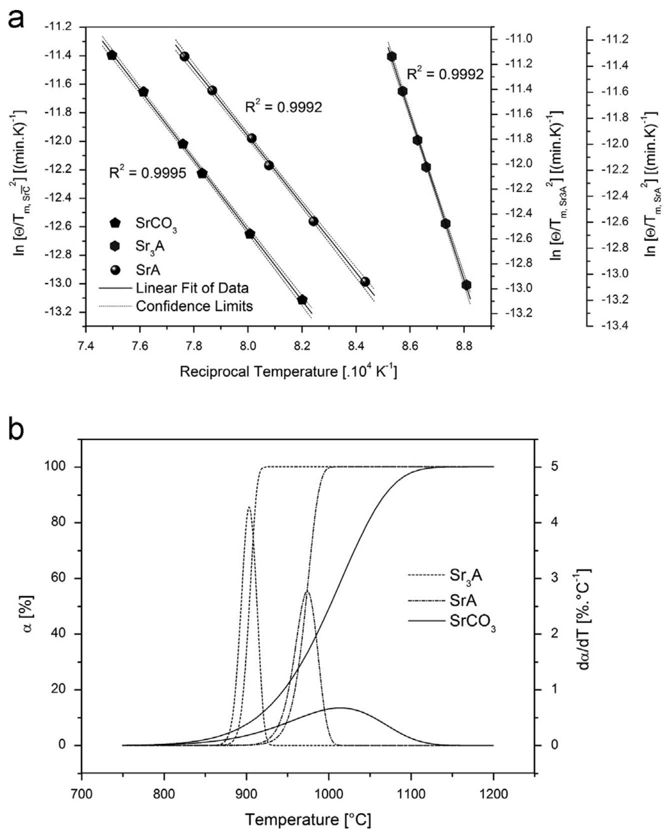

Fig. 7. Kissinger plot (a) and reconstruction of the process for $\Theta = 10\ ^\circ C\ min^{-1}$ (b).

The comparison of infrared spectra of raw material and product (Fig. 5) shows disappearing absorption bands of planar CO_3^{2-} anion with D_3h symmetry [28–30] including strong band of asymmetric stretching at 1465 cm^{-1}, weak band of symmetric stretching at 1072 cm^{-1}, in plane bending at 856 cm^{-1} and out of plane bending vibration at 702 cm^{-1}. Corundum in raw mixture shows four main absorption bands of stretching of (AlO_6) octahedra at 639, 591, 489 and 448 cm^{-1} [31,32]. On the contrary, the $SrAl_2O_4$ structure is built up from the (AlO_4) tetrahedra with T_d symmetry and the structural lattice channels are occupied by Sr^{2+} ions [33]. The bands appearing in spectral regions from 900 to 780 cm^{-1} and from 650 to 550 cm^{-1} belong to antisymmetric and symmetric stretchings of (AlO_4) tetrahedra. The bands related to the doublet of bending of O–Al–O are located at 446 and 418 cm^{-1}.

Grinding and fine milling of strontium aluminate clinker provided cement with the median of particle size of 7.52 μm, which was used for the hydration experiments described in the next section. The density distribution and the cumulative distribution function of prepared binder are shown in Fig. 6.

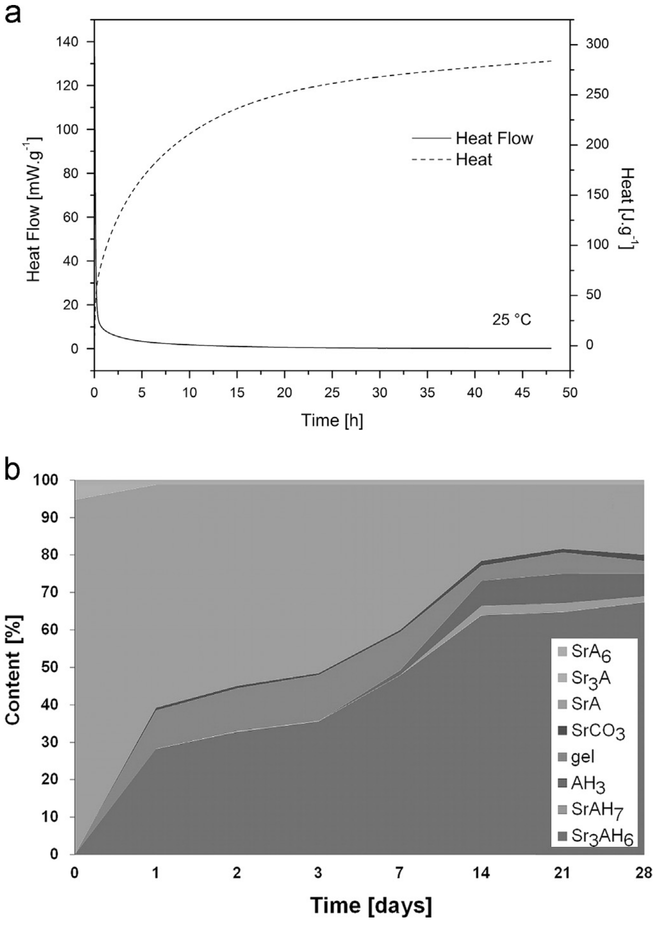

Fig. 8. Isothermal calorimetry of strontium aluminate cement compared to calcium aluminate cement (Secar 71) measured under the same conditions (a) and the changes in phase composition during hydration (b).

The Kissinger plot related to the kinetics of thermal decomposition of $SrCO_3$ and of formation of $Sr_3Al_2O_6$ and $SrAl_2O_4$ is shown in Fig. 7(a). The activation energy of 205 kJ mol^{-1}, the frequency factor of 6.92×10^6 s^{-1} and the kinetic exponent of 1.0 were assessed for the thermal decomposition of strontium carbonate during the synthesis of strontium aluminate clinker.

The apparent activation energy and the frequency factor related to the formation of Sr_3A are 551 kJ mol^{-1} and 1.69×10^{23} s^{-1}, respectively. The value of kinetic exponents calculated according to Eq. (2) is 4.0, hence the process is driven by constant nucleation rate of a new phase. SrA shows the activation energy and the frequency factor of 218 kJ mol^{-1} and 1.63×10^7 s^{-1}, respectively. The value of kinetic exponents is equal to 5.2. Therefore, the crystallization of SrA phase is driven by increasing nucleation rate of a new phase. The results were verified via the recalculation of the processes for the heating rate of 10 °C min^{-1} (Fig. 7(b)). The reconstruction performed with assessed kinetic data shows good agreement with the experiment (refer to Fig. 2).

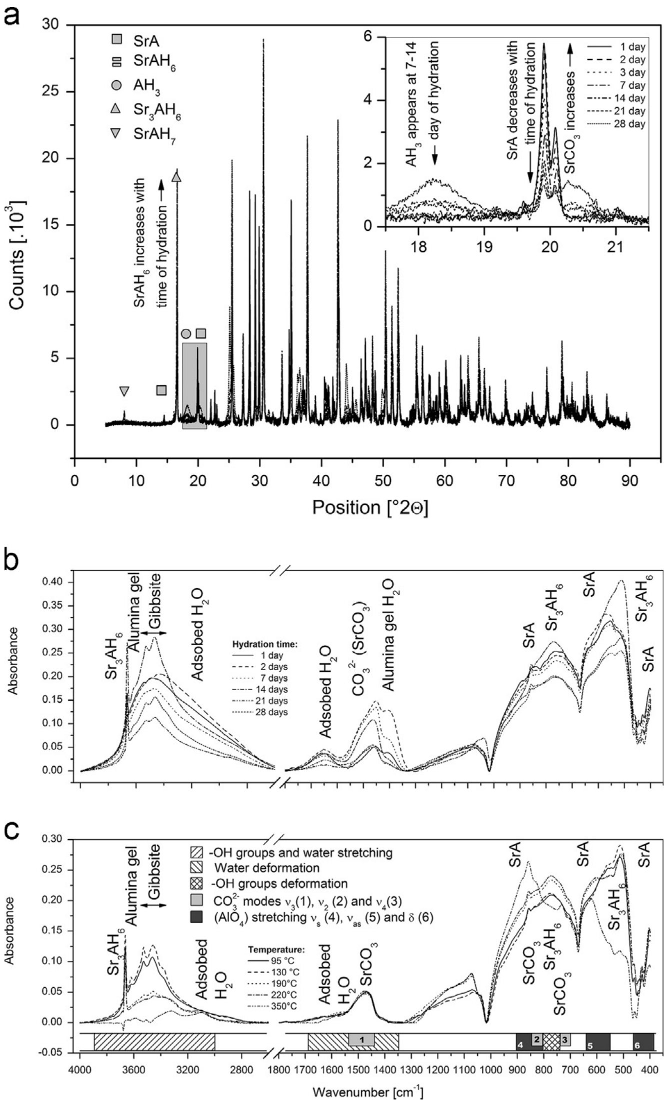

Fig. 9. X-ray diffraction analysis (a) and infrared spectroscopy (b) of hydrated paste prepared from strontium aluminate cement.

3.2. Hydration and hydration products of strontium aluminate cement

The results of isothermal calorimetric experiment (Fig. 8(a)), thermal analysis (Fig. 10), X-ray diffraction analysis (Fig. 9(a)), infrared spectroscopy (Fig. 9(b)) and scanning electron microscopy (Fig. 11) were used to study the evolution of phase composition during the process of hydration of strontium aluminate cement paste with *w/c* of 0.5 (Fig. 8(b)).

For the hydration of strontium aluminate cement an intensive evolution of heat at the beginning of hydration is typical (Fig. 8(a)) and measured pH of cement slurry reaches the value of 12 at the same time. There is not any induction period observed hence the hydration starts immediately after mixing of strontium aluminate cement with water. The cubic tristrontium aluminate hexahydrate phase (Sr_3AH_6) and the high alumina gel phase (AH_3 gel) are recognized as the main products of hydration. $SrAH_7$ hydrate and gibbsite (γ-AH_3) appear after 7 and 14 days of hydration, respectively. The rate of the hydration process is significantly reduced after 14 days and the sample still contains about 20% of un-hydrated strontium aluminate phase in 28th day of hydration.

The formation of Sr_3AH_6 hydrate in hydrated cement paste was identified by x-ray diffraction analysis (Fig. 9(a)) and infrared spectroscopy (Fig. 9(b)). The infrared spectra show sharp absorption band at 3664 cm^{-1}, which is related to stretching of OH groups of Sr_3AH_6. The dehydration of this

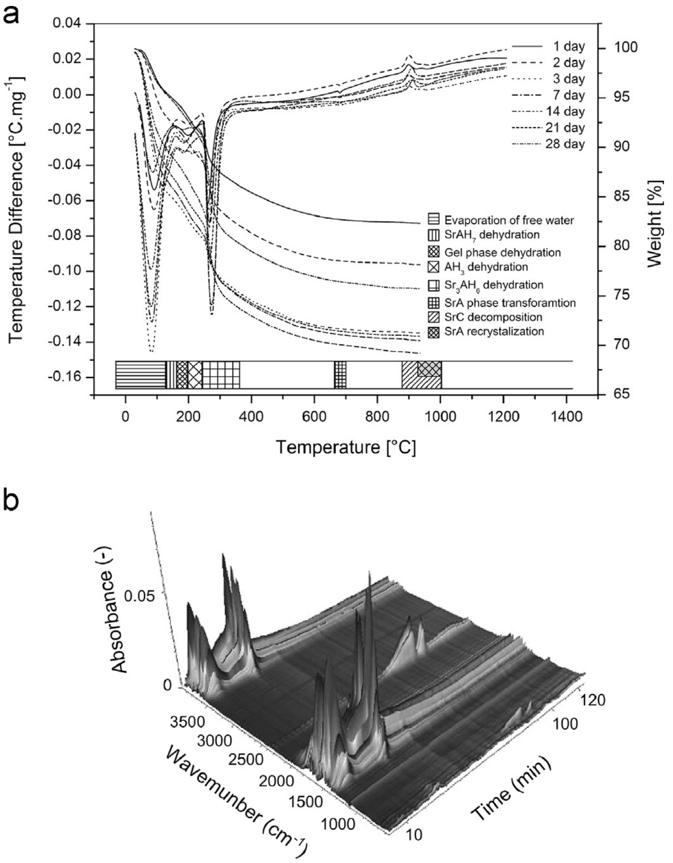

Fig. 10. Simultaneous TG-DTA (a) and EGA (b) of hydrated paste prepared from strontium aluminate cement.

phase shows sharp endothermic peak at the temperature of 262 °C on TG-DTA and EGA (Fig. 10). The test piece area decreases in about 6.0% during this process (Fig. 3(a)). The dehydration of the gel phase shows an endothermic effect on DTA at the temperature of 198 °C, but the peak intensity and the temperature decreases with the time of hydration (Fig. 10).

The dehydration endotherms of $SrAH_7$ and gibbsite (AH_3) are located at the temperatures of 113 and 212 °C, respectively. The decreasing intensity of the peak of endothermic polymorphic transition of monoclinic SrA into hexagonal phase at the temperature of 680 °C is caused by gradual hydration of this phase. Strong CO_2 bands on EGA plot show that certain amount of strontium carbonate is formed (Fig. 10(b)) during hydration. Strontium oxide formed by the decarbonation of $SrCO_3$ reacts with the dehydration products of high alumina phase to strontium aluminate and an exothermic peak at the temperature of 910 °C appears.

The SEM pictures of strontium aluminate cement (a) and hydrated cement stone (b–d) during the first 28 days of hydration

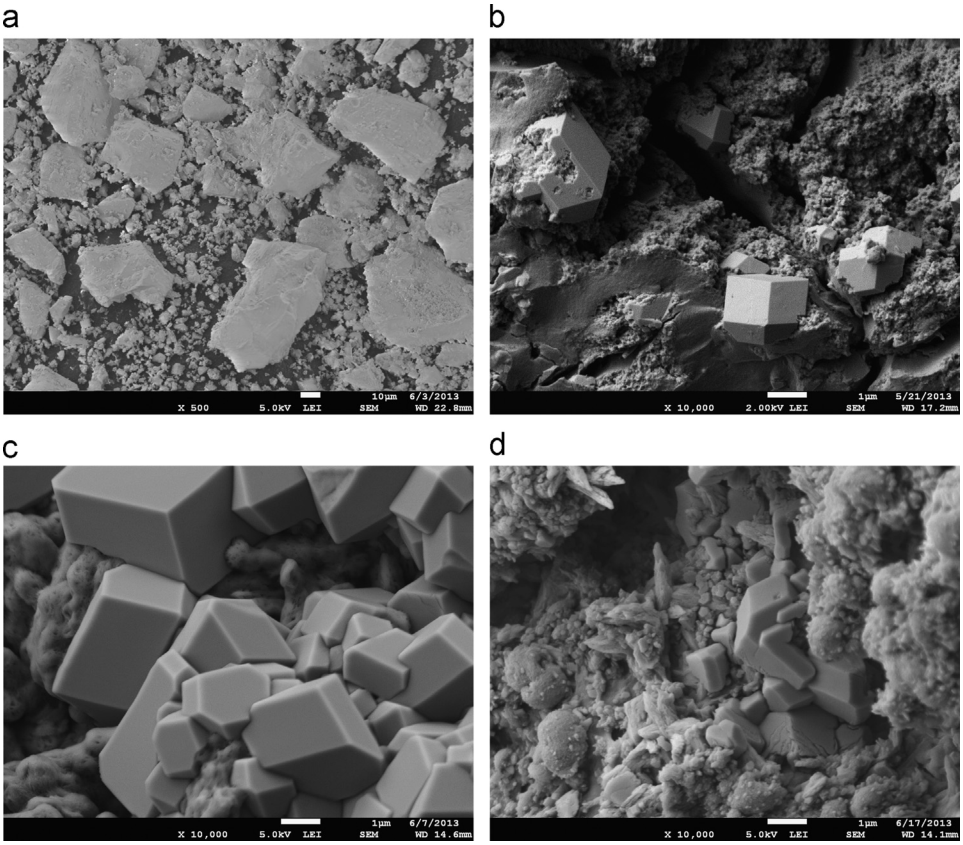

Fig. 11. SEM picture of strontium aluminate cement (a) and hydrated cement stone after 3 (b) and 21(c) and 28(d) days of hydration process.

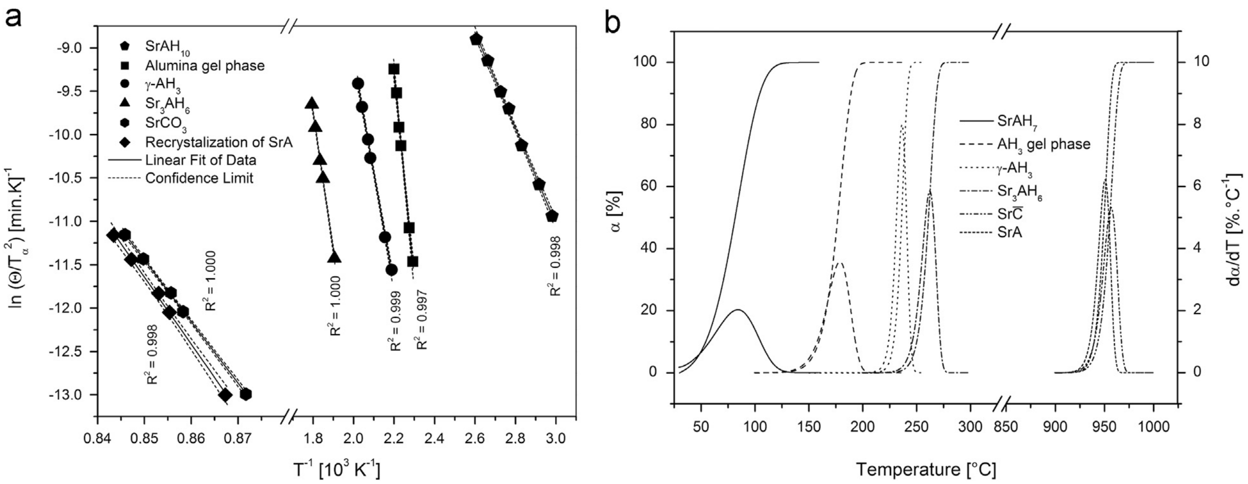

Fig. 12. Kissinger plot (a) and verification of results using assessed kinetic triplets (b).

Table 1
Mechanism and kinetics of thermal decomposition of hydration products of SrA cement.

Phase	E_a (kJ mol^{-1})	A (s^{-1})	α_m (%)	$w_{1/2}$ (°C)	n	The description of the mechanism of process
$SrAH_7$	46	7.79×10^5	49.50	50.0	0.92	Growth of particles of appreciable initial volume, needles and plates of finite long dimensions
AH_3 gel	200	3.46×10^{22}	52.13	24.32	0.79	Growth of particles of appreciable initial volume, thickening of very large plates
γ-AH_3	108	1.45×10^{22}	50.48	9.14	4.18	Interface-controlled growth of a new phase, constant or increasing nucleation rate
Sr_3AH_6	117	3.94×10^{10}	49.70	17.75	2.54	Diffusion-controlled growth of a new phase, constant or increasing nucleation rate
$Sr\overline{C}$	592	2.28×10^{24}	46.11	19.31	2.31	Diffusion-controlled growth of a new phase, decreasing nucleation rate
SrA	642	4.30×10^{26}	54.25	17.95	2.48	Diffusion-controlled growth of a new phase, constant or decreasing nucleation rate

process are shown in Fig. 11. Well-developed crystals of $SrAH_6$ (b) precipitated and grew from supper-saturated liquid phase of cement slurry before setting. During setting the hydration products did not occur in well-developed crystals. The SEM picture of hydrated cement stone shows well-developed Sr_3AH_6 crystal surrounded by kidney-shaped aggregates of $SrAH_7$ after 21 and 28 days of hydration.

Hence the production of refractory materials is one of the most promising applications of strontium aluminate cements. In provided experiments the activation energy, the frequency factor and the mechanism of thermal decomposition of hydration products were determined using Eqs. (1) and (2). The Kissinger plot used for the determination of kinetic triplets of these compounds is shown in Fig. 12(a).

Table 1 summarizes the kinetic results of the behavior of hardened strontium aluminate cement stone during the thermal treatment. The kinetic data were verified via the reconstruction of the processes which took place during the thermal treatment of hardened strontium aluminate cement stone under the heating rate of 10 °C min^{-1}. The calculated temperature range and the temperature related to the maximum rate are shown in Fig. 12(b). A good agreement with the excrement (please consult with Fig. 10) is reached.

The final product of the thermal treatment of hydrated cement stone is also strontium aluminate, i.e. the same compound as in the original clinker phase. Nevertheless it is formed through different reaction pathways compared to the original mixture of raw materials.

4. Conclusion

Strontium aluminate cement with high content of $SrAl_2O_4$ (96%) as the main clinker phase was prepared by calcination and fine milling of the equimolar mixture of strontium carbonate and alumina powders. As the minor clinker phase $Sr_3Al_2O_6$ was also formed. The formations of major and minor clinker phases require the activation energies of 218 and 551 kJ mol^{-1}, respectively. While tri-strontium aluminate is formed at first via prompt in situ nucleation of a new phase, the crystallization of strontium aluminate is driven by increasing nucleation of this new phase. After mixing of clinker with water, the hydration process starts immediately and there is not any measurable induction period. The tri-strontium aluminate hexahydrate and the high alumina gel phase were recognized as the first formed products of hydration. After 7th day of hydration, the formation of gibbsite and strontium aluminate heptahydrate was observed. The rate of hydration of $Sr_3Al_2O_6$ is much higher than that of $SrAl_2O_4$; hence it disappears during the first day of hydration while the cement stone still contains almost 20% of un-hydrated strontium aluminate phase after 28 days of hydration.

The kinetic data related to the thermal decomposition of the hydration product of strontium aluminate cement were determined. The dehydrations of strontium aluminate hexahydrate and alumina gel phase show the activation energies of 117 and 200 kJ · mol^{-1}, respectively. The thermal decompositions of latterly formed γ-AH_3 and $SrAH_7$ require the activation energies of 108 and 46 kJ mol^{-1}, respectively. $SrAl_2O_4$ is the final product of the thermal treatment of hardened cement stone, but the kinetics and the mechanism of formation are different from the crystallization of this phase from original mixture of strontium carbonate and alumina powders due to higher homogeneity of the material after hydration.

Acknowledgments

This work was supported by the project No. CZ.1.05/2.1.00/01.0012 “Centre for Materials Research at FCH BUT” supported by the operational program “Research and Development for Innovations”. The authors also gratefully acknowledge the funding provided from the project “Excellent Teams” No. CZ.1.07/2.3.00/30.0005.

References

[1] A. Douy, M. Capron, Crystallisation of spray-dried amorphous precursors in the SrO–Al_2O_3 system: a DSC study, J. Eur. Ceram. Soc. 23 (12) (2003) 2075–2081.

[2] I. Odler, Special Inorganic Cements, Taylor & Francis, New York, 2000.

[3] A.K. Chatterjee, Re-examining the prospects of aluminous cements based on alkali-earth and rare-earth oxides, Cem. Concr. Res. 39 (11) (2009) 981–988.

[4] N. Illyouka, V. Timofeeva, Development of Hydraulic Zirconia Cements and their Applications for Productions of Refractories Items, T.t. University (Ed.), Kharkov, Ukraine, 1998.

[5] B. Smets, J. Rutten, G. Hoeks, J. Verlijsdonk, $2SrO_{0.3}Al_2O_3:Eu^{2+}$ and $1:29(Ba, Ca)_{0.6}Al_2O_3:Eu^{2+}$ two blue-emitting phosphors, J. Electrochem. Soc. 136 (1989) 2119–2123.

[6] F.C. Pallila, A.K. Levine, M.R. Tomkus, Fluorescent properties of alkaline earth aluminates of the type MAl_2O_4 activated by divalents ions, J. Electrochem. Soc. 115 (1968) 642–644.

[7] H. Song, D. Chen, W. Tang, Y. Peng, Synthesis of $SrAl_2O_4$: Eu2+, Dy3+, Gd3+ phosphor by combustion method and its phosphorescence properties, Displays, 29, , 2008, p. 41–44.

[8] Z. Tang, F. Zhang, Z. Zhang, C. Huang, Y. Lin, Luminescent properties of $SrAl_2O_4$: Eu, Dy material prepared by the gel method, J. Eur. Ceram. Soc., 20, , 2000, p. 2129–2132.

[9] M. Misevicius, O. Scit, I. Grigoraviciute-Puroniene, G. Degutis, I. Bogdanoviciene, A. Kareiva, Sol–gel synthesis and investigation of un-doped and Ce-doped strontium aluminates, Ceram. Int. 38 (7) (2012) 5915–5924.

[10] Y.-L. Chang, H.-I. Hsiang, M.-T. Liang, F.-S. Yen, Phase evolution and thermal behaviors of the solid-state reaction between $SrCO_3$ and Al_2O_3 to form $SrAl_2O_4$ under air and CO_2-air atmospheres, Ceram. Int. 38 (3) (2012) 2269–2276.

[11] T. Sathaporn, S. Niyomwas, Synthesis and characterization of MAl_2O_4 (M= Ba, Ca, Sr) phosphor by self-propagating high temperature synthesis, Energy Proc. 9 (2011) 410–417.

[12] Q. Xiao, L. Xiao, Y. Liu, X. Chen, Y. Li, Synthesis and luminescence properties of needle-like $SrAl_2O_4$:Eu, Dy phosphor via a hydrothermal co-precipitation method, J. Phys. Chem. Solids 71 (7) (2010) 1026–1030.

[13] Z. Xue, S. Deng, Y. Liu, B. Lei, Y. Xiao, M. Zheng, Synthesis and luminescence properties of $SrAl_2O_4$:Eu2+,Dy3+ hollow microspheres via a solvothermal co-precipitation method, J. Rare Earths 31 (3) (2013) 241–246.

[14] N. Setoudeh, N.J. Welham, Ball milling induced reduction of $SrSO_4$ by Al, Int. J. Miner. Process. 98 (3–4) (2011) 214–218.

[15] M. Franco, System SrO–Al_2O_3, in: E.M. Levine, C.R. Robbins, H.F. McMurdie (Eds.), Phase Diagram for Ceramics, The AcerS, Ohio, 1959, p. 118.

[16] R. R., Encyclopedia of the Alkaline Earth Compounds, Elsevier, Amsterdam, 2013.

[17] Z. Fu, S. Zhou, T. Pan, S. Zhang, Band structure calculations on the monoclinic bulk and nano-$SrAl_2O_4$ crystals, J. Solid State Chem. 178 (1) (2005) 230–233.

[18] A.K. Prodjosantoso, B.J. Kennedy, Solubility of $SrAl_2O_4$ in $CaAl_2O_4$—a high resolution powder diffraction study, Mater. Res. Bull. 38 (1) (2003) 79–87.

[19] C.M.B. Henderson, D. Taylor, The structural behaviour of the nepheline family: (1) Sr and Ba aluminates (MAl_2O_4), Mineral. Mag. 45 (335) (1982) 111–127.

[20] K. Fukuda, K. Fukushima, Crystal structure of hexagonal $SrAl_2O_4$ at 1073 K, J. Solid State Chem. 178 (9) (2005) 2709–2714.

[21] W. Hörkner, H. Müller-Buschbaum, Zur kristallstruktur von $CaAl_2O_4$, J. Inorg. Nucl. Chem. 38 (5) (1976) 983–984.

[22] A.R. Schulze, H.M. Buschbaum, Zur Verbindungsbildung von MeO: M2O3. IV. Zur Struktur von monoklinem $SrAl_2O_4$, Z. Anorg. Allg. Chem. 475 (4) (1981) 205–210.

[23] H.E. Kissinger, Reaction kinetics in differential thermal analysis, Anal. Chem. 29 (11) (1957) 1702–1706.

[24] R.L. Blaine, H.E. Kissinger, Homer Kissinger and the Kissinger equation, Thermochim. Acta 540 (2012) 1–6.

[25] J. Augis, J. Bennett, Calculation of the Avrami parameters for heterogeneous solid state reactions using a modification of the Kissinger method, J. Therm. Anal. Calorim. 13 (2) (1978) 283–292.

[26] C.S. Ray, Q. Yang, W.-h. Huang, D.E. Day, Surface and internal crystallization in glasses as determined by differential thermal analysis, J. Am. Ceram. Soc. 79 (12) (1996) 3155–3160.

[27] J. Málek, The applicability of Johnson–Mehl–Avrami model in the thermal analysis of the crystallization kinetics of glasses, Thermochim. Acta 267 (1995) 61–73.

[28] F. Davar, M. Salavati-Niasari, S. Baskoutas, Temperature controlled synthesis of $SrCO_3$ nanorods via a facile solid-state decomposition rout starting from a novel inorganic precursor, Appl. Surf. Sci. 257 (9) (2011) 3872–3877.

[29] N. Tipcompor, T. Thongtem, A. Phuruangrat, S. Thongtem, Characterization of $SrCO_3$ and $BaCO_3$ nanoparticles synthesized by cyclic microwave radiation, Mater. Lett. 87 (2012) 153–156.

[30] M.A. Alavi, A. Morsali, Syntheses and characterization of $Sr(OH)_2$ and $SrCO_3$ nanostructures by ultrasonic method, Ultrason. Sonochem. 17 (1) (2010) 132–138.

[31] A. Boumaza, L. Favaro, J. Lédion, G. Sattonnay, J.B. Brubach, P. Berthet, A.M. Huntz, P. Roy, R. Tétot, Transition alumina phases induced by heat treatment of boehmite: an X-ray diffraction and infrared spectroscopy study, J. Solid State Chem. 182 (5) (2009) 1171–1176.

[32] A. Boumaza, A. Djelloul, F. Guerrab, Specific signatures of α-alumina powders prepared by calcination of boehmite or gibbsite, Powder Technol. 201 (2) (2010) 177–180.

[33] A. Nag, T.R.N. Kutty, Role of B_2O_3 on the phase stability and long phosphorescence of $SrAl_2O_4$:Eu, Dy, J. Alloys Compd. 354 (1–2) (2003) 221–231.

Available online at www.sciencedirect.com

ScienceDirect

Ceramics International 41 (2015) 14116–14123

CERAMICS INTERNATIONAL

www.elsevier.com/locate/ceramint

Mullite-based refractories fabricated by foam casting

Eva Bartonickova*, Petr Ptacek, Tomas Opravil, Frantisek Soukal, Jiri Masilko, Radoslav Novotny, Jiri Svec, Jaromir Havlica

Materials Research Centre, Faculty of Chemistry, Brno University of Technology, Purkynova 118, 612 00 Brno, Czech Republic

Received 30 March 2015; received in revised form 22 June 2015; accepted 4 July 2015
Available online 13 July 2015

Abstract

The research on the structure, behaviour and properties of mullite foams is strongly motivated by industrial demands for high-temperature applications. Sintered mullite foam stabilized by strontium aluminate is an appropriate candidate for industrial refractory applications under elevated temperatures. The preparation technique is based on casting of foamed kaolin slurry using air/surfactant sacrificial fugitive. Wet foam precursors were dried and treated to the temperature of 1250 °C. High-temperature behaviour and bulk properties of obtained products with the porosity up to 85% were characterised by means of high temperature X-ray diffraction analysis, thermal analysis and scanning electron microscopy. The mechanical properties and the thermal conductivity of sintered mullite-based foams were determined to be in the range from 1.7 to 2.5 MPa and from 0.05 to 0.06 W/m K, respectively.

Keywords: C. Thermal conductivity; D. Mullite; Kaolin; Foam casting; Ceramic foams

---

1. Introduction

Ceramic foams have gained a substantive importance in material research over the last decade due to their miscellaneous and versatile applications. The remarkable amount of publications is published only on the macro-porous ceramics topic (i.e. pore size higher than 50 nm). Consequently, two important reviews were devoted to the advanced tailoring technologies regarding the preparation of foam ceramics focusing mainly on macro-porous ceramics with improved properties [1,2]. The application of macro-porous foam can be divided to 4 main applications [1]. A substantial attention is paid to the *filtration processes* – fluids, molten metals [3], water pollutions – bacteria or bacillus trapping [4,5] and consequently as diesel particulate filters intended for capturing the matters in diesel engines [6]. The bone tissue engineering and the usage of ceramic foams /scaffolds in *bio-applications* or as bio-reactor beds are also frequently reported [7,8]. Increasing industrial demand for novel and economically beneficial *electronic devices* strongly influences the development of porous ceramics' fabrication. Porous ceramics are successfully applied as piezoelectrics for ultrasound transducers [9], as components of SOFCs [10,11] or as components of thermo-ceramics modules for waste energy harvesting [12]. The last group of applications is the *refractory* one. The utilisation of porous ceramic foams as the kiln lining, thermal insulators with low thermal conductivity and excellent thermal shock resistance is also in the researcher's interest [13–15]. The present work is devoted to the last aforementioned group of interest.

The mullite-based ceramics is one of the most suitable candidates for refractory applications. Mullite ceramics is widely used due to low thermal conductivity, moderate thermal stability and thermal expansion, excellent thermal shock resistant, good chemical resistance and stability in high temperatures, sufficient mechanical properties [16]. Another benefit of mullite-based ceramics is economically favourable starting materials for its preparation. Especially abundant raw kaolin powders with different amount of kaolinite are much exploited nowadays [3,4,14,15,17–20]. The usage of secondary raw materials as fly ash or slags was also reported [21].

The tailoring/fabrication methods of mullite foams belong to common foaming techniques such as partial sintering, the

---

*Corresponding author. Tel.: +420 541 149 366; fax: +420 541 211 697.
E-mail address: bartonickova@fch.vutbr.cz (E. Bartonickova).

http://dx.doi.org/10.1016/j.ceramint.2015.07.032
0272-8842/

usage of sacrificial fugitives, replica templates or in situ foaming. Recently the most frequently reported method is the pore formation using partial sintering process of synthetised or commercial powders [4,14,15,21–23]. Further the replica template method with different types of polymers such as starch, polyurethane foam, polystyrene beads and graphite powders was described in [19,24–28], respectively. The casting method in combination with sacrificial fugitives such as gel casting [13,29,30] or the combination of surfactant/air precursor implemented to ceramics slurries [17,18,31] was an inspiration for the fabrication method applied in this work.

Hereafter, the fabrication method based on fugitive-like casting is presented. Prepared mullite-based foams were studied as a possible refractory lining material with sufficient thermal stability, porosity, thermal conductivity and mechanical properties. The influence of strontium aluminate addition as a potential agent for thermal stability enhancement and on foam microstructure was also investigated.

2. Experimental

2.1. Foam preparation and thermal treatment

Raw kaolin powder SEDLEC 1A (Sedlecky kaolin, Czech republic), containing 92 wt% of kaolinite with median particle size of D_{50}=3.8 μm was mixed with various amounts of deionized water with/without liquefaction additive (sodium carbonate, Lach-Ner, Czech republic) to prepare starting ceramic suspension. Further the precursor foam from water and surfactant GA 285 (BASF, Germany) (the experimental set-up of foam production is published elsewhere [17,31]) was added to as-prepared ceramic suspension and stirred to homogenous consistence. Finally the stabiliser based on strontium aluminate (further SrA, D_{50}=16.1 μm, the synthesis is published elsewhere [32]) was mixed with deionised water and added to the kaolinite foam.

Prepared foam was poured into a mould and kept to set for 24 h under ambient temperature. Then the samples were demoulded and dried in two steps – firstly under the temperature of 50 °C for 6 h and afterwards under the temperature of 110 °C for 5 h. Dried samples were cut and polished to required dimensions and sintered in kanthal furnace (CLASIC CZ Ltd., Czech Republic) at the temperature of 1200 °C for 2 h with the heating/cooling rate of 2 °C/min. The reference porous samples were prepared in the same way as described above with calcium aluminate cement (CAC, SECAR® 71, Kerneos, France) as the stabiliser [17].

The compositions of prepared samples are given in Table 1 and the procedure is shown in Fig. 1 and summarised in Table 2.

Table 1
Summary of experimental set-up.

Sample	Stabiliser/type (wt%)	w/p (−)	Kaolin (wt%)	Water (wt%)	Additive (wt%)	Foam (ml)
CAC ref[a]	Calcium aluminate/6.7	0.50	59.6	30.1	0.60[b]	500
SrA 20	Stroncium aluminate/8.6	0.68	54.7	40.4	0.15[c]	300
SrA 25	Stroncium aluminate/8.6	0.68	54.8	40.5	–	300
SrA 31/2	Stroncium aluminate/8.6	0.76	52.3	43.2	–	250

Notes: w/p – water to powders ratio (i.e. summary of kaolin and aluminates).
[a] Content of particular entities was assumed from our work recently published elsewhere [17].
[b] The plasticizer CHRYSO FLUID CE40W was used.
[c] The liquefier Na_2CO_3 was used.

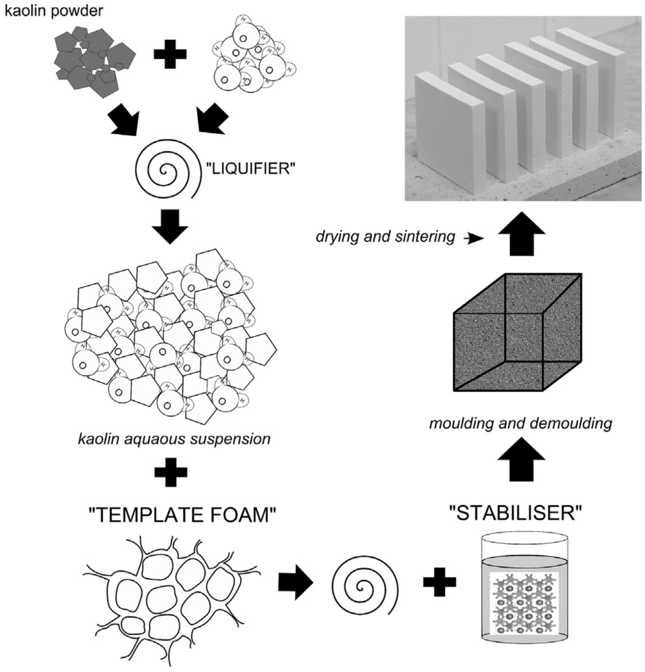

Fig. 1. Experimental set-up of foam fabrication.

Table 2
Summary of processing set-up.

Sample	Stabiliser/type (wt%)	w/p (−)	Setting (h)	Drying (h)		Sintering (°C/h)
				50 °C	110 °C	
CAC ref	Calcium aluminate/6.7	0.50	24	6	5	1200/2
S20	Stroncium aluminate/8.6	0.68	24	6	5	1200/2
S25	Stroncium aluminate/8.6	0.68	24	6	5	1200/2
S31/2	Stroncium aluminate/8.6	0.76	24	6	5	1200/2

Notes: w/p – water to powders ratio (i.e. summary of kaolin and aluminates).

2.2. Characterisation of starting materials and final products

Laser diffraction analyser HELOS (SYMPATEC, Germany) was used for the determination of particle size distribution of powdered materials. The phase composition was determined using X-ray diffraction analyser EMPYREAN (PANalytical, Netherland) in central focusing arrangement using CoKα radiation couples with high temperature chamber HTK 16 (Anton Paar, Austria). The evaluation of the crystallographic structure was done by Highscore programme using the Rietveld method. The foam products were analysed in terms of particle morphology by means of analytical scanning

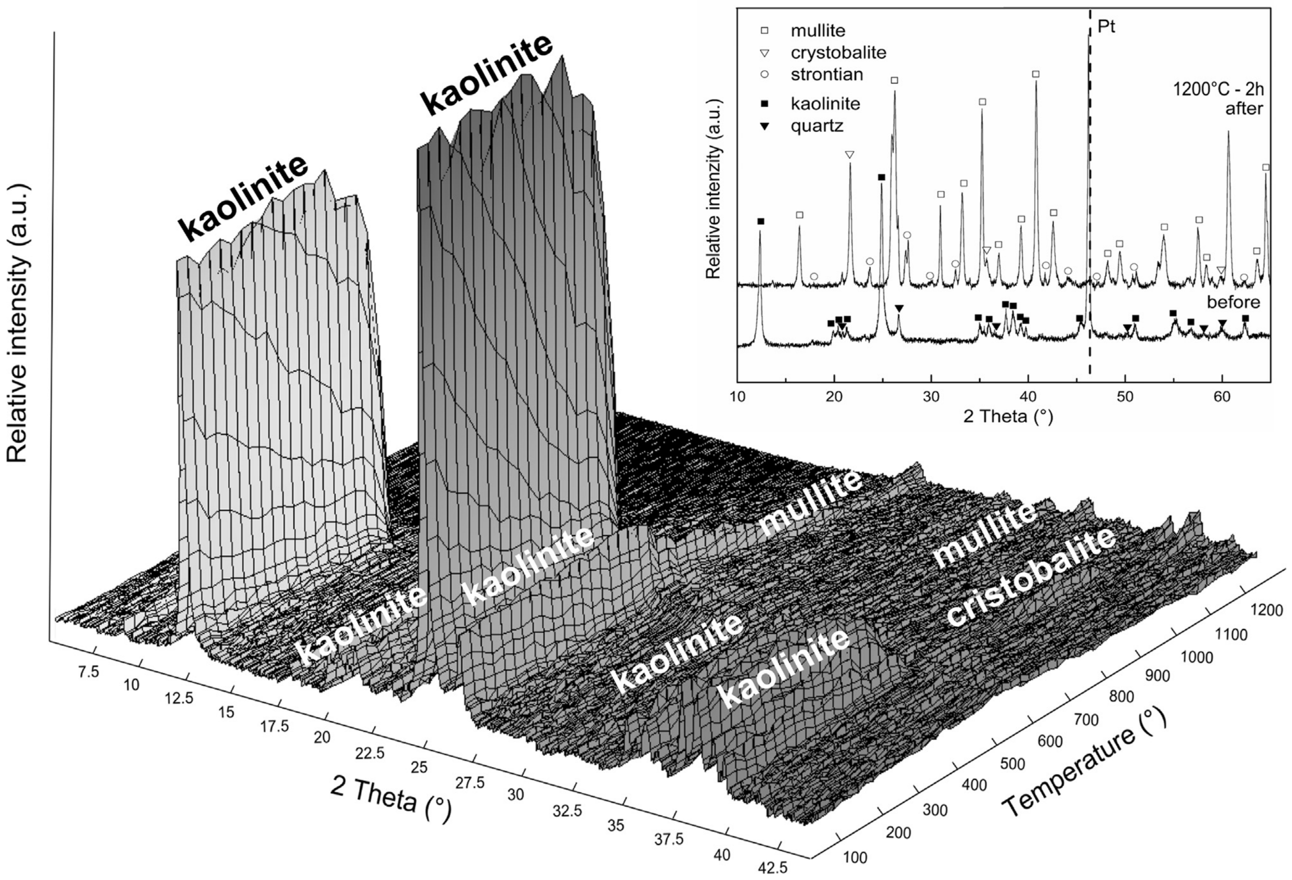

Fig. 2. In situ HT-XRD up to 1200 °C plot of dried foam precursor, XRD spectrum of obtained structure before/after thermal treatment (embedded).

electron microscopy (SEM/EDS) using the device EVO (ZEISS, Germany). The TG–DTA analysis was performed, on cut foam sample, simultaneously using thermal analyser Q600 (TA Instruments, USA.) with the heating rate 10 °C per minute. Horizontal heating microscope with automatic image analysis EM 201 (Hesse Instruments, Germany) was used for sintering behaviour determination. Samples were grinded and press to cylindrical dimensions approximately 3 mm high and 3 mm in diameter. The porosity of prepared foam products was analysed using mercury intrusion pore analyser PoreMaster (Quantachrome, USA) and assed also by image analysis of SEM images performed by Image J software. The mechanical properties were determined by means of compressive test on samples with dimensions $(40\times 25\times 15)\ mm^3$. The compressive strength was determined from the maximal force performed on Instron instruments 5985c (Instron, USA) with loading rate 2 mm per minute. The thermal conductivity measurements were performed on C-Therm TCi (C-Therm, Canada) on the samples with the approximately dimensions $(40\times 25\times 15)\ mm^3$.

3. Results and discussion

The fabrication process of foam preparation is piecewise analysed.

3.1. Thermal and sintering foam behaviour

In situ high temperature XRD analysis of prepared foam samples (SrA 25 without liquifier) before the firing process shown in Fig. 2 reveals the expected kaolinite decomposition and mullite-cristoballite formation with increasing temperature. The presence of stabiliser – monoclinic strontium aluminate phase was also confirmed by the measurements after thermal decomposition (see embedded Fig. 2). The thermal processes and kinetics occurring during the kaolinite heating are well studied and described in several works [33–40]. The Eqs. (1) and (2) summarize general equilibrium of the crystallisation and new phase formation during the thermal treatment – mullite (90 wt%) and cristoballite (5 wt%.) [34,39]:

$$6(Al_2O_3\cdot 2SiO_2\cdot 2H_2O)\xrightarrow{\geq 500^\circ C}6(Al_2O_3\cdot 2SiO_2)\xrightarrow{\geq 950^\circ C}3Al_4Si_3O_{12}+3SiO_{2(amorp.)}\qquad(1)$$

$$3Al_4Si_3O_{12}+3SiO_{2(amorp.)}\xrightarrow{\geq 1200^\circ C}2(3Al_2O_3\cdot 2SiO_2)+8SiO_{2(cryst.)}\qquad(2)$$

The presence of strontium aluminium silicate (anorthite analogue) phase indicates the formation of solid solution with SiO_2 from the reaction between kaolinite and strontium aluminate up to 1200 °C (see Fig. 2 embedded). The thermal stability of strontium aluminate is widely studied elsewhere

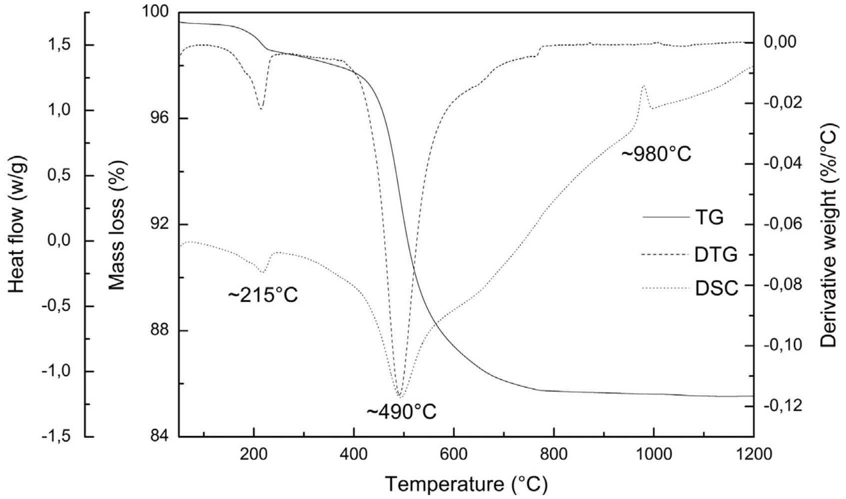

Fig. 3. Simultaneous TG–DTA analysis of dried foam precursor with Na_2CO_3.

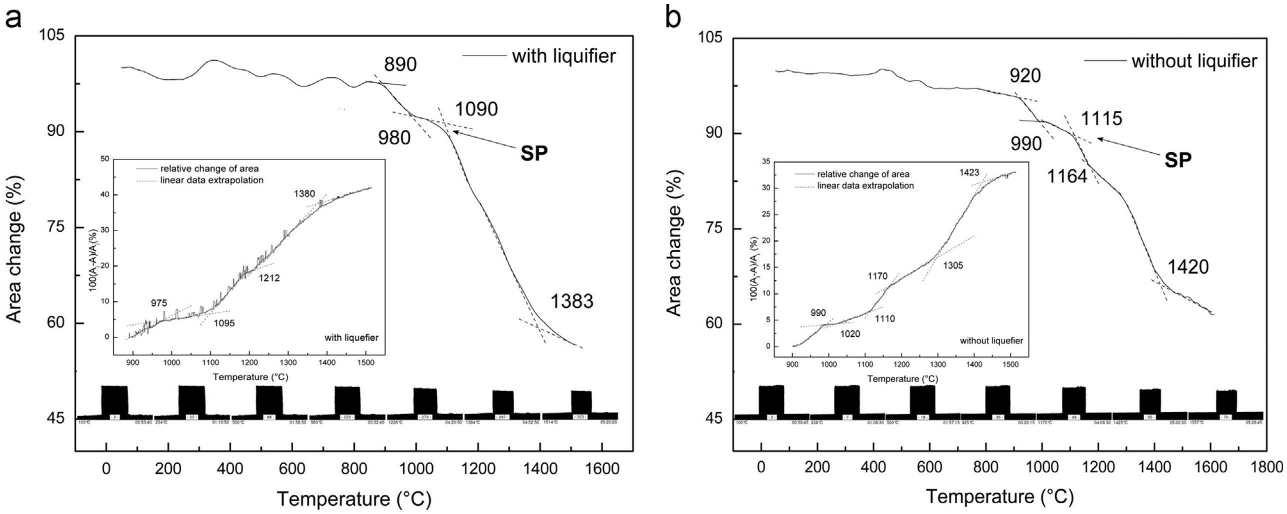

Fig. 4. Sintering behaviour of prepared SrA foams: (a) sintering curve of foam SrA 20 with Na_2CO_3; (b) sintering curve of foam SrA 25 without Na_2CO_3.

[19,32]. The observed structure was determined to as monoclinic and the amount slightly decreased to 5 wt%. The performed TG–DTA analysis SrA 25 (see Fig. 3) confirms the results obtained from in situ HT-XRD.

A small endothermic peak found at 215 °C could correspond to the dehydration of SrA aluminate hydrates formed by the reaction with water during sample preparation [32]. In the temperature region from 400 to 600 °C the broad endothermic peak was determined and could be assigned to two ongoing processes. The first one is the dehydroxylation of kaolinite and the other one is the metakaolinite formation. The small exothermic peak corresponds to Al–Si spinel formation as depicted in Eq. (1). [35, 38, 39]. The results given above confirm that the presence of strontium aluminate shows similar behaviour under high temperatures as in the case where reference CAC stabiliser was used [17]. The heating microscopy experiments (see Fig. 4a and b) were performed in order to show the sintering behaviour of SrA stabilised foams and to achieve optimal sintering conditions and mechanical strength.

The addition of liquefier slightly influenced the sintering behaviour and shifted the end of sintering process from 1420 °C to 1385 °C. For the compositions with or without liquefier the optimal sintering temperature range was determined to be 1090–1383 °C with 9.4% to 40.1% shrinkage and 1115–1420 °C with 10.5% to 32.3% shrinkage, respectively. Fig. 4 (embedded graphics) also showed the extrapolation of area change data in the dependence of temperature in the sintering range. Several ongoing processes can be seen, referring to suggested mullite-cristobalite sintering theories published elsewhere [20,33,34,39]. The temperature 1200 °C, under which the mullite-cristobalite crystallisation and the solid state reaction process take place, was determined as optimal densification temperature. Higher shrinkage and lower temperature stability was observed in samples with liquefier addition.

3.2. Microstructure and properties of prepared foams

Figs. 5 and 6 show the microstructure of prepared foams. The homogenous pore distribution resulting from foam casting/

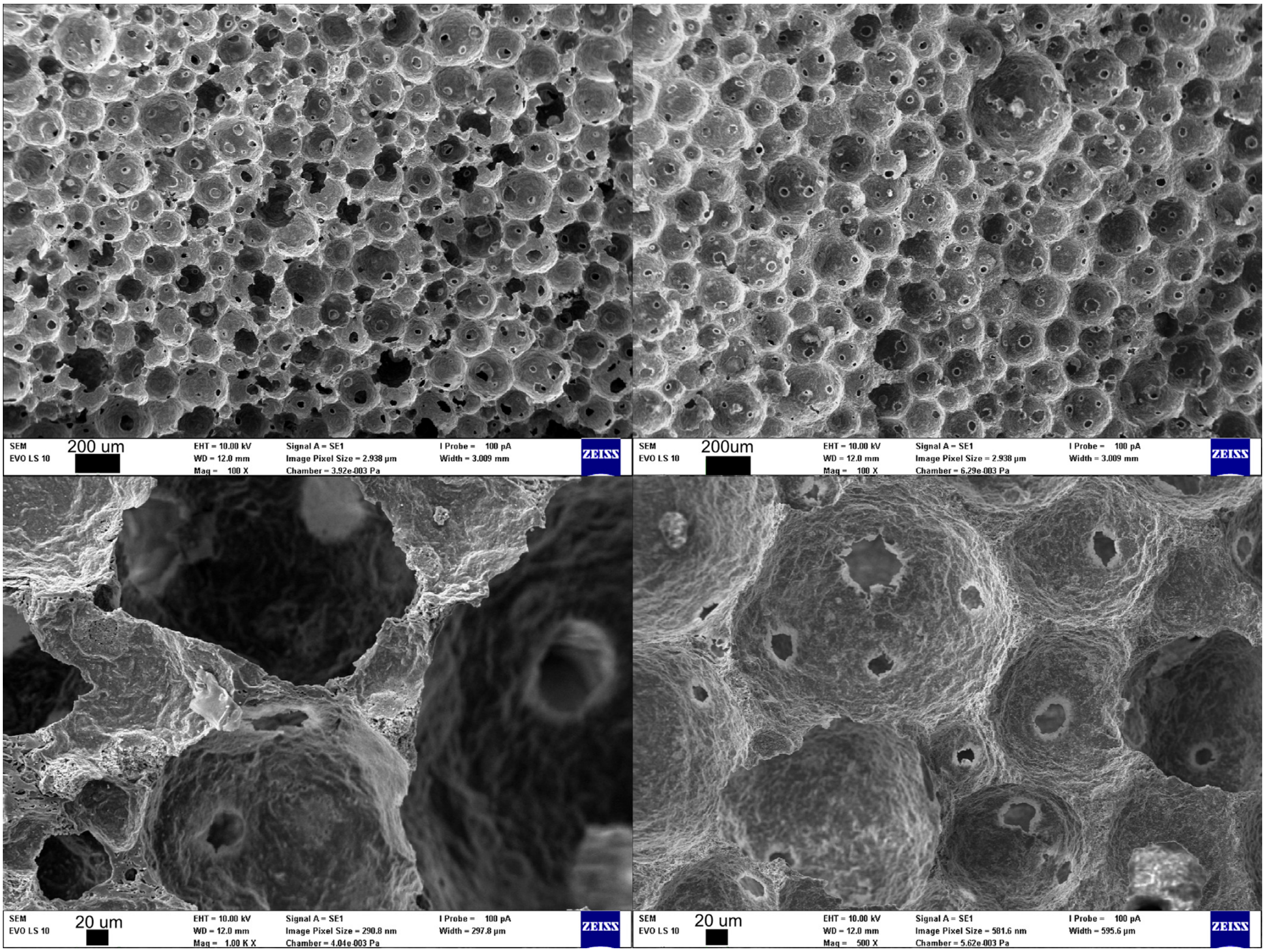

Fig. 5. Microstructure of prepared foams: CAC ref (a, c), SrA (b, d).

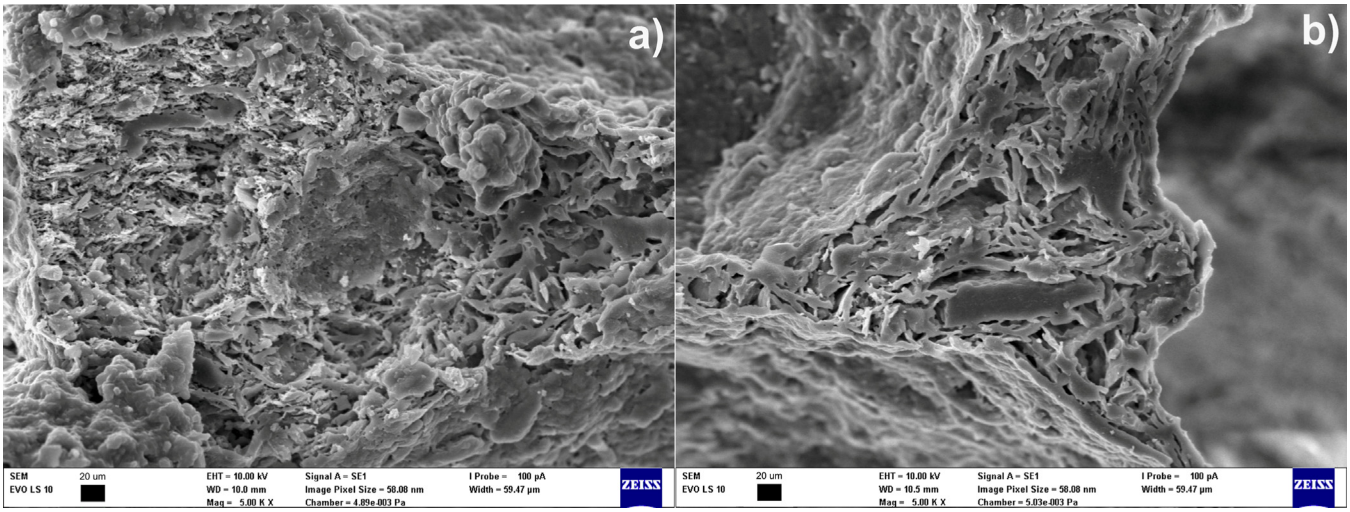

Fig. 6. Fracture surface of prepared SrA foams (SrA 20 with Na_2CO_3 (a), SrA 25 without Na_2CO_3 (b)).

templating process can be seen. The macro-pores with clearly visible open porosity and average pore diameter of 55/230 μm and 45/160 μm were observed for prepared CAC ref and SrA foams (SrA 25), resp. (i.e. mercury porosimetry analysis/image analysis).

The measurements also revealed the presence of smaller pores with macro- and meso-diameter (480 nm, 6–20 nm, resp.). Those cellular pores could result from incomplete sintering process of foam walls. Fig. 6 shows the strut detail with the platelet grain arrangement specific to kaolin based powder structure [18]. The influence of liquefier on the microstructure was not clearly confirmed. Prepared SrA foams with/without (SrA 20a 25) liquefier exhibited very homogenous structure in comparison with CAC ref foam where the collapse of pores was clearly visible. A similar microstructure of kaolin foam collapse was also observed by Bourret et al. [18]. Calculated geometrical density of foams varies from 217 to 341 kg/m^3 (see Fig. 9) and increases with SrA foams system stabilisation and higher w/p ratio. The calculated values of open porosity from the porosimetry measurements were 65.7% to 84.7% for CAC ref and SrA foams, resp.

The thermal conductivity (Figs. 7 and 8) also increased with the same tendency as density. Otherwise the values determined in the range from 0.05 to 0.06 W/m K are lower than recently published ones [13,17,18,22,24,41]. The thermal conductivity measurements were performed under ambient temperature. There are several models how to calculate the thermal conductivity in porous materials [26,42–44]. Porous foams could be described as two phase material (solid and air/pores/voids) with the structure strongly depending on the fabrication way, i.e. homogenous or random phase arrangement. Hashin et al. described the equations predicting effective thermal conductivity, known as Maxwell–Eucken equations, in two forms (see Eqs. (3) and (4)). This model was suggested for homogenous isotropic two phase materials [45]. Finding the optimal continuous heat conduction pathway in homogenously dispersed material could be complicated because of the distances between solid particles. For two phase materials with random phase distribution and with possible uninterrupted conduction pathways, the Effective Medium Theory was considered (see Eq. (5)) [46]. Fig. 8b is based on Maxwell–Eucken and EMT calculations with the assumption of mullite and air bulk thermal conductivity to be 5.10 W/m K [24,25,42] and 0.0257 W/m K respectively. The curves of k_{e1}, k_{e2} and k_{eEMT} divide the area into two regions which is widely discussed by Carson et al. [42]:

$$k_{e1} = k_1 \frac{2k_1 + k_2 - 2(k_1 - k_2)\upsilon_2}{2k_1 + k_2 + (k_1 - k_2)\upsilon_2} \tag{3}$$

$$k_{e2} = k_2 \frac{2k_2 + k_1 - 2(k_2 - k_1)(1-\upsilon_2)}{2k_2 + k_1 + (k_2 - k_1)(1-\upsilon_2)} \tag{4}$$

$$k_{eEMT} = \frac{1}{4}\Big((3\upsilon_2 - 1)k_2 + [3(1-\upsilon_2) - 1]k_1 + \sqrt{[(3\upsilon_2 - 1)k_2 + (3\{1-\upsilon_2\} - 1)k_1]^2 + 8k_1k_2}\Big) \tag{5}$$

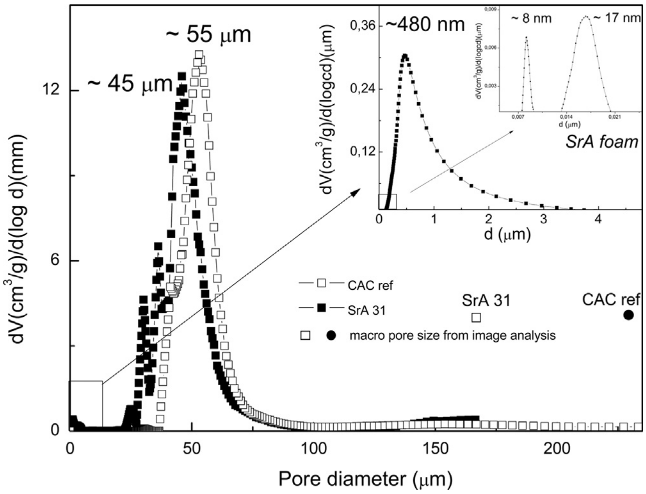

Fig. 7. Pore size distribution of CAC ref and SrA 25 without Na_2CO_3 samples.

The theoretical calculation of effective thermal conductivity by means of Maxwell–Eucken and EMT models shows our experimental values between k_{eEMT} and k_{e2}. Carson et al. [42] proposed the thermal conductivity bounds to “external” and “internal” regions. Experimental data presented in this work belong to “internal region” so the optimal conduction pathway would be established through the solid phase part of foams, which is in agreement with Carson statements [42] and with data published by Gong et al. [25].

Foams were further subjected to the tests of mechanical properties. Fig. 9 shows the results from “crush” compressive strength tests of as-prepared foams. The mechanical strength

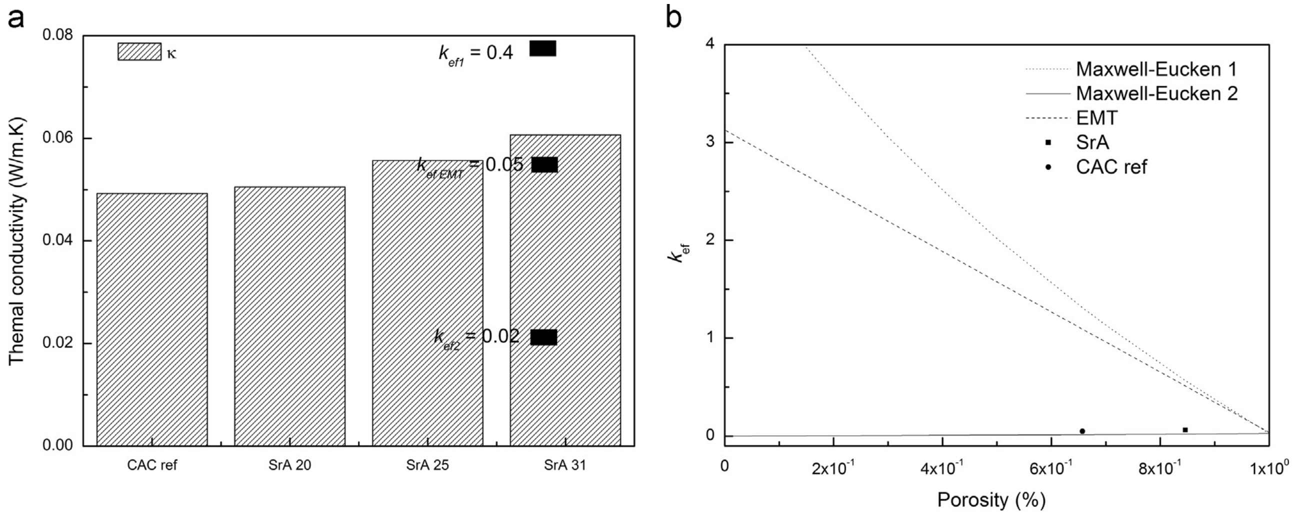

Fig. 8. Thermal conductivity analysis of prepared foams (CAC ref and SrA 25): (a) experimental data; (b) Maxwell–Eucken and EMT models in comparison with experimental data.

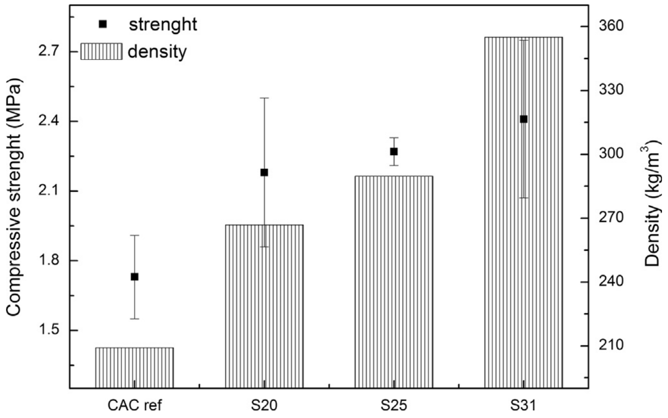

Fig. 9. Mechanical properties of prepared foams.

slightly increased with SrA stabiliser content and without the addition of liquefier. Maximal compressive strength was achieved for the sample with higher w/p ratio and without addition of liquefier. Obtained values are in the range of published ones from 0.5 to 13 MPa [22,29]. Determined mechanical properties were presumably deteriorated due to the presence of macropores, i.e. with low degree of foam wall densification and substantially with low bulk density [3,4,14].

4. Conclusions

The homogenous mullite based foams were successfully prepared via casting-like fabrication method. The addition of strontium aluminate stabiliser showed similar high temperature stability in comparison with calcium aluminate cement. The morphology of obtained foams was very homogenous without any mark of foam collapse and also with thin walls structure (∼2.5 μm). The simple fabrication method provided useful refractory material with high open porosity (up to 85% and macropore size in the range of 480–166 μm), low density (from 200 to 300 kg/m^3), low thermal conductivity (about 0.06 W/m K) and convenient mechanical strength. From low cost and abundant starting material (i.e. fine kaolin powder) excellent ceramics can be produced with possible applications such as an insulation brick working under high temperatures and also due to the strontium content as biocompatible scaffolds for bone tissue engineering.

Acknowledgement

This work was supported by the project “Materials Research Centre at FCH BUT – Sustainability and Development”, REG LO1211, with financial support from National Programme for Sustainability I, (Ministry of Education, Youth and Sports), Czech Republic. The authors also gratefully acknowledge the funding provided from the project “Excellent Teams” No. CZ.1.07/2.3.00/30.0005.

References

[1] T. Ohji, M. Fukushima, Macro-porous ceramics: processing and properties, Int. Mater. Rev. 57 (2) (2012) 115–131.
[2] A.R. Studart, U.T. Gonzenbach, E. Tervoort, L.J. Gauckler, Processing routes to macroporous ceramics: a review, J. Am. Ceram. Soc. 89 (6) (2006) 1771–1789.
[3] A. Harabi, A. Guechi, S. Condom, Production of supports and filtration membranes from Algerian kaolin and limestone, Procedia Eng. 33 (2012) 220–224.
[4] A. Harabi, F. Zenikheri, B. Boudaira, F. Bouzerara, A. Guechi, L. Foughali, A new and economic approach to fabricate resistant porous membrane supports using kaolin and $CaCO_3$, J. Eur. Ceram. Soc. 34 (5) (2014) 1329–1340.
[5] O. Bakhtiari, M. Samei, H. Taghikarimi, T. Mohammadi, Preparation and characterization of mullite tubular membranes, Desalin. Water Treat. 36 (1–3) (2011) 210–218.
[6] A. Shyam, E. Lara-Curzio, T.R. Watkins, R.J. Parten, Mechanical characterization of diesel particulate filter substrates, J. Am. Ceram. Soc. 91 (6) (2008) 1995–2001.
[7] J. Luyten, I. Thijs, M. Ravelingien, S. Mullens, Bone engineering with porous ceramics and metals, Adv. Eng. Mater. 13 (11) (2011) 1002–1007.
[8] G. Tripathi, B. Basu, A porous hydroxyapatite scaffold for bone tissue engineering: physico-mechanical and biological evaluations, Ceram. Int. 38 (1) (2012) 341–349.
[9] E. Roncari, C. Galassi, F. Craciun, C. Capiani, A. Piancastelli, A microstructural study of porous piezoelectric ceramics obtained by different methods, J. Eur. Ceram. Soc. 21 (3) (2001) 409–417.
[10] Y.-F. Wang, J. Yuan, B. Sundén, Y.-L. Hu, Coarse-grained molecular dynamics investigation of nanostructures and thermal properties of porous anode for solid oxide fuel cell, J. Power Sources 254 (0) (2014) 209–217.
[11] M.-J. Lee, J.-H. Jung, K. Zhao, B.-H. Kim, Q. Xu, B.-G. Ahn, S.S.-H. Kim, S.-Y. Kim, Fabrication and electrochemical properties of SOFC single cells using porous yttria-stabilized zirconia ceramic support layer coated with Ni, J. Eur. Ceram. Soc. 34 (7) (2014) 1771–1776.
[12] Y.-F. Yao, C.-H. Shen, W.-F. Chen, P.-Y. Shih, W.-H. Chou, C.-Y. Su, H.-S. Chen, C.-H. Liao, W.-M. Chang, Y.-W. Kiang, C.C. Yang, Void Structures in regularly patterned ZnO nanorods grown with the hydrothermal method, J. Nanomater. 2014 (2014) 11.
[13] T. Shimizu, K. Matsuura, H. Furue, K. Matsuzak, Thermal conductivity of high porosity alumina refractory bricks made by a slurry gelation and foaming method, J. Eur. Ceram. Soc. 33 (15–16) (2013) 3429–3435.
[14] F. Bouzerara, A. Harabi, S. Condom, Porous ceramic membranes prepared from kaolin, Desalin. Water Treat. 12 (1–3) (2009) 415–419.
[15] C.N. Djangang, E. Kamseu, M.K. Ndikontar, G.L.L. Nana, J. Soro, U.C. Melo, A. Elimbi, P. Blanchart, D. Njopwouo, Sintering behaviour of porous ceramic kaolin-corundum composites: phase evolution and densification, Mater. Sci. Eng. A: Struct. Mater. Prop. Microstruct. Process 528 (29–30) (2011) 8311–8318.
[16] H. Schneider, J. Schreuer, B. Hildmann, Structure and properties of mullite—a review, J. Eur. Ceram. Soc. 28 (2) (2008) 329–344.
[17] P. Ptáček, K. Lang, F. Šoukal, T. Opravil, L. Tvrdík, R. Novotný, Preparation and properties of nanostructured ceramic foam from kaolinite, Powder Technol. 253 (2014) 29–34.
[18] J. Bourret, A. Michot, N. Tessier-Doyen, B. Naït-Ali, F. Pennec, A. Alzina, J. Vicente, C.S. Peyratout, D.S. Smith, Thermal conductivity of very porous kaolin-based ceramics, J. Am. Ceram. Soc. 97 (3) (2014) 938–944.
[19] J.H. Bai, Fabrication and properties of porous mullite ceramics from calcined carbonaceous kaolin and alpha-Al_2O_3, Ceram. Int. 36 (2) (2010) 673–678.
[20] E. Kamseu, A. Rizzuti, P. Miselli, P. Veronesi, C. Leonelli, Use of noncontact dilatometry for the assessment of the sintering kinetics during mullitization of three kaolinitic clays from Cameroon, J. Therm. Anal. Calorim. 98 (3) (2009) 757–763.
[21] J. Cao, X. Dong, L. Li, Y. Dong, S. Hampshire, Recycling of waste fly ash for production of porous mullite ceramic membrane supports with increased porosity, J. Eur. Ceram. Soc. 34 (13) (2014) 3181–3194.
[22] F.K. Yang, C.W. Li, Y.M. Lin, C.A. Wang, Effects of sintering temperature on properties of porous mullite/corundum ceramics, Mater. Lett. 73 (2012) 36–39.

[23] E. Garcia, M.I. Osendi, P. Miranzo, Porous mullite templated from hard mullite beads, J. Eur. Ceram. Soc. 31 (8) (2011) 1397–1403.

[24] L.L. Gong, Y.H. Wang, X.D. Cheng, R.F. Zhang, H.P. Zhang, Thermal conductivity of highly porous mullite materials, Int. J. Heat Mass Transf. 67 (2013) 253–259.

[25] L.L. Gong, Y.H. Wang, X.D. Cheng, R.F. Zhang, H.P. Zhang, Porous mullite ceramics with low thermal conductivity prepared by foaming and starch consolidation, J. Porous Mater. 21 (1) (2014) 15–21.

[26] R. Barea, M.I. Osendi, J.M.F. Ferreira, P. Miranzo, Thermal conductivity of highly porous mullite material, Acta Mater. 53 (11) (2005) 3313–3318.

[27] S. Akpinar, I.M. Kusoglu, O. Ertugrul, K. Onel, In situ mullite foam fabrication using microwave energy, J. Eur. Ceram. Soc. 32 (4) (2012) 843–848.

[28] W. Yan, N. Li, B.Q. Han, Effects of sintering temperature on pore characterization and strength of porous corundum-mullite ceramics, J. Ceram. Process. Res. 11 (3) (2010) 388–391.

[29] Z.G. Hou, H.Y. Du, J.C. Liu, R.H. Hao, X. Dong, M.X. Liu, Fabrication and properties of mullite fiber matrix porous ceramics by a TBA-based gel-casting process, J. Eur. Ceram. Soc. 33 (4) (2013) 717–725.

[30] L.Z. Zhou, C.A. Wang, W.Y. Liu, Y. Huang, Fabrication of low density high strength porous mullite ceramics by tert-butyl alcohol-based gelcasting process, J. Inorg. Mater. 24 (6) (2009) 1173–1177.

[31] P. Ptacek, K. Lang, F. Soukal, T. Opravil, E. Bartonickova, L. Tvrdik, Preparation and properties of enstatite ceramic foam from talc, J. Eur. Ceram. Soc. 34 (2) (2014) 515–522.

[32] P. Ptáček, F. Šoukal, T. Opravil, E. Bartoníčková, M. Zmrzlý, R. Novotný, Synthesis, hydration and thermal stability of hydrates in strontium-aluminate cement, Ceram. Int. 40 (7, Part A) (2014) 9971–9979.

[33] P. Ptacek, M. Kreckova, F. Soukal, T. Opravil, J. Havlica, J. Brandstetr, The kinetics and mechanism of kaolin powder sintering I. The dilatometric CRH study of sinter-crystallization of mullite and cristobalite, Powder Technol. 232 (2012) 24–30.

[34] P. Ptacek, F. Soukal, T. Opravil, M. Noskova, J. Havlica, J. Brandstetr, The kinetics of Al-Si spinel phase crystallization from calcined kaolin, J. Solid State Chem. 183 (11) (2010) 2565–2569.

[35] P. Ptacek, F. Soukal, T. Opravil, M. Noskova, J. Havlica, J. Brandstetr, The non-isothermal kinetics analysis of the thermal decomposition of kaolinite by effluent gas analysis technique, Powder Technol. 203 (2) (2010) 272–276.

[36] P. Ptacek, D. Kubatova, J. Havlica, J. Brandstetr, F. Soukal, T. Opravil, Isothermal kinetic analysis of the thermal decomposition of kaolinite: the thermogravimetric study, Thermochim. Acta 501 (1–2) (2010) 24–29.

[37] P. Ptacek, D. Kubatova, J. Havlica, J. Brandstetr, F. Soukal, T. Opravil, The non-isothermal kinetic analysis of the thermal decomposition of kaolinite by thermogravimetric analysis, Powder Technol. 204 (2–3) (2010) 222–227.

[38] K. Heide, M. Földvari, High temperature mass spectrometric gas-release studies of kaolinite $Al_2[Si_2O_5(OH)_4]$ decomposition, Thermochim. Acta 446 (1–2) (2006) 106–112.

[39] Y.-F. Chen, M.-C. Wang, M.-H. Hon, Phase transformation and growth of mullite in kaolin ceramics, J. Eur. Ceram. Soc. 24 (8) (2004) 2389–2397.

[40] O. Castelein, B. Soulestin, J.P. Bonnet, P. Blanchart, The influence of heating rate on the thermal behaviour and mullite formation from a kaolin raw material, Ceram. Int. 27 (5) (2001) 517–522.

[41] C.W. Li, F.K. Yang, Y. Han, C.A. Wang, K.P. Chen, Effects of foaming agent on microstructure and properties of porous mullite ceramics, Rare Metal Mat. Eng. 42 (2013) 931–934.

[42] J.K. Carson, S.J. Lovatt, D.J. Tanner, A.C. Cleland, Thermal conductivity bounds for isotropic, porous materials, Int. J. Heat Mass Transf. 48 (11) (2005) 2150–2158.

[43] R.S. Jagjiwanram, Effective thermal conductivity of highly porous two-phase systems, Appl. Therm. Eng. 24 (17–18) (2004) 2727–2735.

[44] B. Nait-Ali, K. Haberko, H. Vesteghem, J. Absi, D.S. Smith, Thermal conductivity of highly porous zirconia, J. Eur. Ceram. Soc. 26 (16) (2006) 3567–3574.

[45] Z. Hashin, S. Shtrikman, A variational approach to the theory of the effective magnetic permeability of multiphase materials, J. Appl. Phys. 33 (10) (1962) 3125–3131.

[46] S. Kirkpatrick, Percolation and conduction, Rev. Mod. Phys. 45 (4) (1973) 574–588.

Available online at www.sciencedirect.com

SciVerse ScienceDirect

Journal of the European Ceramic Society 34 (2014) 515–522

www.elsevier.com/locate/jeurceramsoc

Preparation and properties of enstatite ceramic foam from talc

Petr Ptáček [a,*], Karel Lang [b], František Šoukal [a], Tomáš Opravil [a],
Eva Bartoníčková [a], Lukáš Tvrdík [b]

[a] *Brno University of Technology, Faculty of Chemistry, Centre for Materials Research CZ.1.05/2.1.00/01.0012, Purkyňova 464/118, Brno CZ-612 00, Czech Republic*

[b] *P-D Refractories CZ, Nádražní 218, Velké Opatovice CZ-679 63, Czech Republic*

Received 2 June 2013; received in revised form 30 July 2013; accepted 6 August 2013
Available online 3 September 2013

Abstract

The effective method of preparation, stabilization and high temperature treatment of enstatite ceramic foam is described in this work. The technique is based on foaming of suspension of talc, on the stabilization of foam structure and on final high temperature treatment after drying. The spontaneous delamination of aggregates and the redistribution of talc particles in foam are driven by decreasing surface energy. The changes of phase composition as well as the mechanism and the kinetics of processes which take place during the thermal treatment were described. The treatment within the temperature range from 1150 to 1250 °C provides the ceramic foam via sintering without melted phase, whereas a liquid phase sintering occurs at higher temperatures. The final temperature of sintering is 1300 °C. Increasing amount of melted phase supports the formation of enclosed porosity and formed glass stabilizes the high temperature protoenstatite polymorph in the foam.

Keywords: Enstatite; Ceramic foam; Talc; Porous materials

1. Introduction

Steatite ceramics based on magnesium metasilicate ($MgO{\cdot}SiO_2$ or $MgSiO_3$) is widely used in high-temperature applications and electronics due to the low dielectric losses, high mechanical strength and high temperature resistance.[1] Enstatite containing glass ceramics is a promising material for the preparation of glass ceramics substrates for recording media due to its high strength, improved impact, vibration resistance and particularly low temperature expansion coefficient.[2,3]

Steatite ceramics together with ceramics based on magnesium orthosilicate forsterite ($2MgO{\cdot}SiO_2$ of Mg_2SiO_4) and cordierite ($2MgO{\cdot}2Al_2O_3{\cdot}5SiO_2$ or $Mg_2Al_4Si_5O_{18}$) ceramics belong to the ternary systems of $MgO–Al_2O_3–SiO_2$, which are prepared from the mixture of talc ($3MgO{\cdot}4SiO_2{\cdot}H_2O$) and kaolin ($Al_2O_3{\cdot}2SiO_2{\cdot}2H_2O$). $BaCO_3$ is often used as a non-alkaline type of flux which provides low dielectric losses of ceramics. Feldspars or barium carbonate added to talc generate the vitreous phase, hence the crystalline magnesium metasilicate grains are surrounded by the glass matrix after cooling.[1,4]

Steatite occurs in four polymorphic forms such as enstatite, protoenstatite, clinoenstatite and high-temperature clinoenstatite. Protoenstatite is thermodynamically stable at the temperatures higher than 985 °C but in ceramic body it is often stabilized by glassy phase. Therefore, if protoenstatite is not stabilized properly, an undesirable transformation to clinoenstatite takes place at the laboratory temperature. The volume change leads to the formation of cracks in the ceramic body and deteriorates the dielectric properties of material.[2,5]

The combination of properties of ceramics or glass-ceramics with highly porous foam structure enables such applications as high temperature carrier of catalysts[6–8] and photocatalysts,[9,10] refractory and thermal insulating materials,[11–13] filters for molten metals and hot gasses,[14,15] bioceramics and biological substrates.[16–18]

Open cell (reticulated) ceramic foams, which are defined as dispersion systems based on the interconnected bubbles of

---

[*] Corresponding author. Tel.: +420 541 149 389.

E-mail addresses: ptacek@fch.vutbr.cz (P. Ptáček), lang@mslz.cz (K. Lang), soukal@fch.vutbr.cz (F. Šoukal), opravil@fch.vutbr.cz (T. Opravil), bartonickova@fch.vutbr.cz (E. Bartoníčková), tvrdik@mslz.cz (L. Tvrdík).

0955-2219/$ – see front matter © 2013 Elsevier Ltd. All rights reserved.
http://dx.doi.org/10.1016/j.jeurceramsoc.2013.08.007

gas phase in continuous ceramic matrix, can be prepared via various manufacturing techniques[19,20] including the transformation of ceramic powder slurry into the solid foam,[21–23] the reticulated sponge method (replica technique)[24–27] or the gel casting.[28–31] The replica technique is based on the pyrolysis of polymeric sponge coated by ceramic slurry. The following high-temperature treatment leads to the ceramic bond via sintering. The gel casting method uses mechanical work and foaming agents in order to foam the ceramic suspension.

The paper deals with the technique of preparation of enstatite based ceramic foam from talc, where the formation of kaolinite framework is driven by decreasing of surface energy of the system and provides a mechanical support to the foam structure. The stabilization of foam by diatomaceous earth significantly increases the time-stability. The structure and the properties of foam as well as the processes occurring during the stabilization and further thermal treatment were investigated.

2. Experimental

2.1. Preparation of foam

Talc, high alumina cement (HAC, Secar 51, Lafarge) and diatomaceous earth (Holland) were used to prepare the solid framework of aqueous foam stabilized by the mixture of anionic surfactant of an alkyl sulfate-type with water (volume ratio 1: 22). Fig. 1 shows the flow chart diagram of the preparation process using foam of the volume density of 50 kg × m^{-3}.

Setting of cement provides the mechanical properties necessary for the manipulation with raw foam before the thermal treatment. In order to avoid the undesirable effect of surfactant on the hydration process, AC was firstly mixed with water. Within the induction period when the hydration had just begun but its rate was very small, talc and diatomaceous earth were stirred into the reaction mixture. Foam (1.5 dm^3) was added at least. After 15 min of stirring the foamed slurry was poured into the mould. After 2–3 days of free curing the samples gained sufficient mechanical properties for manipulation. Further treatment included drying followed by firing to the temperature within the sintering range.

2.2. Sample analysis

The structure and the properties of foam were investigated by scanning electron microscopy (SEM) using Field emission microscope Jeol JSM-7600F. High temperature X-ray diffraction analysis (HT-XRD, X'pert Empyrean, PANanalytical) with high temperature chamber HTK 16 (Anton Paar) and simultaneous TG-DTA and EGA (Q600, TA Instruments connected to infrared spectrometer iS10, Thermo Scientific) were used to investigate the processes and changes in the phase composition during high temperature treatment. The distribution of particle size of kaolinite and diatomaceous earth was investigated by Helos (Sympatec) particle size analyzer.

The behaviour during sintering and melting was investigated by the horizontal type heating microscope EM 201 (Leitz). The cylinder shaped specimen of the diameter and the height of 3 mm was pressed out and put down by the sample holder. The sample was heated under the heating rate of 5 °C min^{-1} up to the temperature of 1400 °C. The behaviour of the specimen during the thermal treatment was investigated via the relative change of area (A):

$$A\ (\%) = 100\left(1 - \frac{A_T - A_0}{A_0}\right) \tag{1}$$

where A_0 and A_T are the initial specimen area and the area measured at the temperature T, respectively. The picture recorded by CCD camera with the step of 25 °C was used to determine the temperatures of standard points which are defined for heating microscopy and from which the points of sintering (SP), deformation (DP), hemisphere (HP) and flowing (FP) were identified.

The apparent density and porosity were assessed by the evacuation method and the hydrostatic weighting and pycnometric measurements were used for the determination of true density. The specimens were prepared in laboratory furnace under the heating rate of 2 °C min^{-1} to the temperatures within the sintering range assed by heating microscopy (1150, 1175, 1200, 1225 and 1250 °C). After 60 min at final temperature the samples were cooled to 800 °C under the cooling rate of 2 °C min^{-1} and next they were left in the furnace to cool down spontaneously to the laboratory temperature. The thermal conductivity at ordinary temperature was measured by TCi (C-Therm) analyzer without the contact agent.

2.3. Kinetics and mechanism of processes during thermal treatment

The apparent activation energy (E_a) and the frequency factor (A) of investigated process were evaluated by the mechanism-free method based on the Kissinger kinetic approach:[32,33]

$$\ln\left[\frac{\Theta}{T_m^2}\right] = \ln\left[\frac{AR}{E_a} n(1-\alpha_m)^{n-1}\right] - \frac{E_a}{RT_m} = \text{const.} - \frac{E_a}{RT_m} \tag{2}$$

where T_m is the peak temperature measured under applied heating rate $\boldsymbol{\Theta}$, n is the empirical reaction order (kinetic exponent), α_m is the fractional conversion reached for the temperature T_m and R is the universal gas constant.

The non-isothermal kinetics experiments were performed using TG-DTA analyzer SDT Q600. 30 mg of sample were heated under the heating rates (Θ) of 2, 3, 5, 7, 10, 15 and 20 °C min^{-1} up to 1100 °C. The points on the plot of ln (AR/E_a) versus ${T_m}^{-1}$ were fitted by the straight line with the slope equal to $-E_\mathrm{a}/R$ whereas the intercept yields to the constant term of Eq. (2).

The mechanism was estimated from the shape of DTG peak via the value of kinetic exponent ($\boldsymbol{n}$) which is related to the empirical order of reaction.[32] The exponent can be calculated from the equation:[34,35]

$$n = \frac{2.5RT_m^2}{w_{1/2}E_a} \tag{3}$$

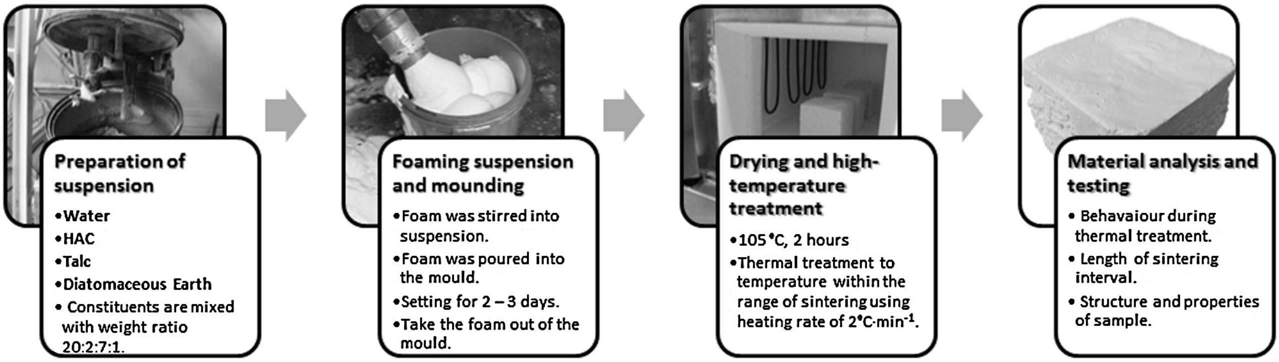

Fig. 1. Preparation of ceramic foam via foaming of the suspension of talc.

where $w_{1/2}$ is the half-width (width at a half height) of peak. The value of kinetic exponent is typical for various mechanisms of the investigated process.[36]

3. Results and discussion

The thermal treatment of foamed talc leads to the ceramic foam based on enstatite. The conditions during this procedure, so called firing curve or firing regime have a considerable effect on such properties of the foam as the mechanical strength, the total porosity and the thermal conductivity. Therefore the knowledge about the processes occurring during the thermal treatment plays an essential role at designing of proper firing regime. Fig. 2 shows the plot of simultaneous TG-DTA (a) and EGA (b) during heating of dry foam up to the temperature of 1350 °C. The data were discussed together with the changes of phase composition investigated by the high-temperature X-ray diffraction analysis (Fig. 3).

Hexagonal dicalcium aluminate hydrate phase (C_2AH_8, $2CaO{\cdot}Al_2O_3{\cdot}8H_2O$) and alumina gel are formed as initial products of hydration of CAC Secar 71[37] but increasing of the temperature during slow drying procedure of wet foam causes formation of the cubic hydrogarnet phase of tricalcium aluminate hexahydrate (C_3AH_6, $3CaO{\cdot}Al_2O_3{\cdot}6SiO_2$) together with aluminium hydroxide in the polymorphic modification of gibbsite (γ-AH_3, $Al(OH)_3$). The thermal decomposition of C_3AH_6 phase and gibbsite shows dual endothermic peak at the temperature of 242 °C and the increasing intensity of water vapor is detected on EGA. The mass of sample decreases by 4.1% during this process. Weak maximum of CO_2 observed at this temperature indicates the C_3AH_6 formation of monocarboaluminate phase (C_4ACH_{11}, $3CaO{\cdot}Al_2O_3{\cdot}CaCO_3{\cdot}11H_2O$)[38] during the hydration of CAC. Large surface of foamed product enhances the reaction of carbonation.

The pyrolysis of surfactant leads to the broad exothermic peak at the temperature of 347 °C connected with the reduction of mass of sample by about 0.2%. The presence of CO bands and various C–H modes in the infrared spectrum of gas phase indicates the formation of short hydrocarbon chains under the moderate reduction condition.

The thermal decomposition of calcium carbonate shows strong endothermic peak at the temperature of 692 °C. The measured weight loss of 2.8% enables to calculate the original amount of $CaCO_3$ in the sample to be 6.4%. EGA shows intensive bands of CO_2 in the spectrum of gas phase. While the diffraction lines of $CaCO_3$ in HT-XRD plot decrease, the lines of formed lime (CaO) grow at the same temperature.

Broad endothermic peak at 905 °C is related to the dehydroxylation of talc (Eq. (4)). Enstatite, amorphous silica and water are formed during this process. The mass of sample is reduced by 3.4% and the increasing intensity of water vapor bands is detected on EGA plot. The diffraction lines of enstatite appear on HT-XRD plot in this temperature range. Cristobalite (c-SiO_2)

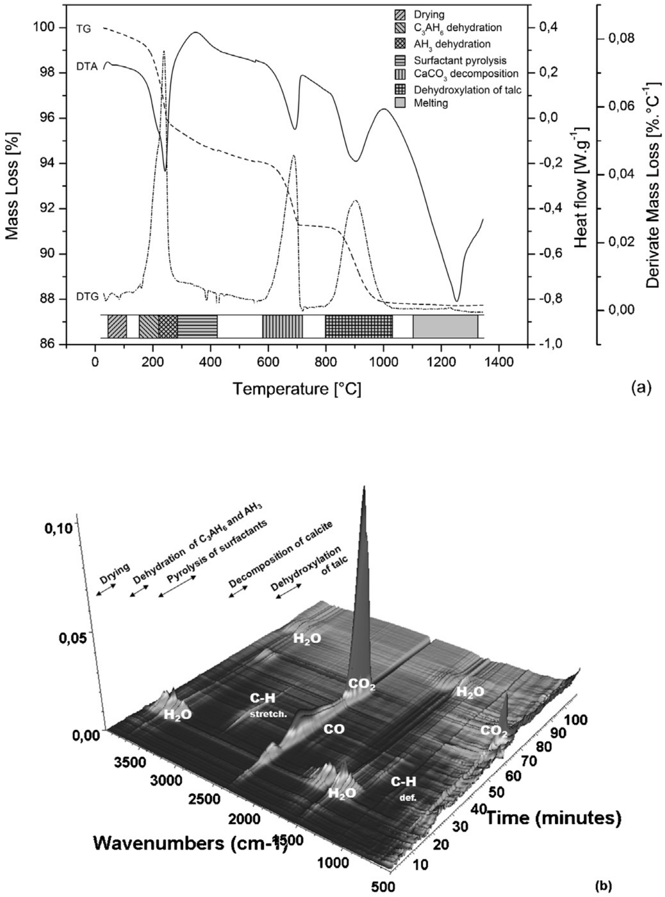

Fig. 2. Simultaneous TG-DTA (a) and EGA (b) of foam based on talc.

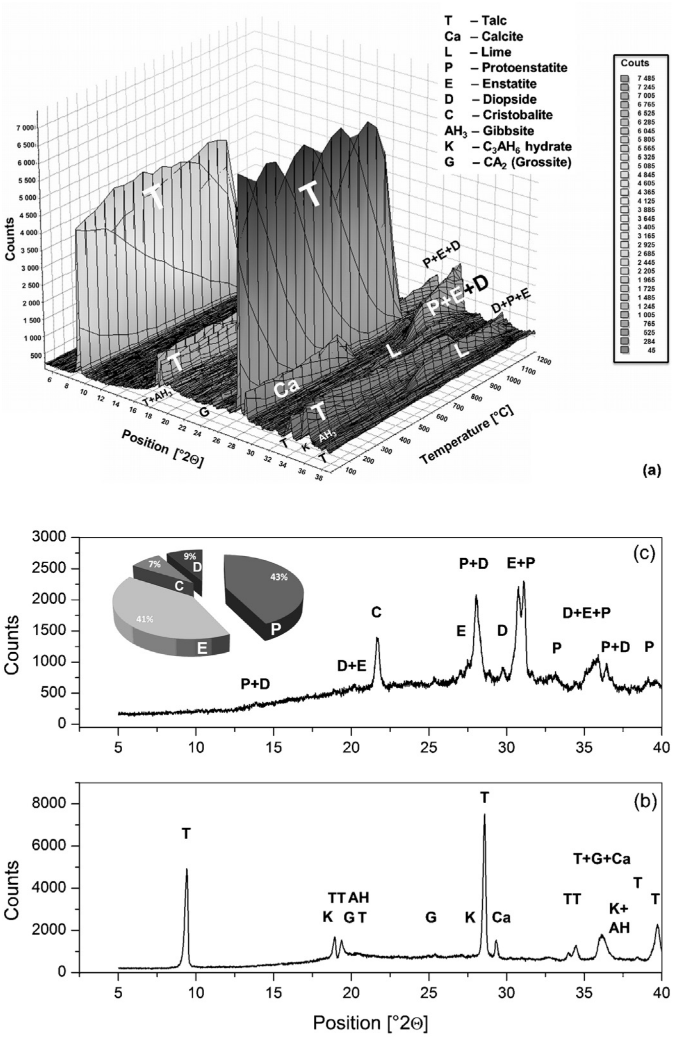

Fig. 3. HT-XRD plot of foam (a) and X-ray diffraction analysis before (b) and after thermal treatment (c).

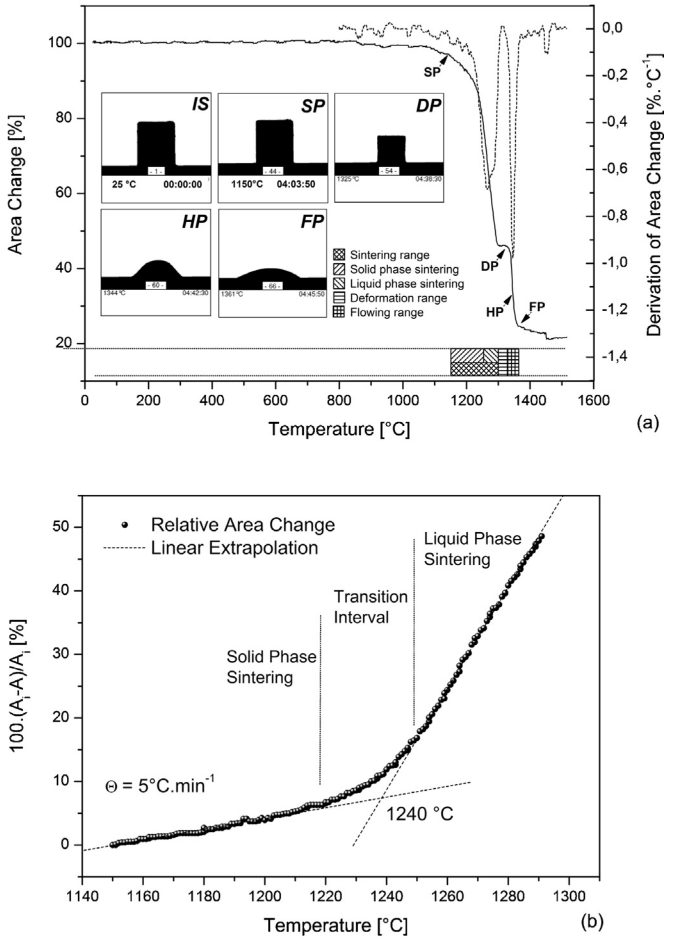

Fig. 4. Heating microscopy plot with photography of test piece related to important temperature points (a): initial state (IS), point of sintering (SP), deformation (DP), hemisphere (HP) and flowing point (FP). The liquid phase participates in the sintering from temperatures higher than 1240 °C (b).

and diopside ($CaMgSi_2O_6$) are originated from the silica phase at the temperature of 1150 °C.

$$3MgO \cdot 4SiO_2 \cdot H_2O \xrightarrow{800-1050^{\circ}C} 3MgO \cdot SiO_2 + SiO_2(amorphous) + H_2O(g) \qquad (4)$$

The Rietveld analysis shows that the sample cooled to the temperature of 1200 °C after the thermal treatment contains 40.9% enstatite, 43.2% protoenstatite, 7.5 % cristobalite and 8.5% diopside (Fig. 3(c)). The HT-XRD plot shows also presence of a certain amount of monoclinic calcium dialuminate phase (CA_2, $CaO{\cdot}2Al_2O_3$) which is a common constituent of high-alumina cement.[39]

The processes of formation of ceramic bond and of melting were investigated by high-temperature heating microscopy (Fig. 4(a)) in order to evaluate the width of sintering range. The initial and final sintering temperatures are 1150 °C and 1300 °C, respectively. Within this 150 °C wide sintering range large amount of melt is formed at the temperature higher than 1240 °C (Fig. 4(b)).This temperature is assessed via the extrapolation of linear parts of relative area change throughout the sintering range ($100\,(\boldsymbol{A}_i-\boldsymbol{A})/\boldsymbol{A}_i$, where $\boldsymbol{A}_i$ is the specimen area at initial sintering temperature) and corresponded to the melt formation endothermic peak at 1255 °C measured by DTA (please refer to Fig. 2).

Large firing shrinkage causes that the temperature higher than 1240 °C is not desirable for foam and proper sintering range is limited by the temperature of 1250 °C. On the other hand, the increasing of amount of melt phase supports the formation of enclosed porosity and stabilizes high temperature protoenstatite polymorph (please referee to Fig. 5).

The melting of sample is indicated by the deformation point. As the temperature increases, the specimen loses its regular shape and a drop of melt is formed. The temperature interval between the points of deformation (1325 °C) and hemisphere (1344 °C) provides the width of deformation range of 19 °C. The flow range of 17 °C is bordered by the hemisphere point and the flowing point at 1361 °C.

The texture of the cross section trough prepared enstatite foam (Fig. 5) shows isolated air bubbles dispersed throughout the ceramic body. The formation of isolated bubbles is given by a hydrophobic nature of talc. The talc particles closest to the inner surface of bubbles show parallel orientation (d) while inside the

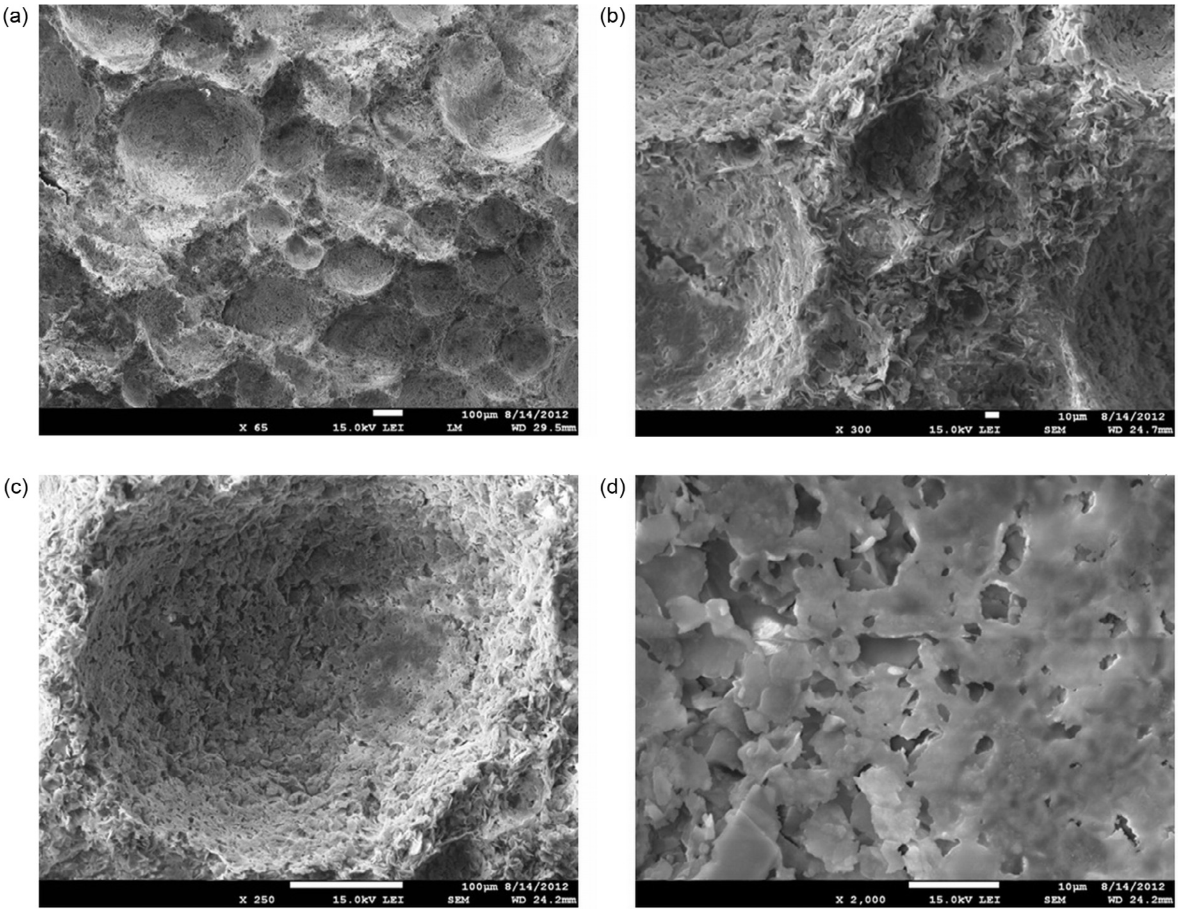

Fig. 5. SEM images of ceramic foam after the thermal treatment: air bubbles enclosed within the ceramic body (a), the wall between two bubbles (b), inner surface wall of bubble (c) and the detail of the sintered particles (d).

wall they are distributed randomly (b). Together with the formation of more spherical bubbles instead of polyhedral cells the interfacial energy of foamed system is reduced. The inner surface of bubbles (c) shows more sintered areas (d) indicating the formation of eutectic melt during the thermal treatment (Fig. 2).

The overview of properties of prepared foam before and after the thermal treatment is listed in Table 1. Increasing final temperature increases the density and shrinkage of ceramic foam while the porosity decreases. The thermal conductivity of samples fired to higher temperatures increases with increasing density, firing shrinkage and decreasing total porosity of foam until the formation of enclosed pores takes place (1225 °C). The formation of enclosed pores reduces the thermal conductivity of foam. Large firing shrinkage and decreasing of total porosity of foam observed at the temperature of 1250 °C causes the thermal conductivity to increase again. Therefore the formation of enclosed pores in the transition zone (please refer to Fig. 4(b)) provides the best firing condition of foam.

The kinetic triplets were determined from the Kissinger plots, which are shown in Fig. 6. The overview of kinetics results regarding to the processes which take place during the

Table 1
Properties of ceramic foam after the thermal treatment.

Final temperature [°C]	Bulk density of foam [kg m^{-3}]			Density [kg·m^{-3}]		Shrinkage [%][c]		Porosity [%][d]		Thermal conductivity [W (m K)$^{-1}$]
	Raw[a]	Dry[b]	Fired	Apparent	True	Firing	Total	Apparent	Total	
1150			180	2430	2720	3.3	4.8	92.6	93.4	0.066
1175			195	2600	2750	5.0	6.5	92.5	92.9	0.082
1200	400	175	210	2740	3040	7.8	9.3	92.3	93.1	0.083
1225			276	2810	3410	8.5	10.0	90.2	91.9	0.072
1250			368	2660	3420	20.2	21.7	86.2	89.2	0.090

[a] Raw foamed talc slurry poured into mould before setting and drying.
[b] Foam after setting and dried to constant weight at the temperature of 105 °C (dry matter).
[c] Drying shrinkage is given by the difference between total and firing shrinkage.
[d] Enclosed porosity is given by the difference between total and apparent porosity.

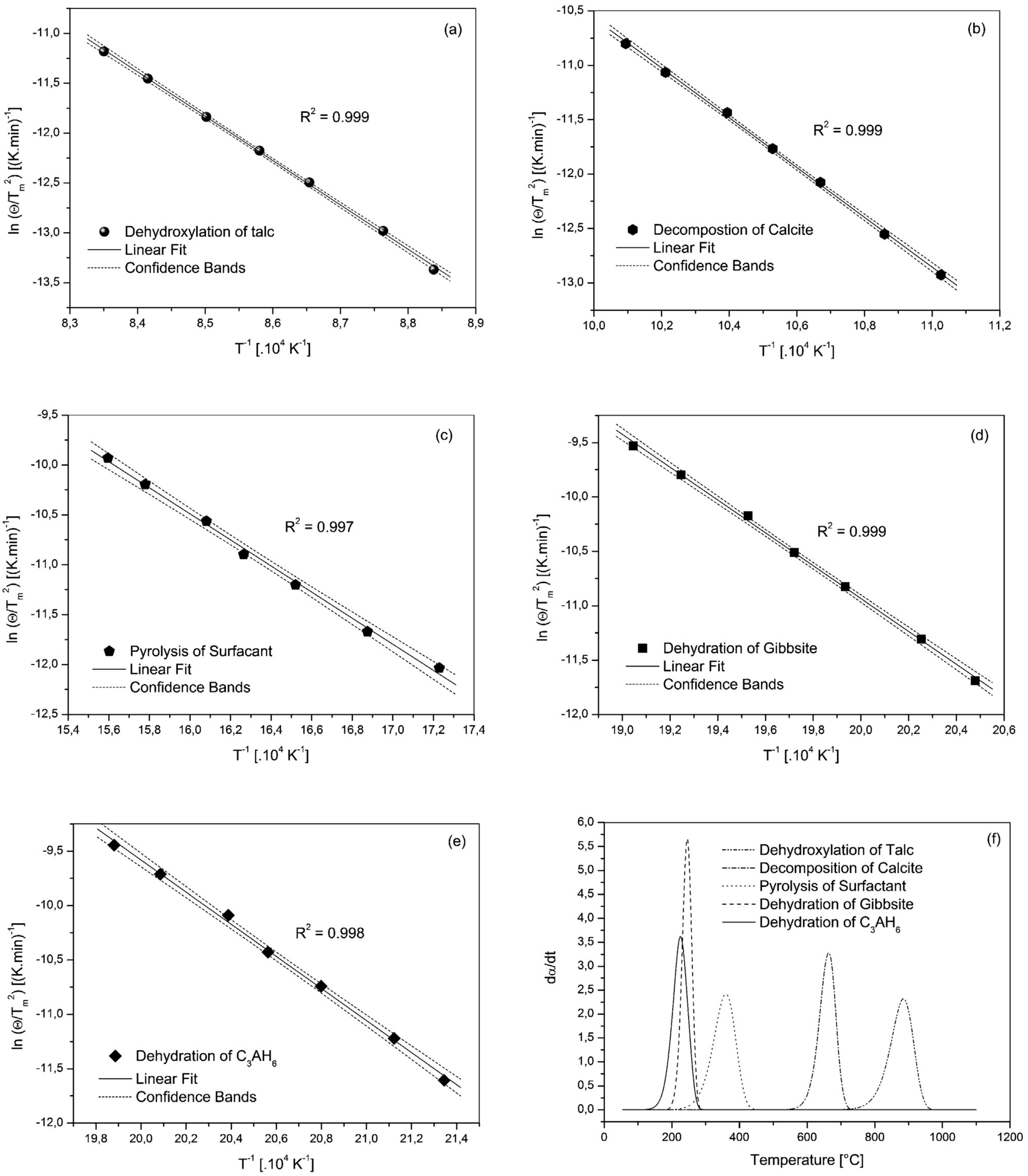

Fig. 6. The Kissinger plots for dehydroxylation of talc (a), thermal decomposition of calcite (b), pyrolysis of surfactant (c), thermal decomposition of C_3AH_6 phase (d) and γ-AH_3 phase (e). Reconstruction of process from assessed kinetic results (f).

thermal treatment of foam is listed in Table 2. The mechanism of the processes was estimated from the values of kinetic factor calculated according to Eq. (3).

Enstatite and protoenstatite are nucleated as direct products of dehydroxylation of talc. Therefore, the kinetic triplet assessed for the dehydroxylation of talc is also related to the formation of magnesium metasilicate phase in the ceramic body. A good agreement with previously published results was reached.[40] The kinetic data were also verified via the reconstruction of the processes from assessed kinetic triplet (Fig. 6(f)). The temperature range and the maximum rate of the process show good agreement with experimental data (please refer to Fig. 2).

Table 2
The kinetics triplet assessed for the processes which occur during firing of foam.

The kinetics of the process	E_a [kJ·mol^{-1}]	A [s^{-1}]	$w_{1/2}$ [°C]	α_m [%]	n	The mechanism of the process
Dehydration of C_3AH_6	120	5.31×10^{10}	15	50	1.0	Random nucleation of a new phase.
Dehydration of AH_3	123	4.42×10^{10}	41	50	3.0	Zero nucleation rate.
Pyrolysis of surfactant	109	7.56×10^{6}	80	46	0.9	
Decomposition of calcite	190	1.54×10^{8}	53	74	1.9	Grain edge nucleation of a new phase.
Dehydroxylation of talc	370	1.45×10^{14}	92	50	1.0	Random nucleation of a new phase.

4. Conclusion

The technique of preparation of ceramic foam of enstatite based on foaming of ceramic suspension was described. The structure indicating spontaneous delamination and redistribution of talc particles near to the bubbles surface was observed in foam. The mechanism and kinetics of dehydration of C_3AH_6 and AH_3, of pyrolysis of surfactant, of thermal decomposition of calcite and of dehydroxylation of talc were determined together with the sintering range correspondent to high temperature treatment of foam. Enstatite and protoenstatite are main constituents of foam after the thermal treatment. The thermal treatment of foam provides the ceramic foam with high service temperature and chemical stability, with high porosity, extremely low volume density and with excellent thermal insulating properties.

Acknowledgments

This work was supported by the project No. CZ.1.07/2.3.00/30.0005, “Excellent Teams” by the project No. TA02010995.

References

1. Gökçe H, Ağaoğulları D, Öveçoğlu ML, Duman İ, Boyraz T. Characterization of microstructural and thermal properties of steatite/cordierite ceramics prepared by using natural raw materials. *J Eur Ceram Soc* 2011;**31**:2741–7.
2. El-Meliegy EAM, Abdel-Hameed SAM. Enstatite–celsian glass ceramics. *Mater Charact* 2005;**55**:28–34.
3. Khater GA, Morsi MM. Glass-ceramics based on spodumene–enstatite system from natural raw materials. *Thermochim Acta* 2011;**519**:6–11.
4. Vela E, Peiteado M, García F, Caballero AC, Fernández JF. Sintering behaviour of steatite materials with barium carbonate flux. *Ceram Int* 2007;**33**:1325–9.
5. Mielcarek W, Nowak-Woźny D, Prociów K. Correlation between $MgSiO_3$ phases and mechanical durability of steatite ceramics. *J Eur Ceram Soc* 2004;**24**:3817–21.
6. Ciambelli P, Palma V, Palo E. Comparison of ceramic honeycomb monolith and foam as Ni catalyst carrier for methane autothermal reforming. *Catal Today* 2010;**155**:92–100.
7. Patcas FC, Garrido GI, Kraushaar-Czarnetzki B. CO oxidation over structured carriers: a comparison of ceramic foams, honeycombs and beads. *Chem Eng Sci* 2007;**62**:3984–90.
8. Twigg MV, Richardson JT. Preparation and properties of ceramic foam catalyst supports. *Stud Surf Sci Catal* 1995;**91**:345–59.
9. Plesch G, Vargová M, Vogt UF, Gorbár M, Jesenák K. Zr doped anatase supported reticulated ceramic foams for photocatalytic water purification. *Mater Res Bull* 2012;**47**:1680–6.
10. Vargová M, Plesch G, Vogt UF, Zahoran M, Gorbár M, Jesenák K. TiO_2 thick films supported on reticulated macroporous Al_2O_3 foams and their photoactivity in phenol mineralization. *Appl Surf Sci* 2011;**257**:4678–84.
11. Juettner T, Moertel H, Svinka V, Svinka R. Structure of kaoline–alumina based foam ceramics for high temperature applications. *J Eur Ceram Soc* 2007;**27**:1435–41.
12. Acimovic Z, Pavlovic L, Trumbulovic L, Andric L, Stamatovic M. Synthesis and characterization of the cordierite ceramics from nonstandard raw materials for application in foundry. *Mater Lett* 2003;**57**:2651–6.
13. Liaw D-W, Tsai Ch Y, Wei W-CJ. Thermal insulation of muscovite/glass ceramic foam for solid oxide fuel cell. *J Power Sources* 2011;**196**:8012–8.
14. Taslicukur Z, Balaban C, Kuskonmaz N. Production of ceramic foam filters for molten metal filtration using expanded polystyrene. *J Eur Ceram Soc* 2007;**27**:637–40.
15. Nacken M, Ma L, Heidenreich S, Verpoort F, Baron GV. Development of a catalytic ceramic foam for efficient tar reforming of a catalytic filter for hot gas cleaning of biomass-derived syngas. *Appl Catal B-Environ* 2012;**125**:111–9.
16. Engin NO, Tas AC. Manufacture of macroporous calcium hydroxyapatite bioceramics. *J Eur Ceram Soc* 1999;**19**:2569–72.
17. Potoczek M, Zima A, Paszkiewicz Z, Ślósarczyk A. Manufacturing of highly porous calcium phosphate bioceramics via gel-casting using agarose. *Ceram Int* 2009;**35**:2249–54.
18. Dorozhkin SV. Bioceramics of calcium orthophosphates. *Biomaterials* 2010;**31**:1465–85.
19. Luyten J, Mullens S, Cooymans J, De Wilde AM, Thijs I, Kemps R. Different methods to synthesize ceramic foams. *J Eur Ceram Soc* 2009;**29**:829–32.
20. Peng HX, Fan Z, Evans JRG. Factors affecting the microstructure of a fine ceramic foam. *Ceram Int* 2000;**26**:887–95.
21. Yu J, Sun X, Li Q, Li X. Preparation of Al_2O_3 and Al_2O_3–ZrO_2 ceramic foams with adjustable cell structure by centrifugal slip casting. *Mat Sci Eng A-Struct* 2008;**476**:274–80.
22. Wang M, Du H, Guo A, Hao R, Hou Z. Microstructure control in ceramic foams via mixed cationic/anionic surfactant. *Mater Lett* 2012;**88**:97–100.
23. Montanaro L, Jorand Y, Fantozzi G, Negro A. Ceramic foams by powder processing. *J Eur Ceram Soc* 1998;**18**:1339–50.
24. Nor MAAM, Ch Hong L, Ahmad ZA, Akil HM. Preparation and characterization of ceramic foam produced via polymeric foam replication method. *J Mater Process Tech* 2008;**207**:235–9.
25. de Sousa E, Rambo CR, Hotza D, de Oliveira APN, Fey T, Greil P. Microstructure and properties of LZSA glass-ceramic foams. *Mat Sci Eng A-Struct* 2008;**476**:89–97.
26. Dressler M, Reinsch S, Schadrack R, Benemann S. Burnout behavior of ceramic coated open cell polyurethane (PU) sponges. *J Eur Ceram Soc* 2009;**29**:3333–9.
27. Akpinar S, Kusoglu IM, Ertugrul O, Onel K. Silicon carbide particle reinforced mullite composite foams. *Ceram Int* 2012;**38**:6163–9.
28. Guo X, Zhou Z, Ma G, Wang S, Zhao S, Zhang Q. Effect of forming process on the integrity of pore-gradient Al_2O_3 ceramic foams by gel casting. *Ceram Int* 2012;**38**:713–9.
29. Bartuli C, Bemporad E, Tulliani JM, Tirillò J, Pulci G, Sebastiani M. Mechanical properties of cellular ceramics obtained by gel casting: characterization and modeling. *J Eur Ceram Soc* 2009;**29**:2979–89.
30. Potoczek M, Zima A, Paszkiewicz Z, Ślósarczyk A. Manufacturing of highly porous calcium phosphate bioceramics via gel-casting using agarose. *Ceram Int* 2009;**35**:2249–54.
31. Prabhakaran K, Ananthakumar S, Pavithran C. Gel casting of alumina using boehmite as a binder. *J Eur Ceram Soc* 1999;**19**:2875–81.

32. Kissinger HE. Reaction kinetics in differential thermal analysis. *Anal Chem* 1957;**29**:1702–6.
33. Blainea RL, Homer EK. Homer Kissinger and the Kissinger equation. *Thermochim Acta* 2012;**540**:1–6.
34. Augis JA, Bennett JD. Calculation of Avrami parameters for heterogeneous solid-state reactions using a modification of Kissinger method. *J Therm Anal* 1978;**13**:283–92.
35. Ray CS, Yang Q, Huang W-H, Day DE. Surface internal crystallization in glasses as determined by differential thermal analysis. *J Am Ceram Soc* 1996;**79**:3155–60.
36. Málek J. The applicability of Johnson-Mehl-Avrami model in the thermal analysis of the crystallization kinetics of glasses. *Thermochim Acta* 1995;**267**:61–73.
37. Edmonds RN, Majumdar AJ. The hydration of Secar 71 aluminous cement at different temperatures. *Cem Concr Res* 1989;**19**:289–94.
38. Bushnell-Watson SM, Sharp JH. The detection of the carboaluminate phase in hydrated high alumina cements by differential thermal analysis. *Thermochim Acta* 1985;**93**:613–6.
39. Odler I. Special Inorganic Cements. In: Bentur A, editor. *Modern Concrete Technology Series*. Publised by E & FN Spon; 2000. ISBN 0-419-22790-3.
40. Ptáček P, Opravil T, Šoukal F, Havlica J, Másilko J, Wasserbauer J. Preparation of dehydroxylated and delaminated talc. *Meta-talc Ceram Int* 2013, http://dx.doi.org/10.1016/j.ceramint.2013.04.109.

Ceramics International 51 (2025) 5505–5513

Contents lists available at ScienceDirect

Ceramics International

journal homepage: www.elsevier.com/locate/ceramint

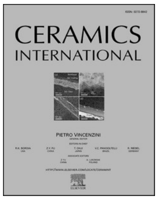

Tailoring microstructure and properties of porous mullite-based ceramics via sol-gel impregnation

E. Bartonickova [a,*], J. Svec [a], L. Dlabajova [a], P. Hruby [a], V. Caba [a], M. Sedlacik [a], L. Kalina [a], J. Koplik [a], F. Soukal [a], L. Kersnerova [b], J. Zach [c], V. Novak [c], K. Dvorak [c]

[a] *Institute of Materials Science, Faculty of Chemistry, Brno University of Technology, Purkynova 118, 612 00, Brno, Czech Republic*
[b] *P-D Refractories CZ JSC, Nadrazni 218, Velke Opatovice, 67963, Czech Republic*
[c] *Institute of Technology of Building Materials and Components, Faculty of Civil Engineering, Brno University of Technology, Veveri 95, 602 00, Brno, Czech Republic*

ARTICLE INFO

Handling Editor: Dr P. Vincenzini

Keywords:
Sol–gel processes (A)
Porosity (B)
Mechanical properties (C)
Mullite (D)

ABSTRACT

Nanotechnology has been introduced into the refractory industry decades ago. However, there are still some peculiarities that hinder its routine application. Poor mechanical strength is one of them. Here we present the fabrication technique for mullite porous ceramics using a calcium-free colloidal binder system followed by secondary sol-gel impregnation intended for fabrication of large up-scaled monoliths. The primary foam was prepared via direct foaming of slurry containing colloidal silica, gelling agents, surfactant, silica fume, and different types of alumina. The foam mixture was cast, de-molded and dried using a cascade drying procedure. The investigation of mullitization that occurred during the high-temperature treatment was studied by XRD and TG-DTA analysis. The optimized sintering curve was then applied to obtain the highest mechanical properties. The resulting foam (with open porosity, volume density about 900 kg/m^3 and mechanical strength about 10 MPa) was further processed by the impregnation step. The applied silica or combined silica/aluminum sol and unreacted alumina underwent secondary mullitization during following high-temperature treatment, which significantly enhanced the mechanical strength (up to 18 MPa). The secondary mullitization process was also investigated by HT-XRD and TG-DTA analysis. Foam microstructure was observed by an electron scanning microscope. Thermal conductivity of as-prepared ceramics foams varied from 0.3 to 0.4 W/m·K. The foam wall porosity evolution was studied by mercury intrusion porosimeter and estimated from image analysis.

1. Introduction

Mullite is the most stable phase in the Al_2O_3–SiO_2 system [1]. Mullite ceramics is refractory material with low thermal conductivity, high corrosion and thermal shock resistance and high refractoriness [2,3]. It serves as a base of castable refractory materials. For castable refractories, the limiting factor in thermal properties is typically the binder phase. Most common binder phase in non-shaped refractory materials are calcium aluminate cements (CAC) [4]. During their hydration, crystalline hydrates are formed, which give mechanical properties sufficient for manipulation of the unfired parts. During the firing process, formed hydrates decompose, which can cause the increase in porosity and in the extreme cases even cracking [5]. The process of dehydration and the loss of hydraulic bond strength causes a decrease in mechanical strength at temperatures lower than 1000 °C. Non-shaped refractory materials with CAC binders therefore require high firing temperatures transition to a ceramic type of bond to achieve desired properties [6]. Another drawback of CAC bonded refractories is linked to the high content of CaO, which can react with other oxides (e.g. MgO, SiO_2), and form low temperature eutectics. These can cause the formation of amorphous phases and decrease of thermal and corrosion resistance of the final material. For these reasons, lowering the CAC content or preparation of CAC free refractory materials, is of interest [4]. Variety of calcium-free binders are used in refractory materials. In general, we can distinguish several binding mechanisms. First one is based on polymerization of –OH groups and formation of CSH gel (geopolymer) or phosphate bonding by the interaction between the binder and the refractory filler [7]. This polymerized bond is transformed into ceramic bond during firing (OH to oxygen bridges). The second one utilizes colloidal particles (e.g. colloidal silica or alumina sols) and the ability to control the process of their coagulation by controlling the temperature/pH or via the addition of coagulation agents. Main advantage of

---

[*] Corresponding author.
E-mail address: bartonickova@fch.vutbr.cz (E. Bartonickova).

https://doi.org/10.1016/j.ceramint.2024.06.019
Received 29 February 2024; Received in revised form 28 April 2024; Accepted 2 June 2024

coagulation binders is easier drying process and lower firing temperature related to the increased sintering ability of nano-sized particles [8].

Colloidal silica is a stable water dispersion of nano-sized amorphous SiO_2 particles with particle sizes generally not exceeding 100 nm. Typical content of SiO_2 in the dispersion varies between 10 and 50 wt %. The stability of the colloidal sol is generally achieved by the addition of stabilizing ions, typically Na^+, K^+ or NH_4^+. The gelation process and therefore the binding properties of colloidal silica are directly linked to the particle size of dispersed species, their content and the pH of the solution, which typically lies between 9 and 11. These types of binders offer great degree of control in terms of behavior in the binder-refractory system [9]. Colloidal silica is the most used coagulation binder as it provides higher particle content in the dispersion compared to alumina sols, which lowers the amount of water in the material, which is directly linked to the final porosity of the material. Nano-sized SiO_2 particles are also able to react with Al_2O_3 at temperatures 900–1100 °C and promote mullite formation in the material. Compared to CAC, colloidal silica also provides better workability of the ceramic suspension since no hydration takes place [10]. Strength development is instead linked to the formation of three-dimensional silicate network due to the gelation of the colloidal suspension. This gel network can then provide sufficient mechanical properties to allow for the manipulation before the firing process [11]. Gelation of colloidal silica is most likely controlled by the addition of gelation agents, most often MgO. MgO reacts with H^+ ions to form $Mg(OH)_2$, which in turn promotes the formation of silicate network [12,13]. Similar effect can also be achieved with CaO addition. The effectivity of the gelation agent is controlled by the solubility of the oxide. Lower solubility of MgO compared to CaO causes faster gelation and makes it the more suitable choice [11]. In the case of lightweight/thermal insulation refractory materials, the binder phase plays even more important role in terms of controlling the final properties of the material. Porous mullite ceramics has excellent thermal and mechanical properties and has been intensively studied for its ability to withstand rather harsh conditions [2]. It can be prepared by various shaping techniques, such as freeze-drying, additive manufacturing, replica templating, sacrificial templating, the addition of pore forming agents, gel casting and other methods [2,14]. Direct foaming is an environmentally friendly method, suitable for the preparation of porous materials with porosity between 40 and 90 % and controlled pore shape. Drawback of this method, however, is the inherent instability of the green body foams. Due to the large surface area of the phase interface, ceramic foams are thermodynamically unstable system. Ceramic foams undergo coalescence, drainage, and Ostwald ripening, which have negative effect on the homogeneity and properties of the formed product. In order to mitigate these processes, methods of fast solidification have been developed, including gel casting, direct solidification and sol-gel methods. Especially the method of non-toxic inorganic sol-gel using silica sol is a typical preparation method at industrial scale [15–18]. **Combination of gel casting with direct foaming has been used in this study**.

Another problem during the direct foaming of ceramic slurries is the formation of very thin walls and open porosity. Both of those can cause deterioration in insulation properties and mechanical and thermal stability of ceramic foams. Strengthening of the material is possible by the impregnation of mullite foam by colloidal suspension of either SiO_2 or Al_2O_3 particles. In addition to physically filling the pore openings and thickening the pore walls, they also allow for the secondary mullite formation which further increases the durability of the refractory foams. Many ways of the impregnation of ceramic foams have been developed, all of which are mostly limited by the degree of open porosity and the pore opening size. Impregnation of ceramic foam is often used in the case of fibrous or whisker-based structures, where the aerogel or xerogel formed after impregnation acts as a coating or support between the fibers [19] or strengthens the pore/bubble walls in the porous structure [20]. Another option is in-situ formation of mullite whiskers which can act as a reinforcement to the primary ceramic structure [21]. This can lead to the formation of a complex bird-nest like structure, where the main fibers of primary mullite can serve as a substrate for the in-situ formation of secondary mullite whiskers [22], which then further reinforces the ceramics structure. Another example of the complex structures of impregnated ceramic foams is the cactus-like structure formed from the combination of the plate-like alumina structure and mullite whiskers [23]. Impregnation of ceramic foams by colloidal suspensions can also be used to apply functionalized coating for e.g. catalytical applications [24].

Generally, in situ foamed refractories exhibit poor mechanical properties. It can be improved by reinforcement of foam wall microstructure by additional mullite layers without significant bulk density and thermal conductivity increase. Here we report the possibility of **vacuum impregnation by colloidal silica or silica-boehmite suspension in order to reinforce the mechanical properties of nanobonded refractory castable**.

2. Experimental

2.1. Foam preparation and thermal treatment

Various commercial silica sols were tested in regard to their possible application in castable refractories. After preliminary gelation experiments using different gelation conditions and agents, commercial silica sol and commercial soft-burned technical grade MgO were selected as a binder and a gelation agent, respectively. Foaming process was carried out by direct foaming using intensive mixing combined with the commercial surfactant. For the laboratory preparation of mullite foams, industry-scale mixture composition was modified. Sol and gelation agent dosage was optimized to achieve sufficient workability. The particle size composition of the final powder mixture, and therefore the dosage of each component, was based on calculations using the modified Andreasen method for optimal densification. Final mixture composition is listed in Table 1.

Mixture components in the dry state were pre-homogenized in a planetary mixer and then mixed for 24 h using an overhead mixer. Zirconia balls were added into the PP mixing vessels to intensify the mixing process. Liquid components were mixed directly in the planetary mixer at low speed to prevent premature foaming. Homogenized mixture of solids was then added. Mixing was first carried out at low speed of 60 rpm for 1 min and for the foaming, mixing speed for increased to 200 rpm for 2 min. Foamed ceramic slurry was poured into small (40 × 40 × 160) mm, larger (200 × 200 × 40) mm and up-scaled (500 × 700 × 250) mm sized molds. Molds were covered to prevent drying of the ceramic slurry. Samples were demolded after 24 h of aging and dried in laboratory conditions for 24 h and then for 24 h at 105 °C. Dried foams were fired in electrical furnace at 1500 °C for 300 min with a heating rate 5 °C/min. Firing regime was designed to simulate firing in an industrial tunnel furnace. Prepared foams were then cut and brushed for further impregnation experiments.

Table 1
Mixture composition for the mullite foam preparation.

Material (D50/μm)	(wt. %)
Mullite cenospheres (200 μm)	29.40
Ground alumina (3 μm)	8.82
Reactive alumina (2 μm)	23.52
Silica fume (4 μm)	29.40
Hydratable alumina (5 μm)	8.82
MgO (5 μm)	0.03
Silica Sol L1530 (15 nm)	60.55
Deionized water	39.18
Surfactant (commercial)	0.27

2.2. Impregnation process

Mixtures used for the impregnation are listed in Table 2. Silica sol (LITHOSOL L 1350) was used as is and SiAl sol (i.e. combined silica boehmite sol (M23 SChem a. s. Czech Republic)) was diluted to one-half of the original concentration and homogenized. In the case of silica fume additive, the suspension was additionally homogenized for 60 min using ultrasonic treatment.

Larger and up-scaled samples were cut to small cubic samples (40 × 40 × 40) mm and were used for the preliminary impregnation experiments. To investigate the penetration depth, an impregnation mixture was colored using Tashiro Blue indicator. Cubic foam samples were placed into a glass vessel and evacuated for 30 min. Impregnation mixture was then added dropwise onto the samples under vacuum until foam samples were fully immersed. Samples fully immersed in the impregnation mixture were then left under vacuum for different durations in order to study the rate and effectivity of the penetration into the foam structure. Optimized procedure was then applied to large samples (200 × 200 × 38) mm.

Impregnated samples were then dried and fired again using the same heating regime of 5 °C/min heating rate up to 1500 °C and holding time 300 min. A s a reference the foam samples without impregnation were also fired for comparison. Samples were then characterized in terms of targeted properties important for unshaped refractories, i.e. porosity, thermal conductivity and mechanical strength. The experimental procedure is shown in Fig.1.

2.3. Sample characterization

The phase composition was determined using X-Ray diffraction analyzer EMPYREAN (PANalytical, Netherlands) in central focusing arrangement using CoKα radiation coupled with high temperature chamber HTK 16 (Anton Paar, Austria). The evaluation of the crystallographic structure was done by Highscore program using the Rietveld method. The foam products were analyzed in terms of microstructure by means of analytical scanning electron microscopy (SEM/EDS) using the device EVO (ZEISS, Germany). The TG-DTA analysis was performed simultaneously using thermal analyzer SDT 650 (TA Instruments, USA.) in dried air atmosphere with heating rate of 5 °C/min. The porosity of prepared foam products was analyzed using mercury intrusion pore analyzer PoreMaster (Quantachrome, USA) and assessed also by image analysis of SEM images performed by Fiji software. Images from impregnation tests were also processed by Fiji image analysis software. The mechanical properties were determined in terms of compressive strength. The compressive strength was determined from the maximal force performed on Instron instruments 5985c (Instron, USA) on samples (40 × 40 × 40) mm. For determination of thermal conductivity, test samples with (200 × 200 × 38) mm were used. Thermal conductivity was determined by FOX 200 Vacuum equipment (TA Instruments USA) according to EN 12667 and ISO 8301. Standard conditions for measurements were 10 °C for mean temperature and 10 °C for temperature difference.

Table 2
Composition of the tested impregnation mixtures.

Impregnation bath	Sol type	Brand	Solids (wt. %)	Additive	Additive dosage (wt. %)
Si IMP	SiO_2	L1530	30	–	–
SiAl IMP	SiO_2–Al_2O_3	SiAl M23	25	H_2O	50
Si IMP	SiO_2	L1530	30	–	–

3. Results

3.1. Foaming and foam characteristics

The direct foaming process was used to produce ceramic foams, controlled by targeted gelation of the colloidal sol with a gelation agent (MgO). The aim was to obtain a stable foam structure without the use of calcium compounds and with the advantage of higher handling strength without the need for drying [25]. The stability of the foam was tested on a pure system without fillers. Fig. 2 shows the effect of sol presence on foam stability and xerogel formation during ageing and free drying. In the foam without sol (surfactant stabilized foam) the bubbles collapse over time, whereas the foam with silica sol (particle stabilized foam) does not collapse. The stability of particle stabilized foams was published by several works [26–28]. The subsequent gel formation has stabilized the foam structure and it remained stable for 24 h. However, some shrinkage and coalescence of pores were observed, most likely due to drying induced gelation in the foam.

For the preparation of the primary mullite foam, it was essential to determine the amount of surfactant to control the quality of the resulting foam and the final bulk density. The tests on the formulation used showed that the dependence of the cold compressive strength and bulk density on the surfactant dose was relatively well correlated, as shown in Fig. 3. Too low a bulk density resulted in open porosity and low strength [13,29]. From an application point of view, mullite foam with this composition and production process (i.e. up-scaled dimensions connected with higher amount of mixed mixture, crack-free monoliths and manipulation strength for automatic processing), required a minimum cold compressive strength of more than 10 MPa. Therefore, based on these findings, the optimal choice was to add 0.27 wt % of surfactant into the liquid part of the foam formulation mixture.

3.2. Primary foam firing and primary mullitization

The solid part of the used mixture allows the formation of mullite and the final foam hardening during thermal treatment only at high temperatures and long dwell times because of the reaction of micron-sized particles with each other [30]. When colloidal SiO_2 is used as a binder phase to fix the foam structure, a xerogel network is formed and serves to cross-link the particles, and also reduces the activation energy required for sintering initiation [31,32]. At elevated temperature, formed Si–OH bond in xerogel network polycondensated to oxygen bridges (Si–O–Si) [33], then gradually crystallized to quartz and later reacted with the reactive Al_2O_3 particles present in the mixture to form mullite. Fig. 4a shows the TG-DTA analysis of the dried sol. The curve can be divided into several phases (1–4). Phase 1 is the drying of the physically bonded water, followed by phases 2 and 3, where dehydroxylation and polycondensation of the Si–OH bonds occurs [15]. In the temperature range 870–940 °C, the transition of quartz to tridymite occurs and in the last high temperature phase (4) the transition to cristobalite occurs [34]. Fig. 4b shows the analysis of the raw foam mixture bonded by the sol-gel process. As in Fig. 4a, one can see first a mass loss up to about 200 °C associated with water loss and drying of the xerogel (1), followed by polycondensation reactions (2) [33]. In phase 4, multiple phenomena occur - around 850 °C, the transformation of quartz to tridymite (from sol, silica fumes and cenospheres) takes place [34], which then starts to react with Al_2O_3 and the mullitization [35]. At a temperature of about 1400 C the crystallization of cristobalite (5) is added to the ongoing mullitization. The resulting phase composition of the ceramic foam according to Rietveld analysis corresponds to 71 wt% of mullite, 10.2 wt% of corundum and 18.8 wt% of cristobalite. The data in Table 3 summarizes the phase composition according to the used firing temperature. As confirmed by XRD analysis (see Table 3), the mullite phase was already present in the sample at 1100 °C. This initial low temperature mullite formation is a result of the rearrangement of SiO_2 and Al_2O_3 particles which causes the initial slow formation of

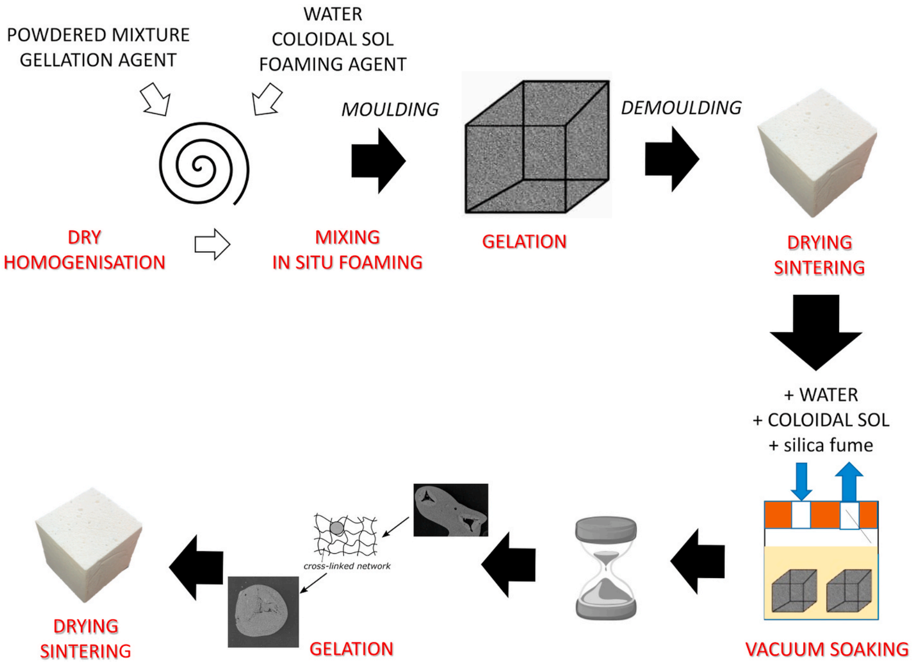

Fig. 1. Illustration of sol-gel foaming procedure and vacuum impregnation process.

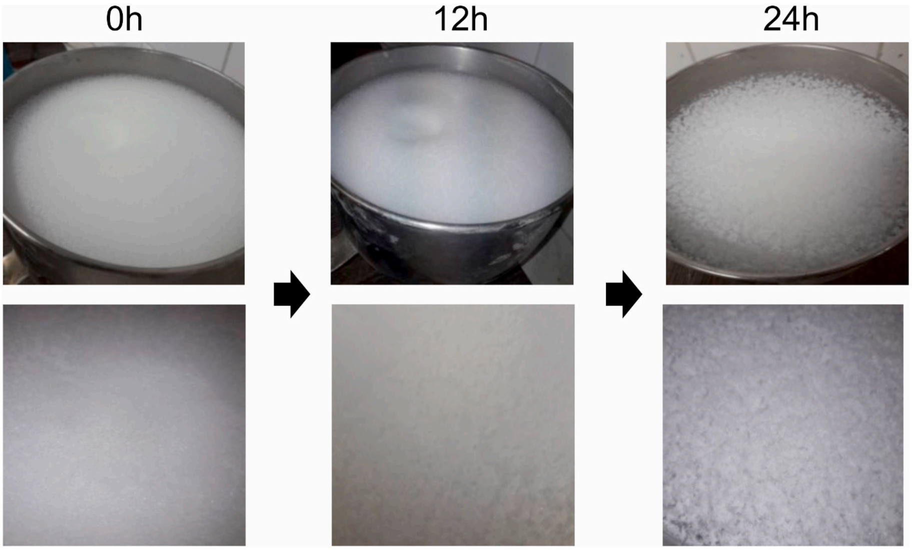

Fig. 2. System stability– water vs. surfactant vs. silica sol.

mullite phase. This process is started around 700 °C and results in the apparent reaction plateau on the TG-DTA curve (during phase 3). The majority of mullite is however formed after this initial reaction plateau in the temperature range 1200–1500 °C, where rapid mullite formation takes place. These data are further confirmed in Fig. 10, where an in situ HT-XRD analysis of the secondary mullitization of the impregnated foam is presented.

After drying and firing, the ceramic foam is formed, which reaches a strength around 2–10 MPa at a bulk density of 520–950 kg/m^3. The microstructure of the pores can be seen in Fig. 5 on the fracture surface of the material. Most of the smaller pores are closed, however, defects can be observed in the walls of the larger pores, and which results in a certain degree of open porosity. A typical whisker-needle-like mullite structure [2] inside the pore can be seen in the detail of Fig. 5c. Fig. 5 a) with overall porosity up to 83 % contain cracks and the preparation of up-scaled samples was impossible. It was not able to withstand the use of standard automatic machine manipulation with monolith samples, resulting in its destruction after the machine grab. Fig. 5 b) shows the microstructure of the samples with a bulk density of around 900 kg/m^3 (i.e. overall porosity up to 70 %), which could be successfully produced in an automated manner.

3.3. Sol-gel impregnation process

The primary foam is already satisfactory for application purposes (operational temperature 1500 °C and cold compressive strength 10 MPa given by industrial demand) in the form of molded parts. For the successful preparation of large volume monoliths, the mechanical strength is no longer sufficient and therefore the vacuum impregnation method was chosen to enhance the monoliths' stability.

The effectiveness of impregnation and the depth of vacuum penetration of the sol into the prepared test bodies was tested by means of a

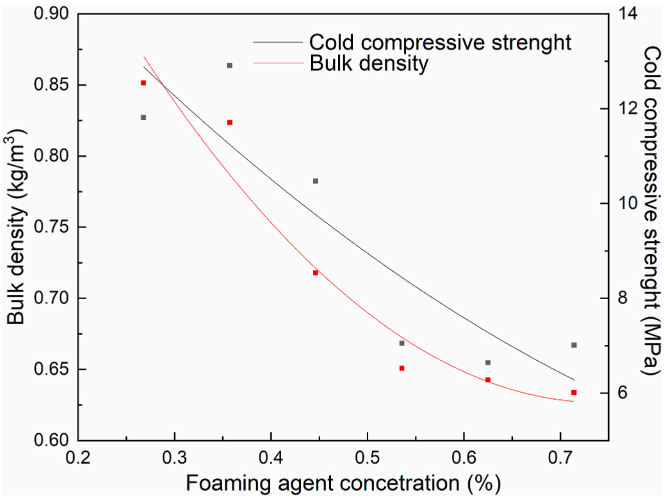

Fig. 3. Foam agent dosage vs. cold compressive strength dependence.

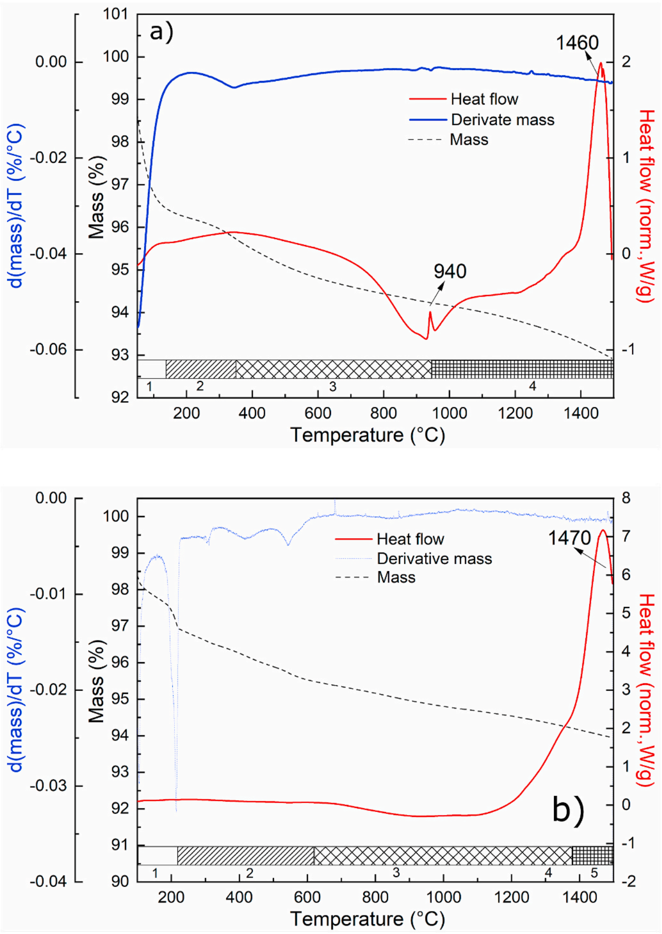

Fig. 4. TG-DTA analysis of sol (a) and „green“ foam mixture (b). (For interpretation of the references to color in this figure legend, the reader is referred to the Web version of this article.)

Table 3
Phase composition of ceramic foam after thermal treatment at different temperatures.

Phase	200 °C	800 °C	1100 °C	1500 °C
Amorphous SiO_2	++++	++++	–	–
Corundum	++++	++++	+++	++
Quartz	–	–	+	–
Cristobalite	–	–	++	++
Mullite	–	–	+	+++

Note: ++++ = 80–100 %, +++ =30–80 %, ++= 30-10 %, += 0–10 %, - = 0 %

coloring experiment. The sol was mixed with dye (Tashiro blue) to reach blue color. Thus, the permeation of the sol through the test body was accurately detected in the mullite foam (see Fig. 6). It was found that for the size of the bodies (40 × 40 × 40) mm an impregnation time of 30 min was sufficient. The dwell time was simultaneously verified by reaching of the constant sample mass. In the case of the combined Si-sol-silica fume bath, there was no need to add dye, the sol replaced the dye function as the grey color of the silica fume allowed for the estimation of the penetration depth.

Impregnation time of 30 min was found to be sufficient for this the (40 × 40 × 40) mm samples. For larger (200 × 200 × 40) mm samples, impregnation dwell time was increased to 60 min to obtain complete penetration.

3.4. Foam impregnation evaluation

Foam wall porosity measurements were performed on (40 × 40 × 40) mm samples of both the fired mullite foam and the secondary fired foam with impregnation (see Fig. 7).

Based on the compressive strength results, it is evident that the impregnation mechanism has an effect on the resulting mechanical properties. In the case of impregnation with Si sol and Si/silica fume, up to 60 % increase in compressive strength values was achieved. The Si sol impregnation was chosen for further testing on large (200 × 200 × 40) mm samples and to evaluate the influence on the thermal conductivity.

Understandably, with increasing strength and decreasing porosity, it was necessary to verify the change in thermal conductivity, and therefore the primary technological parameter of lightweight refractory insulation materials. Table 4 shows that the simple secondary firing of mullite foam without impregnation resulted in densification and a slight increase in thermal conductivity. When the samples were impregnated with Si Sol, a significant increase in bulk density of about 240 kg/m^3 was observed, but the thermal conductivity did not increase dramatically, and this change was compensated for by an increase in strength of about 60 %. Liu et al. and Guo et al. published data with similar λ values of 0.329 W/m·K and needle-like mullite microstructure [3,36].

In addition to macroscopic changes and modifications in physical properties, an assessment of the chemical composition, phase transitions and microstructural transformations that occurred in the silica sol impregnated material was carried out.

Nearly the same behavior [33–35] as is given in Fig. 4 was found by thermal analysis of impregnated samples (Fig. 9): xerogel desiccation up to 200 °C (1), dehydroxylation and polycondensation of Si–OH bonds (2), the gradual reaction plateau of the reactions of the secondary mullitization process where residual unreacted alumina/silica and newly introduced Si–O phases from the xerogel underwent further transformation (3), and final transformation of quartz into cristobalite (4) (see Table 5).

In situ HT-XRD analysis confirmed the processes already analyzed during TG-DTA analysis. Without impregnation (Fig. 10a), there was a gradual increase in mullite and decrease in cristobalite, with corundum and quartz disappearing. In the case of impregnated foam, a significant increase in cristobalite crystallizing from the amorphous xerogel is initially observed. Formed cristobalite phase then reacted with the corundum to form mullite (see Table 5).

Figs. 11–13 show the microstructure of the ceramic foams after the impregnation process. As can be seen in these figures the amount and mullite crystals increased already during the secondary, i.e. repeated firing of the un-impregnated foam itself. This would correspond to both an increase in mechanical strength and would be related to a change in porosity and bulk density.

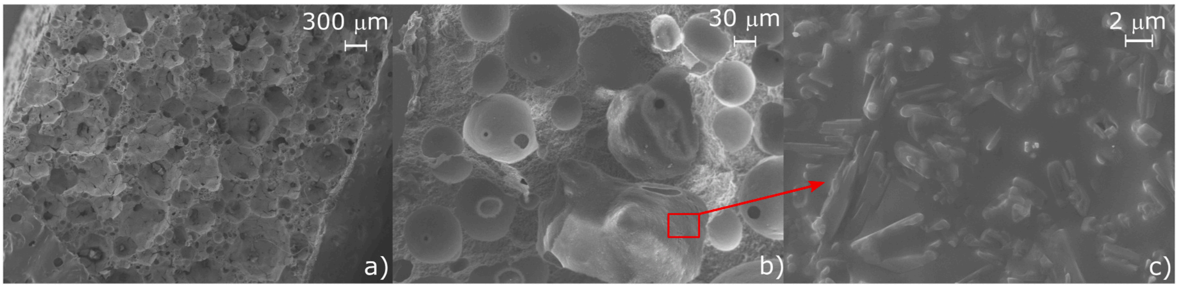

Fig. 5. SEM analysis of ceramic foam after thermal treatment: a, b) overall foam images, c) foam wall in detail.

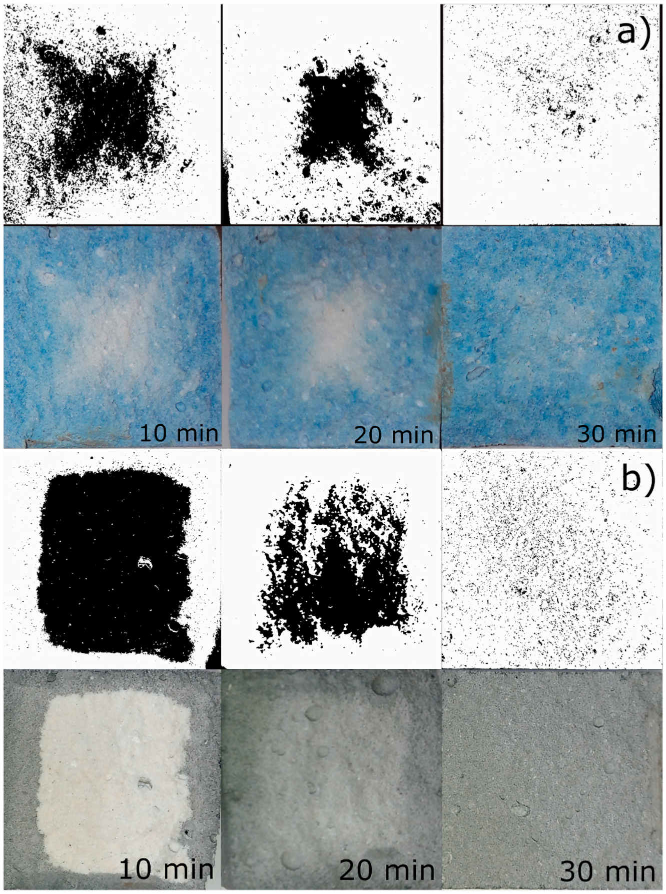

Fig. 6. Coloring experiment data: a) Si Sol without silica fume with Tashiro Blue, b) SiAl sol with silica fume without Tashiro Blue. (For interpretation of the references to color in this figure legend, the reader is referred to the Web version of this article.)

In the sample fired after impregnation with Si Sol, a larger number of slightly larger whisker/needle-like mullite crystals is visible. However, it is evident that secondary mullitization by this route does not produce a large enough number of newly formed crystals to affect the pore wall defects to a greater extent and thus help to close the pores and improve the utility properties.

In the case of Si sol impregnation, newly formed whisker/needle-like mullite crystals are visible inside the bubble walls. Overall, the bubble walls are free of significant defects, as was visible on the original foam. It can be assumed that this newly grown fine mullite, which is formed during secondary mullitization (see Fig. 10 and Table 4), strengthens the internal structure of the foam, and thus increases its mechanical properties [19,22,24], as can be seen in Fig. 8.

Fig. 13 shows the microstructure of the ceramic foam impregnated

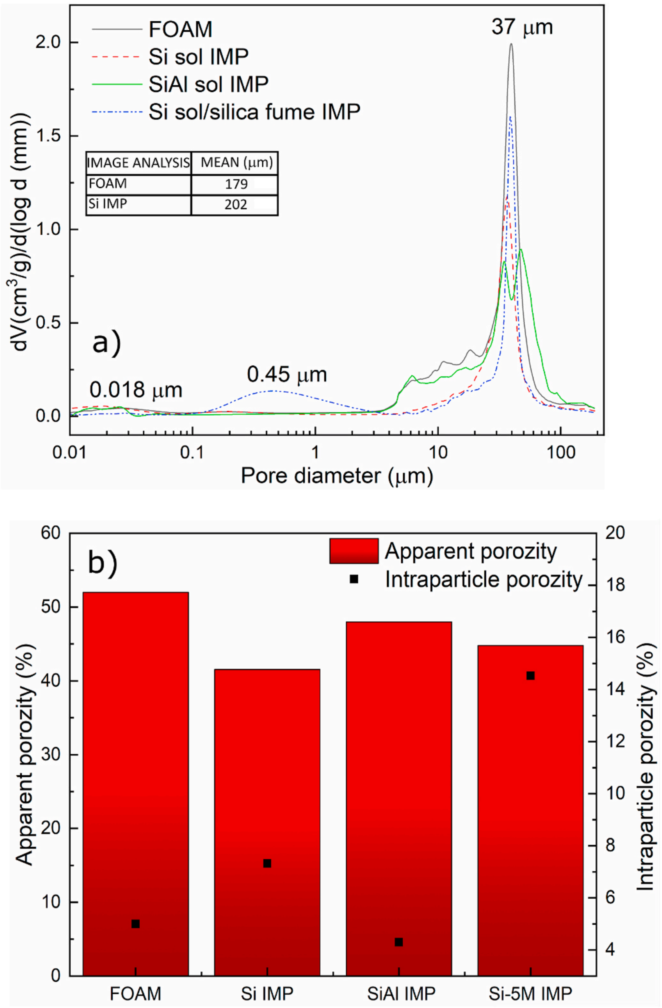

Fig. 7. Porosity evaluation – with and without impregnation (MIP and image analysis).

Table 4
Thermal conductivity data.

	Bulk Density (kg/m^3)	Porozity (%)** %)	λ (W/m·K)
Foam*	**520**	**82.7**	**-**
Foam	940	**68.7**	0.333
2nd SINT	975	**67.5**	0.339
Si IMP	1175	**62.3**	0.411

Note: * laboratory small sample, not validated for up-scaled monoliths.

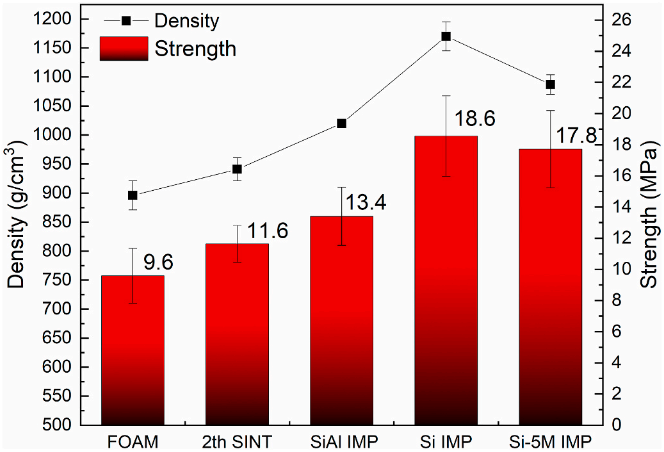

Fig. 8. Strength evolution with impregnation process.

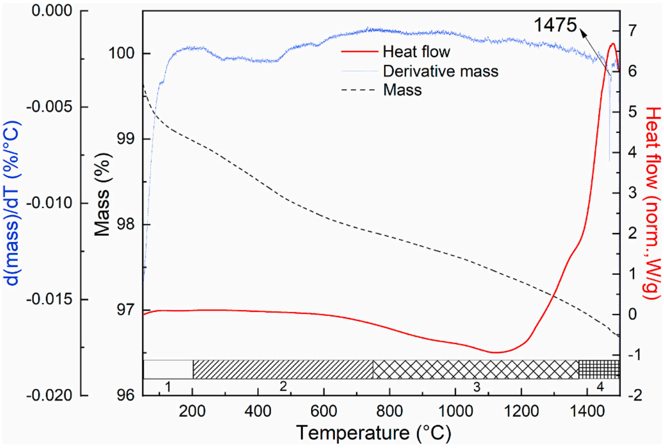

Fig. 9. TG-DTA analysis of Si sol-impregnated ceramic foam.

with SiAl sol, where higher mullitization [18] was expected due to the combined nature of the sols. Both the strength characteristics and the microstructure show that the combination did not produce the expected reinforcement of the foam structure. In Fig. 13 cracks were clearly visible in the coated layer, probably caused by higher shrinkage of the combined xerogel. In the foam wall detail, there was a combination of whisker/needle mullite and spherical particles belonging to unreacted corundum which may have contributed to the increased shrinkage rate.

4. Conclusion

Cold compressive strength, open porosity, and low thermal conductivity are critical product parameters for successful industrial applications. In this study, we developed a porous mullite ceramic under laboratory and up-scaled conditions, eliminating the use of cementitious binders, yielding an overall apparent porosity up to 80 %~~,~~ a strength of 10 MPa, and a thermal conductivity of 0.3 W/m·K. However, these properties did not meet the upscale conditions, i.e. the minimum requirements for mechanical operations during production. To address this limitation, the prepared foams underwent vacuum impregnated using the sol-gel technique (an economically viable method employing substances commonly used in refractory production). Colloidal solutions based on Si and Al were used as gel precursors. The objective of reinforcing the porous structure of the thin walls was successfully achieved through this process. The foams were reinforced with a newly formed needle-like mullite, resulting in strengths of approximately 19 MPa and thermal conductivities of around 0.4 W/m·K. Importantly, the impregnation process was not only successful on small samples (40 × 40 × 40) mm but also scaled up effectively to produce monoliths of industrial scale dimensions.

CRediT authorship contribution statement

E. Bartonickova: Conceptualization, Formal analysis, Investigation, Methodology, Writing – original draft, Writing – review & editing, Data curation. **J. Svec:** Data curation, Formal analysis, Investigation, Methodology. **L. Dlabajova:** Data curation, Investigation, Methodology. **P. Hruby:** Data curation. **V. Caba:** Data curation, Formal analysis, Methodology. **M. Sedlacik:** Data curation, Formal analysis, Methodology. **L. Kalina:** Data curation, Investigation, Methodology. **J. Koplik:** Data curation, Formal analysis, Methodology. **F. Soukal:** Supervision. **L. Kersnerova:** Conceptualization, Supervision. **J. Zach:** Data curation, Formal analysis. **V. Novak:** Data curation, Formal analysis. **K. Dvorak:** Data curation, Formal analysis.

Table 5
Phase composition of ceramic foam after thermal treatment.

Phase	Without Si sol IMP (wt. %)	With Si IMP (wt. %)
Mullite	77.2	88.7
Corundum	11.3	6.5
Quartz	0.2	–
Cristobalite	11.3	4.8

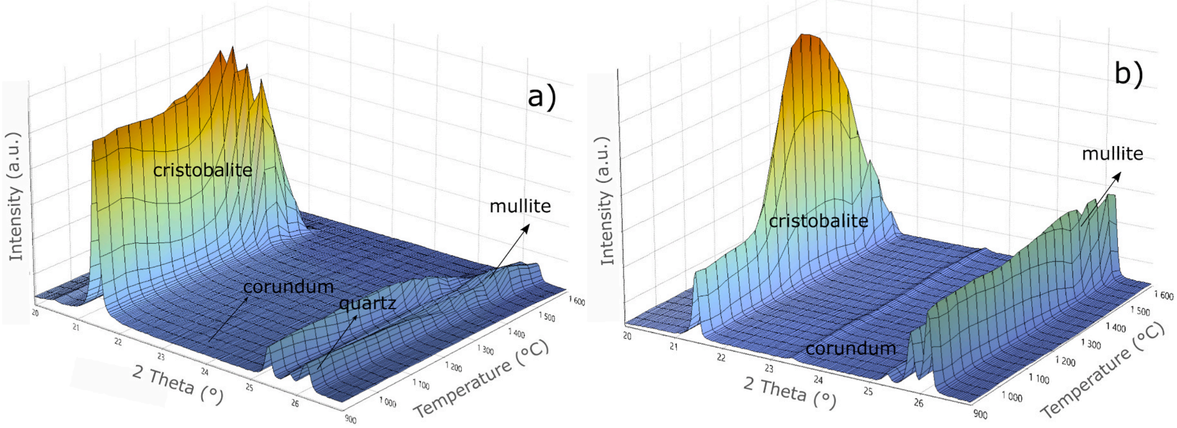

Fig. 10. HT-XRD analyses of ceramic foam without (a) and with Si sol impregnation (b).

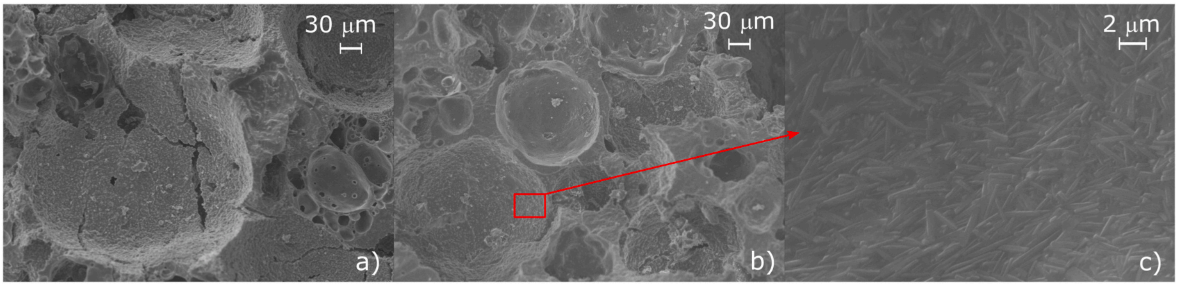

Fig. 11. Microstructure of ceramic foam after 2nd sintering: a) reference sample, b) 2nd sintering, c) foam wall in detail.

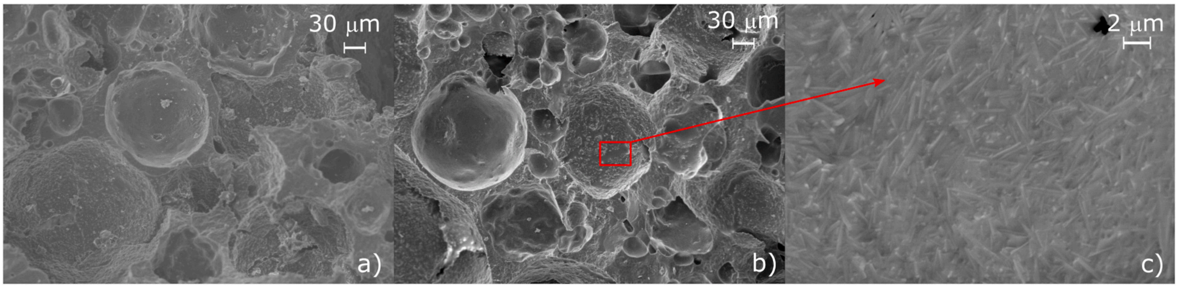

Fig. 12. Microstructure of ceramic foam after Si sol impregnation process: a) reference sample, b) Si so impregnation, c) foam wall in detail.

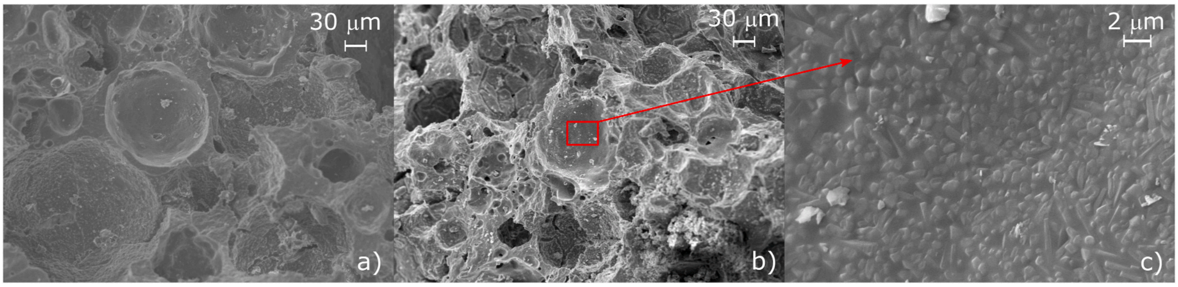

Fig. 13. Microstructure of ceramic foam after SiAl sol impregnation process: a) reference sample, b) SiAl so impregnation, c) foam wall in detail.

Declaration of competing interest

The authors declare that they have no known competing financial interests or personal relationships that could have appeared to influence the work reported in this paper.

Acknowledgements

This research was funded by the Czech Science Foundation (Czechia) under the project number GA22-04828S: Advanced lithium silicate sealers: on the way to sustainable building materials.

References

[1] J.A. Pask, H. Schneider, Phase equilibria and stability of mullite, Mullite (2005) 227–249.
[2] Z. Yang, F. Yang, S. Zhao, K. Li, J. Chen, Z. Fei, G. Chen, In-situ growth of mullite whiskers and their effect on the microstructure and properties of porous mullite ceramics with an open/closed pore structure, J. Eur. Ceram. Soc. 41 (2021) 299–308.
[3] H. Guo, W. Li, F. Ye, Preparation of microporous mullite ceramics by foaming for high temperature thermal isolation, Ceram. Int. 42 (2016) 17332–17338.
[4] W.E. Lee, W. Vieira, S. Zhang, K.G. Ahari, H. Sarpoolaky, C. Parr, Castable refractory concretes, Int. Mater. Rev. 46 (2001) 145–167.
[5] F. Guirado, S. Galí, J.S. Chinchón, Thermal decomposition of hydrated alumina cement (CAH10), Cement Concr. Res. 28 (1998) 381–390.
[6] I.M.I. Bayoumi, E.M.M. Ewais, A.A.M. El-Amir, Rheology of refractory concrete: an article review, Bol. Soc. Esp. Ceram. V 61 (2022) 453–469.
[7] B.P. Bezerra, M.R. Morelli, A.P. Luz, Design, characterization, and incorporation of geopolymer binders in refractory ceramic compositions, Int. J. Appl. Ceram. Technol. 21 (2024) 565–580.
[8] M. Nouri-Khezrabad, M.A.L. Braulio, V.C. Pandolfelli, F. Golestani-Fard, H. R. Rezaie, Nano-bonded refractory castables, Ceram. Int. 39 (2013) 3479–3497.
[9] E. Katoueizadeh, M. Rasouli, S.M. Zebarjad, A comprehensive study on the gelation process of silica gels from sodium silicate, J. Mater. Res. Technol. 9 (2020) 10157–10165.
[10] M. Ismael, R.D. Anjos, R. Salomão, V. Pandolfelli, Colloidal silica as a nanostructured binder for refractory castables, Refract. Appl. News 11 (2015) 16–20.
[11] R.D. dos Anjos, M.R. Ismael, I.R. de Oliveira, V.C. Pandolfelli, Workability and setting parameters evaluation of colloidal silica bonded refractory suspensions, Ceram. Int. 34 (2008) 165–171.
[12] N. Hamedani Golshan, H. Sarpoolaky, A.R. Souri, Microstructure and properties of colloidal silica bonded magnesite castable refractories, Iran, J. Mater. Sci. Eng. 8 (2011) 25–31.
[13] Y. Zhang, L. Zhu, L. Chen, L. Liu, G. Ye, Influence of magnesia on demoulding strength of colloidal silica-bonded castables, Rev. Adv. Mater. Sci. 58 (2019) 32–37.
[14] E. Bartonickova, P. Ptacek, T. Opravil, F. Soukal, J. Masilko, R. Novotny, J. Svec, J. Havlica, Mullite-based refractories fabricated by foam casting, Ceram. Int. 41 (2015) 14116–14123.
[15] B. Dong, Z. Min, L. Guan, X. Zheng, L. Wang, Q. Wang, C. Yin, Y. Wang, R. Zhang, F. Wang, H. Abadikhah, X. Xu, Y. Zhang, G. Wang, Porous mullite-bonded SiC filters prepared by foaming-sol-gel-tape casting for high-efficiency hot flue gas filtration, Sep. Purif. Technol. 295 (2022) 121338.
[16] B. Dong, M. Yang, F. Wang, L. Hao, X. Xu, G. Wang, S. Agathopoulos, Novel fabrication processing of porous alumina/mullite membrane supports by combining direct foaming, sol-gel, and tape-casting methods, Mater. Lett. 240 (2019) 140–143.
[17] F.-Q. Tang, Z. Xiao, J.-A. Tang, L. Jiang, The effect of SiO_2 particles upon stabilization of foam, J. Colloid Interface Sci. 131 (1989) 498–502.

[18] J. Yang, X. Zhang, B. Zhang, F. Liu, W. Li, J. Jian, S. Zhang, J. Yang, Mullite ceramic foams with tunable pores from dual-phase sol nanoparticle-stabilized foams, J. Eur. Ceram. Soc. 42 (2022) 1703–1711.

[19] R. Zhang, X. Hou, C. Ye, B. Wang, Enhanced mechanical and thermal properties of anisotropic fibrous porous mullite–zirconia composites produced using sol-gel impregnation, J. Alloys Compd. 699 (2017) 511–516.

[20] C. Agrafiotis, A. Tsetsekou, Deposition of meso-porous γ-alumina coatings on ceramic honeycombs by sol-gel methods, J. Eur. Ceram. Soc. 22 (2002) 423–434.

[21] F. Yang, S. Zhao, W. Sun, K. Li, J. Chen, Z. Fei, Z. Yang, Fibrous porous mullite ceramics modified by mullite whiskers for thermal insulation and sound absorption, J. Eur. Ceram. Soc. 43 (2023) 521–529.

[22] M. Yang, X. Luo, J. Yi, M. Yu, X. Zhang, A novel way to fabricate fibrous mullite ceramic using sol-gel vacuum impregnation, Ceram. Int. 44 (2018) 12664–12669.

[23] P. Yang, S. Liu, Z. Mao, D. Wang, Preparation and properties of hierarchical structural alumina/mullite composites, J. Eur. Ceram. Soc. 43 (2023) 468–477.

[24] C. Alié, F. Ferauche, A. Léonard, S. Lambert, N. Tcherkassova, B. Heinrichs, M. Crine, P. Marchot, E. Loukine, J.P. Pirard, Pd–Ag/SiO_2 xerogel catalyst forming by impregnation on alumina foams, Chem. Eng. J. 117 (2006) 13–22.

[25] J. Roy, S. Chandra, S. Maitra, Nanotechnology in castable refractory, Ceram. Int. 45 (2019) 19–29.

[26] A.R. Studart, U.T. Gonzenbach, E. Tervoort, L.J. Gauckler, Processing routes to macroporous ceramics: a review, J. Am. Ceram. Soc. 89 (2006) 1771–1789.

[27] C. Chuanuwatanakul, C. Tallon, D.E. Dunstan, G.V. Franks, Controlling the microstructure of ceramic particle stabilized foams: influence of contact angle and particle aggregation, Soft Matter 7 (2011) 11464–11474.

[28] C. Chuanuwatanakul, C. Tallon, D.E. Dunstan, G.V. Franks, Producing large complex-shaped ceramic particle stabilized foams, J. Am. Ceram. Soc. 96 (2013) 1407–1413.

[29] L. Wang, Y. Liang, Y. Yin, L. Zhao, M. Cai, J. Nie, Enhancing the green mechanical strength of colloidal silica-bonded alumina castables using a silane coupling agent, Ceram. Int. 42 (2016) 11496–11499.

[30] T. Ring, Fundamentals of Ceramic Powder Processing and Synthesis, Academic Press Inc., London, 1996.

[31] G.W. Scherer, Aging and drying of gels, J. Non-Cryst. Solids 100 (1988) 77–92.

[32] L.L. Hench, J.K. West, The sol-gel process, Chem. Rev. 90 (1990) 33–72.

[33] M. Nouri-Khezrabad, A.P. Luz, V.R. Salvini, F. Golestani-Fard, H.R. Rezaie, V. C. Pandolfelli, Developing nano-bonded refractory castables with enhanced green mechanical properties, Ceram. Int. 41 (2015) 3051–3057.

[34] S.B. Holmquist, Conversion of quartz to tridymite, J. Am. Ceram. Soc. 44 (1961) 82–86.

[35] K. Okada, Activation energy of mullitization from various starting materials, J. Eur. Ceram. Soc. 28 (2008) 377–382.

[36] H. Liu, X. Xiong, M. Li, Z. Wang, X. Wang, Y. Ma, L. Yuan, Fabrication and properties of mullite thermal insulation materials with in-situ synthesized mullite hollow whiskers, Ceram. Int. 46 (2020) 14474–14480.